Progress in Theoretical Chemistry and Physics B 27
Series Editors: J. Maruani · S. Wilson

Matti Hotokka
Erkki J. Brändas
Jean Maruani
Gerardo Delgado-Barrio *Editors*

Advances in Quantum Methods and Applications in Chemistry, Physics, and Biology

Springer

Advances in Quantum Methods and Applications in Chemistry, Physics, and Biology

Progress in Theoretical Chemistry and Physics

VOLUME 27

The titles published in this series can be found on the web site:
http://www.springer.com/series/6464?detailsPage=titles

Matti Hotokka • Erkki J. Brändas • Jean Maruani •
Gerardo Delgado-Barrio
Editors

Advances in Quantum Methods and Applications in Chemistry, Physics, and Biology

Springer

Editors
Matti Hotokka
Department of Physical Chemistry
Åbo Akademi University
Turku, Finland

Erkki J. Brändas
Department of Chemistry, Ångström Laboratory, Theoretical Chemistry
Uppsala University
Uppsala, Sweden

Jean Maruani
Laboratoire de Chimie Physique
UPMC & CNRS
Paris, France

Gerardo Delgado-Barrio
Instituto de Física Fundamental
CSIC
Madrid, Spain

ISSN 1567-7354 Progress in Theoretical Chemistry and Physics
ISBN 978-3-319-01528-6 ISBN 978-3-319-01529-3 (eBook)
DOI 10.1007/978-3-319-01529-3
Springer Cham Heidelberg New York Dordrecht London

Library of Congress Control Number: 2013950105

Printed on acid-free paper

Springer is part of Springer Science+Business Media (www.springer.com)

PTCP Aim and Scope

Progress in Theoretical Chemistry and Physics

A series reporting advances in theoretical molecular and material sciences, including theoretical, mathematical and computational chemistry, physical chemistry and chemical physics and biophysics.

Aim and Scope

Science progresses by a symbiotic interaction between theory and experiment: theory is used to interpret experimental results and may suggest new experiments; experiment helps to test theoretical predictions and may lead to improved theories. Theoretical Chemistry (including Physical Chemistry and Chemical Physics) provides the conceptual and technical background and apparatus for the rationalisation of phenomena in the chemical sciences. It is, therefore, a wide ranging subject, reflecting the diversity of molecular and related species and processes arising in chemical systems. The book series *Progress in Theoretical Chemistry and Physics* aims to report advances in methods and applications in this extended domain. It will comprise monographs as well as collections of papers on particular themes, which may arise from proceedings of symposia or invited papers on specific topics as well as from initiatives from authors or translations.

The basic theories of physics—classical mechanics and electromagnetism, relativity theory, quantum mechanics, statistical mechanics, quantum electrodynamics—support the theoretical apparatus which is used in molecular sciences. Quantum mechanics plays a particular role in theoretical chemistry, providing the basis for the valence theories, which allow to interpret the structure of molecules, and for the spectroscopic models, employed in the determination of structural information from spectral patterns. Indeed, Quantum Chemistry often appears synonymous with Theoretical Chemistry; it will, therefore, constitute a major part of this book series. However, the scope of the series will also include other areas of theoretical chemistry, such as mathematical chemistry (which involves the use of algebra and topology in the analysis of molecular structures and reactions); molecular mechanics, molecular dynamics and chemical thermodynamics, which play an important

role in rationalizing the geometric and electronic structures of molecular assemblies and polymers, clusters and crystals; surface, interface, solvent and solid state effects; excited-state dynamics, reactive collisions, and chemical reactions.

Recent decades have seen the emergence of a novel approach to scientific research, based on the exploitation of fast electronic digital computers. Computation provides a method of investigation which transcends the traditional division between theory and experiment. Computer-assisted simulation and design may afford a solution to complex problems which would otherwise be intractable to theoretical analysis, and may also provide a viable alternative to difficult or costly laboratory experiments. Though stemming from Theoretical Chemistry, Computational Chemistry is a field of research in its own right, which can help to test theoretical predictions and may also suggest improved theories.

The field of theoretical molecular sciences ranges from fundamental physical questions relevant to the molecular concept, through the statics and dynamics of isolated molecules, aggregates and materials, molecular properties and interactions, to the role of molecules in the biological sciences. Therefore, it involves the physical basis for geometric and electronic structure, states of aggregation, physical and chemical transformations, thermodynamic and kinetic properties, as well as unusual properties such as extreme flexibility or strong relativistic or quantum-field effects, extreme conditions such as intense radiation fields or interaction with the continuum, and the specificity of biochemical reactions.

Theoretical Chemistry has an applied branch (a part of molecular engineering), which involves the investigation of structure-property relationships aiming at the design, synthesis and application of molecules and materials endowed with specific functions, now in demand in such areas as molecular electronics, drug design or genetic engineering. Relevant properties include conductivity (normal, semi- and super-), magnetism (ferro- and ferri-), optoelectronic effects (involving nonlinear response), photochromism and photoreactivity, radiation and thermal resistance, molecular recognition and information processing, biological and pharmaceutical activities, as well as properties favouring self-assembling mechanisms and combination properties needed in multifunctional systems.

Progress in Theoretical Chemistry and Physics is made at different rates in these various research fields. The aim of this book series is to provide timely and in-depth coverage of selected topics and broad-ranging yet detailed analysis of contemporary theories and their applications. The series will be of primary interest to those whose research is directly concerned with the development and application of theoretical approaches in the chemical sciences. It will provide up-to-date reports on theoretical methods for the chemist, thermodynamician or spectroscopist, the atomic, molecular or cluster physicist, and the biochemist or molecular biologist who wish to employ techniques developed in theoretical, mathematical and computational chemistry in their research programs. It is also intended to provide the graduate student with a readily accessible documentation on various branches of theoretical chemistry, physical chemistry and chemical physics.

Preface

This volume collects 20 selected papers from the scientific contributions presented at the Seventeenth International Workshop on Quantum Systems in Chemistry and Physics (and Biology), QSCP-XVII, which was organized by Prof. Matti Hotokka at Åbo Akademi University, Turku, Finland, from August 19 to 25, 2012. Over 120 scientists from 27 countries attended this meeting. Participants of the QSCP-XVII workshop discussed the state of the art, new trends, and future evolution of methods in molecular quantum mechanics, as well as their applications to a wide variety of problems in chemistry, physics, and biology.

The large attendance attained in this conference was particularly gratifying. It is the renowned interdisciplinary character and friendly atmosphere of QSCP meetings that makes them so successful discussion forums.

Turku is located in the southwestern part of Finland. It was the capital city of the country as well as its religious and cultural center throughout the Swedish period. Christina, Queen of Sweden, founded the Åbo Akademi University in Turku in 1630. When Finland became a Grand Duchy under Alexander I, Czar of Russia, in 1809, the former University was transferred to the new capital, Helsinki, and eventually became the University of Helsinki.

The present-day Åbo Akademi University was founded in 1918, shortly after Finland became independent from Russia. Some of the buildings of the old Åbo Akademi University, such as the Ceremonial Hall, are still used by the University. Today, Turku is the seat of the Archbishop of Finland and an active cultural and industrial city endowed with numerous museums, art galleries and historical sites, as well as an important seaport.

Details of the Turku meeting, including the scientific program, can be found on the web site: http://www.qscp17.fi. Altogether, there were 19 morning and afternoon sessions, where 56 plenary talks were given, and one evening poster session, with 21 flash presentations for a total of 55 posters displayed. We are grateful to all participants for making the QSCP-XVII workshop such a stimulating experience and great success.

QSCP-XVII followed the traditions established at previous workshops:
QSCP-I, organized by Roy McWeeny in 1996 at San Miniato (Pisa, Italy);

QSCP-II, by Stephen Wilson in 1997 at Oxford (England);
QSCP-III, by Alfonso Hernandez-Laguna in 1998 at Granada (Spain);
QSCP-IV, by Jean Maruani in 1999 at Marly-le-Roi (Paris, France);
QSCP-V, by Erkki Brändas in 2000 at Uppsala (Sweden);
QSCP-VI, by Alia Tadjer in 2001 at Sofia (Bulgaria);
QSCP-VII, by Ivan Hubac in 2002 near Bratislava (Slovakia);
QSCP-VIII, by Aristides Mavridis in 2003 at Spetses (Athens, Greece);
QSCP-IX, by Jean-Pierre Julien in 2004 at Les Houches (Grenoble, France);
QSCP-X, by Souad Lahmar in 2005 at Carthage (Tunisia);
QSCP-XI, by Oleg Vasyutinskii in 2006 at Pushkin (St Petersburg, Russia);
QSCP-XII, by Stephen Wilson in 2007 near Windsor (London, England);
QSCP-XIII, by Piotr Piecuch in 2008 at East Lansing (Michigan, USA);
QSCP-XIV, by Gerardo Delgado-Barrio in 2009 at El Escorial (Madrid, Spain);
QSCP-XV, by Philip Hoggan in 2010 at Cambridge (England);
QSCP-XVI, by Kiyoshi Nishikawa in 2011 at Kanazawa (Japan).

The lectures presented at QSCP-XVII were grouped into nine areas in the field of *Quantum Systems in Chemistry, Physics, and Biology*, ranging from Concepts and Methods in Quantum Chemistry and Physics through Molecular Structure and Dynamics, Reactive Collisions, and Chemical Reactions, to Computational Chemistry, Physics, and Biology.

The width and depth of the topics discussed at QSCP-XVII are reflected in the contents of this volume of proceedings in the book series *Progress in Theoretical Chemistry and Physics*, which includes four sections:

I. Fundamental Theory (4 papers);
II. Molecular Structure, Properties and Processes (5 papers);
III. Clusters and Condensed Matter (9 papers);
IV. Structure and Processes in Biosystems (2 papers).

In addition to the scientific program, the workshop had its usual share of cultural events. There was an entertaining concert by a tuba orchestra on the premises. The City of Turku hosted a reception on the museum sail ship Suomen Joutsen, and one afternoon was devoted to a visit to the archipelago on board of the old-fashioned steamship Ukkopekka. The award ceremony of the CMOA Prize and Medal took place in the historical Ceremonial Hall of the old Åbo Akademi University.

The CMOA Prize was shared between two selected nominees: Marcus Lundberg (Uppsala, Sweden) and Adam Wasserman (Purdue, USA). The CMOA Medal was awarded to Pr. Martin Quack (ETH, Switzerland). Following an established custom at QSCP meetings, the venue of the next (XVIIIth) workshop was disclosed at the end of the banquet: Paraty (Rio de Janeiro), Brazil, in December 2013.

We are pleased to acknowledge the generous support given to the QSCP-XVII conference by the Federation of Finnish Learned Societies, the Svenska Tekniska Vetenskaps-Akademien i Finland, the City of Turku, the Åbo Akademi University, the Walki company, and Turku Science Park. We are most grateful to the members of the Local Organizing Committee (LOC) for their work and dedication, which made the stay and work of the participants both pleasant and fruitful. Finally, we

would like to thank the members of the International Scientific Committee (ISC) and Honorary Committee (HC) for their invaluable expertise and advice.

We hope the readers will find as much interest in consulting these proceedings as the participants in attending the meeting.

Turku, Finland — Matti Hotokka
Uppsala, Sweden — Erkki J. Brändas
Paris, France — Jean Maruani
Madrid, Spain — Gerardo Delgado-Barrio

Contents

Contributors

S.O. Adamson Department of Chemistry, Lomonosov Moscow State University, Moscow, Russia; MIPT, Moscow, Russia

M.C. Bacchus-Montabonel Institut Lumière Matière, UMR5306, Université Lyon 1-CNRS, Université de Lyon, Villeurbanne Cedex, France

Erkki J. Brändas Ångström Laboratory, Theoretical Chemistry, Department of Chemistry, Uppsala University, Uppsala, Sweden

Daria Brisker-Klaiman Schulich Faculty of Chemistry, Technion—Israel Institute of Technology, Haifa, Israel

A.I. Dementiev Department of Chemistry, Moscow State Pedagogical University, Moscow, Russia

Akira Dobashi School of Pharmacy, Tokyo University of Pharmacy and Life Sciences, Hachioji, Tokyo, Japan

Yi Dong Physical and Theoretical Chemistry, University of Saarland, Saarbrücken, Germany

Masahiro Fukuda Department of Micro Engineering, Kyoto University, Kyoto, Japan

Alexander V. Glushkov Odessa State University—OSENU, Odessa-9, Ukraine

Wei-Chang Hao Department of Chemistry and Biochemistry, National Chung-Cheng University, Chia-Yi, Taiwan

Trygve Helgaker The Centre for Theoretical and Computational Chemistry (CTCC), Department of Chemistry, University of Oslo, Oslo, Norway

Yu-Wei Huang Department of Chemistry and Biochemistry, National Chung-Cheng University, Chia-Yi, Taiwan

Takayoshi Ishimoto Frontier Energy Research Division, INAMORI Frontier Research Center, Kyushu University, Fukuoka, Japan

Kazutomo Kawaguchi Institute of Science and Engineering, Kanazawa University, Kanazawa, Ishikawa, Japan

Ren-Shiou Ke Department of Chemistry and Biochemistry, National Chung-Cheng University, Chia-Yi, Taiwan

D.D. Kharlampidi Department of Chemistry, Moscow State Pedagogical University, Moscow, Russia

Bernard Kirtman Department of Chemistry and Biochemistry, University of California, Santa Barbara, CA, USA

Shyi-Long Lee Department of Chemistry and Biochemistry, National Chung-Cheng University, Chia-Yi, Taiwan

Jean Maruani Laboratoire de Chimie Physique-Matière et Rayonnement, CNRS & UPMC, Paris, France

Takeshi Miyakawa School of Life Sciences, Tokyo University of Pharmacy and Life Sciences, Hachioji, Tokyo, Japan

Ryota Morikawa School of Life Sciences, Tokyo University of Pharmacy and Life Sciences, Hachioji, Tokyo, Japan

David C. Moule Department of Chemistry, Brock University, St. Catharines, ON, Canada

Hidemi Nagao Institute of Science and Engineering, Kanazawa University, Kanazawa, Ishikawa, Japan

Fedor Y. Naumkin Faculty of Science, UOIT, Oshawa, ON, Canada

Taku Onishi Department of Chemistry for Materials, Graduate School of Engineering, Mie University, Mie, Japan; The Center of Ultimate Technology on Nano-Electronics, Mie University (MIE-CUTE), Mie, Japan; The Centre for Theoretical and Computational Chemistry (CTCC), Department of Chemistry, University of Oslo, Oslo, Norway

Uri Peskin Schulich Faculty of Chemistry, Technion—Israel Institute of Technology, Haifa, Israel

N.A. Popova Peoples' Friendship University of Russia, Moscow, Russia

V.A. Popova Peoples' Friendship University of Russia, Moscow, Russia

Svetoslav Rashev Institute of Solid State Physics, Bulgarian Academy of Sciences, Sofia, Bulgaria

Hiroaki Saito Institute of Science and Engineering, Kanazawa University, Kanazawa, Ishikawa, Japan

Masato Senami Department of Micro Engineering, Kyoto University, Kyoto, Japan

E.F. Sheka Peoples' Friendship University of Russia, Moscow, Russia

Tal Simon Schulich Faculty of Chemistry, Technion—Israel Institute of Technology, Haifa, Israel

Michael Springborg Physical and Theoretical Chemistry, University of Saarland, Saarbrücken, Germany

Kimikazu Sugimori Research Center for Higher Education, Kanazawa University, Kanazawa, Ishikawa, Japan

Brian Sutcliffe Service de Chimie Quantique et Photophysique, Université Libre de Bruxelles, Bruxelles, Belgium

Michal Svrček Centre de Mécanique Ondulatoire Appliquée, CMOA Czech Branch, Carlsbad, Czech Republic

Akitomo Tachibana Department of Micro-Engineering, Kyoto University, Kyoto, Japan

Masanori Tachikawa Quantum Chemistry Division, Graduate School of Science, Yokohama-City University, Yokohama, Japan

Masako Takasu School of Life Sciences, Tokyo University of Pharmacy and Life Sciences, Hachioji, Tokyo, Japan

Jorge Vargas Physical and Theoretical Chemistry, University of Saarland, Saarbrücken, Germany

David J. Wales Department of Chemistry, University of Cambridge, Cambridge, UK

Ingolf Warnke Department of Chemistry, Yale University, New Haven, CT, USA

R. Guy Woolley School of Science and Technology, Nottingham Trent University, Nottingham, UK

Part I
Fundamental Theory

Chapter 1
The Potential Energy Surface in Molecular Quantum Mechanics

Brian Sutcliffe and R. Guy Woolley

Abstract The idea of a Potential Energy Surface (PES) forms the basis of almost all accounts of the mechanisms of chemical reactions, and much of theoretical molecular spectroscopy. It is assumed that, in principle, the PES can be calculated by means of clamped-nuclei electronic structure calculations based upon the Schrödinger Coulomb Hamiltonian. This article is devoted to a discussion of the origin of the idea, its development in the context of the Old Quantum Theory, and its present status in the quantum mechanics of molecules. It is argued that its present status must be regarded as uncertain.

1.1 Introduction

> The Coulombic Hamiltonian H' does not provide much obvious information or guidance, since there is [*sic*] no specific assignments of the electrons occurring in the systems to the atomic nuclei involved—hence there are no atoms, isomers, conformations etc. In particular one sees no *molecular symmetry*, and one may even wonder where it comes from. Still it is evident that all of this information must be contained somehow in the Coulombic Hamiltonian H' [1].
>
> Per-Olov Löwdin, Pure. Appl. Chem. **61**, 2071 (1989)

This paper addresses the question Löwdin wondered about in terms of what quantum mechanics has to say about molecules. A conventional chemical description of a stable molecule is a collection of atoms held in a semi-rigid arrangement by chemical bonds, which is summarized as a molecular structure. Whatever 'chemical bonds' might be physically, it is natural to interpret this statement in terms of bonding forces which are conservative. Hence a stable molecule can be associated with a *potential energy* function that has a minimum value below the energy of all the clusters that the molecule can be decomposed into. Finding out about these forces, or equivalently the associated potential energy, has been a major activity for the past century. There is no *a priori* specification of *atomic* interactions from basic physical laws so the approach has been necessarily indirect.

B. Sutcliffe (✉)
Service de Chimie Quantique et Photophysique, Université Libre de Bruxelles, 1050 Bruxelles, Belgium
e-mail: bsutclif@ulb.ac.be

M. Hotokka et al. (eds.), *Advances in Quantum Methods and Applications in Chemistry, Physics, and Biology*, Progress in Theoretical Chemistry and Physics 27,
DOI 10.1007/978-3-319-01529-3_1,

After the discovery of the electron [2] and the triumph of the atomic, mechanistic view of the constitution of matter, it became universally accepted that any specific molecule consists of a certain number of electrons and nuclei in accordance with its chemical formula. This can be translated into a microscopic model of point charged particles interacting through Coulomb's law with non-relativistic kinematics. These assumptions fix the molecular Hamiltonian as precisely what Löwdin referred to as the 'Coulombic Hamiltonian',

$$\mathsf{H} = \sum_{i}^{n} \frac{p_i^2}{2m_i} + \sum_{i<j}^{n} \frac{e_i e_j}{4\pi\varepsilon_0 |\mathbf{q}_i - \mathbf{q}_j|} \tag{1.1}$$

where the n particles are described by empirical charge and mass parameters $\{e_i, m_i, i = 1, \ldots, n\}$, and Hamiltonian canonical variables $\{\mathbf{q}_i, \mathbf{p}_i, i = 1, \ldots, n\}$, which after quantization are regarded as non-commuting operators.

As is well-known classical dynamics based on (1.1) fails completely to account for the stability of atoms and molecules, as evidenced through the facts of chemistry and spectroscopy. And so, starting about a century ago, there was a progressive modification of dynamics as applied to the microscopic world from classical ('rational') mechanics, through the years of the Old Quantum Theory until finally quantum mechanics was defined. This slow evolution left its mark on the development of molecular theory in as much that classical ideas survive in modern Quantum Chemistry. In the following sections we review some aspects of this progression; we also emphasize that a direct approach to a quantum theory of a molecule can be based on the quantized version of (1.1), simply as an extension of the highly successful quantum theory of the atom.

It is of interest to compare this so-called 'Isolated Molecule' model with the conventional account; after all, the sentiment of the quotation from Löwdin reflects the widespread view that the model is the fundamental basis of Quantum Chemistry. Even though there are no closed solutions for molecules, it is certainly possible to characterize important qualitative features of the solutions for the model because they are determined by the *form* of the defining equations [1, 3, 4]. One of the most important ideas in molecular theory is the Potential Energy Surface for a molecule; this is basic for theories of chemical reaction rates and for molecular spectroscopy. In Sect. 1.2 we discuss some aspects of its classical origins. Then in Sect. 1.3 we revisit the same topics from the standpoint of quantum mechanics, where we will see that if we eschew the conventional classical input (classical fixed nuclei), *there are no Potential Energy Surfaces* in the solutions derived from (1.1). It is *not* the case that the conventional approach via the clamped-nuclei Hamiltonian is merely a convenience that permits practical calculation (in modern terms, computation) with results concordant with the underlying Isolated Molecule model that would be obtained if only the computations could be done. On the contrary, a qualitative modification of the formalism is imposed by hand. The paper concludes in Sect. 1.4 with a discussion of these results; some relevant mathematical results are illustrated in the Appendix.

We wish to emphasize that the paper is about a difficult technical problem; it is not a contribution to the philosophy of science. In the traditional picture, (1.15) is widely held to be exact in principle, so if the adiabatic approximation is found to be inadequate we would expect to do 'better' by including coupling terms. Our analysis implies that belief is not well founded because (1.15) is not well founded *a priori* in quantum mechanics; it requires an extra ingredient put in by hand. It might work, or it might not; in other words it is not a sure-fire route to a better account. While we can't offer a better alternative, that information is surely important for chemical physics.

1.2 Classical Origins

The idea of a Potential Energy Surface can be glimpsed in the beginnings of chemical reaction rate theory that go beyond the purely thermodynamic considerations of van 't Hoff and Duhem more than a century ago, and in the first attempts to understand molecular ('band') spectra in dynamical terms in the same period. Thereafter progress was rapid as the newly emerging ideas of a 'quantum theory' were developed; by the time that quantum mechanics was finalized (1925/6) ideas about the separability of electronic and nuclear motions in molecules were common currency, and were carried forward into the new era. In this section we describe how this development took place.

1.2.1 Rates of Chemical Reactions—René Marcelin

The idea of basing a theory of chemical reactions (chemical dynamics) on an energy function that varies with the configurations of the participating molecules seems to be due to Marcelin. In his last published work, his thesis, [5], Marcelin showed how the Boltzmann distribution for a system in thermal equilibrium and statistical mechanics can be used to describe the rate, v, of a chemical reaction. The same work was republished in the Annales de Physique [6] shortly after his death.[1] The main conclusions of the thesis were summarized in two short notes published in Comptes Rendus in early 1914 [7, 8]. His fundamental result can be expressed, in modern terms, as

$$v = M\left(e^{-\Delta G^{\#}_{+}/RT} - e^{-\Delta G^{\#}_{-}/RT}\right) \tag{1.2}$$

where R is the molar gas constant, T is the temperature in Kelvin, the subscripts $+, -$ refer to the forward and reverse reactions, and $\Delta G^{\#}$ is the change in the molar Gibbs (free) energy in going from the initial $(+)$ or final $(-)$ state to the 'activated

[1] René Marcelin was killed in action fighting for France in September 1914.

state'. The pre-exponential factor M is obtained formally from statistical mechanics. Marcelin gave several derivations of this result using both thermodynamic arguments and also the statistical mechanics he had learnt from Gibbs's famous memoir [9]. It is perhaps worth remarking that Gibbs saw statistical mechanics as the completion of Newtonian mechanics through its extension to conservative systems with an arbitrarily large, though finite, number of degrees of freedom. The laws of thermodynamics could easily be obtained from the principles of statistical mechanics, of which they were the incomplete expression, but Gibbs did not require thermodynamic systems to be made up of molecules; he explicitly did not wish his account of rational mechanics to be based on hypotheses concerning the constitution of matter, which at the time were still controversial [10].

From our point of view the most interesting aspect of Marcelin's account is the suggestion that molecules can have more degrees of freedom than those of simple point material particles. In this perspective, a molecule can be assigned a set of Lagrangian coordinates $\mathbf{q} = q_1, q_2, \ldots, q_n$, and their corresponding canonical momenta $\mathbf{p} = p_1, p_2, \ldots, p_n$. Then the instantaneous *state* of the molecule is associated with a 'representative' point in the canonical phase-space $\mathscr{P}$ of dimension $2n$, and so "as the position, speed or structure of the molecule changes, its representative point traces a trajectory in the $2n$-dimensional phase-space" [5].

In his phase-space representation of a chemical reaction the transformation of reactant molecules into product molecules was viewed in terms of the passage of a set of trajectories associated with the 'active' molecules through a 'critical surface' $\mathscr{S}$ in $\mathscr{P}$ that divides $\mathscr{P}$ into two parts, one part being associated with the reactants, the other with the products. Such a [hyper]surface is defined by a relation

$$S(\mathbf{q}, \mathbf{p}) = 0.$$

According to Marcelin, for passage through this surface it is required[2] [5]

> [une molécule] il faudra [...] qu'elle atteigne une certaine région de l'éspace sous une obliquité convenable, que sa vitesse dépasse une certain limite, que sa structure interne corresponde à une configuration instable, *etc.*; ...

In modern notation, the volume of a cell in the $2n$-dimensional phase-space is

$$d\varpi = d\mathbf{q}d\mathbf{p}.$$

The number of points in $d\varpi$ is given by the Gibbs distribution function f

$$d\nu = f(\mathbf{q}, \mathbf{p}, t)d\varpi. \tag{1.3}$$

Marcelin chose the distribution function for the active molecules as

$$f(\mathbf{q}, \mathbf{p}, t) = e^{-G_+^{\#}/RT} e^{-\mathscr{H}(\mathbf{q},\mathbf{p})/k_B T} \tag{1.4}$$

[2] That a molecule must reach a certain region of space at a suitable angle, that its speed must exceed a certain limit, that its internal structure must correspond to an unstable configuration *etc.*; ...

where k_B is Boltzmann's constant, $\mathscr{H}$ is the Hamiltonian function for the molecule, and $G^{\#}_{+}$ is the Gibb's free energy of the active molecules relative to the mean energy of the reactant molecules. It is independent of the canonical variables. There is an analogous expression for the reverse reaction involving $G^{\#}_{-}$. Marcelin quoted a formula due to Gibbs [9] for the number of molecules dN crossing a surface element ds in the critical surface in the neighbourhood of $\mathbf{q}, \mathbf{p}$, in time dt, which may be written in shorthand as

$$dN = dt f(\mathbf{q}, \mathbf{p}, t) J(\dot{\mathbf{q}}, \dot{\mathbf{p}}, \mathbf{q}, \mathbf{p})$$

where $\dot{\mathbf{p}}, \dot{\mathbf{q}}$ are regarded as functions of $\mathbf{q}, \mathbf{p}$ by virtue of Hamilton's equations of motion. The total rate is

$$v = \int d\varpi f(\mathbf{q}, \mathbf{p}) J \delta\big[S(\mathbf{q}, \mathbf{p})\big] \tag{1.5}$$

where the delta function confines the integration to the critical surface $\mathscr{S}$. Equation (1.2) results from taking the difference between this expression for the forward and reverse reactions, and factoring out the terms in $G^{\#}_{\pm}$; the remaining integration, which Marcelin did not evaluate, defines the multiplying factor M.

1.2.2 Molecular Spectroscopy and the Old Quantum Theory

Although the discussion in the previous section looks familiar, it does so only because of the modern interpretation we put upon it.[3] It is important to note that nowhere did Marcelin elaborate on how the canonical variables were to be chosen, nor even how n could be fixed in any given case. The words 'atom', 'electron', 'nucleus' do not appear anywhere in his thesis, in which respect he seems to have followed the scientific philosophy of his countryman Duhem [11]. On other pages in the thesis Marcelin referred to the 'structure' (also 'architecture') of a molecule and to molecular 'oscillations' but never otherwise invoked the atomic structural conception of a molecule due to e.g. van 't Hoff, although he was very well aware of van 't Hoff's Physical Chemistry.

Contemporary with Marcelin's investigation of chemical reaction rates was the introduction of a completely novel model of an atom due to Rutherford. However

[3] Nevertheless it seems proper to regard Marcelin's introduction of phase-space variables and a critical reaction surface into chemical dynamics as the beginning of a formulation of the Transition State Theory that was developed by Wigner in the 1930's [12–15]. The $2n$ phase-space variables $\mathbf{q}, \mathbf{p}$ were identified with the *n nuclei* specified in the chemical formula of the participating species, and the Hamiltonian $\mathscr{H}$ was that for classical nuclear motion on a *Potential Energy Surface*; this dynamics was assumed to give rise to a critical surface which was such that reaction trajectories cross the surface precisely *once*. The classical nature of the formalism was quite clear because the Uncertainty Principle precludes the precise specification of position on the critical surface simultaneously with the momentum of the nuclei.

it quickly became apparent that Rutherford's solar system model of the atom (planetary electrons moving about a central nucleus) cannot avoid eventual collapse if classical electrodynamics applies to it. This is because of Earnshaw's theorem which states that it is impossible for a collection of charged particles to maintain a static equilibrium purely through electrostatic forces [16]. This is the classical result that Bohr alluded to in his 1922 Nobel lecture [17] to rule out an electrostatical explanation for the stability of atoms and molecules.

The theorem may be proved by demonstrating a contradiction. Suppose the charges are at rest and consider the motion of a particular charge e_n in the electric field, $\mathbf{E}$, generated by all of the other charged particles. Assume that this particular charge has $e_n > 0$. The equilibrium position of this particle is the point $\mathbf{x}_n^0$ where $\mathbf{E}(\mathbf{x}_n^0) = \mathbf{0}$, since the force on the charge is $e_n\mathbf{E}(\mathbf{x}_n)$ (the Lorentz force for this static case). Obviously, $\mathbf{x}_n^0$ cannot be the equilibrium position of any other particle. However, in order for $\mathbf{x}_n^0$ to be a stable equilibrium point, the particle must experience a restoring force when it is displaced from $\mathbf{x}_n^0$ in any direction. For a positively charged particle at $\mathbf{x}_n^0$, this requires that the electric field points radially towards $\mathbf{x}_n^0$ at all neighbouring points. But from Gauss's law applied to a small sphere centred on $\mathbf{x}_n^0$, this corresponds to a *negative* flux of $\mathbf{E}$ through the surface of the sphere, implying the presence of a *negative charge* at $\mathbf{x}_n^0$, contrary to our original assumption. Thus $\mathbf{E}$ cannot point radially towards $\mathbf{x}_n^0$ at all neighbouring points, that is, there must be some neighbouring points at which $\mathbf{E}$ is directed away from $\mathbf{x}_n^0$. Hence, a positively charged particle placed at $\mathbf{x}_n^0$ will always move towards such points. There is therefore no static equilibrium configuration. According to classical electrodynamics accelerated charges must radiate electromagnetic energy, and hence lose kinetic energy, so even a dynamical model cannot be stable according to purely classical theory.

Molecular models which can be represented in terms of the (phase-space) variables of classical dynamics had a far-reaching influence on the interpretation of molecular spectra after the dissemination of Bohr's quantum theory of atoms and molecules based on transitions between stationary states [18]. An important feature of his new theory was that classical electrodynamics should be deemed to be still operative when transitions took place, but *not* when the system was in a stationary state, by fiat. Bohr had originally used the fact that two particles with Coulombic interaction lead to a Hamiltonian problem that is completely soluble by separation of variables. With more particles and Coulombic interactions this is no longer true; however by largely qualitative reasoning he was able to develop a quantum theory of the atom and the Periodic Table (reviewed in [17]). Furthermore by the introduction of Planck's constant h through the angular momentum quantization condition, Bohr solved another problem of the classical theory. In classical electrodynamics the only characteristic length available is the classical radius r_o for a charged particle. This is obtained by equating the rest-mass energy for the charge to the electrostatic energy of a charged sphere of radius r_o

$$r_o = \left(\frac{e^2}{4\pi\varepsilon_0 mc^2}\right).$$

For an electron this yields $r_o \approx 2.8 \times 10^{-15}$ m and an even smaller value for any nucleus. It was clear that this was far too small to be relevant to an atomic theory; of course the Bohr radius $a_o \approx 0.5 \times 10^{-10}$ m is of just the right dimension.

Bohr's theory developed into the Old Quantum Theory which was based on a phase-space description of an atomic-molecular system and theoretical techniques originally developed in celestial mechanics. These came from the application of the developing quantum theory to molecular band spectra by Schwarzschild [19] and Heurlinger [20] who used it to describe the quantized vibrational and rotational energies of small molecules (diatomic and symmetric top structures). Schwarzschild, an astrophysicist, was responsible for the introduction of action-angle methods as a basis for quantization in atomic/molecular theory. Heurlinger assumed a quantization of the energy of the nuclear vibration analogous to that used by Planck for his ideal linear oscillators, with the possibility of anharmonic behaviour. Thus a force-law or *potential energy* depending on the separation of the nuclei, for a given arrangement of the electrons, was required.

The basic calculational tool was a perturbation theory approach developed enthusiastically by Born [21] and Sommerfeld [22] with their research assistants. The solution of the Hamiltonian equations of motion could be attempted via the Hamilton-Jacobi method based on canonical transformations of the action-angle variables. This leads to an expression for the energy that is a function of the action integrals only. The action (or 'phase') integrals are constants of the motion, and are also adiabatic invariants [23], and as such are natural objects for quantization according to the 'quantum conditions'. Thus for a separable system with k degrees of freedom and action integrals $\{J_i, i = 1, \ldots, j \leq k\}$, the quantum conditions according to Sommerfeld are

$$J_i \equiv \oint p_i dq_i = n_i h, \quad i = 1, \ldots, j \tag{1.6}$$

where the n_i are non-negative integers ($j < k$ in case of degeneracy). Here it is assumed that each p_i is a periodic function of only its corresponding conjugate coordinate q_i, and the integration is taken over a period of q_i. An important principle, due to Bohr, was that slow, continuous ('adiabatic') deformations of an atomic system kept the system in a stationary state [24, 25]. Thus the action integrals for a Hamiltonian depending on parameters that vary slowly in time are conserved under slow changes of the parameters.[4] This could be applied to the problem of chemical bonding by treating the nuclear positions as the slowly varying parameters in an adiabatic transformation of the Hamiltonian for the electrons in the presence of the nuclei.

We now know that systems of more than 2 particles with Coulomb interactions may have very complicated dynamics; Newton famously struggled to account quantitatively for the orbit of the moon in the earth-moon-sun problem ($n = 3$). The underlying reason for his difficulties is the existence of solutions carrying the signature of chaos [27] and this implies that there are classical trajectories to which

[4] This is strictly true only for integrable Hamiltonians [26].

the quantum conditions simply cannot be applied[5] because the integrals in (1.6) do not exist [28]. We also know that the r^{-1} singularity in the classical potential energy can lead to pathological dynamics in which a particle is neither confined to a bounded region, nor escapes to infinity for good. If the two-body interaction $V(\mathbf{r})$ has a Fourier transform $v(\mathbf{k})$ the total potential energy can be expressed as

$$\begin{aligned} U &= \sum_{i<j}^{n} e_i e_j V\left(|\mathbf{x}_i - \mathbf{x}_j|\right) \\ &= -\frac{n}{2} V(0) + \frac{1}{(2\pi)^3} \int d^3\mathbf{k} v(\mathbf{k}) \left| \sum_i e_i e^{i\mathbf{k}.\mathbf{x}_i} \right|^2 . \end{aligned}$$

In the case of the Coulomb interaction $v(\mathbf{k}) = 4\pi/k^2 > 0$ and so the potential energy U is bounded from below by $-nV(0)/2$; unfortunately for point charges as $r \to 0$, $V(r) \to \pm\infty$ and collapse may ensue [29].

Attempts were made by Born and his assistants to discuss the stationary state energy levels of 'simple' non-trivial systems such as He, H_2^+, H_2, H_2O. The molecular species were tackled as problems in *electronic structure*, that is, as requiring the calculation of the energy levels for the electron(s) in the field of *fixed* nuclei as a calculation separate from the rotation-vibration of the molecule as a whole. Pauli gave a lengthy qualitative discussion of the possible Bohr orbits for the single electron moving in the field of two fixed protons in H_2^+ but could not obtain the correct stationary states [32]. Nordheim investigated the forces between two hydrogen atoms as they approach each other adiabatically[6] in various orientations consistent with the quantum conditions. Before the atoms get close enough for the attractive and repulsive forces to balance out, a sudden discontinuous change in the electron orbits takes place and the electrons cease to revolve solely round their parent nuclei. Nordheim was unable to find an interatomic distance at which the energy of the combined system was less than that of the separated atoms; this led to the conclusion that the use of classical mechanics to discuss the stationary states of the molecular electrons had broken down comprehensively [33, 34]. This negative result was true of all the molecular calculations attempted within the Old Quantum Theory framework which was simply incapable of accounting for covalent bonding [35].

The most ambitious application of the Old Quantum Theory to molecular theory was made by Born and Heisenberg [36]. They started from the usual non-relativistic Hamiltonian (1.1) for a system comprised of n electrons and N nuclei interacting via Coulombic forces. They assumed there is an arrangement of the nuclei which is a stable equilibrium, and use that (a molecular structure) as a reference configuration

[5] The difficulties for action-angle quantization posed by the existence of chaotic motions in non-separable systems [30] were recognized by Einstein at the time the Old Quantum Theory was developed [31].

[6] This is the earliest reference we know of where the idea of *adiabatic* separation of the electrons and the nuclei is proposed explicitly.

for the calculation. Formally the rotational motion of the system can be dealt with by requiring the coordinates for the reference structure to satisfy[7] what were later to become known as 'the Eckart conditions' [37]. Then with a suitable set of internal variables and

$$\lambda = \left(\frac{m}{M}\right)^{\frac{1}{2}}$$

as the expansion parameter, the Hamiltonian was expressed as a series

$$H = H_o + \lambda^2 H_2 + \cdots \tag{1.7}$$

to be treated by the action-angle perturbation theory Born had developed. The 'unperturbed' Hamiltonian H_o is the full Hamiltonian for the electrons with the nuclei fixed at the equilibrium structure, H_2 is quadratic in the nuclear variables (harmonic oscillators) and also contains the rotational energy,[8] while ... stands for higher order anharmonic vibrational terms. H_1 may be dropped because of the equilibrium condition. With considerable effort there follows the usual separation of molecular energies, although of course no concrete calculation was possible within the Old Quantum Theory framework. It is noteworthy that their calculation gives the electronic energies at a *single* configuration because the perturbation calculation requires the introduction of the (assumed) equilibrium structure. This is different from the *adiabatic* approach Nordheim tried (unsuccessfully) to get the electronic energy at *any* separation of the nuclei [33].

1.3 Quantum Theory

With the completion of quantum mechanics in 1925–1926, the old problems in atomic and molecular theory were reconsidered and considerable success was achieved. The idea that the dynamics of the electrons and the nuclei should be treated to some extent as separate problems was generally accepted. Thus the electronic structure calculations of London [39–41] can be seen as a successful reformulation of the approach Nordheim had tried in terms of the older quantum theory, and the idea of 'adiabatic separation' is often said to originate in this work. It is however also implied in the closing section of Slater's early He atom paper where he sketches (but does not carry through) a perturbation method of approximate calculation for molecules in which the nuclei are first held fixed, and the resulting electronic eigenvalue(s) then act as the potential energy for the nuclei [42]. A quantum mechanical

[7] This also deals with the uninteresting overall translation of the molecule.

[8] The rotational and vibrational energies occur together because of the choice of the parameter λ; as is well-known, Born and Oppenheimer later showed that a better choice is to take the quarter power of the mass ratio as this separates the vibrational and rotational energies in the orders of the perturbation expansion [38].

proof of Ehrenfest's adiabatic theorem for time-dependent perturbations was given by Born and Fock [43]. Most famously though, the quantum mechanical basis for the idea of electronic Potential Energy Surfaces is commonly attributed to Born and Oppenheimer, and it is to a consideration of their famous paper [38] that we now turn.

1.3.1 Born and Oppenheimer's Quantum Theory of Molecules

Much of the groundwork for Born and Oppenheimer's treatment of the energy levels of molecules was laid down in the earlier attempt by Born and Heisenberg [36]. The basic idea of both calculations is that the low-lying excitation spectrum of a molecule can be obtained by regarding the nuclear kinetic energy as a 'small' perturbation of the energy of the electrons for stationary nuclei *in an equilibrium configuration*. The physical basis for the idea is the large disparity between the mass of the electron and the masses of the nuclei; classically the light electrons undergo motions on a 'fast' timescale ($\tau_e \approx 10^{-16} \rightarrow 10^{-15}$ s), while the vibration-rotation dynamics of the much heavier nuclei are characterized by 'slow' timescales ($\tau_N \approx 10^{-14} \rightarrow 10^{-12}$ s).

Consider a system of electrons and nuclei and denote the properties of the former by lower-case letters (mass m, coordinates x, momenta p) and of the latter by capital letters (mass M, coordinates X, momenta P). The small parameter for the perturbation expansion must clearly be some power of m/M_o, where M_o can be taken as any one of the nuclear masses or their average. In contrast to the earlier calculation they found the correct choice is

$$\kappa = \left(\frac{m}{M_o}\right)^{\frac{1}{4}}$$

rather than Born and Heisenberg's $\lambda = \kappa^2$. In an obvious shorthand notation using a coordinate representation the kinetic energy of the electrons is then[9]

$$T_e = T_e\left(\frac{\partial}{\partial x}\right)$$

while the nuclear kinetic energy depends on κ

$$T_N = \kappa^4 H_1\left(\frac{\partial}{\partial X}\right).$$

[9]The details can be found in the original paper [38], and in various English language presentations, for example [44–46].

The Coulomb energy is simply $U(x, X)$. They then define the 'unperturbed' Hamiltonian

$$T_e + U = H_o\left(x, \frac{\partial}{\partial x}, X\right) \tag{1.8}$$

and express the total Hamiltonian as

$$H = H_o + \kappa^4 H_1 \tag{1.9}$$

with Schrödinger equation

$$(H - E)\psi(x, X) = 0. \tag{1.10}$$

At this point in their argument they state

> Setzt man in (12) [(1.10) above] $\kappa = 0$, so bekommt man eine Differentialgleichung für die x_k allein, in der die X_l als Parameter vorkommen:
>
> $$\left\{H_o\left(x, \frac{\partial}{\partial x}; X\right) - W\right\}\psi = 0.$$
>
> Sie stellt offenbar die Bewegung der Elektronen bei festgehaltenen Kernen dar.[10]

This splitting of the Hamiltonian into an 'unperturbed' part ($\kappa = 0$) and a 'perturbation' is essentially the same as in the earlier Old Quantum Theory version [36]. The difference here is that the action-angle perturbation theory of the Old Quantum Theory is replaced by Schrödinger's quantum mechanical perturbation theory. In the following it is understood that the overall translational motion of the molecule has been separated off by a suitable coordinate transformation; this is always possible. The initial step in setting up the perturbation expansion involves rewriting the Hamiltonian H_o as a series in increasing powers of κ. This is achieved by introducing new relative coordinates that depend on κ

$$X = X_o + \kappa\zeta \tag{1.11}$$

for some fixed X_o, and using the $\{\zeta\}$ as the nuclear variables, in an expansion of H_o about X_o.

Then as usual the eigenfunction and eigenvalue of (1.10) are presented as series in κ

$$\psi = \psi^{(0)} + \kappa\psi^{(1)} + \kappa^2\psi^{(2)} + \cdots,$$
$$E = E^{(0)} + \kappa E^{(1)} + \kappa^2 E^{(2)} + \cdots,$$

the expansions are substituted into the Schrödinger equation (1.10), and the terms separated by powers of κ. This gives a set of equations to be solved sequentially.

[10] If one sets $\kappa = 0 \ldots$ one obtains a differential equation in the x_k alone, the X_l appearing as parameters:.... Evidently, this represents the electronic motion for stationary nuclei.

The crucial observation that makes the calculation successful is the choice of X_o; the Schrödinger equation for the unperturbed Hamiltonian H_o can be solved for any choice of the nuclear parameters X, and yields[11] an unperturbed energy $E(X)$ for the configuration X. For the consistency of the whole scheme however it turns out (cf. footnote 9) that X_o in (1.11) cannot be arbitrarily chosen, but must correspond to a *minimum* of the electronic energy. That there is such a point is assumed to be self-evident for the case of a stable molecule. The result of the calculation was a triumph; the low-lying energy levels of a stable molecule can be written in the form

$$E_{\text{Mol}} = E_{\text{Elec}} + \kappa^2 E_{\text{Vib}} + \kappa^4 E_{\text{Rot}} + \cdots \tag{1.12}$$

in agreement with a considerable body of spectroscopic evidence. The eigenfunctions that correspond to these energy levels are simple products of an electronic wavefunction obtained for the equilibrium geometry and suitable vibration-rotation wavefunctions for the nuclei.

The Born and Heisenberg calculation [36] had been performed while Heisenberg was a student with Born; Kragh [35] quotes Heisenberg's later view of it in the following terms

> As an exasperated Heisenberg wrote to Pauli, "The work on molecules I did with Born... contains bracket symbols [Klammersymbole] with up to 8 indices and will probably be read by no one." Certainly, it was not read by the chemists.

Curiously that may have initially been the fate of Born and Oppenheimer's paper. As noted by one of us many years ago, a survey of the literature up to about 1935 shows that the paper was hardly if ever mentioned, and when it was mentioned, its arguments were used as *a posteriori* justification for what was being done anyway [47]. What was being done was the general use in molecular spectroscopy and chemical reaction theory of the idea of Potential Energy Surfaces on which the nuclei moved. As we have seen, that idea is *not* to be found in the approach taken by Born and Oppenheimer which used (and had to use) a single privileged *point* in the nuclear configuration space—the assumed equilibrium arrangement of the nuclei [38].

In 1935 a significant event was the publication of the famous textbook *Introduction to Quantum Mechanics* [48] which was probably the first textbook concerned with quantum mechanics that addressed in detail problems of interest to chemists. Generations of chemists and physicists took their first steps in quantum theory with this book, which is still available in reprint form. Chapter X of the book is entitled *The Rotation and Vibration of Molecules*; it starts by summarizing the empirical results of molecular spectroscopy which are consistent with (1.12). The authors then turn to the wave equation for a general collection of electrons and nuclei and remark that its Schrödinger wave equation may be solved approximately by a procedure that they attribute to Born and Oppenheimer; first solve the wave equation for the electrons alone, with the nuclei in a fixed configuration, and then solve the wave equation for the nuclei alone, in which a characteristic energy value [eigenvalue] of

[11] $W(X)$ in the notation of the above quotation.

the electronic wave equation, regarded as a function of the internuclear distances, occurs as a potential function. After some remarks about the coordinates they say

> The first step in the treatment of a molecule is to solve this electronic wave equation for all configurations of the nuclei. It is found that the characteristic values $U_n(\xi)$ of the electronic energy are continuous functions of the nuclear coordinates ξ. For example, for a free diatomic molecule the electronic energy function for the most stable electronic state ($n = 0$) is a function only of the distance r between the two nuclei, and it is a continuous function of r, such as shown in Fig. 34-2.

Figure 34-2 referred to here is a Morse potential function. Later in the book where they give a brief introduction to activation energies of chemical reactions they explicitly cite London [41] as the origin of the idea of adiabatic nuclear motion on a Potential Energy Surface, though there is also a nod back towards Chap. X. Although it is now almost universal practice to refer to treating the nuclei as classical particles that give rise to an electronic energy surface as 'making the Born-Oppenheimer approximation' it is our opinion that the justification for such a strategy is not to be found in *The Quantum Theory of Molecules*, [38]. Nor is it to be found in the early papers of London [39–41] where it was simply assumed as a reasonable thing to do. And it is certainly the case that Born and Oppenheimer did *not* show the electronic energy to be a continuous function of the nuclear coordinates; that was first demonstrated for a diatomic molecule forty years after Pauling and Wilson's book was published (see Sect. 1.3.4).

1.3.2 Born and the Elimination of Electronic Motion

Many years after his work with Heisenberg and Oppenheimer, Born returned to the subject of molecular quantum theory and developed a different account of the separation of electronic and nuclear motion [44, 49]. It is to this method that the expression 'Born-Oppenheimer approximation' usually refers in modern work. Consider the unperturbed electronic Hamiltonian $H_o(x, X_f)$ at a fixed nuclear configuration X_f that corresponds to some molecular structure (not necessarily an equilibrium structure). The Schrödinger equation for H_o is

$$\big(H_o(x, X_f) - E^o(X_f)_m\big)\varphi(x, X_f)_m = 0. \tag{1.13}$$

This equation can have both bound-state and continuum eigenfunctions; the *bound-state* eigenvalues considered as functions of the X_f are the molecular Potential Energy Surfaces. Born proposed to solve the full molecular Schrödinger equation, (1.10) by an expansion

$$\psi(x, X) = \sum_m \Phi(X)_m \varphi(x, X)_m \tag{1.14}$$

with coefficients $\{\Phi(X)_m\}$ that play the role of nuclear wavefunctions. As in the original calculation (Sect. 1.3.1) a crucial step is to assign the nuclear coordinates

the role of parameters in the Schrödinger equation (1.13) for the electronic Hamiltonian; it differs from the earlier approach of Born and Oppenheimer because now the values of X_f range over the whole nuclear configuration space. Substituting this expansion into (1.10), multiplying the result by $\varphi(x, X)_n^*$ and integrating over the electronic coordinates x leads to an infinite dimensional system of coupled equations for the nuclear functions $\{\Phi\}$,

$$\big(T_N + E^o(X)_n - E\big)\Phi(X)_n + \sum_{nn'} C(X, P)_{nn'}\Phi(X)_{n'} = 0 \tag{1.15}$$

where the coupling coefficients $\{C(X, P)_{nn'}\}$ have a well-known form which we need not record here [44].

In this formulation the adiabatic approximation consists of retaining only the diagonal terms in the coupling matrix $\mathbf{C}(X, P)$, for then a state function can be written as

$$\psi(x, X) \approx \psi(x, X)_n^{\mathrm{AD}} = \varphi(x, X)_n\Phi(X)_n \tag{1.16}$$

and a product wavefunction corresponds to additive electronic and nuclear energies. The special character of the electronic wavefunctions $\{\varphi(x, X)_m\}$ is, by (1.13), that they diagonalize the electronic Hamiltonian H_o; they are said to define an 'adiabatic' basis (cf. the approximate form (1.16)) because the electronic state label n is not altered as X varies. The Born approach does not really require the diagonalization of H_o; it is perfectly possible to define other representations of the electronic expansion functions through unitary transformations of the $\{\varphi\}$, with concomitant modification of the coupling matrix $\mathbf{C}$. This leads to so-called 'diabatic' bases; the freedom to choose the representation is very important in practical applications to spectroscopy and atomic/molecular collisions [50, 51].

1.3.3 Formal Quantum Theory of the Molecular Hamiltonian

We now start again and develop the quantum theory of the Hamiltonian for a collection of n charged particles with Coulombic interactions.[12] We remind ourselves again from Sect. 1.1 that for particles with classical Hamiltonian variables $\{\mathbf{q}_i, \mathbf{p}_i\}$ this is

$$\mathsf{H} = \sum_i^n \frac{p_i^2}{2m_i} + \sum_{i<j}^n \frac{e_i e_j}{4\pi\varepsilon_0|\mathbf{q}_i - \mathbf{q}_j|} \tag{1.17}$$

with the non-zero Poisson-bracket

$$\{\mathbf{x}_i, \mathbf{p}_j\} = \delta_{ij}.$$

[12]The reader may find it helpful to refer to the Appendix which summarizes some mathematical notions that are needed here, and illustrates them in a simple model of coupled oscillators with two degrees of freedom.

Let us denote the classical dynamical variables for the electrons collectively as $\mathbf{x}, \mathbf{p}$, and those for the nuclei by $\mathbf{X}, \mathbf{P}$ and denote the classical Hamiltonian by $\mathsf{H}(\mathbf{x}, \mathbf{p}, \mathbf{X}, \mathbf{P})$. After the customary canonical quantization these variables become time-independent operators in a Schrödinger representation

$$\mathbf{x} \to \hat{\mathbf{x}} \quad etc.$$

In the following it will be important to distinguish between operators and c-numbers, so in the following we will use the $\hat{\mathbf{x}}$ notation for operators, and make no special choice of representation.

As we have seen, the idea that the kinetic energy of the massive nuclei could be treated as a perturbation of the electronic motion was first formulated in the framework of the Old Quantum Theory. The idea was to separate the classical Hamiltonian H into two parts to isolate the nuclear momentum variables

$$\mathsf{H}(\mathbf{x}, \mathbf{p}, \mathbf{X}, \mathbf{P}) = H_o(\mathbf{x}, \mathbf{p}, \mathbf{X}) + \kappa^4 H_1(\mathbf{P}). \tag{1.18}$$

According to Hamilton's equations for the unperturbed problem

$$\frac{d\mathbf{X}}{dt} = \{\mathbf{X}, H_o\} = 0, \tag{1.19}$$

using Poisson-bracket notation, which was interpreted (correctly) as describing the dynamics of the electrons in the field of stationary nuclei. This was the starting point of Born and Heisenberg's calculations [36].

Let us now move to quantum theory and recast (1.18) as an operator relation, writing the molecular Hamiltonian operator as

$$\hat{\mathsf{H}}(\hat{\mathbf{x}}, \hat{\mathbf{p}}, \hat{\mathbf{X}}, \hat{\mathbf{P}}) = \hat{H}_o(\hat{\mathbf{x}}, \hat{\mathbf{p}}, \hat{\mathbf{X}}) + \kappa^4 \hat{H}_1(\hat{\mathbf{P}}) \tag{1.20}$$

with equation of motion under $\hat{H}_o$

$$i\hbar \frac{d\hat{\mathbf{X}}}{dt} = [\hat{\mathbf{X}}, \hat{H}_o] = 0 \tag{1.21}$$

from which we infer the nuclear position operators $\hat{\mathbf{X}}$ are constants of the motion under $\hat{H}_o$. We no longer make the interpretation that follows from (1.19) since specifying precisely the positions $\{\mathbf{X}\}$ for *stationary* nuclei violates the Uncertainty Principle. Instead (1.21) leads to a completely different conclusion (see below).

We must now take a little bit of care about the definition of the variables, and dispose of the uninteresting overall motion of the molecule [4]. Since the Coulomb interaction only depends on interparticle distances it is translation invariant, and therefore the total momentum operator $\hat{\mathsf{P}}$

$$\hat{\mathsf{P}} = \sum_n \hat{\mathbf{p}}_n$$

commutes with $\hat{\mathsf{H}}$. It follows that the molecular Hamiltonian may be written as a direct integral

$$\hat{\mathsf{H}} = \int_{\mathbf{R}^3}^{\oplus} \hat{H}(P) dP \tag{1.22}$$

where [52]

$$\hat{H}(P) = \frac{P^2}{2M_T} + \hat{\mathsf{H}}' \tag{1.23}$$

is the Hamiltonian at fixed total momentum P and M_T is the molecular mass. The internal Hamiltonian $\hat{\mathsf{H}}'$ is independent of the centre-of-mass variables and is explicitly translation invariant. The form of $\hat{\mathsf{H}}'$ is not uniquely fixed but whatever coordinates are chosen the essential point is that it is always the same operator specified in (1.23) acting on a Hilbert space $\mathfrak{H}$ that may be parameterized by functions of the electron and nuclear coordinates.

The separation of the centre-of-mass terms from the internal Hamiltonian is the same in quantum mechanics as in classical mechanics so we need not distinguish operators from classical variables in this step. It is convenient to choose the centre-of-nuclear mass for the definition of suitable internal coordinates.[13] Let $\mathbf{t}^{\mathrm{e}}$ be a set of internal electronic coordinates defined as the original electronic coordinates $\mathbf{x}$ referred to the centre-of-nuclear mass, and let $\mathbf{t}^{\mathrm{n}}$ be a set of internal nuclear coordinates constructed purely from the original nuclear coordinates $\mathbf{X}$. If there are s electrons and M nuclei, there are s internal electronic coordinates, and $M-1$ internal nuclear coordinates. There are corresponding canonically conjugate internal momentum variables. In terms of these variables the total kinetic energy of all the particles can be decomposed into the form

$$\mathsf{T}_0 = \mathsf{T}_{\mathrm{CM}} + \mathsf{T}_{\mathrm{N}} + \mathsf{T}_{\mathrm{e}} \tag{1.24}$$

where T_{CM} is the kinetic energy for the centre-of-mass, T_{N} is the kinetic energy for the nuclei expressed purely in terms of the internal nuclear momentum variables, and T_{e} is the kinetic energy for the electrons expressed purely in terms of the internal electronic momentum variables. The Coulomb energy can be expressed purely in terms of the internal coordinates, $U = U(\mathbf{t}^{\mathrm{e}}, \mathbf{t}^{\mathrm{n}})$. These relations are true both classically and in quantum mechanics with a suitable operator interpretation.

In parallel with the decomposition in (1.18), we define the quantum mechanical 'electronic' Hamiltonian as

$$\hat{\mathsf{H}}^{\mathrm{elec}} = \hat{\mathsf{T}}_{\mathrm{e}} + \hat{U}\left(\hat{\mathbf{t}}^{\mathrm{e}}, \hat{\mathbf{t}}^{\mathrm{n}}\right) \tag{1.25}$$

[13] It is always possible to split off the kinetic energy of the centre-of-mass without any approximation; with this choice we retain the separation of the electronic and nuclear kinetic energies as well, as in (1.24). Explicit formulae are given in e.g. [3] where it is shown that the nuclear kinetic energy terms involve reciprocals of the nuclear masses, so that overall, the nuclear kinetic energy is proportional to κ^4.

so that after dropping the uninteresting kinetic energy for the overall centre-of-mass, we see that the internal Hamiltonian has the form,

$$\hat{\mathsf{H}}' = \hat{\mathsf{H}}^{\text{elec}} + \hat{\mathsf{T}}_{\text{N}} \tag{1.26}$$

where, as before, the nuclear kinetic energy term is proportional to κ^4 (see footnote 13). Its Schrödinger equation may be written

$$\hat{\mathsf{H}}'|\Psi_m\rangle = E_m|\Psi_m\rangle \tag{1.27}$$

where m is used to denote a set of quantum numbers (J M p r i): J and M for the angular momentum state: p specifying the parity of the state: r specifying the permutationally allowed irreducible representations within the groups of identical particles, and i to specify a particular energy value. Any bound state (a 'molecule') has an energy lying below the start of the essential spectrum.

Now just as in (1.21) $\hat{\mathsf{H}}^{\text{elec}}$ is independent of the nuclear momentum operators and so it commutes with the internal nuclear position operators

$$\left[\hat{\mathsf{H}}^{\text{elec}}, \hat{t}^{\text{n}}\right] = 0. \tag{1.28}$$

They may therefore be simultaneously diagonalized and we use this property to characterize the Hilbert space $\mathscr{H}$ for $\hat{\mathsf{H}}^{\text{elec}}$. Let $\mathbf{b}$ be some eigenvalue of the $\hat{\mathbf{t}}^{\text{n}}$ corresponding to choices $\{\mathbf{x}_g = \mathbf{a}_g, g = 1, \ldots, M\}$ in the laboratory-fixed frame; then the $\{\mathbf{a}_g\}$ describe a classical nuclear geometry. The set, X, of all $\mathbf{b}$ is $\mathbf{R}^{3(M-1)}$. We denote the Hamiltonian $\hat{\mathsf{H}}^{\text{elec}}$ evaluated at the nuclear position eigenvalue $\mathbf{b}$ as $\hat{\mathsf{K}}(\mathbf{b}, \hat{\mathbf{t}}^{\text{e}})_o = \hat{\mathsf{K}}_o$ for short; this $\hat{\mathsf{K}}_o$ is very like the usual clamped-nuclei Hamiltonian but it is explicitly translationally invariant, and has an extra term, which is often called the Hughes-Eckart term, or the mass polarization term. Its Schrödinger equation is of the same form as (1.13), with eigenvalues $E^o(\mathbf{b})_k$ and corresponding eigenfunctions $\varphi(\mathbf{t}^{\text{e}}, \mathbf{b})_k$,

$$\hat{\mathsf{K}}_o \varphi\left(\mathbf{b}, \mathbf{t}^{\text{e}}\right)_k = E^o(\mathbf{b})_k \varphi\left(\mathbf{b}, \mathbf{t}^{\text{e}}\right)_k. \tag{1.29}$$

As before its spectrum in general contains a discrete part below a continuum,

$$\sigma(\mathbf{b}) \equiv \sigma\left(\hat{\mathsf{K}}\left(\mathbf{b}, \hat{\mathbf{t}}^{\text{e}}\right)_o\right) = \left[E^o(\mathbf{b})_0, \ldots, E^o(\mathbf{b})_m\right) \bigcup \left[\Lambda(\mathbf{b}), \infty\right). \tag{1.30}$$

Note that for other than diatomic molecules, it is not possible to proceed further and separate out explicitly the rotational motion. For any choice of $\mathbf{b}$ the eigenvalues of $\hat{\mathsf{K}}_o$ will depend only upon the shape of the geometrical figure formed by the $\{\mathbf{a}_g\}$, being independent of its orientation. It is possible to introduce a so-called body-fixed frame by transforming to a new coordinate system built out of the $\mathbf{b}$ consisting of three angular variables and $3M - 6$ internal coordinates. In so doing however one cannot avoid angular momentum terms arising which couple the electronic and nuclear variables, and so there is no longer a clean separation of the kinetic energy into an electronic and a nuclear part. Moreover no *single* specification of body-fixed coordinates can be given that describes *all* possible nuclear configurations.

The internal molecular Hamiltonian $\hat{\mathsf{H}}'$ in (1.23) and the clamped-nuclei like operator $\hat{\mathsf{K}}_o$ just defined can be shown to be essentially self-adjoint (on their respective Hilbert spaces) by reference to the Kato-Rellich theorem [53] because in both cases there are kinetic energy operators that dominate the (singular) Coulomb interaction; they therefore have a complete set of eigenfunctions. As regards $\hat{\mathsf{H}}^{\text{elec}}$, we have a family of Hilbert spaces $\{\mathscr{H}(\mathbf{b})\}$ which are parameterized by the nuclear position vectors $\mathbf{b} \in X$ that are the 'eigenspaces' of the family of self-adjoint operators $\hat{\mathsf{K}}_o$; from them we can construct a big Hilbert space as a direct integral over all the $\mathbf{b}$ values

$$\mathscr{H} = \int_X^{\oplus} \mathscr{H}(\mathbf{b}) d\mathbf{b} \tag{1.31}$$

and this is the Hilbert space for $\hat{\mathsf{H}}^{\text{elec}}$ in (1.25).

Equation (1.31) leads directly to a fundamental result; since $\hat{\mathsf{H}}^{\text{elec}}$ commutes with all the $\{\hat{t}^{\text{n}}\}$, it has the direct integral decomposition

$$\hat{\mathsf{H}}^{\text{elec}} = \int_X^{\oplus} \hat{\mathsf{K}}\big(\mathbf{b}, \hat{\mathbf{t}}^{\text{e}}\big)_o d\mathbf{b}. \tag{1.32}$$

Even if the ' clamped-nuclei' Hamiltonian has a set of discrete states—Potential Energy Surfaces—(1.32) implies that the unperturbed Hamiltonian,[14] $\hat{\mathsf{H}}^{\text{elec}}$, *has purely continuous spectrum* (cf. Appendix),

$$\sigma = \sigma\big(\hat{\mathsf{H}}^{\text{elec}}\big) = \bigcup_{\mathbf{b}} \sigma(\mathbf{b}) \equiv [V_0, \infty)$$

where V_0 is the minimum value of $E(\mathbf{b})_0$; in the diatomic molecule case this is the minimum value of the usual ground-state potential energy curve $E_0(r)$. The operator $\hat{\mathsf{H}}^{\text{elec}}$ has no localized eigenfunctions; rather, its eigenfunctions are continuum functions. To avoid any misunderstanding, we emphasize that this result has nothing to do with the continuous spectrum of the full molecular Hamiltonian associated with the centre-of-mass motion which can be dealt with trivially in the preliminaries.

A possibly helpful way to think about this paradoxical result is as follows. The quantum mechanical molecular Hamiltonian for a collection of electrons and nuclei with Coulomb interactions is a function of position and momentum operators for all the specified electrons and all the nuclei. If now we separate off the terms containing all the nuclear momentum operators (the terms proportional to κ^4) what is left must be a function of position and momentum operators for the electrons *and position operators for all the nuclei*. This statement is true in any representation of the operators, and in particular must be respected if one chooses a position representation.

This is *not* what Born and Oppenheimer assumed about their equation (12) [our equation (1.10)] when $\kappa = 0$—see Sect. 1.3.1 above—and which has been assumed ever since in Quantum Chemistry. In effect they chose to work only in the 'small'

[14] After the elimination of the centre-of-mass variables $\hat{\mathsf{H}}^{\text{elec}}$ is playing the role of $\hat{H}_o$ in (1.20).

Hilbert space of a fixed configuration, $\mathscr{H}(\mathbf{X})$, in which $\mathbf{X}$ can be assumed to be a 'parameter' in the position space wavefunction $\psi(\mathbf{x}, \mathbf{X})$, whereas if they had continued with quantum mechanics they would have been working in the 'big' Hilbert space $\mathscr{H}$ with $\hat{\mathbf{x}}$ and $\hat{\mathbf{X}}$ treated on an equal footing as operators, and all possible nuclear configurations being treated simultaneously, rather than one at a time.

The unusual properties of the ('electronic') Hamiltonian $\hat{\mathsf{H}}_o(\hat{\mathbf{x}}, \hat{\mathbf{p}}, \hat{\mathbf{X}}) = \hat{\mathsf{H}}^{\text{elec}}$ in (1.32)[15] considered as a quantum-mechanical operator on the whole space $\mathfrak{H}$, are of exactly the kind to be expected from the work of Kato [54]. In Lemma 4 of his paper he showed that for a Coulomb potential U and for any function f in the domain $\mathcal{D}_0$ of the full kinetic energy operator $\hat{\mathsf{T}}_0$, the domain, $\mathcal{D}_U$, of the internal Hamiltonian $\hat{\mathsf{H}}'$ contains $\mathcal{D}_0$ and there are two constants a, b such that

$$\|Uf\| \leq a\|\hat{\mathsf{T}}_0 f\| + b\|f\|$$

where a can be taken as small as is liked. This result is often summarised by saying that the Coulomb potential is small compared to the kinetic energy. Given this result he proved in Lemma 5 (the Kato-Rellich theorem) that the usual Coulomb Hamiltonian operator is essentially self-adjoint and so is guaranteed a complete set of eigenfunctions, and is bounded from below.

In the present context the important point to note is that the Coulomb term is small only in comparison with the kinetic energy term involving the same set of variables. So the absence of one or more kinetic energy terms from the Hamiltonian may mean that the Coulomb potential term cannot be treated as small. It is evident that one can't use the Kato-Rellich argument to guarantee self-adjointness for the customary representation of H^{elec} in a position representation as a differential and multiplicative operator because it contains the nuclear positions $\{\mathbf{X}\}$ in Coulomb terms that are not dominated by corresponding kinetic energy operators involving the conjugate momentum operators $\{-i\hbar\nabla\}$ since they have been separated off into the 'perturbation' term $\propto \kappa^4$. As a quite separate matter, the abstract direct integral operator (1.32) is self-adjoint since the resolvent of the clamped-nuclei Hamiltonian is integrable. This is demonstrated in Theorem XIII.85 in the book by Reed and Simon [53]. It is in this form that the operator is used in the mathematically rigorous accounts (to be discussed later) of the Born-Oppenheimer approximation in [64] and [70]. The operator used in the standard account of Born and Huang [44] is however simply the usual one which, as discussed above, is not self-adjoint in the Kato sense.

1.3.4 Approximate Calculations

It might have been hoped, in the light of the claim in the original paper by Born and Oppenheimer quoted in Sect. 1.3.1, that the eigensolutions of the $\kappa \to 0$ limit

[15] We assume that the centre-of-mass contributions are eliminated as usual.

of the internal Hamiltonian, $\hat{\mathsf{H}}'$, would actually be those that would have been obtained from (1.10) after separation of the centre-of-mass term, by letting the nuclear masses increase without limit. Although there are no analytically solved molecular problems, the work of Frolov [55] provides extremely accurate numerical solutions for a problem with two nuclei and a single electron. Frolov investigated what happens when the masses of one and then two of the nuclei increase without limit in his calculations. To appreciate his results, consider a system with two nuclei; the natural nuclear coordinate is the internuclear distance which will be denoted here simply as $\mathbf{t}$. When needed to express the electron-nuclei attraction terms, $\mathbf{x}_i^{\mathrm{n}}$ is simply of the form $\alpha_i \mathbf{t}$ where α_i is a signed ratio of the nuclear mass to the total nuclear mass; in the case of a homonuclear system $\alpha_i = \pm\frac{1}{2}$.

The di-nuclear electronic Hamiltonian after the elimination of the centre-of-mass contribution as described in Sect. 1.3.3 is

$$\begin{aligned}\hat{\mathsf{H}}^{\mathrm{elec}}\left(\mathbf{t}^{\mathrm{e}}, \mathbf{t}\right) = &-\frac{\hbar^2}{2m}\sum_{i=1}^{N}\nabla^2\left(\mathbf{t}_i^{\mathrm{e}}\right) - \frac{\hbar^2}{2(m_1+m_2)}\sum_{i,j=1}^{N}\nabla\left(\mathbf{t}_i^{\mathrm{e}}\right)\cdot\nabla\left(\mathbf{t}_j^{\mathrm{e}}\right)\\ &-\frac{e^2}{4\pi\varepsilon_0}\sum_{j=1}^{N}\left(\frac{Z_1}{|\mathbf{t}_j^{\mathrm{e}}+\alpha_1\mathbf{t}|}+\frac{Z_2}{|\mathbf{t}_j^{\mathrm{e}}+\alpha_2\mathbf{t}|}\right)\\ &+\frac{e^2}{8\pi\varepsilon_0}{\sum_{i,j=1}^{N}}'\frac{1}{|\mathbf{t}_i^{\mathrm{e}}-\mathbf{t}_j^{\mathrm{e}}|}+\frac{Z_1Z_2}{R}, \quad R=|\mathbf{t}| \end{aligned} \tag{1.33}$$

while the nuclear kinetic energy part is:

$$\hat{\mathsf{T}}_{\mathrm{N}}(\mathbf{t}) = -\frac{\hbar^2}{2}\left(\frac{1}{m_1}+\frac{1}{m_2}\right)\nabla^2(\mathbf{t}) \equiv -\frac{\hbar^2}{2\mu}\nabla^2(\mathbf{t}). \tag{1.34}$$

The full internal motion Hamiltonian for the three-particle system is then

$$\hat{\mathsf{H}}'\left(\mathbf{t}^{\mathrm{e}}, \mathbf{t}\right) = \hat{\mathsf{H}}^{\mathrm{elec}}\left(\mathbf{t}^{\mathrm{e}}, \mathbf{t}\right) + \hat{\mathsf{T}}_{\mathrm{N}}(\mathbf{t}) \tag{1.35}$$

which is of the same form as (1.26).

It is seen from (1.34), that if only one nuclear mass increases without limit then the kinetic energy term in the nuclear variable remains in the full problem and so the Hamiltonian (1.35) remains essentially self-adjoint. Frolov's calculations showed that when one mass increased without limit (the atomic case), any discrete spectrum persisted but when two masses were allowed to increase without limit (the molecular case), the Hamiltonian ceased to be well-defined and this failure led to what he called *adiabatic divergence* in attempts to compute discrete eigenstates of (1.35). This divergence is discussed in some mathematical detail in the Appendix to Frolov [55]. It does not arise from the choice of a translationally invariant form for the electronic Hamiltonian; rather it is due to the lack of any kinetic energy term to dominate the Coulomb potential.

To every solution of (1.29) there corresponds a function

$$\Phi\left(\mathbf{t}^{\mathrm{e}}, \mathbf{t}^{\mathrm{n}}\right)_m = \varphi\left(\mathbf{b}, \mathbf{t}^{\mathrm{e}}\right)_m \delta\left(\mathbf{t}^{\mathrm{n}} - \mathbf{b}\right) \tag{1.36}$$

in the $(\mathbf{t}^{\mathrm{e}}, \mathbf{t}^{\mathrm{n}})$ position representation which is a formal solution, in the sense of distributions, of the Schrödinger equation for $\hat{\mathsf{H}}^{\mathrm{elec}}$. The energy, $\mathscr{E}_m(\mathbf{b})$ of the function (1.36) is independent of the orientation of the figure defined by the $\mathbf{b}$, and is also unaltered by the parity operation $\mathbf{b} \to -\mathbf{b}$, and by permutations of the labelling of any identical nuclei. Φ_m however depends on the orientation of the body-fixed frame defined by the configuration $\mathbf{b}$ with respect to some space-fixed reference frame. Let the Euler angles relating these two frames be Ω so that

$$\Phi(\mathbf{b})_m = \Phi(\overline{\mathbf{b}}, \Omega)_m$$

in an obvious notation, so we have a continuous family of degenerate states. The dependence on orientation is eliminated by forming a continuous superposition through integration over the Euler angles with some weight function $c(\Omega)$

$$\Psi_m = \int d\Omega' c\left(\Omega'\right) \Phi\left(\overline{\mathbf{b}}, \Omega'\right)_m.$$

Similarly one may form superpositions of the space-inverted and permuted states in order to form a new basis that displays the corresponding symmetries that leave the energy eigenvalue unchanged.

There are two quite distinct approaches to the solution of the molecular Schrödinger equation (1.27) based on the formal theory reviewed in Sect. 1.3.3. Functions of the type (1.36) can be used as the basis of a Rayleigh-Ritz calculation being, hopefully, well-adapted to the construction of useful trial functions. Several different lines have been developed; in the *adiabatic* model the trial function is written as the continuous linear superposition

$$\begin{aligned} \Psi\left(\mathbf{t}^{\mathrm{e}}, \mathbf{t}^{\mathrm{n}}\right)_m &= \int d\mathbf{b} F(\mathbf{b}) \varphi\left(\mathbf{b}, \mathbf{t}^{\mathrm{e}}\right)_m \delta\left(\mathbf{t}^{\mathrm{n}} - \mathbf{b}\right) \\ &= F\left(\mathbf{t}^{\mathrm{n}}\right) \varphi\left(\mathbf{t}^{\mathrm{n}}, \mathbf{t}^{\mathrm{e}}\right)_m \end{aligned} \tag{1.37}$$

where the square-integrable weight factor $F(\mathbf{t}^{\mathrm{n}})$ may be determined by reducing (1.27) to an effective Schrödinger equation for the nuclei in which $F(\mathbf{t}^{\mathrm{n}})$ appears as the eigenfunction [56].

If the $\{\varphi_m\}$ are chosen to be orthonormal we have

$$\langle \Psi_m | \Psi_m \rangle = \iint d\mathbf{t}^{\mathrm{e}} d\mathbf{t}^{\mathrm{n}} \left| \Psi\left(\mathbf{t}^{\mathrm{e}}, \mathbf{t}^{\mathrm{n}}\right)_m \right|^2 = \int d\mathbf{t}^{\mathrm{n}} \left| F\left(\mathbf{t}^{\mathrm{n}}\right) \right|^2.$$

We may choose the weight factor F to be normalized, so that the state function Ψ_m is also normalized. On the other hand

$$\langle \Psi_m | \hat{\mathsf{H}}' | \Psi_m \rangle = \iint d\mathbf{t}^{\mathrm{e}} d\mathbf{t}^{\mathrm{n}} \Psi_m^* \left(\hat{\mathsf{H}}' \Psi_m\right) = \int d\mathbf{t}^{\mathrm{n}} F\left(\mathbf{t}^{\mathrm{n}}\right)^* \left(\hat{\mathsf{H}}_m F\right)\left(\mathbf{t}^{\mathrm{n}}\right)$$

where we have defined the effective nuclear Hamiltonian

$$(\hat{\mathsf{H}}_m F)(\mathbf{t}^{\mathrm{n}}) = \int d\mathbf{t}^{\mathrm{e}} \varphi(\mathbf{t}^{\mathrm{e}}, \mathbf{t}^{\mathrm{n}})_m \big[\hat{\mathsf{H}}' \varphi(\mathbf{t}^{\mathrm{e}}, \mathbf{t}^{\mathrm{n}})_m F(\mathbf{t}^{\mathrm{n}})\big]. \tag{1.38}$$

The Rayleigh-Ritz quotient

$$E[\Psi_m] = \frac{\langle \Psi_m | \hat{\mathsf{H}}' | \Psi_m \rangle}{\langle \Psi_m | \Psi_m \rangle} \tag{1.39}$$

is stationary for those functions that are solutions of the effective nuclear 'Schrödinger equation'

$$\hat{\mathsf{H}}_m F_s = E_{ms} F_s. \tag{1.40}$$

In particular, using the electronic ground state φ_0, the Rayleigh-Ritz quotient leads to an *upper bound* to the ground state energy E_0 of $\hat{\mathsf{H}}'$. Having set up the calculation with square integrable functions the approximate ground-state is naturally a discrete state; the discussion however yields no information about the bottom of the essential spectrum i.e. it does not prove the existence of a bound-state below the continuum. This calculation amounts to the diagonalization of the projection of $\hat{\mathsf{H}}'$ on the one-dimensional subspace spanned by Ψ_0. In principle the subspace may be enlarged, and the accuracy thereby improved, by using the subspace spanned by a set of trial functions $(\Psi_0, \Psi_1, \ldots, \Psi_m)$ of the form of (1.37). Such non-adiabatic calculations which make no use of a Potential Energy Surface are restricted to very small molecules.

In practice the variational approach is implemented as follows; a collection of energies $E(\mathbf{b}_i)$ is found through standard quantum chemical computations for different geometries $\{\mathbf{b}_i\}$ and fitted to produce a function $V(\mathbf{t}^{\mathrm{n}})$ that is treated as a potential energy contribution to the left-hand-side of the Born equation (1.15), rather than (1.40), so the clamped-nuclei assumption enters in an essential way (see Appendix). With considerable computational effort it is possible to construct permutationally invariant energy surfaces for molecules with up to 10 nuclei [57]. Note however that if $\hat{\mathsf{H}}'$ is separated as in (1.26), then it is $\hat{\mathsf{H}}^{\mathrm{elec}}$ that appears in (1.38) rather than the clamped-nuclei Hamiltonian.

Another generalization is to replace the unnormalizable delta function in (1.37) by a square integrable function; the relation

$$\delta^3(\mathbf{x}-\mathbf{y}) = \lim_{a\to\infty} \left(\frac{a}{\pi}\right)^{\frac{3}{2}} e^{-a(\mathbf{x}-\mathbf{y})^2} \equiv \lim_{a\to\infty} \chi_a(\mathbf{x},\mathbf{y})$$

suggests that one might consider trial wavefunctions

$$\Psi(\mathbf{t}^{\mathrm{e}}, \mathbf{t}^{\mathrm{n}})_m^{\mathrm{GCM}} = \int d\mathbf{b} F(\mathbf{b}) \varphi(\mathbf{b}, \mathbf{t}^{\mathrm{e}})_m \chi_a(\mathbf{t}^{\mathrm{n}}, \mathbf{b})$$

for some suitably chosen parameter a. This is the basis of the molecular *Generator Coordinate Method* (GCM) which is a non-adiabatic formalism; as before the

weight factor $F(\mathbf{b})$ is determined by appeal to the Rayleigh-Ritz quotient, although part of its structure can be determined purely by symmetry arguments. In the GCM the effective Schrödinger equation for the weight function becomes an integral equation (the Hill-Wheeler equation) [45]. Again the trial function may be improved, in the sense of a variational calculation, by forming linear superpositions of the wavefunctions $\{\Psi^{\mathrm{GCM}}\}$; this has been done for diatomic molecules for which a fairly complete GCM account has been developed [45, 58]. Usually however the dependence on the nuclear variables $\{\mathbf{t}^{\mathrm{n}}\}$ is not expressed through functions adapted to nuclear permutation symmetry, and the GCM weight functions are determined by molecular structure considerations.

It should be noted here that $\varphi(\mathbf{b}, \mathbf{t}^{\mathrm{e}})$ as a solution to the Schrödinger equation (1.29) where $\mathbf{t}^{\mathrm{n}}$ has been replaced by $\mathbf{b}$, is defined only up to a phase factor of the form

$$\exp\bigl[i\,w(\mathbf{b})\bigr]$$

w is any single-valued real function of the $\{\mathbf{b}_i\}$ which can be different for different electronic states. The phase factor is only trivial in the absence of degeneracies. Specific phase choices may therefore be needed when tying this part to the nuclear part of the product wave function. It is only by making suitable phase choices that the electronic wave function is made a continuous function of the formal nuclear variables, $\mathbf{b}$, and the complete product function, made single valued. This is the origin of the Berry phase in clamped-nuclei calculations involving intersecting Potential Energy Surfaces; for a discussion of these matters see [59, 60]. It is worth noting explicitly that notions of molecular Berry phases and conical intersections of PE surfaces are tied to the clamped-nuclei viewpoint which introduces 'adiabatic parameters'. According to quantum mechanics the eigensolutions of (1.27) are single-valued functions by construction with arbitrary phases (rays) so one does not expect any Berry phase phenomena *a priori*.

The rigorous mathematical analysis of the original perturbation approach proposed by Born and Oppenheimer [38] for a molecular Hamiltonian with Coulombic interactions was initiated by Combes and co-workers [61–64] with results for the diatomic molecule. Some properties of the operator $\mathsf{H}^{\mathrm{elec}}$, (1.32), seem to have been first discussed in this work. A perturbation expansion in powers of κ leads to a singular perturbation problem because κ is a coefficient of differential operators of the highest order in the problem; the resulting series expansion of the energy is an *asymptotic* series, closely related to the WKB approximation obtained by a semiclassical analysis of the effective Hamiltonian for the nuclear dynamics. This requires a more complete treatment than the adiabatic model using the partitioning technique to project the full Coulomb Hamiltonian, $\hat{\mathsf{H}}'$, onto the adiabatic subspace. A normalized electronic eigenvector $|\varphi(\mathbf{b})_j\rangle$ is associated with a projection operator by the usual correspondence

$$\hat{P}(\mathbf{b})_j = \bigl|\varphi(\mathbf{b})_j\bigr\rangle\bigl\langle\varphi(\mathbf{b})_j\bigr|.$$

In view of our earlier discussion of the 'big Hilbert space' $\mathscr{H}$, we can form a direct integral over all nuclear positions

$$\hat{P}_j = \int_X^{\oplus} \hat{P}(\mathbf{b})_j d\mathbf{b}$$

to yield a projection operator on the adiabatic subspace. If we want to include m electronic levels we can form a direct sum of the contributing $\{\hat{P}_j\}$

$$\hat{P} = \bigoplus_{j=0}^{m} \hat{P}_j.$$

This is an Hermitian projection operator and it, and its complement, $\hat{Q}$, have the usual properties

$$\hat{P} + \hat{Q} = \hat{1}, \qquad \hat{P}^2 = \hat{P}, \qquad \hat{Q}^2 = \hat{Q}, \qquad \hat{P}\hat{Q} = \hat{Q}\hat{P} = 0.$$

Using these projection operators the original molecular Schrödinger equation

$$\hat{\mathsf{H}}'|\Psi\rangle = E|\Psi\rangle$$

can be transformed into a pair of coupled equations

$$\hat{P}\hat{\mathsf{H}}'\hat{P}|\psi\rangle + \hat{P}\hat{\mathsf{H}}'\hat{Q}|\chi\rangle = E\hat{1}|\psi\rangle \tag{1.41}$$

$$\hat{Q}\hat{\mathsf{H}}'\hat{P}|\psi\rangle + \hat{Q}\hat{\mathsf{H}}'\hat{Q}|\chi\rangle = E\hat{1}|\chi\rangle \tag{1.42}$$

where

$$|\psi\rangle = \hat{P}|\Psi\rangle, \qquad |\chi\rangle = \hat{Q}|\Psi\rangle.$$

Solving (1.42) for $|\chi\rangle$

$$|\chi\rangle = \frac{1}{E\hat{1} - \hat{Q}\hat{\mathsf{H}}'\hat{Q}}\hat{Q}\hat{\mathsf{H}}'\hat{P}|\psi\rangle$$

and substituting in (1.41) yields the usual Löwdin partitioned equation [65]

$$\left(\hat{P}\hat{\mathsf{H}}'\hat{P} + \hat{P}\hat{\mathsf{H}}'\hat{Q}\frac{1}{E\hat{1} - \hat{Q}\hat{\mathsf{H}}'\hat{Q}}\hat{Q}\hat{\mathsf{H}}'\hat{P}\right)|\psi\rangle = E\hat{1}|\psi\rangle. \tag{1.43}$$

Further progress depends crucially on establishing the properties of the energy dependent operator in (1.43). A detailed consideration of the diatomic molecule case can be found in [63, 64]. The main result is that (1.43) is a generalized version of the effective nuclear Schrödinger equation (1.40) in the adiabatic model, so it contains the nuclear kinetic energy operators and an effective potential $\hat{V}$. The *microscope transformation* used by Combes and Seiler [63] to give a rigorous version of the Born-Oppenheimer theory of a diatomic molecule is essentially a semiclassical theory. It is applicable if there is a minimum in the potential $V_0 = V(\mathbf{x}_0)$ associated

with a particular configuration of the nuclei[16] that is deep enough for the lowest energy eigenstates to be localized about $\mathbf{x}_0$. One can look at these states with a 'microscope' with a certain resolving power that depends on Planck's constant.

The microscope transformation produces a translation to make $\mathbf{x}_0$ the origin of the coordinates, and a dilation (scale transformation)

$$\hat{\mathbf{x}}_\lambda = \hat{\mathbf{x}} - (1-\lambda)(\hat{\mathbf{x}} - \mathbf{x}_0), \qquad \hat{\mathbf{p}}_\lambda = \hat{\mathbf{p}} + \frac{(1-\lambda)}{\lambda}\hat{\mathbf{p}}. \tag{1.44}$$

It is readily verified that the commutation relations are preserved for $\lambda \neq 0$

$$[\hat{\mathbf{x}}_\lambda, \hat{\mathbf{p}}_\lambda] = [\hat{\mathbf{x}}, \hat{\mathbf{p}}].$$

Under this transformation a Hamiltonian of the form

$$\hat{H} = \sum_g \frac{\hat{p}_g^2}{2m_g} + \hat{V}(\mathbf{x})$$

becomes

$$\hat{H}_\lambda = \hat{V}(\mathbf{x}_0) + \lambda^2 \hat{N}(\lambda)$$

where

$$\hat{N}(\lambda) = -\frac{\hbar^2}{\lambda^4} \sum_g \frac{\nabla_g^2}{2m_g} + \frac{1}{\lambda^2}\big(\hat{V}\big(\mathbf{x}_0 + \lambda(\mathbf{x} - \mathbf{x}_0)\big) - \hat{V}(\mathbf{x}_0)\big).$$

We now put $\lambda = \sqrt{\hbar}$ so as to eliminate λ from the kinetic energy term in $\hat{N}(\lambda)$; with this choice for λ, unitary equivalence of the spectrum implies that the eigenvalues of the original Hamiltonian $\hat{H}$ are related to those of $\hat{N}(\lambda)$ by

$$E_n = V(\mathbf{x_0}) + \hbar\mu_n(\lambda).$$

Provided $\hat{V}$ is analytic in λ it can be expanded about $\lambda = 0$, and this puts $\hat{N}(\lambda)$, in lowest order, into the form of a sum of coupled oscillators so that the first approximation for the eigenvalue function μ_n is

$$\mu_n = \sum_k \left(n_k + \frac{1}{2}\right).$$

In the Born-Oppenheimer calculation for the diatomic molecule the potential $\hat{V}$ is identified with the effective potential for the nuclei [63]; analyticity of $\hat{V}$ in λ could be proven, and the role of $\sqrt{\hbar}$ was taken by the usual BO expansion parameter $\kappa = (m_e/M_N)^{\frac{1}{4}}$. In this way the molecular energy level formula (1.12) is recovered as an asymptotic expansion.

[16] The multiminima case can also be treated in this way.

The singular nature of the microscope transformation for $\lambda = 0$ is demonstrated by the modification of the spectrum associated with the limit $\kappa \to 0$. The spectrum of the Coulomb Hamiltonian for a molecule can be discussed in terms of the Hunziker-van Winter-Zhislin theorem [66–68]; for the diatomic molecule, $\sigma_{ess}(\hat{\mathsf{H}}')$ starts at the lowest two-body threshold $\Sigma = \lambda_A(m_A) + \lambda_B(m_B)$ given by the minimal value of the sums of pairs of binding energies for atoms A and B with finite masses m_A and m_B respectively. On the other hand the spectrum of the electronic Hamiltonian, $\hat{\mathsf{H}}^{\text{elec}}$, is purely continuous, $\sigma(\hat{\mathsf{H}}^{\text{elec}}) = [V_0, \infty)$. In the limit $m_A, m_B \to \infty$, Σ does not generally converge to V_0; instead the missing part of the continuous spectrum $[V_0, \lambda_A(\infty) + \lambda_B(\infty)]$ is provided by an accumulation of bound states in this interval [62]. The microscope transformation is formally applicable to the polyatomic case but it may not be sufficient to control the asymptotic behaviour, and has not been used for general molecules.

Since the initial work of Combes, a considerable amount of mathematical work has been published using both time-independent and time-dependent techniques with developments for the polyatomic case; for a recent review of rigorous results about the separation of electronic and nuclear motions see Hagedorn and Joye [69] which covers the literature to 2006. The Hamiltonian (1.26) is the one used by Klein *et al.* [70] in their consideration of the precise formulation of the Born-Oppenheimer approximation for polyatomic systems. Their work was based on a powerful symbolic operator method, the *pseudodifferential calculus* [70, 71] and a formalism related to the partitioning technique described above. In [70] it is assumed that (1.26) has a discrete eigenvalue which has a minimum as a function of the $\mathbf{t}^{\text{n}}$ in the neighborhood of some values $\mathbf{t}^{\text{n}}_i = \mathbf{b}_i$. If it can be assumed that (a) the electronic wavefunction vanishes strongly outside a region close to a particular nuclear geometry and (b) that the electronic energy at the given geometry is an isolated minimum, then it is possible to present a rigorous account of the separation of electronic and nuclear motion which corresponds in some measure to the original Born-Oppenheimer treatment.

A novel feature arises from the requirement that the inversion symmetry of the original problem be respected. If the geometry at the minimum energy configuration is either linear or planar then inversion can be dealt with in terms of a single minimum in the electronic energy. If the geometry at the minimum is other than these two forms, inversion produces a second potential minimum and the problem must be dealt with as a two-minimum problem; then extra consideration is necessary to establish whether the two wells have negligible interaction so that only one of the wells need be considered for the nuclear motion. The nuclei are treated as distinguishable particles that can be numbered uniquely. The symmetry requirements on the total wavefunction that would arise from the invariance of the Hamiltonian operator under the permutation of identical nuclei are not considered. Because of the continuous spectrum of the electronic Hamiltonian $\hat{\mathsf{H}}^{\text{elec}}$, it is not possible to use regular perturbation theory in the analysis; instead asymptotic expansion theory is used so that the result has essentially the character of a WKB approximation [70]. Similar functional analytic techniques have been used to consider such phenomena as Landau-Zener crossing by using a time-dependent approach to the problem

and looking at the relations between the electronic and nuclear parts of a wavepacket [72]. This is essentially a use of standard coherent state theory where again the nuclei are treated as distinguishable particles and the method is that of asymptotic expansion.

1.4 Discussion

Quite generally one needs to make a distinction between an hypothetical Isolated Molecule, and a real observable *individual* molecule. There are no strictly 'isolated' systems of course, but what is striking is that an approach based on the stationary state eigensolutions of the appropriate Coulomb Hamiltonian works so well for atoms and diatomic molecules, but fails with three or more nuclei. We have always been clear that for most of chemistry, molecular eigenstates ('stationary states') are of no relevance since *metastability* is an essential aspect of isomerism. The interesting question is how to get from the quantum theory of an *Isolated Molecule* to a quantum theory of an *individual molecule* by rational mathematics. It is as well to remember that the *generic* molecule is sufficiently complex that the quantum mechanical permutation symmetry of identical nuclei is a feature that cannot be ignored, if one is doing quantum mechanics. The Isolated Molecule model doesn't capture isomerism, nor optical activity. We see no reason at all for Löwdin's optimistic assertion (Sect. 1.1) that molecular symmetry *must* be contained somehow in the Coulomb Hamiltonian.

If a molecule is not isolated it must be interacting with something; that something is loosely referred to as the 'environment'. It might be other molecules, the (macroscopic) substance the molecule finds itself in, or quantized electromagnetic radiation. Blackbody radiation is all pervasive and charges are always coupled to the photon vacuum state in QED and so 'dressed' with clouds of virtual photons. A crucial feature of 'environments' in quantum theory is that generally they are described by Hamiltonians with purely continuous spectra. This is important because a quantum system with a finite number, n, of degrees of freedom described by the usual linear Schrödinger equation does not yield 'broken symmetry' solutions if $n < \infty$. Such matters were discussed at length thirty years ago in the context of molecular structure and quantum theory [73–75]. The characteristic feature of such discussions, and this also applies to more modern formulations under the chic heading of 'decoherence', is that they start with some primitive notion of structure built in: two-state systems, potential energy wells, wavefunctions associated with distinct isomers *etc.* The 'environment' is modelled in the simplest possible way (for example, a free boson quantum field). These crucial ideas are put in by hand at the outset. We don't see that as a 'problem' or 'difficulty'; it is a characteristic feature of many-body physics (condensed matter, nuclei, chemistry) and results in remarkably powerful and fruitful theoretical formalisms; see, for example, Anderson's discussion of what he calls 'adiabatic continuity' [76]. But one can hardly avoid noticing that the models of molecules used are caricatures that contain just the right features

for the answer (for example, loss of permutation symmetry, loss of parity—in the case of chirality) and have no clear connection to Löwdin's's Coulomb Hamiltonian.

An alternative account that *is* based on the Coulomb Hamiltonian may however be possible in the light of the fact that each part of it in the division made in (1.26) has a completely continuous spectrum. As noted in Sect. 1.3.4 the formal eigenvectors of $\hat{\mathsf{H}}^{\text{elec}}$ from the ground state up can exhibit extensive degeneracy. It might be that 'broken symmetry' solutions corresponding to molecular structure could result from treating the two parts as asymptotic states in a scattering or reaction process in a manner analogous to that used in standard S-matrix theory. Such a state would be characterised as a 'resonance' and would have to be long-lived to be describable as a molecule. Only a true bound state, of infinite lifetime, such as a bound eigenstate of the molecular Hamiltonian is really independent of how it was formed; resonant states have histories that describe the environment of their preparation. The Potential Energy Surface would then appear only as an auxiliary concept through the involvement of the clamped-nuclei Hamiltonian in the construction of the states $\{\varphi_m\}$ required for (1.36). That however remains subject to further investigation.

When Bohr introduced his quantum theory of the Rutherford atomic model of the hydrogen atom he made a drastic change in the status of electrodynamics. Hitherto, it had been understood[17] that charged particles affected, and were affected by, the electromagnetic field, and that was the root cause of the failure of a dynamical classical atom ('radiation damping' is a strong coupling interaction). Bohr relegated the electromagnetic field to a perturbation theoretic—*weak coupling*—role; the charges interacted among themselves according to Coulomb's law, to be treated as a strong coupling situation, and would exist permanently in the stationary states selected by the quantization conditions unless perturbed by an 'external' electromagnetic field which produced 'transitions'. That perturbation theory viewpoint was maintained when quantum theory was applied to the atom and the electromagnetic field, and largely survives to this day, to the extent that the electromagnetic field is frequently regarded as a *classical* system. Such a spectroscopic viewpoint is not appropriate in the present context; quantum electrodynamics teaches us that there is no strict separation of charged particles and the (quantized) electromagnetic field, not least because of the requirements of gauge invariance.

The difficulty with quantum mechanical perturbation theory for the interaction of atomic/molecular systems with radiation is this: the spectrum of the unperturbed atom/molecule consists of a continuum corresponding to the half-axis $[\Sigma, \infty)$ for some $\Sigma \leq 0$, and discrete energy levels $E_0, E_1, \ldots$ below the continuum, that is $E_0 \leq E_1 \leq \cdots < \Sigma$ [66–68]. The spectrum of the free electromagnetic field Hamiltonian consists of a simple eigenvalue at 0, corresponding to the vacuum state Ψ_0, and absolutely continuous spectrum on the half-axis $[0, \infty)$. This means that when coupling between particles and radiation is admitted, all the discrete energy levels of the atomic system including E_0 become thresholds of continuous spectra; a quantum theory of matter and the electromagnetic field therefore requires the perturbation theory of continuous spectra. The quantum mechanical theory of electrons

[17] The Lorentz Theory of the electron for example [77].

and nuclei interacting with quantized radiation in the low-energy regime is an active area of research in mathematical physics concerned with the stability of matter, the existence of the thermodynamic limit *etc.*, but with no particular reference to features of chemical interest [78–82].

The presentation of a presumed exact bound state solution of the Schrödinger Coulomb Hamiltonian as a product of electronic and nuclear factors has been considered both by Hunter [83] and, more recently, by Gross et al. [84]. For present purposes the Hunter approach will be employed on the translationally invariant form of the internal Hamiltonian, given earlier (in Sect. 1.3.3). Were the exact solution known, Hunter argues that it could be written in the form

$$\psi\left(\mathbf{t}^{\mathrm{n}}, \mathbf{t}^{\mathrm{e}}\right) = \chi\left(\mathbf{t}^{\mathrm{n}}\right)\phi\left(\mathbf{t}^{\mathrm{n}}, \mathbf{t}^{\mathrm{e}}\right) \tag{1.45}$$

with the nuclear wave function defined by means of

$$\left|\chi\left(\mathbf{t}^{\mathrm{n}}\right)\right|^2 = \int \psi\left(\mathbf{t}^{\mathrm{n}}, \mathbf{t}^{\mathrm{e}}\right)^* \psi\left(\mathbf{t}^{\mathrm{n}}, \mathbf{t}^{\mathrm{e}}\right) d\mathbf{t}^{\mathrm{e}}. \tag{1.46}$$

Providing the function $\chi(\mathbf{t}^{\mathrm{n}})$ has no nodes,[18] an 'exact' electronic wavefunction could be constructed as

$$\phi\left(\mathbf{t}^{\mathrm{n}}, \mathbf{t}^{\mathrm{e}}\right) = \frac{\psi(\mathbf{t}^{\mathrm{n}}, \mathbf{t}^{\mathrm{e}})}{\chi\left(\mathbf{t}^{\mathrm{n}}\right)} \tag{1.47}$$

if the normalization choice

$$\int \phi\left(\mathbf{t}^{\mathrm{n}}, \mathbf{t}^{\mathrm{e}}\right)^* \phi\left(\mathbf{t}^{\mathrm{n}}, \mathbf{t}^{\mathrm{e}}\right) d\mathbf{t}^{\mathrm{e}} = 1$$

is made. The electronic wavefunction (1.47) is then properly defined, and a 'Potential Energy Surface' could be defined in terms of it by integrating out the electronic variables in the expectation value of the internal Hamiltonian in the state ϕ,

$$\mathsf{U}\left(\mathbf{t}^{\mathrm{n}}\right) = \int \phi\left(\mathbf{t}^{\mathrm{n}}, \mathbf{t}^{\mathrm{e}}\right)^* \hat{\mathrm{H}}'\left(\mathbf{t}^{\mathrm{n}}, \mathbf{t}^{\mathrm{e}}\right) \phi\left(\mathbf{t}^{\mathrm{n}}, \mathbf{t}^{\mathrm{e}}\right) d\mathbf{t}^{\mathrm{e}}. \tag{1.48}$$

The nuclear function χ is evidently quite different [86] from the usual approximate nuclear wavefunctions for vibrationally excited states which do have nodes.

Although no closed solutions to the full problem are known for a molecule, some extremely good approximate solutions have been obtained for excited vibrational states of H_2; Czub and Wolniewicz [87] took such an accurate approximation for an excited vibrational state in the $J = 0$ rotational state of H_2 and computed $\mathsf{U}(R)$. They found strong spikes in the potential close to two positions at which the usual vibrational wave function would have nodes. To quote [87]

[18] A similar requirement must be placed on the denominator in (12) of [85] for the equation to provide a secure definition.

> This destroys completely the concept of a single internuclear potential in diatomic molecules because it is not possible to introduce on the basis of non-adiabatic potentials a single, approximate, mean potential that would describe well more than one vibrational level.
> It is obvious that in the case of rotations the situation is even more complex.

Wilson suggested [88] that using the clamped-nuclei Hamiltonian instead of the full one in (1.48) to define the potential might avoid the spikes but Hunter in [86] showed why this was unlikely to be the case, and Cassam-Chenai [89] repeated the work of Czub and Wolniewicz using a clamped-nuclei electronic Hamiltonian and showed that exactly the same spiky behaviour occurred.

Another approach to this problem is in [84]; there is reason to believe however that this sort of difficulty is bound to arise whatever the approach. To see this, simply rewrite (1.45) to recognise that the exact states will actually have definite quantum numbers according to their symmetry, so that it would be more realistic to write

$$\psi_{JMpri}\left(\mathbf{t}^{\mathrm{n}}, \mathbf{t}^{\mathrm{e}}\right) = \chi_{JMPri}\left(\mathbf{t}^{\mathrm{n}}\right)\phi_{JMpri}\left(\mathbf{t}^{\mathrm{n}}, \mathbf{t}^{\mathrm{e}}\right). \tag{1.49}$$

In the H_2 study cited the first four quantum numbers are of no relevance, only i remains and here i labels the vibrational states. There is thus every reason to expect that the best that can be done from this approach is a distinct PES for each nuclear-motion state.

This anticipated behaviour seems to be confirmed in very accurate calculations on H_2 [90] for the electronic Σ ground state of the molecule assumed to dissociate into two hydrogen atoms in their ground states. That work shows that, for example, the $J = 0$ state supports just 14 vibrational states while the $J = 15$ state supports 10 and the $J = 31$ supports only 1 state. Of course in a diatomic molecule, states of different k are states which differ in the electronic angular momentum and these results cannot be regarded as typifying the results for a polyatomic system. However work on H_3^+ shows that in the case of $J = 0$ there are 1280 vibrational states below dissociation [91] and that 46 is the highest value of J for which at least one vibrational state exists [92]. At this level then it cannot be assumed that the potential surface calculated in the usual way is an approximation to anything exact.

The eigenstates of the full molecular Hamiltonian (the Coulomb Hamiltonian for the electrons and nuclei specified by a chemical formula)—a theory of an Isolated Molecule modeled on the quantum theory of the atom which we call the Isolated Molecule model—are reasonably well understood and might have some utility in a limited area of high-resolution experiments on very small molecules where questions of isomerism do not arise [93]. Their computation poses formidable problems, and really belongs to few-body physics. If it is to be taken as underlying Quantum Chemistry then it is worth exploring the consequences of the model without regard to approximations made for practical utility which are a quite separate matter. In this paper we have attempted to discuss the Born-Oppenheimer and Born approaches to the quantum theory of molecules in terms first set out by Combes [61]. The essential point is that the decomposition of the molecular Hamiltonian (with centre-of-mass contribution removed) into the nuclear kinetic energy, proportional to κ^4 and a remainder, is specified by (1.26), not by (1.9), or in other words, *(1.9) cannot be*

written with an = sign if the conventional interpretation of the X acting as parameters is made. Allowing the nuclear masses to increase without limit in $\hat{\mathsf{H}}^{\text{elec}}$ does not produce an operator with a discrete spectrum since this would just cause the mass polarisation term to vanish and the effective electronic mass to become the rest mass. As we have seen it leads to 'adiabatic divergence' [55].

It is thus not possible to reduce the molecular Schrödinger equation to a system of coupled differential equations of classical type for nuclei moving on Potential Energy Surfaces as suggested by Born. An *extra choice* of fixed nuclear positions must be made to give any discrete spectrum and normalizable L^2 eigenfunctions. In our view this choice, that is, the introduction of the clamped-nuclei Hamiltonian into the molecular theory as in Sect. 1.3.1, is the essence of what is commonly meant by the expression,[19] the 'Born-Oppenheimer approximation'

$$\hat{\mathsf{H}}^{\text{elec}} = \int_X^{\oplus} \hat{\mathsf{K}}\big(\mathbf{b}, \mathbf{t}^{\text{e}}\big)_o \, d\mathbf{b} \to \hat{\mathsf{K}}\big(\mathbf{b}, \mathbf{t}^{\text{e}}\big). \tag{1.50}$$

If the molecular Hamiltonian H were classical as in [36], the removal of the nuclear kinetic energy terms would indeed leave a Hamiltonian representing the electronic motion for stationary nuclei, as claimed by Born and Oppenheimer [38, 46]. As we have seen, quantization of H changes the situation drastically, so an implicit appeal to the classical limit for the nuclei is required. The argument is a subtle one, for subsequently, once the classical energy surface has emerged, the nuclei are treated as quantum particles for the determination of the vibration-rotation spectrum (though indistinguishability is rarely carried through); this can be seen from the complexity of the mathematical account given by Klein and co-workers [70].

This *qualitative* modification of the internal Hamiltonian, the extra choice of fixed nuclear positions in the 'electronic' Hamiltonian, is *ad hoc* in the same sense that Bohr's quantum theory of the atom is an *ad hoc* modification of classical mechanics. An essential feature of the answer is put in by hand. We know that both modifications have been tremendously useful and our point is not that something else must be done in practical calculations on molecules. The point is how the successful description of molecules involving the clamped-nuclei modification at some stage can best be understood in terms of quantum mechanics. In the case of the Bohr atom the resolution of the inconsistency in mechanics applied to the microscopic realm was achieved quite quickly with the formulation of quantum mechanics; in the molecular case, no such resolution is at present known.

Appendix

In this appendix we give an heuristic account of the mathematical notion of the direct integral of Hilbert spaces, and then study a simple model problem to illustrate the general ideas discussed in the paper.

[19] In its original form $\mathbf{b} = \mathbf{b}_o$, the equilibrium configuration, on the right-hand side of (1.50).

Consider a self-adjoint operator T that depends on a parameter X, so $T = T(X)$. The parameter $X = -\infty \leq X \leq +\infty$, covers the whole real line $\mathscr{R}$, and $T(X)$ is assumed to be defined for all X. $T(X)$ is an operator on a Hilbert space, which is denoted $\mathscr{H}(X)$; its eigenfunctions $\{\phi\}$ defined by

$$T(X)\phi(X)_k = \lambda_k(X)\phi(X)_k,$$

form a complete orthogonal set for the space $\mathscr{H}(X)$. The scalar product is

$$\langle \phi(X)_k | \phi(X)_j \rangle_X = \int \phi(X,x)^*_k \phi(X,x)_j dx = f(X)_{kj} \equiv f(X)\delta_{kj}, \quad f(X) < \infty \tag{1.51}$$

T may have discrete eigenvalues below a continuous spectrum that starts at Λ, that is

$$\sigma(X) = \sigma\big(T(X)\big) = \big[\lambda_0(X), \lambda_1(X), \ldots, \lambda_k(X)\big) \bigcup \big[\Lambda(X), \infty\big).$$

Now let's introduce a 'big' Hilbert space $\mathscr{H}$ as a *direct integral* over the $\{\mathscr{H}(X)\}$,

$$\mathscr{H} = \int_{\mathscr{R}}^{\oplus} \mathscr{H}(X) dX \tag{1.52}$$

and correspondingly the operator $\mathscr{T}$ acting on $\mathscr{H}$ defined by

$$\mathscr{T} = \int_{\mathscr{R}}^{\oplus} T(X) dX.$$

The scalar product on the big space $\mathscr{H}$ is defined explicitly in terms of (1.51) by

$$\langle \phi(X)_k | \phi(X)_j \rangle_{\mathscr{H}} := \int_{\mathscr{R}} \langle \phi(X)_k | \phi(X)_j \rangle_X dX < \infty. \tag{1.53}$$

In (1.51) one can always chose the functions $\{\phi_k\}$ to be orthonormalized independently of X,

$$f(X) = 1.$$

However this choice is not consistent with (1.53), which requires $f(X)$ to decrease sufficiently fast as $|X| \to \infty$ for the integral to exist. The mathematical motivation for this construction is this: the cartesian product of the spaces $\{\mathscr{H}(X)\}$,

$$\mathscr{F} = \prod_{X \in \mathscr{R}} \mathscr{H}(X)$$

is a field of Hilbert spaces over $\mathscr{R}$ which has a natural vector space structure. In modern geometric language, the Hilbert space $\mathscr{H}(X)$ is a fibre over a point X in a fibre bundle; $\mathscr{F}$ is the vector space of sections of this bundle. The subspace of $\mathscr{F}$ consisting of *square integrable* sections is the direct integral (1.52). The direct integral is the generalization to the continuous infinite dimensional case of the notion of the direct sum of finite dimensional vector spaces.

Purely as a heuristic explanation suppose initially that the parameter X has only two discrete values $\{X_1, X_2\}$. There are then two eigenvalue equations to consider, and two associated Hilbert spaces. In the direct sum space we have

$$\mathscr{T}_2 = T(X_1) \oplus T(X_2), \qquad \mathscr{H} = \mathscr{H}(X_1) \oplus \mathscr{H}(X_2).$$

The eigenfunctions of $\mathscr{T}_2$ are then two-dimensional column vectors, and so

$$\mathscr{T}_2 \begin{bmatrix} \phi(X_1)_k \\ \phi(X_2)_j \end{bmatrix} = \big(\lambda_k(X_1) + \lambda_j(X_2)\big) \begin{bmatrix} \phi(X_1)_k \\ \phi(X_2)_j \end{bmatrix}.$$

The spectrum of $\mathscr{T}_2$ is the union of the spectra of $T(X_1)$ and $T(X_2)$. This discussion is trivially extended to n points $\{X_k : k = 1, \ldots, n\}$, with the spectrum of $\mathscr{T}_n$ given by the union of the n operators $T(X_1), \ldots, T(X_n)$. The limit $n \to \infty$ is not trivial since it brings in important notions from topology and integration (measure theory) which we gloss over [94]. When these are taken into consideration however the result is that the spectrum σ of $\mathscr{T}$ is *purely continuous* since its direct integral representation implies that its spectrum is the union of the spectra of the infinite set of $T(X)$ operators,

$$\sigma = \sigma(\mathscr{T}) = \bigcup_X \sigma(X) \equiv [L_0, \infty) \tag{1.54}$$

where L_0 is the *minimum* value of $\lambda_0(X)$. The eigenvalue equation for $\mathscr{T}$ is,

$$\mathscr{T}\Phi_\Lambda = \Lambda\Phi_\Lambda, \quad L_0 \le \Lambda < \infty$$

with Λ a continuous index for the $\{\Phi\}$. Even if $T(X)$ is self-adjoint, it doesn't follow that its direct integral $\mathscr{T}$ is self-adjoint; that depends on specifics and has to be investigated. So the $\{\Phi\}$ cannot be assumed to be complete.

In the application of this mathematics to the Born-Oppenheimer approximation, the role of x is taken by the electronic coordinates $\mathbf{t}^e$, and X is to be identified with definite choices of the nuclear coordinates $\mathbf{b}$. If there are M nuclei the parameters $\mathbf{b}$ are elements of $\mathscr{R}^{3(M-1)}$. The operator $T(X)$ is the clamped-nuclei Hamiltonian $\hat{\mathsf{K}}(\mathbf{b}, \hat{\mathbf{t}}^e)_o = \hat{\mathsf{K}}_o$. With the conventional normalization of clamped-nuclei electronic eigenfunctions independent of the nuclear positions $\mathbf{b}$, the formal eigenvectors, (1.36), [56] of $\hat{\mathsf{H}}^{\text{elec}}$ do not belong to the Hilbert space $\mathscr{H}$; this simply reflects the loose use of the Dirac delta function for the position operator eigenfunctions.

We now consider a concrete model consisting of coupled harmonic oscillators with two degrees of freedom; we try to mimic the steps taken in the usual Born-Oppenheimer discussion. Consider the following Hamiltonian where κ and a are dimensionless constants[20]

$$\hat{\mathsf{H}} = \hat{\mathsf{p}}^2 + \kappa^4\hat{\mathsf{P}}^2 + \hat{\mathsf{x}}^2 + \hat{\mathsf{X}}^2 + a\hat{\mathsf{x}}\hat{\mathsf{X}}. \tag{1.55}$$

[20]The variables are expressed in dimensionless form for simplicity. The quantum oscillator $\hat{\mathsf{h}} = \frac{1}{2}(\hat{\mathsf{p}}^2 + \hat{\mathsf{q}}^2)$ has eigenvalues $n + \frac{1}{2}$.

The only non-zero commutators of the operators are

$$[\hat{\mathsf{x}}, \hat{\mathsf{p}}] = i, \qquad [\hat{\mathsf{X}}, \hat{\mathsf{P}}] = i.$$

Following the conventional discussion of electron-nuclear separation outlined in Sects. 1.3.1, 1.3.2, define

$$\hat{\mathsf{H}}_o = \hat{\mathsf{p}}^2 + \hat{\mathsf{x}}^2 + a\hat{\mathsf{x}}\hat{\mathsf{X}} + \hat{\mathsf{X}}^2 \tag{1.56}$$

$$\hat{\mathsf{H}}_1 = \hat{\mathsf{P}}^2 \tag{1.57}$$

so that

$$\hat{\mathsf{H}} = \hat{\mathsf{H}}_o + \kappa^4 \hat{\mathsf{H}}_1 \tag{1.58}$$

with Schrödinger equation

$$(\hat{\mathsf{H}} - E)\Psi = 0. \tag{1.59}$$

We note that

$$[\hat{\mathsf{H}}_o, \hat{\mathsf{H}}_1] \neq 0 \tag{1.60}$$

so the two parts cannot be simultaneously diagonalized. A principal axis transformation of the whole expression $\hat{\mathsf{H}}$ brings it to separable form, but we do not need to pursue explicitly the full solution here.

On the other hand

$$[\hat{\mathsf{H}}_o, \hat{\mathsf{X}}] = 0 \tag{1.61}$$

so these two operators may be simultaneously diagonalized, and consider $\hat{\mathsf{H}}_o$ at a definite eigenvalue of $\hat{\mathsf{X}}$, say X

$$\hat{\mathsf{K}}_o = \hat{\mathsf{p}}^2 + \hat{\mathsf{x}}^2 + a\hat{\mathsf{x}}X + X^2. \tag{1.62}$$

This is the Hamiltonian (in the variables $\hat{\mathsf{x}}, \hat{\mathsf{p}}$) of a displaced oscillator in which X is a (c-number) parameter, with Schrödinger equation in position representation

$$\hat{\mathsf{K}}_o \varphi(x, X)_n = E_n(X)\varphi(x, X)_n \tag{1.63}$$

$\hat{\mathsf{K}}_o$ is the analogue in this model of the 'clamped-nuclei' electronic Hamiltonian.

The solution is immediate; we make a unitary transformation by introducing a displaced coordinate involving X

$$\hat{\mathsf{x}}' = \hat{\mathsf{x}} - \frac{1}{2}aX, \qquad \hat{\mathsf{p}}' = \hat{\mathsf{p}} \tag{1.64}$$

$$\hat{\mathsf{U}} = e^{iaX\hat{\mathsf{p}}/2}, \qquad \hat{\mathsf{K}}'_o = \hat{\mathsf{U}}^{-1}\hat{\mathsf{K}}_0\hat{\mathsf{U}} \tag{1.65}$$

so that the transformed $\hat{\mathsf{K}}_o$ in the new variables is

$$\hat{\mathsf{K}}'_o = \hat{\mathsf{p}}'^2 + \hat{\mathsf{x}}'^2 + \left(1 - \frac{a^2}{4}\right)X^2$$

which has oscillator eigenvalues and eigenfunctions

$$E_n(X) = E_n^0 + \left(1 - \frac{a^2}{4}\right)X^2, \qquad \varphi(x')_n \tag{1.66}$$

where $x' = x - \frac{aX}{2}$, the $\{\varphi_n\}$ are the usual harmonic oscillator eigenfunctions and E_n^0 is the energy of the free oscillator $2(n + \frac{1}{2})$. For fixed n the spectrum $\sigma(X)$ is discrete and, as a function of the X parameters, would be conventionally interpreted as a 'potential energy curve'. As far as (1.58) is concerned, $\hat{\mathsf{K}}_o$, evaluated at some point X_0 *cannot* be regarded as an 'approximation' to $\hat{\mathsf{H}}_o$, since obviously

$$\left[\hat{\mathsf{K}}_o(X_0), \hat{\mathsf{H}}_1\right] = 0$$

so they can be simultaneously diagonalized, and $\hat{\mathsf{H}}_1$ has purely continuous spectrum (free motion). So we have to consider X in the full problem in its operator form, $\hat{\mathsf{X}}$.

We make the same unitary transformation of the $\hat{\mathsf{x}}, \hat{\mathsf{p}}$ variables in $\hat{\mathsf{H}}_o$ as before, and it is still brought to diagonal form; however $\hat{\mathsf{H}}_1$ will be modified because $\hat{\mathsf{P}}$ is also translated by the operator $\hat{\mathsf{U}}$ in (1.65) that generates the coordinate displacement (cf. (1.60)); thus

$$\hat{\mathsf{U}}^{-1}\hat{\mathsf{P}}\hat{\mathsf{U}} = \hat{\mathsf{P}} + \frac{1}{2}a\hat{\mathsf{p}}$$

so the transform of $\hat{\mathsf{H}}_1$ contains linear and quadratic terms in $\hat{\mathsf{p}}$.

Nevertheless (1.61) is still valid, and formally we may write $\hat{\mathsf{H}}_0$ as a direct integral

$$\hat{\mathsf{H}}_o = \int_X^{\oplus} \hat{\mathsf{K}}(\hat{\mathsf{x}}, \hat{\mathsf{p}}, X)_o dX. \tag{1.67}$$

The Schrödinger equation for $\hat{\mathsf{H}}_o$ in position representation is now an equation involving functions of x and X

$$\hat{\mathsf{H}}_o \Phi_\varepsilon(x', X) = \varepsilon \Phi_\varepsilon(x', X). \tag{1.68}$$

Just as before (see (1.54)) the direct integral decomposition (1.67) implies that the spectrum is purely continuous, explicitly

$$\sigma(\hat{\mathsf{H}}_o) = \bigcup_X \sigma(X) = [1, \infty). \tag{1.69}$$

ε in (1.68) takes all positive values ≥ 1, where 1 is the *minimum* value of the oscillator eigenvalue $2(n + \frac{1}{2})$. The associated continuum eigenfunctions $\{\Phi\}$ may formally be written as products of oscillator eigenfunctions (in x'), and delta functions (in X). They don't lie in Hilbert space of course and one needs the Gel'fand construction of a rigged space to make sense of the formal calculation [95]. If one returns to the x variable, the $\{\varphi_n\}$ are functions of x and X, since $x' = x'(X)$.

One can't do anything very useful with the direct integral expression (1.67) for $\hat{\mathsf{H}}_o$ apart from adding it onto the κ^4 term, which just returns us to the full problem. The full wavefunction in (1.59) can be expanded as

$$\Psi\left(x', X\right) = \int\!\!\!\!\!\!\sum_{n,X'} \varphi\left(x'\left(X'\right)\right)\delta\left(X - X'\right)c\left(X'\right)_n dX' \tag{1.70}$$

$$= \sum_n c(X)_n \varphi\left(x'(X)\right)_n \tag{1.71}$$

which obviously leads towards a variational approach [56]; such expansions rely on the completeness of the states employed. In this simple problem there is no difficulty, but as noted earlier, in realistic Coulomb systems it is much less clear that a complete set of states is available.

However that may be, let us rehearse again the argument due to Born summarized in Sect. 1.3.2. We substitute (1.71) in (1.59), left multiply by φ_m^* and integrate out the x' variables to leave an equation for the coefficients $\{c(X)_n\}$,

$$\int dx' \varphi\left(x'(X)\right)_m^* \left[\hat{\mathsf{H}}_o + \kappa^4 \hat{\mathsf{H}}_1\right] \sum_n c(X)_n \varphi\left(x'(X)\right)_n$$

$$= E \int dx' \varphi\left(x'(X)\right)_m^* \sum_n c(X)_n \varphi\left(x'(X)\right)_n. \tag{1.72}$$

At this point in the conventional account, $\hat{\mathsf{H}}_o$ is replaced by $\hat{\mathsf{K}}_o$, (1.62), and then the action of $\hat{\mathsf{K}}_o$ on the functions $\{\varphi\}$ in (1.72) can be evaluated using (1.63) in the well-known way,

$$\hat{\mathsf{H}}_o \varphi\left(x'(X)\right)_n \to \hat{\mathsf{K}}_o \varphi\left(x'(X)\right)_n = \varepsilon(X)_n \varphi\left(x'(X)\right)_n.$$

From the foregoing discussion it is clear that the substitution of $\hat{\mathsf{H}}_o$ by $\hat{\mathsf{K}}_o$ makes a *qualitative* change in the theory. This change does seem to be the 'right' thing to do, but so far there is *no* explanation as to *why* this is so.

References

1. Löwdin P-O (1989) Pure Appl Chem 61:2065–2074
2. Thomson JJ (1899) Philos Mag 48:547–567
3. Woolley RG, Sutcliffe BT (2003) In: Brändas EJ, Kryachko ES (eds) Fundamental world of quantum chemistry, vol 1. Kluwer Academic, Dordrecht
4. Sutcliffe BT, Woolley RG (2012) J Chem Phys 137:22A544
5. Marcelin R (1914) Contribution à l'étude de la cinétique physico-chimique. Gauthier-Villars, Paris
6. Marcelin R (1915) Ann Phys 3:120–231
7. Marcelin R (1914) C R Hebd Séances Acad Sci 158:116–118
8. Marcelin R (1914) C R Hebd Séances Acad Sci 158:407–409
9. Gibbs JW (1902) Elementary principles in statistical mechanics. C. Scribner, New York

10. Navarro L (1998) Arch Hist Exact Sci 53:147–180
11. Duhem P (1911) Traité d'énergétique, 2 vols. Gauthier-Villars, Paris
12. Pelzer H, Wigner EP (1932) Z Phys Chem Abt B 15:445–471
13. Wigner EP (1938) Trans Faraday Soc 34:29–41
14. Laidler KJ, King MC (1983) J Phys Chem 87:2657–2664
15. Waalkens H, Schubert R, Wiggins S (2008) Nonlinearity 21:R1–R118
16. Earnshaw S (1842) Trans Camb Philos Soc 7:97–112
17. Bohr N (1922) The structure of the atom. Nobel Lecture, December 11. Available online as http://www.nobelprize.org/nobel_prizes/physics/laureates/1922/Bohr-lecture.html
18. Bohr N (1913) Philos Mag 26:1–25
19. Schwarzschild K (1916) Sitzber Preuss Akad Wiss 1:548–561
20. Heurlinger T (1919) Z Phys 20:188–190
21. Born M (1925) Vorlesungen über Atommechanik. Springer, Berlin. The mechanics of the atom. Translated by JW Fisher (1927). George Bell and Sons, London
22. Sommerfeld A (1919) Atombau und Spektrallinien. Verlag F Vieweg und Sohn, Braunschweig
23. Ehrenfest P (1916) Ann Phys 356:327–352
24. Bohr N (1918) Kgl Danske Vid Selskab 4:1–36
25. Bohr N (1923) Z Phys 13:117–165
26. Berry MV (1984) J Phys A, Math Gen 17:1225–1233
27. Gutzwiller M (1998) Rev Mod Phys 70:589–639
28. Percival IC (1973) J Phys B, Atom Mol Phys 6:L229–L232
29. Thirring W (1987) In: Kilmister CW (ed) Schrödinger, centenary celebrations of a polymath. Cambridge University Press, Cambridge
30. Poincaré H (1899) Les méthodes nouvelles de la mécanique céleste. Gauthier-Villars, Paris
31. Einstein A (1917) Verh Dtsch Phys Ges 19:82–92
32. Pauli W (1922) Ann Phys 68:177–240
33. Nordheim L (1923) Z Phys 19:69–93
34. Kemble EC (1926) Molecular spectra of gases. Bull NRC 11(57):303–304
35. Kragh H (2012) Neils Bohr and the quantum atom: the Bohr model of atomic structure, 1913–1925. Oxford University Press, Oxford, p 239
36. Born M, Heisenberg W (1924) Ann Phys 74:1–31
37. Eckart C (1935) Phys Rev 47:552–558
38. Born M, Oppenheimer JR (1927) Ann Phys 84:457–484
39. Heitler W, London F (1927) Z Phys 44:455–472
40. London F (1928) In: Quantentheorie und Chemie. Hirzel, Leipzig, p 59
41. London F (1928) In: Probleme der modernen Physik. Hirzel, Leipzig, p 104
42. Slater JC (1927) Proc Natl Acad Sci 13:423–430
43. Born M, Fock V (1928) Z Phys 51:165–180
44. Born M, Huang K (1954) Dynamical theory of crystal lattices. Clarendon, Oxford
45. Lathouwers L, van Leuven P (1982) Adv Chem Phys 49:115–189
46. An English language translation of the original paper can be found at www.ulb.ac.be/cpm/people/scientists/bsutclif/main.html
47. Sutcliffe BT (1990) In: Maksic ZB (ed) Theoretical models of chemical bonding, part 1. Springer, Berlin, pp 1–28
48. Pauling L, Wilson EB Jr. (1935) Introduction to quantum mechanics. McGraw-Hill, New York. See especially Chap X, p 262
49. Born M (1951) Nachr. Akad. Wiss. Göttingen. Math-Phys. Klasse IIa. Math Phys Chem Abt, S Art Nr 6:1–3
50. O'Malley TF (1971) Adv At Mol Phys 7:223–249
51. Hall GG (1987) Int J Quant Chem XXXI:383–391
52. Loss M, Miyao T, Spohn H (2007) J Funct Anal 243:353–393
53. Reed M, Simon B (1978) Analysis of operators. Methods of modern mathematical physics, vol IV. Academic Press, New York

54. Kato T (1951) Trans Am Math Soc 70:195–218
55. Frolov AM (1999) Phys Rev A 59:4270–4280
56. Messiah A (1961) Quantum mechanics. North-Holland, Amsterdam
57. Bastiaan JB, Bowman JM (2009) Int Rev Phys Chem 28:577–606
58. Broeckhove J, Lathouwers L, van Leuven P (1991) J Math Chem 6:207–241
59. Mead CA (1992) Rev Mod Phys 64:51–85
60. Faure F, Zhilinskii B (2002) Phys Lett A 302:242–252
61. Combes J-M (1975) In: International symposium on mathematical physics, Kyoto University, Kyoto. Lecture notes in physics, vol 39, pp 467–471
62. Combes J-M (1977) Acta Phys Austriaca Suppl XVII:139–159
63. Combes J-M, Seiler R (1980) Quantum dynamics of molecules. In: Woolley RG (ed) NATO ASI B57. Plenum, New York
64. Combes J-M, Duclos P, Seiler R (1981) In: Velo G, Wightman A (eds) Rigorous atomic and molecular physics. Plenum, New York
65. Löwdin P-O (1966) Perturbation theory and its application in quantum mechanics. In: Wilcox CH (ed) Proceedings of Madison symposium. Wiley, New York
66. Zhislin G (1960) Tr Mosc Mat Obsc 9:81–128
67. van Winter C (1964) Kgl Danske Vid Selskab 1:1–60
68. Hunziker W (1966) Helv Phys Acta 39:451–462
69. Hagedorn GA, Joye A (2007) In: Gesztezy F, Deift P, Galvez C, Perry P, Schlag GW (eds) Spectral theory and mathematical physics. A festschrift in honor of Barry Simon's 60th birthday. Oxford University Press, London, p 203
70. Klein M, Martinez A, Seiler R, Wang XP (1992) Commun Math Phys 143:607–639
71. Feffermann CL (1983) Bull Am Math Soc 9:129–206
72. Hagedorn GA, Joye A (1999) Rev Math Phys 11:41–101
73. Primas H (1983) Chemistry, quantum mechanics and reductionism, 2nd edn. Springer, Berlin
74. Woolley RG (1980) Isr J Chem 19:30–46
75. Woolley RG (1982) Struct Bond (Springer) 52:1–35
76. Anderson PW (1984) Basic notions of condensed matter physics. Benjamin-Cummings, Redwood City
77. Lorentz HA (1909) The theory of electrons and its applications to the phenomena of light and radiant heat. Teubner, Leipzig
78. Lieb EH, Loss M (2003) Adv Theor Math Phys 7:667–710
79. Lieb EH, Loss M (2005) Commun Math Phys 258:675–695
80. Hasler D, Herbst I (2008) Commun Math Phys 279:769–787
81. Loss M, Miyao T, Spohn H (2009) Lett Math Phys 89:21–31
82. Lieb EH, Seiringer R (2010) The stability of matter in quantum mechanics. Cambridge University Press, Cambridge
83. Hunter G (1975) Int J Quant Chem 9:237–242
84. Abedi A, Matra NT, Gross EKU (2010) Phys Rev Lett 105:123002
85. Kutzelnigg W (2007) Mol Phys 105:2627–2647
86. Hunter G (1981) Int J Quant Chem 19:755–761
87. Czub J, Wolniewicz L (1978) Mol Phys 36:1301–1305
88. Wilson EB Jr. (1979) Int J Quantum Chem, Symp 13:5–14
89. Cassam-Chenai P (2006) Chem Phys Lett 420:354–357
90. Pachuki K, Komasa J (2009) J Chem Phys 130:164113
91. Henderson JR, Tennyson J, Sutcliffe BT (1993) J Chem Phys 98:7191–7203
92. Miller S, Tennyson J (1988) Chem Phys Lett 145:117–120
93. Sutcliffe BT, Woolley RG (2005) Phys Chem Chem Phys 7:3664–3676
94. Dixmier J (1981) Von Neumann algebras. Elsevier/North-Holland, Amsterdam
95. Ballentine LE (1990) Quantum mechanics. Prentice-Hall, Englewood Cliffs

Chapter 2
A Comment on the Question of Degeneracies in Quantum Mechanics

Michal Svrček

Abstract The problem of degeneracies, descending from the Born-Oppenheimer (B-O) approximation serves as a "comeback backdoor" of the principle of complementarity, but on a much more subtle level. Quantum mechanics incorporates both mechanical and field theory features, which results in the well-known particle-wave aspects of complementarity. The degeneracy problem, however, prompts a new type of "property-object" complementary phenomena. This leads to serious consequences: Field theoretical methods, unlike mechanical ones, are incapable of separating the internal and the external degrees of freedom with respect to the centre of gravity, but on the other hand adapt relativistically in a natural manner very similar to the space-time formulas of Maxwell's equations. The solutions of the quantum field equations, relativistic in the mentioned specific sense, yield singularities at symmetric points that correspond to the well-known B-O degeneracies giving the latter in actual fact a metaphysical attribute. However, Nature has in this case a more sophisticated method or modus operandi to avoid degenerations and to instigate symmetry violations.

In quantum mechanics, we often encounter degenerate states, which are authentic and experimentally detectable. The most famous case of degeneracy removal is the splitting of states under the influence of external electric or magnetic fields (Stark and Zeeman effects). On the other hand, we also often come across virtual degenerate states that are the product of a simplified Hamiltonian, which we usually have to choose due to the possibility of a realistic analytical solution when the total Hamiltonian does not directly provide such a solution. Since the step toward the answer exploit the principle of superposition, the simplified Hamiltonian may lead to non-existent fictional degenerations, which are eventually eliminated when taking the total Hamiltonian into consideration. This removal is either resolved in perturbation theory or in a non-perturbative approach based on multiconfigurational interaction.

Realistic degenerate states are mostly well defined and they do not therefore need to be considered further here. In contrast, in the case of so-called virtual degenerate

M. Svrček (✉)
Centre de Mécanique Ondulatoire Appliquée, CMOA Czech Branch, Carlsbad, Czech Republic
e-mail: m.sv@o2active.cz

M. Hotokka et al. (eds.), *Advances in Quantum Methods and Applications in Chemistry, Physics, and Biology*, Progress in Theoretical Chemistry and Physics 27,
DOI 10.1007/978-3-319-01529-3_2,

states there are many unresolved questions. A typical example is the situation of degenerate states arising in connection with the use of the Born-Oppenheimer (B-O) approximation [1]. Since the wave function of the system of electrons and nuclei can be decomposed due to their small mass ratio m/M into

$$\Psi(\mathbf{r},\mathbf{R}) = \psi(\mathbf{r},\mathbf{R})\chi(\mathbf{R}) \tag{2.1}$$

we can separately solve the equations for the electron and the nuclear states. Quantization is carried out in a hierarchical manner: First the electron states are parametrically quantized at given internuclear distances $\mathbf{R}$

$$H_e(\mathbf{R})\big|\psi(\mathbf{r},\mathbf{R})\big\rangle = E_e(\mathbf{R})\big|\psi(\mathbf{r},\mathbf{R})\big\rangle \tag{2.2}$$

after which the introduction of the kinetic energy of electrons, T_e, the electron-nuclear and two-electron potentials, E_{eN} and E_{ee}, respectively, the electron Hamiltonian H_e in Eq. (2.2) is expressed as

$$H_e = T_e(\mathbf{r}) + E_{eN}(\mathbf{r},\mathbf{R}) + E_{ee}(\mathbf{r}). \tag{2.3}$$

Finally the nuclear motions are quantized as

$$H_N\big|\chi(\mathbf{R})\big\rangle = E\big|\chi(\mathbf{R})\big\rangle \tag{2.4}$$

where one obtains for the nuclear Hamiltonian in Eq. (2.4) (T_N is the kinetic energy of nuclei and E_{NN} the internuclear potential)

$$H_N = T_N(\mathbf{R}) + E_{NN}(\mathbf{R}) + E_e(\mathbf{R}). \tag{2.5}$$

When Eq. (2.2), at the nuclear equilibrium position, causes a degenerate solution, represented by the crossing of two or more potential surfaces, the Jahn-Teller (J-T) effect [2] shows up. The usual responses to this impasse are the incorporation of standard non-adiabatic corrections as the only cure capable of removing the degeneracies originating from the B-O approximation.

There would be no further reason to think about the origin of this type of degeneracies, if field theoretic methods did not exist. In the latter situation, with an approach, borrowed from quantum electrodynamics and made operational within quantum mechanics and furthermore widely used in the theory of solids, we are in fact facing a similar degeneracy problem, but with a completely different method of solution regarding degeneracy removal. Perhaps the most famous is the model field Hamiltonian

$$H = \sum_{\mathbf{k},\sigma} \varepsilon_{\mathbf{k}} a^{+}_{\mathbf{k},\sigma} a_{\mathbf{k},\sigma} + \sum_{\mathbf{q}} \hbar\omega_{\mathbf{q}} \left(b^{+}_{\mathbf{q}} b_{\mathbf{q}} + 1/2\right) + \sum_{\mathbf{k},\mathbf{q},\sigma} u^{\mathbf{q}} \left(b_{\mathbf{q}} + b^{+}_{-\mathbf{q}}\right) a^{+}_{\mathbf{k}+\mathbf{q},\sigma} a_{\mathbf{k},\sigma}. \tag{2.6}$$

Now the question arises how Eq. (2.6) relates with the B-O approximation. Electron and electron-phonon terms come from the second quantization of Eq. (2.3) neglecting the two-electron term, i.e. $T_e + E_{eN}$. The phonon term comes from the

second quantization of the B-O equation (2.5), i.e. $T_N + E_{NN} + E_e$. This means that whenever the system is in a degenerate situation in a quantum mechanical description, according to Eq. (2.2), it is simultaneously degenerate in the quantum field description, see to Eq. (2.6). What is indeed striking is the way the quantum mechanical approach on the one hand and the field theoretical approach on the other hand, in reality are capable to eliminate the degeneracy. The mechanical approach leads to multiconfigurational interaction descriptions including all intersecting potential surfaces, as is standard practice in the theory of J-T effect [3, 4], while the field theoretical approach uses the Fröhlich transformation [13] (which, unfortunately, is unable to remove the degeneracies) and subsequently the Bogoljubov-Valatin transformation [5], the latter reflecting the BCS theory [6], as is customary in the theory of superconductivity. Both approaches lead to broken symmetries. Again we find here a striking difference: the mechanical approach of the J-T effect leads to a structural symmetry breaking, whereas symmetry violations in the field theoretical approach to BCS theory relates to charge superselection rule violation.

At this point, we may correctly speculate over the differences between the two approaches, quantum mechanical and quantum field theoretical ones, and in particular over the origin of these differences as, e.g., resulting from the B-O approximation, and moreover how to completely bypass this almost undefeatable approximation. It provides a certain type of virtual degeneracies, and therefore the question appears whether these are still justified and if there exists some higher principle, that would entirely circumvent such circumstances and arrive without more ado at the desired lifting of the degeneration.

Actually, there is an, in principle, exact formulation in quantum mechanics, considered by Monkhorst [7, 8], which ignores the B-O approximation, but, however, suffers some disadvantages. Firstly, it is not possible to derive analytic expressions for quantum mechanical measurable quantities, cf. the B-O separation procedure; and secondly, even with the best computers the computations are numerically exceedingly demanding. It is in effect prohibiting even going beyond such a humble endeavour as just about ten considered particles, electrons and nuclei included. Hence, unfortunately, it is quite impossible to consider systems where the B-O approximation leads to electronically degenerated states, such as those leading to the J-T effect or the mechanisms of superconductors.

Regarding quantum field methods, there do not seem to exist any definite techniques in consideration of how to construct a field that is not based on the B-O approximation, or in other words going further than the model Hamiltonian (2.6). This Hamiltonian representation has turned out to be especially advantageous in treating systems like insulators and conductors, but alas in superconductivity it points to the same problems in analogy with non-adiabatic corrections in the J-T problem, i.e. one obtains B-O degenerate states that we then try to eliminate in a subsequent treatment.

The primary problem of the B-O approximation is related to the centre-of-mass (COM) notion. It was indeed one of the main reasons why Monkhorst promoted his concept and entirely avoided to make this approximation. However, it also appears that the mistake to determine the centre of gravity in the B-O approximation may be

compensated via the Born-Huang (or Born-Handy) [9, 10] ansatz, which provides the lowest diagonal adiabatic correction to the B-O formulation. The Born-Handy ansatz has been tested numerous times, and it yields accurate results in agreement with experiment. The reason behind the popularity of the Born-Handy ansatz and why it has been so carefully verified was its approximate avoidance of the COM problem in the B-O separation. Handy's contribution consisted, in addition to formulating the procedure, in convincing the broad scientific community of the value of this pragmatic ansatz, without having to solve the full COM problem, which amongst other things demands the introduction of relative coordinates and masses. Kutzelnigg then gave the proof that the Born-Handy ansatz fully replaces the very complicated and difficult COM solution [11].

Unfortunately, there exists no analogy of the Born-Handy ansatz in the field theoretical equation (2.6), which would compensate for the error in the determination of the centre of mass by means of the B-O approximation. If we perform its generalization for systems without translational symmetry (applicable not only to crystals with translational symmetry but also to molecules), and subsequently applying the Fröhlich transformation (cf. Fröhlich's attempts to explain superconductivity [13]), we obtain, for the ground state of the hydrogen molecule, only about 20 % of the total adiabatic correlation energy, while, in quantum mechanics, the Born-Handy ansatz yields the correct result [14, 15]. Of course, insulators or conductors are not as sensitive to these effects, and there we prevail with Eq. (2.6). Nevertheless, cf. non-adiabatic effects in connection with superconductivity, we have to devote deeper thoughts to the correctness of the Hamiltonian representation (2.6).

As we proceed we will look in more detail at the COM separation problem as it appears in the B-O approximation. Equation (2.4) leads to a solution in terms of coupled oscillators, in which relative coordinates represent normal coordinates of the vibrational modes. After introducing the normal coordinates $B_r = b_r + b_r^+$ and $\tilde{B}_r = b_r - b_r^+$ for the kinetic and potential energies, respectively, of the nuclei in the effective field of the electrons, we have

$$H_{BO} = E_{kin}(\tilde{B}) + E_{pot}(B) \tag{2.7}$$

where the kinetic and potential energies are given by

$$E_{pot} = \frac{1}{4} \sum_{r \in V} \hbar\omega_r B_r^+ B_r \tag{2.8}$$

$$E_{kin} = \frac{1}{4} \sum_{r \in V} \hbar\omega_r \tilde{B}_r^+ \tilde{B}_r . \tag{2.9}$$

From the B-O separation we finally get the well-known vibrational Hamiltonian

$$H_{BO} = \frac{1}{4} \sum_{r \in V} \hbar\omega_r \left(B_r^+ B_r + \tilde{B}_r^+ \tilde{B}_r \right) = \sum_{r \in V} \hbar\omega_r \left(b_r^+ b_r + 1/2 \right). \tag{2.10}$$

The mechanical approach, based on this procedure, clearly separates the internal and the external degrees of freedom. The internal degrees correspond to vibrational

modes r, $r \in V$, and the external degrees are reflected in the translational degrees of freedom corresponding to the de Broglie wave of COM, and the rotational degrees of freedom corresponding to the quantized states of angular momentum, with eigenvalues of L^2 and L_3. An error in the determination of the centre of gravity is then entirely compensated by the Born-Handy ansatz, but only on the adiabatic level, as Kutzelnigg did prove [11].

The field theoretical approach, unfortunately, involves Eq. (2.10) as an ingredient in the total Hamiltonian (2.6) without any possibility to compensate for the COM factual error. Where is, however, the mistake? Is the error to be found in Eq. (2.10)? In considering this question, we get back to one of the fundamental problems of quantum mechanics, which for inexplicable reasons were never brought up for consideration. As is well-known, in quantum mechanics the mechanical and the field attributes are brought together, and this gives rise to recognized microscopic peculiarities, *viz.* the complementarity between the coordinate and the momentum representations, the alleged dualism of the considered entities, e.g., the appearance as particles or as waves, the non-commutativity between different classes of operators. Even if this has been correctly formulated for single-particle states, the general role of complementarity in quantum mechanics is not completely unraveled in this way. There is yet another manifestation of complementarity, which shows up at the many-body level, i.e. the degenerate states in the B-O many-body approximation just emerge as the reappearance through the backdoor of the fundamental principle of complementarity, however on a much more subtle level.

Equations (2.8) and (2.9) represent the standard quantum mechanical picture of vibrations as the properties of the system of electrons and nuclei. However, if we want to further include Eq. (2.10) in the ensuing field Hamiltonian (2.6), the vibrations must not be interpreted as properties only, but instead they are quantum mechanical objects themselves, ontologically equivalent with electrons. Hence, the external degrees of freedom cannot be separated from the internal ones, rather they are materialized in the form of quasiparticles, i.e. rotons and translons, cf. the internal degrees of freedom that are materialized e.g. in the form of phonons. This leads to a surprising deduction: Eqs. (2.8) and (2.9) have two mutually exclusive interpretations: firstly, they are the determining equations for the properties of electrons and nuclei, e.g. vibrations with a clear separation from the external degrees of freedom; or secondly, they are the generic equations for new quasiparticles, e.g. phonons, rotons and translons. In the latter case Eqs. (2.8) and (2.9) have the following solution:

$$E_{pot} = \frac{1}{4} \sum_{r \in V} \hbar \omega_r B_r^+ B_r \tag{2.11}$$

$$E_{kin} = \frac{1}{2} \left(\frac{1}{2} \sum_{r \in V} \hbar \omega_r + \sum_{r \in R} \rho_r + \sum_{r \in T} \tau_r \right) \tilde{B}_r^+ \tilde{B}_r . \tag{2.12}$$

Dual interpretations of the same equations with two alternate solutions, in the form of (2.8), (2.9) and (2.11), (2.12), result in a new type of complementarity.

Hence, in addition to the well-known particle-wave dualism, we discern here a new type of property-object dualism. Equations (2.11), (2.12) thus become the proper opening from the original mechanical formulation of the system of electrons and nuclei to the new field theoretic formulation of electrons, phonons, rotons and translons. There is here no reduction of the system into a subsystem with $3N - 5(6)$ degrees of freedom, as in the B-O case, but we must instead consider all $3N$ degrees, and as a replacement for vibrations, we introduce the concept of hypervibrations (vibrations + rotations + translations) and the corresponding hypervibrational double-vector

$$\boldsymbol{\omega} = \begin{pmatrix} \omega_r \\ \tilde{\omega}_r \end{pmatrix} = \begin{pmatrix} \omega_r & 0 & 0 \\ \omega_r & \frac{2}{\hbar}\rho_r & \frac{2}{\hbar}\tau_r \end{pmatrix} \tag{2.13}$$

from which we get covariant expressions for the boson hypervibrational Hamiltonian with respect to all $3N$ hypervibrational modes.

$$H_B = \frac{1}{4}\sum_r \left(\hbar\omega_r B_r^+ B_r + \hbar\tilde{\omega}_r \tilde{B}_r^+ \tilde{B}_r\right). \tag{2.14}$$

It is important to point out that this hypervibrational Hamiltonian (2.14), and not merely the vibrational Hamiltonian (2.10) must be used in the field equations of type (2.6). Consequently, while the mechanical pattern in quantum mechanics retains the classical separation of the degrees of freedom, the field theory pattern does not permit this, while binding together the internal and the external degrees in a relativistic manner. It may sound astonishing, but it looks like the second time in the history of physics, when we come across something similar. The space-time theory of relativity works in four-dimensions where the time can be seen as the fourth—external degree of freedom. This feature was not present in the classical mechanical laws of Newton, but it was finally discovered in the classical field equations known as Maxwell's equations, where the Lorentz transformation binds together space and time.

Although the property-object complementarity as well as the related relativistic nature of the degrees of freedom was not previously shown, Fröhlich, nevertheless, used the incomplete field Hamiltonian (2.6) and applied his transformation [13]

$$H' = e^{-S(Q,P)} H e^{S(Q,P)} \tag{2.15}$$

which refers only to the internal degrees of freedom. However, by attempting to remove the degeneracy in Eq. (2.6), and further, to get from the initial conducting state to the state of superconductivity the treatment fails since it would not produce the requisite gap. On the other hand we can generalize the Fröhlich transformation, and, instead of the ordinary vibrational modes, we will use the relativistic hypervibrational ones and in addition consider a general case without any translational symmetry requirement.

The following application, in accord with (2.15), of the two quasiparticle transformations, the first Q-dependent

$$\overline{a}_P = \sum_Q c_{PQ}(B) a_Q, \qquad \overline{b}_r = b_r + \sum_{PQ} d_{rPQ}(B) a_P^+ a_Q \tag{2.16}$$

with the unitary conditions

$$\sum_R c_{PR}(B) c_{QR}^+(B) = \delta_{PQ}, \qquad d_{rPQ} = \sum_R c_{RP}^+(B)\big[b_r, c_{RQ}(B)\big] \tag{2.17}$$

and the second P-dependent

$$\overline{a}_P = \sum_Q \tilde{c}_{PQ}(\tilde{B}) a_Q, \qquad \overline{b}_r = b_r + \sum_{PQ} \tilde{d}_{rPQ}(\tilde{B}) a_P^+ a_Q \tag{2.18}$$

with the unitary conditions

$$\sum_R \tilde{c}_{PR}(\tilde{B}) \tilde{c}_{QR}^+(\tilde{B}) = \delta_{PQ}, \qquad \tilde{d}_{rPQ} = \sum_R \tilde{c}_{RP}^+(\tilde{B})\big[b_r, \tilde{c}_{RQ}(\tilde{B})\big] \tag{2.19}$$

will lead to new systems of fermions and bosons. The diagonalization procedures permit choosing an optimal system, where we achieve a realistic separation into individual (quasi) fermions and bosons with minimal interaction between them.

Looking at this problem from the standpoint of group theory, we realize that we must adhere to the Poincaré group, as one of the most general group reflecting the full symmetry of special relativity, a problem seldom treated in full generality. Asking the question what would the most general group be that reflects the full symmetry of the Fröhlich transformation, or in other words, what would be the analogy of the Poincaré group for transformations carried out in the field theoretic methods of quantum mechanics. It can be shown that the Fröhlich transformation in Eq. (2.15) is decomposable into a product of two quasiparticle transformations: the coordinate (adiabatic) and the momentum (non-adiabatic) ones. We can perform the generalization to the case without the implied translational symmetry in a very simple way by replacing the quasimomentum/spin notation, which Fröhlich used in his original work, by the spinorbital notation. A further simple generalization can also be attempted, given that the quasiparticle transformations remain valid, by replacing the vibrational modes r, $r \in V$ by the hypervibrational modes r, $r \in \{V, R, T\}$.

We can now show that (2.16), (2.18) form a group. First we write their inverse transformations:

$$a_P = \sum_Q \overline{c}_{PQ}(\overline{B}) \overline{a}_Q, \qquad b_r = \overline{b}_r + \sum_{PQ} \overline{d}_{rPQ}(\overline{B}) \overline{a}_P^+ \overline{a}_Q \tag{2.20}$$

$$a_P = \sum_Q \overline{\tilde{c}}_{PQ}(\overline{\tilde{B}}) \overline{a}_Q, \qquad b_r = \overline{b}_r + \sum_{PQ} \overline{\tilde{d}}_{rPQ}(\overline{\tilde{B}}) \overline{a}_P^+ \overline{a}_Q. \tag{2.21}$$

It is easy to prove, see e.g. [17], that (2.16), (2.20) contain two invariants: the coordinate operator B and the number of fermion particles N

$$\overline{B}_r = B_r, \qquad \overline{N} = \sum_P \overline{a}_P^+ \overline{a}_P = \sum_P a_P^+ a_P = N \tag{2.22}$$

and further, the transformations (2.18), (2.21) contain also two invariants: the momentum operator $\tilde{B}$ and the number of fermion particles N

$$\overline{\tilde{B}}_r = \tilde{B}_r, \qquad \overline{N} = \sum_P \overline{a}_P^+ \overline{a}_P = \sum_P a_P^+ a_P = N. \tag{2.23}$$

Finally, the transformations (2.16), (2.18) and their inverses (2.20), (2.21) are tied up in a certain way:

$$\overline{c}_{PQ}(\overline{B}) = c_{QP}^+(B), \qquad \overline{d}_{rPQ}(\overline{B}) = -\sum_{RS} c_{PR}(B) d_{rRS}(B) c_{QS}^+(B) \tag{2.24}$$

$$\overline{\tilde{c}}_{PQ}(\overline{\tilde{B}}) = \tilde{c}_{QP}^+(\tilde{B}), \qquad \overline{\tilde{d}}_{rPQ}(\overline{\tilde{B}}) = -\sum_{RS} \tilde{c}_{PR}(\tilde{B}) \tilde{d}_{rRS}(\tilde{B}) \tilde{c}_{QS}^+(\tilde{B}). \tag{2.25}$$

Consequently we realize that (2.16), (2.18) actually form a group and thus all systems of fermions and bosons, obtained by these are equivalent. It is the most general group of transformations of the Fröhlich type. Unfortunately the Fröhlich treatment was sadly undervalued and it is now primarily remembered as an ad hoc transformation that Fröhlich applied to the Hamiltonian describing conductors, while the resulting Hamiltonian was eventually used in the BCS theory of superconductivity. However, from the generalized group structure it follows, that Fröhlich type transformations are of cardinal importance, not only in solids, but also generally in quantum chemistry, where they are regrettably still practically unused. In conclusion we point out that the main interest lies in that this generalized group combines the internal and external degrees of freedom in a relativistic fashion.

As is quite obvious the present understanding only needs a straightforward knowledge of the quantum nature of the harmonic oscillator. As an example we investigate how the harmonic oscillator manifests itself in a different way comparing the mechanical, see (2.8), (2.9), and in the field approach, see (2.11), (2.12). Hence we immediately arrive at the novel type of complementarity as based on the property-object dualism. Continuing further with the degrees of freedom, where they, in classical form, enter directly in the electron-nuclear Hamiltonian. As a result of the COM formulation, they represent the quantum form of vibrational, rotational and translational quanta—as quasiparticles, which transform according to the most general group (2.16), (2.18). In the mechanical method one does not recognize any translational quanta, but the in the field theoretical case one does! It is not possible to separate internal and external degrees of freedom in the field formulation in contrast to the mechanical approach, and therefore we attain a new kind of relativistic flavour in molecular and solid state structures. This variety of relativity is logically

of quantum origin! Again, as already pointed out, all the aforementioned statements are merely a consequence of the properties of the harmonic oscillator.

Let us now continue by applying the general transformations, (2.16), (2.18), to the field Hamiltonian. Here we will only sketch the derivation, since it is, however, very time-consuming. The final formula for the change of the ground state energy has a surprisingly simple analytical form. Details of the derivation have been given in previous work [15] as well as a more comprehensive discussion in [16].

For the correction of the ground state energy we finally get

$$\Delta E_0 = \sum_{AIr} \left(\hbar\tilde{\omega}_r \left| c^r_{AI} \right|^2 - \hbar\omega_r \left| \tilde{c}^r_{AI} \right|^2 \right) \tag{2.26}$$

where the summation refers to virtual spinorbitals A, occupied spinorbitals I, and all hypervibrational modes r, $r \in \{V, R, T\}$. The coefficients c resp. $\tilde{c}$ are related to the adiabatic and the non-adiabatic transformation, respectively, and determined by the set of equations

$$u^r_{PQ} + \left(\varepsilon^0_P - \varepsilon^0_Q\right) c^r_{PQ} + \sum_{AI} \left[\left(\nu^0_{PIQA} - \nu^0_{PIAQ}\right) c^r_{AI} - \left(\nu^0_{PAQI} - \nu^0_{PAIQ}\right) c^r_{IA} \right] - \hbar\omega_r \tilde{c}^r_{PQ} = \varepsilon^r_P \delta_{PQ} \tag{2.27}$$

$$\left(\varepsilon^0_P - \varepsilon^0_Q\right) \tilde{c}^r_{PQ} + \sum_{AI} \left[\left(\nu^0_{PIQA} - \nu^0_{PIAQ}\right) \tilde{c}^r_{AI} - \left(\nu^0_{PAQI} - \nu^0_{PAIQ}\right) \tilde{c}^r_{IA} \right] - \hbar\tilde{\omega}_r c^r_{PQ} = \tilde{\varepsilon}^r_P \delta_{PQ} \tag{2.28}$$

where u are the coefficients of the electron-hyperphonon interaction, ε^0 are one-electron energies, and ν^0 two-electron potential energies.

For the derivation we stress the most interesting three limits of Eq. (2.26):

(a) The adiabatic limit, which means that all non-adiabatic coefficients $\tilde{c}$ will be equal to zero. Thus, we obtain the adiabatic correction

$$\Delta E_{0(ad)} = \sum_{AIr} \hbar\tilde{\omega}_r \left| c^r_{AI} \right|^2 = 2 \sum_{AI} \left(\sum_{r\in V} \frac{1}{2} \hbar\omega_r + \sum_{r\in R} \rho_r + \sum_{r\in T} \tau_r \right) \left| c^r_{AI} \right|^2 \tag{2.29}$$

which we can directly compare with the Born-Handy ansatz. In the author's works [14, 15], the exact CPHF reformulation of the Born-Handy ansatz is displayed, leading to the identity between the field and the mechanical equations at the adiabatic level

$$\Delta E_{0(ad)} = \left\langle \psi(\mathbf{R}) \middle| T_N \middle| \psi(\mathbf{R}) \right\rangle_{R_0} = 2 \sum_{AI} \left(\sum_{r\in V} \frac{1}{2} \hbar\omega_r + \sum_{r\in R} \rho_r + \sum_{r\in T} \tau_r \right) \left| c^r_{AI} \right|^2 . \tag{2.30}$$

Numerical verification was performed on the molecules H_2, HD and D_2 [14]. It was surprising that the vibrational contribution only amounted about 20 %,

while the remaining 80 % consisted of rotational and translational contributions, even if considering molecules at rest, i.e. they neither rotate nor move. This comparison is very important because the field equations used in the theory of solids and derived from the B-O approximation, kept only the first term in (2.30), which is in complete contrast to the Born-Handy ansatz. From the identity of (2.29) and (2.30), we can clearly see how the mechanical and the field approaches get by differently with the inaccurate determination of the centre of gravity, however, eventually leading to the same results, i.e. that the mechanical Born-Handy ansatz is equivalent to the relativistic field correction.

(b) The non-relativistic limit + neglection of the two-electron terms. It means that the summation in Eq. (2.26) will involve only the internal degrees of freedom—phonons.

$$\Delta E_0 = \sum_{AI,r\in V} \left(\hbar\omega_r \left|c^r_{AI}\right|^2 - \hbar\omega_r \left|\tilde{c}^r_{AI}\right|^2\right) = \sum_{AI,r\in V} \left|u^r_{AI}\right|^2 \frac{\hbar\omega_r}{(\varepsilon^0_A - \varepsilon^0_I)^2 - (\hbar\omega_r)^2} \tag{2.31}$$

from which, after changeover from quantum chemical to solid state physics notation, we get exactly the same results as originally derived by Fröhlich [12, 13].

$$\Delta E_0 = 2 \sum_{\mathbf{k},\mathbf{k}';\mathbf{k}\neq\mathbf{k}'} \left|u^{\mathbf{k}'-\mathbf{k}}\right|^2 f_{\mathbf{k}}(1 - f_{\mathbf{k}'}) \frac{\hbar\omega_{\mathbf{k}'-\mathbf{k}}}{(\varepsilon^0_{\mathbf{k}'} - \varepsilon^0_{\mathbf{k}})^2 - (\hbar\omega_{\mathbf{k}'-\mathbf{k}})^2}. \tag{2.32}$$

Unfortunately, as mentioned above, this equation did not acquire the expected superconducting gap, as Fröhlich initially had expected. In fact the optimization of the occupation factors $f_{\mathbf{k}}$ yields some decrease of the total energy and Fröhlich then tried to interpret this new state as the superconducting state.

(c) The complete non-adiabatic and relativistic limit, where we only omit two-electron terms in order to obtain transparent analytical expression:

$$\Delta E_0 = \sum_{AIr} \left|u^r_{AI}\right|^2 \frac{\hbar\tilde{\omega}_r}{(\varepsilon^0_A - \varepsilon^0_I)^2 - (\hbar\omega_r)^2} \tag{2.33}$$

which in the form of the sum of vibrational, rotational and translational parts finally reads

$$\begin{aligned}\Delta E_0 = &\sum_{AI,r\in V} \left|u^r_{AI}\right|^2 \frac{\hbar\omega_r}{(\varepsilon^0_A - \varepsilon^0_I)^2 - (\hbar\omega_r)^2} \\ &+ 2 \sum_{AI,r\in R} \left|u^r_{AI}\right|^2 \frac{\rho_r}{(\varepsilon^0_A - \varepsilon^0_I)^2} + 2 \sum_{AI,r\in T} \left|u^r_{AI}\right|^2 \frac{\tau_r}{(\varepsilon^0_A - \varepsilon^0_I)^2}.\end{aligned} \tag{2.34}$$

After the rewriting Eq. (2.34) in solid state notation we obtain

$$\Delta E_0 = 2\sum_{\mathbf{k},\mathbf{k}'} \left|u^{\mathbf{k}'-\mathbf{k}}\right|^2 \frac{\hbar\omega_{o,\mathbf{k}'-\mathbf{k}}}{(\varepsilon^0_{c,\mathbf{k}'} - \varepsilon^0_{v,\mathbf{k}})^2 - (\hbar\omega_{o,\mathbf{k}'-\mathbf{k}})^2}$$
$$+ 4\sum_{\mathbf{k},r\in R} \left|u^r\right|^2 \frac{\rho_r}{(\varepsilon^0_{c,\mathbf{k}} - \varepsilon^0_{v,\mathbf{k}})^2} + 4\sum_{\mathbf{k},r\in T} \left|u^r\right|^2 \frac{\tau_r}{(\varepsilon^0_{c,\mathbf{k}} - \varepsilon^0_{v,\mathbf{k}})^2} \tag{2.35}$$

where o denotes the optical branches and c, v the conducting and the valence bands respectively.

Equations (2.34), (2.35) are indeed quite intriguing. Here degenerate states cannot exist unless all the matrix elements of electron-roton and electron-translon interactions are equal to zero. If not, these types of interactions induce singularities in symmetric points, where the system would be degenerate according to the B-O approximation. Rotons and translons thus cause symmetry breaking, which results in automatic elimination of system degeneracies. Degenerations resulting from the B-O approximation therefore constitute a metaphysical trait, as well as do the concepts of intersecting potential surfaces.

Unfortunately, many scientists consider real and virtual degeneracies to be of the same nature, as well as their removal, and that the J-T effect and superconductivity should be treated on an equal footing using the same quantum mechanical rules as e.g. the Stark and the Zeeman effects. As we have seen here this is not true. Nature has yet another, more sophisticated means to eliminate virtual degenerations, and not removing them in some perturbative or multiconfigurational way as usually carried out in the case of realistic ones.

The question arises how to interpret the B-O approximation, which entrusts a metaphysical essence to the resulting degeneracies. The development of quantum mechanics due to the practical but misleading B-O paradigm has somehow stalemated halfway between the mechanical and field theoretical methods, and exactly at the unlucky point where the corresponding complementarity cannot be seen at the same time leading to incorrect metaphysical conclusions. As a possible recipe the author recommends either to go back, totally ignoring the B-O procedure, like was done by Monkhorst in his concept which in fact is the only correct mechanical approach, or to go on to the concluding line, where the relativistic field approach ultimately appears. Despite some incongruousness's as regards the theory of special relativity, cf. the fulfillment of the group properties of the Poincaré group, the latter will not be fully solved until we have obtained a consistent quantum gravity theory.

Quantum mechanics is today considered to be a closed discipline; that means, it should not lead to any internal contradictions. As we have shown here, in this work, the transformed standard field Hamiltonian, compared with the Born-Handy ansatz, yields the same paradox as if trying to apply the Galilean transformation to Maxwell's equations. The only way out of this quantum mechanical crisis is to incorporate the concept of a relativistically noncontradictory structure of molecules and crystals, binding together their internal and external degrees of freedom in the same way as the Lorentz transformation binds together space and time. We then arrive at the more general concept of relativity principles, which concern explicitly internal and external degrees of freedom. Relativity of space and time forms

a special subclass, in which the three internal (spatial) and one external (time) coordinates are bound into a four-dimensional spacetime. Brändas recently opened a discussion of the possible quantum origin of Einstein's general relativity [18].

Here we have described a different subclass of relativity considerations, with reference to the structure of molecules and crystals, which follows as a direct result of the overlooked property-object dualism. The particle-wave dualism is not the only manifestation of Bohr's complementarity; there is also a more subtle property-object dualism. In conclusion we refer to the old controversy between Einstein and Bohr, with Einstein's answer to the puzzles of quantum mechanics: "God does not play dice." Thus we can understand the principle of relativity as a direct consequence of the general complementarity principle.

Acknowledgements The author wishes to express his gratitude to E. Brändas for a very careful reading of the manuscript and improvements of many linguistic and stylistic formulations.

References

1. Born M, Oppenheimer R (1927) Ann Phys (Leipzig) 84:457
2. Jahn HA, Teller E (1937) Proc R Soc London A 161:220
3. Köppel H, Domcke W, Cederbaum LS (1984) Adv Chem Phys 57:59
4. Bersuker IB (2006) The Jahn-Teller effect. Cambridge University Press, Cambridge
5. Bogoliubov NN (1958) Nuovo Cim 10 Ser 7:794
6. Bardeen J, Cooper LN, Schrieffer JR (1957) Phys Rev 108:1175
7. Monkhorst HJ (1987) Phys Rev A 36:1544
8. Cafiero M, Adamowicz L (2004) Chem Phys Lett 387:136
9. Born M, Huang K (1954) The dynamical theory of crystal lattices. Oxford University Press, London
10. Handy NC, Lee AM (1996) Chem Phys Lett 252:425
11. Kutzelnigg W (1997) Mol Phys 90:909
12. Fröhlich H (1950) Phys Rev 79:845
13. Fröhlich H (1952) Proc R Soc Lond A 215:291
14. Svrček M, Baňacký P, Biskupič S, Noga J, Pelikán P, Zajac A (1999) Chem Phys Lett 299:151
15. Svrček M (2012) In: Progress in theoretical chemistry and physics, vol 22. Springer, Berlin, pp 511–552. Part 7
16. Svrček M (2012). arXiv:1207.0711 [physics.gen-ph]
17. Svrček M (1992) In: Molecular vibrations. Methods in computational chemistry, vol 4. Plenum, New York, pp 150–202 (Chap 2-6.2) & pp 204–229 (Chap 7)
18. Brändas E (2009) Frontiers in quantum systems. In: Russo N, Antonchenko VYa, Kryachko E (eds) Chemistry and physics. NATO science for peace and security series A: chemistry and biology, vol 18. Springer, Dordrecht, pp 49–87

Chapter 3
The Dirac Electron as a Massless Charge Spinning at Light Speed: Implications on Some Basic Physical Concepts

Jean Maruani

Abstract The Dirac equation, which was derived by combining, in a consistent manner, the relativistic invariance condition with the quantum probability principle, has shown its fecundity by explaining the half-integer spin of fermions and predicting antimatter, the first resulting from a wave beat between a particle and its antiparticle. In the previous paper, it was conjectured that the spinning motion of the electron is that of a *massless charge* vibrating at *light speed*, and that this internal motion is responsible for the *rest mass* measured in external motions (inertia) and interactions (gravitation). In this paper, we develop implications of this concept on such basic properties as time, mass, electric charge, and magnetic moment.

> '[Now let man] search, amidst what he knows, the most delicate things. Let a *small insect* offer him, within his tiny body, incomparably smaller things .... Dividing these latter further, ..., the last object he can attain will be that of our discourse .... I want to present him a *new abyss* ... within this *embryo of an atom*. There, he will see an infinity of universes, each with its firmament, planets, earth, ..., animals, and eventually *small insects*, within which he will meet again what the former have given ....'
>
> Blaise Pascal (1623–1662), *Pensées* (translated from the French)

3.1 Introduction

Wave mechanics originated from a detailed analysis by Louis de Broglie [1] of the Maupertuis and Fermat principles in classical mechanics and classical optics, together with a comparison of Einstein's quantum frequency-energy relationship in for light ($\Delta E = h\nu$) and relativistic matter-energy relationship for matter ($E = mc^2$). This led him to the concept of matter waves:

$$\lambda_B = h/mv, \tag{3.1}$$

where m and v are the mass and velocity of the matter particle.

J. Maruani (✉)
Laboratoire de Chimie Physique-Matière et Rayonnement, CNRS & UPMC,
11, rue Pierre et Marie Curie, 75005 Paris, France
e-mail: jemmaran@gmail.com

M. Hotokka et al. (eds.), *Advances in Quantum Methods and Applications in Chemistry, Physics, and Biology*, Progress in Theoretical Chemistry and Physics 27,
DOI 10.1007/978-3-319-01529-3_3,

However, further developments in quantum mechanics (both in the Schrödinger and Heisenberg representations) used classical kinetic and potential energy expressions (with *spin* added as an *ansatz*), and were not Lorentz invariant. Contrary to the equations for the electric and magnetic components of the light waves, the Schrödinger equation for matter waves contains a first-order time derivative with second-order space derivatives. A relativistic energy was used in the Klein-Gordon equation, bringing time and space on the same footing but in a quadratic form which, while being compatible with the quantum superposition principle, led to a non-definite positive probability density and proved unsuitable for the description of particles endowed with rest mass and spin momentum.

Dirac made a breakthrough [2–5] by designing a relativistic equation which was linearized by introducing anticommutative 4-D matrices, which he expressed in terms of 2-D Pauli matrices. This implied 4-component state vectors or 4-valued wave functions with *double-valued spin and mass* as extra coordinates. It was noticed by de Broglie [6] that the process leading from the Klein-Gordon equation to the Dirac equation is similar to that leading from the second-order equations for the electric and magnetic fields $\underline{E}$ and $\underline{B}$ to the four coupled, first-order, Lorentz-invariant Maxwell equations for the scalar and vector potentials A_4 and $\underline{A}$.

Further consistency was reached by quantizing the electromagnetic field, which led to quantum electrodynamics [7] for the electron and other leptons. This served as a model to quantum chromodynamics [8] for particles involving quarks, such as nucleons and other baryons. Modern quantum field theory [9] encompasses the various cases. In these theories, the entanglement of matter and antimatter is expressed by the necessity to include particles and antiparticles on the same footing to cope with infinities.

De Broglie's wavelength λ_B was an outcome of a (theoretical) encounter of light and matter. Another outcome of a (physical) encounter of light and matter was Compton's wavelength λ_C [10]. When X-rays hit electrons (relatively) at rest, the wavelength λ_2 of a scattered photon differs from that λ_1 of the incident photon by a value: $\lambda_2 - \lambda_1 = \lambda_C(1 - \cos\theta)$, θ being the angle between the two X-rays and λ_C being given by:

$$\lambda_C = h/m_0 c, \tag{3.2}$$

where m_0 is the rest mass of the electron and c, the velocity of light.

From the definitions of λ_B and λ_C it appears that the former depends on the particle velocity v (and may thus vary from ∞ to 0) while the second depends solely on its rest mass (and universal constants). The relation between the two involves the Lorentz 'boost' transformation factor:

$$\lambda_C/\lambda_B = \beta\gamma, \tag{3.3}$$

where $\beta \equiv v/c$ and $\gamma \equiv (1 - \beta^2)^{-1/2}$ are coefficients of the Lorentz proper transformations.

De Broglie's wavelength is linked to the *external motion*, with momentum mv, of the particle wave packet, whereas Compton's wavelength seems to be linked to

some *internal motion*, involving a 'momentum' m_0c, within a 'ball' of width $2r_C$ determined by the Heisenberg uncertainty relation:

$$m_0c \cdot 2r_C \sim \hbar \quad \rightarrow \quad 2r_C \sim \hbar/m_0c = \lambda_C/2\pi. \tag{3.4}$$

This internal motion was identified by Schrödinger [11, 12] as a 'trembling motion' (*Zitterbewegung*), which vanishes when one takes expectation values over wave packets made up entirely of positive (or negative) energy solutions of the Dirac equation. This was understood by de Broglie [6] as resulting from a *wave beat* between the positive and negative energy states: $\pm mc^2$, the beat frequency being the difference of the two wave frequencies: $\nu_e = 2mc^2/h$. The amplitude of this internal motion was shown to be precisely $2r_C$.

Various authors have seen the electron as a *point charge* oscillating at *velocity* c within a ball of *radius* r_C [13–16, 18–21], and identified the *orbital momentum* of this motion to its *spin momentum* [17–21]. In a previous paper [22], we have conjectured that the *rest mass* involved in external motions (inertia) and interactions (gravitation) results *from this very internal motion*. In the present paper, we reassess our previous discussion and see how this may lead to some insights into basic physical concepts.

3.2 The Dirac Equation and the Electron Internal Motion

Today, the Dirac equation can be deduced from more general theoretical frameworks [7, 9, 23–26]. But the inductive derivation originally given by Dirac [2–5] has shown great heuristic value, and we shall summarize it with only a few notation changes. He started with the time-dependent wave equation for a free particle in the Schrödinger representation, the Hamiltonian being given the relativistic expression, $H = mc^2$:

$$i\hbar\partial\Psi/\partial(ct) = mc\Psi, \tag{3.5}$$

with the expanded form for mc:

$$mc = \left(m_0^2c^2 + p^2\right)^{1/2}. \tag{3.6}$$

Here, $p^2 = p_1^2 + p_2^2 + p_3^2$ with $p_i = mv_i$ along x_i, and $m = m_0\gamma$. Dimensionwise, one can define an overall 'momentum' $p_4 \equiv mc$ corresponding, according to Eq. (3.5), to the *time* coordinate $x_4 \equiv ct$, and an invariant 'momentum' $p_0 \equiv m_0c$ for a particle *at rest*. With these notations, Eq. (3.6) can be rewritten:

$$p_4^2 = p_0^2 + p_1^2 + p_2^2 + p_3^2. \tag{3.7}$$

This expression for the invariant (rest mass) 'momentum' p_0 is similar to that for the invariant (proper interval) 'coordinate' x_0:

$$x_4^2 \equiv x_0^2 + x_1^2 + x_2^2 + x_3^2. \tag{3.8}$$

The Minkowski 4-D relativistic space-time has a Lorentz (non-Euclidean) hyperbolic metric. However, as $x_4 \equiv ct$ appears as a *Pythagorean* sum of the three x_i's

plus x_0, and $p_4 \equiv mc$ of the three p_i's plus p_0, one may wonder if the Lorentz-invariant x_0 and p_0 do not point to some wrapped dimension related to a different metric. This is not to be confused with the fifth dimension designed to unify gravitation and magnetism in Kaluza-Klein theories [27], which pointed the way to string theories.

The Dirac equation was derived in several steps [5]. By analogy, Dirac first wrote:

$$p_i \rightarrow -i\hbar\partial/\partial x_i \quad (i = 1, 2, 3) \quad \text{and} \quad p_4 \rightarrow i\hbar\partial/\partial(ct). \tag{3.9}$$

One notices that there is no 'coordinate' derivative associated with the fifth, combined, invariant 'momentum' p_0. It has been proposed [26] to formally assign to this rest-mass momentum a combined operator: $i\hbar d/d(ct) = i\hbar[\partial/\partial(ct) + \boldsymbol{\alpha}.\nabla]$. But this amounts to a tautological reformulation of Eq. (3.11), not to a definition of a specific fifth dimension.

Substituting Eq. (3.7) into Eq. (3.5) with the generalized momenta p_μ replaced by their respective operators from Eq. (3.9) yields:

$$\left[p_4 - \left(p_0^2 + p_1^2 + p_2^2 + p_3^2\right)^{1/2}\right]\Psi = 0, \tag{3.10}$$

which is linear in p_4 but not in the other p_i's. Multiplying on the left side by the conjugate expression yields an equation that is *symmetric in all* p_μ's but *not linear in* p_4. Dirac's feat was to design a relativistic wave equation that was both symmetric and linear:

$$\left[p_4 - (\boldsymbol{\alpha_0} p_0 + \boldsymbol{\alpha_1} p_1 + \boldsymbol{\alpha_2} p_2 + \boldsymbol{\alpha_3} p_3)\right]\Psi = 0. \tag{3.11}$$

In order to yield the same solutions as Eq. (3.10), the $\boldsymbol{\alpha}_\mu$'s must be 4-D matrices commuting with the four p_μ's and satisfying, for $\mu, \nu = 0, 1, 2, 3$, the relations:

$$\boldsymbol{\alpha}_\mu^2 = \mathbf{1}, \qquad \boldsymbol{\alpha}_\mu \boldsymbol{\alpha}_\nu + \boldsymbol{\alpha}_\nu \boldsymbol{\alpha}_\mu = \mathbf{0}. \tag{3.12}$$

In the original, most common representation of the Dirac 4-D matrices $\boldsymbol{\alpha}_\mu$, the Pauli 2-D matrices $\boldsymbol{\sigma_i}$ are used as off-diagonal elements.

A result is that Ψ must be a *four-valued* wave function or a *four-component* state vector. It was already known that, in order to satisfy Pauli's antisymmetry condition, Ψ had to be endowed with a *two-valued internal dynamical variable*, which Dirac interpreted as being the *spin angular momentum*. But he also discovered that this number must be doubled because Eq. (3.11) has additional, *negative energy* solutions, which he assigned to an 'antielectron' with *opposite charge* [2–5]. The entanglement of the four components of Ψ when Eq. (3.11) is written in the explicit form of four coupled equations [6] shows that spin itself is related to the negative-energy states.

The electron spin first entered quantum mechanics through an *intrinsic magnetic moment* interacting with an external field. To have the electron magnetic moment show up, Dirac made it interact with an external field. And to have its spin momentum appear, he made it combine with an orbital momentum. Equation (3.11) was thus extended to include interactions with an electromagnetic field, with scalar and vector potentials A_4 and $\underline{A}$:

$$\left[(p_4 + eA_4/c) - \boldsymbol{\alpha}_0 p_0 - \boldsymbol{\alpha}.(\underline{p} + e\underline{A})\right]\Psi = 0. \tag{3.13}$$

One may notice that, while the 'time momentum' p_4 is affected by the electric potential A_4/c and the 'space momenta' $\underline{p}$ by the magnetic potential $\underline{A}$, the 'invariant momentum' p_0 is not affected by the external electromagnetic field.

Writing $H = m_0c^2 + H'$ and using the Heisenberg representation one obtains, to first order:

$$H' = p_4c - p_0c = -eA_4 + (\underline{p} + e\underline{A})^2/2m_0 + (e\hbar/2m_0)\underline{\boldsymbol{\sigma}} \cdot \underline{B}. \tag{3.14}$$

In addition to the classical potential and kinetic energy terms, there appears an extra term which was interpreted as being due to the interaction of an *intrinsic magnetic moment*: $\mu = -(e\hbar/2m_0)\underline{\boldsymbol{\sigma}}$, with the magnetic field $\underline{B}$.

The spin angular momentum does not give rise to any *potential* energy. To show its existence, Dirac computed the angular momentum integrals for an electron moving in a central *electric* field (e.g., that of a nucleus), i.e.:

$$H = p_4c = -eA_4(r) + c\boldsymbol{\alpha_0}p_0 + c\underline{\boldsymbol{\alpha}} \cdot \underline{p}. \tag{3.15}$$

For a component l_1 of the *orbital* angular momentum: $\underline{l} = -i\hbar \underline{r} x \underline{\nabla}$, Dirac obtained a non-zero expression for $i\hbar\partial l_1/\partial t$, and similarly for the corresponding component σ_1 of the Pauli matrix/operator vector used to build the Dirac matrices $\boldsymbol{\alpha}_\mu$. Neither $\underline{l}$ nor $\underline{\sigma}$ was then a constant of the motion; but the sum was:

$$\partial l_1/\partial t + (\hbar/2)\partial\sigma_1/\partial t = 0. \tag{3.16}$$

Dirac interpreted this as the electron having a *spin* angular momentum: $\underline{s} = (\hbar/2)\underline{\boldsymbol{\sigma}}$, that has to be added to the *orbital* angular momentum, $\underline{l}$, to get a constant of the motion. The directions of $\underline{s}$ and $\underline{\mu}$ are defined by the *same* matrix/operator vector $\underline{\boldsymbol{\sigma}}$. It was noticed by de Broglie [6] that it is not possible to separate the spin and orbital momenta because uncertainties on the latter would be larger than the former, due to the electron having a finite size defined by the Compton diameter $2r_C$.

In another computation [5] Dirac used a field-free Hamiltonian to determine *at which velocity* the electron 'rotates' to acquire kinetic and magnetic spin momenta:

$$H = c(\boldsymbol{\alpha_0}p_0 + \boldsymbol{\alpha_1}p_1 + \boldsymbol{\alpha_2}p_2 + \boldsymbol{\alpha_3}p_3). \tag{3.17}$$

The linear momentum $\underline{p}$ commutes with H and thus is a constant of the motion. Making use of the properties of the $\boldsymbol{\alpha}_k$'s (Eqs. (3.12)), it can be written, for an arbitrary component v_k $(k = 1, 2, 3)$ of the electron velocity:

$$i\hbar\partial x_k/\partial t = [x_k, H] = i\hbar c\boldsymbol{\alpha}_k \quad \rightarrow \quad \boldsymbol{v_k} = |\partial \boldsymbol{x_k}/\partial \boldsymbol{t}| = \pm \boldsymbol{c}, \tag{3.18}$$

which means the electron moves *at the speed of light*!

This paradox was elucidated by Schrödinger [11, 12] while investigating the Dirac velocity operators $v_k = c\boldsymbol{\alpha}_k$. He showed that:

$$i\hbar\partial\boldsymbol{\alpha}_k/\partial t = 2\boldsymbol{\alpha}_k H - 2cp_k.$$

Since H and p_k are time-independent, this entails:

$$i\hbar\partial^2\boldsymbol{\alpha}_k/\partial t^2 = 2(\partial\boldsymbol{\alpha}_k/\partial t)H.$$

This differential equation can be integrated twice, yielding first the explicit time dependence of the velocity and then that of the position. One first obtains:

$$v_k = c\boldsymbol{\alpha}_k = c^2 p_k H^{-1} + (i\hbar c/2)\gamma_k^0 e^{-i\omega t} H^{-1}, \tag{3.19}$$

where $\omega = 2H/\hbar$ and $\gamma_k^0 = \partial\boldsymbol{\alpha}_k/\partial t$ at $t = 0$. As $H = mc^2$, the first term is a constant of the order of p_k/m, the classical relation between momentum and velocity. But there is, here again, an extra term, which is oscillating at the electron *Zitterbewegung* frequency [11, 12]:

$$\nu_e = 2mc^2/h. \tag{3.20}$$

The *constant part* gives the *average velocity*, through a time interval larger than ν_e^{-1}, which is observed in practical measurements, whereas the *oscillatory part* explains why the *instantaneous velocity* has eigenvalues $\pm c$ [5]. Further integration yields the time dependence of the electron coordinate x_k, and it appears that the *Zitterbewegung* amplitude is of the order of $r_C = \hbar/2m_0c$, the Compton radius given by Eq. (3.4).

3.3 The Electron as a Quasi-Bohr Subsystem

Since its introduction by Uhlenbeck and Goudsmit in 1925, spin has been the subject of a number of speculations [28–31]. The three additional terms which emerged in Eqs. (3.14), (3.16), and (3.19) stemming from the very same properties of the 4-D $\boldsymbol{\alpha}$ matrices introduced by Dirac to linearize his quadratic equation, the *internal motion* giving rise to both the spin angular momentum and intrinsic magnetic moment can be identified to *Zitterbewegung* [13–21], which occurs *at the velocity of light*. As the rest masses of both the electron and positron are non-zero, one may then wonder *why they do not go to infinity*.

If *Zitterbewegung* is interpreted as a *wave beat* between the positive and negative energy states [6], then the *average mass* of the *vibrating entity* can be considered as being null, departures from this value being allowed by the Heisenberg uncertainty principle. A related point of view [26] is to consider a *vacuum fluctuation*, with frequency ν_e, associated with a particle of mass m_0, this latter becoming a wave with momentum p_0 when it yields its energy to the vacuum and recovering its mass when it is restored as a corpuscle.

If one writes the Heisenberg uncertainty relation for the energy:

$$\Delta\left(2mc^2\right) \cdot \Delta t = \Delta(2mc) \cdot \Delta(ct) \sim \hbar,$$

and the Δ's are removed and appropriate substitutions are made, one obtains:

$$2m_0c \cdot c\tau_0 \sim \hbar \quad \rightarrow \quad \tau_0 \sim \hbar/2m_0c^2 = (2\pi\nu_0)^{-1}, \tag{3.21}$$

where $\nu_0 = 2m_0c^2/h$ is the *Zitterbewegung* frequency for the electron at rest, and $\tau_0 \sim 0.645 \times 10^{-21}$ sec is the time scale for the electron internal motion. To the *rest mass* 'momentum' $m_0c \equiv p_0$ is associated an *internal time* 'coordinate' $c\tau_0 \equiv x_0$.

One may then see Eq. (3.8) as involving formally *three* space dimensions and *two* time dimensions.

In the simple classical picture of a particle endowed with charge e and mass m_0 moving at velocity c around a loop of radius r_C, the intrinsic angular momentum would be: $s = m_0 c \cdot r_C = r_C \cdot 2\pi\hbar/\lambda_C$, from the definition of λ_C in Eq. (3.2). As in the *Bohr model* for the orbital motion of an electron around a nucleus, the quantum number $s/\hbar = 2\pi r_C/\lambda_C$ takes on a (half) integer value if the circumference $2\pi r_C$ involves a (half) integer number of wave-lengths λ_C (the half stemming from the *Zitterbewegung* frequency being that of a wave beat between the positive and negative energy states). This loop could then be seen as a kind of 'intrinsic orbit' with range $2r_C$.

If then the *electron* ($m_0 \sim 0.5$ MeV) is viewed as the 'lowest (stable) state' of a kind of 'hidden structure' similar to the Bohr atom, then the related *muon* and *tau* particles ($m_\mu \sim 106$ MeV, $m_t \sim 1800$ MeV) could be seen as 'excited (unstable) states' of this quasi-Bohr substructure. In a classical (*spinless*) extensible model of the electron as a charged conducting surface [32], Dirac showed that its first excited state with spherical symmetry has a rest mass about four times smaller ($m^*_{1s} \sim 27$ MeV) than the *muon*'s. A large part of the rest mass should then arise from the spin motion.

The *muon* and *tau* particles belonging to the same (lepton) family as the *electron*, their Compton wavelength λ_C, Eq. (3.2), if it was measurable in spite of their very short lifetime ($\tau_\mu \sim 2.10^{-6}$, $\tau_t \sim 3.10^{-13}$), would be much smaller than the electron's. In hydrogenoid atoms, the *smaller* the 'Bohr' (average) radius $\langle r \rangle_n$ of a given (spherically symmetric) ns orbital, the *larger* the ionization energy I_n from this state. In our quasi-Bohr lepton substructure, the *smaller* the 'Compton radius' r_C, the *larger* the rest mass energy $m_0 c^2$.

In the hydrogen atom, there is an infinite sequence of excited states, with higher and higher discrete energies bounded by the *Rydberg energy* R_H ($\sim$13.6 eV) and ending in the continuum. Similarly, one may conjecture that in the electron family, there is an infinite sequence of excited states, with larger and larger discrete energies bounded by the *Planck energy* E_P ($\sim 1.96 \times 10^9$ J $\sim 1.22 \times 10^{22}$ MeV), corresponding to a Planck spinning range $2r_P$ ($\sim 1.62 \times 10^{-35}$ m) and a Planck time scale τ_P ($\sim 5.39 \times 10^{-44}$ s).

We have tried to find some regularity in the sequence of known members of the electron family, so as to estimate what could be the next member in the series. Results of a quadratic fit of the logarithms of reduced energies, including the Planck limit, are shown in Table 3.1. The next member would have a rest mass $m_\upsilon \sim 122$ GeV, very close to that (125 GeV) of the particle identified in 2012 at CERN as the celebrated 'Higgs boson': it could be detected in the same energy range. Figure 3.1 displays a fit of these masses.

The *proton* and the *neutron* belong to a different (baryon) family: they are *composite* particles (both are made up of three quarks) and are sensitive to the *strong* nuclear force. Their *charge radii* r_N (N for nucleon), measured by electron scattering, differ from their *Compton radii* r_C by one to two orders of magnitude, and their magnetic moments μ_N from the nuclear magneton $\mu_P = ecr_P$ (r_P being the Compton radius of the proton) by factors 2.79285 and -1.91315, respectively.

Table 3.1 The lepton series of the electron family

Name	Rank	E/MeV	$\log(E/E_e)$	Ratio
Electron	1	0.5110	0.	"
Muon	2	105.7	2.316	"
Tau	3	1 777	3.541	1.529
'Next'	4	122.5×10^3	5.380	1.519
Planck limit	Limit	1.221×10^{22}	22.378	Limit

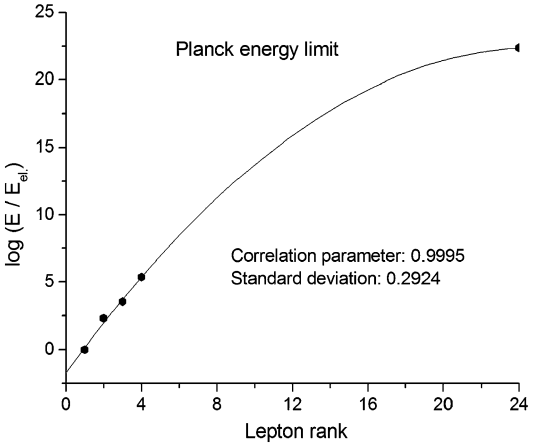

Fig. 3.1 Quadratic fit of the logarithms of reduced energies in the electron family

In our earlier paper [22] we noted that the Compton diameter (reduced wavelength): $\lambda\!\!\!^{-}_C \equiv \lambda_C/2\pi = 2r_C \sim 3.86159 \times 10^{-13}$ m, is a geometric average of the classical electrostatic radius: $r_0 = k_e e^2/m_0 c^2 \sim 2.81794 \times 10^{-15}$ m, and the Bohr hydrogen radius: $a_0 = \hbar^2/k_e m_e e^2 \sim 5.29177 \times 10^{-11}$ m, k_e being the Coulomb constant ($k_e = 1/4\pi\varepsilon_0$):

$$2r_C/a_0 = r_0/2r_C = \alpha, \quad \alpha = k_e e^2/\hbar c \sim 0.729735 \times 10^{-2}. \tag{3.22}$$

The Compton diameter $2r_C$ was also shown to be a geometric average of the *space-time curvatures*, defined from general relativity theory, 'inside' the electron: $r_G = (G/c^2)m_0$, and 'outside' a volume of radius r_Q: $R_G = r_Q^2/r_G$ [22]. For $r_Q = r_C$, one is led to define a *gravitational invariant* δ similar to the *fine-structure constant* α:

$$2r_C/4R_G = r_G/2r_C = \delta, \quad \delta = Gm_0^2/\hbar c \sim 1.751 \times 10^{-45}. \tag{3.23}$$

Auxiliary relations resulting from Eqs. (3.22) and (3.23) can be written:

$$r_G/r_0 = \delta/\alpha, \qquad r_G/2r_C = \delta, \qquad r_G/a_0 = \delta \cdot \alpha. \tag{3.24}$$

The gravitational invariant δ introduced here differs from that, α_p, introduced by Carr and Rees [33] while discussing cosmological issues raised by Dirac, Dicke, Jordan, and others: α_p involves the mass of the proton, m_p, instead of that of the

electron, m_0. It is involved, for instance, in estimating the minimum size and age of the Universe [34] and in building universe models.

In one of these models [35, 36], the whole Universe undergoes a kind of *Zitterbewegung*. Let $M_U \sim N_H \cdot m_H \times 10/3$ be, according to Eddington [34], the total mass of the Universe, N_H and m_H being the number and the mass of hydrogen atom equivalents: $N_H \sim 0.53 \times 10^{80} \rightarrow M_U \sim 0.88 \times 10^{53}$ kg. The Universe resulting radius is given by the relativistic formula: $R_U = 2G \times M_U/c^2 \sim 13.0 \times 10^{25}$ m $\sim 13.8 \times 10^9$ light-years. A 'cosmic flickering' frequency is then defined as: $\nu_U = 2M_U c^2/h \sim 0.24 \times 10^{104}$ s^{-1}, which is a kind of 'wave beat' between matter and antimatter, reminding of *Zitterbewegung* [6].

According to Sanchez et al. [35, 36], this frequency is coordinated with the electron and other fermion frequencies—which occur in widely different ranges—through an extended 'holographic principle' [37]. In the hydrogen atom, for instance, there is a 'holographic relation' between the Bohr radius and the electron and proton radii. If ordinary matter results from an oscillation between positive and negative energy states [6], what we call antimatter then amounts to a totally dephased oscillation [35, 36]. But this does not explain the dissymmetry of the occurrences of the two species.

Expressing the distance r between two identical particles (e, m_0) as a multiple N of the Compton diameter: $2r_C = \hbar/m_0 c$ (Eq. (3.4)), and scaling both the electrostatic force: $F_e = k_e \cdot e^2/r^2$, and the gravitational force: $F_g = G \cdot m_0^2/r^2$, to Planck units: $F_P = c^4/G$, $E_P = (\hbar c^5/G)^{1/2}$ [38], Macken [39] managed to express the two widely different forces as two different powers of the rest mass energy of the particles ($E_0 = m_0 c^2$):

$$\underline{F_e} = \alpha \underline{E_0}^2/N^2, \qquad \underline{F_g} = \underline{E_0}^4/N^2, \tag{3.25}$$

where $\underline{F_e} \equiv F_e/F_P$, $\underline{F_g} \equiv F_g/F_P$, and $\underline{E_0} \equiv E_0/E_P$ are dimensionless quantities. For $N = 1$, the two particles are contiguous: $r = 2r_C = \hbar/m_0 c$, and Eq. (3.25) yields a harmonic relation [39] similar to Eqs. (3.22) and (3.23):

$$\alpha^{-1} F_e/F_P = F_g/\alpha^{-1} F_e = \delta. \tag{3.26}$$

According to this relation, within the fine-structure constant α, *the Planck force is to the electromagnetic force as the electromagnetic force is to the gravitational force*, the ratio of this relation being the gravitational constant δ [22]. This is an indication that these forces are deeply related to the Compton wavelength and, following our previous comments, to the spin of the particles.

It may be interesting to put side by side the analogies revealed by Eqs. (3.22)–(3.26) (with the involved constants in parentheses):

$$\text{Classical radius} \sim \text{Inside curvature} \sim \alpha \text{ Gravitational force}$$

$$\text{Compton diameter } (\alpha) \sim \text{Compton diameter } (\delta) \sim \text{Electromagnetic force } (\delta)$$

$$\text{Bohr radius} \sim \text{Outside curvature} \sim \alpha \text{ Planck force.}$$

The Compton radius r_C thus appears as playing a privileged role in the description of the electron. Of the various definitions of electron radii, only that emerging

from the analysis of X-ray inelastic scattering has direct experimental evidence. The Compton radius r_C defines the amplitude of the *Zitterbewegung* responsible for the electron spin angular momentum and intrinsic magnetic moment. Equation (3.4) also relates Planck's energy E_P, length $2r_P$, and time τ_P of the Big-Bang singularity [38].

In Dirac's semi-classical model of the electron as a charged conducting surface [32], the potential 'inside' the surface is constant, according to Gauss' theorem, and equal to:

$$V = -k_e e/r_C = -k_e e 2\alpha/r_0 = -\alpha\left(2m_0c^2/e\right). \tag{3.27}$$

The second equality results from Eq. (3.22) and the third one, which is obtained by replacing r_0 by its expression given above, means that the constant electric potential 'inside' the electron, acting on the proton charge, generates an energy that is *not infinite* but proportional to that of a particle-antiparticle pair (times the fine-structure constant). There is *no Coulomb singularity*, and *no cusp condition* [40–42] is required for the wave function if the wave equation is reformulated accordingly.

There is no discontinuity either when the nucleus moves away from the 'electron core' through the 'Compton frontier' to distances larger than the Compton radius. Its interaction energy with the electron simply decreases as: $H = -k_e e^2/r (r \geq r_C)$. If the interaction energy of the proton 'inside' the ball was exactly that of the creation of a pair (the quantum-like equivalent to infinity), then the effective factor k_e within this *no man's land* would be divided by α.

That there is no singularity when the nucleus is at the electron core is not contradictory with the existence of *contact* Darwin and Fermi terms entering the expressions of isomer shifts e_i and hyperfine couplings a_i measured in Mössbauer and magnetic resonance spectroscopies [43]:

$$e_i = (2\pi/3) R_i^2 Z_i e^2 \rho(r_i); \qquad a_i = (8\pi/3)\hbar^2 \gamma_i \gamma_e \sigma(r_i), \tag{3.28}$$

where $\rho(r_i)$ and $\sigma(r_i)$ are the effective charge and spin densities at nucleus i.

Although the volume 'inside' the Compton radius may have different properties than that 'outside', the electron cannot be considered as a micro black hole. Consider a particle with rest mass $M \cdot m_e$, electric charge $Q \cdot e$, and angular momentum $J \cdot s$, where m_e, e, and s are the mass, charge, and spin of the electron, used as units. For this particle to be a black hole having an *event horizon*, these properties must satisfy the relation [44]:

$$Q^2\alpha + \left(J^2/4\right)/\left(M^2\delta\right) \leq M^2\delta, \tag{3.29}$$

with α and δ defined in Eqs. (3.22)–(3.24). For the electron, $Q = J = M = 1$. Then, the positive solution for M in the *extremal case* obeys: $M^2\delta = [\alpha + (1+\alpha^2)^{1/2}]/2 \sim 0.504$, yielding $M \sim 0.170 \times 10^{23}$, i.e. 0.028 Avogadro numbers of electron masses ($\sim$15 μg). In addition, the Schwartzschild radius, given in our previous paper [22] as $2r_G$ ($\sim 1.353 \times 10^{-57}$ m), would be considerably smaller than the Planck limit, $2r_P$ ($\sim 1.616 \times 10^{-35}$ m).

In one of his conjectures [45, 46], de Broglie described the *photon* as resulting from the *fusion* of a particle-antiparticle *pair* (real or virtual). In our model for the

electron, the metastable hydrogenoid species *positronium* ($\tau \sim 0.1$ ns) would be viewed as a couple of oppositely charged vortices rotating around a barycentre. As in hydrodynamics, the two vortices would attract each other if they spin in the same direction and eventually merge into a single vortex, which would be our compound photon (in fact, both *para* and *ortho* positronium decay into several lower-energy photons). There results a charge oscillating along an axis orthogonal to the motion [22], generating an electromagnetic field.

Thus, *Zitterbewegung* is what relates a *real* electron and a *virtual* positron, their mass and spin being linked by a wave beat between the two states; *positronium* is a Bohr-like structure associating a *real* electron and a *real* positron, with resulting spin $S = 0/1$; and a *photon* is what results for $S = 1$ when the fermion pair merges.

3.4 Rest Mass and Spin Motion

The essential idea in this paper is that the *rest mass* of the electron stems from the *spinning motion* of a *massless charge* at *light speed*, in a confined region defined by the *Compton radius*. That a mass may stem from motion already appears in the increase of inertial mass with increasing speed: $m_v = m_0/(1 - v^2/c^2)^{1/2}$. And that a massless entity moving at light speed may display mass properties also appears in the photon showing kinetic momentum: $p = h/\lambda$ (e.g. in the Compton effect) and gravitational mass: $m = p/c$ (e.g. in a Mössbauer shift).

Rewording in classical terms the interpretation of *Zitterbewegung* resulting from Eq. (3.19), one may say that the *intrinsic orbit* (Sect. 3.3), which defines the 'internal structure' of the electron, is described at *velocity* c, whereas the *external orbit*, in an atom for instance, is described at *velocity* v. This makes it necessary to consider that the charged entity describing the intrinsic orbit has *zero rest mass*. The *rest mass observed* with respect to an external body, such as an atomic nucleus, must then arise from the *intrinsic motion* of the charged entity at velocity c.

Rest mass induction by space confinement also holds for massless bosons like photons. It has been shown [39, 47] that photons trapped in optical resonators acquire mass properties similar to those of fermions. For a similar reason, light trapped on the photon sphere of a black hole or a neutron star acquires a rest mass much larger than that resulting from the finite size of the Universe, $R_U \sim 1.3 \times 10^{26}$ m. Its total energy would be given by:

$$E^2 = m_0^2 c^4 + p^2 c^2 = \hbar^2 c^2 / 4 r_C^2 + \hbar^2 \omega^2. \tag{3.30}$$

For a blue radiation ($\lambda \sim 4.10^{-7}$ m) trapped around a stellar black hole ($M \sim 2.10^{31}$ kg, $R \sim 3.10^4$ m), the ratio of the two contributions in Eq. (3.30) would be: $E_1/E_2 \sim 10^{-12}$.

However, a rest mass induced by a confined motion must draw its energy from an immaterial source which, for a massless charge, should be an electromagnetic field (A_4, $\underline{A}$). For immaterial particles, the expression for the energy reduces to: $E = p \cdot c$. For photons, one has: $p = h/\lambda$, yielding: $E = h\nu$. For a spinning charge, one would

have: $p = (\hbar/2)/r_C$, yielding: $E = \hbar c/2r_C = m_0c^2$ according to Eq. (3.4). Writing $E = eV$ and making use of Eq. (3.4), one obtains:

$$V = \hbar c/2er_C = k_e\alpha^{-1}e/2r_C. \tag{3.31}$$

What maintains the *massless charge* $-e$ in a spinning orbit and provides it with the energy accounting for the *electron rest mass* would then be the *electric potential* V exerted by an opposite charge at a distance equal to twice the Compton radius, as if the spheres of the electron and its mirror image were contiguous. This is indeed the occurrence leading to Eq. (3.26). However, in this *no man's land* (cf. Eq. (3.27)), the inverse permittivity of the medium or, alternatively, the attracting virtual charge would be multiplied by $\alpha^{-1} \sim 137$.

That an *internal* potential V acting on a *massless* charge $-e$ be responsible for its *spin motion* and *rest mass* is not contradictory with p_0 and x_0 (Eqs. (3.7) and (3.8)) being invariant under an *external* field, while p_4 is modified by A_4 and $\underline{p}$ by $\underline{A}$ (Eq. (3.13)). The spin momentum $s = p_0r_C$ and rest mass $m_0 = p_0/c$ are also insensitive to $(A_4, \underline{A})$, although these potentials can act on the associated magnetic moment and electric charge. The deep connection between spin and mass also appears in the unitary irreducible representations of the group of isometries in relativistic space-time being indexed by spin and mass.

A corroboration of our conjecture can be found in more formal treatments. Barut and Bracken [18–21] have derived the Dirac equation for a finite quantum system in an arbitrary moving frame. There, *spin* appears as the *orbital* momentum associated with the *internal system*, while the *rest mass* is the internal energy in the *rest frame*. In another, stochastic electrodynamics approach [48], Haisch, Rueda and Puthoff have shown that *Zitterbewegung* arises from the electromagnetic interaction of a subelementary charged particle (*parton*) with the vacuum zero-point field (ZPF). *Inertia* was interpreted as a *resistance* of ZPF to spectral distortion in an accelerated frame, and the *van der Waals force* generated by this oscillating motion was identified with the *Newtonian gravitational force*. In addition, the inertial and gravitational masses thus derived were shown to be equivalent.

In Sect. 3.5, we shall see that *charge* is the only independent quantity that remains when one identifies time with length, and mass with length inverse. It is not surprising then that the three related quantities: length, time, and mass, vary with velocity, but *not charge*. If the electron rest mass essentially results from the spinning motion, over a sphere of radius r_C, of a massless charge $-e$ at light speed, then the contribution of the electrostatic potential due to the charge distribution over this sphere is [22]:

$$E_0 \sim k_e e^2/2r_C = \alpha \cdot m_0c^2. \tag{3.32}$$

The contribution of the *electrostatic self-energy* to the electron rest mass is less than 1 % of the kinetic contribution due to the spin motion around the effective virtual charge $\alpha^{-1}e$ (Eq. (3.31)). This energy can be compared to the electron-nucleus 'contact energy' (Eq. (3.27)).

Using again the semi-classical picture of an electron ball, the *hidden confined motion* of a massless charge at velocity c can be related to the *visible free motion*

of the resulting particle at velocity v by the Compton formula, which connects the mass increase to the radius decrease:

$$m_v = \hbar/2r_v c = \hbar\gamma/2r_C c = m_0\gamma. \tag{3.33}$$

A *velocity increase* in the *outer motion* entails an *amplitude decrease* in the *inner motion*. This may be the deep reason why c is a limiting velocity for all motions, and why inertial frames play a specific role in relativity theory. However, contrary to what we stated in our previous paper [22], the contraction of the radius with increasing velocity should appear as uniform [49, 50] and not just along the direction of the motion.

3.5 Homologies in the Hierarchy of Complexity and Dimensional Analysis of Fundamental Physical Properties

> 'Analogy is the key to the understanding of … the universal law that governs all things as a whole and every thing in its detail'.
>
> (*Attributed to Hermês ho Trismégistos*)

This part is intended to trigger reflections on possible impacts of the inner structure, as discussed above, of the Dirac electron on the properties and interactions of structures generated at the various levels of complexity.

The number and nature of the quantities that can be defined in a given field of science (physics, chemistry, biology, ecology, …) is a matter of convenience and, whenever it is possible, of coherence. This is true also for the units that can be designed to measure or, at least, to scale these quantities. In fact, thousands of units have been used (and are still in use) in various periods of history (and various regions of the world) to quantify scores of quantities: from distance, duration, and weight to radioactivity level, viscosity grade, earthquake strength, nutritional value, or music interval [51]. However, since Aristotle, and even more since Galileo, it has been admitted that physics, especially mechanics, is a science more fundamental than others. This led to a mechanistic vision of Nature, which prevailed until it became partly challenged by the paradoxes of relativity and quantum theories [52, 53].

This paradigm of modern sciences is based on an analytical and deterministic approach to natural phenomena, which has made obsolete the holistic and finalistic vision of traditional sciences. Nevertheless, it is still admitted that the biological realm, even though it keeps obeying physical laws, has properties and laws of its own (called *emergences* in the theories of complex systems), including holistic and finalistic characters [54]. In the 19th century, Louis Pasteur (who refuted the old belief in spontaneous generation) expressed an even more radical view, contrasting with the prevailing materialistic and reductionist views:

> 'Who tells you that the steady progress of science will not compel scientists who will live in a hundred, a thousand years … to state that *life* has existed from all eternity, *not* matter …. Who ensures me that in ten thousand years, one will not consider that it is *from life* … that it is impossible to proceed *to matter*?'

Even in the physical sciences, the Newtonian concept of interaction at a distance, as well as Mach's idea of a mass being determined by all masses in the Universe, had an odd holistic flavour. In fact, in classical mechanics as in classical optics one can use, to compute the trajectory of a matter particle or a light ray, either a deterministic, derivative formulation (Hamilton's equations for position and momentum, Descartes' laws of reflection and refraction), or a finalistic, integral approach (Maupertuis' principle of least action integral, Fermat's principle of stationary optical path). The latter formulations are now well understood as resulting from interferences between waves associated with matter particles or light rays, constructive along the effective, real trajectory and destructive along other, virtual paths [1, 55].

In the biological sciences, only deterministic approaches to microevolution (as those involving Darwinian mechanisms of natural and sexual selection) have indeed been rationalized. There is no real understanding of the macroevolution process *in which we are embedded* (and not just external observers, as in the physical sciences). However, the existence of *selected trajectories for phylum evolution* cannot be discarded. In a way, *chance and necessity* play a role similar in the Darwinian theory of biological evolution and in the Copenhagen interpretation of quantum mechanics. In the former, the *ecosystem* acts as an 'observer' reducing the *species* 'wave packet' (population variety) generated by 'subquantum' (genotype) fluctuations. If biological phenomena are indeed, as Schrödinger had foreseen it [56], a *manifestation of quantum laws at the macroscopic level*, then *constructive and destructive interferences* may operate also among living systems, and hence within social structures [57]. There remains a Maupertuis or Fermat-like principle to be built on a quantification model for biological evolution.

Schrödinger's argumentation on the quantum nature of living systems, together with Darwin's theory of biological evolution, reminds of Epicure's conjecture that matter is made up of atoms driven by chance and necessity. Schrödinger's idea was expressed before the discovery of DNA (which actually it inspired). But, still earlier, life quantization was implicit in Mendel's laws of heredity and Morgan's theory of genes. This may be seen as the latest step in a *fractal progress of complexity*. Among the so-called elementary particles, some of the most stable (electrons and nucleons) build up a few scores of atoms, which constitute a *kind of alphabet* making up usual matter. Some of the molecules (words) built up with a few light atoms constitute a *higher-order alphabet* making up molecules of life (sentences). These assemble into cells (paragraphs), tissues (chapters), organisms (books), species (bookseries), and eventually ecosystems (libraries).

This evolving auto-organization process [58] follows four main rules [59]. 1. *At every level of complexity*, the forces that have driven the lower-level structures become less relevant, and *new forces take over*. 2. *The higher the level of complexity, the weaker the driving force:* nucleons are held together by the strong nuclear force; atoms and molecules by the weaker, electromagnetic force; and living organisms communicate by exchanging energy-free signals (*languages*). 3. *At every level of complexity*, *a new variety of structures emerge*, while only a few of those that emerged at the lower level are retained (*natural selection*). 4. Subsidiary to this rule, *at critical levels of complexity* there is a *dissymmetry in the entities retained*: matter

over antimatter for elementary particles, levogyre over dextrogyre amino-acids in protein macro-molecules.

The *third rule* starts applying at the lowest level: particles may constitute complex systems without going through molecular structures and living organisms. Hydrogen is the main constituent of complex stars like the Sun while nucleons make up neutron stars. Some Sun-like stars drive complex systems of planets and satellites, and in turn they belong to galaxies. At the cosmic scale, the *first two rules* make the very weak gravitational force control the auto-organization process, although nuclear forces are still effective in the core of stars and electromagnetic radiation in their environment. In fact, the rise of complexity in the micro-systems seems to be conditioned by that in the macro-structures. It is as if the whole process aims at producing life in the Universe: changes in the original conditions or in universal constants may not allow the process to be completed [33, 34].

The *electrostatic force*, in its quantum version involving *antisymmetry of the wave function* for particles obeying the Fermi-Dirac statistics, plays the main role in *chemical bonding* and in the structure and properties of molecules, including biomolecules. However, according to our *second rule*, the magnetostatic and weak nuclear forces could also affect specific biological phenomena. On line with this idea, investigations have since long been made on a possible role of the *weak nuclear force* in *biomolecular homochirality* [60].

Regarding *magnetism* (which is due mainly to the *electron spin*), it occurs in various aspects of our daily life, from the oxygen we breathe to the hard disks of our computers. It is also involved in *magnetoreception* [61], an extra sense that allows various species to detect magnetic fields due to motions in the Earth nucleus or storms in the Sun corona. It has been detected in bacteria, mushrooms, insects, sea animals, small mammals, and migrating birds [61]. In most cases, it is due to *magnetosensitive proteins* in the brain (hippocampus) or in sense organs (especially in the eyes).

Living organisms may also be sensitive to *electromagnetic waves*, irrespective of their energy content [62, 63]. The gigantic amount of *invisible information* surrounding us (decoded by radio, TV, computer or cell-phone devices) might act, in the long run, on proteins or nucleic acids in the brain or in the body, with unpredictable effects.

Regarding the *gravitational force*, an influence on biological phenomena, in particular through natural selection, has been recognized [64]. In addition to acting indirectly on the environment through the seasons and daily cycles, gravitation may act directly at the cell level. Observations on cosmonauts undergoing *microgravity* will tell more.

The relevance of this discussion to our topic is that, according to our conjecture, not only the magnetic moment but also the rest mass of the electron is related to its spin motion (and its interplay with its antiparticle), the resulting fermion properties being responsible for chemical bonding. Deeper knowledge of the electron microcosm may then be a key to better understanding of biological phenomena.

Coming back to the physical realm, a convenient and consistent system of quantities (and units) has eventually been designed: the *International System* (SI). In

this system, there are seven *basic* quantities/units: *length*/meter, *mass*/kilogram, *time*/second, *electric current*/ampere, *temperature*/kelvin, *substance amount*/mole, and *light intensity*/candela. There are also twenty-two *derived* quantities (and units), designed to quantify such entities as planar or solid angle, force and pressure, energy and power, electric charge and circuit properties, magnetic and light properties, radioactivity, and biocatalysis. Multiples and fractions of these units are defined according to the *decimal system*.

One may wonder why the plane or solid angle was not retained as a basic quantity, for *angle* is linked to *isotropy*, a basic symmetry which entails conservation of angular momentum. A property like magnetic flux density could also have been selected, although magnetism is related to electricity, contrary to gravitation. It seems strange that radioactivity is relegated to derived quantities and measured in s^{-1}, no more lethal than a music note! On the other hand, one may argue about the theoretical relevance (though not the practical convenience) of such basic units as the kelvin, mole, or candela, all related to energy through heat, mass, or light.

One may also wonder if *different units* could not be defined for the three dimensions of space: length, width, and height. For Aristotle, it made sense to distinguish between going up or down, East or West, South or North. Contrary to the two horizontal directions, the *vertical* seemed oriented, as *time* is for us. Medieval painters represented objects on two dimensions, ignoring perspective display by projective geometry (and, of course, holographic storing and retrieval by diffraction patterns of coherent light). Until Descartes' analytical geometry in the 17th century, it was not clearly understood that space has *three dimensions*, with axis representations and measuring units that are both *rotatable* (due to space *isotropy*) and *translatable* (due to space *homogeneity*) [65].

In general relativity theory, the *vertical* relative to a massive body is different indeed from the other two space dimensions, due to space curvature resulting from gravitational attraction; and in special relativity theory, *time* is already a different dimension, involving an imaginary axis. Hence, a non-Euclidean metric in the two theories. Having reduced the *vertical* to the two horizontal dimensions, one could further simplify by reducing *time* to the three spatial dimensions, writing in dimensional terms: $c \sim L/T \sim 1$ (the length associated with 1 second being 1 parsec).

The velocity of light c, assumed to be an upper limit in relativity theory, is one of the fundamental constants of Nature. The quantum of action $\hbar$, assumed to be a lower limit in quantum theory, is another fundamental constant. If it is also taken as dimensionless, one has: $\hbar \sim 1 \rightarrow ML^2T^{-1} \sim ML \sim 1 \rightarrow M \sim L^{-1} \sim T^{-1}$. This is consistent with Eq. (3.4) for the Compton radius when both $c \sim 1$ and $\hbar \sim 1$ (dimensionwise), as well as with mass being identical to energy when $c \sim 1$ (and with time inverse when $\hbar \sim 1$). In Table 3.2, we show how some universal constants and physical properties are related in this dimensional system, commonly used in relativistic quantum mechanics.

This system should not be confused with the natural system of units proposed in 1881 by George Stoney, who derived units for length, time, and mass by normalizing G, c, and e to unity. This system was extended in 1899 by Max Planck, who derived also units for temperature by normalizing G, c, $\hbar$, and k_B (the Boltzmann constant),

Table 3.2 Some universal constants and electron properties (upper half) and a few physical properties (lower half) with dimensions scaled to $\hbar \sim c \sim 1$ (dimensionwise)

Name	Symbol	Formula	Dim.
Newton constant	G	$F_{grav} = Gmm'/d^2$	$L^2 \sim T^2$
Coulomb constant	k_e	$F_{elec} = k_e ee'/d^2$	Q^{-2}
Planck constant	$\hbar$	$\Delta E = \hbar\omega$	1
Light velocity	c	Constant in all frames	1
Elementary charge	e	Negative or positive	Q
Fine-structure constant	α	$k_e e^2/\hbar c$	1
Electron rest mass	m_e	Negative for positrons	$L^{-1} \sim T^{-1}$
Gravitational invariant	δ	$Gm_e^2/\hbar c$	1
Classical electron radius	r_0	$k_e e^2/m_e c^2$	L
Compton electron radius	r_C	$\hbar/2m_e c$	L
Hydrogen Bohr radius	a_0	$k_e^{-1}\hbar^2/m_e e^2$	L
Gravitational electron radius	r_G	$(G/c^2)m_e$	L
Force	$\boldsymbol{F}$	$\boldsymbol{F} = m\boldsymbol{g}$	$L^{-2} \sim T^{-2}$
Pressure	P	$P = F/d^2$	$L^{-4} \sim T^{-4}$
Energy	E	$E = Fd$	$L^{-1} \sim T^{-1}$
Power	W	$W = E/t$	$L^{-2} \sim T^{-2}$
Electric potential	V	$V = E/Q$	$Q^{-1}T^{-1}$
Electric resistance	Ω	$\Omega = V/A$	Q^{-2}
Electric inductance	$\mathcal{H}$	$\mathcal{H} = Vt/A$	$Q^{-2}T$
Electric capacitance	$\mathcal{F}$	$\mathcal{F} = Q/V$	Q^2T
Electric field	$\boldsymbol{E}$	$\boldsymbol{E} = V/l$	$Q^{-1}T^{-2}$
Magnetic flux density	$\boldsymbol{B}$	$\boldsymbol{B} = Vt/l^2$	$Q^{-1}T^{-2}$
Electric moment	$\boldsymbol{d}$	$\boldsymbol{d} = e\boldsymbol{r}$	QL
Magnetic moment	$\boldsymbol{\mu}$	$\boldsymbol{\mu} = e\hbar/2m_e$	QL

to which was later added $k_e = (4\pi\varepsilon_0)^{-1}$ [38]. As they are free of anthropocentric choices, these units help physicists to reframe fundamental questions such as the smallness of G relative to k_e in *SI* units. Expressing Universe properties such as age or temperature in terms of Planck units discloses a regular occurrence of large dimensionless numbers, which led Weyl, Hoyle, Eddington, Wheeler, Dirac, and others to speculations which inspired Carter's *Anthropic Principle* in 1973 [33, 34]. Table 3.3 gives expressions of some Planck units and their values in the *SI* system. Those for E_P and F_P were used in deriving Eq. (3.25).

In the system we use here (Table 3.2), only c and $\hbar \sim 1$ (dimensionwise). As expected, both the fine-structure constant α (pregnant in quantum electrodynamics) and the similar gravitational invariant δ (introduced in our previous paper) remain dimensionless. This choice also will help to reframe some basic physical concepts.

Table 3.3 Expressions and values of a few Planck units

Planck unit	Expression	Dimension	Value/SI units
Length	$l_P = (\hbar G/c^3)^{1/2}$	L	1.6162×10^{-35} m
Time	$t_P = l_P/c = (\hbar G/c^5)^{1/2}$	T	5.3911×10^{-44} s
Mass	$m_P = \hbar/c^2 t_P = (\hbar c/G)^{1/2}$	M	2.1765×10^{-8} kg
Charge	$q_P = (\hbar c/k_e)^{1/2}$	Q	1.8755×10^{-18} C
Linear momentum	$P_P = \hbar/l_P = m_P c$	MLT^{-1}	6.5249 kg m s^{-1}
Force	$F_P = \hbar/l_P t_P = c^4/G$	MLT^{-2}	1.2103×10^{44} N
Energy	$E_P = \hbar/t_P = m_P c^2$	ML^2T^{-2}	1.9561×10^{9} J

In Table 3.2, it can be seen that, while all mechanical quantities appear homologous to powers of length (or time), charge and related electromagnetic quantities are not reducible to space-time. It can also be seen that, since k_e expresses a property of free space relative to electricity similar to that expressed by G relative to gravitation, *the role played by* ***charge in electricity*** *is homologous to that played by* ***curvature in gravitation***. This is, of course, due to the homology between M and L^{-1} in the dimensional system we have used. However, this suggests that a property related to the *charge inverse* may have to be included as an *additional dimension* to space-time in a general unification scheme.

While length and time allow continuous (translation and rotation) as well as discrete (P and T reversal) operations, charge is a discrete, pseudo-scalar quantity, eligible only to C conjugation. Now, whereas there is exact invariance of usual Hamiltonians with respect to translations/rotations in space-time, only combined CPT is a rigorous symmetry operation [60, 66]. There may then be a hidden dimension, homologous to Q^{-1}, allowing continuous operations also for charge (as for length and time), whose visible aspect would be discrete conjugation. The Poincaré group would then have to be extended to account for this extra dimension. However, it has been suggested that charge may just be a relativistic-invariant quantum whole number [35, 36], while a space-time interpretation for charge has also been proposed [39].

In Table 3.2, force and power are homodimensional to L^{-2} or T^{-2} (the inverse of G), due to our choice $c \sim 1$. For the same reason, energy (mc^2) and momentum (mc) are homodimensional, which is consistent with energy being the fourth component of a four-vector momentum in relativity theory. Electric resistance Ω is, as expected, homologous to the Coulomb constant k_e. Electric field and magnetic flux density also appear homologous, and both electric and magnetic moments are homologous to the inverse electric potential.

The Lorentz transformation equations for the electric and magnetic components, E_i and B_j, of an electromagnetic field between two inertial frames, S and S', moving with relative velocity v along a common axis x, are similar to those for the space and time coordinates, x and ct, of a free particle (Eqs. (2.4) of Ref. [22]). But here, E_x and B_x remain unchanged while E_y transforms as x and B_z as ct (or,

alternatively, E_y as ct and B_z as x), with similar correspondences for the other two components:

$$E_y(B_z) \sim x, \qquad B_z(E_y) \sim ct; \qquad E_z(B_y) \sim \pm x, \qquad B_y(E_z) \sim \pm ct. \quad (3.34)$$

Just as p_0^2 and x_0^2 (Eqs. (3.7) & (3.8)) are invariant under a change of frame, here also there are two invariants [65]:

$$Y^2 = \underline{E}^2 - \underline{B}^2, \qquad Z^2 = \underline{E} \cdot \underline{B}. \quad (3.35)$$

As (dimensionwise) $E \sim B \sim MLT^{-2}Q^{-1} \sim L^{-2}Q^{-1}$ (in our system), these two invariants are homologous to $L^{-4}Q^{-2}$. According to our previous remark on the analogy between charge Q and curvature L^{-1}, one may then write: $Y \sim Z \sim L^{-1}$, homologous to p_0, then to rest mass.

The electric and magnetic fields are different in that $\underline{E}$ is a *polar* vector (translational symmetry) while $\underline{B}$ in an *axial* vector (rotational symmetry). Now, in the Dirac equation, space coordinates $\underline{x}$ are related to the external, *linear* momentum $\underline{p}$ while the time coordinate $x_0 = c\tau_0$ is related to the internal, *spin* momentum $p_0 = m_0 c$. There is thus a correspondence between electric field, translation, linear momentum, and space, and a similar one between magnetic field, rotation, spin momentum, and time.

While *space homogeneity* entails conservation of $\underline{p}$, and *time homogeneity* conservation of $p_4 \equiv E/c$, *space-time isotropy* entails conservation of $\underline{l} + \underline{s}$, for $\underline{l}$ and $\underline{s}$ cannot be measured independently [6]. A definition of isotropy consistent with relativistic quantum mechanics then necessarily involves full space-time.

3.6 Conclusions

In this paper we have conforted our previous conjecture that the visible properties of the electron, especially its rest mass, are determined by a subquantum massless charge spinning at light speed within a Compton radius. In complement to the conclusions drawn in our previous paper [22], the following points can be stressed.

1. The *rest mass* energy m_0c^2 of the electron is essentially a *kinetic* self-energy related to its *spin* motion, with a contribution α-smaller of the *potential* self-energy related to its *charge* content. For *photons*, $p = \hbar\omega/c$ (p being the external *linear* momentum), whereas for *electrons*, $1/2\hbar/r_C = m_0c^2/c$ ($1/2\hbar$ being the spin *angular* momentum). This sets the Compton radius: $r_C = \hbar/2m_0c$, as the range of the spin motion.
2. *Spin* itself being the 'orbital momentum' of *Zitterbewegung*, which in turn stems from a *wave beat* between the *electron* and its mirror twin the *positron*, there is *no matter without antimatter*: there is no need to search for antimatter *for it is around us and in us*, as the two faces of a same coin *or the two poles of a magnetic moment*.

   The question now is, why 'only one face of the coin' shows up regarding the electric charge, *while magnetic poles always appear in couple*. If charge is

interpreted as a *quantized curvature* involving an *additional dimension*, then this dissymmetry means that *a single sign is privileged* for this curvature, charge conjugation amounting to its reversal. Mass arises from the confined motion of the extra-dimension curvature over usual space-time.

3. By relating *rest mass* to *spin motion*, quantum theory brings an insight into such relativistic concepts as the *proper interval* x_0, which is the residual interval when the space coordinates $\underline{r}^2$ are subtracted from the time coordinate c^2t^2. The *velocity of light* c is not simply that of electromagnetic waves, but also that of basic motions at the heart of matter. Time is deeply related to the inner clock: $\tau_0 = x_0/c$, spin momentum: $s = p_0 r_C$, and rest mass: $m_0 = p_0/c$, of the matter particles.
4. If the *electron* is regarded as the *ground state* of a *subsystem* analogous to the Bohr atom, then a regular series of *excited states*, with *decreasing* Compton wavelength, may occur, starting with the parent *muon* and *tau* leptons and ending at the *Planck limit*. Being charged fermions, the *two quark families* could follow a similar pattern.

Acknowledgements I wish to thank Erkki Brändas, Roland Lefebvre, John Macken, and Francis Sanchez for useful discussions and critical comments.

References

1. de Broglie L (1925) Recherches sur la théorie des quanta. Ann Phys 10(III):22–128. (Thesis, Sorbonne, Paris, 1924)
2. Dirac PAM (1928) Quantum theory of the electron. Proc R Soc Lond A 117:610–624
3. Dirac PAM (1931) Quantised singularities in the electromagnetic field. Proc R Soc Lond A 133:60–72
4. Dirac PAM (1933) Theory of electrons and positrons. Nobel lectures 320–325
5. Dirac PAM (1930) The principles of quantum mechanics, 1st edn. Clarendon Press, Oxford. 4th edn (1958), Chaps 11–12
6. de Broglie L (1934) L'électron magnétique: théorie de Dirac. Hermann, Paris. Chaps 9–22
7. Feymann RP (1998) Quantum electrodynamics. Addison-Wesley, Reading
8. Cottingham WN, Greenwood DA (1998) Introduction to the standard model of particle physics. Cambridge University Press, Cambridge
9. Weinberg S (1995) The quantum theory of fields. Cambridge University Press, Cambridge
10. Compton AH (1923) A quantum theory of the scattering of x-rays by light elements. Phys Rev 21:483–502
11. Schrödinger E (1930) Über die kräftefreie Bewegung in der relativistischen Quantenmechanik. Sitzungsber Preuss Akad Wiss Berlin, Phys Math Kl 24:418–428
12. Schrödinger E (1931) Zur Quantendynamik des Elecktrons. Sitzungsber Preuss Akad Wiss Berlin, Phys Math Kl 25:63–72
13. Hönl H (1938) Ann Phys (V) 33:565
14. Hönl H, Papapetrou A (1939) Über die innere Bewegung des Elecktrons. Z Phys 112:512
15. Hönl H, Papapetrou A (1939) Über die innere Bewegung des Elecktrons. Z Phys 114:478
16. Hönl H, Papapetrou A (1940) Über die innere Bewegung des Elecktrons. Z Phys 116:153
17. Huang K (1952) On Zitterbewegung of the Dirac electron. Am J Phys 20:479–484
18. Barut AO, Bracken AJ (1981) Zitterbewegung and the internal geometry of the electron. Phys Rev D 23:2454–2463

19. Barut AO, Bracken AJ (1981) Zitterbewegung and the internal geometry of the electron. Phys Rev D 24:3333–3342
20. Barut AO, Zanghi N (1984) Classical model of the Dirac electron. Phys Rev Lett 52:2009–2012
21. Barut AO, Pavšič M (1987) Quantization of the Zitterbewegung in the Schrödinger picture. Class Quantum Gravity 4:L131–L136, and references therein
22. Maruani J (2012) The Dirac electron ... and the kinetic foundation of rest mass. In: Nishikawa K et al (eds) Prog theor chem & phys B, vol 26. Springer, Berlin, pp 23–46
23. Infeld L, Schield AE (1945) A new approach to kinematic cosmology. Phys Rev 68:250–272
24. Infeld L, Schield AE (1946) A new approach to kinematic cosmology. Phys Rev 70:410–425
25. Chapman TC, Leiter DJ (1976) On the generally covariant Dirac equation. Am J Phys 44:858–862
26. Arbab AI, Yassein FA (2012) A new formulation of quantum mechanics. J Mod Phys 3:163–169
27. Appelquist T, Chodos A, Freund PGO (eds) (1987) Modern Kaluza-Klein theories. Addison-Wesley, Reading, and references therein
28. Dahl JP (1977) The spinning electron. Det Kongelige Danske Vid. SM-FM 39(12):1–33
29. Ohanian HC (1986) What is spin? Am J Phys 54:500–505
30. Rahmani Nejad A (2009) A new approach to the concept of electron spin. Private communication
31. Tiwari SC (2012) Gordon decomposition of the Dirac current. Private communication
32. Dirac PAM (1962) An extensible model of the electron. Proc R Soc Lond A 268:57–67
33. Carr BJ, Rees MJ (1979) The anthropic principle and the structure of the physical world. Nature 278:605–612
34. Barrow JD, Tipler FT (1986) The anthropic cosmological principle. Oxford University Press, London, and references therein
35. Sanchez FM, Kotov VA, Bizouard C (2011) Towards a synthesis of two cosmologies: the steady-state flickering universe. J Cosmol 17:7225–7237
36. Sanchez FM, Kotov VA, Bizouard C (2012) Towards coherent cosmology. Galilean Cosmol 24(4):63–81, and private communication
37. Bousso R (2002) The holographic principle. Rev Mod Phys 74:825–874, and references therein
38. Pavšič M (2001) The landscape of theoretical physics: a global view. Kluwer Academic, Dordrecht, pp 347–352. See also http://en.wikipedia.org/wiki/planck_units
39. Macken JA (2013) The Universe is only spacetime (http://onlyspacetime/home); wave-based insights into the relationship between forces. Private communication
40. Kato T (1957) On the eigenfunctions of many-particle systems in quantum mechanics. Commun Pure Appl Math 10:151–157
41. Pack RT, Byers Brown W (1966) Cusp conditions for molecular wavefunctions. J Chem Phys 45:556–559. Cusp conditions involve averaging of the wavefunction over small spheres about the singularities, which is an indirect way of accounting for the finite size of the electron
42. Kutzelnigg W (2003) Theory of electron correlation. In: Rychlewski J (ed) Explicitly correlated wave functions in chemistry and physics. Prog theor chem & phys A, vol 13. Kluwer Academic, Dordrecht, pp 3–90, and references therein
43. Maruani J (1980) Magnetic resonance and related techniques. In: Becker P (ed) NATO ASI proceedings. Plenum, New York. It should be noted that the Darwin term is the contact correction to the interaction between two (pseudo-scalar) electric charges, while the Fermi term is the contact correction to the interaction between two (pseudo-vectorial) magnetic moments
44. Shapiro SL, Teukolsky SA (1983) Black holes, white dwarfs, and neutron stars: physics of compact objects. Wiley, New York, p 357
45. de Broglie L (1954) Théorie générale des particules à spin: méthode de fusion. Gauthier-Villars, Paris
46. de Broglie L (1961) Introduction à la nouvelle théorie des particules. Gauthier-Villars, Paris, Chap 3

47. André J-M, Jonnard P (2011) Effective mass of photons in a one-dimensional photonic crystal. Phys Scr 84:035708, and references therein
48. Haisch B, Rueda A, Puthoff HE (1994) Inertia as a zero-point field Lorentz force. Phys Rev A 49:678–694, and references therein
49. Penrose R (1958) The apparent shape of a relativistically moving sphere. Research notes, Cambridge, pp 137–139
50. Poincaré H (1905) Sur la dynamique de l'électron. C R Acad Sci (Paris) 140:1504–1508. In this prerelativistic paper, in addition to the first rigorous introduction of the homogeneous Lorentz group, Poincaré discusses the views of Lorentz and Langevin about the shape and size changes of the electron under fast motion, with implications for the electromagnetic and gravitational forces
51. Rowlett R (2012) How many? A dictionary of units of measurement. University of North Carolina at Chapel Hill, last update August 2012. http://www.unc.edu/~rowlett/units/
52. Costa de Beauregard O et al (1968) Relativité et quanta: les grandes théories de la physique moderne. Masson, Paris
53. Karlsson EB, Brändas EJ (eds) (1998) Modern studies of basic quantum concepts and phenomena. Proc Nobel Symp 104, Physica Scripta T, vol 76, and references therein
54. Brändas EJ (2011) Gödelian structures and self-organization in biological systems. Int J Quant Chem 111:1321–1332. Also a chapter in this volume, and references therein
55. Feynman R (1948) Space-time approach to non-relativistic quantum mechanics. Rev Mod Phys 20:367–387
56. Schrödinger E (1967) What is life? Cambridge University Press, Cambridge, 180 pp. Combined publication with Mind and Matter. 1st edn in 1944
57. Maruani J (2009) An illustrated overview of QSCP meetings. In: Piecuch P et al (eds) Prog theor chem & phys B, vol 19. Springer, Berlin, pp 1–32
58. Nicolis G, Prigogine I (1977) Self-organization in non-equilibrium systems: from dissipative structures to order through fluctuations. Wiley, New York, and references therein
59. Maruani J, Lefebvre R, Rantanen M (2003) Science and music: from the music of the depths to the music of the spheres. In: Maruani J et al (eds) Prog theor chem & phys B, vol 12. Kluwer Academic, Dordrecht, pp 479–514, and references therein
60. Quack M (2012) Molecular parity violation and chirality: the asymmetry of life and the symmetry violations in physics. In: Nishikawa K et al (eds) Prog theor chem & phys B, vol 26. Springer, Berlin, pp 47–76, and references therein
61. Winklhofer M (2010) Magnetoreception. J R Soc Interface 7(S2):131–134. Also: http://en.wikipedia.org/wiki/magnetoreception, and references therein
62. Crabtree V Electromagnetic radiation and the human body. humantruth.info/radiation.html
63. McRill D Effects of radio waves on living organisms. ehow.com/list_6376744..., and references therein
64. Ross MD (1984) Influence of gravity on the structure and function of animals. Adv Space Res 4:305–314. Also: http://en.wikipedia.org//wiki/gravitational_biology, and references therein
65. Kaempffer FA (1967) The elements of physics: a new approach. Blaisdell, Toronto. Chaps 1, 11 & 15
66. Kaempffer FA (1965) Concepts in quantum mechanics. Academic Press, New York. Chaps 13–15 & 26–28

Chapter 4
Some Biochemical Reflections on Information and Communication

Erkki J. Brändas

Abstract The biochemical aspects of communication have been investigated via an extended framework of original quantum-statistical concepts. The key idea develops from the notion of a so-called Spatio-Temporal Neumatic, *STN*, configuration, an open dissipative structure resting on the boundaries connecting micro-, meso- and macroscopic levels. In this category one finds *de novo* self-organization of molecular motion, enzymatic catalysis and the self-assembly of nano-structures all the way to biologically relevant processes like cell evolution, cellular neurobiology etc. The possibility to store and communicate coded messages in this enlarged organization is documented and recognized, unifying various proposals of theoretical understanding including in particular the law of Gödelian self-reference. It is demonstrated that intra-cell and inter-cell order leads to differentiation through a Poissonian modus operandi. The latter lacks intrinsic memory, but its statistical nature gives way to something non-intrinsic of teleonomic significance. Various consequences of this idea prompt a broadened notion of communication and information, generating encodable cell differentiation through cell quality value factors resonating through original communication channels accessible through Poisson statistics. It is shown that inter-cell communication is temporally dominated while intra-cell information is largely spatio-controlled. The nested (spatio-temporal) property of the "code of codes" extends from the genetic- through the socio-, ecological- and to the cosmological rank, while taking account of a more stringent and appraisable representation of the contemporary concept of a meme.

4.1 Introduction

Communication is a fundamental concept that covers as well as demands a deeper and philosophical understanding at all levels of physical, chemical and biological (even social) processes. Communication appears between the various parts of a microscopic system, e.g. to interpret single-molecule-information transfer or in

E.J. Brändas (✉)
Ångström Laboratory, Theoretical Chemistry, Department of Chemistry, Uppsala University, Box 518, 751 20 Uppsala, Sweden
e-mail: erkki.brandas@kemi.uu.se

M. Hotokka et al. (eds.), *Advances in Quantum Methods and Applications in Chemistry, Physics, and Biology*, Progress in Theoretical Chemistry and Physics 27,
DOI 10.1007/978-3-319-01529-3_4,

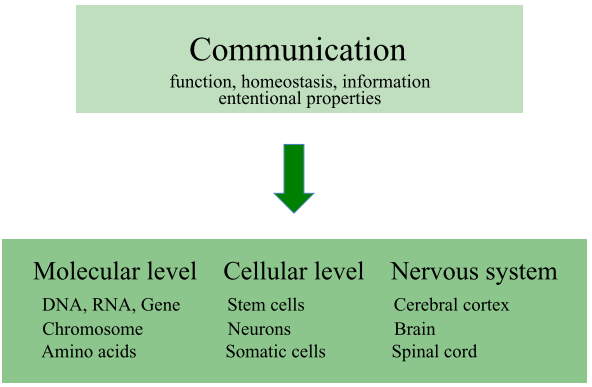

Fig. 4.1 Levels of communication from molecules to living organisms

understanding molecular, enzymatic and protein catalytic properties of biological systems [1, 2].

On the mesoscopic level there appears macro-molecular structures and their dynamics, self-organization and autocatalytic processes, chemical waves and patterns [1–3]. Communication and pattern recognition play a decisive role in the specific evolution of the cell. Concepts such as microtubules, spindles, molecular propellers etc., are contained in biological information systems governing the conversion of chemical energy to mechanical energy [4]. An analogous challenge relates to metabolism, i.e. the proxy of the classical Helmholtz free energy with its quantum analogue including the functional emergence of quantum-thermal correlations and associated microscopic self-organization.

The enormous development within nano-science is based on a fundamental understanding of quantum mechanical meso- macro systems, e.g. characteristic polymers [5]. This in turn leads to the formation of new molecular electronics building communication systems for the future [6]. One can safely predict that quantum technology will revolutionize our new information society, not only by dramatically reducing the size of ingoing components, but also via the exploitation of an entirely new and completely different theory for information transfer, based on quantum communication [7].

In the present description the concept of communication, including aspects like function, information, reception, submission, transmission, regulation and adaptation have been extended. In Fig. 4.1 a sketch of the levels of communication presently discussed in this contribution, have been made. The figure will be completed with a larger picture in the final concluding section.

Target-directed behaviour was already generalized by Mayr [8] to conceive of biological functions to so-called teleonomic processes, which owe their goal-directness to the operation of a program, see also Pittendrigh [9] for an early introduction of the term. Following Deacon, Ref. [10], one may attempt to divide dynamics into three separate categories, *viz*. homeo- (thermo-), morpho- (self-organization) and teleo-dynamics. The view conveyed here indicates incompleteness in our scientific vision and physical representation. The word “intentional” is a philosophical expression that corresponds to a metaphysical concept that also

admits purpose. However, to introduce a general term for all phenomena that are intrinsically incomplete in the sense of being arranged or ordered to accomplish something non-intrinsic, Deacon in his excellent monograph [10] introduced the generic attribute "ententional".

In order to disentangle the dilemma of separating the world into a physical and a mental part, we will introduce the concept of an open dissipative structure that in effect corresponds to active transitions between germane states of biological significance. The ensuing spatio-temporal adaptation exhibits teleonomy, since their autogenetic epithet is controlled by diverse factorizations of the apt transformation. This allows transcended encodings [11, 12], a feature that will be expounded below.

To realize this agenda we will establish a basic statistical relationship between the spatio-temporal neumatic structure (*STN*), [13], mentioned above, see Appendices A, B, and the infinitely divisible probability distribution a.k.a. the Poisson distribution. For a recent discussion and application of the latter in connection with cell-radiation interactions in radiotherapy, see Advances in Quantum Chemistry, volume 65 edited by Dz. Belkic [14]. Although the number of occurrences of an event, within a unit of time, if characterized as Poissonian, lacks memory, i.e. is independent of previous occurrences, it will be demonstrated that the transformation properties of *STN* systems carry encodable factorizations. Thus the intrinsic statistical property of the Poisson distribution gives way to something non-intrinsic with ententional significance. This insight will provide realistic modelling of genetic and epigenetic factors interlocking cell differentiation and cell communication, chaotic neuron dynamics and bestow additional understanding of the general binding problem, a central issue in cognitive neuroscience. The energetics of the teleonomic processes, to be considered here, recognizes the quantum statistical emergence and self-organisational mode of quantum-thermal correlations, the latter yet in concert with the second law. This undertaking will conclusively make possible the communicative aspects of evolution, as it will extend also to the socio-ecological and the cosmological ranks.

4.2 Theoretical Basis and Background

In order to confront the challenges enunciated above, it is essential to incorporate the examination of microscopic systems that exhibit irreversible behavior as well as the associated time asymmetry of entropic increase. Thus one needs to consider the following requirement: In what way could thermodynamics possibly emerge from the abstract concept of statistical mechanics, where temporal asymmetry materializes from perfectly time symmetric microscopic dynamics. To remove unnecessary detailed theoretical formulae and their derivations in the main text they have been collected in Appendices A and B, see also Refs. [11–13, 15–25]. In these so-called *STN*-structures it is particularly emphasized that the synergetic emergence of the quantum- and the thermally activated correlations operates as a constructive driving force in far from equilibrium situations. Note that the present quantum-classical fusion, reminiscent of the notion of quantum discord, a recent hot topic in quantum

information theory [26, 27], is in fact a quite different conception. As demonstrated in the appendices further below, the *STN* configuration reproduces evolution in that it inhibits loss of ordering between the phases of the system or otherwise stated is decoherence code forbidden leading to atypically longer lifetimes.

To complete the picture, we call attention to the sub-dynamics programme of the Brussels School [22, 28], a derivation that combines classical and quantum mechanics employing the Nakajima-Zwanzig projection and the Liouville operator technique [29, 30]. Making use of the dilation analytic properties of the many-body molecular Hamiltonian, i.e. employing the universal complex scaling method for the subsequent analytical continuation via a mathematical theorem due to Balslev and Combes [31] the author derived and developed the advanced-retarded representation of the Prigogine Generalized Master Equation [32], see e.g. Refs. [15, 33, 34]. These extensions are not merely technical as the possibility to formulate and analyze the *STN* concept rests on the incorporation of broken symmetry solutions (parity violations, time irreversibility, non-probabilistic evolution etc.) resulting in the above mentioned quantum-thermal unification. Moreover it will be easy to separate, in the Master Equation, the appropriate residue contributions of its key partaker, the non-hermitian collision operator, in addition to calculate related creation- and destruction operators via proper analytic continuation as ascertained by the mathematical theorem just mentioned. The ensuing spectral limit on the real axis gives the dissipativity condition for a quantum mechanical system with an absolutely continuous spectrum as well as rigorously defining necessary analytic extensions.

In summary the primary differences between the causal dynamics of the Brussels School and the present formulation is appended. Thus it is advocated [13, 37]:

(i) a retarded-advanced (homeo-, morpho-, teleo-) dynamics, allowing conversion of the authentic time evolution into contracted semigroups
(ii) a relaxed positivity preserving condition, compelling a non-probabilistic interpretation
(iii) an entrenched integration of an inevitable objective loss of information
(iv) a wide-ranging self-organization through integral quantum-thermal correlations as established by the instituted Bloch thermalization.

This progression begets a new concept, *viz*. the Spatio-Temporal Neumatic structure, *STN*, which in addition to perpetuating microscopic self-organization including a rich variation of timescales as well as (code-forbidden) protection against decoherence, also brings about transmissible encodable transformations yielding authorization to consecutive changes between germane, e.g. polymorph biological states.

4.3 Nucleic Acids Versus Proteins as Cell Discriminator in Vivo

The recent Nobel Prize in Physiology and Medicine, recognized work that concerned the remarkable possibility to reprogram somatic cells to so-called induced pluripotent stem cells, IPS [35, 36]. This achievement is not only predicted to stimulate progress and providing new tools to scientists around the world in many areas

of medicine, but it also brings up new challenges, such as what differentiates various somatic cells from each other and how does the cell in a stable culture environment, including other cells of similar mode (homeostasis), communicate its tasks and responsibilities to the cell nucleus thereby starting the appropriate program to generate the necessary information in agreement with its position in the hierarchy of the organism.

In Appendices A and B, we have examined the dynamics of the DNA structure of the cell nucleus and on the next level described the evolution of the cell. The central request for information concerns the cellular signal opening up the program stored in the cell nucleus. In the search for answers one recognizes the conditions related to one of Darwin's basic evolutionary mechanism, i.e. Natural Selection, *NS*. In the entropic language of Shannon the constraints of the signal probability, and further the dynamics of the signal generator is entailed, while maintaining the far from equilibrium situation. In consequence one must incorporate simultaneously, thermo-, morpho-, and teleodynamics, using the term self-organization more or less synonymously with morphodynamics. In other words, therefore, self-organisation is the expression of the intrinsic thermodynamics of the *STN* constitution that gets "articulated" within a specific non-equilibrium boundary condition. *NS*, quoting Ref. [10], is a function of the organization of the system's internal non-equilibrium dynamics with respect to non-intrinsic external conditions.

The properties of the so-called *STN* configurations and their role in *NS*, are examined in the Appendices A, B, see below. Hence one might characterize the cell C_i as derived for M base pairs (the DNA double helix joined together by hydrogen bonded nucleotide bases will be further detailed below) via the m-dimensional *STN* configuration. Rewriting (4.25) and using the normalization condition

$$\mathrm{Tr}\{\rho\rho^{\dagger}\} = 1$$

one obtains

$$C_i = \frac{1}{\sqrt{10}}\left\{3\left|f_1^i\right\rangle\left\langle f_m^i\right| + \frac{1}{(m-1)}\sum_{k=1}^{m-1}\left|f_k^i\right\rangle\left\langle f_{k+1}^i\right|\right\}. \tag{4.1}$$

Here the preferred molecular basis $\boldsymbol{h}$ refers to the molecular double proton tunnelling motion of the various base pairs adenine-thymine, guanine-cytosine, the canonical basis $\boldsymbol{f}$ obtains from the transformation $\boldsymbol{h} = \boldsymbol{f}\boldsymbol{B}$, where $\boldsymbol{B}$ becomes the crucial bearer of phonon induced channel information, see Eq. (4.12) in Appendix A, i.e.

$$\boldsymbol{B} = \frac{1}{\sqrt{m}}\begin{pmatrix} 1 & \omega & \omega^2 & \cdot & \omega^{m-1} \\ 1 & \omega^3 & \omega^6 & \cdot & \omega^{3(m-1)} \\ \cdot & \cdot & \cdot & \cdot & \cdot \\ \cdot & \cdot & \cdot & \cdot & \cdot \\ 1 & \omega^{2m-1} & \omega^{2(2m-1)} & \cdot & \omega^{(m-1)(2m-1)} \end{pmatrix}; \quad \omega = \mathrm{e}^{\frac{i\pi}{m}}. \tag{4.2}$$

Although M and m in general satisfies $M < m$ (or even $M \ll m$), it is natural, in the case of a description related to the DNA helix, to choose $m = 4M$, since the

account refers to four different nucleotides, alternatively one can also make the optimal choice $m = 2M$ preferring the general tautomeric structures of the two basic proton configurations, see Appendix B for more details on the origin of Eq. (4.1). The *STN* structure Eq. (4.1) describes a dynamical situation, which mimics the helical structure of the nucleotides. Note that the transformation engenders two fundamental undertakings: (i) it diagonalises the apposite second order reduced density matrix, which in ideal cases might develop ODLRO, see Appendix A and Eq. (4.13), (ii) it transforms the thermalized density, fulfilling the far from equilibrium boundary conditions (4.18), to classical canonical form (4.21)–(4.23). Hence $\boldsymbol{B}$ emerges to "store information" in the helical arrangement before the cell division, where the structure represented by Eq. (4.1) mimics the step operator properties of e.g. angular momentum. The former property is wide-ranging and has actually been respected in the context of cosmological evolution, see Ref. [37] and in the conclusion.

The opening up of the double helix, the copying of the gene, leads to a very complex process (here much oversimplified) where the copy is made via the so-called messenger ribonucleic acid mRNA. In the subsequent step transfer RNA (tRNA), is bound to mRNA. The former carry an amino acid at one end of the chain. Hence the anticodon of the tRNA is bound to the complementary codon of the mRNA. Note that in RNA the nucleotide base is uracil instead of thymine and of course it forms no double helix. Note also that the anticodon defines the group of the three complementary nucleotide bases coding for the amino acid carried by the tRNA. The process describes the generation of a protein from the complete sequence coding of one gene, where triples of nucleotide bases code for one of the twenty natural amino acids building up the protein. In addition to the protein coding genes, the so-called extrons, there are interruptions by long DNA sequences, introns (missing in the mRNA synthesis), which do not code proteins and whose biological role for a long time appeared uncertain. We will return to this exon-intron mechanism below.

Before examining the factorization properties of the transformation $\boldsymbol{B}$ it is important to realize that the molecular constituents of the cell as formulated in Eq. (4.1) and in the appendices is a coarse grained simplification and require further details. At the outset the reader is reminded of the Watson and Crick stereo-model utilizing the hydrogen bond complementarity between the nucleotide base pairs, see e.g. Löwdin [38] and references therein for the state-of-the-art of that period. Thus it is important to model the preferred basis as essentially developed from the double proton tunnelling movements inside the DNA helical order even if the description refers to an open dissipative system. This is clearly not the whole story since the dynamics is intrinsically defined by the highly complex correlated motions of the light fermionic carriers e.g. the electrons that accompany nuclear position changes and vice versa. In this procedure one usually invokes the purported Born-Oppenheimer (BO) approximation, implying essentially that electrons, being much lighter and quicker, moves in a more or less nuclear equilibrium configuration. Obviously this is not adequate here, cf. Ref. [39] where the mirroring between the "light carrier" and its "heavy partner" should be perceived beyond the BO picture via corresponding traces over all nuclear degrees of freedom in the electronic picture and vice versa for the nuclear dynamics. Without going into more details it will be sufficient

to consider the nuclear organization, while knowing in principle that one can recover the complementary portrait in the more complex world of the light carrier via the Generalized Master Equation.

The intimate relation between the guardians of the blue print (DNA-RNA) and the proteins as responsible for the business of life, see Refs. [40, 41], prompts the establishment of a nested code, where the codon triplets defines the actual amino acid and the sequence of amino acids builds the protein. Note that Szent-Györgyi [40, 41], already more than 70 years ago, did postulate electron conduction along the main polypeptide chain of the main protein, a hypothesis that the scientific community did not originally accept, see e.g. Ref. [42]. It was, however, corroborated by Ladik and Ye [43] half a century later. Incidentally we have here a clear indication of the mirroring symmetry between the non-equilibrium nuclear degrees of freedom and the electronic motion. The proton tunnelling movement in the hydrogen bond is, at this juncture, commensurate with electron transfer through several different proteins, similar to the situation in photosynthesis or the case of oxidation-reduction enzymes. As will be seen below, this relationship calls for an encoding that incorporates at the same time the molecular-, the super-molecular and the cellular levels.

4.4 The Nested Code and the Cell Quality Factor

The puzzle or question: why are there four bases in DNA and what role is played by the natural selection, *NS*, of the coding form has been belaboured on and off since the origin of the work of Watson and Crick, see e.g. Ref. [44] for various inherent constraining requirements on the coding system itself considering the efficiency of performing the code's biological roles. As seen below, we will attempt to go beyond the model of a linear sequence of symbols "under the constraint of a constant number of units in a symbol pool", Ref. [44], and assemble a more flexible scheme based on non-commutative factorizations of the *STN*-graph.

To appreciate the coding possibilities of the transformation $\boldsymbol{B}$ in Eq. (4.2), one can take the case of $m = 12$ as an example. The display of $\sqrt{}12\boldsymbol{B}$ will be portrayed as a diagram below, where the dimension of the cyclic vectors is given in parenthesis. For simplicity the first vector of one-dimensional units (1) have been removed and hence there will only be 11 columns, i.e.

$$\begin{matrix}(12)\\(6)\\(6)\end{matrix}\begin{matrix}(4)\\(4)\\(4)\end{matrix}\begin{matrix}(3)\\(3)\\(3)\\(3)\end{matrix}\begin{matrix}(12)\\(2)\\(2)\\(2)\\(2)\\(2)\\(2)\end{matrix}\begin{matrix}(12)\\(3)\\(3)\\(3)\\(3)\end{matrix}\begin{matrix}(4)\\(4)\\(4)\end{matrix}\begin{matrix}(6)\\(6)\end{matrix}\begin{matrix}(12)\end{matrix} \tag{4.3}$$

bearing in mind, at the same time, the manifest symmetry in the diagram. A realistic consideration of the cyclic nature of the columns above elicits the implication that

certain input locations or key subject areas of the system are spatio-temporally correlated. In addition the nested characteristic of the non-commutative map recognize interlevel communication and dynamics.

Belabouring the factorizations one could also simplify the graph, Eq. (4.3), as the seven noncommuting factors below including the first column of (1)'s, leaving out the final 5 repetitions, i.e.

$$\{12\} = \big\{12 \times (1) \oplus 1 \times (12) \oplus 2 \times (6) \oplus 3 \times (4) \oplus 4 \times (3) \oplus 1 \times (12) \oplus 6 \times (2)\big\}.$$

In particular one sees that amongst the 12 columns there are 4 columns that are of the type $1 \times (12)$, i.e. that one third of the columns are not factorizable, while the remaining two thirds are. Also the choice of $m = 12$ has a particular relevance since the diagram supports the codon triplets as fundamental cycles. To include cycles corresponding to the 20 amino acids one could append the example to the case $m = 12 \times 5 = 60$, i.e. including the factor "5", which will add columns divisible by 5, 10, 15, 20, 30. Here one finds that 40 columns of 60 are not factorizable, increasing the abundance of the latter ($m = 12$) from 1/3 to 2/3, a number rapidly increasing with m. Already at this instance, one is able to predict the characteristic that a large number of vectors in fact do not convey any information as they contain no closed cycles of order smaller than m compared to the number of those that did contain such cycles, not to mention the situation when m equals a prime number. It has not escaped our notice that the specific property postulated above immediately suggests a possible exon-intron mechanism for the genetic material; see the comment in the previous section.

The general diagram for a number n, with an initial factorial progression would essentially read ($n_k = n/k$)

$$\begin{array}{ccccccccccccccccccc}
 & & & & & & & & (n_{\frac{n}{2}}) & & & & & & & & & & \\
 & & & & (n_{p_k}) & & & & (\cdot) & & & & (n_{p_k}) & & & & & & \\
 & & & \cdot & \cdot & (\cdot) & \cdot & & \cdot & & \cdot & & \cdot & (\cdot) & \cdot & \cdot & & & \\
 & & (n_3) & \cdot & & & \cdot & & (n_{\frac{n}{2}}) & \cdot & & & \cdot & & \cdot & (n_3) & & & \\
 & (n_2) & & & (n_{p_k}) & & & & & & & & (n_{p_k}) & & & & (n_2) & & \\
(n) & & (n_3) & \cdot & & & \cdot & (n) & \cdot & (n_{\frac{n}{2}}) & \cdot & (n) & \cdot & & & \cdot & (n_3) & & (n) \\
 & (n_2) & & & (n_{p_k}) & & & & & & & & (n_{p_k}) & & & & (n_2) & & \\
 & & (n_3) & \cdot & & & \cdot & & (n_{\frac{n}{2}}) & \cdot & & & \cdot & & \cdot & (n_3) & & & \\
 & & & \cdot & \cdot & (\cdot) & \cdot & & \cdot & & \cdot & & \cdot & (\cdot) & \cdot & \cdot & & & \\
 & & & & & (n_{p_k}) & & & (\cdot) & & & & (n_{p_k}) & & & & & & \\
 & & & & & & & & (n_{\frac{n}{2}}) & & & & & & & & & &
\end{array} \tag{4.4}$$

In fact one can use the unique prime decomposition of every number n to devise a so-called Gödel numbering identifying any "proposition", cf. the famous Gödel incompleteness theorem in propositional logic [21], see also [11, 12], the "proposition" here in general meaning anything from amino acid identification to higher order ententional meanings [10]. To account for the nested combination of characteristics in (4.4), Nature must develop a more compact and flexible code than the Gödel numbering, for instance bijective K-numeral systems e.g. the bijective base

26 without a zero, which make compact strings of alphabetic labels (which finally gives rise to languages as developed from mathematics). It is also required that the decoding depends on the prior "knowledge" of each "receiver" and in this sense the code may have different interpretations and versions.

In Appendix B the cell's Q-value factor was obtained, the latter essentially being equal to the dimensional number m. Rewriting Eq. (4.27) (here ω_0 is the thermal frequency, τ the lifetime corresponding to the resonance half-width, and τ_{corr} is the short time scale defined in Eq. (4.18), see Appendices A, B for details)

$$\mathcal{P} = (\omega_0 \tau - i)\mathcal{I} + \mathcal{J} = m\left(\omega_0 \tau_{corr} - \frac{i}{m}\right)\mathcal{I} + \mathcal{J} \tag{4.5}$$

it is easy to see that resonance between correlated cells and *STN* structures of the cell nucleus occurs when the dimension of the *STN* matches (essentially) the Q-value of the cell, noting that the first term in Eq. (4.1) is short-lived compared the second one.

Metaphorically the cell can be imagined as a tuning fork coupled to a resonance box, i.e. the cell confinement containing the cell nucleus. The Q-value depends on the actual position of the cell in the hierarchy of the organism and the corresponding assignment for the business of building material structures of a particular kind. As an example one might consider nerve cells or neurons, which regulates the flow of information from sensory input to motor output, via the production of appropriate neurotransmitters. Obviously high Q-factors contribute to various types of memory and learning, see e.g. Kandel [45] for an excellent summary of the state of the art in memory research.

Continuing the metaphor one can envisage the phonon assisted communication between the cells as a number of "phone calls" between the cells during a given time, t, being multiples of the characteristic time $\tau = \tau_{rel}$, see Eqs. (4.31)–(4.34) in the appendices. The probability that k "calls" are exchanged during a specific time interval, with each "telephone call" occurring with a known average (intensity) parameter $\lambda_l = (l-1)\tau_{rel}/\tau_{rel} = (l-1)$; $l = 2, 3..m$ i.e. with a specific distribution for each value of l, is trivially given by

$$P_{\lambda_l}(k) = \frac{(l-1)^k}{k!} e^{-(l-1)} \tag{4.6}$$

with the mean and variance given by $\lambda = l - 1$. The mean maximum number of events during $\mathcal{T}_l = (l-1)\tau_{rel}$ are clearly given by $l = m$, with $\lambda_m = (m-1)$ or counting $l = 0$ as an event, the community of cells encompasses during $\mathcal{T}_{m-1}$, according (4.6), m communications between M cells distributed over m possible "sites" in the organism. From the properties of the Poisson distribution one can recognize that the maximum length m, of a message set, is directly matched by the variance and the mean λ.

To put it concisely, each cell is characterized as an *STN* system, i.e. an open dissipative system, containing nested encodings, programmed in the factorized canonical vectors of the transformation $\boldsymbol{B}$, from the genetic to higher order codes, e.g. the blueprint for the protein build up, stored in the genetic alphabet and converted via a resonating mechanisms (depending on the Q-value) from cell to cell.

While the intercell interconnection essentially emerges temporally, the intracell communication is also spatially linked. This is simply recognized since the intra-cell configuration, as analysed by the Zubarev-like double time Green function [25], see Appendix B, entails a cumulative Poisson statistics, see Eq. (4.38), with the parameter $\lambda = 4\pi/3m$ and where communication divides into much smaller packages, i.e. dividing up the unit sphere of the cell into m units for various values of m (remember its relation to the Q-factor of the "resonating tuning fork"). In this vein it is tempting to speculate how the choices of various factors in this super-genetic game permits factors that include essentially the first prime factors plus some key elements from the knowledge of the organized structure of DNA and protein. In addition to observing the presence of the factors $2, 3, 4, 5, 10, 12, 15, 20, 30, 60$, see discussions above, one also observes the inevitable choice of the factor 23 for the human chromosome (consisting of 23 pairs), each containing 400–4000 genes and 50–250 million base pairs. Some further comments will be given in the conclusion.

Lastly, noting the curious choice $3m = 12$, yields a close proximity to the key case ($\lambda = 1$), i.e. $\lambda = 1.047$, which favours the one-event case over the zero event situation while at the same time rapidly approaching the cumulative distribution with an increasing number of terms, the latter a critical property of the code transfer process on the microscopic stratum. Unless this observation is an artefact of the formulation, the deviation of λ from unity, should be experimentally noticeable, cf. the hypofractionation modality of radiotherapy, Belkic and Belkic [14].

Finally the column vectors of $\boldsymbol{B}$, i.e. the actual canonical vectors $\boldsymbol{f}$ or $\boldsymbol{F}$, give the contents of "telephone calls". While the encoded diagrams (4.3), (4.4) concern the memory storage of information, the decoding is read (column wise) via the inverse (unitary) transformation $\boldsymbol{B}^{-1}$ corresponding to the transpose rotated diagram, see the tilted view in Fig. 4.2 below. Thus in the revolved diagram, the various column vectors start with a "1" in the first entry, supplied by the omitted column in (4.3). Hence data messages, scanned during the decoding process, are scrambled compared to the stored information given by the vectors of $\boldsymbol{B}$, but nevertheless simplified by the obvious symmetry of the portrait in Fig. 4.2. Although it is appealing to continue a more detailed examination and interpretation of neuron dynamics and their adaptability as well as their potential for any organisms' behaviour, as built into the brain, we will here only emphasize the commensurateness of the present idea with regular genetic and developmental control. Some evidence will, however, be enunciated in the final stages below.

4.5 Conclusion

As the conclusion is approached, we should briefly address the question how humans had retained some of the cellular mechanisms of learning and memory storage found in simple animals and further, during evolution, developed higher quality neurons, e.g. the pyramidal neurons in the prefrontal cortex. The modern state of the art, i.e. how the flow of information from sensory input, coding for a perception and

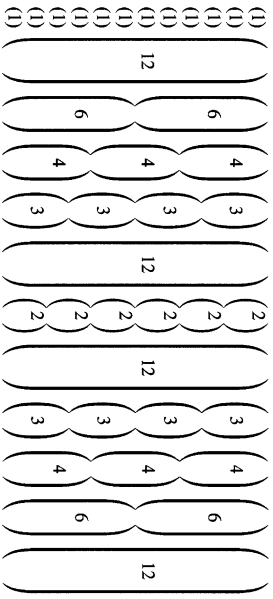

Fig. 4.2 The 90 degree rotated diagram for the case $m = 12$ corresponding to the decoding process, i.e. the inverse transformation $\boldsymbol{B}^{-1}$

couples the information, via the interneurons, to motor output, emerged primarily from the research group of the Nobel Laureate Erik Kandel in their fundamental studies of the giant marine snail (Aplysia) [45] via simple neuronal circuits of originally a small number of nerve cells. In general, different forms of learning give rise to different patterns of neuronal activity. A fundamental feature of memory is that it is formed in stages and that fixation onto long-term memory requires the synthesis of new proteins. Further, memory is distributed and stored throughout the circuit and without going into detail regarding the synaptic transmissions; it is realized that the important point is that chemical synapses predominate in the brain. It is hence tempting to analyse the spinal cord and its neuronal activities in terms of the model put forward here. For instance combining the factor 60 from the triplet codon analysis with 23 (the number of chromosome pairs), one obtains a possible Q-number for single sensory neurons of $m = 23 \times 60 = 1380$ or using a more compact factorization $m = 23 \times 6 \times 4 = 552$, numbers that is slightly larger than those found in Aplysia [45]. These figures (or multiples thereof) correspond to active neural terminals serving as classical communication channels for synaptic transmission, with shifting Q-values, each linked to a particular schema, Fig. 4.2.

Obviously the present understudy of numbers may be a great deal too naïve not only in comprehending its nested attributes, but also in the entreating appeal to understand the detailed structure of the chromatin strands, the estimated gene content of a particular chromosome, its size and associated gene prediction. Nevertheless the structure of the DNA packing in general and the DNA and protein in the cell cycle in particular, provide important communicative information about e.g. centromeres and other chromosomal components, which should become transferrable information for code entanglement.

Although it is too early to draw specific conclusions it is obvious that the Q-factor representation of the cell actually becomes more like a passive Q-switching model. The synchronization of so-called spike trains may be examined in terms of their Poissonian property, cf. Eq. (4.6), where classes of statistical distributions with $\lambda = l - 1$ for $l = 2, 3, \ldots, m - 1$; provides the necessary channel for communication. The somewhat ambiguous interpretation that free will, interpreted in its naïve form, should be contradicted by incompatible time lags between increasing brain activity and its conscious perception in the cortex, does not appear here if one avoids to conflate time as an evolving (generalized) observable with the various biological time scales building up the actual organism under reasonable statistical conditions. In fact the self-referential nature of our theoretical formulation, cf. the analogy between Gödel's theorem(s) and multiple surface intersections in molecular chemical physics, introduces decision making processes already working at the microscopic level. Since communicative semiology, at various levels, with its basis in the fundamental idea of self-reference, produce teleodynamic encodings, then, irrespective of the location of the spatio-temporal site for any decisions made, the only agent is by definition the self!

A central question in cognitive neuroscience is the way the collection of neurons combines external signals with internal memories. Although different in perspective, i.e. studying quantum aspects of chaotic neuron dynamics, Arecchi [46], did put forward a novel conjecture in terms of homoclinic chaotic systems and studied the problem mentioned above, also known as the Feature Binding Problem, finding that mutual synchronizations of spike trains may contribute to well-defined perceptions. Homoclinic chaos then appears suitable for encoding of information of equal spikes occurring at apparently erratic times via a given metric structure of a so-called percept space, the latter displaying fundamental quantum features. Nevertheless the conjecture, of great interest, is wanting in the verification of an explicit code.

In our model one might well anticipate expanding the encoding and decoding processes to the appropriate regions in the cortex, viewing higher-level perceptions, "codes of codes", as an extended *STN* configuration in which it should be possible to incorporate a more distinct gene-based definition of the reproductive "social gene", known as the meme, a notion coined as a concept for discussion by Dawkins [47]. For instance, the actual physical representation of an information processing capability in the brain leads to neural circuits in action and the question how e.g. hippocampus processes sensory information. Neurons in the hippocampus register information, not with respect to a single sensory attribute, or one of the five senses individually, but more precisely, to a modality that depends on the synchronized information from several senses including spatial and temporal recognition. It is not unreasonable to sanction the spatial map that maintains the unitary and subjective nature of the conscious state, i.e. feature bindings via the present nesting of the "codes of codes".

In passing one note our attempts to find answers to the question, whether it is possible to reduce biological explanations to chemistry and/or physics. In more detail we have tried to advance a positive response at the same time amalgamating the systematic- and selectionist viewpoint. While pursuing natural selection to its basic

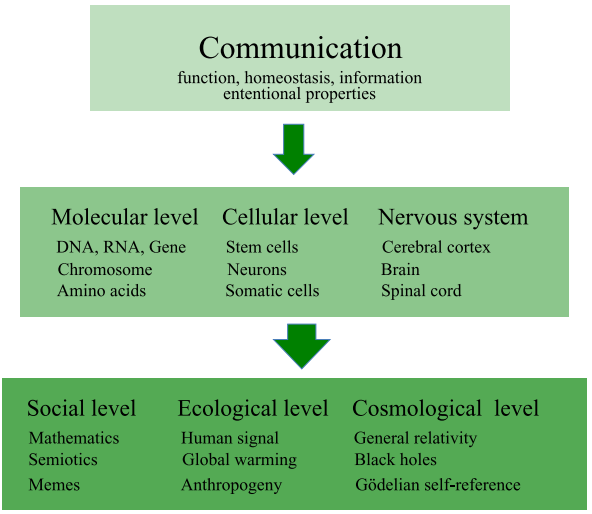

Fig. 4.3 Ranks of communication from the micro level to cosmos

level, we end up with a genotypic position. Nevertheless, the teleonomic dynamics, i.e. the view of biology as a goal-directed evolution according to the operation of a program inevitably puts a more complete answer closer to the scientific borders between physics, metaphysics and philosophy. Not only do we hypothesize whether macro- and micro evolution are instigated by the same process, but in addition, even if we believe that the answer should be "yes", the unattainable question arise, *viz.* when and how did the origin of life emerge in the universe? The answer that we want to communicate in this article, i.e. an assertion at the highest branch of evolution, as is presently known, without religious implications, complies with Fig. 4.3, containing an extended forethought of Fig. 4.1, in the introduction, to the socio-, ecological- and cosmological rank.

In the present investigation it is stressed as well that a different contention or query has been made, i.e. rather than asking the problematical question: what is consciousness, we have attempted to delineate a more specific problem; i.e. what distinguishes animate from inanimate behaviour. Obviously our analysis gives a valid picture of continual evolutionary transitions, entailing decoherence protection, with physical observables represented by operators and their conjugate ones [11–13, 37]. Surprisingly these properties do not only show up at the microscopic biological arena, but also on the cosmic level, see more on this below. Hence the origin of life, although of great interest as far as discovering its first indicators, is already an intrinsic property of a Heraclitean universe.

In the present scenario, Fig. 4.3, it has been added, to the individual level of an organism, the "larger" portrait, exploiting communication between life forms, their interaction with the terrestrial environment, and finally the universal cosmological echelon, as understood today. Also the development or evolution of social structures based on sophisticated meme-like "codes of codes", like mathematics, linguistics, fine arts, music etc. have been examined as well as providing metaphors like tuning forks etc., in anticipation of other phonon-induced communications. For more

considerations and assessments, see e.g. the excellent account of the science of music that goes back to the very remote periods of history including the Neanderthal flute by Maruani et al. [48]. On the ecological level, semiotic investigations concern the anthropogenic impact on our climate. Even if we have succeeded to reduce the patterns of communication to a principle that defines "the self" and that it is "the self" that, in our representation, is the director of its cell-based orchestra, there still remain puzzles. The director acts as a scheduler of the partiture and participates in the upgrading, hence the director-composer becomes a member of the Universal Composers' Guild that includes the universality of knowledge and coding, i.e. information in its semiotic-, anthropogenic- and self-referential connotation. Therefore far and beyond the macro- as well as by and within the microscopic level concealed and unrequited questions are hiding: What is the origin of teleonomy? Is the composition of the universal symphony a built in property of our Universe? Our present conjecture portrays evolution as a natural physical law founded on the principle of self-reference.

In discussing the cosmological category of the chart above, it is necessary to provide a more penetrating assessment of the general concept of teleology. The concept was largely in disrepute until the work of Mayr [8, 49], where he categorized various types of teleology, but unfortunately ruled out the cosmological domain. A surprising relationship between propositional logics (Gödel's theorem [21]), *STN* (then referred to as coherent dissipative structure) [11, 12], and Einstein's theory of general gravity [50], were suggested, proved and exploited [11–13, 37]. The relation suggests a general heuristic Gödelian arrow of time [51] and then a Gödelian structure of the general "codes of codes". Using this allegory, communication on all levels, can be characterized as Gödelian absentia, see also Deacon's analogy, i.e. the concept of the absential as a paradoxical intrinsic property of existence with respect to something missing and as a defining attribute of life and mind [10].

Note that Penrose [52] unequivocally considered the Gödelian theorem(s) of mathematical logic, the latter asserting the inherent limitations of all nontrivial systems, in connection with the main positions of Artificial Intelligence, AI. The critique of his view, i.e. essentially that appropriate physical action of the brain, evoking awareness, can not be properly simulated computationally, has been unforgiving from the philosophical community, but all the same the logically based view finds support in the light of the present report, see also [11, 12] for an earlier account.

It is quite compelling to recognize that our present project rests on analogies with Gödel's work in propositional logic, which unexpectedly did lead to a consistent formulation of gravity [11–13, 37] without any inclusion of a cosmological constant. Nevertheless Gödel is famous also for another paradox [53], namely his cosmological solution to Einstein's field equations [50]. Since this example results in a metric, which allows closed time loops; it implies that Einstein's general relativity supports time as being ideal rather than subscribing to our own primitive intuition. This paradox can be eliminated, however, by the realization that our present operator-conjugate operator method rules out the Gödel metric on account of its dependence on the cosmological constant. As already demonstrated in Ref. [54], the relativistic Kepler problem, e.g. the perihelion movement of Mercury can here be given a

treatment that agrees with general relativity. Whether probing the small or the large, communication in its most general sense seems to follow comparable patterns, i.e. originating from a certain awareness of absentia complying with the law of self-reference. In this way we are all children of evolving time [22], making our way through the sanctuary of spatio-temporal communication via Gödelian Absentia.

Note Added in Proof The meme-based evolution of culture has been vividly illustrated by Deutsch [55], who concludes that knowledge changes the very structure of the Universe, i.e. that the creativity program is a combination of genes and memes and that replicating genes evolve the hardware that support better memes, cf. also the Blackmore "meme machine" [56]. These ideas find support in the present theory that indicates a more detailed gene-oriented meme structure. In addition our teleonomic approach provides backing to the authors simple resolution to the two puzzles presented [55], (a) why was human creativity evolutionary advantageous at a time where there was almost no innovation, and (b) why did human memes successfully replicate, given that brains have no mechanism to download them from other brains. As also confirmed here, complex memes do mandate rules. It remains a conundrum that Richard Semon's views [57] on human memory, that emerged in a biological context for more than 100 years ago, have been ignored not only by his contemporaries, but almost forgotten until this day. For more details on this, see Schacter's remarkable book on Semon's life and work, as well as considerations raised about recognition and neglect of ideas in science [58]. It goes without saying that the actual concept of a *mneme*, introduced in Ref. [57], notwithstanding its introduction, long before the conceptual development of modern genetics, should play a significant role also in our present investigation.

Acknowledgements The author thanks the organiser of QSCP XVII, Prof. Matti Hotokka, Åbo Akademi University, Turku for friendly cooperation, an excellent programme and outstanding organization as well as generous hospitality. The present research has, over the years, been supported by the Swedish Natural Science Research Council, the Swedish Foundation for Strategic Research, The European Commission and the Nobel Foundation.

Appendix A: Derivation of the *STN* Configuration

To ease the reader I will sketch the theoretical background for the so-called Spatio-Temporal Neumatic (*STN*) configuration, earlier also denoted a coherent dissipative structure, including a list of the relevant equations needed for the formulation. Neumatic stands for the basic element, "neum", used in medieval musical notation prior to the invention of the modern staff notation. It could also relate to the ancient Greek word, "pneuma", and meaning breath. For further details on the development, see the work of the author, [11–13, 15] and references therein, where also more thorough accounts can be found. The focal point will be the density matrix ρ (the fundamen-

tal particles are fermions like electrons or protons), subject to the Liouville equation ($\hbar$ briefly omitted)

$$i\frac{\partial\rho}{\partial \boldsymbol{t}} = \hat{L}\rho \tag{4.7}$$

where the Liouvillian is defined as usual from the Hamiltonian $\boldsymbol{H}$ describing the system, e.g. the molecular configuration under investigation, i.e.

$$\hat{L} = H\rho - \rho H^{\dagger}. \tag{4.8}$$

Normally H is self-adjoint, but to carry out analytic continuation a "dagger" is inserted in (4.8). Since the microscopic system might be very complex, not to mention depicting biological structures and organization, it is convenient to start by introducing the Nth particle fermionic (and its q-reduced) representable density matrix $\Gamma^{(q)}$ as follows

$$\begin{aligned}&\Gamma^{(q)}\big(x_1\cdots x_q|x_1'\cdots x_q'\big)\\ &=\binom{N}{q}\int \Psi(x_1\cdots x_q, x_{q+1}\cdots x_N)\Psi^*\big(x_1'\cdots x_q', x_{q+1}\cdots x_N\big)dx_{q+1}\cdots dx_N\end{aligned} \tag{4.9}$$

defined in terms of the many body (normalized) wave function Ψ (here Γ represents a pure state, with obvious extensions for an ensemble) in Eq. (4.9). In particular we will discuss the 2-particle reduced density matrix below, since it is of fundamental importance in connection with the all-embracing electronic correlation problem in *ab initio* quantum chemistry, primarily in connection with strongly correlated structures [16, 17], like e.g. high-T_C cuprates [18]. In the so-called extreme case [17] the density matrix takes on a very simple form. For instance defining an m-dimensional preferred real localized basis $|\boldsymbol{h}\rangle$ of geminals (two-particle functions) on suitable sites of correct symmetry, one can show that the finite dimensional representation essentially writes [13, 19]

$$\begin{aligned}&\Gamma^{(2)} = \rho = \sum_{k,l}^{m}|h_k\rangle\rho_{kl}\langle h_l|; \qquad \mathrm{Tr}\{\rho\} = \frac{N}{2}\\ &\rho_{kk} = p; \qquad \rho_{kl} = p(1-p); \qquad k\neq l;\ p = \frac{N}{2m}.\end{aligned} \tag{4.10}$$

In Eq. (4.10) N is the number of fermions or $N/2$ (quasi-)bosonic pairs and p is "the probability to find" a pair in the state m. The number of possible states must fulfill $m \geq N/2$. The associated secular equation renders a non-degenerate large eigenvalue $\lambda_L = mp - (m-1)p^2$ and a small $(m-1)$-degenerate $\lambda_S = p^2$. Note that for large m and p small ($m \gg N$), $\lambda_L \approx N/2$. Hence the density operator writes

$$\Gamma^{(2)} = \rho = \lambda_L|g_1\rangle\langle g_1| + \lambda_S\sum_{k,l=1}^{m}|h_k\rangle\left(\delta_{kl} - \frac{1}{m}\right)\langle h_l|. \tag{4.11}$$

Although the diagonalisation of the degenerate subspace corresponding to the "small" eigenvalue is not unique, a particularly simple form results from the transformation $|\boldsymbol{h}\rangle \boldsymbol{B} = |\boldsymbol{g}\rangle = |g_1, g_2, \ldots, g_m\rangle$, see e.g. Refs. [15, 20] for the origin of this transformation

$$\boldsymbol{B} = \frac{1}{\sqrt{m}} \begin{pmatrix} 1 & \omega & \omega^2 & \cdot & \omega^{m-1} \\ 1 & \omega^3 & \omega^6 & \cdot & \omega^{3(m-1)} \\ \cdot & \cdot & \cdot & \cdot & \cdot \\ \cdot & \cdot & \cdot & \cdot & \cdot \\ 1 & \omega^{2m-1} & \omega^{2(2m-1)} & \cdot & \omega^{(m-1)(2m-1)} \end{pmatrix}; \quad \omega = \mathrm{e}^{\frac{i\pi}{m}} \tag{4.12}$$

from which our reduced density operator reduces to a very simple and compact form

$$\begin{aligned} \Gamma^{(2)} = \rho &= \lambda_L |g_1\rangle\langle g_1| + \lambda_S \sum_{k=2}^{m} |g_k\rangle\langle g_k| \\ \mathcal{E} &= \mathrm{Tr}\{H_2 \Gamma^{(2)}\}. \end{aligned} \tag{4.13}$$

Before proceeding to discuss open or so-called dissipative systems, which in effect are characterized as exchanging energy and/or entropy with its surroundings, one learns a very uncomplicated yet signifying lesson. The formulation above, that under certain optimal conditions, would develop Off-Diagonal Long-Range Order, ODLRO [16], displays a rather trivial construction, i.e. the diagonal elements of ρ is the probability p to find a pair in the state m, while the off-diagonal ρ_{kl} is the answer to the question "what is the transition probability for a particle to go from the state k to l". Since the preferred basis is localized on the various sites one could also "loosely" replace the state "k" with the site "k". Note that this type of reasoning is non-classical in the sense that it is prompted by the general structure of the density matrix under the extreme form or the precursor to ODLRO. Normally one would think about electronic systems here, but it is equally appropriate to discuss mirroring dynamics in the nuclear skeleton, and e.g. model the nuclear degrees of freedom instead tracing over all the electron variables, for more on the mirroring mapping, see Ref. [39]. Hence the present formulation is completely general as the quantum correlations incorporated here can be modeled as a means to describe propositional logics in a consistent manner that also includes a formal mathematical solution to the Gödel enigma [11, 12, 21].

In order to extend the discussion to include dissipativity, i.e. invoking the temperature of the environment or in other words to merge quantum and thermal correlations one continues by employing the traditional trick of letting the time parameter, t, include the temperature through

$$t \to t + i\hbar\beta; \quad \beta = \frac{1}{k_B T} \tag{4.14}$$

where k_B is the Boltzmann constant and T the absolute temperature. Thermalization is straightforwardly carried out via the Bloch equation

$$-\frac{\partial \rho}{\partial \beta} = \hat{L}_B \rho; \qquad \hat{L}_B = \frac{1}{2}\{H|\,\rangle\langle *| + |\,\rangle\langle *|H\}; \qquad \mathcal{E} = \mathrm{Tr}\{H_2 \Gamma^{(2)}\} \tag{4.15}$$

where the energy (anticommutator) superoperator, see Prigogine [22], is equipped with a complex conjugate sign in the bra-position. The latter is a necessity in order to analytically continue the resonance solution into the complex plane, for more details see Ref. [15]. Writing the Hamiltonian as a sum of two-body operators the total energy follows from a simple trace formula. The formal solution of Eq. (4.15) obtains uncomplicatedly as

$$e^{-\beta\hat{L}_B}\Gamma^{(2)} = \lambda_L \sum_{k,l}^{m} |h_k\rangle e^{i\beta\frac{1}{2}(\varepsilon_k+\varepsilon_l)}\langle h_l| + \lambda_S \sum_{k,l}^{m} |h_k\rangle e^{i\beta\frac{1}{2}(\varepsilon_k+\varepsilon_l)}\left(\delta_{kl} - \frac{1}{m}\right)\langle h_l| \tag{4.16}$$

with the standard relation observed between the imaginary part of the energy and the appropriate lifetime as

$$\varepsilon_k = \frac{\Gamma_k}{2} = \frac{\hbar}{2\tau_k}. \tag{4.17}$$

The thermalized density portrays a complex symmetric representation containing apposite phases due to the thermal fluctuations instigated at the temperature T. To merge the thermal and the quantum correlations, i.e. relating the lifetimes above with the absolute temperature of the environment one might make take advantage of the following boundary conditions [19, 20] ($\tau_2 = \tau_{rel}$)

$$\begin{aligned} \beta\varepsilon_l &= \frac{2\pi(l-1)}{m}; \quad l = 2, \ldots, m \\ m &= \frac{4\pi kT}{\hbar}\tau_{rel}; \quad \tau_{rel} = \tau_2 = \tau_l(l-1) = \tau_{corr} \end{aligned} \tag{4.18}$$

which is due to an important observation [19, 20, 23, 24], *viz*. Eq. (4.16) becomes a Jordan block provided (4.18) holds. Not only will the condition Eq. (4.18) lead to anomalous time evolutions, see the subsequent appendix, but it will also provide us with a unique transformation, cf. (4.12), with specific coding properties as well as providing in retrospect a cumulative Poisson statistics to be used in the main text in connection with cell characteristics and cell differentiation. The first realization is that $\mathcal{E} = \mathrm{Tr}\{H_2\Gamma_T^{(2)}\}$; $\Gamma_T^{(2)} = e^{-\beta\hat{L}_B}\Gamma^{(2)}$, i.e. exhibiting an m-dimensional degeneracy. Secondly it follows surprisingly, inserting the condition (4.18) into (4.16), that

$$\Gamma_T^{(2)} = \lambda_L \sum_{k,l}^{m} |h_k\rangle e^{i\frac{\pi}{m}(k+l-2)}\langle h_l| + \lambda_S \sum_{k,l}^{m} |h_k\rangle e^{i\frac{\pi}{m}(k+l-2)}\left(\delta_{kl} - \frac{1}{m}\right)\langle h_l| \tag{4.19}$$

under the inverse transformation $\boldsymbol{B}^{-1}$ transforms to a more accessible canonical form, i.e. using the knowledge [20, 23] that $\boldsymbol{Q}$

$$\boldsymbol{Q}_{kl} = \left(\delta_{kl} - \frac{1}{m}\right)e^{i\frac{\pi}{m}(k+l-2)}; \quad k, l = 1, 2, \ldots, m \tag{4.20}$$

and the classical canonical form $\boldsymbol{J}$ defined by $\boldsymbol{J}^{(m-1)} \neq 0;\ \boldsymbol{J}^{(m)} = 0$

$$\boldsymbol{J} = \begin{pmatrix} 0 & 1 & 0 & \cdot & 0 \\ 0 & 0 & 1 & \cdot & \cdot \\ \cdot & \cdot & \cdot & \cdot & 0 \\ \cdot & \cdot & \cdot & \cdot & 1 \\ 0 & \cdot & \cdot & \cdot & 0 \end{pmatrix} \tag{4.21}$$

are similar through the unitary transformation

$$\begin{aligned} \boldsymbol{Q} &= \boldsymbol{B}^{-1}\boldsymbol{J}\boldsymbol{B} \\ |\boldsymbol{h}\rangle\boldsymbol{B}^{-1} &= |\boldsymbol{f}\rangle = |f_1, f_2, \ldots, f_m\rangle. \end{aligned} \tag{4.22}$$

In terms of the basis $|\boldsymbol{f}\rangle$ one can finally rewrite Eq. (4.19) in classical canonical form

$$\Gamma_T^{(2)} = \lambda_L \mathcal{J}^{(m-1)} + \lambda_S \mathcal{J}; \quad \mathcal{J} = \sum_{k=1}^{m-1} |f_k\rangle\langle f_{k+1}| \tag{4.23}$$

with

$$\mathcal{E} = \mathrm{Tr}\left\{H_2 \Gamma_T^{(2)}\right\} = 0. \tag{4.24}$$

Looking back, we have in fact carried out a sequence of steps, i.e. complex scaling and localized thermal fluctuations leading up to two orthogonal many-body functions, $\Psi(g)$ and $\Psi(g^*)$, see Eq. (4.9) above. Thus the degenerate structure characterized by Eq. (4.23) is in actual fact not a standard quantum mechanical state as it does represent more accurately a sequence of successive transitions. It is an open spatio-temporal structure, which does not exist under a certain minimum "size" and lifetime, see Refs. [19, 24], with anomalous time evolutions and, as will be demonstrated below, subject to a (cumulative) Poisson-like statistics. A final attribute of far-reaching importance is the factorization property of transformation $\boldsymbol{B}$ as displayed in Eq. (4.12).

Appendix B: Time Evolution of the *STN* Configuration

As portrayed in the central part of the text there are many distinct realizations of *STN* structures to amorphous condensed matter in general and biological, complex enough systems in particular [11–13, 19, 24]. For instance describing cellular interactions and their various properties and differentiation, it is convenient to model each cell as an *STN* entity, based on tunneling proton pairs (quasibosonic degrees of freedom) as sites for the preferred basis. The dimension of the *STN* organization gives rise to a particular transformation $B = \boldsymbol{B}_m$ where the associated factorizing structure of the vectors exhibits nested encoded programs, e.g. the genetic- and higher level codes, as will be pursued in the main script.

Lifting the argument from the molecular- to the cellular level it is straightforward to set up an extended Liouville equation for the cell i, i.e. C_i defined via Eq. (4.23)

$$C_i \propto \left\{ |f_1^i\rangle\langle f_m^i| + \frac{1}{m'}\sum_{k=1}^{m-1} |f_k^i\rangle\langle f_{k+1}^i| \right\} \tag{4.25}$$

where the proportionality sign $\propto$ signifies appropriate normalization, see also Eq. (4.1) regarding the normalization, and

$$m' = m\frac{(1-p)}{p}. \tag{4.26}$$

The value of the "probability" p depends on the context, e.g. for the base pair system discussed in the main text the choice $m = 4M$ yields $p = 1/4$, $m' = 3m$, while the optimal value of the large eigenvalue obtains from $m = 2M$, i.e. $p = 1/2$ and $m' = m$.

In order to formulate the cellular correlations one repeats the trick of constructing the appropriate reduced density matrix [19, 24] derived from the symmetric product of all cells. The (quasibosonic) one matrix describes a cell in the environment of all the others. Note that the energy degeneracy (4.24) for each cell rests on the quasi-equilibrium reached at temperature T with the energy equal to $k_B T$ and the relaxation time, (4.18), $\hbar/\Gamma = \tau = \tau_{rel}$, where Γ, not to be confused with the density matrix notation above, is the width of the resonance profile. For reasons to be clear below the Liouvillian generator of the time evolution is subject to a Poisson-like statistics and it is by now well-known that this follows simply from the inclusion of Jordan-like perturbations. Hence in the space spanned by the cell basis C_i the propagator/generator $\mathcal{P}$ writes

$$\mathcal{P} = (\omega_0\tau - i)\mathcal{I} + \mathcal{J} \tag{4.27}$$

where ω_0 is the thermal frequency corresponding to $k_B T$ and $\mathcal{I}, \mathcal{J}$ are the unit matrix and the Jordan canonical form respectively. For simplicity we take the dimension to be denoted by m although the dimension here in general should be separated from the intracell dimension in (4.25). Note also that the corresponding transformations $\boldsymbol{B}$ and $\boldsymbol{B}^{-1}$ of the "localized" cell basis $\boldsymbol{C}_i$ holds yielding the correspondences $|\boldsymbol{G}\rangle$ to $|\boldsymbol{g}\rangle$ and $|\boldsymbol{F}\rangle$ to $|\boldsymbol{f}\rangle$. From Eq. (4.27) follows directly the causal propagator $\mathcal{G}(t)$ and the resolvent $\mathcal{G}(z)$ defined by

$$\mathcal{G}(t) = e^{-i\mathcal{P}\frac{t}{\tau}}; \qquad \mathcal{G}(\omega\tau) = (\omega\tau\mathcal{I} - \mathcal{P})^{-1} \tag{4.28}$$

with the recognized polynomially perturbed time evolution of the propagator and the associated multipole expansion of its Fourier transform, i.e.

$$e^{-i\mathcal{P}t/\tau} = e^{-i\omega_0 t}e^{-t/\tau}\sum_{k=0}^{m-1}\left(\frac{-it}{\tau}\right)^k \frac{1}{k!}\mathcal{J}^{(k)} \tag{4.29}$$

$$(\omega\tau\mathcal{I} - \mathcal{P})^{-1} = \sum_{k=1}^{m}\big((\omega-\omega_0)\tau + i\big)^{-k}\mathcal{J}^{(k-1)}. \tag{4.30}$$

From the degeneracy with $F_k(t) = e^{-i\omega_0 t} e^{-t/\tau} F_k$, one gets for the rth power of t (note that only F_1 is an eigenfunction, while the others complete the root manifold)

$$N(t) \propto \left|\langle F_1 | \mathcal{J}^{(r)} | F_{r+1} \rangle\right| \left(\frac{t}{\tau}\right)^r \frac{1}{r!} e^{-\frac{t}{\tau}} = \left(\frac{t}{\tau}\right)^r \frac{1}{r!} e^{-\frac{t}{\tau}} \tag{4.31}$$

where the r'th power of $\mathcal{J}$ writes (note the relation between (4.31) and the statistical projection below)

$$\mathcal{J}^{(r)} = \sum_{k=1}^{m-r} |F_k\rangle\langle F_{k+r}|. \tag{4.32}$$

For e.g. the highest power $m-1$ one obtains from Eq. (4.31)

$$dN = t^{m-2}\left(m - 1 - \frac{t}{\tau}\right) N(t) dt \tag{4.33}$$

with an altered microscopic law of evolution

$$dN(t) > 0; \quad t < (m-1)\tau. \tag{4.34}$$

Hence it has been demonstrated (i) that Eq. (4.31) suggests a Poisson-like statistics, see more below, and (ii) that Jordan blocks appearing in the generator of the *STN* teleo-dynamical system results in a non-decaying evolution law that supports microscopic self-organization. The total evolution, being non-statistical, with maximum information becomes "chaotic" when summing over all terms in Eq. (4.29). Note that any reference to statistics here concerns events where genetic code data is transferred between cells.

To proceed one makes the substitution Eq. (4.14), i.e. using the analogue of the Zubarev double-time Green function [25], implying that $\mathcal{P}$ in formula (4.28) is converted into

$$\mathcal{G}(t) \to \mathcal{G}(t + i\hbar\beta) = e^{-i\mathcal{P}\frac{(t+i\hbar\beta)}{\tau}}. \tag{4.35}$$

Since $\omega_0 = \tau/\hbar\beta = M/4\pi$, see Eq. (4.18), the formula (4.29) becomes statistically projected

$$\left|e^{-i\mathcal{P}\frac{(t+i\hbar\beta)}{\tau}}\right| = e e^{-\frac{t}{\tau}} \left|e^{-i\mathcal{J}\frac{t}{\tau}}\right| \sum_{r=0}^{m-1} \left(\frac{4\pi}{m}\right)^r \frac{1}{r!} \mathcal{J}^{(r)} \tag{4.36}$$

which inserted below, using the relation $C_1 = (1/\sqrt{m}) \sum_{l=0}^{m-1} F_{l+1}$, becomes

$$\begin{aligned} N(t + i\hbar\beta) &= \left|\langle C_1 | e^{-i\mathcal{P}\frac{t_i \hbar\beta}{\tau}} | C_1 \rangle\right| = \left|\sum_{r=0}^{m-1} \langle F_1 | \mathcal{J}^{(r)} | F_{r+1} \rangle \left(\frac{4\pi}{m}\right)^r \frac{1}{r!} e^{-\frac{(t-\tau)}{\tau}}\right| \\ &= \sum_{r=0}^{m-1} \left(\frac{4\pi}{m}\right)^r \frac{1}{r!} e^{-\frac{(t-\tau)}{\tau}}. \end{aligned} \tag{4.37}$$

Note that the term containing powers of the operator $\mathcal{J}$ in (4.36) inserted into (4.37) translates to the sum

$$\sum_{k=0}^{m-1}\left(\frac{-it}{\tau}\right)^k\frac{1}{k!}\approx e^{-it/\tau}$$

who's magnitude is essentially one for large m and $|t|<\tau$.

From Eq. (4.37) follows, dividing the lifetime τ into $m/4\pi$ discrete time units, or going from $t-\tau$ to t in single steps, defines a cumulative Poisson distribution with the intensity (rate) parameter $\lambda=4\pi/m$ (or factoring out the triplet codon $\lambda=4\pi/3m$)

$$P\{(t-\tau)/\tau<m/4\pi\}=\sum_{k=0}^{m-1}\left(\frac{4\pi}{m}\right)^k\frac{1}{k!}e^{-4\pi/m}. \tag{4.38}$$

Equation (4.38) sustains the statistical response to the quantum-thermal chaos, for each cell C_i, via collective intra-cell quantum-thermal correlations leading up to a cumulative statistical distribution. It is interesting to ponder whether the choice $m=|4\pi|=12$ carries any particular meaning, since it yields an almost critical case with $\lambda=1.047$, with $P(0)=e^{-1.047}$ and $P(1)=1.047\times e^{-1.047}$, where the probability for one event of communication is larger than that for no event, being exactly the same for $\lambda=1$.

In summary we have mapped the basic constituents of the cell onto an *STN* configuration, i.e. spatio-temporally structured on the electron-proton transfer molecular level of the gene. Examining cell evolution and cell differentiation, based on thermalization along with a degeneracy analysis, where the dimension of the largest Jordan block, m, defines the so-called Segrè characteristic of the degenerate level, one finds a particular type of statistics known as the (cumulative) Poisson distribution (4.31), (4.38). The number $m\propto\omega_0\tau$ is essentially the cell's Q-value factor, cf. its use in regard to quality aspects of an oscillator or a resonator. One can e.g. imagine the cell as a tuning fork coupled to a resonator or in the case of overdamping a "slamming door". The factor 4π obtains naturally in the derivation and may be given a geometric interpretation as being related to space angle integrations. Note that standard practice usually gives the quality factor in terms of energy ratios times 2π.

References

1. Eigen M (1931) Molecular self-organization and the early stages of evolution. Q Rev Biophys 4(2):149
2. Lehn J-M (2007) From supramolecular chemistry towards constitutional dynamic chemistry and adaptive chemistry. Chem Soc Rev 36(2):151
3. Karsenti E (2007) Self-organization processes in living matter. Interdiscip Sci Rev 32(2):163
4. Michl J, Vacek J (1997) A molecular "Tinkertoy" construction kit: computer simulation of molecular propellers. New J Chem 21(12):1259
5. Ladik J (1999) Polymers as solids: a quantum mechanical treatment. Phys Rep 313(4):171

6. Ratner M, Ratner D (2003) Nanotechnology a gentle introduction to the next big idea. Prentice Hall, New York
7. Karlsson EB, Brändas EJ (1998) Modern studies of basic quantum concepts and phenomena. In: Karlsson EB, Brändas E (eds) Proceedings Nobel symposium, vol 104. World Scientific, Singapore
8. Mayr E (1974) Teleological and teleonomic: a new analysis. Boston Stud Philos Sci 14:91
9. Pittendrigh CS (1958) Adaptation, natural selection, and behavior. In: Roe A, Simpson GG (eds) Behavior and evolution. Yale University Press, New Haven
10. Deacon TW (2010) Incomplete nature. How mind emerged from matter. Norton, New York
11. Brändas EJ (2011) Int J Quant Chem 111:215
12. Brändas EJ (2011) Int J Quant Chem 111:1321
13. Brändas EJ (2012) In: Nicolaides CA, Brändas EJ (eds) Unstable states in the continuous spectra, part II: interpretation, theory and applications. Adv quant chem, vol 63. Elsevier, Amsterdam, p 33
14. Belkic Dz, Belkic K (2013) In: Belkic Dz (ed) Theory of heavy ion collision physics in hadron therapy. Adv quant chem, vol 65. Elsevier, Amsterdam, p 407
15. Obcemea CH, Brändas EJ (1983) Ann Phys 151:383
16. Yang CN (1962) Rev Mod Phys 34:694
17. Coleman AJ (1963) Rev Mod Phys 35:668
18. Dunne LJ, Brändas EJ, Murrell JN, Coropceanu V (1998) Solid State Commun 108:619–623
19. Brändas EJ, Chatzidimitriou-Dreismann CH (1991) Int J Quant Chem 40:649
20. Reid CE, Brändas EJ (1989) Lect Notes Phys 325:476
21. Gödel KG (1931) Über Formal Unentscheidbare Sätze der Principia Matematica und Verwandter Systeme. Monatshefte Math Phys 38:173
22. Prigogine I (1980) From being to becoming. Freeman, San Fransisco
23. Brändas EJ (2009) Int J Quant Chem 109:2860
24. Brändas EJ (1995) In: Lippert E, Macomber JD (eds) Dynamics during spectroscopic transitions. Springer, Berlin, p 148
25. Zubarev DN (1960) Usp Fiz Nauk 71:71
26. Oliver H, Zurek WH (2001) Phys Rev Lett 88:017901
27. Henderson L, Vedral V (2001) J Phys A 34:6899
28. Antoniou I, Goldbeter A, Lefever R (eds) (2004) Complexity: microscopic and macroscopic aspects, workshop in honour of Ilya Prigogine on the occasion of his 85th birthday. Int J Quant Chem 98(2)
29. Nakajima S (1958) Prog Theor Phys 20:948
30. Zwanzig R (1960) J Chem Phys 33:1338
31. Balslev E, Combes JM (1971) Commun Math Phys 22:280
32. Prigogine I, George C, Henin F, Rosenfeld L (1973) Chem Scr 4:5
33. Kumicák J, Brändas E (1993) Int J Quant Chem 46:391
34. Brändas EJ, Antoniou IE (1993) Int J Quant Chem 46:419
35. Gurdon JB (1962) J Embryol Exp Morphol 10:622
36. Yamanaka TK (2006) Cell 126:663
37. Brändas EJ (2012) In: Hoggan P, Brändas EJ, Maruani J, Piecuch P, Delgado-Barrio G (eds) Advances in the theory of quantum systems in chemistry and physics, vol 21. Springer, Dordrecht, p 3
38. Löwdin P-O (1965) Adv Quantum Chem 2:213
39. Brändas EJ (2004) Int J Quant Chem 98:78
40. Szent-Györgyi A (1941) Nature 148:157
41. Szent-Györgyi A (1941) Science 93:609
42. Ladik J, Förner W (1994) The beginnings of cancer in the cell. An interdisciplinary approach. Springer, Berlin
43. Ye Y-J, Ladik J (1994) Int J Quant Chem 52:491
44. Seybold PG (1976) Int J Quant Chem S3:39

45. Kandel ER (2006) Search of memory the emergence of a new science of mind. Norton, New York
46. Arecchi FT (2003) Mind Matter 1:15
47. Dawkins R (1976) The selfish gene. Oxford University Press, New York
48. Maruani J, Lefebvre R, Rantanen M (2003) In: Maruani J, Lefebvre R, Brändas E (eds) Advanced topics in theoretical chemical physics, vol 12. Kluwer Academic, Dordrecht, p 479
49. Mayr E (2004) What makes biology unique? Cambridge University Press, New York
50. Einstein E (1915) Zur Allgemeine Relativitätstheorie. Sitz Ber Der Preuss Akad der Wissenschaften, Berlin, p 778
51. Brändas EJ (2013) Int J Quant Chem 113:173
52. Penrose R (1994) Shadows of the mind: a search for the missing science of consciousness. Oxford University Press, Oxford
53. Gödel K (1949) Rev Mod Phys 21:447
54. Brändas EJ (2012) In: Nishikawa K, Maruani J, Brändas EJ, Delgado-Barrio G, Piecuch P (eds) Quantum systems in chemistry and physics. Progress in methods and applications, vol 22. Springer, Berlin, p 3
55. Deutsch D (2011) The beginning of infinity. Viking/Penguin, New York
56. Blackmore S (1999) The meme machine. Oxford University Press, Oxford
57. Semon R (1904) Die Mneme. Engelmann, Leipzig. Yale University Press, New Haven (2004)
58. Schacter DL (2001) Forgotten ideas, neglected pioneers: Richard Semon and the story of memory. Psychology Press, Oxford

Part II
Molecular Structure, Properties and Processes

Chapter 5
Application of the Uniformly Charged Sphere Stabilization for Calculating the Lowest ^1S Resonances of H^-

S.O. Adamson, D.D. Kharlampidi, and A.I. Dementiev

Abstract The uniformly charged sphere stabilization method has been used to calculate the lowest ^1S resonances of H^-. It was shown that this method is sensitive to the choice of basis set and parameters of the stabilization potential. The conclusion on the suitability of this method for calculating resonance energies and widths is based on the analysis of our computational results.

5.1 Introduction

Considering the progress in development of the direct methods for resonance calculations [1–3], the uniformly charged sphere stabilization (UCS-stabilization) approach now can be considered as the simple "first-aid" tool for the estimation of resonance parameters of molecular negative ions [4–12]. This method, based on the ideas from the previous works [13, 14], has two advantages distinguishing it from the other stabilization techniques [1, 10, 12, 15–17]. First, the calculations may be carried out by almost all modern quantum chemistry programs, including multi-reference ab initio methods. Secondly, the scope of this approach isn't limited to consideration of only the single-channel problem (but up to now there are no examples of multi-channel calculations). On the other hand, for a long time this method was applied in the absence of the theoretical base proving possibility to estimate the resonance energy and width using only the known parameters of the potential, and the energies of the discrete levels. Later it was shown, that these parameters allow to estimate the amplitudes of the incoming and outgoing waves of the partial solution [18–20]. One more lack of this method is the absence of recommendations for creating the optimal computational scheme (the construction of the single- and many-particle functions, choice of the external potential parameters, etc.).

S.O. Adamson (✉)
Department of Chemistry, Lomonosov Moscow State University, Leninskie Gory 1, Moscow 119991, Russia
e-mail: sergey.o.adamson@gmail.com

S.O. Adamson
MIPT, Moscow, Russia

M. Hotokka et al. (eds.), *Advances in Quantum Methods and Applications in Chemistry, Physics, and Biology*, Progress in Theoretical Chemistry and Physics 27,
DOI 10.1007/978-3-319-01529-3_5,

Taking into account that all the listed problems of the UCS-stabilization method will be solved only through systematic investigations of the well studied molecular systems, the aim of this paper is to assess the influence of the UCS-potential parameters on the accuracy of the resonance energy and width calculation. It is expected that the choice of the UCS-potential parameters (charge and radius of the uniformly charged sphere) should also influence the accuracy of the estimated resonance parameters by analogy with the optical potential method [21, 22]. Two lowest ^1S resonances of H^- below the threshold $n = 2$ were chosen as the computational examples because both theoretical calculations performed by different methods [1, 23–34] and measurements [35] are known for these resonances. The experiments give the energy and width ($E_{res} = 0.35092 \pm 0.00048$ and $\Gamma = 0.00232 \pm 0.0003$ a.u.) for the lowest resonance and prove the existence of one more resonance ($E_{res} \approx 0.37403$ a.u.) [35]. The energies and widths for the six ^1S resonances below the threshold $n = 2$ were estimated in the later theoretical works and for the first and second resonances $E_{res} = 0.35122025$, $\Gamma = 0.00173870$ and $E_{res} = 0.373979753$, $\Gamma = 9.0934 \times 10^{-5}$ a.u. [1, 33]. The energies and widths given in other mentioned works were calculated less accurately and differ from the above ones by about 10^{-4} a.u. [24–32, 34].

The theoretical background is described in the next section. Following parts contain the details of the Hamiltonian matrix construction and method used for the resonance parameters calculation. In conclusion the obtained results and their discussion are presented.

5.2 Theory

Within the limit of the infinite nuclear mass approximation the Hamiltonian of the H^- system has the form

$$\hat{H}_s = \sum_{i=1}^{2} \hat{H}_s(i) + \frac{e^2}{r_{12}}, \tag{5.1}$$

where $\hat{H}_s(i) = -\hbar^2 \Delta_i / 2m - e^2/r_i + V_s(r_i)$, m is electron mass, e is elementary charge, r_i is distance between the nucleus and i-th electron, and r_{12} is distance between electrons. The external (stabilization) potential is given by the formula

$$V_s(r_i) = \begin{cases} 0, & r_i < R, \\ V_0 - Z_0 e^2/r_i, & r_i \geq R, \end{cases} \tag{5.2}$$

where V_0 and R are independent parameters, and Z_0 is determined by the condition $Z_0 = RV_0$.

Consider the application of the variational method for the calculation of the stationary eigenfunctions $\overline{\Psi}^{LS}$ with eigenvalues $\overline{E}$ lying in the continuum spectrum of the system, which consists of a target and an electron. The brief notation LS is used for the full set of the quantum numbers $\{\alpha, L, S, L_z, S_z\}$, where L, S—are the total

angular and spin moments, L_z, S_z—its projections on the z-axis and α—all quantum numbers, which were not introduced explicitly. For the two-electron system the wave function can be represented by [23, 36–39]

$$\Psi^{LS} = \sum_{\mu} a_\mu D_\mu + \hat{A}_{SL} \sum_{\nu} f_\nu(1)\Gamma_\nu(2). \tag{5.3}$$

The first term on the right-hand side of (5.3) refers to the electron correlation and it is defined as the linear combination of Slater determinants D_μ with coefficients a_μ. The second term refers to the asymptotic part of the wave function at $r_i \geq R$ and it can be written as a set of antisymmetrized products of the single-particle functions $f_\nu(1)$ and $\Gamma_\nu(2)$. The operator $\hat{A}_{SL}$ is taken in the form $\hat{A}_{SL} = (1 - P_{12})/\sqrt{2}$, where P_{12} is the permutation operator.

Let's define the finite set of single-particle functions $\{\varphi_i\}$, $i = 1, 2, \ldots, N$, where each function is a product of independently normalized spatial and spin parts: $\varphi_i = \chi_i(\mathbf{r})\tau(\sigma)$, $\langle\varphi_i|\varphi_j\rangle = \delta_{ij}$. To define both terms of (5.3) the $\{\varphi_i\}$ set is split in the subsets $\{\varphi_i^\Gamma\}$, $\{\varphi_i^f\}$ and $\{\varphi_i^D\}$. The first subset $\{\varphi_i^\Gamma\}$ determines the orthonormal target states $\{\Gamma_\nu\}$, $\Gamma_\nu = \sum_i c_{\nu i}\varphi_i^\Gamma$, where $c_{\nu i}$ are some coefficients and index ν corresponds to the full set of quantum numbers $\{n_\nu, l_\nu^\Gamma, s_\nu^\Gamma, l_{z\nu}^\Gamma, s_{z\nu}^\Gamma\}$, characterizing uniquely the state of target. The target functions should satisfy the condition $\langle\Gamma_\mu(i)|\hat{H}_s(i) - E_{\nu s}|\Gamma_\nu(i)\rangle = 0$, i.e. these functions may be exact or obtained by the linear variational method. To describe the scattered electron state let's introduce the single-particle functions $f_\nu = \sum_j b_{\nu j}\varphi_j^f$ expanded over the subset $\{\varphi_j^f\}$ of the initial set $\{\varphi_i\}$ with coefficients $b_{\nu j}$. The last subset is used to define the functions $D_\mu = \hat{A}_{SL}\{\varphi_i^D(1)\varphi_j^D(2)\}$.

In the general case the basic formulation of the variational method depends on the choice of $\{\varphi_i^\Gamma\}$, $\{\varphi_i^f\}$ and $\{\varphi_i^D\}$ sets. For example, the case when the initial choice does not provide the orthogonality conditions $\langle A_{SL}(f_\nu(1)\Gamma_\nu(2))|D_\mu(1,2)\rangle = 0$ was discussed earlier [23, 37]. Further it will be assumed that the wave function variation preserves the orthogonality of both terms of (5.3) due to the corresponding choice of the single-particle subsets. In this case the basic equations of the variational method are

$$\left(\Gamma_\nu(2)\middle|\hat{H}_s - \overline{E}\middle|\overline{\Psi}^{LS}\right) = 0, \tag{5.4}$$

$$\left\langle D_\mu\middle|\hat{H}_s - \overline{E}\middle|\overline{\Psi}^{LS}\right\rangle = 0, \tag{5.5}$$

where the integration in (5.4) is realized over all the variables of the second particle and in (5.5) over all the variables of both particles. As has been shown earlier, if the wavefunction of the scattered electron f_ν is written in the form $f_\nu(1) = {r_1}^{-1}F_\nu(r_1)Y_{l_\nu m_\nu}(\hat{r}_1)\tau_\nu(\sigma_1)$, where $\hat{r}_1$ represents the polar (θ) and azimuthal (ϕ) angles, $m_\nu + l_{z\nu}^\Gamma = L_z$ and $Y_{lm}(\hat{r})$ is a spherical harmonic, (5.4) can be transformed to a system of the radial integro-differential equations. In our case this system of equations will differ slightly from its original form [23, 36–39] and have the form

$$\left(-\frac{\mathrm{d}^2}{\mathrm{d}r^2} + \frac{l_\nu(l_\nu+1)}{r^2} + \tilde{V}_s(r) - k_{\nu s}^2\right)F_\nu(r) = \sum_{\nu'} A_{\nu\nu'}(r) + \sum_{\mu} B_{\nu\mu}(r), \tag{5.6}$$

where $r = r_1$ is radial variable of the first electron, $k_{\nu s}^2 = 2m(\overline{E} - E_{\nu s})/\hbar^2$, $\tilde{V}_s(r) = 2mV_s(r)/\hbar^2$ and $A_{\nu\nu'}(r)$, $B_{\nu\mu}(r)$ are coupling functions.

If the parameter R is acceptably large to provide the conditions $A_{\nu\nu'}(r) \to 0$ and $B_{\nu\mu}(r) \to 0$ in the region $r \geq R$ for the all coupling elements then the radial functions $F_\nu(r)$ for the open channels ($k_{\nu s} > 0$) can be represented in the asymptotic form

$$\lim_{r \to R-0} F_\nu(r) = A_\nu I_{l_\nu}(z_\nu) + B_\nu O_{l_\nu}(z_\nu), \tag{5.7}$$

where $z_\nu = k_{\nu s} r$, A_ν, B_ν are amplitude coefficients, $I_{l_\nu}(z)$ and $O_{l_\nu}(z)$ are linearly independent solutions ($\lim_{z\to\infty} I_l(z) = \sin(z - l\pi/2)$ and $\lim_{z\to\infty} O_l(z) = \cos(z - l\pi/2)$), which can be represented as the Riccati-Bessel functions of the first and second kind $I_l(z) = z j_l(z)$ and $O_l(z) = -z y_l(z)$ [40]. As the functions $F_\nu(r)$ and their first derivatives are continuous at the point $r = R$, the coefficients A_ν and B_ν are obtained from the expressions

$$A_\nu = -k_{\nu s}^{-1} W_r\big(F_\nu(r), O_{l_\nu}(z_\nu)\big)\big|_{r=R}, \tag{5.8}$$

$$B_\nu = k_{\nu s}^{-1} W_r\big(F_\nu(r), I_{l_\nu}(z_\nu)\big)\big|_{r=R}, \tag{5.9}$$

where $W_r(f, g) = f\frac{\mathrm{d}g}{\mathrm{d}r} - g\frac{\mathrm{d}f}{\mathrm{d}r}$ is the Wronskian. As discussed below, in the case of a single open channel the scattering phase can be calculated as $\tan\delta_l(k) = B/A$, where subscript ν is omitted.

After the premultiplying by single-particle functions $\varphi_i^f(1)$ and the integrating over coordinates of the first electron the system of (5.4) is reduced to

$$\big\langle \varphi_i^f(1)\Gamma_\nu(2)\big|\hat{H}_s - \overline{E}\big|\overline{\Psi}^{LS}\big\rangle = 0. \tag{5.10}$$

These equations together with (5.5) formulate the generalized eigenvalue problem and its solution gives the optimal value of $\overline{E}$ and coefficients $\{b_{\nu j}, a_\mu\}$, which are necessary to calculate the scattering parameters.

It is possible to introduce another method to estimate the scattering phase using only the known values of $\overline{E}$ and external potential parameters (V_0 and R). The optimal function $\overline{\Psi}^{LS}$ that satisfies the condition $\langle\overline{\Psi}^{LS}|H_s - \overline{E}|\overline{\Psi}^{LS}\rangle = 0$ can be considered to approach the exact solution of the Schrödinger equation $(H_s' - \overline{E})\Psi^{LS} = 0$ with the Hamiltonian H_s', which differs from (5.1) by the parameters of potential V_s' only. Denoting the difference between exact and approximate solutions as $\Delta\Psi = \overline{\Psi}^{LS} - \Psi^{LS}$, one obtains

$$\begin{aligned}\big\langle\overline{\Psi}^{LS}\big|H_s - \overline{E}\big|\overline{\Psi}^{LS}\big\rangle = \big\langle\overline{\Psi}^{LS}\big|V_s - V_s'\big|\overline{\Psi}^{LS}\big\rangle + \langle\Delta\Psi|H_s' - \overline{E}\big|\Psi^{LS}\big\rangle \\ + \big\langle\Psi^{LS}\big|H_s' - \overline{E}|\Delta\Psi\rangle + \langle\Delta\Psi|H_s' - \overline{E}|\Delta\Psi\rangle.\end{aligned} \tag{5.11}$$

The second term on the right-hand side of (5.11) is equal to zero because Ψ^{LS} is the exact solution of the Schrödinger equation and it can be shown using the Green's theorem that the third term is equal to zero as well. Hence the formula (5.11) is simplified to the equality

$$\big\langle\overline{\Psi}^{LS}\big|V_s - V_s'\big|\overline{\Psi}^{LS}\big\rangle + \langle\Delta\Psi|H_s' - \overline{E}|\Delta\Psi\rangle = 0. \tag{5.12}$$

Assuming that $\Delta\Psi$ is small, we obtain the condition $\langle\overline{\Psi}^{LS}|V_s - V_s'|\overline{\Psi}^{LS}\rangle = 0$ which leads to the approximate equality $V_s \approx V_s'$ only if one of the external potential parameters (V_0 or R) has the same value for both potentials. It has been shown earlier [19, 20], that the exact solution $F(r)$ for the external interval ($r \geq R$) is

$$F(r) = U(l+1-a, 2l+2, y)y^{l+1}\mathrm{e}^{-y/2}, \tag{5.13}$$

where (using the notations introduced above) $r = \lambda y$, $\lambda^2 = \hbar^2/8m_e(V_0 - \overline{E} + E_s)$, $E_s = E(H,^2 S, n = 1)$, $a = 2m_e e^2 Z_0\lambda/\hbar^2$ and $U(l+1-a, 2l+2, y)$ is the Tricomi function [40, 41]. Taking into account the approximate equality between the external potential V_s used in variational calculation and $V_s^{'}$ required for exact calculations, the function $F(r)$ from (5.8) and (5.9) can be calculated using the relation (5.13) with the parameters of the external potential and $\overline{E}$. Because the parameters of the external potential V_0 and R were chosen as constants in each energy calculation, the stationarity condition $\delta E|_{E=\overline{E}} = 0$ leads to the stationarity of the parameter $\lambda(\overline{E})$ which is included in the equation for the exact radial function (5.13). Thus, if (5.13) is used, the coefficients (5.8) and (5.9) and their ratio $\tan\delta_l(k) = B/A$ are stationary with respect to small variations of λ.

Because this method to estimate the scattering parameters doesn't require the calculation of the coefficients b_{vi}, one can solve the eigenvalue problem in the basis of Slater determinants (CI method) instead of the system of equations (5.5) and (5.10). The asymptotic part of the wave function (5.3) can be always written as $\hat{A}_{SL}\sum_v f_v(1)\Gamma_v(2) = \sum_i\sum_j d_{ij}\hat{A}_{SL}\varphi_j^f(1)\varphi_i^\Gamma(2)$, where coefficients $d_{ij} = \sum_v b_{vj}c_{vi}$. Accordingly, the calculation of the coefficients b_{vj} with the known d_{ij} and c_{vi} is possible only if the set of functions $\{\Gamma_v\}$ has the same dimension as the set $\{\varphi_i^\Gamma\}$. At least two variants of the wave function construction in the Slater determinant basis satisfying this requirement are possible. In the first variant the initial set $\{\varphi_i\}$ is separated onto the non-overlapping subsets $\{\varphi_i^\Gamma\}$ and $\{\varphi_i^f\}$, which are used to define the asymptotic part. The correlation part includes the complete set of the antisymmetrized products constructed from the single-particle functions $\{\varphi_i^\Gamma\}$. This variant corresponds to the restricted CI (RCI). In the second one wave function contains the complete set of the antisymmetrized products of φ_i without the explicit fragmentation in the asymptotic and correlation parts (full CI method, or FCI).

5.3 The Calculation Method

The trial wave function was taken as the linear combination of configuration-state functions (CSF) which are proper for the operators $\hat{S}_z(1,2)$ and $\hat{S}^2(1,2)$

$$\Psi^{LS} = \sum_{i,j} c_{ij}\Phi_{ij}(1,2), \tag{5.14}$$

where indexes 1, 2 denote the spatial and spin variables of electrons and indexes i and j satisfy the condition $i \leq j$. For singlet states functions $\Phi_{ij}(1,2)$ are defined as

$$\begin{aligned}\Phi_{ii}(1,2) &= \frac{1}{\sqrt{2}}\chi_i(1)\chi_i(2)\Theta(\alpha,\beta),\\ \Phi_{ij}(1,2) &= \frac{1}{2}\big[\chi_i(1)\chi_j(2)+\chi_j(1)\chi_i(2)\big]\Theta(\alpha,\beta),\end{aligned} \tag{5.15}$$

where $\Theta(1,2)=\alpha(1)\beta(2)-\beta(1)\alpha(2)$, $\alpha(j)$ and $\beta(j)$ $(j=1,2)$ are the spin functions of electron j with $S_z=\pm 1/2$, and $\chi_i(j)$ is the spatial part of the single-particle function.

The key moment in using ab initio methods is the basis construction of single-particle functions (atomic orbitals, or AO). As a rule, in this procedure AOs are approximated by the linear combination of non-orthogonal nodeless Gaussians with the purpose of minimizing calculation error of the target parameter (energy, electron density, etc.) [42–45]. The AO bases created in this manner give the opportunity to find, with acceptable accuracy, the energies of the lowest bound electronic states and matrix elements of one- and two-particle operators for molecular systems. Nevertheless they show a rather essential disadvantage: non-orthogonality of Gaussians doesn't allow to infinitely increase the existing AO set using additional functions, as this procedure results in so-called "computational linear dependence" [46, 47]. To avoid the computational linear dependence problem, the set of the orthogonal single-particle functions was used for the CSF construction

$$\chi(b\mathbf{r}) = |nlm\rangle = R_{nl}(br)Y_{lm}(\hat{r}), \tag{5.16}$$

where

$$R_{nl}(br) = N_{nl}(br)^l \mathrm{e}^{-br/2} L_n^{2l+2}(br), \tag{5.17}$$

with the normalizing multiplier $N_{nl}=(b^3 n!/(n+2l+2)!)^{1/2}$, the scaling factor b and the associated Laguerre polynomial $L_n^{2l+2}(br)$ [40, 41]. To preserve the spin and angular degeneracy of the target states, the number of basis functions (5.16) with the moments $l>0$ was chosen to be equal to $(N-l)$, where N—the number of functions with $l=0$: $Ns, (N-1)p, (N-2)d, \ldots, (N-l)l$. Further, for simplicity the basis sets being used are represented by the pairs of parameters: (N, l_{max}), where l_{max}—maximal moment l value. The details of the matrix elements computation are described in the Appendix. When calculating the scattering phase the R parameter was chosen sufficiently large to consider $E_{vs}(n=1)$ in (5.13) being equal to the energy of the hydrogen ground state.

For calculating the Tricomi function and its derivatives the computational scheme similar to [19, 20] was used. At the first step the values of functions $U(\beta-[\beta],\gamma,x)$ and $U(\beta-[\beta]+1,\gamma,x)$ ($[\beta]$ being the integer part of β) were calculated according to the algorithm [48]. Further these values were applied for initiating an ascending recursion $U^- + (\gamma-2\beta-x)U + \beta(1+\beta-\gamma)U^+ = 0$, where $U=U(\beta,\gamma,x)$ and $U^{\pm}=U(\beta\pm 1,\gamma,x)$, and the derivative $U'=U(\beta,\gamma,x)$ were calculated by the formula $\beta(1+\beta-\gamma)U^+ - \beta U - xU' = 0$ [40, 41, 49]. Because the lowest ^1S

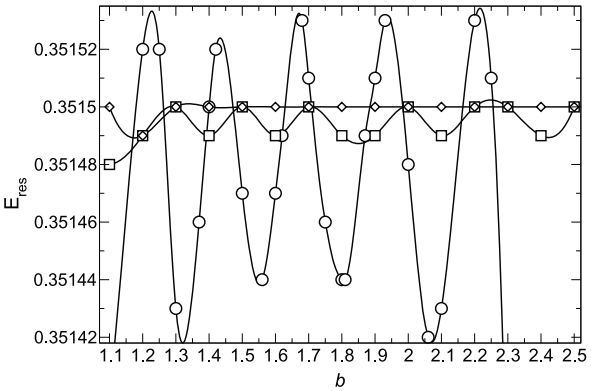

Fig. 5.1 Energy of the lowest ^1S resonance with respect to the scaling factor (b) for bases (19,2) (◯), (23,2) (□) and (27,2) (◇). The 8th eigenvalue is used, $V_0 = 1$ a.u., $R_{res} \approx 20$ a.u. All data are given in a.u.

resonances were previously interpreted as the Breit-Wigner ones, their energies and widths are calculated by the approximation of the phase shift derivative $d\delta_l(k)/dE$ by the Lorentz function.

5.4 Results and Discussion

The full CI method was chosen as the main way for the wave function construction. If no additional conditions provided, the results being discussed are obtained by this method. The resonance parameters were calculated with the use of the AO bases with $N \leq 39$ and $l_{max} \leq 3$. The values of scaling factor ($1.0 \leq b \leq 2.5$) with the step 0.1 and the parameter V_0 ($1 \leq V_0 \leq 10$ a.u.) were varied.

The phase shift function $\delta_l(k)$ was built for each of the lowest eigenvalues, calculated at the gradual increasing the radius of the charged sphere in the range 10.0–75.0 a.u. with the fixed value of the parameter V_0. Like the box stabilization this procedure results in the family of monotonously decreasing curves $\overline{E}_i(R)$ (i.e. stabilization curves) [16, 50]. So, it seems appropriate to enumerate these curves in order of the eigenvalues starting with the ground state of H^-. In addition, any stabilization curve can be characterized also by the R parameter value approximately corresponding to the resonance energy (R_{res}).

In the preliminary series of calculations with the fixed value of $V_0 = 1.0$ a.u., the energy and width of the lowest resonance were found to depend on the value of scaling factor b and for both parameters these dependencies show the oscillations in the vicinity of some average value. The dependencies for one of the stabilization curves are given below as an example (Figs. 5.1, 5.2). To take this dependence into account the average values $P = \sum_{i=1}^{n} P(b_i)/n$ instead of $P(b)$ ($P = E_{res}, \Gamma$) and average linear deviations $\Delta P = \sum_{i=1}^{n} |P(b_i) - P|/n$ are used for all the available results determined for the scaling factor 1.0–2.5.

The comparison of the resonance parameters calculated for the stabilized solutions with various R_{res} shows that with increasing R_{res} the estimations of energy

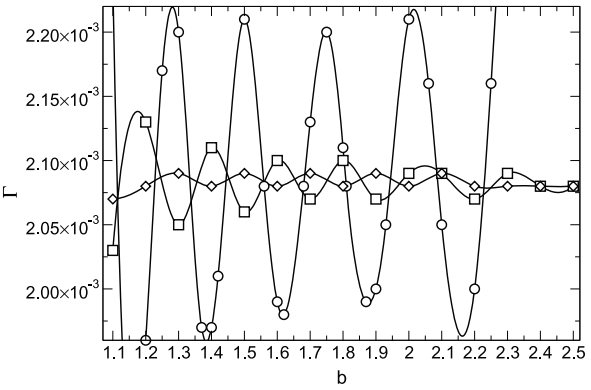

Fig. 5.2 Width of the lowest ^1S resonance with respect to the scaling factor (b) for bases (19,2) (◯), (23,2) (□) and (27,2) (◊). The 8th eigenvalue is used, $V_0 = 1$ a.u., $R_{res} \approx 20$ a.u. All data are given in a.u.

and width are going to the reference ones. The simultaneous increase of the average deviations and R_{res} can be explained by the incompleteness of AO bases that don't give the opportunity to correctly reproduce the asymptotic behavior of the wave function at the long distances from the nucleus (Table 5.1). The analysis of the results demonstrates that the average values of energy and width of the lowest resonance for the chosen basis (N, l_{max}) depend on the values V_0 and R_{res}. The average deviations of E_{res} and Γ grow with the increasing of parameter V_0 (Table 5.2).

For the fixed value V_0 the largest differences between the average parameters and reference ones are observed for the bases included only single-particle functions (AO) with $l = 0$. If the AO set is extended by functions with $l \leq 2$ the differences decrease quickly. The further basis set enlarging by orbitals with $l > 2$ does not considerably change the resonance energy and width (Table 5.3). The comparison of the calculated phase shift with the exact one [30, 32] shows that the stabilization curves with the acceptable accuracy of the average E_{res} and Γ do not provide the accurate estimation of the phase shift (Fig. 5.3). The observed error in the phase shift demonstrates that the used AO sets provide the correct asymptotic part of the wave function only for the curves with $R_{res} < 25.4$ a.u. (this corresponds to stabilization curves with numbers 8 and 9).

In addition to FCI method the RCI one was applied to the phase shift and lowest resonance parameters calculations. In this case the correlation part of the wave function included the full set of CSF constructed in the bases (8,2), (11,2) or (15,2). The asymptotic part was represented by the full set of the CSF created by one-electron excitations from the CSF of the correlation part. It is found that the phase shift values obtained by the RCI even for the wave function with correlation part of the minimal size (corresponding to (8,2) AO set) practically coincide with the FCI ones (Fig. 5.4) and the difference in resonance parameters does not exceed 2×10^{-5} a.u.

Taking into account the dependence of the resonance energy and width on the V_0 value, the second ^1S resonance was calculated with $V_0 = 1.0$ a.u. for sphere radius $R = 25.0$–75.0 a.u. The RCI approach with correlation part constructed from the single-particle basis set (11,2) was used in all cases. It was found that this resonance appears at $R_{res} > 45$ a.u. and the results which agree better with reference

Table 5.1 Average parameters and its linear deviations ($\times 10^5$) of the lowest ^1S resonance for $V_0 = 1$ a.u. All data are given in a.u.

Basis	Root	E_{res}	ΔE_{res}	Γ	$\Delta\Gamma$	R_{res}
(19,2)	7	0.35209	1	0.00286	3	16.8
	8	0.35146	4	0.00211	11	19.8
	9	0.35123	15	0.00182	19	23.1
	10	0.35115	24	0.00173	25	26.6
	11	0.35116	44	0.00151	16	30.8
	12	0.35113	62	0.00135	17	35.9
(23,2)	7	0.35210	0	0.00285	0	16.8
	8	0.35149	1	0.00208	2	19.7
	9	0.35129	3	0.00186	5	22.6
	10	0.35122	7	0.00174	9	25.6
	11	0.35123	7	0.00174	28	28.8
	12	0.35121	14	0.00169	50	32.1
(27,2)	7	0.35210	0	0.00285	0	16.8
	8	0.35150	0	0.00208	0	19.7
	9	0.35131	0	0.00185	1	22.6
	10	0.35126	1	0.00178	2	25.4
	11	0.35123	2	0.00176	6	28.3
	12	0.35120	6	0.00174	17	31.5
(31,2)	7	0.35210	0	0.00286	0	16.8
	8	0.35150	0	0.00208	0	19.6
	9	0.35131	0	0.00185	0	22.5
	10	0.35126	1	0.00177	1	25.4
	11	0.35123	1	0.00175	1	28.3
	12	0.35121	3	0.00172	5	31.1

ones were obtained for the stabilization curves with $R_{res} \approx 70$ a.u. (Table 5.4). Nevertheless, the good agreement between our estimations and reference results has not been found for the all used AO sets but the tendency to improve our estimations is observed.

The presented method should be considered as a modification of the uniformly charged sphere stabilization including the new routine of the phase shift calculation. This routine has two significant features. First one is in the using the parameters of the external potential and energy of discrete level only. Second one is in the stationarity of the $\tan\delta_l(\overline{E})$ with respect to the small variations of the energy of quasidiscrete level. It should be noted that the requirement $\delta E|_{E=\overline{E}} = 0$ is not a unique way to introduce the variational method. Another way is to define the optimal V_0 value for the fixed energy from the variational equations.

Table 5.2 Average parameters and its linear deviations ($\times 10^5$) of the lowest ^1S resonance with respect to V_0 value at the same R_{res}. All data are given in a.u.

Basis	V_0	E_{res}	ΔE_{res}	Γ	$\Delta\Gamma$	R_{res}	Root
(19,2)	1.0	0.35116	44	0.00151	16	30.8	11
	2.0	0.35116	28	0.00188	68	32.5	10
	5.0	0.35124	20	0.00176	58	31.0	9
	10.0	0.35125	28	0.00172	62	32.1	9
(23,2)	1.0	0.35123	7	0.00174	28	28.8	11
	2.0	0.35122	16	0.00169	20	30.6	10
	5.0	0.35121	10	0.00173	32	29.7	9
	10.0	0.35120	12	0.00172	36	30.8	9
(27,2)	1.0	0.35123	2	0.00176	6	28.3	11
	2.0	0.35123	5	0.00176	12	30.0	10
	5.0	0.35124	4	0.00175	11	28.9	9
	10.0	0.35123	7	0.00174	13	29.7	9
(31,2)	1.0	0.35123	1	0.00175	1	28.3	11
	2.0	0.35123	1	0.00175	4	29.7	10
	5.0	0.35124	2	0.00176	4	28.7	9
	10.0	0.35124	3	0.00176	8	29.6	9

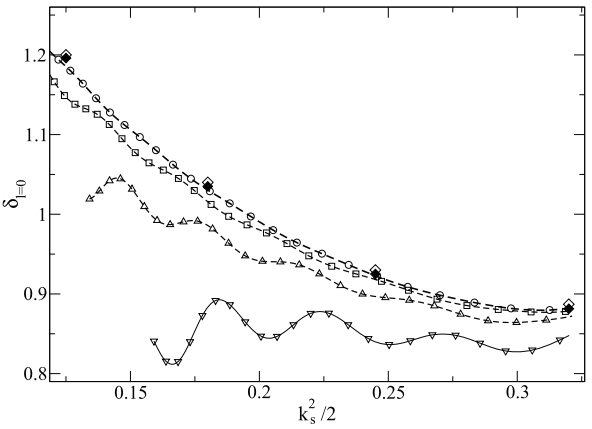

Fig. 5.3 Phase shift functions obtained by FCI method (basis (31,2)) with respect to $k_s^2/2 = (E(H^-, ^1S) - E(H, ^2S))m_e/\hbar^2$. Symbol ◯ corresponds to 8th eigenvalue (stabilization curve), □—9th, △—10th, and ∇—11th. Symbols ◊ and ⧫ correspond to the exact phase shift [30, 32]. $k_s^2/2$ is given in a.u., phase shift—in radians

The main condition to successful application of the considered method is in using the AO sets which provide the correct representation of the asymptotic part of the wave function and allow to use sufficiently large values of the parameter R. The analysis of the results shows that the phase shift can be obtained for $R > 25$ a.u. with acceptable accuracy in narrow energy intervals required to estimate the energy and width of isolated resonances located far from the channel threshold. To calculate

Table 5.3 Average parameters and its linear deviations ($\times 10^5$) of the lowest ^1S resonance with respect to the size of single-particle basis. (10th eigenvalue corresponding to $R_{res} \approx 24$–27). All data are given in a.u.

l_{max}	N							
	19		23		27		31	
	E_{res}	ΔE_{res}	E_{res}	ΔE_{res}	E_{res}	ΔE_{res}	E_{res}	ΔE_{res}
0	0.37453	5	0.37465	2	0.37468	0	0.37468	0
1	0.35155	25	0.35164	8	0.35167	1	0.35167	0
2	0.35115	24	0.35122	7	0.35126	1	0.35126	1
3					0.35125	1		
	Γ	$\Delta\Gamma$	Γ	$\Delta\Gamma$	Γ	$\Delta\Gamma$	Γ	$\Delta\Gamma$
0	0.00096	13	0.00091	3	0.00090	1	0.00090	0
1	0.00161	33	0.00178	10	0.00181	3	0.00181	0
2	0.00173	25	0.00174	9	0.00178	2	0.00177	1
3					0.00177	2		

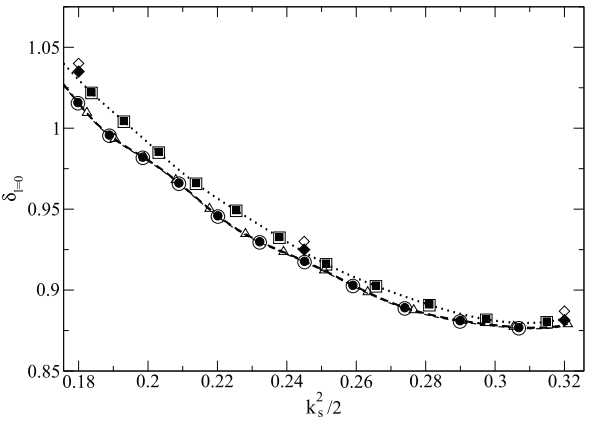

Fig. 5.4 Phase shift functions (9th stabilization curve) with respect to $k_s^2/2 = (E(H^-, ^1S) - E(H, ^2S))m_e/\hbar^2$. Symbol △ corresponds to FCI results, ◯—RCI (8,2), •—RCI (11,2), obtained in basis set (31,2). Symbol □—RCI (8,2) and ■—RCI (11,2) correspond to the results obtained in basis set (35,2). Symbols ◊ and ♦ correspond to the exact phase shift [30, 32]. $k_s^2/2$ is given in a.u., phase shift—in radians

the phase shift in wide energy intervals the chosen way based on using curves $\overline{E}_j(R)$ with fixed V_0 is not effective and should be replaced by technique which operates with the curves $\overline{E}_j(V_0)$ with changed V_0.

Earlier it was found that the use of neighboring stabilization curves leads to slightly different estimations of the resonance energy and width [7, 8]. This effect was explained by unsatisfactory account of electron correlation, so checking up the stability of the estimations with respect to the variation of AO basis was not carried out [7, 8]. On the other hand, it has been previously shown that for the model single-channel systems the resonance parameters deviate only in the case of specific choice of the basis set [18]. Taking into account the oscillations of the resonance energy and width (Figs. 5.1, 5.2), demonstrated in this paper, it is reasonable to as-

Table 5.4 Average energy and width of the second ^1S resonance of H^- ($V_0 = 1$ a.u.). All data are given in a.u.

Root	(31,2)			(35,2)			(39,2)		
	E_{res}	Γ	R_{res}	E_{res}	Γ	R_{res}	E_{res}	Γ	R_{res}
18	0.37506	0.00059	45.2	0.37526	0.00058	43.5	0.37532	0.00058	43.0
19	0.37470	0.00048	49.5	0.37492	0.00047	46.9	0.37499	0.00048	46.2
20	0.37439	0.00043	54.3	0.37465	0.00036	50.5	0.37472	0.00040	49.4
21	0.37423	0.00020	60.2	0.37447	0.00028	54.5	0.37452	0.00034	52.8
22				0.37433	0.00022	58.8	0.37435	0.00028	56.6
23				0.37423	0.00018	63.9	0.37422	0.00022	60.7
24				0.37416	0.00016	70.3	0.37413	0.00018	65.4
25							0.37406	0.00014	70.3

sume that the main cause of the resonance parameters deviation in many-electron anions is connected with the used method of constructing the AO basis, but not with the correlation effects.

5.5 Conclusions

Thus, the method considered in this paper is the most comprehensive variant of the uniformly charged sphere stabilization. It can be applied for the resonance parameters calculation with a good accuracy only if the formulated above requirements are taken into account. Nevertheless, the optimal strategy of the wave function construction which provides the reasonable accuracy of the calculations for the real atomic or molecular systems is still open.

Acknowledgements The study has been carried out with the financial support of the Russian Foundation for Basic Research, grant No. 12-03-00821.

Appendix: Calculation of Matrix Elements for One- and Two-Electron Operators

The matrix elements of the one-electron operators can be written as

$$\left\langle n'l'm'\right|\frac{1}{r}|nlm\rangle = \frac{1}{b^2}Q^{l'+l+1}_{n'l'nl}(0)N_{n'l'}N_{nl}\delta_{l'l}\delta_{m'm}, \tag{5.18}$$

$$\begin{aligned}\left\langle n'l'm'\right| - \frac{1}{2}\Delta|nlm\rangle = -\frac{1}{2b}\Bigg\{&\frac{1}{4}Q^{l'+l+2}_{n'l'nl}(0) - (n+l+1)Q^{l'+l+1}_{n'l'nl}(0)\\ &- nQ^{l'+l}_{n'l'nl}(0) + (n+2l+2)Q^{l'+l}_{n'l'n-1l}(0)\Bigg\}N_{n'l'}N_{nl}\delta_{l'l}\delta_{m'm},\end{aligned} \tag{5.19}$$

$$\langle n'l'm'|V_{st}(r)|nlm\rangle = \frac{V_0}{b^3}\left\{Q^{l'+l+2}_{n'l'nl}(bR) - bRQ^{l'+l+1}_{n'l'nl}(bR)\right\}N_{n'l'}N_{nl}\delta_{l'l}\delta_{m'm}, \tag{5.20}$$

where $Q^m_{n'l'nl}(x)$ is the auxiliary integral

$$Q^m_{n'l'nl}(x) = \int_x^\infty \mathrm{e}^{-z}z^m L^{2l'+2}_{n'}(z)L^{2l+2}_n(z)dz. \tag{5.21}$$

For the calculation of integrals (5.18)–(5.20) the method based on the recurrence relation for product of Laguerre polynomials has been used [51]. The main relation of this method can be obtained by substituting the recursion $(n+1)L^k_{n+1}(z) - (2n+k+1-z)L^k_n(z) + (n+k)L^k_{n-1}(z) = 0$ [40] for L^{2l+2}_n or $L^{2l'+2}_{n'}$ polynomial in (5.21) which gives two different three-term recursions for integrals over the indexes n and n'. Elimination of the integral $Q^{m+1}_{n'l'nl}(x)$ from the both recursions leads to the new relation

$$\begin{aligned} nQ^m_{n'l'nl}(x) = {} & \left(n'+1\right)Q^m_{n'+1l'n-1l}(x) + \left(n'+2l'+2\right)Q^m_{n'-1l'n-1l}(x) \\ & - (n+2l+1)Q^m_{n'l'n-2l}(x) + 2\left(n+l-n'-l'-1\right)Q^m_{n'l'n-1l}(x). \end{aligned} \tag{5.22}$$

This relation is applied for construction of the ascending recursion which starts from the elements $Q^m_{kl0l}(x)$ with $n'-n+1 \le k \le n'+n-1$ and finishes at $Q^m_{n'lnl}(x)$ (assume that $n \le n'$). The integrals with $m = 2l+2$ and $x = 0$ can be evaluated directly using the orthogonality relation

$$Q^{2l+2}_{n'lnl}(0) = \frac{(n+2l+2)!}{n!}\delta_{n'n}. \tag{5.23}$$

For integrals with $m < 2l+2$ and $x = 0$ the recursion (5.22) is initialized by the elements

$$Q^m_{0l0l}(0) = m!, \tag{5.24}$$

$$Q^m_{1l0l}(0) = Q^m_{0l1l}(0) = m!(2l+2-m), \tag{5.25}$$

$$Q^m_{1l1l}(0) = m!\left((m+1)(m+2) - 2(m+1)(2l+3) + (2l+3)^2\right). \tag{5.26}$$

All elements $Q^m_{kl0l}(0)$ needed for the evaluation of integrals (5.18) and (5.19) are calculated by means of the special three-term recursion $(n'+1)Q^m_{n'+1l0l}(x) - (2n'+2l+1)Q^m_{n'l0l}(x) + (2n'+2l+1)Q^{m+1}_{n'l0l}(x) + (n'+2l+2)Q^m_{n'-1l0l}(x) = 0$.

The case of the integrals (5.20) is more complicate. The elements $Q^m_{n'l0l}(x)$ and $Q^m_{n'l1l}(x)$ ($m = 2l+2$ or $m = 2l+1$) needed for the initializing (5.21) can be taken analytically

$$Q^m_{n'lnl}(x) = \sum_{t=0}^{n'+n}\Gamma(m+t+1,x)W_t\left(n',l',n,l\right), \tag{5.27}$$

where $\Gamma(a,x) = \int_x^\infty z^{a-1}\mathrm{e}^{-z}dz$—incomplete gamma function, $W_t(n',l,n,l)$—coefficient of the term z^t in the product of two associated Laguerre polynomials. This coefficient is calculated by the formula

$$W_t\left(n',l',n,l\right) = \sum_{u=0}^{u\le n,t-u\le n'} \frac{(-1)^t(n'+v)!(n+v)!}{u!(t-u)!(n'-t+u)!(n-u)!(v'+t-u)!(v+u)!}. \tag{5.28}$$

In this formula $v = 2l+2$ and $v' = 2l'+2$. The function $\Gamma(a,x)$ from expression (5.27) can be derived analytically at the integer values of parameter a. For this purpose the function is represented as the product $\Gamma(a,x) = \mathrm{e}^{-x}x^a g(a,x)$, where $g(a,x)$—the auxiliary function defined for the $a = 1$ as $g(1,x) = 1/x$. This representation allows to use the standard recurrence relation for incomplete gamma function $\Gamma(a+1,x) = a\Gamma(a,x) + \mathrm{e}^{-x}x^a$ by $g(a+1,x) = \frac{a}{x}g(a,x) + \frac{1}{x}$ with the minimal numerical error [52]. The analytical method of calculation is suitable for integrals with $n' \le 23$, that one can see by the comparison of the values obtained from the formula (5.27) with ones obtained by Gauss-Laguerre integration. For the integrals with $n' > 23$ the quadrature method was applied.

During the calculation of electron-electron repulsion integrals the operator $1/r_{12}$ can be represented by the series

$$\frac{1}{r_{12}} = \sum_{l=0}^{\infty}\sum_{m=-l}^{l}\frac{4\pi}{2l+1}Y_{lm}(\hat{r}_1)Y^*_{lm}(\hat{r}_2)\frac{r_<^l}{r_>^{l+1}}, \tag{5.29}$$

where $r_< = \min(r_1,r_2)$ and $r_> = \max(r_1,r_2)$ [53–57]. With this expression the two-electron integral is

$$\begin{aligned}&\left\langle n_1'l_1'm_1'n_2'l_2'm_2'\right|\frac{1}{r_{12}}\left|n_1l_1m_1n_2l_2m_2\right\rangle \\ &\quad = N_{n_1'l_1'}N_{n_2'l_2'}N_{n_1l_1}N_{n_2l_2}b^{-5}\sum_{L=0}^{\infty}R_L\sum_{M=-L}^{L}D_{LM},\end{aligned} \tag{5.30}$$

where R_L—radial integral in the form

$$R_L = \int_0^\infty\int_0^\infty dxdyf_1(x)f_2(y)\frac{x_<^L}{x_>^{L+1}}, \tag{5.31}$$

in which variables r_1, r_2 and $r_{</>}$ are replaced by x, y and $x_{</>}$, and $f_i(x) = \mathrm{e}^{-x}x^{l_i'+l_i+2}L_{n_i'}^{2l_i'+2}(x)L_{n_i}^{2l_i+2}(x)$ $(i = 1,2)$. The multiplier D_{LM} from the formula (5.30) is

$$\begin{aligned}D_{LM} = (-1)^{m+m_1'+m_2'}&\sqrt{\frac{(2l_1'+1)(2l_2'+1)(2l_1+1)(2l_2+1)}{(2L+1)^2}} \\ &\times C^{L0}_{l_1'0,l_10}C^{L0}_{l_2'0,l_20}C^{L-M}_{l_1'-m_1',l_1m_1}C^{LM}_{l_2'-m_2',l_2m_2},\end{aligned} \tag{5.32}$$

where $C^{lm}_{l_1m_1,l_2m_2}$—Clebsch-Gordan coefficients.

Substitution $x_{</>}$ by x and y the integral (5.31) can be represented as

$$R_L = \int_{x>y} \int \mathrm{d}x\mathrm{d}y f_1(x) f_2(y) \frac{y^L}{x^{L+1}} + \int_{x<y} \int \mathrm{d}x\mathrm{d}y f_1(x)\mathrm{d}y f_2(y) \frac{x^L}{y^{L+1}}, \quad (5.33)$$

where the integration over variables x, y is realized on the region $[0, \infty)$; integrals from the right part correspond to $x > y$ and $x < y$ cases, respectively. As the integration order in this relation is arbitrary, each of integrals from the right part can be taken in two variants [53–57]. For the first integral there is the expression

$$\int_0^\infty \mathrm{d}x f_1(x) \int_0^x \mathrm{d}y f_2(y) \frac{y^L}{x^{L+1}} = \int_0^\infty \mathrm{d}x f_2(x) \int_x^\infty \mathrm{d}y f_1(y) \frac{x^L}{y^{L+1}}. \quad (5.34)$$

The second integral from the right part of (5.33) can be obtained from (5.34) by substitution f_2 for f_1 (and vice versa). Using the expressions with the internal integration over the interval $x \le y \le \infty$, the integrals from (5.33) can be modified as

$$R_L = \int_0^\infty \mathrm{d}x f_2(x) \int_x^\infty \mathrm{d}y f_1(y) \frac{x^L}{y^{L+1}} + \int_0^\infty \mathrm{d}x f_1(x) \int_x^\infty \mathrm{d}y f_2(y) \frac{x^L}{y^{L+1}}. \quad (5.35)$$

The expansion of Laguerre polynomials from (5.35) over powers of variables x and y permits to present R_L as

$$R_L = \sum_{t=0}^{n_1+n_1'} \sum_{u=0}^{n_2+n_2'} W_t\left(n_1', l_1', n_1, l_1\right) W_u\left(n_2', l_2', n_2, l_2\right) [H_{\alpha+t,\beta+u-\gamma} + H_{\beta+u,\alpha+t-\gamma}], \quad (5.36)$$

where $\alpha = l_1' + l_1 + L + 2$, $\beta = l_2' + l_2 + L + 2$, $\gamma = 2L + 1$ and $H_{a,b}$—integral in the form

$$H_{a,b} = \int_0^\infty x^a \mathrm{e}^{-x} \Gamma(b+1, x) dx = \frac{\Gamma(a+b+2)}{(a+1)2^{a+b+2}} {}_2F_1(1, a+b+2, a+2; 1/2). \quad (5.37)$$

By means the integral $\int_0^\infty x^a \mathrm{e}^{-x} \gamma(b+1, x)\mathrm{d}x = \frac{\Gamma(a+b+2)}{(b+1)2^{a+b+2}} {}_2F_1(1, a+b+2, b+2; 1/2) = H_{b,a}$ it can be shown that $H_{a,b} = \Gamma(a+1)\Gamma(b+1) - H_{b,a}$ and $H_{a,a} = (\Gamma(a+1))^2/2$. Putting the recurrence relation $\Gamma(b+1, x) = b\Gamma(b, x) + x^b \mathrm{e}^{-x}$ into integral (5.37), one obtains

$$H_{a,b} = bH_{a,b-1} + \frac{\Gamma(a+b+1)}{2^{a+b+1}}. \quad (5.38)$$

To evaluate the $H_{a,b}$ it is useful to introduce the new formula $h_{a,b} = H_{a,b} \frac{2^{a+b+1}}{\Gamma(a+b+1)}$ ($h_{0,0} = 1$), which allows to rewrite recursion (5.38) as $h_{a,b} = \frac{2b}{a+b} h_{a,b-1} + 1$.

The numerical tests demonstrated, that the evaluation of the radial integral by formulas (5.36)–(5.38) gives the accuracy up to 12th significant digits for the basis functions with $\max(n_1', n_1, n_2', n_2) \le 7$, if the 64th bits representation of real numbers is used. The 128th bit representation allows to preserve the same accuracy

level for the basis functions with $\max(n_1', n_1, n_2', n_2) \leq 10$. The check of the two-indexes recursion, which is analogous to the (5.22) [51], showed that this one provides a good precision only for integrals with $\max(n_1', n_1, n_2', n_2) \leq 13$ when 128th bit representation of real numbers is used. This is in accord with the remark in [51] about the possibility of using this recursion for integral calculation with a good accuracy $\max(n_1', n_1, n_2', n_2) \leq 14$. As it was not known beforehand if in constructing a wave function one can select polynomials with $n \leq 13$ only, the combined scheme was used. Calculations have been done with the formulas (5.36)–(5.38), if $\max(n_1', n_1, n_2', n_2) < 11$ and the quadrature integration being used in the opposite case. Using the replacement of $u = x$ and $v = y - x$, similar to [57], the integral (5.35) can be represented as

$$R_L = \int_0^\infty \mathrm{d}u f_1(u) \int_0^\infty \mathrm{d}v f_2(u+v) \frac{u^L}{(u+v)^{L+1}} + \int_0^\infty \mathrm{d}u f_2(u) \int_0^\infty \mathrm{d}v f_1(u+v) \frac{u^L}{(u+v)^{L+1}}. \tag{5.39}$$

Thus, it is possible to use Gauss-Laguerre integration for calculation (5.39). Note, that the relation as $\sum_{m=0}^{n} L_m^\alpha(x) L_{n-m}^\beta(y) = L_n^{\alpha+\beta+1}(x+y)$ [41] allows to factorize the two-dimensional integral completely.

References

1. Nicolaides CA (2010) Theory and state-specific methods for the analysis and computation of field-free and field-induced unstable states in atoms and molecules. In: Nicolaides CA, Brändas E (eds) Unstable states in the continuous spectra, Part I: analysis, concepts, methods, and results. Advances in quantum chemistry, vol 60. Elsevier, Amsterdam, pp 163–267, and references therein
2. Moiseyev N (2011) Non-Hermitian quantum mechanics. Cambridge University Press, Cambridge
3. Nicolaides CA, Brändas E (eds) (2012) Unstable states in the continuous spectra, Part II: interpretation, theory and applications. Advances in quantum chemistry, vol 63. Elsevier, Amsterdam
4. Sabelli NH, Gislason EA (1984) SCF study of the lowest $^2\Sigma_u^+$ resonance of H_2^-. J Chem Phys 81:4002–4007
5. DeRose E, Gislason EA, Sabelli NH (1985) A new method for computing properties of negative ion resonances with application to $^2\Sigma_u^+$ states of H_2^-. J Chem Phys 82:4577–4584
6. Chao JS-Y, Falcetta MF, Jordan KD (1990) Application of the stabilization method to the $N_2^-(1^2\Pi_g)$ and $Mg^-(1^2\Pi)$ temporary anion states. J Chem Phys 93:1125–1135
7. Izmaylov AF, Adamson SO, Zaitsevskii A (2004) Multipartitioning many-body perturbation theory calculations on temporary anions: applications to N_2^- and CO^-. J Phys B, Atom Mol Phys 37:2321–2329
8. Izmaylov AF, Shchegoleva LN, Scuseria GE, Zaitsevskii A (2005) Ab initio study of temporary anions of benzene and fluorobenzenes using the multipartitioning many-body perturbation theory. Phys Chem Chem Phys 7:3933–3937
9. Adamson S et al (2007) Multiscale multiphysics non-empirical approach to calculation of light emission properties of chemically active non-equilibrium plasma: application to Ga-I3 system. J Phys D, Appl Phys 40:3857–3881

10. Simons J (2008) Molecular anions. J Phys Chem A 112:6401–6511, and references therein
11. Adamson SO, Deminskii MA et al (2010) The role of dissociative electron attachment to metal halides in a low pressure glow discharge. Russ J Phys Chem B 4:1–7
12. Simons J (2011) Theoretical study of negative molecular ions. Annu Rev Phys Chem 62:107–128, and references therein
13. Watson RE (1958) Analytic Hartree-Fock solutions for O_2^-. Phys Rev 111:1108–1110
14. Liebman JF, Yeager DL, Simons J (1977) A simple approach to predicting resonance levels. Chem Phys Lett 48:227–232
15. Hazi AU, Taylor HS (1970) Stabilization method of calculating resonance energies: model problem. Phys Rev A 1:1109–1120
16. Lefebvre R (1985) Box quantization and resonance determination: the multichannel case. J Phys Chem 89:4201–4206
17. Kukulin VI, Krasnopolsky VM, Horáček J (1989) Resonances in atomic physics. In: Kukulin VI, Krasnopolsky VM, Horáček J (eds) Theory of resonances. Principles and applications. Academia, Praha, pp 303–340, and references therein
18. Adamson S, Kharlampidi D, Dementiev A (2008) Stabilization of resonance states by an asymptotic Coulomb potential. J Chem Phys 128:024101, and references therein
19. Kharlampidi DD, Dementiev AI, Adamson SO (2010) Using of stabilization by uniformly charged sphere for resonance states calculations. Russ J Phys Chem A 84:611–616
20. Adamson SO, Kharlampidi DD, Dement'ev AI (2011) Calculation of the parameters of resonance states using stabilization with non-Coulomb potentials. Russ J Phys Chem B 5:915–920
21. Jolicard G, Austin E (1986) Optical potential method of calculating resonance energies and widths. Chem Phys 103:295–302
22. Jolicard G, Leforestier C, Austin E (1988) Resonance states using the optical potential model. Study of Feshbach resonances and broad shape resonances. J Chem Phys 88:1026–1031
23. Callaway J (1978) The variational method in atomic scattering. Phys Rep 45:89–173, and references therein
24. Ho YK (1981) Complex-coordinate calculations for doubly excited states of two-electron atoms. Phys Rev A 23:2137–2149
25. Pathak A, Kingston AE, Berrington KA (1988) Resonances in H^- associated with the $n = 2, 3$ and 4 hydrogenic thresholds. J Phys B, At Mol Opt Phys 21:2939–2951
26. Scholz T, Scott P, Burke PG (1988) Electron-hydrogen-atom scattering at intermediate energies. J Phys B, Atom Mol Phys 21:L139–LI45
27. Ho YK (1990) High-lying doubly excited states of H^-. J Phys B, At Mol Opt Phys 23:L71–L78
28. Botero J, Shertzer J (1992) Direct numerical solution of the Schrodinger equation for quantum scattering problems. Phys Rev A 46:R1155–R1158
29. Sadeghpour HR (1992) Resonant electron-hydrogen atom scattering using hyperspherical coordinate method. J Phys B, At Mol Opt Phys 25:L29–L35
30. Shertzer J, Botero J (1994) Finite-element analysis of electron-hydrogen scattering. Phys Rev A 49:3673–3679
31. Gien TT (1998) Observation of a triplet D-wave resonance below the $n = 2$ H excitation threshold in electron-hydrogen scattering. J Phys B, At Mol Opt Phys 31:L629–L635
32. Gien TT (1998) Feshbach resonances below the $n = 2$ H excitation threshold in electron—hydrogen scattering. J Phys B, At Mol Opt Phys 31:L1001–L1008
33. Bylicki M, Nicolaides C (2000) Theoretical resolution of the H^- resonance spectrum up to the $n = 4$ threshold. II. States of ^1S and ^1D symmetries. Phys Rev A 61:052509
34. Zhang SB, Wang JG, Janev RK (2010) Electronhydrogen-atom elastic and inelastic scattering with screened Coulomb interaction around the $n = 2$ excitation threshold. Phys Rev A 81:032707
35. Warner CD, King GC, Hammond P, Slevin J (1986) Resonance structure in elastic scattering of electrons from atomic hydrogen. J Phys B, At Mol Opt Phys 19:3297–3308
36. Burke PG, Taylor AJ (1966) Correlation in the elastic and inelastic S-wave scattering of electrons by H and He^+. Proc Phys Soc Lond 88:549–562

37. Burke PG, Seaton MJ (1971) In: Alder B, Frenbach S, Rotenberg M (eds) Methods in computational physics. Atomic and molecular scattering, vol 10. Academic Press, New York. Chap. 1, and references therein
38. Harris FE, Michels HH (1971) In: Alder B, Frenbach S, Rotenberg M (eds) Methods in computational physics. Atomic and molecular scattering, vol 10. Academic Press, New York. Chap. 4, and references therein
39. Matese JJ, Oberoi RS (1971) Choosing pseudostates in the close-coupling formalism for electron-atomic-hydrogen system. Phys Rev A 4:569–579
40. Abramowitz M, Stegun I (eds) (1964) Handbook of mathematical functions with formulas, graphs, and mathematical tables. NBS app math series, vol 55. Government Printing Office, Washington
41. Bateman H, Erdlyi A (1953) Higher transcendental functions, vols 1, 2. McGraw-Hill, New-York
42. O-ohata K, Taketa H, Huzinaga S (1966) Gaussian expansions of atomic orbitals. J Phys Soc Jpn 21:2306–2313
43. Hehre WJ, Ditchfield R, Stewart RF, Pople JA (1970) Self-consistent molecular orbital methods. IV. Use of Gaussian expansions of Slater-type orbitals. Extension to second-row molecules. J Chem Phys 52:2769–2773
44. Widmark P-O, Persson BJ, Roos BO (1991) Density matrix averaged atomic natural orbital (ANO) basis sets for correlated molecular wave functions. Theor Chim Acta 79:419–432
45. Sadlej AJ (1992) Medium-size polarized basis sets for high-level-correlated calculations of molecular electric properties. Theor Chim Acta 81:339–354
46. Wallis A, McElwain DLS, Pritchard HO (1969) The variation method and the algebraic eigenvalue problem. Int J Quant Chem 3:711–722
47. Moncrieff D, Wilson S (2005) Computational linear dependence in molecular electronic structure calculations using universal basis sets. Int J Quant Chem 101:363–371, and references therein
48. Yoshida T (1995) Computation of Kummer functions $U(a, b, x)$ for large argument x by using the τ-method. Inf Process Soc Jpn 36:2335–2342
49. Temme NM (1983) The numerical computation of the confluent hypergeometric function $U(a, b, z)$. Numer Math 41:63–82
50. Maier CH, Cederbaum LS (1980) A spherical-box approach to resonances. J Phys B, Atom Mol Phys 13:L119–L124
51. Gersbacher R, Broad JT (1990) Resonances in helium photoionisation. J Phys B 23:365–384
52. Guseinov II, Mamedov BA (2004) Evaluation of incomplete Gamma functions using downward recursion and analytical relations. J Math Chem 36:341–346
53. Eyring H, Walter J, Kimball GE (1944) Quantum chemistry. Wiley, New York
54. Holøien E, Midtdal J (1955) On a metastable energy state of the negative helium ion. Proc Phys Soc A 68:815–823
55. Condon EU, Shortley GH (1959) The theory of atomic spectra, 6th edn. Cambridge University Press, Cambridge
56. Schwartz C (1962) Importance of angular correlations between atomic electrons. Phys Rev 126:1015–1019
57. Goldman SP (1997) Accurate modified configuration interaction calculations for many electron systems made easy. Phys Rev Lett 78:2325–2328, and references therein

Chapter 6
Charge Transfer Rate Constants in Ion-Atom and Ion-Molecule Processes

M.C. Bacchus-Montabonel

Abstract The theoretical treatment of charge transfer processes in collisions of ions with atomic and molecular targets is developed using ab initio molecular calculations. An analysis of quantum and semi-classical dynamics is presented in order to determine the limit of validity of such methods. Accurate cross sections and rate constants are determined which provide important data for space chemistry models. Additionally, such theoretical approaches give an insight into the mechanism of these processes with consideration of anisotropic effects for collisions with diatomic molecular targets.

6.1 Introduction

Charge transfer processes are involved in the description of a number of astrophysical environments, astrophysical plasmas, interstellar medium, atmospheres of planets and stars... The knowledge of their rate constants is determinant for the modelisation of these mediums. However experimental data remain very scarce and theoretical approaches appear to be a very efficient tool for evaluation of such rate constants. With regard to the environment, the temperature and consequently the energy to be considered in the collision process may vary significantly, from 10 K for example in the interstellar medium, to more than 10^4 K in some stellar environments. This requires developing different collision approaches in order to analyze such processes. Charge transfer recombination with neutral atoms has been widely investigated; this is indeed a fundamental process in the description of the interstellar medium which drives the ionization balance of charged species [1–5]. But charge transfer between multiply charged ions and molecular targets has also to be taken into account and appears to play a quite important role [6, 7]. In that sense, we present in this paper significant results on collisions of carbon ions with atomic and molecular targets. First of all, we consider the $C^+(^2P) + S(^3P)$ collision and its reverse reaction which is determinant in the chemistry of sulfur and carbon species. It

M.C. Bacchus-Montabonel (✉)
Institut Lumière Matière, UMR5306, Université Lyon 1-CNRS, Université de Lyon, 69622 Villeurbanne Cedex, France
e-mail: bacchus@univ-lyon1.fr

M. Hotokka et al. (eds.), *Advances in Quantum Methods and Applications in Chemistry, Physics, and Biology*, Progress in Theoretical Chemistry and Physics 27,
DOI 10.1007/978-3-319-01529-3_6,

is crucial in the chemistry of the photon dominated regions (PDR's) of the interstellar medium [8] and drives the ionic carbon chemistry at the origin of the formation of the complex carbon molecules observed in the PDR's. The rate constant generally accepted for this process from the UMIST database [9] is 1.5×10^{-9} cm^3 s^{-1} between 10 K and 41000 K, but it appears uncertain for such a large temperature domain and accurate calculations have been performed [10, 11].

We have also investigated the charge transfer of C^{2+} ions with CO and N_2 diatomic targets [7, 12]. Up to now, most of the theoretical studies involving molecular targets have been devoted to molecular hydrogen [13, 14] and experiments between carbon ions and diatomic targets have been performed mainly at keV collision energies [15, 16]. But recent measurements of Gao and Kwong provide a precise determination of the charge transfer rate coefficients for the C^{2+} collision with CO and N_2 targets at $T_{equiv} = 1.17 \times 10^4$ K [17] which may be compared with theoretical studies.

6.2 Theoretical Approach

6.2.1 Molecular Hamiltonian

The single charge transfer process $A^{q+} + B \rightarrow A^{*(q-1)+} + B^+$ may be treated in the framework of the molecular description of the collisions. The Hamiltonian is the sum of the radial and rotational parts of the kinetic energy and the electronic Hamiltonian:

$$H = T_R + T_{rot} + H^{el}. \tag{6.1}$$

The spin-orbit effects are neglected in the energy range of interest; spin manifolds are thus considered separately and spin is taken into account via its multiplicity when calculating the charge transfer cross sections. The total time dependent wave function is expanded in a parity adapted ro-electronic basis set [18, 19]:

$$\zeta_{m K M \Omega} = \frac{1}{[2(1+\delta_{\Lambda 0})]^{1/2}} \left[\psi_{m\Lambda} | K M \Omega \rangle + (-1)^K \varepsilon_{m,-\Lambda} | K M, -\Omega \rangle \right] \tag{6.2}$$

where m numbers the electronic states $\psi_{m\Lambda}$ and Λ is the quantum number for the projection on the molecular axis of the total electronic orbital angular momentum $\mathbf{L}$. We consider here Σ ($\Lambda = 0$) and Π ($\Lambda = 1$) states. The total angular momentum is $\mathbf{K} = \mathbf{N} + \mathbf{L}$ where $\mathbf{N}$ is the rotational angular momentum. $|K M \Omega\rangle$ are the states of the total angular momentum representation of quantum number K. M and Ω are the projection of the total angular momentum on the laboratory Z axis and on the internuclear z axis, respectively. The two cases $\varepsilon = 1$ and $\varepsilon = -1$ correspond to the e and f states.

The adiabatic electronic functions $\psi^{adia}_{m\Lambda}$ diagonalize H^{el}. The charge transfer process is driven mainly by non-adiabatic interactions in the vicinity of avoided crossings [20]. The corresponding radial coupling matrix elements between all pairs

of states of the same symmetry and multiplicity are calculated by means of the finite difference technique [21]:

$$g_{m\Lambda,n\Lambda}(R) = \left\langle \psi_{m\Lambda}^{adia} \middle| \partial_R \middle| \psi_{n\Lambda}^{adia} \right\rangle = \lim_{\Delta \to 0} \frac{1}{\Delta} \left\langle \psi_{m\Lambda}^{adia}(R) \middle| \psi_{n\Lambda}^{adia}(R+\Delta) \right\rangle, \tag{6.3}$$

with the parameter $\Delta = 0.0012$ a.u. previously tested [22].

The rotational coupling matrix elements $\langle \psi_K | iL_y | \psi_L \rangle$ between states of angular moment $\Delta\Lambda = \pm 1$ have been calculated directly from the quadrupole moment tensor with the centre of mass of the system chosen as origin of electronic coordinates [23].

6.2.2 Collision Dynamics

In the time-dependent quantum approach [24, 25], the adiabatic electronic functions $\psi_{m\Lambda}^{adia}$ are transformed into diabatic electronic functions by means of the transformation matrix $\mathbf{D}(R)$ obtained by solving the equation $\partial_R \mathbf{D}(R) + \mathbf{g} \cdot \mathbf{D}(R) = 0$ with the asymptotic condition $\mathbf{D}(R_\infty) = \mathbf{I}$ where $\mathbf{I}$ is the identity matrix and $\mathbf{g}$ the matrix containing the radial coupling matrix elements.

For each value of K, the coupled equations for the radial functions $\chi_{m\Lambda}^{dia,K}$ corresponding to the electronic channels in the diabatic representation take the form

$$\boldsymbol{\chi}^{dia,K}(R,t) = e^{\frac{-i\mathbf{H}^{dia,K}(t-t_0)}{\hbar}} \boldsymbol{\chi}^{dia,K}(R,t_o) \tag{6.4}$$

where

$$\mathbf{H}^{dia,K}(R) = \hbar^2 \left(-\frac{1}{2\mu} \frac{\partial^2}{\partial R^2} + \frac{K(K+1) - \Lambda^2}{2\mu R^2} \right) \times \mathbf{I} + \mathbf{H}^{el,dia}(R) + \mathbf{T}_{rot}^{dia,K}(R). \tag{6.5}$$

$\mathbf{T}_{rot}^{dia,K}(R)$ contains the rotational off diagonal elements in the diabatic representation.

A Gaussian wave packet in entrance channel $\zeta_{m\Lambda K}$ is then propagated by the coupled equations in the diabatic representation by using the split operator formalism [26] extended to take into account non-adiabatic interactions [27]. The propagation is stopped when the norm is smaller than a threshold fixed to 10^{-6}, ensuring that the entire wave packet has been absorbed. The $\chi_{n\Lambda'}^{K}(R,t)$ are Fourier transformed to get the eigenstates $\bar{\chi}_{n\Lambda'}^{K}(R,E)$ in the same domain and finally determine the square modulus of the collision matrix element $|S_{n\Lambda',m\Lambda}^{K}(E)|^2$.

The cross section for the transfer of an electron from an initial state $\psi_{m\Lambda}$ to a final state $\psi_{n\Lambda'}$ is obtained by summing over the total angular momentum values up to convergence

$$\sigma_{n\Lambda',m\Lambda}(E) = \frac{\pi}{k_{m\Lambda}^2(E)} \sum_K (2K+1) \left| S_{n\Lambda',m\Lambda}^{K}(E) - \delta_{nm}\delta_{\Lambda'\Lambda} \right|^2. \tag{6.6}$$

In the semiclassical approach, the nuclei are considered to follow a classical trajectory $R(t) = b + vt$ with regard to the impact parameter b and the velocity v [28]. The time-dependent Schrödinger equation reduces thus to:

$$\left(H^{el}\big[r, R(t)\big] - i\frac{\partial}{\partial t}\right) \times \Psi(r, b, v, t) = 0 \tag{6.7}$$

where r stands for the electronic coordinates. It may be solved for each velocity v and impact parameter b by expanding the total wave function on the eigenfunctions $\psi_{m\Lambda}^{adia}$ of H^{el} with eigenvalues $\varepsilon_{m\Lambda}$:

$$\Psi(r, b, v, t) = \sum_{m\Lambda} a_{m\Lambda}(b, v, t)\psi_{m\Lambda}^{adia}\big[r, R(t)\big] \times \exp\left(-i\int_o^t \varepsilon_{m\Lambda}\big[R\big(t'\big)\big]dt'\right). \tag{6.8}$$

By integration of equation (6.7), the capture probabilities are given by $P(b, v) = \sum_{m\Lambda} |a_{m\Lambda}(b, v, \infty)|^2$ with summation over all charge exchange channels. The cross section is then defined by:

$$\sigma(v) = 2\pi \int bP(b, v)db. \tag{6.9}$$

In this approach, the collision dynamics was treated using the EIKONXS program [29] taking into account radial and rotational coupling matrix elements, as well as translation effects, although they are expected to be low at these energies.

6.2.3 Thermal Rate Constant

The rate constants $k(T)$ are calculated by averaging the cross sections $\sigma(E)$ over a Maxwellian velocity distribution at temperature T [30]:

$$k(T) = \left(\frac{8}{\pi\mu}\right)^{1/2}\left(\frac{1}{k_B T}\right)^{3/2}\int_0^\infty E\sigma(E) \times \exp\left(-\frac{E}{k_B T}\right)dE. \tag{6.10}$$

The rate constant for the reverse ionization process $k_{rev}(T)$ may be determined easily by means of the micro-reversibility relation from the corresponding charge transfer rate constant $k(T)$:

$$k_{rev}(T) = g\exp\left(-\frac{\Delta E}{k_B T}\right)k(T), \tag{6.11}$$

where g is the ratio of the statistical weights of initial and final states, and ΔE is the energy gain of the charge transfer reaction.

6.3 Molecular Calculations

The electron spin being conserved in the collision process, we have to determine the potential energies of the different molecular states involved in the process for all

Table 6.1 Correlation diagram

Configuration	Molecular states	Asymptotic energies (eV)		
		NIST database [34]	$^2\Pi/^2\Sigma$	$^4\Pi/^4\Sigma$ states
$C(2s^22p^2)^1D + S^+(3s^23p^3)^4S$	$^4\Sigma, ^4\Pi, ^4\Delta$	1.26		1.32
$C^+(2s^22p)^2P + S(3s^23p^4)^3P$	$^{2,4}\Sigma, ^{2,4}\Pi, ^{2,4}\Delta$	0.92	0.98	0.93
$C(2s^22p^2)^3P + S^+(3s^23p^3)^4S$	$^{2,4,6}\Sigma, ^{2,4,6}\Pi$	0.0	0.0	0.0

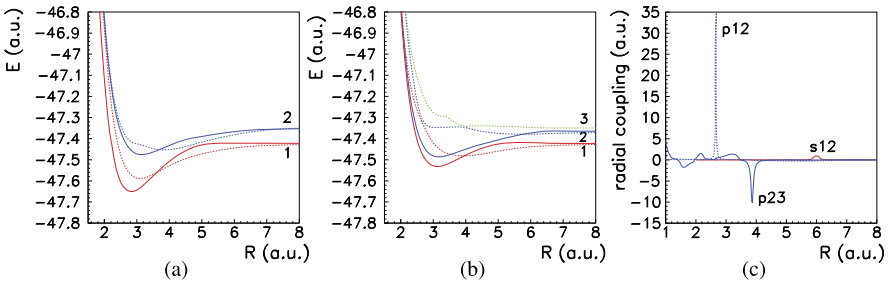

Fig. 6.1 (**a**) Adiabatic potential energy curves for the Σ (*full lines*) and Π (*dashed lines*) states of the doublet manifold of the CS^+ molecular system. (1) $\{C(2s^22p^2)^3P + S^+(3s^23p^3)^4S\}$. (2) $\{C^+(2s^22p)^2P + S(3s^23p^4)^3P\}$ entrance channel. (**b**) Adiabatic potential energy curves for the Σ (*full lines*) and Π (*dashed lines*) states of the quartet manifold of the CS^+ molecular system. (1) and (2), same labels as in Fig. 6.1a. (3) $\{C(2s^22p^2)^1D + S^+(3s^23p^3)^4S\}$. (**c**) Radial coupling matrix elements between the $^4\Pi$ and $^4\Sigma$ states of the CS^+ molecular system: s12, $\langle 1\Sigma|\partial/\partial R|2\Sigma\rangle$; p12, $\langle 1\Pi|\partial/\partial R|2\Pi\rangle$; p23, $\langle 2\Pi|\partial/\partial R|3\Pi\rangle$

spin symmetries, as well as the couplings between these states. They are determined by means of *ab initio* quantum chemistry approaches. For all systems, the potentials have been calculated by means of state-average CASSCF/MRCI (Complete Active Space Self Consistent Field/ Multi-Reference Configuration Interaction) calculations using the MOLPRO code [31] with the correlation-consistent quadruple-ζ aug-cc-AVQZ basis sets of Dunning for all atoms [32]. The ECP10sdf (Effective Core Potential) relativistic pseudo-potential has been used to describe the 10 core-electrons of sulfur [33]. The active space includes the $n = 2$ orbitals for carbon, and the $n = 3$ orbitals for sulfur.

At low temperatures in the interstellar medium, the different species involved in the $C^+(^2P) + S(^3P)$ collision process may be in their ground state. With regard to the correlation diagram (Table 6.1), only two molecular states $\{C^+(2s^22p)^2P + S(3s^23p^4)^3P\}$ and $\{C(2s^22p^2)^3P + S^+(3s^23p^3)^4S\}$ could thus be involved in the direct charge transfer reaction for the doublet manifold. However, for quartet states the higher $\{C(2s^22p^2)^1D + S^+(3s^23p^3)^4S\}$ configuration is close in energy to the entrance channel and has to be considered.

The potential energy curves are presented in Figs. 6.1a, b for doublet and quartet manifolds. Both $^2\Sigma$ and $^2\Pi$ potentials show a smooth avoided crossing around $R = 5$ a.u., in agreement with previous calculations [35, 36]. In the quadruplet

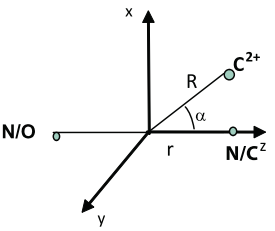

Fig. 6.2 Internal Jacobi coordinates

manifold, a similar smooth avoided crossing is observed for the $^4\Sigma$ potential energy curves. But a strong interaction between the $^4\Pi$ entry channel and the upper $^4\Pi\{C(2s^22p^2)^1D + S^+(3s^23p^3)^4S\}$ level is exhibited around $R = 4$ a.u. It corresponds to a strong radial coupling, about 10 a.u. high which might be determinant in the description of the charge transfer process (Fig. 6.1c). A very peaked radial coupling appears also between states $1^4\Pi$ and $2^4\Pi$ in the repulsive part of the potential energy curves.

We have performed the same theoretical treatment for the $C^{2+} + CO$ and $C^{2+} + N_2$ isoelectronic collision systems. The geometry has been described using the internal Jacobi coordinates $\{R, r, \alpha\}$ with the origin at the centre of mass of the target molecule (see Fig. 6.2). The equilibrium geometries of the CO and N_2 diatomics have been optimized, respectively $r_{CO} = 2.140535$ a.u. and $r_{N_2} = 2.0749$ a.u., and provide accurate ionization potentials [7, 12]. The orientation of the projectile toward the molecular target may be studied for different values of the angle α, from linear to perpendicular geometry ($\alpha = 90°$). The angle $\alpha = 180°$ corresponds to the collision in the linear approach toward the oxygen atom for the $C^{2+} + CO$ charge transfer.

Considering the symmetry of the entrance channels, respectively $C^{2+}(1s^22s^2)^1S + CO(^1\Sigma^+)$ and $C^{2+}(1s^22s^2)^1S + N_2(^1\Sigma_g^+)$, only $^1\Sigma^+$ levels could be involved in the process by means of radial coupling, and $^1\Pi$ levels by means of rotational coupling. Seven levels have thus been taken into account in the calculation for each system:

$C^{2+}(1s^22s^2)^1S + CO(1\Sigma^+)/N_2(^1\Sigma_g^+)$	$4^1\Sigma^+$
$C^+(1s^22s^22p)^2P + CO^+(B^2\Sigma^+)/N_2^+(^2\Sigma_u^+)$	$3^1\Sigma^+, 3^1\Pi$
$C^+(1s^22s^22p)^2P + CO^+(A^2\Pi)/N_2^+(^2\Pi_u)$	$2^1\Sigma^+, 2^1\Pi$
$C^+(1s^22s^22p)^2P + CO^+(A^2\Sigma^+)/N_2^+(^2\Sigma_g^+)$	$1^1\Sigma^+, 1^1\Pi$

The potential energy curves of these isoelectronic systems are presented respectively in Figs. 6.3a, c. They show very similar features, with a relatively smooth avoided crossing around 6–7 a.u. between the entrance channel and the $3^1\Sigma^+$ level, as well as between respectively the 2–$3^1\Sigma^+$ and 1–$2^1\Sigma^+$ states. A sharper avoided crossing may be observed at shorter range between the entrance channel and the highest $3^1\Sigma^+$ exit channel as exhibited in Fig. 6.3b for the $C^{2+} + CO$ system.

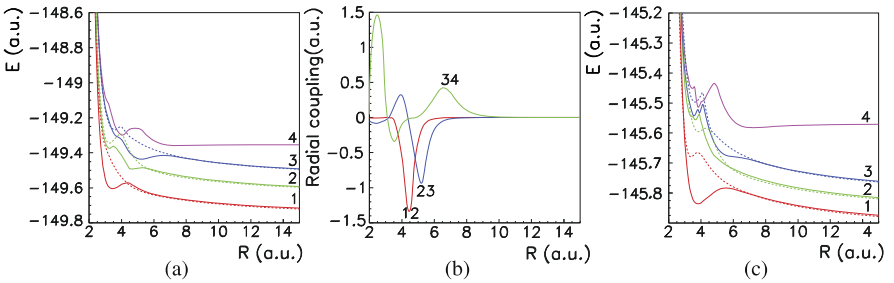

Fig. 6.3 (**a**) Potential energy curves for the $^1\Sigma^+$ (*full lines*) and $^1\Pi$ (*dashed lines*) states of the C^{2+} + CO molecular system at equilibrium, internal Jacobi coordinates $\{R, r, \alpha\}$ $\alpha = 180°$. (1) $C^+(1s^22s^22p)^2P$ + $CO^+(A^2\Sigma^+)$; (2) $C^+(1s^22s^22p)^2P$ + $CO^+(A^2\Pi)$; (3) $C^+(1s^22s^22p)^2P$ + $CO^+(B^2\Sigma^+)$; (4) $C^{2+}(1s^22s^2)^1S$ + $CO(^1\Sigma^+)$ entrance channel. (**b**) Corresponding radial coupling matrix elements between $^1\Sigma^+$ states: ij, $\langle i\,\Sigma|\partial/\partial R|j\,\Sigma\rangle$. (**c**) Potential energy curves for the $^1\Sigma^+$ (*full lines*) and $^1\Pi$ (*dashed lines*) states of the C^{2+} + N_2 molecular system at equilibrium in linear geometry. (1) $C^+(1s^22s^22p)^2P$ + $N_2^+(^2\Sigma_g^+)$; (2) $C^+(1s^22s^22p)^2P$ + $N_2^+(^2\Pi_u)$; (3) $C^+(1s^22s^22p)^2P$ + $N_2^+(^2\Sigma_u^+)$; (4) $C^{2+}(1s^22s^2)^1S + N_2(^1\Sigma_g^+)$ entrance channel

6.4 Collision Rate Constants

The total cross section for each charge transfer is calculated from all the space and spin symmetry states involved in the process, taking account of their respective statistical weights.

In the $C^+(2s^22p)^2P + S(3s^23p^4)^3P \rightarrow C(2s^22p^2)^3P + S^+(3s^23p^3)^4S$ reaction where the entrance channel may be of doublet and quartet spin symmetry, the total cross section is thus $\sigma_{tot} = \frac{1}{3}{}^2\sigma + \frac{2}{3}{}^4\sigma$ with regard to the statistical weights between doublet and quartet manifolds. In this expression, the cross sections for doublet and quartet manifolds are expressed respectively from the cross sections σ^{Σ} and σ^{Π} for Σ and Π states:

$$^{2,4}\sigma = 1/3\sigma^{\Sigma} + 2/3\sigma^{\Pi}. \tag{6.12}$$

The partial and total cross sections $C^+ + S \rightarrow C + S^+$ are presented in Fig. 6.4 and an interesting analysis on the domain of validity of the semi-classical approach may be discussed. The quartet states provide the main contribution to the total cross section at low collision energies and the consideration of the upper $^4\Pi\{C(2s^22p^2)^1D + S^+(3s^23p^3)^4S\}$ level is necessary for an accurate description of the charge transfer from the quadruplet $^4\Sigma$ and $^4\Pi$ entrance channels. For the doublet manifold, the partial cross sections calculated with a semiclassical approach are in excellent agreement with the results of quantum wave packet dynamics for collision energies higher than 8–10 eV. As expected, of course, the semiclassical calculation deviates at lower energies from the quantum one. However, the semiclassical method appears to be valid down to energies far below its generally accepted domain of accuracy. The variation is even less sensitive for the quartet cross sections which correspond to a statistical weight two times higher than the doublet one. The

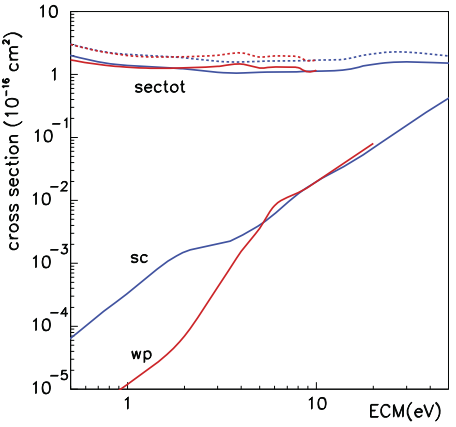

Fig. 6.4 Semiclassical (*blue*) and wave packet (*red*) partial and total cross sections for the CS^+ molecular system in the 0.5–50 eV E_{CM} energy range: doublet manifold (*full lines*); quartet manifold (*dashed lines*); total cross section (*full lines*)

Table 6.2 Rate coefficients for the $C^+ + S$ reaction (in $cm^3\,s^{-1}$)

T (K)	$C^+(^2P) + S(^3P) \rightarrow C(^3P) + S^+(^4S)$	
	Semiclassical dynamics	Quantum dynamics
10		6.0×10^{-12}
50		1.3×10^{-11}
100		1.9×10^{-11}
500	1.8×10^{-11}	4.1×10^{-11}
1000	3.8×10^{-11}	5.6×10^{-11}
5000	7.3×10^{-11}	9.0×10^{-11}
10000	7.3×10^{-11}	1.0×10^{-10}
50000	1.3×10^{-10}	1.5×10^{-10}

total cross section remains close in wave packet and semiclassical approaches, even at eV energies. Such a result is very encouraging in order to have, at a low price, an order of magnitude of cross sections, and consequently rate coefficients, for a number of astrophysical processes.

This is visualized on the corresponding rate constants presented in Table 6.2 using, on one hand, the semi-classical cross sections, and, on the other hand, the wave packet quantum approach. Integration over the whole collision energy domain down to 10^{-3} eV for the quantum dynamics may provide charge transfer rate constants at low temperature. This is of course not possible with semiclassical methods for which rate constants cannot be established for temperatures lower than 500 K. However, such semiclassical approaches may provide the correct order of magnitude, in particular at higher temperatures. The absolute values are significantly lower than the 1.5×10^{-9} $cm^3\,s^{-1}$ rate constant given in the UMIST data base for the 10–41000 K temperature range, in particular at low temperature. The variation is relatively smooth, between about 10^{-11}–10^{-10} $cm^3\,s^{-1}$, which could be in relative accordance with the constant rate considered in astrophysical models, but the usual value seems to be overestimated at least by a power of 10.

Table 6.3 Rate coefficients for the $C^{2+} + CO$ and $C^{2+} + N_2$ collision systems (in $cm^3\,s^{-1}$)

T (K)	$C^{2+} + CO$	exp [17]	$C^{2+} + N_2$	exp [17]
10	5.4×10^{-15}		1.7×10^{-15}	
50	6.3×10^{-14}		2.4×10^{-14}	
100	1.2×10^{-13}		6.1×10^{-14}	
500	1.1×10^{-12}		3.2×10^{-13}	
1000	6.7×10^{-12}		8.4×10^{-13}	
5000	9.6×10^{-11}		1.1×10^{-11}	
10000	2.4×10^{-10}		4.2×10^{-11}	
11700	2.9×10^{-10}	4.6×10^{-10}	5.5×10^{-11}	1.1×10^{-10}

Similar calculations may provide charge transfer cross sections and rate constants for the $C^{2+} + CO$ and $C^{2+} + N_2$ collision systems (Table 6.3). In that case, the total cross section is averaged over the different orientations of the projectile ion toward the molecular target, at the equilibrium distance optimized for each diatomic target. The process is highly anisotropic, markedly inefficient in the perpendicular orientation ($\alpha = 90°$), and clearly preferred in the linear orientation for both collision systems. In the case of the $C^{2+} + CO$ reaction, the charge transfer is favoured in the collision toward the oxygen atom ($\alpha = 180°$) in correspondence with a higher value of the main $\langle 3^1\Sigma^+|\partial/\partial R|4^1\Sigma^+\rangle$ radial coupling.

For both systems, the rate constants increase with increasing temperatures in the whole temperature range. The calculated values appear in relative good agreement with experiment. At $T_{equiv} = 1.17 \times 10^4$ K, the calculated rate constants are 2.88×10^{-10} $cm^3\,s^{-1}$ for $C^{2+} + CO$, and 5.55×10^{-11} $cm^3\,s^{-1}$ for $C^{2+} + N_2$, slightly underestimated compared to experimental data, respectively 4.58×10^{-10} $cm^3\,s^{-1}$ and 1.08×10^{-10} $cm^3\,s^{-1}$, but the relative difference between the rate coefficients for the CO and N_2 targets is correctly reproduced. This comparison has however to take into account several uncertainties in both experimental and theoretical studies. Experimental measurements are performed using an ion trap combined with a laser-plasma electron beam ion source. In such technique, the determination of the temperature, T_{equiv}, remains always questionable as it is given by a mean value between the temperature T_i of the incident ion and the temperature T_n of the target molecule:

$$T_{equiv}/\mu = T_i/m_i + T_n/m_n \tag{6.13}$$

with μ the reduced mass of the system and m_i and m_n, respectively, the masses of the C^{2+} ion and target molecule [17]. As T_i ($\sim 1.7 \times 10^4$ K) and T_n (300 K) are very different and the collision process very fast, it is hard to imagine the collision system at equilibrium. On the other hand, the theoretical calculation has been performed for a number of given orientations between the molecular target and the projectile ion, a full 3D calculation would be necessary to take account completely of the anisotropy of the process, besides, the calculation of rate constants needs the determination of very low-energy cross sections. Such approach provides anyway

a quantitative determination of charge transfer rate constants and our treatment enlightens the mechanism involved in the process.

6.5 Conclusion

The present results exhibit some interesting features of charge transfer processes with atomic or molecular targets. Rate constants can be determined theoretically for such processes. The charge transfer mechanism is driven mainly by non-adiabatic interactions between the molecular states, and correlations between non-adiabatic radial couplings and charge transfer cross sections may be pointed out. The process is highly anisotropic, favoured in the linear approach toward the more electronegative atom.

Acknowledgements This work was granted access to the HPC resources of [CCRT/ CINES/ IDRIS] under the allocation i2012081566 made by GENCI [Grand Equipement National de Calcul Intensif]. The support of the COST Action CM0805 'Chemical Cosmos' is gratefully acknowledged.

References

1. Nussbaumer H (1986) Astron Astrophys 155:205
2. Honvault P, Gargaud M, Bacchus-Montabonel MC, McCarroll R (1995) Astron Astrophys 302:931
3. Gargaud M, Bacchus-Montabonel MC, McCarroll R (1993) J Chem Phys 99:4495
4. Honvault P, Bacchus-Montabonel MC, Gargaud M, McCarroll R (1998) Chem Phys 238:401
5. Wakelam V et al (2012) Astrophys J Suppl Ser 199:21
6. Bene E, Vibók Á, Halász GJ, Bacchus-Montabonel MC (2008) Chem Phys Lett 455:159
7. Bene E, Martínez P, Halász GJ, Vibók Á, Bacchus-Montabonel MC (2009) Phys Rev A 80:012711
8. Teyssier D, Fossé D, Gerin M, Pety J, Abergel A, Roueff E (2004) Astron Astrophys 417:135
9. The UMIST database for Astrochemistry. http://www.udfa.net
10. Bacchus-Montabonel MC, Talbi D (2008) Chem Phys Lett 467:28
11. Chenel A, Mangaud E, Justum Y, Talbi D, Bacchus-Montabonel MC, Desouter-Lecomte M (2010) J Phys B 43:245701
12. Bacchus-Montabonel MC, Tergiman YS (2010) Chem Phys Lett 497:18
13. Bacchus-Montabonel MC (1999) Phys Rev A 59:3569
14. Errea LF, Macías A, Méndez L, Riera A (1999) J Phys B 32:4065
15. Unterreiter E, Schweinzer J, Winter HP (1991) J Phys B 24:1003
16. Burns D, Greenwood JB, Bajajova KR, McCullough RW, Geddes J, Gilbody HB (1997) J Phys B 30:1531
17. Gao H, Kwong VHS (2003) Phys Rev A 68:052704
18. Zare RN (1988) Angular momentum. World Scientific, New York
19. Shtermin PS, Vasyutinskii OS (2008) J Chem Phys 128:194314
20. Bacchus-Montabonel MC, Vaeck N, Lasorne B, Desouter-Lecomte M (2003) Chem Phys Lett 374:307
21. Bacchus-Montabonel MC (1987) Phys Rev A 36:1994
22. Bacchus-Montabonel MC, Courbin C, McCarroll R (1991) J Phys B 24:4409

23. Gargaud M, Fraija F, Bacchus-Montabonel MC, McCarroll R (1994) J Phys B 27:3985
24. Vaeck N, Bacchus-Montabonel MC, Baloïtcha E, Desouter-Lecomte M (2001) Phys Rev A 63:042704
25. Baloïtcha E, Desouter-Lecomte M, Bacchus-Montabonel MC, Vaeck N (2001) J Chem Phys 114:8741
26. Feit MD, Fleck JA, Steiger A (1982) J Comput Phys 47:412
27. Alvarellos J, Metiu H (1988) J Chem Phys 88:4957
28. Bransden BH, McDowell MRC (1992) Charge exchange and the theory of ion-atom collisions. Clarendon, Oxford
29. Allan RJ, Courbin C, Salas P, Wahnon P (1990) J Phys B 23:L461
30. Linguerri R, Hochlaf M, Bacchus-Montabonel MC, Desouter-Lecomte M (2013) Phys Chem Chem Phys 15:824
31. Werner HJ, Knowles P, MOLPRO package of ab initio programs
32. Woon DE, Dunning TH Jr (1993) J Chem Phys 98:1358
33. Nicklass A, Dolg M, Stoll H, Preuss H (1995) J Chem Phys 102:8942
34. NIST atomic spectra database levels. http://www.physics.nist.gov/cgi-bin/AtData:main_asd
35. Larsson M (1985) Chem Phys Lett 117:331
36. Honjou N (2008) Chem Phys 344:128

Chapter 7
Spin Torque and Zeta Force in Allene-Type Molecules

Masahiro Fukuda, Masato Senami, and Akitomo Tachibana

Abstract The spin torque, the zeta force, and the zeta potential, which are significant quantities to describe the local picture of spin dynamics, are studied by using allene-type molecules (C_3H_4 and $C_3H_2Li_2$) in their stationary states. We show that the two molecules have different distribution patterns of these quantities though their structures are very similar to each other. It is also shown that the zeta potential distribution is almost independent of the electron density distribution.

7.1 Introduction

Due to the great innovation of the field of spintronics, the electron spin is now one of the most interesting quantities for electronic devices. The control of the spin is the key element of the spintronics. Hence, the further knowledge of the nature of the electron spin enables us to improve spintronics devices. The size of spintronics materials is already about nano-scale. For these microscopic materials, local effects are relatively important for the evolution of the electron spin. However, few studies for the local evolution of the electron spin are reported in spite of its necessity. We consider that it is important to analyze the local evolution from the first principles calculation.

In our laboratory, nano-materials have been studied by using several local quantities proposed by one of the authors [1–4]. For example, the local dielectric constant and local polarizability clarify the local dielectric response in high dielectric constant thin films. We have reported the local dielectric property of hafnium dioxide, which is a candidate for materials of a future semiconductor [5–10]. For the study of the local electric conductive property, the local conductivity is used to investigate the conductive property of nanowire materials [11–14]. For the description of local torque for the electron spin, the local spin torque and the zeta force have been proposed based on quantum field theory [1–4] and we have studied these quantities for atoms of transition elements and dimers of alkali metal atoms [15, 16]. In these

A. Tachibana (✉)
Department of Micro-Engineering, Kyoto University, Kyoto 615-8540, Japan
e-mail: akitomo@scl.kyoto-u.ac.jp

M. Hotokka et al. (eds.), *Advances in Quantum Methods and Applications in Chemistry, Physics, and Biology*, Progress in Theoretical Chemistry and Physics 27,
DOI 10.1007/978-3-319-01529-3_7,

works, we have reported that the local description of the torque for the electron spin is available in quantum field theory due to the existence of the zeta force, while in relativistic quantum mechanics we cannot use the local description. In quantum mechanics, when the Heisenberg equation of the electron spin is considered at a point, this equation gives nonzero result even for spin steady states [16], though the expectation value of the whole region is zero, of course. Hence, the zeta force plays an important role to describe the local picture of the spin even for the stationary state. In this article, we study the local spin torque and zeta force following our preceding works.

This paper is organized as follows. In Sect. 7.2, we introduce the definitions of the spin angular momentum density and the zeta potential. The spin torque and the zeta force are derived from the equation of motion of the spin angular momentum density. We also mention the comparison with the Heisenberg equation in relativistic quantum mechanics. In Sect. 7.2.2, we explain computational details. In Sect. 7.3, our results of the spin torque, the zeta force, and the zeta potential of allene-type molecules (C_3H_4, $C_3H_2Li_2$) are shown. The last section is devoted to our conclusion.

7.2 Theory and Calculation Method

In this section, we briefly review the equation of motion of the spin angular momentum density and the quantities of the spin torque density and the zeta force density [1–4]. These quantities play important roles to investigate the local electronic spin dynamics. In this work, relativistic quantum field theory is adopted. It is known that the electronic spin is intrinsically included in the Dirac equation. In the relativistic quantum theory, the electronic spin and orbital angular momentums are not conserved separately, for example due to the spin-orbit interaction. Hence, if we treat the spin degree of freedom correctly, we should rely on the relativistic quantum theory. In addition, we adopt the quantum field theory, which is considered to be more correct than quantum mechanics, since one of the authors found the novel contribution to the torque for the electron spin, the zeta force.

7.2.1 Spin Torque Density and Zeta Force Density

The electronic spin angular momentum density operator is represented as

$$\hat{s}_e^k(x) = \frac{1}{2}\hbar\hat{\psi}^\dagger(x)\Sigma^k\hat{\psi}(x), \tag{7.1}$$

where $\hat{\psi}$ is the four-component Dirac spinor operator and Σ^k is the Pauli matrix in the four-component representation.

The torque density for the electron spin is derived by the time derivative of the spin angular momentum density,

$$\frac{\partial \hat{s}_e^k(x)}{\partial t} = \frac{\partial}{\partial t}\left(\frac{1}{2}\hbar\hat{\psi}^\dagger(x)\Sigma^k\hat{\psi}(x)\right). \tag{7.2}$$

The time derivative of the field operators in the right-hand side can be calculated by using the Dirac equation,

$$i\hbar\gamma^\mu \hat{D}_\mu(x)\hat{\psi}(x) = mc\hat{\psi}(x), \tag{7.3}$$

where γ^μ is the gamma matrix and m is the mass of electron. The covariant derivative is given by

$$\hat{D}_\mu(x) = \partial_\mu + i\frac{Z_e e}{\hbar c}\hat{A}_\mu(x), \quad Z_e = -1, \tag{7.4}$$

where $\hat{A}_\mu(x)$ is the photon field operator. As a result, we obtain the equation of motion of the spin angular momentum density, and the right-hand side can be arranged in two terms,

$$\frac{\partial \hat{s}_e^k(x)}{\partial t} = \hat{t}_e^k(x) + \hat{\zeta}_e^k(x), \tag{7.5}$$

where the first term, $\hat{t}_e^k(x)$, is the spin torque, which is the same as that of quantum mechanics, and the second term, $\hat{\zeta}_e^k(x)$, is the zeta force, respectively [1, 3, 4]. (In this article, we call only $\hat{t}_e^k(x)$ the spin torque, and the sum of the terms in the right-hand side is called the torque for the spin.) The spin torque density operator is defined with the relativistic stress tensor density, $\hat{\tau}_e^{\Pi ln}(x)$, as

$$\hat{t}_e^k(x) = -\varepsilon_{lnk}\hat{\tau}_e^{\Pi ln}(x), \tag{7.6}$$

where ε_{lnk} is the Levi-Civita tensor. The relativistic stress tensor operator is given by [1, 3, 4, 17–22],

$$\hat{\tau}_e^{\Pi ln}(x) = \frac{i\hbar c}{2}\left[\hat{\psi}^\dagger(x)\gamma^0\gamma^n\hat{D}_l(x)\hat{\psi}(x) - \left(\hat{D}_l(x)\hat{\psi}(x)\right)^\dagger\gamma^0\gamma^n\hat{\psi}(x)\right]. \tag{7.7}$$

The zeta force density operator is defined with the zeta potential, $\hat{\phi}_5$, as

$$\hat{\zeta}_e^k(x) = -\partial_k\hat{\phi}_5. \tag{7.8}$$

The zeta potential is given by

$$\hat{\phi}_5(x) = \frac{\hbar c}{2}\left[\hat{\psi}^\dagger(x)\gamma_5\hat{\psi}(x)\right], \tag{7.9}$$

where $\gamma_5 = i\gamma^0\gamma^1\gamma^2\gamma^3$.

The stress tensor (Eq. (7.7)) is known to classify the chemical bond. The third eigenvalue of the stress tensor characterize compressive (negative) and tensile (positive) stress in a molecule. For a covalent bond, the region between bonding atoms is associated with tensile stress and a spindle structure of an inter-atomic region [22].

The spin torque density (Eq. (7.6)) is defined so that it is the same as the well-known spin torque term in relativistic quantum mechanics. The Heisenberg equation of the spin angular momentum in quantum mechanics is given by

$d\hat{\mathbf{s}}_e/dt = -c\hat{\pi} \times \alpha$ [23, 24]. The zeta force density (Eq. (7.8)), which does not appear in quantum mechanics, gives a novel local contribution to the torque for the electron spin. The potential of the zeta force, zeta potential, is proportional to $\hat{j}_5^0(x)$, which is the zeroth-component of the chiral current,

$$\hat{j}_5^\mu(x) = cZ_e e\big[\hat{\bar{\psi}}(x)\gamma^\mu\gamma_5\hat{\psi}(x)\big]. \tag{7.10}$$

We note that the spin angular momentum density is also represented by the chiral current as $\hat{s}_e^k(x) = \frac{\hbar}{2cZ_e e}\hat{j}_5^k(x)$. The zeta potential can be cast into another form,

$$\hat{\phi}_5(x) = \frac{\hbar c}{2}\big(\hat{\psi}_R^\dagger(x)\hat{\psi}_R(x) - \hat{\psi}_L^\dagger(x)\hat{\psi}_L(x)\big), \tag{7.11}$$

where $\hat{\psi}_L(x)$ and $\hat{\psi}_R(x)$ are the spinor with the left-handed and right-handed chirality, respectively. These operators are defined as

$$\hat{\psi}_L(x) = \frac{1-\gamma_5}{2}\hat{\psi}(x), \qquad \hat{\psi}_R(x) = \frac{1+\gamma_5}{2}\hat{\psi}(x). \tag{7.12}$$

We now proceed to the discussion of the physical interpretation of the equation of motion of the spin. It can be seen from Eq. (7.5) that the electronic spin can be accelerated by two torque terms: the spin torque and zeta force. One may wonder whether this new contribution disturbs the consistency between experimental observations and the prediction by quantum mechanics. The expectation value of the zeta force is zero after the integration over the whole region, since the zeta force density operator is given as the gradient of the zeta potential operator (see Eq. (7.8)). Hence, Eq. (7.5) is the same as the Heisenberg equation in quantum mechanics, and this new contribution can safely be neglected in past experiments. However, if we consider a local region in target materials, the contribution from the zeta force can give a nonzero effect even after the integration over a restricted local region. Hence, the effect of the zeta force can be observed if an experimental setup is carefully designed for this purpose. Therefore, our equation, Eq. (7.5), based on quantum field theory can predict the correct local picture of electron spin dynamics.

Next, we mention a time-independent stationary state of the electron spin. In the state, as seen in Eq. (7.5), the spin torque and zeta force are canceled out with each other. Hence, we can obtain a new local picture of a time-independent stationary state of the electron spin. In quantum mechanics, any local spin dynamics prediction cannot be derived, since the Heisenberg equation cannot give zero torque for a local region even for the spin stationary state. Of course, the quantum mechanics is defined for the expectation value, and hence the local description is theoretically out of scope of quantum mechanics.

In a time-dependent spin evolution state, this balance is not maintained. In the viewpoint of quantum electrodynamics (QED), which is a kind of quantum field theory, the dynamical local picture of the spin is summarized as follows: When some photons enter a system, the balance between the spin torque and the zeta force is disturbed, and the electronic spin is driven by the photons. Then the photons are also affected by the back reaction from this torque.

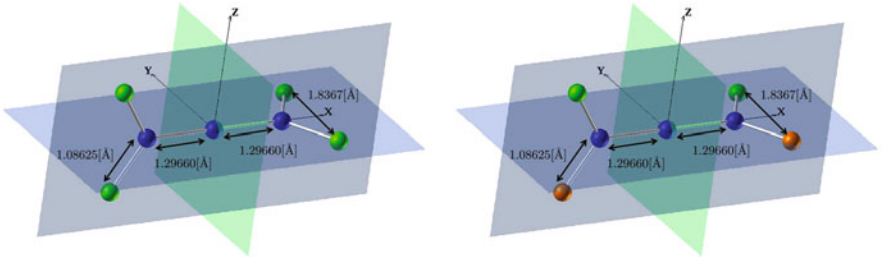

(a) Structure of C_3H_4 (b) Structure of $C_3H_2Li_2$

Fig. 7.1 Structures of molecules. *Blue*, *green* and *orange* spheres represent C, H, and Li atoms, respectively. In C_3H_4 (**a**), the lengths of C–C, C–H, and H–H bonds are 1.29660 [Å], 1.08625 [Å], and 1.83670 [Å], respectively. In $C_3H_2Li_2$ (**b**), the lengths of C–C, C–Li, and Li–H bonds are 1.29660 [Å], 1.08625 [Å], and 1.83670 [Å], respectively

Table 7.1 Details of CI calculations

	Number of electrons (excluding frozen core)	Active space number	Active orbitals (electronic eigenvalue no.)	Number of spinors in the RAS1 (1A, 2A)	Number of spinors in the RAS3 (1A, 2A)
C_3H_4	16	19	4–22	(8, 8)	(11, 11)
$C_3H_2Li_2$	20	18	4–21	(10, 10)	(8, 8)

7.2.2 Computational Details

We study the spin torque and zeta force of allene-type molecules, an achiral molecule (C_3H_4) and a chiral molecule ($C_3H_2Li_2$), in this work. The achiral and chiral molecules in the steady state are compared from the viewpoint of chirality.

To calculate the spin torque and zeta force, a state derived by quantum field theory is required. However, the state is not available for our purpose, since most computation code is based on quantum mechanics. Hence, in this work, we use the four-component wave function by relativistic quantum mechanics as a substitution. This is derived by using DIRAC11 program package [25]. Structures of C_3H_4 and $C_3H_2Li_2$ are shown in Fig. 7.1. In this calculation, the cc-pVTZ basis set [26] is used with the uncontraction for large components of H, Li, and C atoms. The small component basis is generated by restricted kinetic balance. After Hartree-Fock calculations with Dirac-Coulomb Hamiltonian, Configuration Interaction (CI) calculations are performed by the restricted active space (RAS) method by using DIRRCI module. The details of CI calculations are summarized in Table 7.1. The screening technique [27] is not used in our computations in order to derive higher accuracy.

After these quantum chemistry computations, the spin torque and zeta force are calculated for derived wave functions. The lowest energy singlet state is used for these calculations. These calculations are performed by QEDynamics program package [28–30]. The effect of vector potential is ignored in our calculations, since

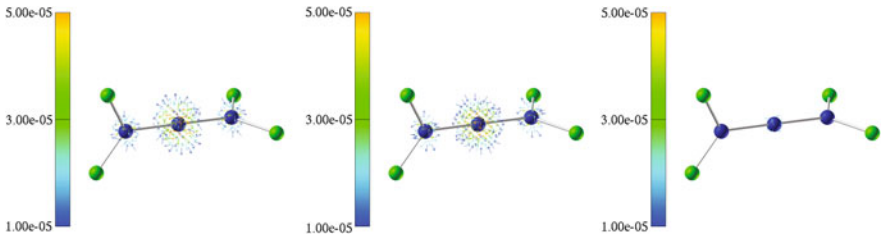

(a) spin torque (b) zeta force (c) spin torque + zeta force

Fig. 7.2 The distributions of the spin torque (**a**), the zeta force (**b**), and the sum of them (**c**) in C_3H_4. The threshold value is 1.0×10^{-5} [a.u.]

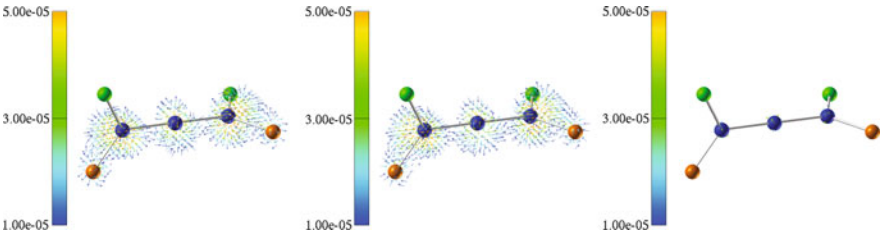

(a) spin torque (b) zeta force (c) spin torque + zeta force

Fig. 7.3 The distributions of the spin torque (**a**), the zeta force (**b**), and the sum of them (**c**) in $C_3H_2Li_2$. The threshold value is 1.0×10^{-5} [a.u.]

it is quantitatively small for the states by quantum mechanics. All the physical quantities, such as the spin torque and zeta force, are depicted for only active electrons of CI calculations.

7.3 Result and Discussion

7.3.1 Spin Torque and Zeta Force

We investigate the spin torque and the zeta force of C_3H_4 and $C_3H_2Li_2$. The results are shown in Figs. 7.2 and 7.3 for C_3H_4 and $C_3H_2Li_2$, respectively. It can be seen that the sum of the spin torque and the zeta force is much smaller than the spin torque and the zeta force itself in the whole region. This result is consistent with the fact that the nonzero spin torque is in balance with the zeta force for the spin steady state. Hence, although our computational result is derived from wave functions of quantum mechanics, it is considered that we can study the behavior of the spin torque and zeta force by using these wave functions.

The values of the norm of the spin torque and zeta force in the vicinity of nuclei amount to 10^{-4}–10^{-5} [a.u.] for both molecules. In C_3H_4, the spin torque and zeta

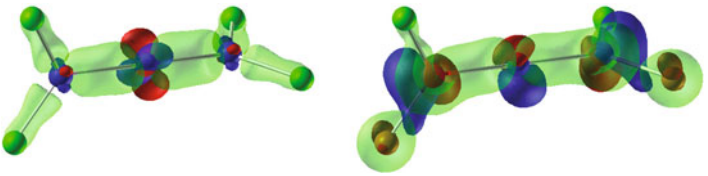

(a) C_3H_4 (b) $C_3H_2Li_2$

Fig. 7.4 Electron density and zeta potential. *Blue* and *red* envelopes represent positive and negative zeta potential iso-surfaces, respectively. The threshold value of iso-surfaces of the zeta potential is taken as $\pm 7.5 \times 10^{-6}$ [a.u.]. *Green* envelopes represent electron density iso-surfaces. The threshold value of iso-surfaces of the electron density is taken as 0.25 [a.u.]

force are concentrated in the vicinity of C nuclei, especially around the center of them. In contrast, the spin torque and zeta force in $C_3H_2Li_2$ are also distributed around the vicinity of Li nuclei. In both molecules, the spin torque around H atoms are very small. In comparison between two molecules, the distribution around the center C atom is almost similar to each other. On the other hand, around C atoms at both ends, the distribution of the spin torque (zeta force) of $C_3H_2Li_2$ is wide and its values are large. The cause to make this difference is discussed in the next subsection from the viewpoint of the electron density.

7.3.2 Zeta Potential

In this section, the distribution of the zeta potential introduced in Sect. 7.2.1 is discussed. The zeta potential is principally an observable quantity and hence this quantity is one of the most significant physical quantities to discuss spin dynamics as well as the spin angular momentum density. As denoted in Sect. 7.2.1, the zeta potential is the difference between the electron density with right-handed chirality and left-handed one. Only left-handed electrons interact with neutrinos and/or weak gauge bosons (W/Z bosons) according to the standard model of particle physics. Hence we can principally observe the zeta potential, for example if we can prepare appropriate neutrino beam and detector.

The distributions of the electron density and the zeta potential are shown in Fig. 7.4. Blue and red envelopes represent positive and negative zeta potential iso-surfaces, respectively. The threshold value of these iso-surfaces of the zeta potential is taken as $\pm 7.5 \times 10^{-6}$ [a.u.]. Green envelopes represent electron density iso-surfaces. The threshold value of the iso-surfaces of the electron density is taken as 0.25 [a.u.]. It can be seen from this figure that the distribution of the zeta potential is almost independent of the electron density distribution for both models, while around the C atom at both ends where the zeta potential of $C_3H_2Li_2$ is larger than that of C_3H_4, the electron density is seen to be also large.

We have anticipated that the zeta potential of a chiral molecule is larger than that of an achiral one because it is considered that molecular chirality is probably related

to the electron chirality. While our result supports our conjecture, it cannot yet be concluded whether our conjecture is correct, since we cannot separate the effect of the difference between H and Li atoms and that between the chiral and achiral structures. It can be confirmed that the zeta force distribution is closely related to the zeta potential distribution and the increase of the zeta potential of $C_3H_2Li_2$ from C_3H_4 is inevitably accompanied by the increase of the spin torque.

7.4 Conclusion

In this study, we have studied the spin torque density, the zeta force density, and zeta potential of allene-structure molecules (C_3H_4, $C_3H_2Li_2$), whose states are in the time-independent stationary singlet one. The local picture of the electronic spin stationary states have been described in terms of these density quantities based on quantum field theory. We have shown the local spin torque and zeta force distributions of allene-structure molecules. We have pointed out that the distribution pattern of the zeta potential is not related to the distribution of the electron density. It is considered that the torque for the electrons in a molecule is dependent on the spin orbit interaction. Hence we visualize the distribution of the spin orbit interaction in these molecules and compare the distributions of the spin torque and the zeta force, in our next work.

In our near future work, the local pictures of the electronic spin are studied for chiral and achiral molecules, which interact with photons by using the time evolution simulation based on quantum electrodynamics.

Acknowledgements This work was partially supported by a Grant-in-Aid for Scientific Research from the Japan Society for the Promotion of Science (JSPS) (22550011). M.S. is supported by a Grant-in-Aid for Young Scientists (B) from JSPS (24760028) and Mizuho Foundation for the Promotion of Sciences.

References

1. Tachibana A (2001) J Chem Phys 115:3497
2. Tachibana A (2003) In: Brändas EJ, Kryachko ES (eds) Fundamental world of quantum chemistry, a tribute to the memory of Per-Olov Löwdin, vol 2. Kluwer Academic, Dordrecht, p 211
3. Tachibana A (2005) J Mol Model 11:301
4. Tachibana A (2010) J Mol Struct, Theochem 943:138
5. Doi K, Nakamura K, Tachibana A (2006) In: International workshop on nano CMOS. IEEE Press, New York, pp 209–235
6. Doi K, Mikazuki Y, Sugino S, Doi T, Szarek P, Senami M, Shiraishi K, Iwai H, Umezawa N, Chikyo T, Yamada K, Tachibana A (2008) Jpn J Appl Phys 47:205
7. Szarek P (2008) PhD dissertation, Kyoto University
8. Fukushima A, Tsuchida Y, Senami M, Tachibana A (2010) Jpn J Appl Phys 49:111504
9. Fukushima A, Sugino S, Tsuchida Y, Senami M, Tachibana A (2010) Jpn J Appl Phys 49:121504

10. Senami M, Tsuchida Y, Fukushima A, Ikeda Y, Tachibana A (2012) Jpn J Appl Phys 51:031101
11. Senami M, Ikeda Y, Fukushima A, Tachibana A (2010) Jpn J Appl Phys 49:115002
12. Senami M, Ikeda Y, Tachibana A (2011) Jpn J Appl Phys 50:010103
13. Senami M, Ikeda Y, Tachibana A (2012) AIP Adv 2:042168.
14. Senami M, Ikeda Y, Tachibana A (2013) To be pulished in J Phys Conf Ser
15. Senami M, Nishikawa J, Hara T, Tachibana A (2010) J Phys Soc Jpn 79:084302
16. Hara T, Senami M, Tachibana A (2012) Phys Lett A 376:1434
17. Szarek P, Tachibana A (2007) J Mol Model 13:651
18. Szarek P, Sueda Y, Tachibana A (2008) J Chem Phys 129:94102
19. Szarek P, Urakami K, Zhou C, Cheng H, Tachibana A (2009) J Chem Phys 130:084111
20. Tachibana A (2001) J Chem Phys 115:3497
21. Tachibana A (2003) In: Brändas E, Kryachko E (eds) Fundamental perspectives in quantum chemistry: a tribute to the memory of Per-Olov Löwdin, vol 2. Kluwer Academic, Dordrecht, pp 211–239
22. Tachibana A (2004) Int J Quant Chem 100:981
23. Messiah A (1961) Quantum mechanics. North-Holland, New York
24. Sakurai JJ (1967) Advanced quantum mechanics. Addison-Wesley, Reading
25. DIRAC, a relativistic ab initio electronic structure program, Release DIRAC11 (2011), written by R. Bast, H. J. Aa. Jensen, T. Saue, and L. Visscher, with contributions from V. Bakken, K. G. Dyall, S. Dubillard, U. Ekström, E. Eliav, T. Enevoldsen, T. Fleig, O. Fossgaard, A. S. P. Gomes, T. Helgaker, J. K. Lærdahl, J. Henriksson, M. Iliaš, Ch. R. Jacob, S. Knecht, C. V. Larsen, H. S. Nataraj, P. Norman, G. Olejniczak, J. Olsen, J. K. Pedersen, M. Pernpointner, K. Ruud, P. Sałek, B. Schimmelpfennig, J. Sikkema, A. J. Thorvaldsen, J. Thyssen, J. van Stralen, S. Villaume, O. Visser, T. Winther, and S. Yamamoto (see http://dirac.chem.vu.nl)
26. Dunning TH Jr (1989) J Chem Phys 90:1007
27. Saue T, Fægri K, Helgaker T, Gropen O (1997) Mol Phys 91:937
28. Senami M, Ichikawa K, Tachibana A, QEDynamics (http://www.tachibana.kues.kyoto-u.ac.jp/qed)
29. Ichikawa K, Fukuda M, Tachibana A (2012) Int J Quant Chem 113:190
30. Senami M, Miyazato T, Takada S, Ikeda Y, Tachibana A (2013) To be published in J Phys Conf Ser

Chapter 8
A Refined Quartic Potential Surface for S_0 Formaldehyde

Svetoslav Rashev and David C. Moule

Abstract We present an improved quartic potential energy surface for S_0 formaldehyde. The field was refined starting from the original Martin, Lee, Taylor ab initio field (Martin et al. in J. Mol. Spectrosc. 160:105, 1993). In the calculations we have been using our recently developed variational vibrational calculation method. During the refinement procedure, all (80) harmonic, cubic and quartic force constants of the original field have been varied sequentially in groups of ten, until the best possible fit between the calculated and experimentally measured results has been obtained for a set of carefully selected 29 frequencies (of A_1 symmetry), extending up to $\sim$6000 cm^{-1} of excess vibrational energy.

8.1 Introduction

Formaldehyde is a benchmark polyatomic molecule that has been thoroughly studied spectroscopically [1–6] and has frequently served as a model for large scale vibrational calculations [7–19]. To the present day, 276 vibrational levels in the ground electronic state (up to 12500 cm^{-1}) have been experimentally observed and assigned [3–6]. There have been a number of ab initio determinations of the S_0 ground electronic state molecular force field and equilibrium geometry parameters [20–24], of steadily improving quality. The first exact variational calculation of vibrational levels in formaldehyde, using an exact analytical expression for the kinetic energy [25] and the Martin, Lee, Taylor (MLT) quartic field [22], was carried out by Carter, Pinnavaia and Handy [11]. There have been numerous adjustments and refinements of the MLT quartic force field based on extensive vibrational calculations [11–14]. Burleigh et al. [14] performed a calculation and adjustment to experimental data of 138 vibrational levels in formaldehyde, using 4th and 6th order canonical Van Vleck perturbation theory [6, 14]. Lee and Light [18] applied their iterative solutions/energy selected bases variational method

S. Rashev (✉)
Institute of Solid State Physics, Bulgarian Academy of Sciences, Tsarigradsko chaussee 72, 1784 Sofia, Bulgaria
e-mail: rashev@issp.bas.bg

M. Hotokka et al. (eds.), *Advances in Quantum Methods and Applications in Chemistry, Physics, and Biology*, Progress in Theoretical Chemistry and Physics 27,
DOI 10.1007/978-3-319-01529-3_8,

to calculate 729 A_1 symmetry states up to 13500 cm^{-1} of excess vibrational energy, based on a slightly modified version of the Burleigh et al. adjusted PES [14]. More recently, Yachmenev et al. [24] produced an ab initio PES for ground electronic state formaldehyde, that surpassed the quality of the MLT field [22] being closer to spectroscopic accuracy. The authors [24] designed an analytical expression for their field, determined by 110 parameters. Next, these authors varied the values of the parameters, aiming to obtain a PES of spectroscopic accuracy.

In our recent work we described and implemented an alternative method [26] for the calculation of exact frequencies in S_0 formaldehyde that is based on the exact kinetic energy expression [25], a PES expression that should be given in separable form (as a sum of products; the quartic expression [22] and the analytical expression [24] satisfy this requirement) and the employment of a specific iterative procedure for deriving the most economic Hamiltonian matrix of the vibrational problem, complemented by a Lanczos manipulation of the Hamiltonian matrix. The main asset of our method is the possibility to achieve arbitrarily high precision as well as to extend the calculations to extremely high vibrational excitation energies [26–29]. We first assessed the performance of our method [26], by reproducing exactly the vibrational energy levels of S_0 formaldehyde, corresponding to the ab initio MLT PES, calculated earlier by Carter et al. [11] and Luckhaus [15] and next demonstrated the ability of our method to extend the calculations up to extremely high levels of vibrational excitation energy [26]. We also performed converged large scale calculations on deuterated species D_2CO [27] and HDCO [28, 29] and compared the calculated frequencies to experimentally measured values. We also studied the IVR behavior at very high vibrational excitations and compared the mode selectivity and vibrational redistribution of different formaldehyde isotopomers [26–29]. In all these calculations the original ab initio MLT PES was used without any adjustment.

This work is organized as follows. In Sect. 8.2 we give a very brief description of our variational vibrational procedure for calculation of vibrational energy levels, that has been described in detail in our recent work [26]. Next in Sect. 8.3 we first briefly describe our experience with the recently computed formaldehyde PES by Yachmenev et al. [24] and then we describe our strategy employed for adjustment of the force constants of the original MLT field to yield vibrational frequencies of S_0 H_2CO, possibly closest to a set of well defined experimentally measured H_2CO frequencies. In Sect. 8.4 we present the newly obtained set of quartic force constants, and a selection of H_2CO and HDCO vibrational level energies, calculated with this new set of force constants and compared to the experimentally measured frequencies. Finally in Sect. 8.5 we conclude. Our code for computation of the obtained refined quartic PES is given in a supplement to this work.

8.2 Variational Vibrational Calculation Procedure for Formaldehyde

In our calculations we use the expression of Handy for the kinetic energy of formaldehyde [25], in terms of his curvilinear coordinates q_k (three bond stretches, two interbond angles and one dihedral "book" angle [22, 25]). For the PES of S_0 formaldehyde, we use a quartic expansion in terms of the shifts from equilibrium of the above internal curvilinear coordinates, exactly in the form, given by MLT [22]. This surface does not give spectroscopic accuracy, but it is quite realistic as a starting point of the fitting procedure and very well adapted to our vibrational method, allowing the calculations to access very high vibrational excitation energies (E_v).

Our 6D basis functions are products of 6 1D basis functions $\Psi_i = \prod \chi_{n_k}(q_k)$. The 1D basis functions are chosen to resemble most closely the lower excited molecular vibrational eigenfunctions so that the nondiagonal Hamiltonian matrix elements be as small as possible. For the three stretching coordinates of the C–H_1, C–H_2 and C–O bonds, we employ Morse oscillator eigenfunctions $\chi_{n_k}(q_k), k = 1, 2, 3$ $n_k = 0, 1, \ldots, n_{k0}$ that are optimally adapted to the relevant molecular motions, by setting appropriately the two parameter values of the Morse oscillators. For the out of plane bend, we employ harmonic oscillator eigenfunctions $\chi_{n_4}(q_4)$ [$q_4 = \varphi$—the out-of-plane bend ("book") angle]. Finally, for the two O–C–H(θ) bends (coordinates $q_5 = \cos\theta_1$, $q_6 = \cos\theta_2$), we use a set of normalized associated Legendre polynomials $P_n^2(\cos\theta)$, $n = 2, 3, \ldots$, that cancel the singularities in the KE operator. However since they have no free parameters to adjust and are not well adapted to the molecular vibrations, for them we apply a prediagonalization of the 1D basis (using a simple 1D Hamiltonian) in order to obtain suitable 1D basis functions as linear combinations of the original wavefunctions. This procedure was described in detail in our previous work [26].

Our specific search/selection procedure for constructing the Hamiltonian matrix H in a vibrational calculation, designed for selection of a characteristic and representative active space (AS) of basis vectors from a huge primitive space, involves the intermediate calculation of a great number of Hamiltonian matrix elements (that are employed to test whether a state should be selected or not), greatly exceeding the final number of elements in H. Therefore we need a very fast method for calculation of matrix elements that does not include numerical integrations. For this purpose, prior to each actual vibrational calculation, we compute a number of 2D arrays $P^{i,\alpha_i}_{m_i,n_i} = \langle \chi_{m_i}(q_i)|F^{\alpha_i}(q_i)|\chi_{n_i}(q_i)\rangle$, $m_i, n_i = 0, 1, 2, \ldots, n_{i0}$, corresponding to all vibrational coordinates q_i and each function or operator $F^{\alpha_i}(q_i)$, occurring in either KE or PES expressions, using either Gauss-Hermite, Gauss-Laguerre or Gauss-Legendre numerical integrations [30], where n_{i0} is the number of basis functions employed for the vibrational coordinate q_i. All computed $n_{i0} \times n_{i0}$ arrays are stored in computer core memory, ready to use in the subsequent matrix elements calculations. As a result of this and of the separable forms of the KE and PES, each matrix element is obtained as the sum of products of the appropriate values, thus reducing the actual calculation to a number of multiplications and summations and no integrations, which greatly accelerates the calculation of matrix elements.

Our search/selection procedure, serves to select an optimally small however representative active space of basis states, that are most relevant to the particular vibrational calculation. A search/selection procedure is started from a particular basis (feature) state $|0\rangle$, chosen to be the best zeroth-order representation of the vibrational levels to be calculated. The algorithm is symmetrically adapted to search and select only such basis states whose symmetry coincides with the symmetry species of the initial state $|0\rangle$. During the implementation of the search/selection algorithm, many basis states are probed and each state that satisfies the criteria for sufficient coupling strength is selected and consecutively added to the previously selected AS. There are three parameters, determining the scope and the quality of the search, C, f and R, whose values have to be fixed at the outset, that have been defined and discussed in our previous work [26]. According to the values chosen for the three parameters C, f and R, the search/selection procedure will select a varying number of basis states, i.e., include more and more weakly coupled basis states into the selected AS, which will result in enhanced accuracy and convergence in the calculation of the desired molecular vibrational levels. All selected basis states are stored in an array in computer core memory. Simultaneously the Hamiltonian matrix is being built, containing the diagonal and nondiagonal matrix elements of all selected basis states.

The Hamiltonian matrix H constructed in the course of the search/selection procedure, besides being optimal in size, is also quite sparse, because the algorithm employed automatically discards the matrix elements that are too small according to the criteria of the search. This makes our vibrational procedure both memory and time efficient. For the tridiagonalization of H we employ a conventional Lanczos iteration without reorthogonalization [31, 32], started again with the vector $|0\rangle$. We diagonalize the obtained tridiagonal Lanczos matrix using the routine *tqli()* from Numerical recipes [31], in slightly modified form.

8.3 Adjustment of the Original MLT PES to the Experimentally Measured Frequencies

Prior to presenting our adjustment procedure and the obtained refined quartic potential field for formaldehyde, we shall have to discuss the recently ab initio computed and refined field by Yachmenev et al. [24]. In fact, before starting our own work on the refinement of the MLT field, we wanted to use the refined field of the authors [24] for our large scale calculations on formaldehyde and its deuterated species [26–29]. For that purpose we have spent much effort to present in the required product form the analytic expression for the PES, supplied in the supplementary material to [24], in order to incorporate it into our vibrational code. Then we performed converged variational calculations on the vibrational frequencies of S_0 H_2CO, using both the set of ab initio parameters as well as the refined set from [24]. Our experience with the field [24] is briefly summarized below.

In Table 8.1 are presented the results from our calculations on the H_2CO vibrational frequencies of A_1 symmetry ($J = 0$), using both the ab initio and refined

Table 8.1 Calculated A_1 vibrational states (in cm^{-1}) in S_0 H_2CO, using both the ab initio and refined PES from Ref. [24] (columns 3 and 5 respectively), the corresponding calculated values by the authors [24] themselves (columns 4 and 6 respectively) and the experimentally measured frequencies [6] (column 2) with their assignments (column 1)

Assign.	Observed [6]	Ab initio		Refined	
		Our calc.	Ref. [24]	Our calc.	Ref. [24]
ν_3	1500.2	1499.03	1499.10	1495.64	1500.19
$\nu_?$	1746.1	1744.53	1744.61	1745.75	1746.03
$2\nu_4$	2327.5	2324.94	2325.18	2350.27	2327.54
$2\nu_6$	2495.1	2487.45	2487.73	2495.53	2494.34
ν_1	2782.2	2781.70	2781.74	2783.13	2782.46
$2\nu_3$	2998.1	2997.07	2997.24	2989.94	2998.94
$\nu_2 + \nu_3$	3239.0	3235.91	3236.11	3233.39	3238.36
$2\nu_2$	3471.6	3469.22	3469.39	3470.39	3471.23
$\nu_3 + 2\nu_4$	3825.3	3822.00	3822.43	3840.48	3825.94
$\nu_3 + 2\nu_6$	3937.4	3928.92	3929.86	3931.95	3936.02
$\nu_2 + 2\nu_4$	4058.3	4054.26	4054.60	4077.50	4058.53
$\nu_5 + \nu_6$	4083.1	4078.67	4078.88	4084.79	4083.21
$\nu_2 + 2\nu_6$	4248.7	4240.61	4241.02	4247.97	4247.13
$\nu_1 + \nu_3$	4253.8	4253.60	4253.86	4250.83	4254.58
$\nu_1 + \nu_2$	4529.4	4527.30	4527.54	4529.55	4529.82
$4\nu_4$	4629.0	4624.73	4625.12		4628.59
$\nu_2 + 2\nu_3$	4730.8	4725.71	4726.16	4722.72	4732.59
$2\nu_4 + 2\nu_6$	4842.0	4834.03	4834.67		4840.93
$2\nu_2 + \nu_3$	4955.2	4952.37	4952.81	4947.92	4954.65
$\nu_1 + 2\nu_4$	5092.4	5089.58	5089.97	5117.39	5092.32
$3\nu_2$	5177.6	5174.67	5175.01	5174.27	5177.82
$2\nu_3 + 2\nu_4$	5321.3	5316.83	5317.59	5311.29	5324.51
$4\nu_6$	5389.4	5381.17	5380.66	5380.77	5386.16
$2\nu_1$	5462.7	5460.30	5460.43	5463.49	5462.94
$\nu_2 + \nu_3 + 2\nu_4$	5546.5	5539.81	5540.40	5542.45	5545.43
$\nu_3 + \nu_5 + \nu_6$	5551.3	5548.26	5548.73	5554.23	5553.13
$2\nu_5$	5651.0	5649.87	5650.04	5648.79	5651.38
$\nu_2 + \nu_3 + 2\nu_6$	5687.9	5681.43	5681.97	5682.61	5688.20
$\nu_1 + 2\nu_3$	5729.2	5727.19	5727.84	5721.69	5729.86
$\nu_2 + \nu_5 + \nu_6$	5809.5	5803.66	5804.16	5807.79	5810.02
$2\nu_2 + 2\nu_6$	5986.2	5984.88	5985.47	5982.72	5984.48
$\nu_3 + 4\nu_4$	6123.6	6118.43	6119.14		6123.36
$\nu_1 + 2\nu_2$	6254.7	6251.95	6252.59	6249.15	6253.93
$\nu_3 + 2\nu_4 + 2\nu_6$	6263.1	6257.86	6258.82	6275.16	6262.05
$\nu_3 + 4\nu_6$	6373.4	6365.06	6357.54	6370.65	6372.06

Table 8.1 (Continued)

Assign.	Observed [6]	Ab initio		Refined	
		Our calc.	Ref. [24]	Our calc.	Ref. [24]
$2\nu_4 + \nu_5 + \nu_6$	6401.2	6394.49	6395.01	6414.91	6399.83
$\nu_1 + \nu_3 + 2\nu_4$	6562.7	6560.57	6561.59	6544.88	6565.39
$\nu_2 + 2\nu_4 + 2\nu_6$	6578.8	6570.28	6570.97	6572.47	6575.74
$3\nu_2 + \nu_3$	6652.2	6648.93	6649.83	6641.00	6653.34
$3\nu_3 + 2\nu_4$	6815.2	6808.70	6809.16	6791.27	6816.11
$\nu_1 + \nu_2 + 2\nu_4$	6825.5	6821.30	6821.88	6838.86	6823.88
$6\nu_4$	6909.0	6902.46	6903.18	6915.02	6910.15
$\nu_2 + 2\nu_3 + 2\nu_6$	7137.4	7127.24	7139.51	7135.45	7140.25

fields [24], that are compared to the results from the respective calculations by the authors themselves. Given are also the experimentally measured frequencies [6] and assignments. This Table essentially corresponds to Table III from Ref. [24], but we have changed most of the assignments in accord with Ref. [6] and excluded several states, that do not have the correct A_1 symmetry. From a comparison of columns 3 and 4 in Table 8.1 it is seen that the results of our calculations using the parameters, corresponding to the ab initio field, are close to those of the authors [24], but consistently somewhat lower, the difference starting from $\sim$0.1 cm^{-1} for the lowest levels and ranging up to $\sim$1 cm^{-1} or even more, for the highest excited levels in the Table. This slight mismatch between the two sets of calculated data might be attributed to the program suite TROVE [34], used by the authors [24] that involves a truncation of both the kinetic as well as the potential energy operators and a limitation $P_{max} = 14$ for the highest polyad number accessed in the calculation, which limits the active space to about 21000 basis states. On the other hand, our variational vibrational code is based on the exact expressions for both the kinetic and the potential energy operators and a search/selection procedure, that selects as many basis states (of almost unlimited high excitation) as needed for the calculation at hand, the AS dimensions ranging up to 50000 or much more, when necessary. As a result, our calculated results are converged to $\sim$0.01 cm^{-1}. Anyway, the overall results show, that the ab initio computed PES in [24] presents an improvement over the MLT quartic field [22].

Next, our calculations using the parameter set corresponding to the refined PES in [24] are displayed in column 5 of Table 8.1 and the calculated results of the authors [24] are given in the last column 6. It is obvious from a comparison of columns 5 and 6, that both sets of results are substantially different. Our calculated results are substantially different both from the calculated results by the authors [24] and from the experimentally measured frequencies in column 2, of Table 8.1, as well. In fact, according to our calculations, the so called refined field is not an improvement over the ab initio field but a deterioration. Similar is the situation with the other sets of calculated vibrational energy levels (of symmetries A_2, B_1 and B_2), displayed in Tables IV, V and VI of Ref. [24]. Our guess could be, that either there

might be some formal errors in the supplied electronic file for the set of refined parameters or that the authors [24] might have serious problems with their fitting code. Anyway, we were not able to confirm the spectroscopic quality of the refined field in Ref. [24] and we decided to carry out our own refinement of the MLT quartic field.

For the adjustment procedure, we employed the Marquardt's method for nonlinear parameter estimation through the "chi-square" minimization (chi-square is equal to the sum of squares of the differences between calculated and experimental values for all 29 frequencies, involved in the fitting process), essentially implemented in the routine *mrqmin( )* from [30]. We incorporated our vibrational calculation code into the least squares fitting routine *mrqmin( )* [30]. We fitted the calculated 29 frequencies to the corresponding experimentally measured values (indicated in Table 8.3 by an asterisk), all of them of the same symmetry type A_1, in order to be able to obtain all required frequencies in a single calculation. However most of these 29 vibrational energy levels represented combinations and overtones of all six molecular vibrational modes, which meant that all molecular modes of all symmetries were involved into the refinement process. We proceeded to carry out the fitting process by varying all 80 force constants sequentially, in groups of 10. We first started with harmonic force constants, next cubic and finally quartic force constants were varied. The whole sequence was repeated a second time. The three equilibrium parameters (two bond lengths and one interbond angle) were left unchanged, equal to the values used by MLT themselves [22]. In the vibrational calculations for the fitting routine, the state 1_1 (A_{1g} symmetrized combination of the one quantum excitation in the C–H stretching mode) was used as the initial state of the search $|0\rangle$. The convergence of the results obtained in this calculation was better than 0.01 cm^{-1} for the frequencies up to $\sim$6000 cm^{-1} and 0.1 cm^{-1} for the higher excited ones, as discussed in detail in our recent work [26, 27]. The final chi-square value achieved in the fitting process was 9.27 for the 29 frequencies employed.

8.4 Results and Discussion

The set of harmonic, cubic and quartic force constants, that were obtained as a result of our fitting process, are displayed in Table 8.2. In the Supplement to this work we have provided a C++ code, for calculation of the potential energy for arbitrary input values of the deviations of all six vibrational coordinates from equilibrium. In Table 8.2 are displayed the resulting vibrational energy levels of various symmetry types for S_0 H_2CO, up to $\sim$6000 cm^{-1}, that were obtained from a series of calculations with the final adjusted set of force constants (Table 8.2). The vibrational energy levels in Table 8.3, calculated using our newly determined set of force constants (Table 8.2), are compared with the experimentally measured values [6], as well as with the vibrational level energies calculated by the authors, for two earlier refined fields: Ref. [12] and Ref. [14]. As it is seen from Table 8.3, the agreement between the calculated and the experimentally measured frequencies as well as with the calculated results by the authors [12, 14], up to $\sim$6000 cm^{-1} is quite satisfactory (with very few exceptions). In addition we have also performed calculations

Table 8.2 A set of adjusted quartic force constants, determined in this work, using our vibrational code [equilibrium configuration: r(C–O) = 1.2096 Å, r(C–H) = 1.1033 Å, ∠(H–C–H) = 116.19 deg]

F11 = 3.0049422	F1113 = 0.0435328
F22 = 9.5205955	F1122 = −1.3352289
F33 = 0.83487867	F1123 = −1.1744012
F44 = 0.1305192	F1133 = −0.2543632
F55 = 2.9252182	F1144 = −.0422238
F66 = 0.4132887	F1155 = −.2210200
F12 = 1.0322378	F1156 = 0.31075900
F13 = −0.2385655	F1166 = −0.1931805
F23 = 0.7845680	F1222 = −0.3903829
F56 = 0.1283040	F1223 = −7.1392288
F111 = −0.3338075	F1233 = 3.32196713
F112 = 1.4975541	F1244 = 0.05576686
F113 = 1.0129728	F1255 = −10.5728899
F122 = −0.1992566	F1256 = −6.94089592
F123 = 0.8324351	F1266 = 1.671599806
F133 = −0.5153881	F1333 = 0.408204336
F144 = −0.08179475	F1344 = 0.053017191
F155 = −2.0146801	F1355 = 0.9230410
F156 = 0.675122	F1356 = 0.9919296
F166 = −0.1216545	F1366 = 0.5599576
F222 = −6.5754184	F2222 = −7.5345681
F223 = 0.21434682	F2223 = −1.5646255
F233 = −0.0618665	F2233 = −1.3061651
F244 = −0.3294825	F2244 = −0.2222958
F255 = 3.50491397	F2255 = −1.3966364
F256 = −0.8697603	F2256 = 20.0713766
F266 = −0.9656138	F2266 = −0.64347064
F333 = 0.3176335	F2333 = 0.23759968
F344 = 0.0881654	F2344 = 0.01078432
F355 = −1.1731703	F2355 = −7.4242240
F356 = 0.0434476	F2356 = −2.4665830
F366 = −0.3536357	F2366 = 0.87704112
F1111 = −0.8396216	F3333 = 0.18653205
F1112 = −0.9988350	F3344 = 0.06039921
F3355 = −1.5720053	F4466 = −0.0663805
F3356 = −2.4342667	F5555 = 0.3666690
F3366 = −0.0918158	F5556 = 3.2674870
F4444 = 0.01642359	F5566 = −0.3661640
F4455 = −0.2304280	F5666 = −0.3584239
F4456 = −0.0743773	F6666 = 0.04302172

Table 8.3 Calculated vibrational levels [in cm^{-1}] of S_0 formaldehyde, using the refined PES in this work (column 2). The 29 frequencies that were employed in the fitting process are indicated with an asterix (column 2). Results from calculations by the authors for two earlier refined fields: Ref. [12] (column 3) and Ref. [14] (column 4). The experimentally measured values are also given in the Table for comparison (column 5)

Assignment	Calculated this work	Calculated [12]	Calculated [14]	Experimental [6]
0_0	5777.90			
4_1	1167.26	1167.3	1167.3	1167.4
6_1	1249.89	1249.8	1248.9	1249.6
3_1	1500.40*	1499.6	1499.5	1500.2
2_1	1746.41*	1745.8	1746.1	1746.1
4_2	2327.50*	2327.5	2327.9	2327.1
$4_1 6_1$	2422.74	2421.3	2422.0	2422.4
6_2	2496.08*	2495.9	2495.0	2496.1
$3_1 4_1$	2666.80	2666.8	2666.1	2667.1
$3_1 6_1$	2719.47	2718.9	2718.0	2718.6
1_1	2782.58*	2782.2	2782.3	2782.5
5_1	2843.61	2842.6	2842.5	2843.0
$2_1 4_1$	2905.22	2905.7	2905.9	2906.0
3_2	2999.84*	2999.0	2998.2	2998.1
$2_1 6_1$	3001.12	3000.0	2999.9	3000.6
$2_1 3_1$	3238.87*	3238.0	3238.4	3239.0
2_2	3471.85*	3471.1	3472.4	3471.7
4_3	3480.40	3481.0	3482.3	3480.7
$4_2 6_1$	3585.60	3585.7	3585.6	3586.6
$4_1 6_2$	3676.26	3672.5	3675.9	3673.5
$3_1 4_2$	3824.83*	3825.3	3825.0	3825.3
$3_1 4_1 6_1$	3889.41	3886.3	3886.6	3886.5
$3_1 6_2$	3938.13*	3935.9	3935.2	3937.4
$1_1 4_1$	3941.99	3942.2	3942.0	3940.2
$4_1 5_1$	4002.45	3995.6	3996.0	3995.8
$2_1 4_2$	4057.53*	4057.8	4058.2	4058.3
$5_1 6_1$	4082.79*	4083.2	4083.0	4083.1
$2_1 4_1 6_1$	4164.99	4164.2	4163.6	4163.9
$2_1 6_2$	4247.07*	4250.0	4248.1	4248.7
$1_1 3_1$	4254.13*	4253.7	4255.2	4253.8
$2_1 3_1 4_1$	4396.10	4397.9	4397.3	4397.5
$2_1 3_1 6_1$	4467.04	4467.0	4466.2	4466.8
$1_1 2_1$	4528.77*	4527.5	4528.9	4529.4
$2_1 5_1$	4572.78	4572.2	4570.7	4571.5
$2_2 4_1$	4622.90	4624.3	4624.5	4624.3

Table 8.3 (Continued)

Assignment	Calculated this work	Calculated [12]	Calculated [14]	Experimental [6]
4_4	4629.29*	4628.2	4630.6	4629.0
$2_1 3_2$	4730.34*	4729.6	4729.5	4730.8
$2_2 6_1$	4736.46	4735.0	4734.3	4733.8
$4_3 6_1$	4740.83	4744.4	4741.6	4741.9
$4_2 6_2$	4841.77*	4840.4	4842.6	4842.0
$2_2 3_1$	4956.43*	4956.3	4957.1	4955.2
$3_1 4_3$	4975.70	4976.4	4977.2	4977.1
$3_1 4_2 6_1$	5046.88	5042.5	5042.4	5043.7
$1_1 4_2$	5092.73*	5094.2	5094.4	5092.4
$3_1 4_1 6_2$	5114.44	5105.8	5109.8	5104.0
$4_2 5_1$	5146.88	5140.9	5141.5	5140.1
$3_1 6_3$	5152.62	5151.7	5152.5	5151.0
2_3	5176.92*	5177.1	5179.5	5177.6
$2_1 4_3$	5205.11	5204.0	5204.9	5205.2
$4_1 5_1 6_1$	5250.29	5242.6	5246.5	5244.1
$5_1 6_2$	5314.45	5314.2	5312.9	5312.2
$3_2 4_2$	5319.69	5321.0	5320.6	5321.3
$2_1 4_2 6_1$	5324.80	5325.6	5325.3	5325.6
$3_2 4_1 6_1$	5360.10	5357.4	5357.6	5353.2
$3_2 6_2$	5388.56*	5386.2	5384.5	5389.4
$2_1 4_1 6_2$	5418.61	5417.4	5414.5	5417.6
$1_1 3_1 6_1$	5435.68	5432.4	5434.3	5433.4
1_2	5462.85*	5462.0	5467.1	5462.7
$3_1 4_1 5_1$	5498.14	5489.3	5489.1	5489.0
$1_1 5_1$	5543.66	5531.4	5533.7	5530.5
$2_1 3_1 4_2$	5544.81	5543.8	5544.5	5546.5
$3_1 5_1 6_1$	5551.46*	5553.6	5552.5	5551.3
$2_1 3_1 4_1 6_1$	5628.52	5625.8	5625.8	5625.5
5_2	5651.00*	5651.0	5651.7	5651.0
$1_1 2_1 4_1$	5678.90		5681.2	5680.0
$2_1 3_1 6_2$	5688.20*		5687.1	5687.9
$2_1 4_1 5_1$	5722.89		5718.1	5717.7
$1_1 3_2$	5727.87*		5730.1	5729.2
$2_2 4_2$	5769.00*		5769.2	5768.8
4_5	5771.35		5772.8	5771.0
$2_1 5_1 6_1$	5809.58*		5809.9	5809.5
$2_2 4_1 6_1$	5891.76		5888.2	5887.5
$4_4 6_1$	5889.12		5890.6	5891.8

Table 8.3 (Continued)

Assignment	Calculated this work	Calculated [12]	Calculated [14]	Experimental [6]
$2_2 6_2$	5986.74		5985.4	5986.2
$1_1 2_1 3_1$	5998.87		5997.8	5996.0
$2_1 3_1 5_1$	6057.55		6052.3	6051.7
$2_2 3_1 4_1$	6105.21		6108.1	6106.2
$3_1 4_4$	6119.98		6122.9	6123.6
$3_1 4_3 6_1$	6195.63		6189.3	6189.1
$2_2 3_1 6_1$	6198.55		6196.7	6194.8
$1_1 4_3$	6235.88		6239.9	6235.2
$1_1 2_2$	6252.96		6254.6	6254.7
$3_1 4_2 6_2$	6272.80		6264.8	6263.1
$2_2 5_1$	6276.04		6275.4	6276.4

on the much higher excited vibrational levels (up to $\sim$12500 cm^{-1} and higher) and compared them to the experimentally measured and calculated frequencies from Ref. [6], as well as with the results from calculations by Lee and Light [18], who used essentially the PES of Burleigh et al. [14], with a slight modification for the out-of-plane mode. Our calculated results were found to be reasonably close to the experimentally measured frequencies as well as to the calculated frequencies by Burleigh et al. [6, 14] and by Lee et al. [18].

In order to demonstrate that in spite of our using only vibrational levels of A_1 symmetry in the adjustment process, the levels of other symmetries were also well approximated, we have provided the Table 8.4, containing calculated vibrational levels using our refined PES, of A_2, B_1 and B_2 symmetries, up to $\sim$5000 cm^{-1}, compared to the experimentally measured frequencies [6]. It is readily seen from the table, that the agreement between the calculated and the experimentally measured values is quite satisfactory.

Lee and Light [18] calculated all vibrational levels of A_1 symmetry up to 13500 cm^{-1} in S_0 H_2CO and they found their exact number to be 729. In our present calculation with the newly obtained quartic PES (Table 8.1) we have counted 727 A_1 vibrational levels in this energy range. There is a remarkable agreement between the two calculations. This can be considered as evidence, that the two fields are of the same quality. In addition we have found 422 A_2 levels, 501 B_1 levels, and 615 B_2 levels in the same energy range (0–13500 cm^{-1}).

In order to find out whether our refined field retains the physically justified character of the ab initio computed fields, we have calculated cuts through all four types of vibrational curvilinear coordinates in formaldehyde (1-CH and 2-CO stretches, 3-HCO in plane bend and 4- out of plane bend of the two HCO planes), in each case holding all the remaining coordinates fixed at equilibrium. For the sake of comparison, we have also calculated the corresponding cuts for three other fields: the original MLT field [22] and the ab initio and refined fields by Yachmenev et al. [24]. These cuts for all four fields are displayed in Figs. 8.1, 8.2, 8.3, and 8.4, for the

Table 8.4 Calculated vibrational states in S_0 H_2CO, of other symmetries (A_2, B_1, B_2), using the refined PES in this work (column 2). The experimentally measured frequencies [6] are displayed in column 2, for comparison. Assignments and symmetries of the states are given in column 1

Assignment and symmetry	Calculated with the refined PES	Measured [6]
ν_4 (B_1)	1167.26	1167.4
ν_6 (B_2)	1249.89	1249.6
$\nu_4 + \nu_6$ (A_2)	2422.74	2422.4
$\nu_3 + \nu_4$ (B_1)	2666.80	2667.1
$\nu_3 + \nu_1$ (B_2)	2719.47	2718.6
ν_5 (B_2)	2843.61	2843.0
$\nu_2 + \nu_4$ (B_1)	2905.22	2906.0
$\nu_2 + \nu_6$ (B_2)	3001.12	3000.6
$3\nu_4$ (B_1)	3481.40	3480.7
$2\nu_4 + \nu_6$ (B_2)	3585.60	3586.6
$\nu_4 + 2\nu_6$ (B_1)	3676.26	3673.5
$\nu_3 + \nu_4 + \nu_6$ (A_2)	3889.41	3886.5
$\nu_1 + \nu_4$ (B_1)	3941.99	3940.2
$\nu_3 + \nu_4 + \nu_6$ (A_2)	4164.99	4163.9
$\nu_2 + \nu_3 + \nu_4$ (B_1)	4396.10	4397.5
$\nu_2 + \nu_3 + \nu_6$ (B_2)	4467.04	4466.8
$\nu_2 + \nu_5$ (B_2)	4572.78	4571.5
$2\nu_2 + \nu_4$ (B_1)	4622.90	4624.3
$2\nu_2 + \nu_6$ (B_2)	4736.46	4733.8
$2\nu_4 + \nu_6$ (A_2)	4740.83	4741.9
$\nu_3 + 3\nu_4$ (B_1)	4975.65	4977.1
$\nu_3 + 2\nu_4 + \nu_6$ (B_2)	5046.88	5043.7

above coordinates 1–4, respectively. As it is seen from the figures, all four fields show very similar behavior up to quite high excitation levels, with only the ab initio Yachmenev et al. field [24] showing marked deviation, for the CH stretch.

Using the obtained refined quartic PES in this work, we have also carried out a calculation on the vibrational frequencies in HDCO. It was our purpose to find how well does the PES, fitted to the vibrational frequencies of H_2CO, perform for the isotopomer HDCO. In Table 8.5 are displayed the results from our calculation of all A' (even number of ν_4 quanta) vibrational states in S_0 HDCO, in the range up to $E_v = 5000$ cm^{-1}. In this table, the results from the calculations with our newly obtained refined PES, are compared to the results from our recent calculations [29], using the original ab initio MLT PES [22], as well as to the set of experimentally measured frequencies in the recent work of Ellsworth et al. [33]. It can be seen from Table 8.5, that there is a marked improvement in the calculations with the refined PES over the results obtained with the original MLT field, as regards the comparison with experimental results [33]. However the improved frequencies are still too far

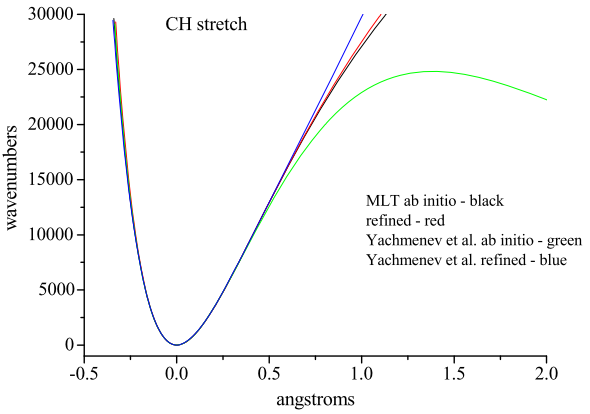

Fig. 8.1 Cut through the CH stretch mode for the four formaldehyde fields indicated in the figure, with all remaining coordinates fixed at equilibrium

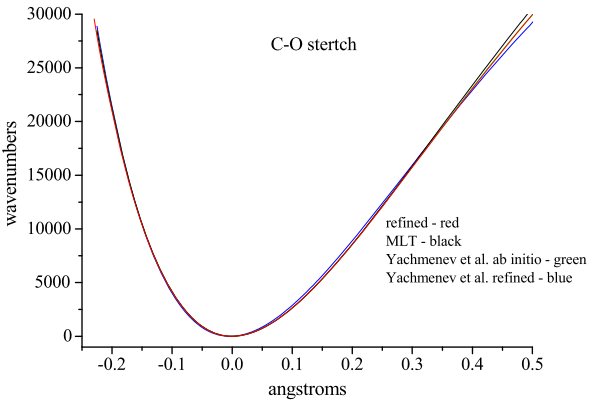

Fig. 8.2 Cut through the CO stretch mode for the four formaldehyde fields indicated in the figure, with all remaining coordinates fixed at equilibrium

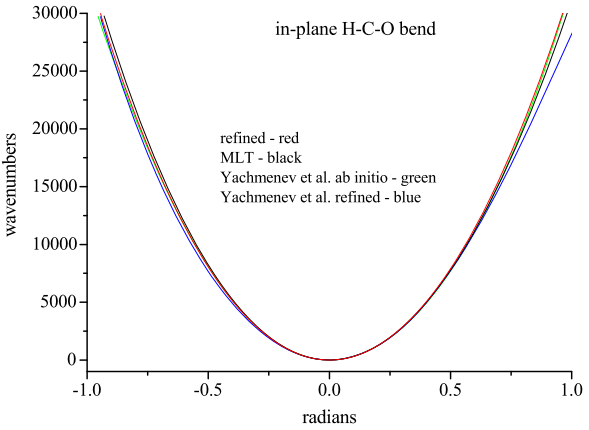

Fig. 8.3 Cut through the HCO in plane bend mode for the four formaldehyde fields indicated in the figure, with all remaining coordinates fixed at equilibrium

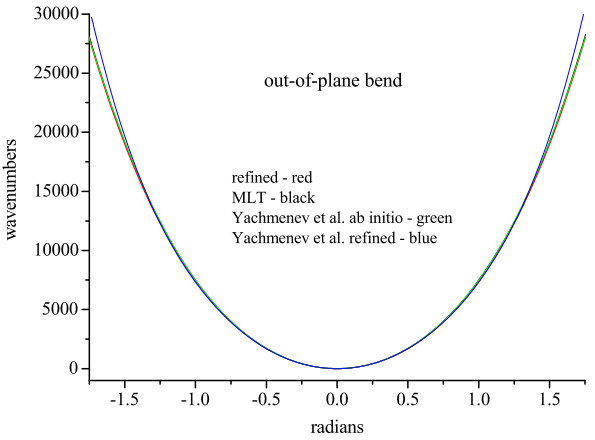

Fig. 8.4 Cut through the out-of-plane plane bend mode (book angle) for the four formaldehyde fields indicated in the figure, with all remaining coordinates fixed at equilibrium

from the experimental measurements. This means that in order to obtain an universal PES for formaldehyde, that would be valid for the other isotopomers besides H_2CO as well, a refinement should be carried out, including the experimentally measured frequencies of the other isotopomers as well.

8.5 Conclusions

In this work we have carried out a careful adjustment of all the 80 force constants (harmonic, cubic and quartic), comprising the quartic PES of MLT [22], defined as a quartic expansion in terms of the shifts from equilibrium of their internal curvilinear coordinates. Using Marquardt's method for nonlinear parameter estimation through the "chi-square" minimization, we have varied all the force constants sequentially in groups of ten, until we have obtained the best possible agreement of a particular set of our calculated frequencies (29), corresponding to well assigned vibrational energy levels, with the corresponding set of experimentally measured frequencies [6]. For the vibrational calculations we have employed our recently developed variational vibrational method, based on an iterative search/selection/diagonalization procedure to obtain the eigenvalues and some eigenvectors of the vibrational problem (using the exact kinetic energy expression [25]). The calculations, performed with the newly obtained refined quartic PES (Table 8.2, Supplement) have been shown to yield vibrational frequencies for H_2CO that are in reasonably good agreement with the experimentally measured frequencies, up to quite high vibrational excitation energies. However the calculation performed on the vibrational frequencies of the asymmetric formaldehyde isotopomer HDCO, using the refined PES did not show very good agreement with the experimentally measured frequencies [33]. This means, that an additional fitting procedure should be carried out, by including into the set of fitting frequencies some frequencies belonging to the isotopic species of formaldehyde.

Table 8.5 All calculated A′ (even number of ν_4 quanta) vibrational states in S_0 HDCO, in the range up to $E_v = 5000$ cm^{-1}, using the refined PES in this work (column 2). The frequencies calculated with the original MLT PES, taken from our recent work [29] are in column 1. Experimentally measured frequencies [33] are in column 3

Calculated with MLT PES [29]	Calculated with refined PES	Measured [33]
1032.2	1029.15	1027.1
1404.2	1397.49	
1725.8	1722.14	1724.0
2042.2	2035.28	2028.2
2100.6	2095.11	2104.4
2133.9	2138.31	2129.0
2435.7	2426.99	
2742.3	2730.19	2737.2
2767.6	2762.22	
2849.1	2845.61	2846.8
3045.6	3034.15	
3125.6	3112.53	
3143.2	3135.11	3125.1
3166.8	3168.35	3163.9
3431.9	3424.45	3428.5
3443.8	3433.59	
3503.0	3494.23	
3540.1	3535.40	3521.4
3751.1	3735.19	3745.9
3791.4	3781.44	
3819.0	3806.45	3813.6
3851.8	3849.87	3851.2
3880.3	3874.53	3869.5
4033.7	4021.54	
4103.1	4087.70	
4111.8	4101.15	4111.6
4145.8	4139.54	4144.4
4154.2	4143.38	4168.8
4195.0	4185.71	4192.1
4212.2	4215.58	
4259.7	4243.41	4258.5
4261.0	4277.37	
4443.0	4424.26	
4447.6	4434.16	4435.6
4488.9	4474.18	
4546.1	4535.87	

Table 8.5 (Continued)

Calculated with MLT PES [29]	Calculated with refined PES	Measured [33]
4569.4	4565.42	4564.5
4573.0	4566.70	
4747.8	4727.45	
4801.2	4790.32	
4827.5	4807.85	
4837.8	4820.04	4825.0
4864.6	4853.38	
4867.9	4861.47	4864.5
4887.3	4878.85	4883.0
4894.2	4893.81	
4946.1	4935.19	4945.2
4976.5	4975.58	

8.6 Supplement

C++ code for calculation of the refined (and the original MLT) potential field at arbitrarily chosen values for the 6 curvilinear vibrational coordinates: z1, z2—C–H stretches; z3—CO stretch; t1, t2—in plane bending angles; f—out of plane angle (stretches are in A, angles are in radians; the input values are deviations from equilibrium, which is obtained for zero values of all coordinates).

```
// PES.cpp : MLT PES of S0 H2CO in wavenumbers

#include "stdafx.h"
#include <iostream>
#include <cmath>
#include <cstdlib>
#include <fstream>
#include <iomanip>
#include <cstdio>
using namespace std;

/*
// MLT force ctes:
double F11=3.00134, F22=9.53546, F33=0.84581, F44=0.13237, F55=2.89965,
F66=0.41504, F12=1.00934, F13=-0.24764, F23=0.78790, F56=0.11165;
double F111=-0.35451, F112=0.89040, F113=0.08391, F122=-1.42689, F123=-0.36867,
F133=-0.41373, F144=-0.10521, F155=-1.33402, F156=0.26701, F166=-0.12874;
double F222=-6.81287, F223=-0.23282, F233=-0.81319, F244=-0.09166, F255=1.45247,
F256=-0.77602, F266=-0.78182, F333=0.19412, F344=0.11961;
double F355=-0.57006, F356=0.00180, F366=-0.29413;
```

```
double F1111=-0.70019, F1112=0.34900, F1113=0.30059, F1122=-0.53308,
F1123=-0.83581, F1133=-0.30456, F1144=-0.04892, F1155=-3.84204, F1156=0.19062,
F1166=-0.20060;
double F1222=-0.84544, F1223=0.91400, F1233=0.35388, F1244=0.06732,
F1255=2.36355, F1256=-1.18313, F1266=0.63147, F1333=-0.07450, F1344=-0.01473;
double F1355=-0.49110, F1356=-0.21855, F1366=0.12851;
double F2222=-5.16837, F2223=-0.85737, F2233=-0.06649, F2244=-0.21414,
F2255=-1.20379, F2256=1.01391, F2266=-0.29680, F2333=0.02937, F2344=0.00279;
double F2355=-0.08514, F2356=0.00854, F2366=0.66654, F3333=0.09006,
F3344=-0.05665, F3355=-1.09814, F3356=0.14720, F3366=-0.02848;
double F4444=0.01628, F4455=-0.20953, F4456=0.03736, F4466=-0.06331,
F5555=-0.51645, F5556=0.08444, F5566=-0.21524, F5666=0.03680, F6666=0.03321;
double r_CO=1.2096, r_CH=1.1033; //equilibrium bond lengths
*/
// Refined PES:
double F11=3.00494217108178, F22=9.52059546762136, F33=0.834878668759375,
F44=0.1305192, F55=2.92521820970712, F66=0.413288662007181,
F12=1.03223777792455;
double F13=-0.238565486726518, F23=0.784568001214077, F56=0.128304035672759,
F111=-0.333807527166278, F112=1.49755408987174, F113=1.01297276169864;
double F122=-0.199256642842184, F123=0.832435133553144,
F133=-0.515388146213856, F144=-0.0817947526301169, F155=-2.01468041534641,
F156=0.675122316448874, F166=-0.121654497183245;
double F222=-6.57541838669074, F223=0.214346818916391,
F233=-0.0618665114342241, F244=-0.329482480919666, F255=3.50491397221967,
F256=-0.869760304068994;
double F266=-0.965613840212784, F333=0.317633458279646,
F344=0.0881654357764115, F355=-1.17317028629488, F356=0.043447613736584,
F366=-0.353635660595592;
double F1111=-0.839621603756803, F1112=-0.998834983017552,
F1113=0.043532837827995, F1122=-1.33522886259013, F1123=-1.17440119152888,
F1133=-0.254363171447765;
double F1144=-0.0422237648905299, F1155=-2.22101995214809,
F1156=0.310758985970269, F1166=-0.193180509345745, F1222=-0.390382928902052,
F1223=-7.13922876943697;
double F1233=3.32196712897583, F1244=0.0557668588009518,
F1255=-10.5728898743163, F1256=-6.94089592039379, F1266=1.67159980627772,
F1333=0.408204336193871, F1344=0.0530171916146628;
double F1355=0.923041047680587, F1356=0.991929635564585,
F1366=0.559957611225298, F2222=-7.53456809141082, F2223=-1.56462546139935,
F2233=-1.30616512098343, F2244=-0.222295773473732;
double F2255=-1.39663644279243, F2256=20.0713765590419,
F2266=-0.643470636292006, F2333=0.237599682525006, F2344=0.0107843208366685,
F2355=-7.42422396175545, F2356=-2.46658300013839;
double F2366=0.877041118643844, F3333=0.186532054408352,
F3344=0.0603992076591577, F3355=-1.5720053307153, F3356=-2.43426672835613,
F3366=-0.0918157894206982, F4444=0.0164235874521334;
double F4455=-0.23042803656397, F4456=-0.0743772882717946,
F4466=-0.0663805139499858, F5555=0.366668964397229, F5556=3.26748699700024,
```

```
F5566=-0.366164046715441, F5666=-0.358423904173009, F6666=0.0430217192246419;
double r_CO=1.2096, r_CH=1.1033; //equilibrium bond lengths

double Fact2=50341.17, x1, x2, x3, mt=0;
double z1=0, z2=0, z3=0, t1=0, t2=0, f=0;// input values for the calculation
// z1,z2 - C–H stretches; z3 - CO stretch; t1,t2 - in plane bending angles; f - o.p. angle
(stretches are in A, angles are in radians)

void main()
x1=z1/(z1+r_CH); x2=z2/(z2+r_CH); x3=z3/(z3+r_CO);

// harmonic
mt+=.5*F11*(x1+x2)*(x1+x2);
mt+=.5*F55*(x1-x2)*(x1-x2);
mt+=F22*x3*x3;
mt+=F44*f*f;
mt+=F12/sqrt(2.)*(x1+x2)*x3;
mt+=0.5*(F33+F66)*(t1*t1+t2*t2) + (F33-F66)*t1*t2;
mt+=F13/2.*(x1+x2)*(t1+t2);
mt+=F23/sqrt(2.)*x3*(t1+t2);
mt+=F56/2.*(x1-x2)*(t1-t2);

// cubic
mt+=F111/2./sqrt(2.)*(x1+x2)*(x1+x2)*(x1+x2);
mt+=F155/2./sqrt(2.)*(x1*x1-x2*x2)*(x1-x2);
mt+=F222*x3*x3*x3;
mt+=F112/2.*x3*(x1+x2)*(x1+x2);
mt+=F255/2.*x3*(x1-x2)*(x1-x2);
mt+=F122/sqrt(2.)*x3*x3*(x1+x2);
mt+=F144/sqrt(2.)*(x1+x2)*f*f;
mt+=F244*x3*f*f;
mt+=F113/2./sqrt(2.)*(x1+x2)*(x1+x2)*(t1+t2);
mt+=F355/2./sqrt(2.)*(x1-x2)*(x1-x2)*(t1+t2);
mt+=F133/2./sqrt(2.)*(x1+x2)*(t1+t2)*(t1+t2);
mt+=F156/2./sqrt(2.)*(x1*x1 - x2*x2)*(t1-t2);
mt+=F166/2./sqrt(2.)*(x1+x2)*(t1-t2)*(t1-t2);
mt+=F356/2./sqrt(2.)*(x1-x2)*(t1*t1 - t2*t2);
mt+=F223/sqrt(2.)*x3*x3*(t1+t2);
mt+=F233/2.*x3*(t1+t2)*(t1+t2);
mt+=F266/2.*x3*(t1-t2)*(t1-t2);
mt+=F123/2.*x3*(x1+x2)*(t1+t2);
mt+=F256/2.*x3*(x1-x2)*(t1-t2);
mt+=F344/sqrt(2.)*(t1+t2)*f*f;
mt+=F333/2./sqrt(2.)*(t1+t2)*(t1+t2)*(t1+t2);
mt+=F366/2./sqrt(2.)*(t1*t1 - t2*t2)*(t1-t2);

// quartic
mt+=F1111/4.*(x1+x2)*(x1+x2)*(x1+x2)*(x1+x2);
mt+=F5555/4.*(x1-x2)*(x1-x2)*(x1-x2)*(x1-x2);
mt+=F1155/4.*(x1*x1*x1*x1 - 2.*x1*x1*x2*x2 + x2*x2*x2*x2);
mt+=F1112/2./sqrt(2.)*x3*(x1+x2)*(x1+x2)*(x1+x2);
```

```
mt+=F1122/2.*x3*x3*(x1+x2)*(x1+x2);
mt+=F2255/2.*x3*x3*(x1-x2)*(x1-x2);
mt+=F1222/sqrt(2.)*x3*x3*x3*(x1+x2);
mt+=F1255/2./sqrt(2.)*x3*(x1*x1-x2*x2)*(x1-x2);
mt+=F1244/sqrt(2.)*x3*(x1+x2)*f*f;
mt+=F1144/2.*(x1+x2)*(x1+x2)*f*f;
mt+=F4444*f*f*f*f;
mt+=F2222*x3*x3*x3*x3;
mt+=F2244*x3*x3*f*f;
mt+=F4455/2.*(x1-x2)*(x1-x2)*f*f;
mt+=F1123/2./sqrt(2.)*x3*(x1+x2)*(x1+x2)*(t1+t2);
mt+=F2355/2./sqrt(2.)*x3*(x1-x2)*(x1-x2)*(t1+t2);
mt+=F1223/2.*x3*x3*(x1+x2)*(t1 + t2);
mt+=F1233/2./sqrt(2.)*x3*(x1+x2)*(t1+t2)*(t1+t2);
mt+=F1256/2./sqrt(2.)*x3*(x1*x1 - x2*x2)*(t1-t2);
mt+=F1266/2./sqrt(2.)*x3*(x1+x2)*(t1-t2)*(t1-t2);
mt+=F2256/2.*x3*x3*(x1-x2)*(t1-t2);
mt+=F2356/2./sqrt(2.)*x3*(x1-x2)*(t1*t1 - t2*t2);

mt+=F1113/4.*(x1+x2)*(x1+x2)*(x1+x2)*(t1+t2);
mt+=F1355/4.*(x1*x1-x2*x2)*(x1-x2)*(t1+t2);
mt+=F1133/4.*(x1+x2)*(x1+x2)*(t1+t2)*(t1+t2);
mt+=F3355/4.*(x1-x2)*(x1-x2)*(t1+t2)*(t1+t2);
mt+=F1156/4.*(x1+x2)*(x1+x2)*(x1-x2)*(t1-t2);
mt+=F5556/4.*(x1-x2)*(x1-x2)*(x1-x2)*(t1-t2);
mt+=F1166/4.*(x1+x2)*(x1+x2)*(t1-t2)*(t1-t2);
mt+=F5566/4.*(x1-x2)*(x1-x2)*(t1-t2)*(t1-t2);
mt+=F1356/4.*(x1*x1 - x2*x2)*(t1*t1 - t2*t2);
mt+=F1366/4.*(x1+x2)*(t1*t1-t2*t2)*(t1-t2);
mt+=F1333/4.*(x1+x2)*(t1+t2)*(t1+t2)*(t1+t2);
mt+=F3356/4.*(x1-x2)*(t1*t1-t2*t2)*(t1-t2);
mt+=F5666/4.*(x1-x2)*(t1-t2)*(t1-t2)*(t1-t2);
mt+=F1344/2.*(x1+x2)*(t1+t2)*f*f;
mt+=F2223/sqrt(2.)*x3*x3*x3*(t1+t2);
mt+=F2233/2.*x3*x3*(t1+t2)*(t1+t2);
mt+=F2266/2.*x3*x3*(t1-t2)*(t1-t2);
mt+=F2333/2./sqrt(2.)*x3*(t1+t2)*(t1+t2)*(t1+t2);
mt+=F2366/2./sqrt(2.)*x3*(t1*t1-t2*t2)*(t1-t2);
mt+=F2344/sqrt(2.)*x3*(t1+t2)*f*f;
mt+=F3333/4.*(t1+t2)*(t1+t2)*(t1+t2)*(t1+t2);
mt+=F3366/4.*(t1*t1-t2*t2)*(t1*t1-t2*t2);
mt+=F6666/4.*(t1-t2)*(t1-t2)*(t1-t2)*(t1-t2);
mt+=F3344/2.*(t1+t2)*(t1+t2)*f*f;
mt+=F4456/2.*(x1-x2)*(t1-t2)*f*f;
mt+=F4466/2.*(t1-t2)*(t1-t2)*f*f;

mt*=Fact2;
cout<<"\nPotential energy="<<mt<<"\n";

return;
```

Acknowledgements This research was supported by the National Research and Engineering Council of Canada.

References

1. Moule DC, Walsh AD (1975) Chem Rev 75:67
2. Clouthier DJ, Ramsay DA (1983) Annu Rev Phys Chem 34:31
3. Hardwick JL, Till SM (1979) J Chem Phys 70:2340
4. Brown LR, Hunt RH, Pine AS (1979) J Mol Spectrosc 75:406
5. Reisner DE, Field RW, Kinsey JL, Dai HL (1984) J Chem Phys 80:5968
6. Bouwens RJ, Hammerschmidt JA, Grzeskowiak MM, Stegink TA, Yorba PM, Polik WF (1996) J Chem Phys 104:460
7. Romanowski H, Bowman JM, Harding LB (1985) J Chem Phys 82:4156
8. Aoyagi M, Gray SK, Davis MJ (1990) J Opt Soc Am B 7:1859
9. Aoyagi M, Gray SK (1991) J Chem Phys 94:195
10. Bramley MJ, Carrington T (1993) J Chem Phys 99:8519
11. Carter S, Pinnavaia N, Handy NC (1995) Chem Phys Lett 240:400
12. Carter S, Handy NC (1996) J Mol Spectrosc 179:65
13. Poulin NM, Bramley MJ, Carrington T Jr, Kjaergaard HG, Henry R (1996) J Chem Phys 104:7807
14. Burleigh DC, McCoy AB, Sibert EL III (1996) J Chem Phys 104:480
15. Luckhaus D (2000) J Chem Phys 113:1329
16. Ribeiro F, Iung C, Leforestier C (2002) Chem Phys Lett 362:199
17. Bernal R, Lemus R (2006) J Mol Spectrosc 235:218
18. Lee H-S, Light JC (2004) J Chem Phys 120:4626
19. Mladenovic M (2002) Spectrochim Acta A 58:809
20. Harding LB, Ermler WC (1985) J Comput Chem 6:13
21. Clabo DA Jr, Allen WD, Remington RB, Yamaguchi Y, Schaeffer HF III (1988) Chem Phys 123:187
22. Martin JML, Lee TJ, Taylor PR (1993) J Mol Spectrosc 160:105
23. Yagi K, Oyanagi C, Taketsugu T, Hirao K (2003) J Chem Phys 118:1653
24. Yachmenev A, Yurchenko SN, Jensen P, Thiel W (2011) J Chem Phys 134:244307
25. Handy NC (1987) Mol Phys 61:207
26. Rashev S, Moule DC (2012) Spectrochim Acta A, Mol Biomol Spectrosc 87:286–292
27. Rashev S, Moule DC, Rashev V (2012) Spectrochim Acta A, Mol Biomol Spectrosc 97:111–118
28. Rashev S, Moule DC (2013) Cent Eur J Chem 11(1):1–7
29. Rashev S, Moule DC, J Molec Spectrosc, submitted
30. Press WH, Flannery BP, Teukolsky SA, Vetterling WT (1988) Numerical recipes in C. Cambridge University Press, Cambridge
31. Wyatt RE (1989) Adv Chem Phys 73:231
32. Cullum JK, Willowghby RA (1985) Lanczos algorithms for large symmetric eigenvalue computations, vols I, II. Birkhauser, Boston
33. Ellsworth KK, Lajiness BD, Lajiness JP, Polik WP (2008) J Mol Spectrosc 252:205
34. Yurchenko SN, Thiel W, Jensen P (2007) J Mol Spectrosc 245:126

Chapter 9
Operator Perturbation Theory for Atomic Systems in a Strong DC Electric Field

Alexander V. Glushkov

Abstract A consistent uniform quantum approach to the solution of the non-stationary state problems including the DC (Direct Current) strong-field Stark effect and also scattering problem is presented. It is based on the operator form of the perturbation theory for the Schrödinger equation. The method includes the physically reasonable distorted-waves approximation in the frame of the formally exact quantum-mechanical procedure. The zero-order Hamiltonian possessing only stationary states is determined only by its spectrum without specifying its explicit form. The method allows calculating the resonance complex energies and widths plus a complete orthogonal complementary of the scattering state functions. The calculation results of the Stark resonance energies and widths for the hydrogen and sodium atoms are presented and compared with other theoretical data.

9.1 Introduction

The Stark effect [1] is one of the best known problems in quantum mechanics, but at the same time one of the most difficult (outside the weak-field region) [1–8]. A new interest in this effect has been stimulated in the last two decades. A range of the interesting phenomena to be studied includes: quasi-discrete state mixing; a zoo of Landau-Zener anticrossings in non-hydrogenic (non-H) atoms; autoionization in non-H atoms; the effects of potential barriers (shape resonances); new kinds of resonances above threshold etc. [1–63]. The dielectronic recombination involves highly excited (Rydberg) atomic states, which are very strongly affected by relatively weak fields [3–6]. In fact these states provide the gateway for ion-electron recombination processes. Now it is well known that weak-field effects on Rydberg states can cause the large changes in electron-ion collision cross sections. One subject stands out quite clearly: possible non-perturbative effects of the electric fields on the autoionization states responsible for dielectronic recombination. It is of a great importance for a consistent treating the different processes in a laser plasma, astrophysical en-

A.V. Glushkov (✉)
Odessa State University—OSENU, L'vovskaya str., 15, Odessa-9, 65016, Ukraine
e-mail: glushkovav@gmail.com

M. Hotokka et al. (eds.), *Advances in Quantum Methods and Applications in Chemistry, Physics, and Biology*, Progress in Theoretical Chemistry and Physics 27,
DOI 10.1007/978-3-319-01529-3_9,

vironments etc. [4–14]. Naturally in the last two decades a great progress has been made on the Stark effect for the hydrogen atom as well as for non-H atoms [2–62].

An external electric field shifts and broadens the bound state atomic levels. The standard quantum -mechanical approach relates complex eigenenergies (EE) $E = E_r + i\Gamma/2$ and complex eigenfunctions (EF) to the shape resonances. The field effects drastically increase upon going from one excited level to another. The highest levels overlap forming a "new continuum" with lowered boundary. The calculation difficulties inherent to the standard quantum mechanical approach are well known. Here one should mention the well-known Dyson phenomenon. The Wentzel-Kramers-Brillouin (WKB) approximation overcomes these difficulties for the states lying far from the "new continuum" boundary. Some modifications of the WKB method [4, 6–8, 50, 56, 63–66] are introduced in [4, 50, 66] and Glushkov, Ivanov and Letokhov, where the first theoretical estimation of the effectiveness of the selective ionization of the Rydberg atom using electric and laser fields has been fulfilled. The usual WKB approximation applicability is substantiated in the case of a relatively weak electric field [2, 3]. One can show that the standard form of the WKB method applicability condition can be reformulated as the requirement that the examined resonances be well separated one from other. The same is so regarding the widespread asymptotic phase method [42], based on the Breit-Wigner parameterization for the asymptotic phase shift dependence on scattering energy and the method by Luc-Koenig and Bachelier, who have used a normalization constant [42, 48]. Different calculational procedures are used in the Pade and then Borel summation of the divergent Rayleigh-Schrödinger perturbation theory (PT) series [45, 66] and in the sufficiently exact numerical solution of the difference equations following from expansion of the wave function over finite basis [41, 46, 48, 51, 52], complex-scaling method [17–55]. It should be noted that the latter has been extensively used to describe the resonance behavior in different atomic and even molecular systems. Its mathematical foundation is linked with the theory of dilatation analyticity [27, 28]. Surely, though the Hamiltonian of an atom in a DC electric field is not a dilatational analytic operator, Reinhardt [44] has performed the numerical experiments on the diagonalization of the complex-scaled Stark Hamiltonian for a hydrogen with a real L basis set. The same method has been used by Cerjan et al. [40] to get new data on the ground and low-excited states of a hydrogen atom in a DC and AC fields. Farrelly and Reinhardt [47] have used the complex coordinate rotation method in combination with numerical integration of the separated equation. Ivanov and Ho [54] have applied the method for the Dirac Hamiltonian. Different applications are reviewed in Ref. [53].

Hehenberger, McIntosh and E. Brändas [21] have applied the Weyl's theory to the Stark effect in the hydrogen atom. They have shown that one of the interesting features of Weyl's theory is that it requires a complex parameter and complex solutions to the differential equations making it a powerful tool for the treatment of resonance states [21]. Rittby, Elander and Brändas [25] have applied the Weyl's theory and the complex-rotation method to phenomena associated with a continuum spectrum. Brändas and Froelich [23] have shown that a complex scale transformation of the time-dependent Schrödinger equation leads to a symmetric EE value

problem containing both bound states and resonance (complex) EE values as solutions. They have stated the extended virial theorem and developed an original approach to determination of the resonance eigenvalues by means of elementary matrix manipulations. The error estimates for the approximate complex eigenvalues of the dilated Schrödinger operator are derived in Ref. [24], where the calculation data for the resonances of the DC Stark effect in the hydrogen are presented. In the complex-coordinate method a dilation transformation is used to make the resonance EF square integrable. The resonance of nondilation analytic potentials can be obtained numerically by using Simons exterior-scaling procedures within the finite-basis-set approximation [27, 28]. The exterior-scaling procedure has been used only with direct numerical integration methods [27–30]. The use of a finite basis set in these calculations will enable one to use numerical techniques developed for bound states in calculating resonance positions and widths for nondilation potentials [27–36].

Rao, Liu and Li [18] have studied theoretically the DC strong-field Stark resonances by a complex-scaling plus B-spline approach and shown that the high accuracy is attributed to the good stationarity behavior of eight trajectories with a well-adjusted 8-spline basis. Rao and Li [19] have also studied the behavior of the resonances of a hydrogen atom in parallel magnetic and electric fields with a complex scaling plus B-spline method too and received a consistent data on the corresponding resonance parameters in dependence upon the ratio of the magnetic-field strength to the electric-field strength. It is worth to remind that the similar approaches have been developed to describe the Zeemane resonances. Namely, for hydrogen atoms in pure magnetic fields, the properties of resonant states were calculated by the complex scaling, the R matrix, the operator PT (OPT) and other methods (look, for example, [4–7]. The generalization of methods to account for the resonance interference, non-H and relativistic effects is still an important problem, though here a definite progress has been reached too. One should mention such approaches as a model potential method, quantum defect approximation, the OPT, complex scaling plus B-spline method etc. [3–19, 64–76]. Regarding the quantum chaos phenomenon in atoms in electromagnetic fields (look, for example, [77–80]) note that this topic should not be considered here. Let us only note that the approach presented below together with the various methods of the theory of chaos in options [80–82] has been effectively used to describe the chaotic behavior of the hydrogen and non-H atoms in the magnetic and microwave fields.

Here a consistent uniform quantum-mechanical approach to the solution of the non-stationary state problems including the DC strong-field Stark effect and also scattering problem is presented. It allows calculation of complex EE and especially is destined for investigation of the spectral region near the new continuum boundary. The essence of the method is the inclusion of the well known "distorted waves approximation" method in the frame of the formally exact PT. The zero-order Hamiltonian H_0 of this PT possesses only stationary bound and scattering states. To overcome formal difficulties, we define the zero-order Hamiltonian by the set of orthogonal eigenfunctions (EF) and EE without specifying the explicit form of the corresponding zeroth-order potential. To ensure rapid PT convergence, a physically reasonable spectrum (EE and EF) must be chosen as the zero order, similar

to the "distorted waves" method [6, 56–58]. In a case of the optimal zeroth-order spectrum, the PT smallness parameter is of the order of Γ/E, where Γ and E are the field width and bound energy of the state level examined. The successive PT corrections can be expressed through the matrix elements of the total Hamiltonian calculated between the zeroth-order basis functions. This method is called the OPT. We will define H_0 so that it coincides with the total Hamiltonian H at $\varepsilon \Rightarrow 0$ (ε is the electric field strength). Let us emphasize that perturbation in our theory does not coincide with the electric field potential though they disappear simultaneously. We also present a generalization of the OPT for calculation of the DC strong field Stark effect in the non-H atoms in an electric field [59–61]. The difference between the atomic and Coulomb field is taken into account by introducing the quantum defects on a parabolic basis. The results of calculation of the Stark resonance energies and widths for the H and sodium atoms are listed and compared with other theoretical and experimental data.

9.2 Operator Perturbation Theory for DC Strong-Field Stark Effect

9.2.1 DC Strong-Field Stark Effect for the Hydrogen Atom

The Schrödinger equation for the electron function taking into account the uniform electric field and field of the nucleus (Coulomb units are used: for length, 1 unit is h^2/Ze^2m; for energy 1 unit is mZ^2e^4/h^2) is [6, 57]:

$$\left[-(1-N/Z)/r + V_m(r) + \varepsilon z - 1/2\Delta - E\right]\psi = 0, \tag{9.1}$$

where E is the electron energy, Z is the nucleus charge, N is the number of electrons in the atomic core (for the hydrogen atom: $Z = 1$, $N = 0$), V_m is an model potential (for the hydrogen atom $V_m = 0$). Firstly, we only deal with the Coulomb part of the electron- atomic residue interaction. The non-Coulomb part, as well as relativistic effects, can be approximately accounted for next step. The separation of variables in the parabolic coordinates ($\xi = r + z$, $\eta = r - z$, $\varphi = \tan^{-1}(y/x)$):

$$\psi(\zeta, \eta, \varphi) = f(\zeta)g(\eta)(\zeta \cdot \eta)^{|m|/2}\exp(\mathrm{im}\,\varphi)/(2\pi)^{1/2} \tag{9.2}$$

transforms it to the system of two equations for the functions f, g:

$$f'' + \frac{|m|+1}{t}f' + \left[1/2E + (\beta_1 - N/Z)/t - 1/4\varepsilon(t)t\right]f = 0, \tag{9.3}$$

$$g'' + \frac{|m|+1}{t}g' + \left[1/2E + \beta_2/t + 1/4\varepsilon(t)t\right]g = 0, \tag{9.4}$$

coupled through the constraint on the separation constants:

$$\beta_1 + \beta_2 = 1. \tag{9.5}$$

For the uniform electric field $\varepsilon(t) = \varepsilon$. In principle, the more realistic models can be considered in the framework of our approach. Potential energy in (9.4) has the barrier. Two turning points for the classical motion along the η axis, t_1 and t_2, at a given energy E are the solutions of the quadratic equation ($\beta = \beta_1$, $E = E_0$):

$$t_2 = \left\{\left[E_0^2 - 4\varepsilon(1-\beta)\right]^{1/2} - E_0\right\}/\varepsilon, \tag{9.6}$$

$$t_1 = \left\{-\left[E_0^2 - 4\varepsilon(1-\beta)\right]^{1/2} - E_0\right\}/\varepsilon, \quad t_1 < t_2. \tag{9.7}$$

Here and below t denotes the argument common for the whole equation system. To simplify the calculational procedure, the uniform electric field ε in (9.3) and (9.4) should be substituted by the function [57, 58]:

$$\varepsilon\,(t) = \frac{1}{t}\varepsilon\left[(t-\tau)\frac{\tau^4}{\tau^4 + t^4} + \tau\right] \tag{9.8}$$

with sufficiently large τ ($\tau = 1.5t_2$). The function $\varepsilon(t)$ practically coincides with the constant ε in the inner barrier motion region ($t < t_2$) and disappears at $t \gg t_2$. The minimal acceptable value of τ introduced in the spatial dependence of the electric field, which does not influence the final results, can be established experimentally. Thus, the final results do not depend on the parameter τ (the further calculation has entirely confirmed this fact). Besides the pure technical convenience, the case of an asymptotically disappearing electric field is more realistic from the physical point of view. Now we deal with the asymptotically free (without electric field) motion of the ejected electron along the η-axis. The corresponding effective wavenumber is:

$$k = (E/2 + \varepsilon\tau/4)^{1/2}. \tag{9.9}$$

The scattering states energy spectrum now spreads over the range $(-\varepsilon\tau/2, +\infty)$, compared with $(-\infty, +\infty)$ in the uniform field. In contrast to the case of a free atom in scattering states in the presence of the uniform electric field remain quantified at any energy E, i.e. only definite values of β_1 are possible. The latter are determined by the confinement condition for the motion along the η-axis. The same is true in our case, but only for $E \subset (-\frac{1}{2}\varepsilon\tau, +\frac{1}{2}\varepsilon\tau)$. The motion with larger E is non-quantified, similar to the free atom case.

9.2.2 Energy and Width of the Stark Resonance

The total Hamiltonian $H(\varsigma, \nu, \varphi)$ does not possess the bound stationary states. According to OPT [6, 56–58]), one has to define the zero order Hamiltonian H_0, so that its spectrum reproduces qualitatively that of the initial one. In contrast to H, it must have only stationary states. To calculate the width Γ of the concrete quasistationary state in the lowest PT order one needs only two zeroth-order EF of H_0: bound state function $\Psi_{Eb}(\varepsilon, \eta, \varphi)$ and scattering state function $\Psi_{Es}(\varepsilon, \eta, \varphi)$ with the

same EE. We solve a more general problem: a construction of the bound state function along with its complete orthogonal complementary of scattering functions Ψ_E with $E \subset (-\frac{1}{2}\varepsilon\tau, +\infty)$. First, one has to define the EE of the expected bound state. It is the well known problem of states quantification in the case of the penetrable barrier [65, 66]. Following [57], we solve the system (9.3) and (9.4) with the total Hamiltonian H under the conditions:

$$f(t) \to 0 \quad \text{at } t \Rightarrow \infty, \tag{9.10a}$$

$$\partial x(\beta, E)/\partial E = 0 \tag{9.10b}$$

with

$$x(\beta, E) = \lim_{t \Rightarrow \infty} \left[g^2(t) + \left\{ g'(t)/k \right\}^2 \right] t^{|m|+1}. \tag{9.11}$$

The first condition ensures the finiteness of motion along the ς-axis, the second condition minimizes the asymptotic oscillation amplitude for the function describing the motion along the η-axis. These two conditions quantify the bound energy E and separation constant β_1. We elaborated a special numerical procedure for this two-dimensional eigenvalue problem. Our procedure deals repeatedly with the solving of the system of the ordinary differential equations (9.3) and (9.4) with probe pairs of E, β_1. The corresponding EF:

$$\psi_{Eb}(\zeta, \eta, \varphi) = f_{Eb}(\zeta) g_{Eb}(\eta) (\zeta\eta)^{|m|/2} \exp(\mathrm{i}m\varphi)(2\pi)^{-1/2}. \tag{9.12}$$

Here $f_{Eb}(t)$ is the solution of (9.3) (with the just determined E, β_1) at $t \subset (0, \infty)$ and $g_{Eb}(t)$ is the solution of (9.4) (with the same E, β_1) at $t < t_2$ (inside barrier) and $g(t) = 0$ otherwise. These bound state EE, eigenvalue β_1 and EF for the zero-order Hamiltonian H_0 coincide with those for the total Hamiltonian H at $\varepsilon \Rightarrow 0$, where all the states can be classified due to the quantum numbers n, n_1, n_2, m (principal, parabolic, azimuthal) connected with E, β_1, m by the well known expressions. We preserve the n, n_1, m states classification in the non-zero ε case. The scattering state functions:

$$\psi_{E's}(\zeta, \eta, \varphi) = f_{E's}(\zeta) g_{E''s}(\eta) (\zeta\eta)^{|m|/2} \exp(\mathrm{i}m\varphi)(2\pi)^{-1/2} \tag{9.13}$$

must be orthogonal to the above defined bound state function and to each other. In addition, these functions must describe the motion of the ejected electron, i.e. $g_{E's}$ must satisfy (9.4) asymptotically. Following the OPT ideology [57], we choose the next form of $g_{E's}$:

$$g_{E's}(t) = g_1(t) - z_2' g_2(t) \tag{9.14}$$

with $f_{E's}$ and $g_1(t)$ satisfying the differential equations (9.3) and (9.4). The function $g_2(t)$ satisfies the non-homogeneous differential equation, which differs from (9.4) only by the right-hand term, disappearing at $t \Rightarrow \infty$. The total equation system,

determining the scattering function, reads

$$f''_{E's} + \frac{|m|+1}{t} f'_{E's} + \left[1/2E' + \left(\beta'_1 - N/Z\right)/t - 1/4\varepsilon(t)t\right] f_{E's} = 0,$$
$$g''_1 + \frac{|m|+1}{t} g'_1 + \left[1/2E' + \beta'_2/t + 1/4\varepsilon(t)t\right] g_1 = 0, \qquad (9.15)$$
$$g''_2 + \frac{|m|+1}{t} g'_2 + \left[1/2E + \beta'_2/t + 1/4\varepsilon(t)t\right] g_2 = 2g_{Eb},$$

($\beta'_1 + \beta'_2 = 1$). As mentioned above there remains motion quantification for $E' \subset (-\frac{1}{2}\varepsilon\tau, +\frac{1}{2}\varepsilon\tau)$. At the given E', the only quantum parameter β'_1 is determined by the natural boundary condition: $f_{E's} \Rightarrow 0$ at $t \Rightarrow \infty$. Of course: $\beta'_1 = \beta_1$, $f_{E's} = f_{Eb}$ at $E' = E$; only this case is needed in the particular problem we deal with here. The coefficient z'_2 ensures the orthogonality condition $\langle \Psi_{Eb} | \Psi_{E's} \rangle = 0$:

$$z'_2 = \left\{ \iint d\zeta d\eta (\zeta + \eta) f^2_{Eb}(\zeta) g_{Eb}(\eta) g_1(\eta) \right\}$$
$$\Big/ \left\{ \iint d\zeta d\eta (\zeta + \eta) f^2_{Eb}(\zeta) g_{Eb}(\eta) g_2(\eta) \right\}. \qquad (9.16)$$

One can check that

$$\langle \psi_{Es'} | \psi_{E''s} \rangle = 0 \quad \text{for } E' \neq E''.$$

The imaginary part of state energy in the lowest PT order is

$$\operatorname{Im} E = \Gamma/2 = \pi \left| \langle \Psi_{Eb} | H | \Psi_{Es} \rangle \right|^2 \qquad (9.17)$$

with the total Hamiltonian H. The state functions Ψ_{Eb} and Ψ_{Es} are assumed to be normalized to 1 and by the $\delta(k - k')$ condition, accordingly. The action of H on Ψ_{Eb} is defined unambiguously by (9.15):

$$\left(H - E'\right)\psi_s = 2|m|\left(\zeta \cdot \eta^2\right) \cdot f_{E's}(\zeta) g_{Eb}(\eta) z'_2 \exp(\mathrm{i}m\varphi/) / \left[(2\pi)^{1/2}(\zeta + \eta)\right],$$
$$\langle \psi_{Eb} | H | \psi_{E's} \rangle = \iint d\zeta d\eta (\zeta\eta)^{|m|} \eta f^2_{Eb}(\zeta) f^2_{E's}(\zeta) g_{Eb}(\eta) z'_2. \qquad (9.18)$$

The matrix elements $\langle \Psi_{Eb} | H | \Psi_{E's} \rangle$ entering the high- order PT corrections can be determined in the same way. All the two-dimensional integrals in (9.16)–(9.18) and the normalization coefficients can be expressed through the next set of one-

dimensional integrals:

$$
\begin{aligned}
I_1 &= \int dt f_b^2(t) t^{|m|}, \qquad I_2 = \int dt f_b^2(t) t^{|m|+1}, \\
I_3 &= \int dt g_b(t) g_1(t) t^{|m|}, \qquad I_4 = \int dt g_b(t) g_1(t) t^{|m|+1}, \\
I_5 &= \int dt g_b(t) g_2(t) t^{|m|}, \qquad I_6 = \int dt g_b(t) g_2(t) t^{|m|+1}, \\
I_7 &= \int dt g_b^2(t) t^{|m|}, \qquad I_8 = \int dt g_b^2(t) t^{|m|+1},
\end{aligned}
\tag{9.19}
$$

calculated with the arbitrary normalized functions f_{Eb}, g_{Eb}, f_2, g_2, and $f_1 = f_{Eb}$, $g_1 = g_{Eb}$. In this notation

$$
\begin{aligned}
\Gamma &= 32\pi z_2^2 N_s^2 I_1^2 I_8^2 / [I_2 I_7 + I_1 I_8], \\
z_2 &= [I_1 I_4 + I_2 I_3] / [I_1 I_6 + I_2 I_5]
\end{aligned}
\tag{9.20}
$$

with

$$
\begin{aligned}
N_s^2 &= \lim_{t \Rightarrow \infty} X(t) / \left\{ 2\pi \eta^{2|m|+1} \left[g_s^2(\eta) X^2(t) + g_s'^2(\eta) \right] \right\}, \\
X(t) &= \left\{ E/2 + (\beta - N/Z)/t - Et/4 \right\}^{1/2}.
\end{aligned}
\tag{9.21}
$$

Remember that arbitrary normalized state functions are assumed in (9.20) and (9.21). The whole calculational procedure at known resonance energy E and separation parameter β_1 has been reduced to the solution of one system of the ordinary differential equations. This master system includes the differential equations for the state functions f_{Eb}, g_{Eb}, f_{Es}, g_{Es}, as well as the equations for the integrals I_1–I_8. Thus, our calculational procedure is one-dimensional. The procedure is sufficiently simple and realized as the numerical code with using the fourth-order Runge–Kutta method of solving the differential equations (the atomic code "Superatom-ISAN-Stark").

9.2.3 *Operator Perturbation Theory for Non-H Atoms in Electric Field*

In contrast to the hydrogen atom, the non-relativistic Schrödinger equation for an electron moving in the field of the atomic core in many-electron atom (in particular, an alkali element) and a uniform external electric field does not allow separation of variables in the parabolic coordinates ξ, η, φ [2, 3]. This separation is not possible, in particular, due to the fact that the potential of the atomic core is essentially non-Coulomb. This makes difficult to take into account an external field, e.g., as the zeroth approximation of the PT [71, 75, 76] in order to calculate the spectral

characteristics of multi-electron atoms in an external electric field, regardless of its strength. Obviously, such a method would be extremely useful and effective. Note, however, that one of the ways this problem could be related to the use of effective potentials, chosen in such a way that to achieve the separation of variables in the Schrödinger equation. Here the model potential approach or the quantum defect approximation can be used. One may introduce the ion core charge z^* for the multielectron atom. According to standard quantum defect theory, the relation between quantum defect value μ_1, electron energy E and principal quantum number n is: $\mu_1 = m - z^*(-2E)^{-1/2}$. The quantum defect in the parabolic coordinates $\delta(n_1 n_2 m)$ is connected to the quantum defect value of the free ($\varepsilon = 0$) atom by the following relation [59]:

$$\delta(n_1 n_2 m) = (1/n)\sum_{l=m}^{n-1}(2l+1)\left(C^{JM}_{J,M-mlm}\right)^2\mu_l, \qquad J = (n-1)/2, \qquad M = (n_1 - n_2 + m)/2. \tag{9.22}$$

Using the quantum defect approximation allow to use the above OPT method for the non-H atoms. Naturally, it is possible to use more complicated forms for the ion core potential. As alternative approach, it should be mentioned the finite difference methods of calculation without separation of variables in the Schrödinger equation for atom in an electric field [5, 6]. The long-term possibility of solving the problems associated with the use of a screened Coulomb approximation and further taking into account the non-Coulomb potential of the atomic residue in the calculation of mixing levels of an atom in an external field. In this way, we also reserve the separability of variables. Let us separate the Coulomb part V_C of the model Ivanova-Ivanov potential V [9]:

$$v(r) = N_C\left[1 - e^{-2br}(1-br)\right]/Zr = N_c/Zr - N_c e^{-2br}(1-br)/Zr = v_c - v_{nc} \tag{9.23}$$

and put it in our potential into the Schrödinger equation for the hydrogen-like atom with nuclear charge Z. The rest of the non-Coulomb part is factorized. The matrix element in parabolic coordinates on the screened H-like functions f and g:

$$\begin{aligned}
&\langle i|v_{nc}|j\rangle \\
&= (-N_C/2Z)\int d\xi f_i(\xi) f_j(\xi)\exp(-b\xi)\int d\eta g_i(\eta) g_j(\eta)\exp(-b\eta) \\
&\quad + (-bN_C/4Z)\int d\xi f_i(\xi) f_j(\xi)\exp(-b\xi)\int d\eta g_i(\eta) g_j(\eta)\exp(-b\eta) \\
&\quad + (-bN_C/4Z)\int d\xi f_i(\xi) f_j(\xi)\exp(-b\xi)\int d\eta\eta g_i(\eta) g_j(\eta)\exp(-b\eta).
\end{aligned} \tag{9.24}$$

As indicated above, the inclusion of an electric field rearranges atomic spectrum so that the states become autoionization ones (the shape resonances). An energy

of the state becomes complex: $E = E_r - i\Gamma/2$. The total problem is thus reduced to the diagonalization of the energy complex matrix for a many-electron atom (see details in Refs. [12, 59–63, 71–76]). The matrix of interaction operator should be then calculated [6, 61, 75]:

$$E^{(i-j)} = \mathrm{Re}\, E^{(i-j)} + i\, \mathrm{Im}\, E^{(i-j)}. \tag{9.25}$$

Further it is possible to limit the calculation accuracy to the relationship $\mathrm{Im}\, E / \mathrm{Re}\, E$ (the justification for this approach is set out in detail, for example, in [6, 75]). The components of the eigenvectors of states can be obtained as a result of the diagonalization of the real part of the energy matrix. The imaginary part of the energy matrix is as follows:

$$\mathrm{Im}\, E_{ik} = \sum_{n,m} \hat{C}^*_{in}\, \mathrm{Im}\, E^{i-j}_{nm}\, \hat{C}_{mk}, \tag{9.26}$$

where C is the matrix of eigenvectors. The widths of the resonances are determined by the corresponding imaginary parts. As a result, this approach allows in principle to calculate the characteristics of the Stark resonances in the spectrum of an arbitrary multi-electron atom in a strong external electric field, which is a great interest to a wide range of applications in modern atomic, molecular and laser physics, quantum electronics, plasma physics and chemistry etc.

9.3 Calculation Results and Discussion

9.3.1 The Stark Resonances Energies and Widths of Hydrogen Atom

The calculation results for the Stark resonances energies and widths of the ground state hydrogen atom in the DC electric field with the strength $\varepsilon = 0.04, 0.08, 0.10, 0.80$ a.u. are presented in Tables 9.1 and 9.2. The comparison with earlier similar results, obtained within the generalized WKB approximation, summation of divergent PT series, the numerical solution of the differential equations following from expansion of the wave function over finite basis, a complex scaling plus B-spline calculation [15–51] shows quite acceptable agreement.

The calculation results of the Stark resonances parameters for the excited state H atom ($n = 2, 5, 15$) for different strength values are listed in Table 9.3. The comparison with earlier similar results, obtained within the summation of divergent PT series, the numerical solution of the differential equations with using the finite basis expansion of the wave function again shows acceptable agreement. It is important to compare the theoretical values of the resonance energy and width for the H atom in the field $\varepsilon = 16.8$ kV/cm with experimental data [4]. There is quite good agreement between theory and experiment. Note that our results are obtained in the first PT

Table 9.1 The energies and widths (a.u.) of the Stark resonances of the ground state hydrogen atom ($\varepsilon = 0.04, 0.08$ a.u.). Notation: (a1) Mendelson [15], (a2) Alexander [17], (b1) Hehenberger, McIntosh and Brändas [21], (b2) Brändas and Froelich [23], (c) Benassi and Grecchi [46], (d) Cerjan et al. [40], (e) Farrelly and Reinhardt [47], (f) Franceschini, Greechi, and Silverstone [45], (g) Reinhardt [44], (h) Maquet, Chu, and Reinhardt [41], (i) Kolosov [48], (j) Damburg and Kolosov [42], (k) Anokhin and Ivanov [51], (l) Ivanov and Ho (relativistic and non-relativistic results respectively) [54], (m) Rao, Liu and Li [18], (n) the OPT method (our data), (o) Filho et al. [49]

ε, a.u.	Method	E_r, a.u.	$\Gamma/2$, a.u.
0.04	a1	−0.5038	–
	a2	−0.5038	0.2×10^{-5}
	b1	−0.5037714	0.195×10^{-5}
	b2	−0.5037715	0.191×10^{-5}
	c	−0.5037716	0.1946×10^{-5}
	f	−0.5037716	0.1946×10^{-5}
	j	−0.5037716	0.195×10^{-5}
	k	−0.5038	0.248×10^{-5}
	l	−0.5037780	0.205×10^{-5}
		−0.5037716	0.195×10^{-5}
	m	−0.5037716	0.1946×10^{-5}
	n	−0.5037714	0.1945×10^{-5}
	o	−0.503752	–
0.08	a1	−0.5193	–
	a2	−0.5175	0.230×10^{-2}
	b1	−0.51756	0.227×10^{-2}
	c	−0.51756	0.2270×10^{-2}
	f	−0.51756	0.2270×10^{-2}
	g	−0.51756	0.2269×10^{-2}
	h	−0.51756	0.2270×10^{-2}
	j	−0.51749	0.2255×10^{-2}
	k	−0.5176	0.220×10^{-2}
	l	−0.51757	0.2270×10^{-2}
		−0.51756	0.2270×10^{-2}
	m	−0.51756	0.2270×10^{-2}
	n	−0.51757	0.2270×10^{-2}
	o	−0.51745	–

order, i.e. already the first PT order provides the physically reasonable results. Naturally its accuracy can be increased by an account of the next PT order. The range of validity of the proposed method which uses the Fermi golden rule is quite wide and it is not restricted to resonances lying far from the continuum boundary.

Table 9.2 The energies and widths of the Stark resonances of the ground state hydrogen atom ($\varepsilon = 0.10, 0.80$ a.u.). Notation: (a1) Mendelson [15], (a2) Alexander [17], (b1) Hehenberger, McIntosh and Brändas [21], (b2) Brändas and Froelich [23], (c) Benassi and Grecchi [46], (d) Cerjan et al. [40], (e) Farrelly and Reinhardt [47], (f) Franceschini, Greechi, and Silverstone [45], (g) Reinhardt [44], (h) Maquet, Chu, and Reinhardt [41], (i) Kolosov [48], (j) Damburg and Kolosov [42], (k) Anokhin and Ivanov [51], (l) Ivanov and Ho (relativistic and non-relativistic results respectively) [54], (m) Rao, Liu and Li [18], (n) the OPT method (our data), (o) Filho et al. [49], (p) Popov et al. [66]

E, a.u.	Method	E_r, a.u.	$\Gamma/2$, a.u.
0.10	a1	−0.556	–
	a2	−0.527	0.750×10^{-2}
	b1	−0.52743	0.725×10^{-2}
	b2	−0.52742	0.727×10^{-2}
	c	−0.527418	0.7269×10^{-2}
	d	−0.527417	0.727×10^{-2}
	f	−0.527418	0.7269×10^{-2}
	g	−0.527425	0.7271×10^{-2}
	h	−0.527418	0.7269×10^{-2}
	i	−0.527418	0.7269×10^{-2}
	j	−0.526905	0.7170×10^{-2}
	l	−0.527423	0.7268×10^{-2}
		−0.527418	0.7269×10^{-2}
	m	−0.527418	0.7269×10^{-2}
	n	−0.527419	0.7269×10^{-2}
	o	−0.53109	–
	p	−0.5274	0.727×10^{-2}
0.80	e	−0.6304	0.5023
	i	−0.630415	0.50232
	m	−0.630415	0.50232
	n	−0.630416	0.50232

9.3.2 DC Stark Effect for the Sodium Atom

Observation of the DC Stark effect near threshold in alkali atoms led to the discovery by Freeman and colleagues of resonances extending into the ionization continuum (look Refs. [4–6, 64–66]). The unique characteristics in a photoionization spectrum are connected to the presence of a non-H core, which produces the interference dips below threshold and attenuates the modulations above threshold.

As an application of the presented method, in Table 9.4 we present the calculation results for the Stark resonance energies for some Rydberg states of the Na atom in an electric field with the strength 3.59 kV/cm. For comparison, we also list the experimental data, the results of calculation within the $1/n$-expansion method by Popov et al. [4, 5, 57, 59, 65, 66]. Agreement between both the theory and the

Table 9.3 The energies and widths of the Stark resonances of the hydrogen atom ($n = 2, 5$). Notation: a, OPT calculation; b, Damburg and Kolosov [42]; c, Kolosov [48]; d, Benassi and Grecchi [46]; e, Telnov [52]; f, Popov et al. [66]; exp—experimental data (from Refs. [4, 42, 46, 48, 57, 58, 65, 66]

$(n\ n_1\ n_2\ m)$	ε, a.u.	Method	E_r, a.u.	Γ, a.u.
2 0 1 0	0.005	a	0.1426	0.102×10^{-3}
		c	0.1426	0.106×10^{-3}
		e	0.1426	0.106×10^{-3}
	0.01	a	0.1661	0.108×10^{-1}
		c	0.1661	0.109×10^{-1}
		d	0.1661	0.109×10^{-1}
		e	0.1661	0.109×10^{-1}
2 0 0 1	0.005	a	0.1272	0.267×10^{-4}
		c	0.1272	0.262×10^{-4}
		e	0.1272	0.262×10^{-4}
	0.01	a	0.1345	0.637×10^{-2}
		c	0.1345	0.628×10^{-2}
		e	0.1345	0.628×10^{-1}
5 2 2 0	1.8×10^{-4}	a	0.2062	0.278×10^{-5}
		b	0,2062	0.228×10^{-5}
		f	0.2062	0.228×10^{-5}
		f	0.2062	0.222×10^{-5}
15 10 4 0	3.27×10^{-6}	a	1.9098×10^{-3}	2.782×10^{-7}
		f	1.9095×10^{-3}	2.278×10^{-7}
		exp	1.91×10^{-3}	2.92×10^{-7}

Table 9.4 The energies (in cm^{-1}) of the Stark resonances for Na atom ($\varepsilon = 3.59$ kV/cm)

State: $(n_1\ n_2\ m)$	δ	Exp Data	Method by Popov et al.	This method
26, 0, 0	0.140	15.5	15.5	15.5
25, 0, 1	0.007	21.1	21.1	21.1
25, 0, 0	0.145	35.5	35.5	35.5
24, 0, 1	0.008	41.1	40.4	41.0
24, 1, 0	0.130	50.5	50.3	50.5
24, 0, 0	0.151	56.5	57.0	56.5
23, 0, 1	0.008	61.2	60.7	61.1
23, 0, 0	0.157	79.3	80.3	79.4
22, 0, 1	0.009	84.1	83.1	83.9
22, 1, 1	0.016	75.0	74.9	75.1

experiment is good. Our results are obtained in the first PT order, i.e., the first PT order provides physically reasonable results.

9.4 Conclusions

In this chapter it is presented a new uniform quantum-mechanical approach to the solution of the non-stationary state problems including the DC strong-field Stark effect and also scattering problem. New OPT method allows sufficiently exact calculating the complex EE and resonance widths and especially is destined for investigation of the spectral region of an atom near the new continuum boundary in a strong field. The essence of the method is the inclusion of the well known "distorted waves approximation" in the frame of the formally exact PT. The method is generalized to provide the description of the DC strong field Stark effect for the non-H atoms. The results of the calculation of the Stark resonance energies and widths for the hydrogen and sodium atoms are presented and in a physically reasonable agreement with the best results of the alternative theoretical methods and experiment. It is noted that the zeroth model approximation, including the potential of a strong external electric field, can be implemented into the general formalism of the formally exact PT for many-electron atom [6, 12, 59–63, 71–76].

The range of validity of the presented method which uses the Fermi golden rule is sufficiently wide and it is not restricted to resonances lying far from the continuum boundary. Let us conclude that the OPT method has been also successfully applied to correct description of the resonances of the Zeeman effect in a strong magnetic field, crossed electric and magnetic fields, the resonances in molecular systems, as well as descriptions of resonant states in nuclear systems such as the resonances of the compound nucleus and the resonances arising from the collision of heavy ions (nuclei), accompanied by the electron-positron pairs production (look the details in Refs. [6, 80, 83–91]).

Acknowledgements The author would like to thank Prof. Jean Maruani and Prof. Matti Hotokka (the organizer of QSCP XVII-2012, Turku, Finland) for the friendly cooperation and invaluable advises.

References

1. Stark J (1914) Ann Phys 43:965
2. Bethe HA, Salpeter EE (1957) Quantum mechanics of one- and two-electron atoms. Springer, Berlin
3. Landau LD, Lifshitz EM (1977) Quantum mechanics. Pergamon, Oxford
4. Stebbings RF, Dunning FB (eds) (1983) Rydberg states of atoms and molecules. Cambridge University Press, Cambridge
5. Nayfeh MN, Clark CW (eds) (1984) Atomic excitation and recombination in external fields. NBS, Gaithersburg
6. Glushkov AV (2005) Atom in an electromagnetic field. KNT, Kiev, pp 1–450

7. Lisitsa VS (1987) Phys Usp 153:369
8. Ivanov LN, Letokhov VS (1975) Quantum Electron 2:585
9. Ivanov LN, Ivanova EP (1979) At Data Nucl Data Tables 24:95
10. Glushkov AV, Ivanov LN (1992) Phys Lett A 170:33
11. Ivanova EP, Grant IP (1998) J Phys B, At Mol Opt Phys 31:2871
12. Glushkov AV (2012) In: Nishikawa K, Maruani J, Brändas E, Delgado-Barrio G, Piecuch P (eds) Advances in the theory of quantum systems in chemistry and physics. Frontiers in theoretical physics and chemistry, vol 26. Springer, Berlin, pp 231–254
13. Delone NB, Fedorov MV (1989) Phys Usp 158:215
14. Siegert AJF (1939) Phys Rev 56:750
15. Mendelson LB (1968) Phys Rev 176:90
16. Dolgov AD, Turbiner AV (1977) Phys Lett A 77:15
17. Alexander MH (1969) Phys Rev 178:34
18. Rao J, Liu W, Li B (1994) Phys Rev A 50:1916
19. Rao J, Li B (1995) Phys Rev A 51:4526
20. Meng H-Y, Zhang Y-X, Kang S, Shi T-Y, Zhan M-S (2008) J Phys B, At Mol Opt Phys 41:155003
21. Hehenberger M, McIntosh HV, Brändas E (1974) Phys Rev A 10:1494
22. Hehenberger M, McIntosh HV, Brändas E (1975) Phys Rev A 12:1
23. Brändas E, Froelich P (1977) Phys Rev A 16:2207
24. Brändas E, Hehenberger M, McIntosh HV (1975) Int J Quant Chem 9:103
25. Rittby M, Elander N, Brändas E (1981) Phys Rev A 24:1636
26. Froelich P, Davidson ER, Brändas E (1983) Phys Rev A 28:2641
27. Lipkin N, Moiseyev N, Brändas E (1989) Phys Rev A 40:549
28. Rittby M, Elander N, Brändas E (1983) Int J Quant Chem 23:865
29. Simon B (1979) Phys Lett A 7(1):211
30. Nicolaides CA, Beck DR (1978) Phys Lett A 65:11
31. Brändas E, Froelich P, Obcemea CH, Elander N, Rittby M (1982) Phys Rev A 26:3656
32. Engdahl E, Brändas E, Rittby M, Elander N (1986) J Math Phys 27:2629
33. Engdahl E, Brändas E, Rittby M, Elander N (1988) Phys Rev A 37:3777
34. Brändas E, Elander N (eds) (1989) Resonances: the unifying route towards the formulation of dynamical processes—foundations and applications in nuclear, atomic and molecular physics. Lecture notes in physics, vol 325. Springer, Berlin, pp 1–564
35. Scrinzi A, Elander N (1993) J Chem Phys 98:3866
36. Ostrovsky VN, Elander N (2005) Phys Rev A 71:052707
37. Sigal JM (1988) Commun Math Phys 119:287
38. Herbst IW, Simon B (1978) Phys Rev Lett 41:67
39. Silverstone HJ, Adams BG, Cizek J, Otto P (1979) Phys Rev Lett 43:1498
40. Cerjan C, Hedges R, Holt C, Reinhardt WP, Scheibner K, Wendoloski JJ (1978) Int J Quant Chem 14:393
41. Maquet A, Chu SI, Reinhardt WP (1983) Phys Rev A 27:2946
42. Damburg RJ, Kolosov VV (1976) J Phys B, At Mol Phys 9:3149
43. Luc-Koenig E, Bachelier A (1980) J Phys B, At Mol Phys 13:1743
44. Reinhardt WP (1982) Int J Quant Chem 21:133
45. Franceschini V, Grecchi V, Silverstone HJ (1985) Phys Rev A 32:1338
46. Benassi L, Grecchi V (1980) J Phys B, At Mol Phys 13:911–924
47. Farrelly D, Reinhardt WP (1983) J Phys B, At Mol Phys 16:2103
48. Kolosov VV (1987) J Phys B, At Mol Phys 20:2359
49. Filho O, Fonseca A, Nazareno H, Guimarães P (1990) Phys Rev A 42:4008
50. Kondratovich VD, Ostrovsky VN (1984) J Phys B, At Mol Phys 17:2011
51. Anokhin SB, Ivanov MV (1984) Opt Spectrosc 59:499
52. Telnov DA (1989) J Phys B, At Mol Opt Phys 22:1399–1403
53. Ho Y-K (1983) Phys Rep 99:3
54. Ivanov IA, Ho Y-K (2004) Phys Rev A 69:023407

55. González-Férez R, Schweizer W (2000) In: Hernández-Laguna A, Maruani J, McWeeny R, Wilson S (eds) Quantum systems in chemistry and physics. Progress in theoretical chemistry and physics, vol 2/3. Springer, Berlin, p 17
56. Glushkov AV, Ivanov LN (1992) Proc of 3rd symposium on atomic spectroscopy. Moscow, Chernogolovka
57. Glushkov AV, Ivanov LN (1993) J Phys B, At Mol Phys 26:L379
58. Glushkov AV, Malinovskaya SV, Ambrosov SV, Shpinareva IM, Troitskaya OV (1997) J Tech Phys 38:215
59. Glushkov AV, Ambrosov SV, Ignatenko AV, Korchevsky DA (2004) Int J Quant Chem 99:936
60. Glushkov AV, Loboda AV (2007) J Appl Spectrosc (Springer) 74:305
61. Glushkov AV, Khetselius OYu, Loboda AV, Svinarenko AA (2008) In: Wilson S, Grout PJ, Maruani J, Delgado-Barrio G, Piecuch P (eds) Frontiers in quantum systems in chemistry and physics. Progress in theoretical chemistry and physics, vol 18. Springer, Berlin, pp 523–588
62. Glushkov AV, Khetselius O, Malinovskaya S (2008) Eur Phys J T 160:195
63. Glushkov AV, Khetselius OYu, Svinarenko AA, Prepelitsa GP (2011) In: Duarte FJ (ed) Coherence and ultrashort pulsed emission. Intech, Vienna, pp 159–186
64. Zimmerman ML, Littman MG, Kash MM, Kleppner D (1979) Phys Rev A 20:2251
65. Harmin DA (1982) Phys Rev A 26:2656
66. Popov V, Mur V, Sergeev A, Weinberg V (1990) Phys Lett A 149:418, 425
67. Grutter M, Zehnder O, Softley T, Merkt F (2008) J Phys B, At Mol Opt Phys 41:115001
68. Stambulchik E, Maron Y (2008) J Phys B, At Mol Opt Phys 41:095703
69. Dunning FB, Mestayer JJ, Reinhold CO, Yoshida S, Burgdörfer J (2009) J Phys B, At Mol Opt Phys 42:022001
70. Bryant HC, Clark DA, Butterfield KB et al (1983) Phys Rev A 27:2889
71. Glushkov AV, Ambrosov S, Khetselius OYu, Loboda AV, Gurnitskaya E (2006) In: Julien J-P, Maruani J, Mayou D, Wilson S, Delgado-Barrio G (eds) Recent advances in theoretical physics and chemistry systems. Progress in theoretical chemistry and physics, vol 15. Springer, Berlin, pp 285–300
72. Khetselius OYu (2012) J Phys Conf Ser 397:012012
73. Khetselius OYu (2009) Int J Quant Chem 109:3330
74. Khetselius O, Florko T, Svinarenko A, Tkach T (2013) Phys Scr T 153:01437
75. Ivanova EP, Ivanov LN, Glushkov AV, Kramida AE (1985) Phys Scr 32:512
76. Ivanova EP, Glushkov AV (1986) J Quant Spectrosc Radiat Transf 36:127
77. Benvenuto F, Casati G, Shepelyansky DL (1994) Z Phys B 94:481
78. Buchleitner A, Delande D (1997) Phys Rev A 55:1585
79. Gallagher TF, Noel M, Griffith MW (2000) Phys Rev A 62:063401
80. Glushkov AV, Ambrosov SV (1996) J Tech Phys 37:347
81. Glushkov AV, Khokhlov V, Tsenenko I (2004) Nonlinear Process Geophys 11:285
82. Glushkov A, Khohlov V, Loboda N, Bunyakova Yu (2008) Atmos Environ 42:7284
83. Glushkov AV, Khetselius OYu, Malinovskaya SV (2008) Mol Phys 106:1257
84. Glushkov AV, Rusov VD, Ambrosov SV, Loboda AV (2003) In: Fazio G, Hanappe F (eds) New projects and new lines of research in nuclear physics. World Scientific, Singapore, pp 126–142
85. Glushkov AV (2005) In: Grzonka D, Czyzykiewicz R, Oelert W, Rozek T, Winter P (eds) Low energy antiproton physics, vol 796. AIP, New York, pp 206–210
86. Glushkov AV (2007) In: Krewald S, Machner H (eds) Meson-nucleon physics and the structure of the nucleon, vol 2. IKP, Juelich. SLAC eConf C070910 (Menlo Park, CA, USA, 2007), pp 111–117
87. Glushkov AV, Khetselius OYu, Loboda AV, Malinovskaya SV (2007) In: Krewald S, Machner H (eds) Meson-nucleon physics and the structure of the nucleon, vol 2. IKP, Juelich. SLAC eConf C070910 (Menlo Park, CA, USA, 2007), pp 118–122
88. Glushkov AV, Khetselius OYu, Lovett L, Gurnitskaya EP, Dubrovskaya YuV, Loboda AV (2009) Int J Mod Phys A, Part Fields Nucl Phys 24:611

89. Glushkov AV, Khetselius OYu, Lovett L (2010) In: Piecuch P, Maruani J, Delgado-Barrio G, Wilson S (eds) Advances in the theory of atomic and molecular systems: dynamics, spectroscopy, clusters, and nanostructures. Progress in theoretical chemistry and physics, vol 20. Springer, Berlin, pp 125–151
90. Glushkov AV, Khetselius OYu, Svinarenko AA (2012) In: Hoggan P, Brändas E, Maruani J, Delgado-Barrio G, Piecuch P (eds) Advances in the theory of quantum systems in chemistry and physics. Progress in theoretical chemistry and physics, vol 22. Springer, Berlin, pp 51–70
91. Glushkov AV (2008) Relativistic quantum theory. Quantum mechanics of atomic systems Astroprint, Odessa, pp 1–704

Part III
Clusters and Condensed Matter

Chapter 10
Structural and Thermodynamic Properties of Au_{2-58} Clusters

Yi Dong, Michael Springborg, and Ingolf Warnke

Abstract In this study, we have used a parametrized density-functional tight-binding method combined with genetic algorithms for an unbiased global optimization to study systematically neutral gold clusters with from 2 to 58 atoms. The ground states of the clusters are identified and different descriptors are used to analyze the properties of the clusters, including stability, overall shape, similarity, growth patterns, and structural motifs. The vibrational heat capacity of the ground state of neutral gold clusters at different temperatures are calculated by a newly developed method. The results show that the heat capacity is strongly size-dependent, particularly at low temperature.

10.1 Introduction

Clusters science has been an active research area for some decades because of the fascinating properties of the clusters. Thus, quantum-size effects combined with the fact that the number of surface atoms relative to the total number of atoms is far from vanishing may be held responsible for the unique, size-dependent properties of clusters. Moreover, there is a highly non-trivial dependence of the properties on the size and composition of the clusters. Since, on the other hand, the properties depend sensitively on the structure of the clusters, one of the most fundamental challenges in the study of clusters is related to the determination of their ground-state structures.

Without any further information the theoretical identification of the structure of the ground state of a cluster of N atoms requires searching in a geometry space of $3N - 6$ dimensions, which for even small values of N is hardly possible. Accordingly, even for not too large clusters, an unbiased determination of the structure of the global total-energy minimum will easily require that very many structures are studied whereas for each structure the calculation of the total energy is computationally demanding. Therefore, theoretical studies of the properties of the clusters have

Y. Dong (✉)
Physical and Theoretical Chemistry, University of Saarland, Campus B2.2, 66123 Saarbrücken, Germany
e-mail: y.dong@mx.uni-saarland.de

M. Hotokka et al. (eds.), *Advances in Quantum Methods and Applications in Chemistry, Physics, and Biology*, Progress in Theoretical Chemistry and Physics 27,
DOI 10.1007/978-3-319-01529-3_10,

to incorporate one or more approximations. For instance, one may choose to study only small(er) clusters or clusters of selected sizes and/or structures. Furthermore, by employing empirical potentials that depend only on the interatomic distances it may become possible to study more structures and/or larger systems at the cost of possible inaccuracies due to the approximate descriptions of the interatomic interactions. As a compromise, parametrized methods that include electronic degrees of freedom can be used. Besides the use of such approximate methods for the determination of the total energy for a given structure, various approaches for the determination of the structure of the global total-energy minimum have been suggested. These include Simulated Annealing, the Basin-Hopping method, and Genetic Algorithms [1–9].

Gold clusters constitute a special case that has attracted much attention partly because of their application as catalysts and in nanoscience, and partly because these systems provide a useful model system with surprising results for theoretical studies. However, it has turned out to be particularly difficult to determine the properties of gold cluster because the calculated structures depend very sensitively on the applied methods [10, 11], which is to a much lesser extent the case for most other elemental clusters. Therefore, the reported theoretical results for gold clusters show a particularly large scatter and a strong dependence on the approximations of the calculations.

Interesting information on the clusters can be obtained by studying their thermodynamic properties, both experimentally and theoretically. This includes the melting of small clusters [12–14] but also their low-temperature properties can provide useful information.

In this contribution we shall present results of a theoretical study of the properties of gold clusters. We shall partly review our earlier results on the structural and energetic properties of gold clusters [15] and, in addition, present and apply a new method for studying the vibrational contributions to the thermodynamic low-temperature properties of the clusters. Our computational methods will be described in Sect. 10.2, followed by a discussion of the results in Sect. 10.3. Finally, our results are summarized in Sect. 10.4.

10.2 Computational Method

10.2.1 Parametrized Density-Functional Method

In the present work the total energy and the electronic properties of a given structure were calculated using a parametrized tight-binding density-functional (DFTB) method [16]. According to this method, the relative total energy of a compound with a chosen structure can be written as the difference of the orbital energies of the compound ($\{\varepsilon_i\}$, with i being an orbital index) minus those of the isolated atoms ($\{\varepsilon_{im}\}$

with i and m being an orbital and an atom index, respectively) augmented with pair potentials,

$$E_{\text{tot}} = \sum_i \varepsilon_i - \sum_m \sum_i \varepsilon_{im} + \sum_{m_1,m_2} U_{m_1 m_2}\big(|\mathbf{R}_{m_1} - \mathbf{R}_{m_2}|\big). \tag{10.1}$$

Here, $U_{m_1,m_2}(R)$ is the pair potential between atom m_1 and m_2 that depends on their interatomic distance R.

In order to determine the orbital energies, the single-particle Kohn-Sham operator is written as the kinetic-energy operator plus an effective potential. The latter is approximated as the superposition of the potentials of the isolated atoms,

$$V_{\text{eff}}(\mathbf{r}) = \sum_m V_m^0\big(|\mathbf{r} - \mathbf{R}_m|\big). \tag{10.2}$$

The single-particle wavefunctions, $\{\psi_i\}$, are expanded in terms of atom-centered functions,

$$\psi_i(\mathbf{r}) = \sum_{jm} c_{ijm}\phi_{jm}(\mathbf{r} - \mathbf{R}_m) \tag{10.3}$$

with m identifying the atom and j used in distinguishing between different functions centered on the same atom.

We assume that $\langle\phi_{j_1 m_1}|V_m^0|\phi_{j_2 m_2}\rangle$ vanishes unless at least one of the two basis functions is centered at $\mathbf{R}_m$. Thereby, all relevant information for the secular equation can be extracted from accurate density-functional calculations on the two-atomic molecules. The short-ranged pair potentials are determined by requiring that the total energy of two-atomic systems (in our case, of Au_2) as a function of interatomic distance as determined through accurate density-functional calculations is accurately reproduced.

Finally, in the present study only the $5d$ and $6s$ electrons of the isolated Au atom are explicitly included in the calculations, whereas the other electrons are treated within a frozen-core approximation.

10.2.2 Genetic Algorithms

The DFTB calculations provide information on the total energy of the cluster as a function of structure and can also be used in determining local total-energy-minima structures. In order to find the global total-energy-minimum structures of the clusters we have used a method based on genetic algorithms, which was developed in connection with our earlier studies on HAlO clusters [17]. Such methods are based on the principles of natural evolution and are, therefore, also called evolutionary algorithms [18]. They have been found to provide an efficient tool for global geometry optimizations.

Our version of the genetic algorithms is as follows. Suppose that we have optimized the structure of the cluster with N atoms. Using this structure we create a

set of M initial structures (which define the first generation) for the $(N+1)$-atom system by randomly adding one Au atom and afterward letting each of these structures relax to its nearest total-energy minimum. Subsequently, the next generation of M new $(N+1)$-atomic clusters is formed by cutting each of the original clusters randomly into two parts that are interchanged and requiring that no atom should be too close to any other atom or too far from all the other ones. Also these structures are relaxed to their nearest total-energy minima. Out of the total set of $2M$ structures, those M of the lowest total energy define the next generation. This procedure is repeated until the lowest total energy is unchanged for a large number of generations. We add that even if this unbiased structure-optimization is reliable and efficient, there is no absolute certainty that the global total-energy minimum has been identified.

10.2.3 Jellium Model

Because the jellium model has been intensively used for metal clusters, we considered that model, too. Within this model we assumed that the total charge formed by all but the $5d$ and $6s$ valence electrons of each gold atom as well as of the nuclei is smeared out to a spherical medium (jellium) with a constant density within which the valence electrons are moving. The value of the density of the jellium is taken as that of crystalline Au, and a local-density approximation within density-functional theory is assumed valid for the valence electrons. The resulting one-dimensional, single-particle equations are then solved numerically and self-consistently.

10.2.4 Thermodynamics Calculations

Within the Normal Mode Harmonic Oscillator (NMHO) approximation [19], the total energy, E, is approximated with a Taylor expansion up to second order in the coordinates of the atoms relative to the equilibrium positions, $\{q_i\}, i = 1, 2, \ldots, 3N$. Since the first order derivatives vanish at the equilibrium structure, we have accordingly

$$E \simeq E_0 + \frac{1}{2}\sum_{i,j=1}^{3N}\left(\frac{\partial^2 E}{\partial q_i \partial q_j}\right)_0 q_i q_j + \cdots \equiv E_0 + \frac{1}{2}\sum_{i,j=1}^{3N} f_{ij} q_i q_j + \cdots . \tag{10.4}$$

Here, the subindex 0 indicates properties at the equilibrium structure.

For the vibrational properties, we need the $3N \times 3N$ the dynamical matrix that can be constructed from the force constants f_{ij},

$$D_{ij} = \frac{1}{\sqrt{M_i M_j}} f_{ij}, \tag{10.5}$$

with M_i being the mass for the ith coordinate. Then, the vibrational frequencies, ω_i, are found as the square roots of the eigenvalues of the dynamical matrix.

In order to calculate the force constants f_{ij} we use a finite-difference approximation

$$f_{ij} = \frac{\partial}{\partial q_i}\frac{\partial E}{\partial q_j} = \frac{\partial}{\partial q_j}\frac{\partial E}{\partial q_i} = \frac{1}{2}\left(\frac{\partial}{\partial q_i}\frac{\partial E}{\partial q_j} + \frac{\partial}{\partial q_j}\frac{\partial E}{\partial q_i}\right) = \frac{-1}{2}\left(\frac{\partial F_i}{\partial q_j} + \frac{\partial F_j}{\partial q_i}\right)$$
$$\simeq \frac{-1}{4\Delta s}\left[F_i(q_j + \Delta s) - F_i(q_j - \Delta s) + F_j(q_i + \Delta s) - F_j(q_j - \Delta s)\right] \quad (10.6)$$

where Δs is a small but finite change in the coordinates, and $F_m(q_n \pm \Delta s)$ denotes the mth force component for the structure where the nth coordinate has been changed by $\pm\Delta s$. From test calculations we found that $\Delta s = 0.01$ a.u. results in numerically stable results.

From the calculated vibrational frequencies we can use Boltzmann statistics in determining first the vibrational partition function and subsequently the vibrational heat capacity,

$$C_{\text{vib}} = k_B \sum_{i=1}^{\text{NVM}} \frac{\alpha_i^2 e^{\alpha_i}}{(e^{\alpha_i} - 1)^2} \quad (10.7)$$

with

$$\alpha_i = \frac{\hbar\omega}{k_B T} \equiv \frac{T_i}{T} \quad (10.8)$$

and k_B being the Boltzmann constant. NVM is the number of non-zero frequencies and equals $3N - 6$ ($3N - 5$) for non-linear (linear) systems. Moreover, for each mode T_i is a characteristic temperature that describes that temperature ($T \simeq 2.35T_i$) at which the contribution of the given mode changes most rapidly as a function of temperature. At $T \simeq 2.35T_i$ the contribution of the ith node equals roughly 64 % of its maximal contribution (at $T \to \infty$).

Finally, it is easily seen that

$$\lim_{T\to\infty} C_{\text{vib}} = \text{NVM} \cdot k_B. \quad (10.9)$$

10.3 Results

For the Au_N clusters with N up to 6 the calculations give that the lowest total energy is found for planar structures, whereas for larger clusters the structure is purely three dimensional. As discussed elsewhere [15] this result is only partly in agreement with findings of more accurate studies for these relatively small systems. In those, planar structures are found for clusters with more than 10 atoms. However, our studies show also that the inaccuracies that lead to the discrepancies in the optimized structures indeed are small [15]. In agreement with other studies, we find that the optimized structures of the gold clusters in general possess a low symmetry.

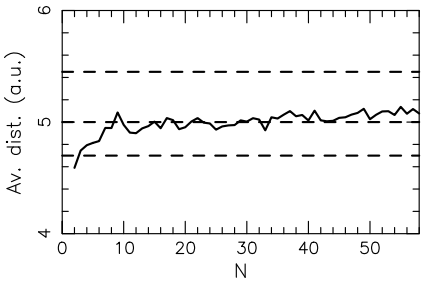

Fig. 10.1 The average nearest-neighbor bond length as a function of cluster size. The *horizontal dashed lines* give (from below) the experimental value for the gold dimer, the theoretical value for a linear chain of gold atoms, and the experimental value for crystalline gold

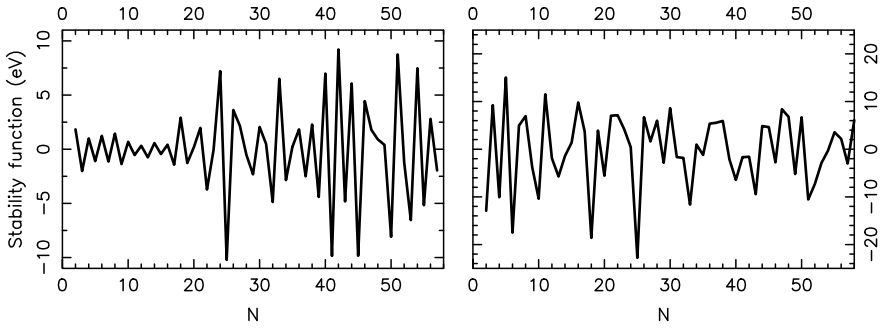

Fig. 10.2 The *left panel* shows the stability function from the DFTB results; the *right panel* that of the jellium calculations

With the purpose of obtaining general information on the structural properties of the clusters we shall use various simplifying descriptors. At first we study (Fig. 10.1) the average of the nearest-neighbour interatomic distances for the gold clusters as a function of size N, whereby we assume that two atoms are nearest neighbors when their interatomic distance is below the average of the nearest-neighbor and the next-nearest-neighbor distances of crystalline gold (6.58 a.u.). From the figure we can see that our calculated bond length of Au_2 is slightly smaller than the experimental value. Furthermore, we observe that the bond lengths for all cluster sizes lie between the (experimental) length for the dimer and the experimental value for crystalline gold and are close to the theoretical value for the linear chain of gold atoms. This finding is in accordance with the fact that the atoms of the gold clusters have a fairly low coordination.

Particularly stable clusters can be identified from the stability function, defined as

$$\Delta_2 E(N) = E(N+1) + E(N-1) - 2E(N) \tag{10.10}$$

[with $E(K)$ being the total energy of Au_K], and shown in Fig. 10.2 both for the DFTB and for the jellium calculations. We see that there is hardly any similarity be-

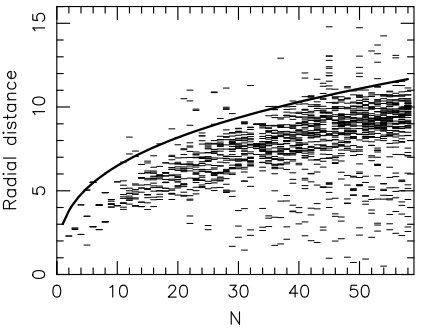

Fig. 10.3 The radial distances as a function of cluster size. For a given cluster size, N, *each small line* represents (at least) one atom with that value of the radial distance. The *smooth curve* shows the radius of the spherical jellium with a density as in the crystal

tween the two sets of results, implying that the jellium approximation is not adequate for the Au_N clusters. Moreover, for the DFTB calculations, the stability function is much more smooth for $N < 20$ than for $N > 20$. For $N \leq 20$, there is a clear odd-even oscillatory pattern, which suggests that those clusters with even N are more stable than those with odd N. But for the clusters with size above 20, the stability function does not follow the even-odd oscillatory pattern. The most pronounced maxima are found for $N = 8$, 18, and 20 for $N \leq 20$ and for $N = 24$, 33, 40, 42, 51, and 54 for $N \geq 20$.

More detailed information on the structural properties of the clusters can be obtained with the help of the so called radial distances that are defined as follows. For the cluster with N atoms we first define its center,

$$\mathbf{R}_0 = \frac{1}{N} \sum_{i=1}^{N} \mathbf{R}_i , \tag{10.11}$$

(here, $\mathbf{R}_i$ is the position of the ith atom), and subsequently the radial distance of the ith atom is given as

$$r_i = |\mathbf{r}_i| = |\mathbf{R}_i - \mathbf{R}_0| . \tag{10.12}$$

At first we show in Fig. 10.3 the radial distances themselves and compare with the radius of the spherical jellium. The figure shows that for $8 \leq N \leq 24$ no atom has a small value of the radial distance suggesting that the clusters have cage-like structures as also was found in the study by Bulusu et al. [23].

Information on the overall shape of the clusters can be obtained by analyzing, for each N, the eigenvalues of the 3×3 matrix containing the elements $\sum_i s_i t_i$ with s_i and t_i being the x, y, and/or z components of $\mathbf{r}_i$. The eigenvalues $I_{\alpha\alpha}$ of this matrix are used to identify the overall cluster shape. At first, their average (divided by $N^{5/3}$ which is the N dependence of the value for the spherical jellium) gives the overall spatial extension of the cluster, whereas three identical eigenvalues suggest a spherical shape, and two large and one small (two small and one large) value suggest a lens-like (cigar-like) shape.

The results are summarized in Fig. 10.4. Only in one single case ($N = 1$), the cluster is characterized as being spherical, whereas in all other cases the clusters

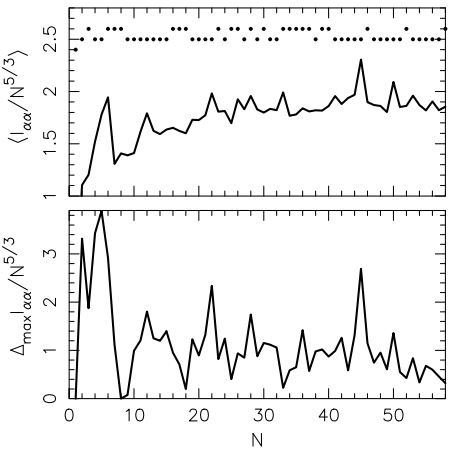

Fig. 10.4 Properties related to the eigenvalues $I_{\alpha\alpha}$ that describe the overall shape of the clusters. The *upper panel* shows the average value (scaled by $N^{-5/3}$) together with marks indicating whether the Au_N cluster is overall spherical (*dots* in the *lowest row*), overall cigar-like shaped (*middle row*) or overall lens-like shaped (*upper row*). The *lower panel* shows the largest difference in the eigenvalues

have a low(er) symmetry, although for some sizes ($N = 8$, 9, 18, 25, and 33) the eigenvalues are very close.

A highly relevant issue for, e.g., the understanding of growth mechanisms is to study the structural similarity between clusters of different sizes. To this end, we have developed a new scheme for introducing a so called similarity function [24] that works as follows when comparing the structures of Au_n and Au_m for which we will assume that $m \geq n$. At first, the two structures are scaled (using the average of the nearest-neighbor and next-nearest-neighbor distances in the crystal), and subsequently the two resulting structures are placed upon each other so that

$$Q = \sum_{i=1}^{n} \left| \frac{1}{d_A} \mathbf{R}_{A,i} - \frac{1}{d_B} \mathbf{R}_{B,i} \right|^2 \tag{10.13}$$

is minimized. Here, d_A and d_B are the two scaling factors for the two systems, $\mathbf{R}_{A,i}$ is the position of the ith atom of the A cluster, and $\mathbf{R}_{B,i}$ is the position of that atom of the B cluster that (after scaling) is closest to the ith atom of the A cluster (also after scaling). From the minimum value of Q we define a similarity function,

$$S = \frac{1}{1 + (Q/n)^{1/2}}. \tag{10.14}$$

In Fig. 10.5 we show S for the comparison between the clusters with $m = N$ atoms with those with $n = N - 1$, $N - 2$, $N - 3$, and $N - 4$. With few exceptions, S takes relatively low values, implying that for the cluster sizes of the present study, there is only little structural similarity. An interesting exception is found for the comparison between the clusters with $N = 12$ or $N = 13$ atoms with that with $N = 11$ atoms. Here, S takes large values (close to 1), although the comparison between $N = 13$ and $N = 12$ gives a small values for S. Thus, both of the two latter structures resemble the 11-atomic cluster, although they are not similar to each other. Our approach can also be used in comparing the structures with a fragment of the crystalline (fcc) structure. The result in shown in Fig. 10.6 and imply that these clusters have structures markedly different from that of the crystal.

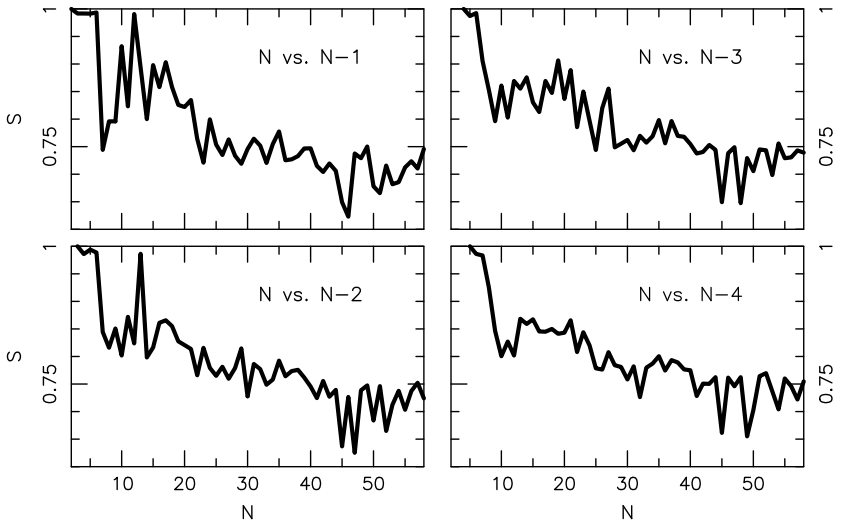

Fig. 10.5 The similarity function for the comparison between Au_N with Au_{N-1}, Au_{N-2}, Au_{N-3}, and Au_{N-4}

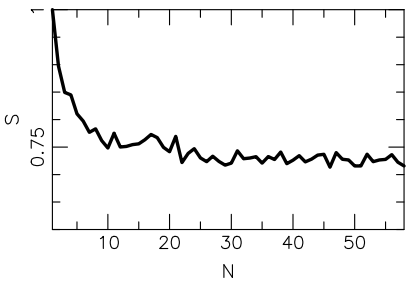

Fig. 10.6 The similarity function for the comparison between the Au_N cluster and the crystal

Alternatively, we may use the common-neighbor analysis [20–22] for the purpose of identifying structural motifs. At first, a cut-off distance is defined that describes whether two atoms are bonded (again, we use the average of the nearest- and next-nearest-neighbor distances in the fcc crystal) and to each pair of atoms, three indices, (i, j, k), are defined. i is the number of common neighbors, j is the number of bonds between those, and k is the number of bonds in the longest unbroken sequence of bonds. For an infinite fcc crystal, the four sets (2,1,1), (1,0,0), (4,2,1), and (4,4,4) occur with a relative occurrence of $4 : 2 : 2 : 1$. Thus, if a cluster has a structure that is identical to a cutout of the crystal, we will for this system find those three sets of indices with roughly the above mentioned relative occurrence and hardly any other set. However, as shown in Fig. 10.7 we recognize a very different behavior for all cluster sizes of the present study. Thus, also this analysis does not at all suggest that fragments of the crystal are found.

As an extension of our earlier study [15] on the structural properties of the gold clusters, we shall here present results related to their vibrational properties. At first,

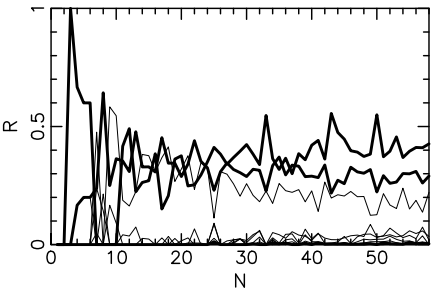

Fig. 10.7 Results of a common-neighbor analysis. *Each curve* shows the relative occurrence of a certain set of indices (i, j, k) (described in the text), when excluding $(i, j, k) = (0, 0, 0)$, and the *thicker curves* show the occurrences for $(i, j, k) = (1, 0, 0)$, $(i, j, k) = (2, 1, 1)$, and $(i, j, k) = (4, 2, 1)$, whereas $(i, j, k) = (4, 4, 4)$ is not found in this size range

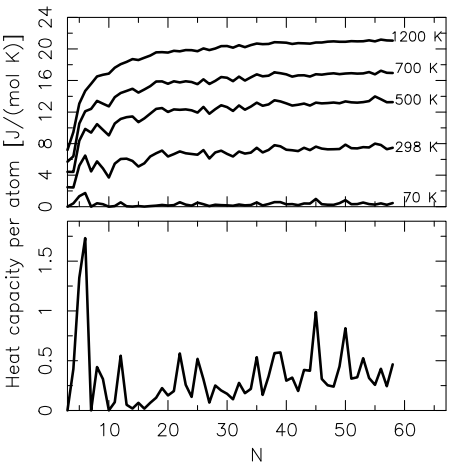

Fig. 10.8 The vibrational contribution to the heat capacity per atom for different temperatures (given in the *upper panel*) as function of the size of the clusters. The *lower panel* shows an expanded version of the results for 70 K

we show in Fig. 10.8 the heat capacity per atom of the Au_N clusters for temperatures of 70, 298.25, 500, 700, and 1200 K. We observe a strong size dependence of the vibrational heat capacity per atom in particularly for the smallest clusters and lowest temperatures. That this is so can be understood from Eqs. (10.7) and (10.9). Thus, for the highest temperatures the vibrational heat capacity per atom approaches $(3 - \frac{6}{N})k_B$ for non-linear clusters, which is smooth and monotonically increasing as a function of N and converges to $3k_B$ for $N \to \infty$. On the other hand, for a low temperature, T, only those clusters for which there exist one or more vibrational modes with characteristic temperatures $T_i < T$ will have significant heat capacities.

An interesting issue is whether a correlation between stability and heat capacity exists. One may speculate that clusters that are particularly stable (unstable) also are particularly rigid (soft), i.e., have particularly high (low) vibrational frequencies. That would imply that the heat capacity then has a minimum (maximum) for those clusters. Since, in Fig. 10.8, the results for $T = 70$ K are those that show the most pronounced size dependence, we shall use those in comparing with the stabil-

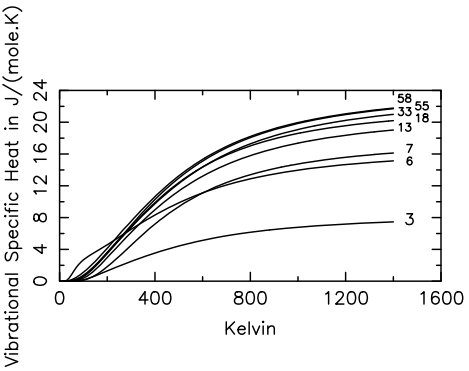

Fig. 10.9 Heat capacity as a function of temperature for clusters of different size

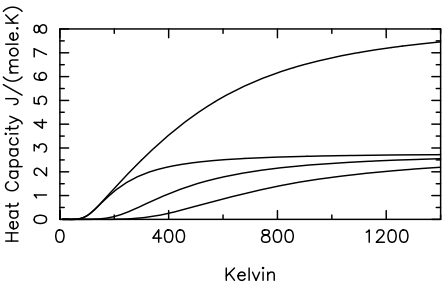

Fig. 10.10 The temperature dependence of the individual modes (*thin curves*) to the total vibrational heat capacity (*thick curve*) for the $N = 3$ cluster

ity function of Fig. 10.2. Then, it is clearly seen that there is no correlation between stability and heat capacity. Thus, the largest values for the heat capacity are found for $N = 5$ and 6, for which, however, the stability function does not show any pronounced minima. On the other hand, the most stable clusters according to Fig. 10.2 are found for $N = 42$ and 51, for which the heat capacity has average values.

Next we study the temperature dependence of the vibrational heat capacity, C_{vib}, of individual clusters. Accordingly, Fig. 10.9 shows the heat capacity as function of temperature for the cluster sizes 3, 6, 7, 13, 18, 33, 55, and 58. As expected and in agreement with Eqs. (10.7) and (10.8), for each size, C_{vib} is a monotonously increasing function of temperature. An interesting result is that the heat capacity for $N = 6$ is a much more rapidly increasing function of temperature at low temperature than is the case for other cluster sizes. In order to explain this, we first observe that the heat capacity is a superposition of the contributions of the individual modes, whereby each mode gives a contribution that is a decreasing function of frequency. This is illustrated in Fig. 10.10 where we present the contributions from the three modes with non-vanishing frequencies for the cluster size $N = 3$. For low temperatures, the modes with the lowest frequencies or lowest characteristic temperatures [see Eq. (10.8)] are the most important for C_{vib}. By plotting the characteristic temperatures as a function of cluster size (this is done in Fig. 10.11) we can identify those clusters that have a particularly large value C_{vib} at low temperatures as those that have modes with particularly low characteristic temperatures. As seen in the figure, this is the case for $N = 5, 6, 12, 22, 25, 32, 35, 38, 39, 40, 45, 50, 51$, and 53,

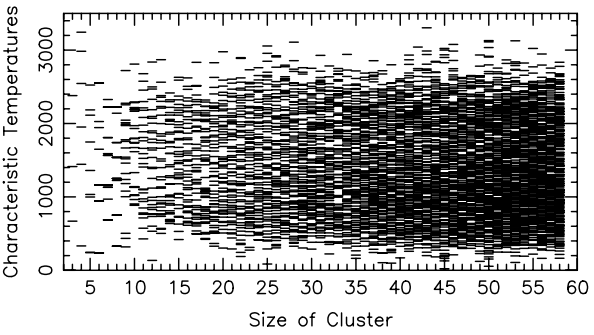

Fig. 10.11 The characteristic temperatures for the different vibrational modes as function of the size, N, of the clusters. For a given N, *each line* marks that at least one mode has that characteristic temperature

which agrees well with the cluster sizes for which C_{vib} is particularly large (see the lower panel in Fig. 10.8).

The reason that the $N = 6$ cluster has a mode with a particularly low frequency can be explained by considering its structural and vibrational properties in detail. As mentioned above, the $N = 6$ size cluster has a planar structure, and this planar structure results in energetically low-lying wagging modes (see [25]). Since it is known that also slightly larger clusters have planar structure, we suggest that also these larger clusters will have particularly large heat capacities at low temperatures.

10.4 Summary

In this work, we have used a parametrized density-functional method combined with genetic algorithms to systemically study the properties of the global total-energy minima of gold clusters with size from 2 to 58 atoms. The use of an approximate total-energy method allows us to perform unbiased structure-determination studies also for larger clusters, although the approximations may lead to (smaller) inaccuracies in the final results. We believe, however, that our study will give the overall trends. As an extension of our earlier work we have developed a new method to calculate some thermodynamic properties of the clusters for low temperatures.

Our study shows that the gold clusters in general have a low symmetry and that for up to $N = 6$ the clusters are planar. For larger values of N our approach finds that the clusters have a three dimensional structure, although more accurate studies give that clusters with slightly more than 10 atoms should be planar. By analyzing the structures we find that the clusters do not resemble those with 1, 2, 3, or 4 atoms less, and that the clusters do not resemble fragments of the fcc crystal. The vibrational heat capacity of the gold clusters is found to be strongly size dependent at low temperatures and for the smallest clusters. This becomes less pronounced when the size and/or temperature increases. An interesting observation is that some structures have a particularly large vibrational heat capacity at low temperatures, and that this is not correlated with particularly high or low stability of those clusters.

Acknowledgements This work was supported by the German Research Council (DFG) through project Sp439/23.

References

1. Rossi G, Ferrando R (2006) Chem Phys Lett 423:17
2. Donnelly RA (1994) Chem Phys Lett 136:274
3. Wales DJ, Doye JPK (1997) J Phys Chem 101:5111
4. Deaven DM, Ho KM (1995) Phys Rev Lett 75:288
5. Morris JR, Deaven DM, Ho KM (1996) Phys Rev B 53:R1740
6. Deaven DM, Tit N, Morris JR, Ho KM (1996) Chem Phys Lett 256:195
7. Ge Y-B, Head JD (2004) Chem Phys Lett 398:107
8. Ge Y-B, Heas JD (2004) J Phys Chem B 108:6025
9. Joswig J-O, Springborg M (2003) Phys Rev B 68:085408
10. Baletto F, Ferrando R (2005) Rev Mod Phys 77:371
11. Fa W, Luo C, Dong J (2005) J Phys Rev B 72:205428
12. Schmidt M, Donger J, Hippler T, Haberland H (2003) Phys Rev Lett 90:103401
13. Calvo F, Spiegelman F (2004) J Chem Phys 120:9684
14. Breaux GA, Neal CM, Cao B-P, Jarrold MF (2005) Phys Rev Lett 94:173401
15. Dong Y, Springborg M (2007) J Phys Chem C 111:12528
16. Seifert G, Porezag D, Fraunheim Th (1996) Int J Quant Chem 58:185
17. Dong Y, Burkhart M, Veith M, Springborg M (2005) J Phys Chem B 109:22820
18. Goldberg DE (1986) Genetic algorithms in search optimization and machine learning. Addison-Wesley, Reading
19. Bowman JM (1986) Acc Chem Res 19:202
20. Hunnycutt JD, Andersen AC (1987) J Phys Chem 91:4950
21. Clarke AS, Jónsson H (1993) Phys Rev E 47:3795
22. Faken D, Jónsson H (1994) Comput Mater Sci 2:279
23. Bulusu S, Li X, Wang L-S, Zeng XC (2006) Proc Natl Sci 103:8326
24. Dong Y, Springborg M, Pang Y, Morillon FM. Comput Theor Chem, in press. doi:10.1016/j.comptc.2013.06.004
25. Dong Y, Springborg M, Warnke I (2011) Theor Chem Acc 130:1001

Chapter 11
An Evaluation of Density Functional Theory for CO Adsorption on Pt(111)

Yu-Wei Huang, Ren-Shiou Ke, Wei-Chang Hao, and Shyi-Long Lee

Abstract In this study, serveal different density functionals were applied to study the CO adsorption on Pt(111) clusters. When adding more contribution of HF exchange energy, it can be found that the HOMO energy is decreased and LUMO energy is increased, thus increasing the HOMO-LUMO energy gap. The accuracy of S-T excitation energy can also be largely improved when increasing the ratio of HF exchange energy. For CO adsorption at Pt_{7-3} cluster, most functionals predict that CO favors to adsorb at fcc site. Only when adding more than 40 % HF exchange energy, the M06HF, BMK, wB97 and M06-2X functionals can predict the top-site preference. For CO adsorption at Pt_{9-9-9} cluster, when adding more than 40 % HF exchange energy, the CO prefers to adsorb at top site than fcc site. Among these functionals, the M06HF strongly predicts the top-site preference. The chemical bonding analysis shows that the effects of σ-repulsion are reduced as the CO S-T excitation energy increasing, and the effect of reduction for CO at top site is more remarkable than that for CO at fcc site. Therefore, CO would more favor to adsorb at top site in those functionals which can give better CO S-T excitation energy. Although the opposite trend can be found for the π-attraction, the overall effect also supports CO favoring to adsorb at top site.

11.1 Introduction

The CO adsorption on Pt surface has been studied extensively with great academic and industrial interest because it is an important step of various CO catalytic reactions, such as CO oxidation, hydrogenation, Fischer-Tropsch reaction, and many others [1, 2]. Due to its importance, the adsorption behaviors of CO on Pt have been investigated not only experimentally but also theoretically [3–47]. Especially, CO adsorption on Pt(111) has been long known as a puzzle and attracted much attention in surface science [9]. Experimentally, low-energy electron diffraction (LEED) and electron energy loss spectroscopy (EELS) indicates that the top site is favored for

S.-L. Lee (✉)
Department of Chemistry and Biochemistry, National Chung-Cheng University, Chia-Yi 621, Taiwan
e-mail: chesll@ccu.edu.tw

M. Hotokka et al. (eds.), *Advances in Quantum Methods and Applications in Chemistry, Physics, and Biology*, Progress in Theoretical Chemistry and Physics 27,
DOI 10.1007/978-3-319-01529-3_11,

CO adsorption on Pt(111) surface at low coverage [34]. However, theoretically the density functional theory calculation based on LDA and GGA failed to predict the correct adsorption site for CO on Pt(111) [9]. Up to now, it is still hard to find a suitable and complete DFT functional to solve this puzzle. In this study, we would like to evaluate the performance of computational schemes including 21 different density functionals, HF and MP2 for CO adsorption on Pt(111) cluster model. The chemical bonding analyses were also adopted to investigate the effect of DFT functionals to the adsorption behavior of CO on Pt nanocluster.

Investigations of CO on Pt(111) by using density functional theory has been long back to early 90's. Philipsen et al. applied the BP86 [48] functional to calculate CO adsorption on Pt(111) surface showing that the adsorption energies are 0.83 and 1.02 eV for CO adsorption on top site and hollow site [43]. Lynch et al. applied the PW91 [49] functional with ultrasoft pseudopotentials to calculate the CO/Pt(111) obtaining the adsorption energies of 1.87 and 2.00 eV for CO adsorption at top and fcc sites, respectively [25]. Both results did not agree with the experimental observation. In order to check this problem of site preference, Feibelman et al. considered different DFT functionals including LDA [50], PW91, PBE [51] and RPBE [52], and different numerical condition to calculate the CO on Pt(111) surface [9]. However, all LDA and GGA functionals predicted the wrong site preferences and then coined this interesting problem, "CO/Pt(111) puzzle". Since then this "puzzle" has been addressed and studied further by several groups [7, 14, 16, 19, 20, 23, 26, 30, 31, 37, 44].

Grinberg et al. carefully studied the influence of pseudopotentials and DFT functional on the CO binding energy and site preference [16]. Their results show the wrong prediction of site preference was due to the poor treatment of CO bonding for LDA and GGA functional. Gil et al. applied several different GGA and hybrid-GGA B3LYP [53] to calculate CO adsorption on Pt clusters [14]. The results show that the inaccuracy in site preference may come from the underestimation of unoccupied CO $2\pi^*$ orbital by DFT-GGA, which leads to the unrealistic strengthening of the $2\pi^*$-d bonding interaction. Kresse and co-workers also report that a linear relationship between the CO LUMO energy and the top-hollow adsorption energy difference by using slab model [23]. Mason et al. also found out the relationship between singlet-triplet excitation and adsorption energy [26]. These results all implied that the CO/Pt(111) puzzle may be attributed to the incorrect underestimation of CO LUMO energy in the conventional LDA or GGA DFT schemes. Therefore, the modification of the CO LUMO energy by improving the DFT functional may be a feasible way to solve this puzzle.

On the other hand, Gil et al. applied the B3LYP and cluster model to study the CO adsorption on Pt(111) and also compared their results with other LDA/GGA functional and slab model [14]. They found that both slab and cluster models, irrespective of the functionals used, always favor CO adsorption at hollow site than at top site. However, the B3LYP functional can largely reduce the adsorption energy difference between the top site and hollow site. The predicted adsorption energies under the B3LYP and Pt_{12-6} cluster model are 1.42 and 1.49 eV for CO adsorption at top and fcc sites. They also found that the CO LUMO energy increased when

including more exact HF exchange contribution, and thus may improve the results for the site preference of CO adsorption. By adopting the slab model calculation with hybrid B3LYP functional, Doll described better LUMO property and successfully predicted top-CO adsorption preference [7]. The adsorption energies are 1.44 and 1.40 eV for CO at top and fcc sites, respectively. However, the energy splitting between top site and fcc site is still too small and hard to confirm the experimental observation. Similar results are also reported by Stroppa et al. who apply hybrid PBE0 [54] and HSE03 [55] methods in the CO/Pt(111) slab model calculation with the plane wave basis set [35]. Although hybrid-GGA functionals can improve the results of site preference, it still cannot reproduce experimental observation in most case. Hence, the CO/Pt(111) puzzle is still a unsolved problem up to now.

Recently many new density functionals were developed for different purpose. For instance, Truhlar et al. developed M-series hyper-GGA functionals which are better than conventional hybrid functionals in thermodynamics and kinetics calculations [56–63]. Boese et al. developed the hyper BMK functional which includes the kinetic energy term and a large percentage of Hartree-Fock (HF) exchange energy (42 %). Zhao et al. has also tested the performance of these DFT functionals, the results show that BMK, M052X, M062X and M06HF owns the better performance in the calculation of excitation energies of CO [63].

Therefore, in this study, we would like to apply various density functional theory including LDA, GGA, meta-GGA, hybrid-GGA and hyper-GGA to calculate CO adsorption on Pt(111) cluster model. Through the chemical bonding analysis, the effect of different functionals to CO adsorption behavior on Pt(111) cluster can be clearly presented.

In Sect. 11.2, a brief description of the computational method and cluster construction are given. In Sect. 11.3, the results and discussion of the adsorption energies and chemical bonding analyses on CO/Pt(111) cluster for different DFT functionals are presented. Conclusions are drawn in the final section.

11.2 Computational Method

In this study, the density functional theory (DFT) and the wavefunction theory (WFT) were performed with the program package Gaussian 09 [64]. Several density functionals, including LDA (SVWN) [50], GGAs (BLYP [65], PBE, PW91, B97D [66] and BP86, meta-GGA (M06-L) [59] and hybrid-GGAs (HSE03, HSE06, B3PW91 [53], PBE0, B3LYP, B1B95 [67], BHandHLYP [68], BHandH [68], wB97 [69], wB97X [69], M052X [58], M062X [63], M06HF [61], BMK), were adopted to check the effect of exchange-correlation functional on computed CO adsorption energy on Pt(111). The wavefunction theory HF and MP2 were also applied for the comparison. The LANL2DZ basis set as well as effective core potentials was used for Pt atom [70]. In our previous study, several different basis sets including 6–31G, 6–31G*, 6–31 + G, 6–31 + G*, 6–311G, 6–311G*, 6–311 + G and 6–311 + G*, were adopted to check the effect to CO properties. Among these

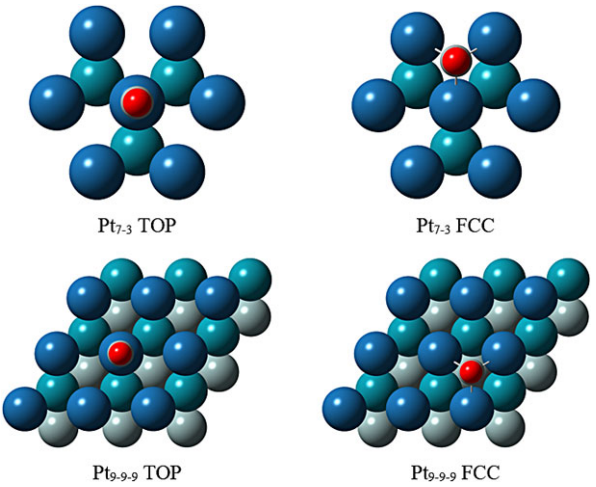

Fig. 11.1 The adsorption geometries of CO on two-layer Pt_{7-3} and three-layer Pt_{9-9-9} cluster models

basis sets, the 6–31G* can predict the better CO LUMO properties. Due to this reason and consideration of CPU cost, the 6–31G* basis set was chosen for CO molecule in all calculations. Although the effect of spin multiplicity is important in cluster calculation, it would be an artifact when adopting to mimic Pt(111) surface if lacking detailed examination. Hence, all calculations on Pt nanocluster are spin-unpolarized.

In order to simulate the Pt surface structure, geometry parameters for Pt clusters are fixed in bulk platinum geometry with the Pt-Pt distance of 2.775 Å, calculated from the experimental lattice constant 3.92 Å over the square root of 2. Two different size Pt clusters, Pt_{7-3} and Pt_{9-9-9}, are used as model systems and shown in Fig. 11.1.

Due to the convergence problem for LDA, GGA and meta-GGA functionals, only the hybrid-GGA functionals were adopted to calculate the CO on Pt_{9-9-9} cluster. The adsorption energy E_{ads} is obtained according to

$$E_{ads} = E_{Pt-CO} - E_{Pt} - E_{CO} \tag{11.1}$$

where E_{Pt-CO} is the total energy of CO-adsorbed Pt clusters, E_{Pt} is the total energy of Pt cluster, and E_{CO} is the total energy of CO molecule.

The surface atom-projected density of states and overlap population density of states were computed based on the orbital analysis of Mulliken formulation by using the AOMIX software 6.5 [71, 72]. The projected d-band center E_{dbc} is defined as

$$E_{dbc} = \frac{\sum_{i \in \text{d-band}} E_i P_{E_i}}{\sum_{i \in \text{d-band}} P_{E_i}} \tag{11.2}$$

where the E_i is the i-th orbital energy of metal cluster and P_{E_i} is the projected proportion of specific metal orbitals.

Table 11.1 The calculated singlet-triplet excitation, HOMO, LUMO, HOMO-LUMO energies (eV) and electronic dipole moment (Debye) of CO and the ratio of HF exchange (%) for several wavefunction theories (WFT) and density functional theories (DFT)

Level	Method	E_{S-T}	[a]E_{S-T}^{err}	E_{HOMO}	E_{LUMO}	$E_{LUMO-HOMO}$	E_x^{HF}	μ_e
WFT	MP2	6.41	0.09	−14.97	4.14	19.11	100	0.188
WFT	HF	5.19	−1.13	−14.86	4.57	19.43	100	−0.264
Hybrid	M06HF	6.29	−0.03	−14.61	3.17	17.77	100	−0.068
Hybrid	BMK	6.12	−0.20	−11.47	0.57	12.04	42	−0.001
Hybrid	M052X	6.11	−0.21	−12.10	1.16	13.26	56	−0.032
Hybrid	wB97	6.03	−0.29	−13.40	2.59	15.99	100	0.022
Hybrid	M062X	5.99	−0.33	−11.91	1.08	13.00	54	−0.002
Hybrid	wB97X	5.93	−0.39	−13.09	2.26	15.35	100	0.025
Hybrid	BHandH	5.92	−0.40	−11.85	1.30	13.15	50	−0.025
Hybrid	BHandHLYP	5.91	−0.41	−12.10	1.21	13.31	50	−0.064
Hybrid	B1B95	5.90	−0.42	−10.43	−0.03	10.40	28	0.039
Hybrid	B3LYP	5.83	−0.49	−10.11	−0.59	9.51	20	0.060
Hybrid	PBE0	5.71	−0.61	−10.40	−0.27	10.13	25	0.063
Hybrid	B3PW91	5.71	−0.61	−10.14	−0.61	9.53	20	0.068
Hybrid	HSE03	5.70	−0.62	−10.27	−0.92	9.35	25	0.057
Hybrid	HSE06	5.70	−0.62	−9.98	−0.67	9.31	25	0.062
mGGA	M06L	5.66	−0.66	−9.07	−1.42	7.65	0	0.068
GGA	BP86	5.70	−0.62	−8.76	−1.79	6.97	0	0.144
GGA	B97D	5.68	−0.64	−8.70	−1.59	7.12	0	0.103
GGA	PW91	5.64	−0.68	−8.66	−1.71	6.95	0	0.165
GGA	PBE	5.64	−0.68	−8.60	−1.66	6.94	0	0.172
GGA	BLYP	5.73	−0.59	−8.51	−1.55	6.96	0	0.144
LDA	SVWN	5.86	−0.46	−9.13	−2.31	6.82	0	0.186
Exp.		6.32						0.123

[a]The error of singlet-triplet excitation energies comparing with the experimental result of 6.32 eV

11.3 Results and Discussion

11.3.1 The Properties of CO

Table 11.1 shows the computed single-triplet (S-T) excitations, HOMO, LUMO, HOMO-LUMO energies and electronic dipole moment of CO and the ratio of HF exchange energy by HF, MP2 and 21 different level density functional theories. Performance of DFT on excited states can be revealed by examining the S-T excitation

energies. As can be seen in Table 11.1, the HF method strongly underestimates the S-T excitation energy as compared to the experimental value of 6.32 eV [73]. After considering the second order perturbation correction, the error of S-T excitation energy for MP2 is largely reduced to 0.09 eV. For the density functional theories, the error of S-T excitation energy at LDA (SVWN) is −0.46 eV.

For the GGA and meta-GGA functionals, the error of S-T excitation energies is increased to ca. −0.65 eV. For the hybrid GGA functionals, the errors of S-T excitation at functionals with low ratio of HF exchange energy, like HSE03, HSE06, B3PW91 and PBE0 are only slightly reduced by ca. 0.03 eV. Increasing the ratio of HF exchange energy, the accuracy of S-T excitation energy can be largely improved. It can be found that the S-T excitation energy of M06HF agrees excellently well with the experimental value.

The electronic dipole moment of CO was also collected in Table 11.1. As is well known [74], the HF method predicts wrong sign of CO dipole moment and MP2 method overestimates the CO dipole moment comparing with the experimental value of 0.123 D [75]. It can also be found that the LDA and GGA functionals all overestimate the CO dipole moment except for B97D. However, the meta-GGA and hybrid functional all underestimates the CO dipole moment. When adding more than 40 % HF contribution, it can be found most functionals predict wrong sign of CO dipole moment except for wB97 and wB97X.

It is well-known that DFT schemes of LDA and GGA levels give a poor description of CO LUMO. As can be seen in Table 11.1, LDA and GGA levels give a negative energy for CO LUMO. By adding the HF exchange contribution, the hybrid functional can raise the LUMO energy, lower the HOMO energy, and thus increase the HOMO-LUMO gap. This is important as the CO LUMO energies become positive after adding more than 40 % HF contribution in exchange-correlation functionals. It can also be found that the linear relationship exists between HOMO-LUMO gap and S-T excitation energy except only for the case of HF which the HOMO-LUMO gap is high but the S-T excitation energy is far from the experimental value.

11.3.2 The Properties of Pt_{7-3} and Pt_{9-9-9} Clusters

Performance of DFT on metal clusters has long been an intense subject however the accurately calculating properties of metal cluster has been shown to be problematic [76]. Here HF, MP2 and 21 DFT schemes were adopted to calculate the electronic structure of Pt clusters. To understand the effect of functionals to the electronic structure of Pt clusters, the projected d-band center (DBC) energy is analyzed. According to the adsorption position and symmetry, the projected d-band center energies for one Pt atom at top site and three Pt atoms at fcc site, and the σ/π-projected DBC energies at top site are considered. Figure 11.2 shows the projected DBC as respect to the ratio of HF exchange energy for Pt_{7-3} and Pt_{10-6} cluster. As can be seen in Fig. 11.2, the projected DBC energies are strongly dependent on the

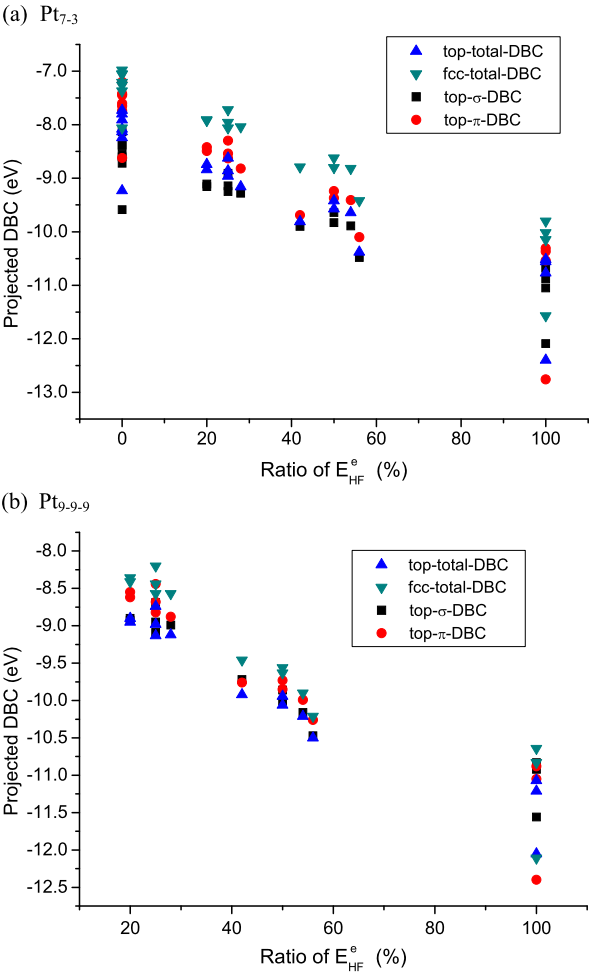

Fig. 11.2 The projected d-band center energies for (**a**) $Pt_{7–3}$ and (**b**) $Pt_{9–9–9}$ clusters as respect to the ratio of HF exchange energy

ratio of HF exchange energy. When increasing the ratio of HF exchange energy, the projected DBC energies are decreased. Our results also show that the top-DBC energies are ca. 0.9 and 0.4 eV smaller than the fcc-DBC energies except for the case of M06HF in $Pt_{9–9–9}$. For M06HF, the top-DBC energy is almost the same with the fcc-DBC energy. As a reasonable expectation, the top-DBC energy should be the same with the fcc-DBC energy in real extended Pt surface, and thus the M06HF can give the better description among the 21 functionals used in this study. Comparing the σ-top-DBC and π-top-DBC energies, it can be found that the σ-top-DBC energy is higher than the π-top-DBC energy in most cases. However, the differences between σ-top-DBC and π-top-DBC energies are reduced as increasing Pt cluster size and adding more ratio of HF exchange energy. For the case of M06HF in $Pt_{7–3}$ and M06HF, BMK, wB97 and wB97X in $Pt_{9–9–9}$, the π-top-DBC energies become higher than the σ-top-DBC energies.

Table 11.2 The adsorption energies (eV) for CO on Pt_{7-3} by using several wavefunction theories (WFT) and density functional theories (DFT)

Level	Method	E_{TOP}	E_{FCC}	$E_{TOP-FCC}$
WFT	MP2	−2.70	−2.79	0.09
WFT	HF	−1.09	−0.86	−0.23
Hybrid	M06HF	−1.62	−1.48	−0.14
Hybrid	BMK	−2.68	−2.46	−0.22
Hybrid	M052X	−1.93	−2.47	0.54
Hybrid	wB97	−1.83	−1.22	−0.61
Hybrid	M062X	−1.76	−1.35	−0.41
Hybrid	wB97X	−1.85	−2.28	0.43
Hybrid	BHandH	−2.70	−3.12	0.42
Hybrid	BHandHLYP	−1.78	−1.89	0.11
Hybrid	B1B95	−1.88	−2.46	0.58
Hybrid	B3LYP	−1.50	−1.83	0.33
Hybrid	PBE0	−1.82	−2.49	0.67
Hybrid	B3PW91	−1.64	−2.20	0.56
Hybrid	HSE03	−1.76	−2.38	0.62
Hybrid	HSE06	−1.77	−2.35	0.58
mGGA	M06L	−1.56	−2.00	0.44
GGA	BP86	−1.64	−1.91	0.27
GGA	B97D	−2.24	−2.27	0.03
GGA	PW91	−1.81	−2.18	0.37
GGA	PBE	−1.79	−2.17	0.38
GGA	BLYP	−1.26	−1.38	0.12
LDA	SVWN	−2.76	−3.48	0.72

11.3.3 The CO Adsorption on Pt Clusters

Table 11.2 collects the adsorption energies of CO on Pt_{7-3} for HF, MP2 and 21 different level density functional theories. It is found that HF method predicts CO adsorption favoring at top site than at fcc site. However, the MP2 method predicts that the adsorption strengths at both sites are almost the same. For the LDA (SVWN), it can be found that the CO strongly favors to adsorb at fcc site than at top site, and the predicted adsorption energies are strongly overestimated compared to the experimental value of ca. 1.0–1.3 eV at top site.

For the GGA and meta-GGA, the adsorption energies and energy differences between top and fcc sites are both reduced comparing with these obtained at LDA level. Among these functionals, the energy differences between top and fcc sites for

Table 11.3 The adsorption energies for CO on Pt_{9-9-9} by using 14 hybrid density functional theories

Level	Method	E_{TOP}	E_{FCC}	$E_{TOP-FCC}$
Hybrid	M06HF	−1.37	−0.41	−0.96
Hybrid	BMK	−1.40	−1.21	−0.19
Hybrid	M052X	−1.35	−1.15	−0.20
Hybrid	wB97	−1.32	−1.12	−0.20
Hybrid	M062X	−1.29	−1.29	0.00
Hybrid	wB97X	−1.26	−1.23	−0.03
Hybrid	BHandH	−1.96	−1.95	−0.01
Hybrid	BHandHLYP	−1.01	−0.81	−0.20
Hybrid	B1B95	−1.44	−1.61	0.17
Hybrid	B3LYP	−1.13	−1.12	−0.01
Hybrid	PBE0	−1.53	−1.70	0.17
Hybrid	B3PW91	−1.33	−1.47	0.14
Hybrid	HSE03	−1.46	−1.61	0.15
Hybrid	HSE06	−1.47	−1.61	0.14

BLYP and B97D are 0.12 and 0.03 eV, respectively, smaller than those for other GGA and meta-GGA functionals. For the hybrid functionals with low ratio of HF exchange energy, the energy differences between top and fcc sites are increased comparing with those at GGA level. It can also be found that the energy difference between top and fcc sites for B3LYP method is smaller than those for other functionals with low ratio of HF exchange energy. When increasing the ratio of HF exchange energy more than 40 %, half of the 8 DFT schemes, i.e., M06HF, BMK, wB97 and M062X functionals, give the correct site preference of CO adsorption.

In order to further check the effects of geometry relaxation, the symmetry-constrained optimization was adopted for CO on Pt_{7-3} [77], which the Pt^{7-3} cluster can be freely relaxed but still maintains the C_{3V} symmetry. The results show that adsorption energies are −1.30 and −1.59 eV for CO adsorption at top and fcc sites, respectively by using B3LYP functional, and −1.83 and −1.04 eV for CO adsorption at top and fcc, respectively by using BMK functional. It can be found that the site preference is still not changed when considering the effect of geometry relaxation.

Table 11.3 shows the adsorption energies for CO on Pt_{9-9-9} for 14 different hybrid density functionals. Comparing with the results of Pt_{7-3}, it can be found that the adsorption energies are reduced for all functionals. For functionals with low ratio of HF exchange energy, the energy differences are ca. 0.15 eV favoring fcc site except B3LYP which predicts no site preference for CO adsorption. When increasing the ratio of HF exchange more than 40 %, it can be found that the CO prefers to adsorb at top site than fcc site in most functionals. Comparing with other functionals, the M06HF strongly predicts the top-site preference.

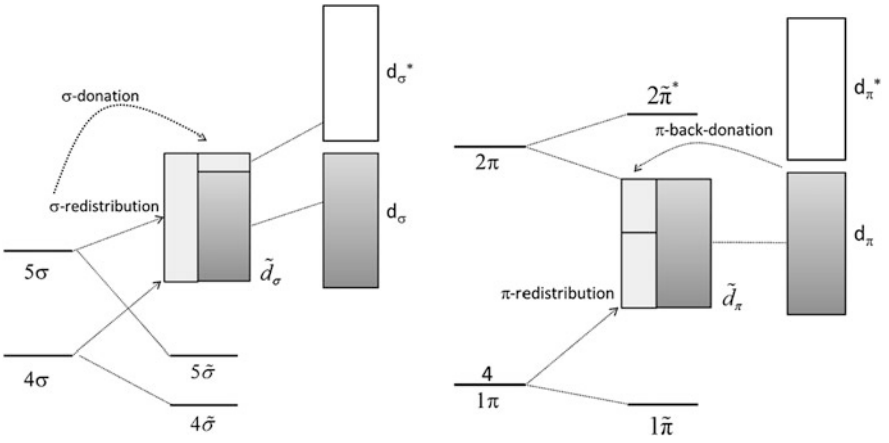

Fig. 11.3 The bonding model for CO adsorption on Pt cluster

Alaei et al. have reported that the CO adsorption on Pt(111) by using the PBE and BLYP functional [44]. Their results show that BLYP functional own the better preference to deal with the CO/Pt(111) puzzle comparing with PBE functional. It can be seen from Table 11.3 that B3LYP and BHandHLYP functionals predict the top-site preference for CO adsorption while PBE0 and HSE03/06 give fcc preference. Our results also agree with their point.

11.3.4 The Bonding Analysis for CO on Pt Clusters

In order to further analyze the effect of density functionals to CO adsorption behavior on Pt clusters, the chemical bonding analyses were considered. The bonding model between CO and Pt surface was firstly proposed by Blyholder based on the frontier orbital theory [78]. According to the frontier orbital theory, the interaction between CO and metal surface can be separated into two parts. First one is a dative bond between CO HOMO 5σ and metal empty d-band. The second is the π-back donation from filled Pt d-band to CO LUMO $2\pi^*$ orbital. Some experimental and theoretical evidence shows that 1π and 4σ levels should also have contribution for CO-metal bonding [4, 45–47]. A latest bonding model was proposed by Nilsson and Föhlisch et al. combining the X-ray emission spectroscopy and density functional theory [10, 11, 79, 80]. They proposed the π-attraction σ-repulsion model to explain the behavior of CO adsorption on metal surface. As can be seen in Fig. 11.3, the CO 1π and $2\pi^*$ orbitals can interact with the metal sp- and d-band and form the tilde-type hybrid CO-metal orbitals $1\tilde{\pi}$, $2\tilde{\pi}^*$ and $\tilde{d}_\pi$. Comparing with the Blyholder model, the π–σ model includes the contribution of 1π orbital and does not assume the direct back-donating from metal to CO. For the σ repulsion in the π–σ model, the CO 4σ and 5σ-orbitals can mix with the metal sp- and d-band and form

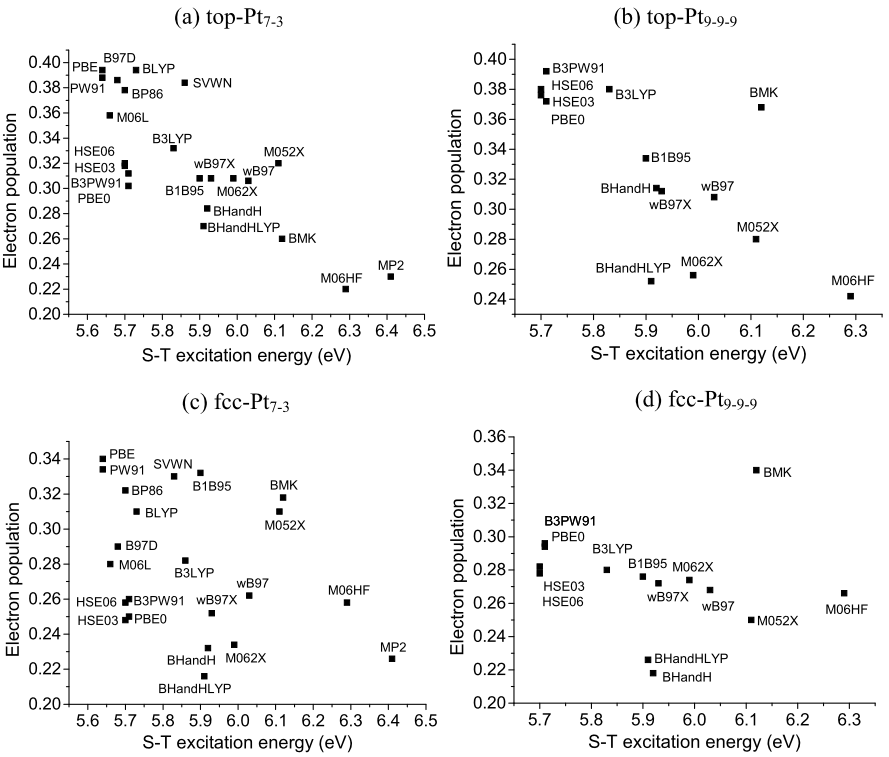

Fig. 11.4 The redistributed σ-electrons population with respect to the singlet-triplet excitation energy of CO adsorbed at (**a**) top-Pt_{7-3}, (**b**) top-Pt_{9-9-9}, (**c**) fcc-Pt_{7-3} and (**d**) fcc-Pt_{9-9-9}

the tilde-type orbitals $4\tilde{\sigma}$, $5\tilde{\sigma}$ and $\tilde{d}_{\sigma}$. The origin of the repulsion comes from the electron density redistribution in the CO region. Basing on the Nilsson and Föhlisch's model, we can examine the performance of different computation schemes on CO/Pt(111) adsorption.

In order to clarify the effect of density functionals, the charge contribution to adsorbed CO orbitals are collected under the π-attraction σ-repulsion model framework.

Figure 11.4 shows the redistributed σ-electron population respect to the CO S-T excitation energy. As can be seen in Fig. 11.4(a) for CO adsorption at top-Pt_{7-3}, the redistributed σ-electron population is decreased with the CO S-T excitation energy increasing. It clearly shows the effect of σ-repulsion for CO adsorption at top site is reduced as the CO S-T excitation energy increases. This trend can also be seen in Fig. 11.4(b) for CO adsorption at top-Pt_{9-9-9} except the case for BMK, M06-2X and BHandHLYP. It can be found that the BMK method predicts larger redistributed σ-electron population and M06-2X and BHandHLYP predict lower one.

Figure 11.4(c) shows the redistributed σ-electron population for CO adsorption at fcc-Pt_{7-3}. It can be found that the LDA and GGA functionals predict lager redistributed σ-electron population. Among these LDA and GGA functionals, BLYP and

B97D can predict smaller redistributed σ-electron population. Most hybrid functionals predicted redistributed σ-electron population within the range of 0.24–0.28. However, it can be found that BMK and M052X functionals predict higher redistributed σ-electron population ($\sim$0.31) and BHandH, M062X and BHandHLYP predict lower one ($\sim$0.22). The wavefunction methods HF and MP2 all predict quite low redistributed σ-electron population of 0.20 and 0.23, respectively. No observable relation between the redistributed σ-electron population and CO S-T excitation energy can be found for CO fcc-Pt_{7-3}.

As can be seen in Fig. 11.4(d) for CO adsorption at fcc-Pt_{9-9-9}, the redistributed σ-electron population only slightly decreases with the CO S-T excitation energy increasing except in the case for BMK, BHandHLYP and BHnadH functionals. The BMK functional gives higher redistributed σ-electron population and the BHandHLYP and BHnadH functionals gives lower one. Comparing with CO adsorption at top-Pt_{9-9-9}, it can be found that as the computed CO S-T excitation energy increasing, the reduction of σ-repulsion for top site is more observable than that for fcc site, and thus CO favors to adsorb at top site in those functionals which can give better CO S-T excitation energy.

Figure 11.5 shows the redistributed π-electron population as respect to the CO S-T excitation energy. As can be seen in Fig. 11.5(a) for CO adsorption at top-Pt_{7-3}, the LDA(SVWN) predict quite high redistributed π-electron population of 0.76. However, for most other GGA and hybrid functionals, the redistributed π-electron populations are within the range of 0.4–0.5. The PW91 and BP86 functionals predict higher redistributed π-electron population ($\sim$0.58) and BHandHLYP predicts lower one (0.34). For CO adsorption at top-Pt_{9-9-9}, as can be seen in Fig. 11.5(b), it can be found that the BHandHLYP predicts quite low redistributed π-electron population (0.38), but redistributed π-electron populations for most hybrid functionals are within 0.45–0.55. As can be seen in Fig. 11.5(c) that for CO adsorption at fcc-Pt_{7-3}, LDA and GGA functionals predict higher redistributed π-electron population comparing with hybrid functionals and WFT. For most hybrid functionals, the predicted redistributed π-electron population are within the range of 1.0–1.2 except for the case of BHandHLYP and M05-2X ($\sim$0.9). The predicted redistributed π-electron population for HF and MP2 are 0.70 and 0.99, respectively. As can be seen in Fig. 11.5(d) that for CO adsorption at fcc-Pt_{9-9-9}, it can be found that the B3PW91, PBE0, HSE03/06 and BMK functionals predict higher redistributed π-electron population, and BHandHLYP predicts lower one (1.05) comparing with other functionals. The predicted redistributed π-electron populations for most functionals are within the range of 1.15–1.28. No observable dependence between the redistributed π-electron population and CO S-T excitation energy can be found for CO adsorption at fcc-Pt_{9-9-9}.

Figure 11.6 shows the π-electron population transferred from metal with respect to the CO singlet-triplet excitation energy for CO adsorption at top site and fcc site on Pt_{7-3} and Pt_{9-9-9}. As can be seen in Fig. 11.6(a) that for CO adsorption at top-Pt_{7-3}, the transferred π-electron population is decreased with the CO S-T excitation energy increasing. Similar trends can also be seen in Fig. 11.6(b) that for CO adsorption at top-Pt_{9-9-9}. It implies that the effect of π-attraction through π-back bonding is reduced with the CO S-T excitation energy increasing. In contrast,

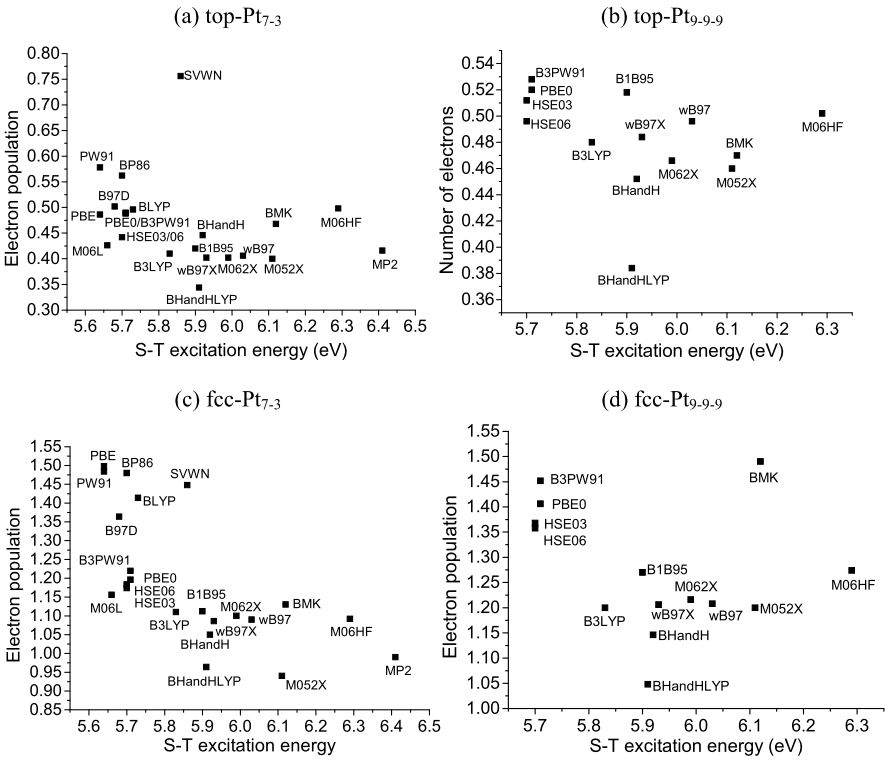

Fig. 11.5 The redistributed π-electron population of with respect to the singlet-triplet excitation energy for CO adsorbed at (**a**) top-Pt_{7-3}, (**b**) top-Pt_{9-9-9}, (**c**) fcc-Pt_{7-3} and (**d**) fcc-Pt_{9-9-9}

for CO adsorbed at fcc site on Pt_{7-3}, it can be seen in Fig. 11.6(c) that the transferred π-electron population is increased with the CO S-T excitation energy increasing. Similar trends can also be seen in Fig. 11.6(d) for CO adsorption at fcc-Pt_{9-9-9}. It implies that the effect of π-attraction through π-back bonding is enhanced with the CO S-T excitation energy increasing.

In summary, both the effects of σ-repulsion for CO adsorption at top and fcc sites are reduced with the CO S-T excitation energy increasing. However, the effect of σ-repulsion reduction for CO at top site is more remarkable than that for CO at fcc site. In contrast, the effect of π-attraction is reduced with the CO S-T excitation energy increasing for CO at top site, but enhanced for CO at fcc site. Even so, the overall effect also supports CO favor to adsorb at top site when increasing the CO S-T excitation energy.

11.4 Conclusion

Summarizing, we have evaluated the performance of HF, MP2 and 21 DFT functionals including LDA, GGA, meta-GGA, hybrid-GGA and hyper-GGA for CO ad-

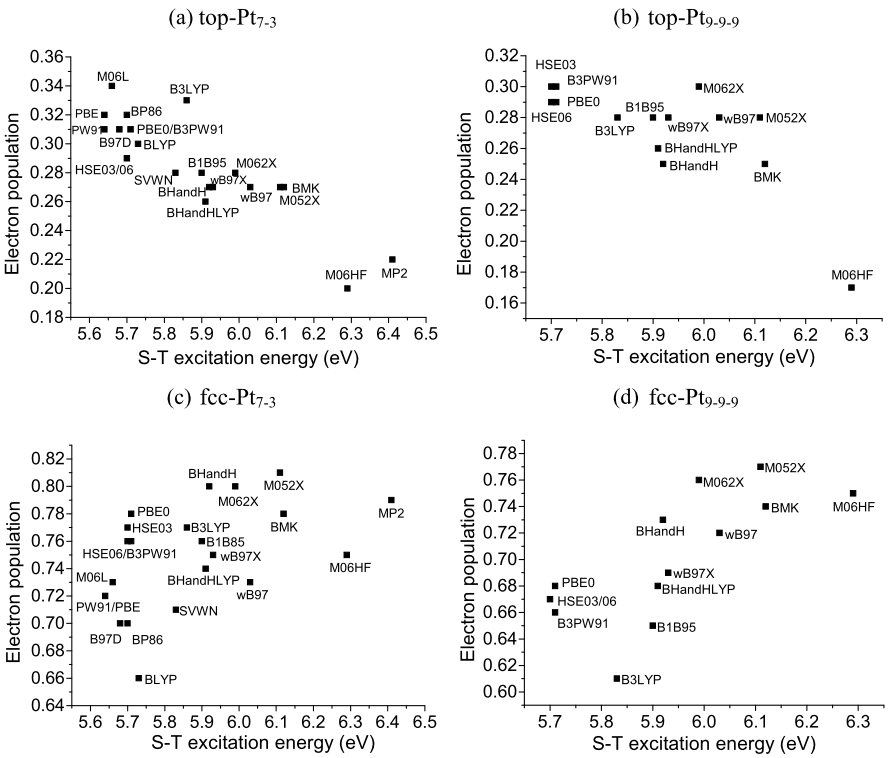

Fig. 11.6 The π-electron population transferred from metal with respect to the singlet-triplet excitation energy for CO adsorbed at (**a**) top-Pt_{7-3}, (**b**) top-Pt_{9-9-9}, (**c**) fcc-Pt_{7-3} and (**d**) fcc-Pt_{9-9-9}

sorption on Pt(111) cluster. When adding more contribution of HF exchange energy, it can be found that the HOMO energy is decreased and LUMO energy is increased, thus increasing the HOMO-LUMO energy gap. The accuracy of S-T excitation energy can also be largely improved when increasing the ratio of HF exchange energy.

For CO adsorption at Pt_{7-3} cluster, it can be found that LDA, GGA and meta-GGA all predict that CO favors to adsorb at fcc site. For the hybrid functionals with low ratio of HF exchange energy (<40 %), it still predicts the fcc-site preference. However, when adding more than 40 % HF exchange energy, half of the 8 DFT functionals, including M06HF, BMK, wB97 and M06-2X, predict the top-site preference.

For CO adsorption at Pt_{9-9-9} cluster, all the hybrid functionals with low ratio of HF exchange predict the fcc-site preference except the B3LYP functional. When adding more than 40 % HF exchange energy, it can be found that the CO prefers to adsorb at top site than fcc site. Among these functionals, the M06HF strongly predicts the top-site preference.

The chemical bonding analysis shows that the effects of σ-repulsion are reduced as the CO S-T excitation energy increasing, and the reduction of σ-repulsion for

CO at top site is more remarkable than that for CO at fcc site. Therefore, CO would more favor to adsorb at top site in those functionals which can give better CO S-T excitation energy. Although the opposite trend can be found for the π-attraction, the overall effect also supports CO favoring to adsorb at top site.

Acknowledgements Financial assistance from National Science Council, Taiwan is gratefully acknowledged. We are also grateful to the National Center for High-performance Computing, Hsinchu, Taiwan for computer time and facilities.

References

1. Dry ME (2002) Catal Today 71:227
2. Somorjai GA (1994) Introduction to surface chemistry and catalysis. Wiley, New York
3. Abild-Pedersen F, Andersson MP (2007) Surf Sci 601:1747
4. Bagus P, Nelin C, Bauschlicher C (1983) Phys Rev B 28:5423
5. Delbecq F (1997) Surf Sci 389:L1131
6. Dimakis N, Cowan M, Hanson G, Smotkin ES (2009) J Phys Chem C 113:18730
7. Doll K (2004) Surf Sci 573:464
8. Ertl G, Neumann M, Streit KM (1977) Surf Sci 64:393
9. Feibelman PJ, Hammer B, Nørskov JK, Wagner F, Scheffler M, Stumpf R, Watwe R, Dumesic J (2001) J Phys Chem B 105:4018
10. Föhlisch A, Nyberg M, Bennich P, Triguero L, Hasselström J, Karis O, Pettersson LGM, Nilsson A (2000) J Chem Phys 112:1946
11. Föhlisch A, Nyberg M, Hasselström J, Karis O, Pettersson LG, Nilsson A (2000) Phys Rev Lett 85:3309
12. Froitzheim H, Hopster H, Ibach H, Lehwald S (1977) Appl Phys 13:147
13. German ED, Sheintuch M (2008) J Phys Chem C 112:14377
14. Gil A, Clotea A, Ricart JM, Kresse G, García-Hernández M, Rösch N, Sautet P (2003) Surf Sci 530:71
15. Giuffrida S, Barone G, Duca D (2009) J Chem Inf Model 49:1223
16. Grinberg I, Yourdshahyan Y, Rappe AM (2002) J Chem Phys 117:2264
17. Heyden BE, Bradshaw AM (1983) Surf Sci 125:787
18. Hopster H, Ibach H (1978) Surf Sci 77:109
19. Hu Q-M, Reuter K, Scheffler M (2007) Phys Rev Lett 98:1
20. Huang Y-W, Lee S-L (2010) Chem Phys Lett 492:98
21. Jennison D, Schultz P, Sears M (1996) Phys Rev Lett 77:4828
22. Kelemen SR, Fischer TE, Schwarz JA (1979) Surf Sci 81:440
23. Kresse G, Gil A, Sautet P (2003) Phys Rev B 68:3
24. Liu W, Zhu YF, Lian JS, Jiang Q (2007) J Phys Chem C 111:1005
25. Lynch M, Hu P (2000) Surf Sci 458:1
26. Mason S, Grinberg I, Rappe A (2004) Phys Rev B 69:1
27. McCabe RW, Schmidt LD (1977) Surf Sci 65:189
28. Morikawa Y, Mortensen JJ, Hammer B, Nørskov JK (1997) Surf Sci 386:67
29. Norton PR, Goodale JW, Selkirk EB (1979) Surf Sci 83:189
30. Olsen RA, Philipsen PHT, Baerends EJ (2003) J Chem Phys 119:4522
31. Orita H, Itoh N, Inada Y (2004) Chem Phys Lett 384:271
32. Poelsema B, Palmer RL, Comsa G (1984) Surf Sci 136:1
33. Seebauer EG, Kong ACF, Schmidt LD (1986) Surf Sci 176:134
34. Steininger H, Lehwald S, Ibach H (1982) Surf Sci 123:264
35. Stroppa A, Termentzidis K, Paier J, Kresse G, Hafner J (2007) Phys Rev B 76:1

36. Surman M, Hagans PL, Wilson NE, Baily CJ, Russell AE (2002) Surf Sci 511:L303
37. Wang Y, de Gironcoli S, Hush NS, Reimers JR (2007) J Am Chem Soc 129:10402
38. Westerberg S, Wang C, Somorjai GA (2005) Surf Sci 582:137
39. Wong YT, Hoffmann R (1991) J Phys Chem 95:859
40. Yeo YY, Vattuone L, King DA (1997) J Chem Phys 106:392
41. Fielicke A, Gruene P, Meijer G, Rayner DM (2009) Surf Sci 603:1427
42. Collins DM, Spicer WE (1977) Surf Sci 69:85
43. Philipsen P, van Lenthe E, Snijders J, Baerends E (1997) Phys Rev B 56:13556
44. Alaei M, Akbarzadeh H, Gholizadeh H, de Gironcoli S (2008) Phys Rev B 77:085414
45. Allyn CL, Gustafsson T, Plummer EW (1977) Chem Phys Lett 47:127
46. Neumann H-JFaM (1988) Appl Phys A 47:3
47. Rogozik J, Dose V (1986) Surf Sci 176:847
48. Perdew JP, Yue W (1986) Phys Rev B 33:8800
49. Perdew JP, Chevary JA, Vosko SH, Jackson KA, Pederson MR, Singh DJ, Fiolhais C (1992) Phys Rev B 46:6671
50. Perdew JP, Zunger A (1981) Phys Rev B 23:5048
51. Perdew JP, Burke K, Ernzerhof M (1996) Phys Rev Lett 77:3865
52. Ernzerhof M, Perdew JP (1998) J Chem Phys 109:3313
53. Becke AD (1993) J Chem Phys 98:5648
54. Adamo C, Barone V (1999) J Chem Phys 110:6158
55. Heyd J, Scuseria GE, Ernzerhof M (2003) J Chem Phys 118:8207
56. Zhao Y, Chen F (2008) J Multivar Anal 99:215
57. Zhao Y, Schultz NE, Truhlar DG (2005) J Chem Phys 123:161103
58. Zhao Y, Schultz NE, Truhlar DG (2006) J Chem Theory Comput 2:364
59. Zhao Y, Truhlar DG (2006) J Chem Phys 125:194101
60. Zhao Y, Truhlar DG (2006) J Phys Chem A 110:13126
61. Zhao Y, Truhlar DG (2006) J Phys Chem 110:5121
62. Zhao Y, Truhlar DG (2008) J Chem Theory Comput 4:1849
63. Zhao Y, Truhlar DG (2008) Theor Chem Acc 120:215
64. Frisch GW, Schlegel HB, Scuseria GE, Robb MA, Pople JA et al Gaussian 09, Revision A.1 (Gaussian Inc, Wallingford CT2009)
65. Lee C, Yang W, Parr RG (1988) Phys Rev B 37:785
66. Grimme S (2006) J Comput Chem 27:1787
67. Becke AD (1996) J Chem Phys 104:1040
68. Becke AD (1993) J Chem Phys 98:1372
69. Chai J-D, Head-Gordon M (2008) J Chem Phys 128:084106
70. Hay PJ, Wadt WR (1985) J Chem Phys 82:299
71. Gorelsky SI, AOMix: program for molecular orbital analysis. University of Ottawa, version 6.5 2011. http://www.sg-chem.net/
72. Gorelsky SI, Lever ABP (2001) J Organomet Chem 635:187
73. Huber KP, Herzberg G (1979) Molecular spectra and molecular structure. IV. Constants of diatomic molecules. Van Nostrand-Reinhold, New York
74. Bak KL, Gauss J, Helgaker T, Jørgensen P, Olsen J (2000) Chem Phys Lett 319:563
75. Meerts WL, Leeuw FHD, Dymanus A (1977) Chem Phys 22:1557
76. Addicoat MA, Buntine MA, Metha GF, Gilbert ATB, Gill PMW (2007) J Phys Chem A 111:2625
77. Zhanpeisov NU, Fukumura H (2006) J Chem Theory Comput 2:801
78. Blyholder G (1964) J Phys Chem 68:2772
79. Nilsson A, Pettersson LGM (2004) Surf Sci Rep 55:49
80. Nilsson A, Weinelt M, Wiell T, Bennich P, Karis O, Wassdahl N, Stöhr J, Samant M (1997) Phys Rev Lett 78:2847

Chapter 12
Hydrogen in Light-Metal Cage Assemblies: Towards a Nanofoam Storage

Fedor Y. Naumkin and David J. Wales

Abstract Isomeric alternatives to usual metal-hydrides as hydrogen-storage materials are considered. Presented are results of ab initio calculations for Be_n ($n \leq 18$) clusters with up to two endohedral H_2 molecules which undergo in-cage dissociation. The systems structures and stabilities are discussed, including energy barriers for hydrogen exit from the cage. The origin of the observed metastability, allowing for a lower-temperature release of H_2, is explored. Preservation of the cage integrity and hydrogen confinement is investigated when such core-shell units are merged into larger assemblies structurally resembling fragments of hydrogen-filled metal nanofoams, possible isomeric forms of metal-hydride solid. Different "nanofoam" isomers are composed of pairs or single H atoms suspended electrostatically inside the metal cage units ("nanobubbles"). Interesting features include simultaneous exit of two H atoms, etc. Structural extrapolations suggest potential hydrogen storage capacity up to ~10 weight-%.

12.1 Introduction

Reliable storage of hydrogen with an easy release on demand is a bottleneck problem of hydrogen-based energy solutions. Solid metal hydrides (e.g. MgH_2) offer high capacity but are so far problematic due to strong metal-H bonds needing high temperature (>300 °C for MgH_2) for releasing H_2 [1].

Corresponding clusters face similar problem, while being smaller and less rigid, both factors reducing the hydrogen-desorption temperature—see, e.g., recent advances for MgH_2-related species [2, 3]. Another class of such systems is represented by mixed/doped metal clusters M_nA_k (M = Be, B, Al; A = Li, Na, Mg, B, P, etc.), both physi- and chemisorbing hydrogen [4–7]. Here the hydrogen binding energies can be close to estimated ideal ~0.5 eV [1], larger or smaller up to negative values (corresponding to metastable systems, e.g. for CAl_{12} or $SiAl_{12}$ substrates [6, 7]), usually with ad-/desorption barrier of ~1 eV.

F.Y. Naumkin (✉)
Faculty of Science, UOIT, Oshawa, ON L1H 7K4, Canada
e-mail: fedor.naumkin@uoit.ca

M. Hotokka et al. (eds.), *Advances in Quantum Methods and Applications in Chemistry, Physics, and Biology*, Progress in Theoretical Chemistry and Physics 27,
DOI 10.1007/978-3-319-01529-3_12,

In particular, H_2 encapsulated in small Mg_n cluster cages can form weakly bound or even metastable species, although with a low storage capacity (∼1 weight-%) [8]. In order to try to improve the situation, the present work has two aims: (1) investigate similar systems of a lighter metal, Be; (2) evaluate feasibility of merging them into assemblies as a step to material.

Previous relevant work includes modeling adsorption of atomic H on solid Be (see [9] and references therein). The desorption temperature for molecular hydrogen has been predicted as ∼450 °C, with the desorption energy of ∼1 eV, which is even higher than for bulk MgH_2. Another family of systems studied have been BeH_2 aggregates and "polymers" [10], for which species, however, the hydrogen desorption temperature or energy has not been specified. The present work employs the earlier results indicating cage isomers of small Be_n clusters as most stable [11].

12.2 Computational Methods and Tools

Calculations have been carried out at the MP2/aug-cc-pvtz level, followed by the standard counterpoise BSSE correction [12]. This level of theory is employed as implemented in the NWChem ab initio package [13], and is preferred due to capability to deal reliably with anticipated non-covalent interactions and strong charge-transfer in the systems studied.

The system geometries have been fully optimized for all atomic coordinates, with no constraints (for the C_1 symmetry). Vibrational frequencies have been calculated to verify local minima of energy. The Be_n cages have been preoptimized, then hydrogen molecules have been put inside with different orientations, and the system then reoptimized. The potential energy barriers (e.g. for hydrogen exit from the cages) were estimated by pulling H in proper direction (e.g. through a gap between Be atoms): an appropriate Be–H distance was fixed at a series of values and all the other coordinates were reoptimized for each displacement.

Higher-spin states have been checked to confirm the ground state multiplicity. Natural charges on atoms have been calculated using the natural bonding orbital formalism [14].

12.3 Results and Discussion

12.3.1 H_2@Be_n

It is found that H_2 molecule can be trapped inside small Be_n clusters starting from $n = 8$ [15]. In particular, this and $n = 10$ cages generally preserve their shapes enveloping the dihydrogen oriented along their symmetry axis. This is different from the analogous case of Mg_8 cage which changes its shape [8]. Inside the Be_9 cage, however, the inserted molecule is trapped perpendicular to the original symmetry

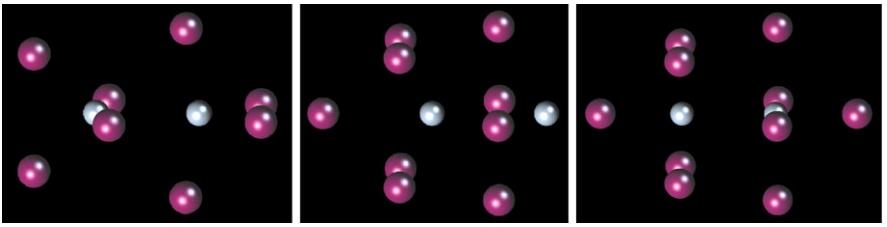

Fig. 12.1 Optimized geometries of $H_2@Be_8$, $H_2@Be_9$, $H_2@Be_{10}$

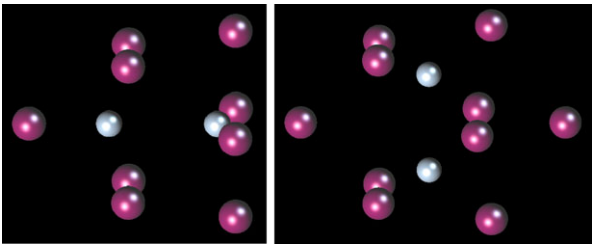

Fig. 12.2 Optimized geometries of higher-energy isomers of $H_2@Be_9$ and $H_2@Be_{10}$

axis of the cage which therefore transforms slightly, adopting a matching shape (capped square antiprism) now axially symmetric around the molecule. In all these cases, the H_2 molecule dissociates into H atoms suspended electrostatically (noncovalently) in the cage (Fig. 12.1).

For $n = 9$ one H atom protrudes from the cage, while adding another axial Be atom pushes it inside for $n = 10$. A higher-energy (by 1.7 eV relative to the isomer with the protruding H atom), "sunken" isomer of $H_2@Be_9$ has both H atoms inside the cage (Fig. 12.2), with a very low (∼0.04 eV) potential energy barrier separating this isomer from the more stable one. Another, "radial" isomer of $H_2@Be_{10}$ with the H_2 molecule perpendicular to the cage axis is 0.7 eV higher in energy (relative to the isomer with the axial orientation of H_2), with the potential energy barrier for turning the dihydrogen into axial orientation (in the lower-energy isomer) of only ∼0.06 eV.

The apparent reason for the H_2 molecule to dissociate is a considerable charge-transfer from the beryllium cage. According to calculations, each H atom is charged by −1.5e and −1.3e for $n = 8$ and 10, respectively. The high negative charge is apparently due to the number of Be atom neighbours donating the electron density. This charge is much larger than −0.15e for analogous $H_2@Mg_{10}$ [8], contrary to the opposite relation in the BeH and MgH diatoms as well as to the higher ionization energy of Be, but consistent with considerably shorter Be–H distances in $H_2@Be_n$. Accordingly, each Be atom is charged by +0.2e to +0.4e (Table 12.1).

For $n = 9$, the charge drops to −0.7e on the protruding H atom while remaining at −1.2e on the other one, the system asymmetry producing an axial dipole moment of 0.76 D. The two charges become about equal for the "sunken" isomer which, however, exhibits a fourfold dipole value of 3.1 D. The "radial" isomer of $H_2@Be_{10}$ is also slightly polar (0.35 D) due to the introduced slight asymmetry.

Table 12.1 Equilibrium parameters (in eV and Å) and atomic charges (in e) of $H_2@Be_n$

System	D_e^{total}/D_e[a]	R_e(H–H)	R_e(Be–H)	R_e(Be–Be)	q(H)	q(Be)
$H_2@Be_8$	11.41/−1.47	1.71	1.42	1.97–2.38	−1.56	0.36, 0.42
$H_2@Be_9$	17.30/1.44	1.96	1.68–1.87[b]	2.06–2.25	−1.19, −0.70[c]	0.17–0.32[d]
$H_2@Be_{10}$	18.98/−1.72	1.70	1.48–1.57[b]	2.13–2.22	−1.33	0.23, 0.41[d]

[a]For $H_2@Be_n \rightarrow H_2 + n$ Be / $\rightarrow H_2 + Be_n$

[b]To axial Be

[c]Protruding atom

[d]Axial atom

The Coulomb explosion of H_2 upon the shell-to-core charge-transfer is confined by the Be_n cage, which is the reason of the metastability of $H_2@Be_n$ for $n = 8$ and 10. These systems are, respectively, 1.5 and 1.7 eV higher in energy relative to the isolated relaxed molecule and cage. The $n = 9$ system, however, allows one H atom to stick outside, and, as a result, exhibits stability of 1.4 eV to such a dissociation. The "sunken" isomer of $H_2@Be_9$ is thus nearly iso-energetic with the dissociation products, such a stabilization relative to $n = 8$ and 10 being consistent with the "magic" number (20) of valence electrons in $H_2@Be_9$.

Calculations predict a low barrier of ∼0.06 eV for H atom to escape from the Be_8 cage which then opens up and lets both hydrogen atoms to surface. The resulting system is only marginally lower in energy (by 0.2 eV) than the original one, hence still metastable. For $n = 9$, the further axial withdrawal of the protruding H atom shows a similar barrier (∼0.08 eV), with the other H atom escaping to the surface as well. The Be_9 cage recovers its shape and the system further stabilizes by 1.3 eV relative to the original one. For $n = 10$, however, the barrier experienced by H atom on its way to the cage surface reaches 0.6 eV, the resulting system having almost the same (marginally higher) energy as original $H_2@Be_{10}$. However, the cage distorts and, as a result, the other hydrogen atom can leave the cage with almost no barrier. This lowers the system energy by 2.2 eV, thereby making it stable by about 1 eV to dissociation into Be_{10} and H_2.

The relative stabilities of $H_2@Be_n$ to dissociation into $H_2 + Be_n$ are reflected in their total dissociation energies D_e^{total} (into $H_2 + n$ Be) as compared to those for respective Be_n. Metastable $H_2@Be_8$ and $H_2@Be_{10}$ have D_e^{total} decreased relative to the original cages by about 0.2 eV per Be atom, while $H_2@Be_9$ is stabilized by a similar amount relative to relaxed Be_9. The overall trend of D_e^{total} increasing with n (in the range of 1.4–1.9 eV per Be atom) is, however, preserved (see Table 12.1).

12.3.2 $(H_2)_2@Be_n$

Both $H_2@Be_8$ and $H_2@Be_{10}$ are employed as units in cluster assemblies [16]. Merging two $n = 8$ systems axially via two shared atoms produces $(H_2)_2@Be_{14}$

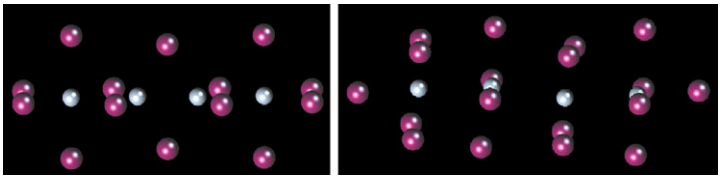

Fig. 12.3 Optimized geometries of $(H_2)_2@Be_{14}$ and $(H_2)_2@Be_{18}$

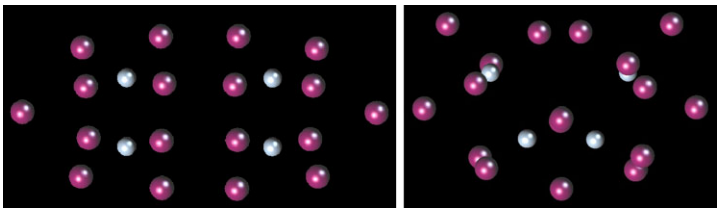

Fig. 12.4 Optimized geometries of "radial" $(H_2)_2@Be_{18}$ and $(H_2)_2@Be_{17}$

with slightly zig-zagging chain of four H atoms inside the Be_{14} cage (Fig. 12.3). The system is triply more metastable, being 4.3 eV above the relaxed cage plus two hydrogen molecules, as compared to $H_2@Be_8$, while the barrier for escape of H remains about same.

A similar situation is found when axially merging two $n = 10$ units while removing two Be atoms. In fact, the resulting system resembles two $H_2@Be_9$ units joined by their open ends, with protruding H atoms being pushed back inside (Fig. 12.3). The system is twice as high in energy (by 3.4 eV) relative to relaxed $Be_{18} + 2H_2$ as $H_2@Be_{10}$ relative to $Be_{10} + H_2$, the difference from the $(H_2)_2@Be_{14}$ versus $H_2@Be_8$ case being due to longer distances between the hydrogen anions (Table 12.2).

The higher-energy isomers of $H_2@Be_{10}$ can also be merged in a similar way, in which case, however, the resulting $(H_2)_2@Be_{18}$ isomer is only 2.4 eV above $Be_{18} + 2H_2$, i.e. significantly lower in energy than the previous isomer. The apparent reason of this is a larger distance between the hydrogen diatoms oriented perpendicularly, even though each "radial" $H_2@Be_{10}$ unit is higher in energy.

Finally, two $H_2@Be_{10}$ units have been merged via a shared triatomic Be_3 face at their ends, with the units twisting relative to one another to adopt a staggered arrangement of atoms at the other ends. The resulting $(H_2)_2@Be_{17}$ system is composed of a C-shaped chain of four H atoms inside a bent Be_{17} cage (Fig. 12.4). An interesting feature of this species is its almost identical metastability (about 1.7 eV higher in energy than relaxed $Be_{17} + 2H_2$) as compared to that of $H_2@Be_{10}$.

In all above systems, the charges on the H atoms only slightly reduce (by 0.2e for $(H_2)_2@Be_{14}$ and 0.1e for the $H_2@Be_{10}$-based species) relative to those in the respective units (Table 12.2). This, together with shorter distances between the hydrogen anions in $(H_2)_2@Be_{17}$ as compared to "radial" $(H_2)_2@Be_{18}$, could not explain such a stabilization of the former. One possible interpretation could be based

Table 12.2 Equilibrium parameters (in eV and Å) and atomic charges (in e) of $(H_2)_2@Be_n$

System	D_e^{total}/n; D_e[a]	R_e(H–H)	R_e(Be–H)	R_e(Be–Be)	q(H)	q(Be)
$(H_2)_2@Be_{14}$	1.73; −4.25	1.46[b], 1.63	1.39–1.72	1.95–2.58	−1.27, −1.30[c]	0.15–0.46[d]
$(H_2)_2@Be_{18}$	2.08; −3.45	1.80, 1.82[b]	1.48–1.67	2.05–2.48	−1.15[c], −1.23	0.04–0.38[d]
"Radial"	2.14; −2.36	1.56	1.37–1.62	2.09–2.46	−1.22	0.05–0.43[d]
$(H_2)_2@Be_{17}$	2.14; −1.71	1.74–1.78[b]	1.45–1.78	2.05–2.35	−1.16[c], −1.20	0.09–0.45[e]

[a] $\rightarrow 2H_2 + nBe$; $\rightarrow 2H_2 + Be_n$

[b] Between inner H atoms

[c] Inner H atoms

[d] Outermost Be atoms

[e] Innermost shared Be atom

on the specific structure with Be atoms located between H atoms and resulting in a charge distribution "negative-positive-negative" creating a significant quadrupole moment of such a layered centre polarizing the outer beryllium atoms.

In addition, the $(H_2)_2@Be_{17}$ system exhibits a significant stability to the hydrogen escape from the cage, with the potential energy barrier of 0.3 eV. This is a half of the barrier for the $H_2@Be_{10}$ unit, the reduction likely being due to increased repulsion between the larger number of closely-spaced hydrogen anions.

Further 1D structural extension of the above $(H_2)_2@Be_{14}$ and $(H_2)_2@Be_{18}$ systems into a beryllium "nanotube" with a hydrogen "wire" inside by adding more units would lead to the hydrogen storage capacity up to 3.6 and 2.7 weight-% (one H per three and four Be), respectively. This value could be increased via merging the units by their sides as well, i.e. for 2D and 3D extensions. In particular, when the $(H_2)_2@Be_{10}$ units are merged by a shared Be_3 face at their ends, as in the above $(H_2)_2@Be_{17}$ system, the storage capacity is evaluated to have an upper limit of about 8 weight-%.

12.3.3 $H_k@Be_n$

Since H_2 dissociates in Be_n, encapsulation of separate H atoms in such cages has been considered as well [17]. The Be_6 cluster is found to be the smallest one able to accommodate an H atom inside. The centrally positioned hydrogen atomic core transforms the beryllium shell from a bipyramid into a perfect octahedron (Fig. 12.5). Unlike the metastable $H_2@Be_{10}$ counterpart, the system is stable to dissociation into relaxed $Be_6 + H$ by appreciable 1.7 eV. The isomers with H attached to Be_6 outside are more stable (bound by 3 eV), both Be_2-edge and Be_3-face sites being nearly degenerate (within 0.1 eV). The barrier for the hydrogen exit from the cage is found to be 0.5 eV.

In endohedral $H@Be_6$, the H atom is charged by −0.95e, which is only slightly more negative than −0.8e for the other, HBe_6 isomers. The charge on H is smaller

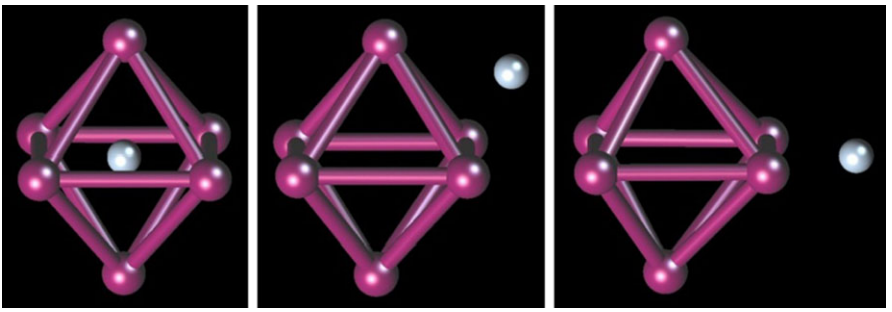

Fig. 12.5 Optimized geometries of endohedral H@Be_6 and two HBe_6 isomers

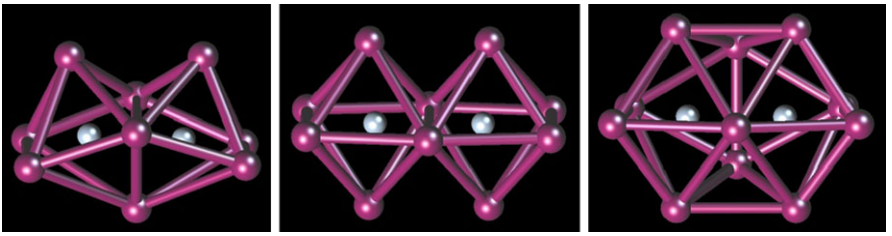

Fig. 12.6 Optimized geometries of (2H)@Be_9, (2H)@Be_{10}, and (2H)@Be_{11}

than in H_2@Be_{10}, even though in the latter case each hydrogen atom has less neighbouring electron-density donors.

The stability of the H@Be_6 species suggests a possibility of building larger assemblies from such blocks. Merging two H@Be_6 units via a shared Be_3 face produces a (2H)@Be_9 species with the units distorted but generally preserved (Fig. 12.6). The repulsion of two hydrogen anions makes the system metastable, 1.2 eV above relaxed $Be_9 + H_2$, hence a higher-energy isomer relative to the above H_2@Be_9. When empty, the relaxed beryllium cage generally preserves its shape of two face-merged Be_6 units, as a higher-energy isomer of Be_9. Due to strain in the system, the barrier for H exit from the cage reduces to 0.2 eV. The two hydrogen centres close to one another in (2H)@Be_9 carry significantly increased negative charges as compared to H@Be_6, $-1.4e$ on each, in spite of the smaller number of Be atoms per H. The system has a small dipole moment of 0.2 D, close to that for the (H_2)@Be_{17} counterpart.

When two H@Be_6 units are merged via a shared Be_2 edge, a (2H)@Be_{10} system is produced (Fig. 12.6), with the shared edge stretched. The H anions are slightly further apart as compared to (2H)@Be_9 (see Table 12.3), which stabilizes the system which is now 0.8 eV above relaxed $Be_{10} + H_2$. This value is a half that for (H_2)@Be_{10}, but is relative to the relaxed empty beryllium cage preserving its shape of two Be_6 edge-sharing units, which is a higher-energy isomer of Be_{10}. As a result, (2H)@Be_{10} remains 1.9 eV higher in energy as compared to (H_2)@Be_{10}. The po-

Table 12.3 Equilibrium parameters (in eV and Å) and atomic charges (in e) of (kH)@Be_n

System	D_e^{total}[a]/n; D_e[b]	R_e(H–H)	R_e(Be–H)	R_e(Be–Be)	q(H)	q(Be)
H@Be_6	1.56; 1.72		1.51	2.13	−0.95	+0.08–0.31
(2H)@Be_9	1.62; −1.19	1.68	1.50–1.72	2.14–2.43	−1.38	+0.15–0.42
(2H)@Be_{10}	1.71; −0.77	1.95	1.51–1.58	1.96–2.48	−1.26	−0.08–+0.40
(2H)@Be_{11}	1.94; −1.52	1.71	1.51–2.01	2.01–2.24	−1.21	+0.11–0.35
(3H)@Be_{11}	1.99; 0.41	1.67	1.52–1.69	1.99–2.32	−1.36	+0.16–0.46

[a] (kH)@$Be_n \rightarrow n$Be + H/H_2/(H + H_2) for $k = 1/2/3$

[b] (kH)@$Be_n \rightarrow Be_n$ + H/H_2/(H + H_2) for $k = 1/2/3$

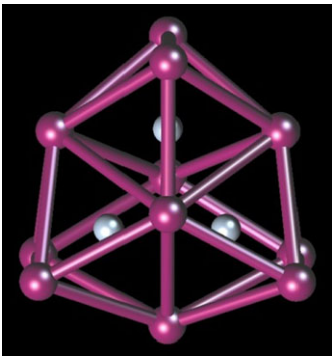

Fig. 12.7 Optimized geometry of (3H)@Be_{11}

tential energy barrier between the two isomers is 0.15 eV, and this isomerization occurs along the pathway followed by H atom exiting the cage.

An attempt to separate the H anions even further by merging two H@Be_6 units via a shared atom results in a collapse of the units into a Be_{11} cage encapsulating both H atoms (Fig. 12.6). The (2H)@Be_{11} system is metastable, being higher in energy than relaxed Be_{11} + H_2 by 1.5 eV which is the largest value among those for (2H)@Be_n, n = 9–11. The Be–Be interactions holding the cage together thus overcome the repulsion of the hydrogen anions. The charges on the H atoms slightly decrease with increasing n (Table 12.3), to −1.2e for $n = 11$, opposite to the number of the donating Be atoms. The asymmetry of the cage leads to a small dipole moment of 0.34 D.

As a next step, a third H@Be_6 unit is merged to (2H)@Be_9 via two shared Be_3 faces, leading to a D_{3h}-symmetric (3H)@Be_{11} assembly with three H atoms forming an equilateral triangle (Fig. 12.7). The beryllium frame keeps its shape when empty, the (3H)@Be_{11} system being weakly stable by 0.4 eV to dissociation into relaxed Be_{11} + H_2 + H. Such a stabilization of (3H)@Be_{11} can be viewed as being due to combination of metastable (2H)@Be_9 and stable H@Be_6. An alternative channel is represented by dissociation into (2H)@Be_{11} + H, in which case the above $n = 11$ species with two H atoms is recovered. These products correspond to the dissociation energy of 0.6 eV. The barrier for H atom exit from the cage is back to 0.5 eV

(as for $H@Be_6$), apparently due to a lower strain in the beryllium cage. The charge on each of the H atoms is $-1.4e$, same as for $(2H)@Be_9$.

Similar to $(H_2)@Be_n$, the relative stabilities of the above $(kH)@Be_n$ systems to separation into the hydrogen and beryllium components translate into their total dissociation energies D_e^{total} (corresponding to Be_n dissociated into atoms). Inserting H into Be_6 and $H + H_2$ into $Be_{11}(D_{3h})$ stabilizes these clusters, significantly (by 0.3 eV per Be atom) for the former and slightly for the latter. While insertion of H_2 into Be_9, Be_{10} and Be_{11} destabilizes them by about 0.1 eV per Be atom. Overall, the D_e^{total} values increase with the system size, as for $(H_2)@Be_n$, from 1.6 to 2 eV per Be atom (Table 12.3).

12.4 Conclusions

Beryllium cluster cages form metastable (by a few eV) core-shell systems when endohedrally doped by molecular hydrogen dissociating due to a strong electron donation from, and confined in, the cage. When small $H_2@Be_n$ units are merged together, they can generally preserve shapes and integrity in the larger assemblies. In some cases, this can result in a further stabilization of the system, as for $(H_2)_2@Be_{17}$. Another feature is a possible higher stability of the assemblies composed of higher-energy isomers of the units, as for $(H_2)_2@Be_{18}$. Energy barriers to extraction of H_2 can be low ($\sim$0.1 eV for $n = 8, 9, 14$) to appreciable ($\sim$0.6 eV for $n = 10$), suggesting low-temperature conditions for stabilization. Extraction of both H atoms at once is more likely.

The metastability may offer two benefits: (1) easier release of hydrogen, (2) direct storage of extra energy ($\sim$0.5–2 eV per H_2 molecule here). Hydrogen storage capacity can be increased in cluster assemblies/materials, e.g. nanofoams. This is confirmed for face-sharing $H_2@Be_{10}$ units, with extrapolated upper bound of $\sim$8 weight-%. Feasibility of such materials is supported experimentally by a recent progress reported for Mg [18].

Such an endohedral doping may also offer options for modification of mechanical and electronic characteristics (shape, dipole moment) of clusters. This suggests potential applications in nanomaterials and molecular electronics.

Be_6 is able to accommodate H atom inside and is significantly stable (by $\sim$2 eV) to its release. This stability can be reduced by design via merging such units into assemblies which are metastable to release of molecular H_2, with a desorption barrier of $\sim$0.5 eV (matching the suggested ideal binding energy [1]). Hydrogen storage capacity of such systems extrapolated to a nanofoam material, composed of face-sharing $H@Be_6$ units filling space, can reach $\sim$10 weight-%. This may exceed the value for the counterparts with encapsulated H_2 (e.g. inside Be_{10} units) due to higher symmetry and better packing.

Such cluster-assembled materials could be more straightforward to develop than macro-assemblies of clusters preserving multiple surface sites for external binding of H_2 molecules. Firm conclusions, however, would benefit from relevant experiments as well as modelling of molecular dynamics related to hydrogen entering and

exiting the cages, in particular for refilling the nanofoam. It is hoped that the present work will stimulate such studies in the near future.

Acknowledgements The authors thank the RSC and the NSERC of Canada for the financial support of this work via a travel grant to FN. The staff of the HPC facilities of the UOIT Faculty of Science and of the Sharcnet network of Ontario are acknowledged for their invaluable technical support. FN is grateful to the University of Cambridge Department of Chemistry for their hospitality during his sabbatical visit.

References

1. Graetz J (2009) Chem Soc Rev 38:73
2. Wagemans RWP et al (2005) J Am Chem Soc 127:16675
3. Harder S et al (2011) Angew Chem, Int Ed 50:4156
4. Srinivasu K et al (2012) RSC Adv 2:2914
5. Bandaru S et al (2012) Int J Quant Chem 112:695
6. Wang L et al (2009) J Comput Chem 30:2509
7. Henry DJ, Yarovsky I (2009) J Phys Chem A 113:2565
8. McNelles P, Naumkin FY (2009) Phys Chem Chem Phys 11:2858
9. Allouche A (2008) Phys Rev B 78:085429
10. Lingam CB et al (2011) Comput Theor Chem 963:371
11. Sun Y, Fournier R (2005) Comput Lett 1:1
12. Boys SF, Bernardi F (1970) Mol Phys 19:553
13. Valiev M et al (2010) NWChem, version 6.x. Comput Phys Commun 181:1477
14. Reed AE, Curtiss LA, Weinhold F (1988) Chem Rev 88:899
15. Naumkin FY, Wales DJ (2012) Int J Quant Chem 112:3068
16. Naumkin FY, Wales DJ (2011) J Phys Chem A 115:12105
17. Naumkin FY, Wales DJ (2012) Chem Phys Lett 545:44
18. Skorb EV et al (2010) Nanoscale 2:722

Chapter 13
A Theoretical Study on a Visible-Light Photo-Catalytic Activity in Carbon-Doped $SrTiO_3$ Perovskite

Taku Onishi

Abstract Carbon-doping has been explored to enhance the visible-light photocatalytic activity in $SrTiO_3$ perovskite. Here, we considered carbon anion (C^{2-})-doping at oxygen site, because no oxygen vacancy is then formed. From our density functional theory (DFT) calculations for carbon anion-doped cluster models, it was found that carbon anion-doping enhances the visible-light photocatalytic activity, realizing a stable crystal structure. Finally, we concluded that carbon anion-doped $SrTiO_3$ is one of the best visible-light active photocatalysts.

13.1 Introduction

Hydrogen has been considered as one of the next-generation energy resources. Hydrogen is generally produced by steam reforming of natural gas. Recently, it has been much expected that hydrogen is produced from water splitting by a photocatalyst. Titanium oxides such as $SrTiO_3$ perovskite [1–3] and TiO_2 [4, 5] have been widely utilized as photocatalysts. $SrTiO_3$ has a large bandgap (3.27 eV) [6], corresponding to absorption of ultraviolet (UV) light which is less than 5 % of sunlight. To use the whole spectrum of sunlight effectively, visible-light active photocatalysts have been explored.

Previously, we investigated the effect of nitrogen-doping to enhance a visible-light photocatalytic activity of $SrTiO_3$, by the use of molecular orbital (MO) calculation [7–9]. Experimental works reported that nitrogen anion-doping (N^{3-}) at oxygen site realizes the high visible-light photocatalytic activity, as the decreased bandgap corresponds to visible light region [10, 11]. However, oxygen vacancy is accompanied by nitrogen-doping, to compensate charge. We concluded that photocatalytic activity becomes inactive, when oxygen vacancy exists in the vicinity of

T. Onishi (✉)
Department of Chemistry for Materials, Graduate School of Engineering, Mie University, 1577 Kurimamachiya-cho, Tsu, Mie 517-8507, Japan
e-mail: taku@chem.mie-u.ac.jp

T. Onishi
The Center of Ultimate Technology on Nano-Electronics, Mie University (MIE-CUTE), 1577 Kurimamachiya-cho, Tsu, Mie 517-8507, Japan

M. Hotokka et al. (eds.), *Advances in Quantum Methods and Applications in Chemistry, Physics, and Biology*, Progress in Theoretical Chemistry and Physics 27,
DOI 10.1007/978-3-319-01529-3_13,

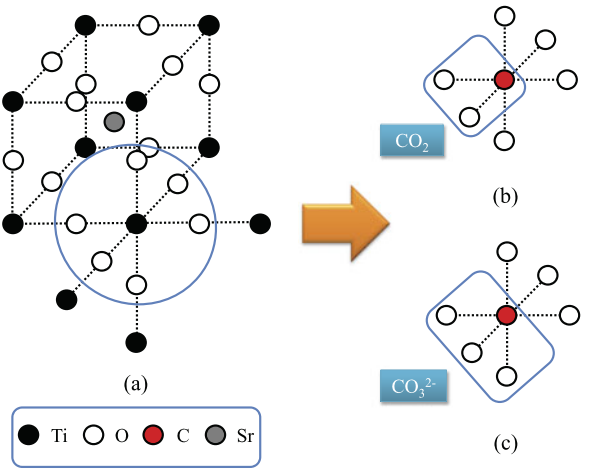

Fig. 13.1 (**a**) The crystal structure of $SrTiO_3$ perovskite, and (**b**) CO_2 and CO_3^{2-} formation around doped carbon

doped nitrogen [9]. It is because bandgap becomes much smaller, due to the direct chemical bonding between titanium atoms.

We consider carbon-doping for $SrTiO_3$, as an alternative to nitrogen-doping. Carbon cation-doping (C^{4+}) at titanium site can be considered [12]. However, carbon cation-doping is unrealistic for $SrTiO_3$ and TiO_2 photocatalysts. It is because the elimination reaction of CO_2 or CO_3^{2-} [13] can be easily caused, due to the stable double bond (C = O) formation, as shown in Fig. 13.1. On the other hand, in TiO_2, it was reported that carbon anion (C^{2-})-doping at oxygen site lowers the bandgap, and enhances a visible-light photocatalytic activity [14, 15]. In $SrTiO_3$, as the photocatalytic activity of carbon anion-doped $SrTiO_3$ has not been investigated enough, we perform carbon anion (C^{2-})-doping at oxygen site. In general, carbon has a strong covalency with transition metals such as titanium, in comparison with nitrogen and oxygen [16]. However, the details of chemical bond formation between titanium and carbon are still unclear. In this study, we perform hybrid density functional theory (DFT) calculations to examine a visible-light photocatalytic activity in carbon anion-doped $SrTiO_3$.

13.2 Theoretical Background

13.2.1 Onishi Chemical Bonding Rule

MO analysis is very useful to examine the mechanism of chemical bonding formation. Beyond Kanamori-Goodenough rule, Onishi chemical bonding rule [7] (see Fig. 13.2) can be applicable to judge chemical bonding character (covalency or ionicity) for strongly correlated M–X–M system (M = transition metal, X = O, F etc.).

1. In MOs including outer shell electrons, check whether the orbital overlap between M and X exists or not.

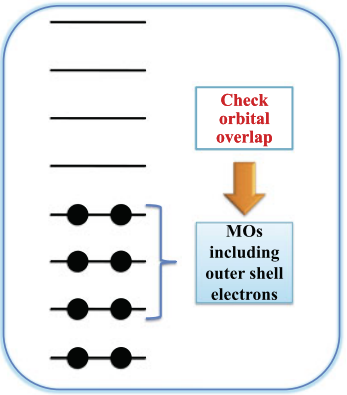

Fig. 13.2 The schematic picture of Onishi chemical bonding rule

2. With orbital overlap, bonding character is covalent. Without orbital overlap, bonding character is ionic.

13.2.2 Calculation Method

The calculations presented here have been performed using BHHLYP hybrid DFT method [17], which properly reproduces the electronic structure of the strongly correlated perovskite-type transition metal oxides. In hybrid DFT, the total exchange and correlation energies are given by

$$E_{XC} = C_1 E_X^{HF} + C_2 E_X^{Slater} + C_3 E_X^{Becke} + C_4 E_C^{VWN} + C_5 E_C^{LYP} \qquad (13.1)$$

where E_X^{HF}, E_X^{Slater}, E_X^{Becke}, E_C^{VWN} and E_C^{LYP} denote HF exchange, Slater exchange, Becke exchange, VWN correlation and LYP correlation, respectively. C_1 coefficients are 1.0, 0.5, 0.2 and 0.0 in Hartree-Fock (HF), BHHLYP, B3LYP and BLYP, respectively. We have used the Tatewaki–Huzinaga MINI basis [18] for titanium and strontium, combined with the 6–31G(d) basis for oxygen and carbon. All calculations were performed with the GAMESS program [19]. MOs have been plotted using MOLEKEL 4.3 [20].

13.2.3 Bandgap Estimation

Previously, we demonstrated a theoretical approach to estimate the bandgap quantitatively for the strongly correlated perovskite-type titanium oxide by the use of MO [7–9]. Bandgap is defined as the orbital energy difference between highest occupied MO (HOMO) and lowest unoccupied MO (LUMO), as shown in Fig. 13.3. In the case of $SrTiO_3$, HOMO and LUMO correspond to oxygen 2p valence band and titanium 3d conduction band, respectively. It is known that bandgap is very sen-

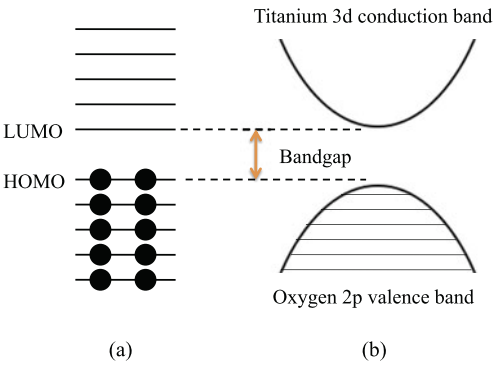

Fig. 13.3 The schematic picture of bandgap definition: (**a**) molecular orbital (MO), (**b**) band structure

sitive to the coefficient of HF exchange term (C_1) in hybrid DFT [7, 8]. As bandgap is proportional to C_1, the corrected bandgap (Δ) can be practically estimated from the calculated one by BHHLYP (Δ_{BHHLYP}).

$$\Delta = k\Delta_{BHHLYP} \tag{13.2}$$

In $SrTiO_3$, the scaling factor (k) was determined to be 0.73 [7, 8].

13.2.4 Calculation Model

Our cluster model approach is not only applicable for bandgap estimation but also useful to examine the relationship between bandgap and chemical bond formation related to doped defect (In this case, carbon). In fact, we illustrated that Ti–Ti and Ti–N–Ti bondings affect bandgap in oxygen vacancy-doped and nitrogen-doped $SrTiO_3$, respectively [7–9].

$SrTiO_3$ has a simple cubic structure, with a lattice parameter (the Ti–O–Ti distance) of 3.905 Å [21]. We constructed mono-carbon-doped $SrTi_8O_{11}C$ and di-carbon-doped $SrTi_8O_{10}C_2$ models, to examine the effect of carbon-doping on bandgap. Referring to Fig. 13.4, one divalent carbon anion is introduced in $SrTi_8O_{11}C$ model. Two divalent carbon anions are introduced in $SrTi_8O_{10}C_2$ (I) and $SrTi_8O_{10}C_2$ (II) models, where two carbon atoms are allocated in parallel. It is because a large structural strain occurs if second carbon atom is doped at neighbouring oxygen position, and two carbon atoms are allocated in anti-parallel. It is considered that Ti–C–Ti bonding forms a strong covalent bonding, due to a strong covalency of doped carbon. In this study, we investigate the change of orbital energy, when titanium atoms in Ti–C–Ti are displaced along z axis.

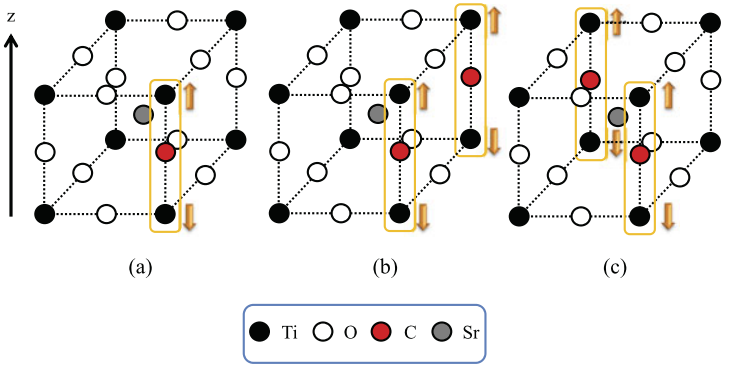

Fig. 13.4 The carbon-doped cluster models for $SrTiO_3$ perovskite: (**a**) mono-carbon doped $SrTi_8O_{11}C$ model, (**b**) di-carbon doped $SrTi_8O_{10}C_2$ (I) model, (**c**) di-carbon doped $SrTi_8O_{10}C_2$ (II) model. The *arrows* depict a titanium displacement direction

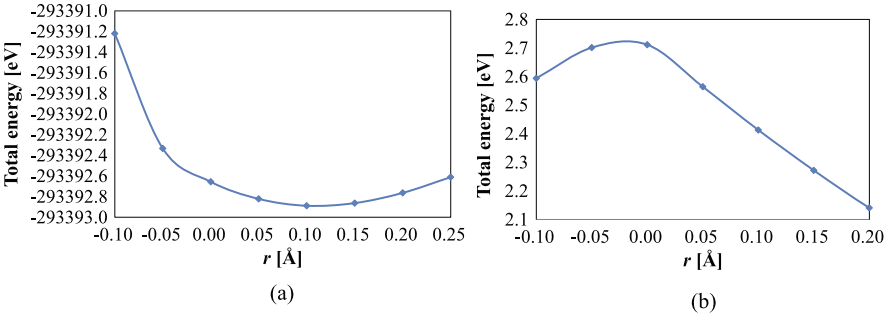

Fig. 13.5 (**a**) Potential energy curve and (**b**) bandgap change in $SrTi_8O_{11}C$ model, displacing titanium atom along z axis. r is the displacement distance from the initial lattice position

13.3 Results and Discussion

13.3.1 Mono-Carbon-Doping

Figure 13.5(a) shows the potential energy curve in $SrTi_8O_{11}C$ model, displacing titanium atom from the initial lattice position along z axis. The minimum total energy was given at $r = 0.10$ Å (Ti–C = 2.15 Å). Mulliken charge densities of doped carbon and titanium neighbouring carbon are −0.25 and 1.94, respectively. It is concluded that the weak ionic bonding between titanium and carbon is responsible for the structural relaxation such as Ti–C elongation. In order to examine the relationship between bandgap and structural relaxation, we calculated bandgap, displacing titanium atom from the initial lattice position along z axis, as shown in Fig. 13.5(b). It is found that bandgap decreases when Ti–C is elongated or shrinks. At the local minimum ($r = 0.10$ Å), bandgap is 2.41 eV (513 nm), corresponding to a visible light region (see Fig. 13.6).

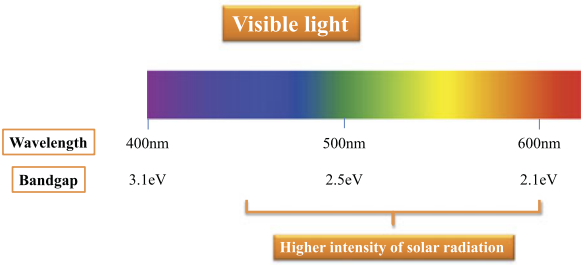

Fig. 13.6 The schematic picture of the relationship between wavelength and bandgap in a visible light

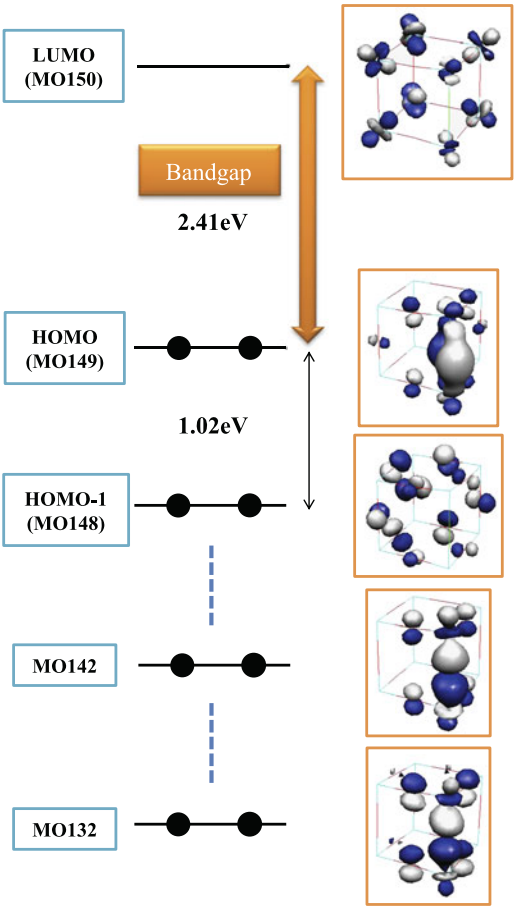

Fig. 13.7 The figures of selected molecular orbitals (MOs) and corresponding energy diagram at the local minimum for $SrTi_8O_{11}C$ model

Figure 13.7 depicts the figures of selected MOs and corresponding energy diagram at the local minimum for $SrTi_8O_{11}C$ model. The π-type Ti–C–Ti covalent bonding in HOMO is the impurity level of carbon. HOMO-1 and LUMO are valence band and conduction band, respectively. It is concluded that visible light absorption energy corresponds to the orbital energy difference between impurity level

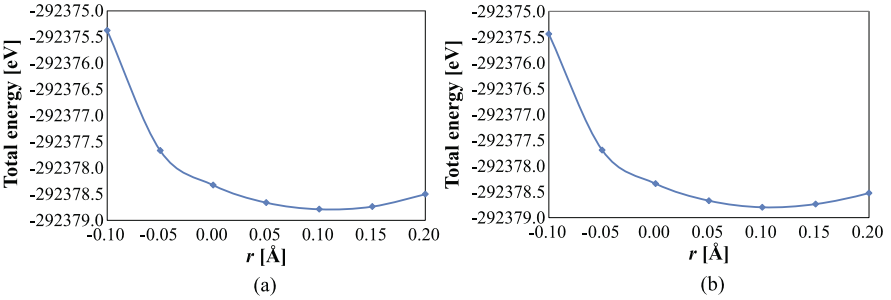

Fig. 13.8 The potential energy curves in (**a**) $SrTi_8O_{10}C_2$ (I) and (**b**) $SrTi_8O_{10}C_2$ (II) models, coincidently displacing titanium atoms along z axis. r is the displacement distance from the initial lattice position

(HOMO) and titanium 3d conduction band (LUMO). In MO132 and MO142, σ-type orbital overlap exists between titanium $3d_{z^2}$ orbital and carbon $2p_z$ orbital. From Onishi chemical bonding rule, a strong covalent bonding is formed in Ti–C–Ti of $SrTi_8O_{11}C$ model. However, it is concluded that Ti–C–Ti covalent bonding is not strong enough to cause an elimination reaction, because of Ti–C elongation.

Let us explain bandgap change from the viewpoint of MO. At $r > 0$, HOMO orbital energy is unstabilized and LUMO orbital energy is unchanged. The orbital overlap between titanium and carbon in HOMO becomes smaller by Ti–C elongation. As the result, bandgap decreases, when r increases. On the other hand, at $r < 0$, HOMO orbital energy is stabilized and LUMO orbital energy is also stabilized. As covalencies of HOMO and LUMO become larger by Ti–C shrink, the two effects are competitive. As the result, bandgap decreases in $SrTi_8O_{11}C$ model.

13.3.2 Di-Carbon-Doping

Figures 13.8(a) and 13.8(b) show the potential energy curves in $SrTi_8O_{10}C_2$ (I) and $SrTi_8O_{10}C_2$ (II) models, coincidently displacing titanium atoms from the initial lattice position along z axis. The minimum total energies were given at $r = 0.10$ Å (Ti–C = 2.15 Å) in both curves. Mulliken charge densities of doped carbon and titanium neighbouring carbon are -0.26 and 1.93 in $SrTi_8O_{10}C_2$ (I) model, respectively. On the other hand, those are -0.25 and 1.94 in $SrTi_8O_{10}C_2$ (II) model, respectively. As same as mono-carbon-doped case, it is concluded that the weak ionic bonding between titanium and carbon is responsible for the structural relaxation such as Ti–C elongation. At the local minimum ($r = 0.10$ Å), bandgap is 2.23 eV (556 nm) in $SrTi_8O_{10}C_2$ (I) model and 2.40 eV (517 nm) in $SrTi_8O_{10}C_2$ (II) model, corresponding to a visible light region (see Fig. 13.6).

Figure 13.9(a) depicts the figures of selected MOs and corresponding energy diagram at the local minimum for $SrTi_8O_{10}C_2$ (I) model. HOMO-2 and LUMO+1 correspond to valence band and conduction band, respectively. LUMO and LUMO+1

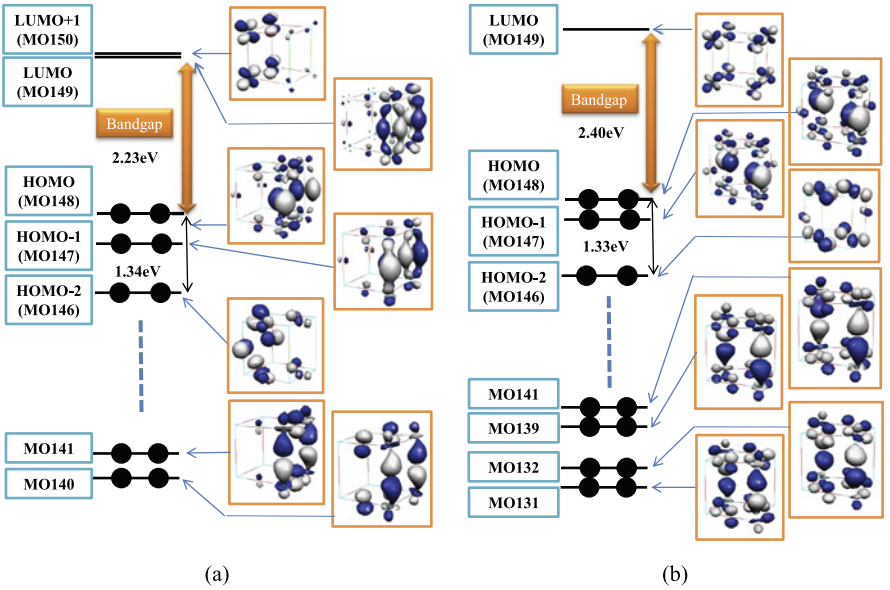

Fig. 13.9 The figures of selected molecular orbitals (MOs) and corresponding energy diagram at the local minimum for (**a**) $SrTi_8O_{10}C_2$ (I) and (**b**) $SrTi_8O_{10}C_2$ (II) models

are degenerated, though the π-type Ti–C–Ti covalent bondings are only formed in LUMO. The π-type Ti–C–Ti covalent bondings in HOMO and HOMO-1 are to the impurity level. It is concluded that a visible light absorption energy corresponds to the orbital energy difference between impurity level (HOMO) and titanium 3d conduction band (LUMO+1). In MO141, titanium $3d_{z^2}$ orbitals have σ-type and π-type orbital overlaps with carbon $2p_z$ orbital and oxygen $2p_z$ orbital, respectively. In MO140, σ-type orbital overlaps exist between titanium $3d_{z^2}$ orbital and carbon $2p_z$ orbital. Figure 13.9(b) depicts the figures of selected MOs and corresponding energy diagram at the local minimum for $SrTi_8O_{10}C_2$ (II) model. HOMO-2 and LUMO correspond to valence band and conduction band, respectively. The π-type Ti–C–Ti covalent bondings in HOMO and HOMO-1 are the impurity level. It is concluded that a visible light absorption energy corresponds to the orbital energy difference between impurity level (HOMO) and titanium 3d conduction band (LUMO). In MO131, MO132, MO139 and MO141, σ-type orbital overlaps exist between titanium $3d_{z^2}$ orbital and carbon $2p_z$ orbital. From Onishi chemical bonding rule, a strong covalent bonding is formed in Ti–C–Ti of $SrTi_8O_{10}C_2$ (I) and $SrTi_8O_{10}C_2$ (II) models. However, it is concluded that Ti–C–Ti covalent bonding is not strong enough to cause an elimination reaction, because of Ti–C elongation.

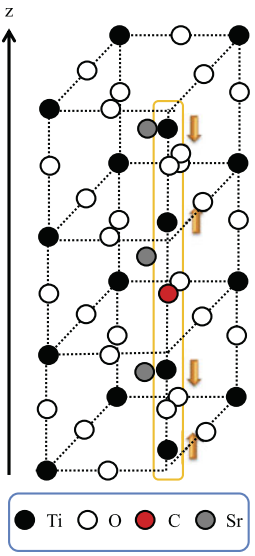

Fig. 13.10 The schematic picture of Ti–C elongation in the carbon-doped $SrTi_8O_{11}C$ unit and Ti–O shrink in the neighbouring $SrTi_8O_{12}$ unit. The *arrows* depict a titanium displacement direction

13.3.3 Concentration of Carbon-Doping

Let us explain the relationship between bandgap and concentration of carbon-doping. The orbital energy difference between valence band and conduction band is getting larger, when the concentration of carbon-doping is higher. In $SrTi_8O_{12}$, $SrTi_8O_{11}C$, $SrTi_8O_{10}C_2$ (I) and $SrTi_8O_{10}C_2$ (II) models, they are 3.27 eV, 3.43 eV, 3.57 eV and 3.73 eV, respectively. However, bandgap decreases, due to the existence of carbon 2p impurity level. The smallest bandgap (2.23 eV) is given in $SrTi_8O_{10}C_2$ (I) model. It is because HOMO is more unstabilized, due to the anti-bonding covalent bonding between titanium 3d orbital and oxygen $2p_z$ orbital. The bandgap of $SrTi_8O_{10}C_2$ (II) model (2.40 eV) is as same as $SrTi_8O_{11}C$ model (2.41 eV), though the orbital energy difference between valence band and conduction band is larger in $SrTi_8O_{10}C_2$ (II) model. It is because HOMO is more unstabilized in $SrTi_8O_{10}C_2$ (II) model, due to the scare orbital overlap between titanium 3d orbital and carbon 2p orbital.

13.3.4 Effect of Structural Relaxation

As shown in Fig. 13.10, in carbon-doped $SrTiO_3$, Ti–C elongation and Ti–C shrink along z axis occur in carbon-doped $SrTi_8O_{11}C$ unit and neighbouring $SrTi_8O_{12}$ unit, respectively. Figure 13.11 depicts three types of Ti–O shrinks in $SrTi_8O_{12}$ model, corresponding to Ti–C elongations in $SrTi_8O_{11}C$, $SrTi_8O_{10}C_2$ (I) and $SrTi_8O_{10}C_2$ (II) models.

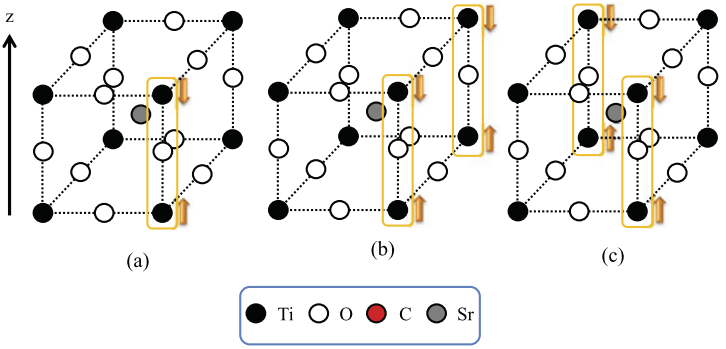

Fig. 13.11 The three types of Ti–O shrinks in $SrTi_8O_{12}$ model, corresponding to Ti–C elongations in (**a**) $SrTi_8O_{11}C$, (**b**) $SrTi_8O_{10}C_2$ (I) and (**c**) $SrTi_8O_{10}C_2$ (II) models. The *arrows* depict a titanium displacement direction

Figure 13.12 shows the potential energy curves for three types of Ti–O shrinks, displacing titanium atoms from the initial lattice position along z axis. The minimum total energies are given at $r = -0.1$ Å in all curves. Ti–C elongation and Ti–O shrink coincidently occur in carbon-doped $SrTi_8O_{11}C$ unit and neighbouring carbon-undoped $SrTi_8O_{12}$ unit, respectively. Hence, it is concluded carbon anion-doped $SrTiO_3$ has a stable crystal structure. In addition, bandgap change is slight, when titanium atoms are displaced in $SrTi_8O_{12}$ model. At the local minima, bandgaps are 3.29 eV, 3.32 eV and 3.34 eV for (a), (b) and (c) types of Ti–O shrinks, respectively.

13.4 Concluding Remarks

13.4.1 General Conclusions

We performed hybrid DFT calculations to examine a visible-light photocatalytic activity in carbon anion-doped $SrTiO_3$ perovskite. The potential energy curve, bandgap and MO were obtained. We concluded as follows.

1. Ti–C–Ti covalent bonding is formed.
2. Ti–C elongation occurs, due to the weak ionic bonding between titanium and carbon.
3. Ti–C–Ti covalent bonding is not strong enough to cause an elimination reaction, because of Ti–C elongation.
4. Bandgap is in the range between 2.23 eV and 2.41 eV, corresponding to a visible light region.
5. A stable crystal structure is realized, due to Ti–C elongation in $SrTi_8O_{11}C$ unit and Ti–O shrink in $SrTi_8O_{12}$ unit.

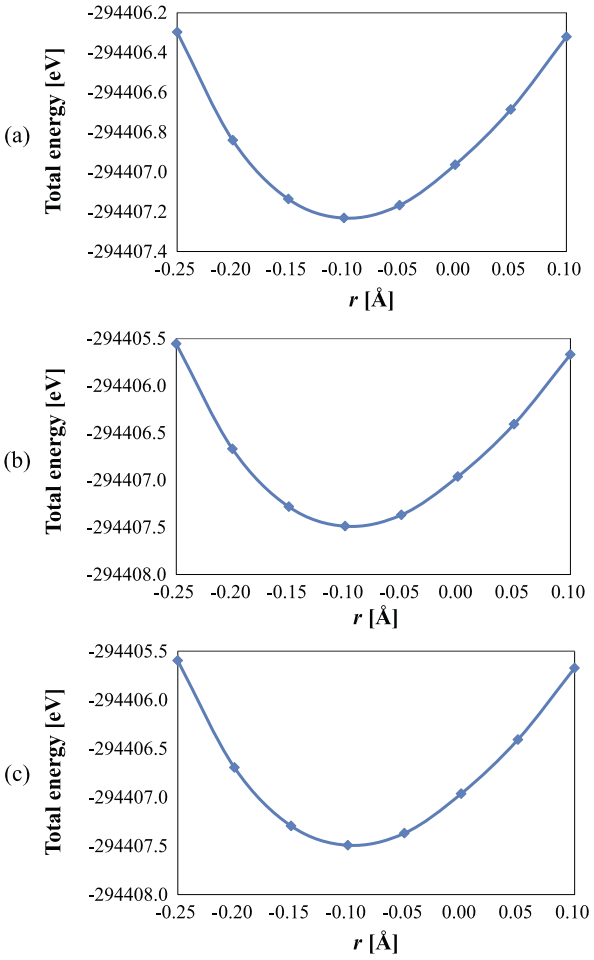

Fig. 13.12 The potential energy curves for three types of Ti–O shrinks in $SrTi_8O_{12}$ model, corresponding to Ti–C elongations in (**a**) $SrTi_8O_{11}C$, (**b**) $SrTi_8O_{10}C_2$ (I) and (**c**) $SrTi_8O_{10}C_2$ (II) models. Titanium atoms are displaced along z axis. r is the displacement distance from the initial lattice position

13.4.2 Comparison with Nitrogen-Doping

In nitrogen-doped $SrTiO_3$, we concluded that oxygen vacancy leads the degradation of visible light photocatalytic activity [9]. On the other hand, in $LaTiO_2N$ perovskite with a bandgap of 2.1 eV [22], no oxygen vacancy is formed. However, it is considered that the local strain by the covalent Ti–N–Ti bonding cannot be negligible. It may be difficult for $LaTiO_2N$ to obtain a stable structure.

In carbon-doped $SrTiO_3$, no oxygen vacancy is formed. The stable structure is kept, as the alternate Ti–C–Ti elongation and Ti–O–Ti shrink are caused. We concluded that carbon anion-doped $SrTiO_3$ is one of the best photocatalysts, from the viewpoints of both a visible light photocatalytic activity and structural stability. The efficient synthesis of carbon anion-doped $SrTiO_3$ perovskite should be explored. This work is in progress.

References

1. Wrighton MS, Ellis AB, Wolczanski PT, Morse DL, Abrahamson HB, Ginley DG (1976) J Am Chem Soc 98:2774–2779
2. Domen K, Naito S, Onishi T, Tamaru K, Soma M (1982) J Phys Chem 86:3657–3661
3. Domen K, Kudo A, Onishi T, Kosugi N, Kuroda H (1986) J Phys Chem 90:292–295
4. Fujishima A, Honda A (1972) Nature 238:37–38
5. Nozik AJ (1975) Nature 257:383–386
6. Capizzi M, Frova A (1970) Phys Rev Lett 25:1298–1302
7. Onishi T (2012) Adv Quantum Chem 64:31–81
8. Onishi T (2008) Int J Quant Chem 108:2856–2861
9. Onishi T (2010) Top Catal 53:566–570
10. Wang J, Yin S, Komatsu M, Zhang Q, Saito F, Sato T (2004) Appl Catal B 52:11–21
11. Miyauchi M, Takashio M, Tobimatsu H (2004) Langmuir 20:232–236
12. Ohno T, Tsubota T, Nakamura Y, Sayama K (2005) Appl Catal A 288:74–79
13. Ohno T, Tsubota T, Nishijima K, Miyamoto Z (2004) Chem Lett 33:750–751
14. Khan SUM, Shahry MA, Ingler WB Jr (2002) Science 297:2243–2245
15. Irie H, Watanabe Y, Hashimoto K (2003) Chem Lett 32:772–773
16. Crabtree RH (2005) The organometallic chemistry of the transition metals. Wiley, New York
17. Becke AD (1993) J Chem Phys 98:1372–1397
18. Tatewaki H, Huzinaga S (1979) J Chem Phys 71:4339–4348
19. Schmidt MW, Baldridge KK, Boatz JA, Elbert ST, Gordon MS, Jensen JH, Koseki S, Matsunaga N, Nguyen KA, Su S, Windus TL, Dupuis M, Montgomery JA (1993) J Comput Chem 14:1347–1363
20. Varetto U ⟨MOLEKEL 4. 3.⟩; Swiss National Supercomputing Centre: Manno, Switzerland
21. Haeni JH, Irvin P, Chang W, Uecker R, Reiche P, Li YL, Choudhury S, Tian W, Hawley ME, Craigo B, Tagantsev AK, Pan XQ, Streiffer SK, Chen LQ, Kirchoefer SW, Levy J, Schlom DG (2004) Nature 430:758–761
22. Kasahara A, Nokumizu K, Hitoki G, Takata T, Kondo J, Hara M, Kobayashi H, Domen K (2002) J Phys Chem A 106:6750–6753

Chapter 14
A Theoretical Study on Proton Conduction Mechanism in $BaZrO_3$ Perovskite

Taku Onishi and Trygve Helgaker

Abstract Hybrid Kohn-Sham calculations were performed to clarify the proton conduction mechanism in $BaZrO_3$ perovskite, from the viewpoint of energetics and bonding. The calculated activation energy for proton conduction was much larger than the experimental one. It is because O–H covalent bonding formation affects the low-frequency real part in AC impedance spectra. The higher proton conductivity in wet condition is derived from "proton pumping effect". We concluded that N-doping at oxygen site enhances the proton conductivity, due to the existence of much hydrogen atoms. We also investigated hydrogen defect around zirconium vacancy.

14.1 Introduction

The perovskite-type cubic $BaZrO_3$ shows proton conductivity in high temperature range (over 500 K) [1]. Many experimental [2–7] and theoretical [8–12] works were performed to investigate the proton conduction mechanism. Two proton conduction paths were theoretically proposed [10–12]. However, our previous studies [13, 14] discovered that three different proton conduction paths exist in cubic $SrTiO_3$ perovskite.

Figure 14.1 shows three proton conduction paths in $BaZrO_3$ perovskite: O–O diagonal path, two-dimensional O–H rotation within Zr_4O_4 square, and three-dimensional (3D) O–H rotation cross Zr_4O_4 square. The 3D O–H rotation was neglected in other previous studies. In general, pure Kohn-Sham methods such as

T. Onishi (✉)
Department of Chemistry for Materials, Graduate School of Engineering, Mie University, 1577 Kurimamachiya-cho, Tsu, Mie 517-8507, Japan
e-mail: taku@chem.mie-u.ac.jp

T. Onishi
The Center of Ultimate Technology on Nano-Electronics, Mie University (MIE-CUTE), 1577 Kurimamachiya-cho, Tsu, Mie 517-8507, Japan

T. Onishi
The Centre for Theoretical and Computational Chemistry (CTCC), Department of Chemistry, University of Oslo, Postbox 1033, Blindern 0315 Oslo, Norway
e-mail: taku.onishi@kjemi.uio.no

M. Hotokka et al. (eds.), *Advances in Quantum Methods and Applications in Chemistry, Physics, and Biology*, Progress in Theoretical Chemistry and Physics 27,
DOI 10.1007/978-3-319-01529-3_14,

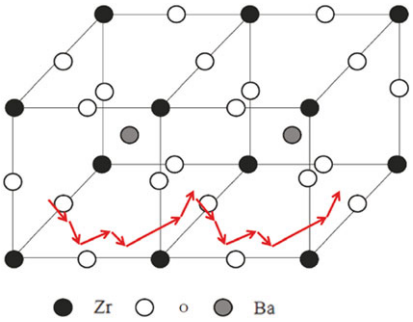

Fig. 14.1 The three proton conduction paths in cubic $BaZrO_3$ perovskite: two-dimensional O–H rotation within Zr_4O_4 square, O–O diagonal path, and three-dimensional O–H rotation cross Zr_4O_4 square

GGA, LDA and BLYP underestimate bandgap, and overestimate orbital overlap between transition metal and oxygen, due to neglecting the delocalization effect [15]. It is considered that pure Kohn-Sham method underestimates or overestimates activation energy. In this study, we calculated activation energy by several hybrid Kohn-Sham methods.

Many experimental studies have estimated activation energy from AC impedance spectra [3, 5, 7]. In wet (dry) condition, it is in 0.44–0.49 eV (0.71–0.80 eV) range. The experimental values are the same as lithium ion conductive perovskite at room temperature (below 0.4 eV) [15–17]. Hybrid Kohn-Sham method provides a reasonable activation energy. However, the operation temperature is much higher than lithium ion conduction. Here, we reconsider the calculated large activation energy for proton conduction, from the viewpoint of O–H covalent bonding formation.

In dry condition, H^+ dissolves directly to oxygen anion. On the other hand, in wet condition, OH^- and H^+ from water dissolve into an oxygen vacancy and an oxygen site, respectively:

$$H_2O + V_O^{\bullet\bullet} + O_O^X \rightarrow 2OH^{\bullet}. \tag{14.1}$$

It is considered that proton conduction starts form the stable O–H position. We investigate the effect of OH conduction through oxygen vacancy on proton conduction. We also discuss the effect of Y-doping and Sc-doping, which are performed to introduce an oxygen vacancy, on proton conduction.

Previously, we concluded that nitrogen doping at oxygen site enhances proton conductivity in $SrTiO_3$ perovskite [13]. It is because much hydrogen atoms as a part of NH^{2-} enhances proton conductivity. We discuss the effect of nitrogen doping at oxygen site on proton conductivity.

Hydrogen defects in proton conductors have attracted much scientific interest, due to difficulty of characterizing hydrogen defects in experimental measurement. Recently, Norby et al. investigated hydrogen defects in rutile-type TiO_2 by band calculations using hybrid Kohn-Sham method [18, 19]. It was concluded that titanium vacancy and OH defects are created under oxidizing conditions.

$$2H_2O + 2O_O^X \rightarrow V_{Ti}^{////} + 4OH_O^{\bullet}. \tag{14.2}$$

They investigated the number of OH defects around titanium vacancy and formation enthalpies. However, the details of O–H covalent bonding formation around

titanium vacancy, and proton conduction mechanism related to O–H defect are still unknown. In $BaZrO_3$ perovskite, zirconium vacancy and O–H defects are created under oxidizing conditions in the same manner.

$$2H_2O + 2O_O^X \rightarrow V_{Zr}'''' + 4OH_O^\bullet. \tag{14.3}$$

In this study, we investigate the effect of a hydrogen defect around zirconium vacancy on proton conductivity, from energetics and bonding.

14.2 Computation

14.2.1 Calculation Method

The calculations presented here were performed using the BHHLYP hybrid Kohn-Sham method [20], which properly reproduces the electronic structure of the strongly correlated perovskite-type transition metal oxides. In BHHLYP theory, the total exchange and correlation energy is expressed by 50 % Hartree-Fock (HF) exchange, 50 % Becke exchange and LYP correlation energies. Previously, we demonstrated that bandgap and effective exchange integral depend on HF exchange coefficient [21, 22] because M–O (M = transition metal) bonding character is controlled by localization effect. In this study, HF, B3LYP and BLYP theories with 100 %, 20 % and 0 % HF exchange, respectively, was also used to investigate the dependence of localization effect on activation energy. We used the Tatewaki-Huzinaga MINI basis [23] for zirconium, barium, yttrium and scandium, combined with the 6-31G(d) basis for oxygen and hydrogen. All calculations were performed with the GAMESS program [24]. The molecular orbitals (MOs) were plotted using MOLEKEL 4.3 [25].

14.2.2 Calculation Model

$BaZrO_3$ has a simple cubic structure, with a lattice parameter (the Zr–O–Zr distance) of 4.20 Å [26]. In our previous work, several ionics models were constructed to investigate an ionic conduction in perovskite-type solids [13–16, 27, 28]. The positions of the atoms in perovskite-type solids were kept fixed while the conductive ions migrated inside these models. To introduce hydrogen atom in $BaZrO_3$ perovskite, trivalent cation or trivalent anion is doped at zirconium or oxygen site, respectively. As the doped concentration is below 10 %, the pseudo-cubic structure can be adapted to construct cluster models.

$Ba_2Zr_4O_4H$ model was constructed to investigate the energetics and bonding in three proton conduction paths (see Fig. 14.2). In our ionics models [27], counter cation (in this case, barium) is included. It is because it participates in O–H and O–H–O bond formation. Figure 14.3 illustrates four proton conduction paths in

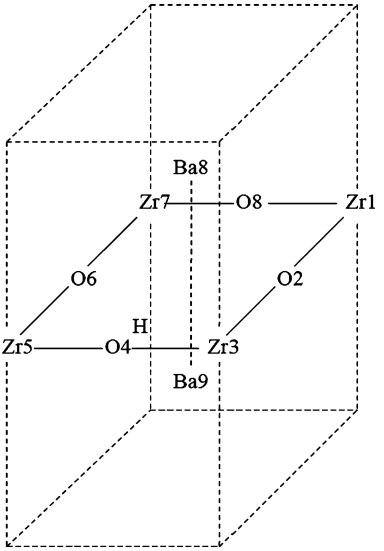

Fig. 14.2 The proton conductive ionics model $Ba_2Zr_4O_4H$

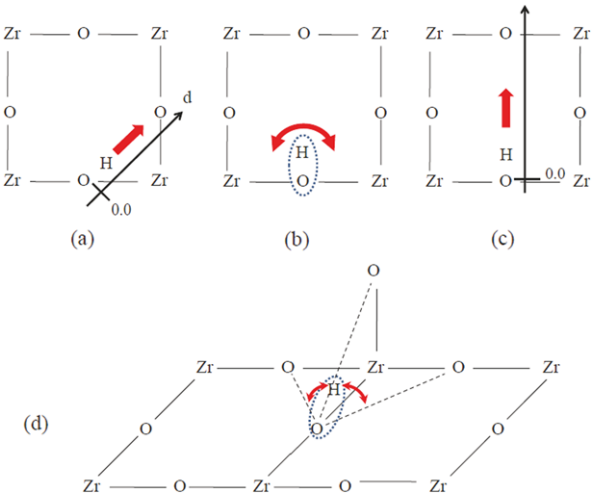

Fig. 14.3 The four proton conduction paths in $Ba_2Zr_4O_4H$ model: (**a**) O–O diagonal path (A path), (**b**) O–H rotation path within Zr_4O_4 square (B path), (**c**) O–O path along y axis (B′ path), (**d**) three-dimensional out-of-plane proton conduction path (C path). The *arrows* denote hydrogen-migration direction

$BaZrO_3$ perovskite. One is the O–O diagonal path (A path), corresponding to proton conduction along O–O diagonal line. The second is O–H rotation path within Zr_4O_4 square (B path). To investigate the stable point along y axis, the proton conduction along y axis (B′ path) was also considered. Note that B′ path is a virtual path in proton conduction in $BaZrO_3$ perovskite. The last is three-dimensional out-of-plane proton conduction path (C path), noting that the positions of the local minima along these paths are needed in order to construct the three-dimensional paths [13, 14].

The N-doped ionics model $Ba_2Zr_4O_3NH$ was constructed to examine the effect of N-doping on proton conduction. Referring to Fig. 14.2, nitrogen is introduced at

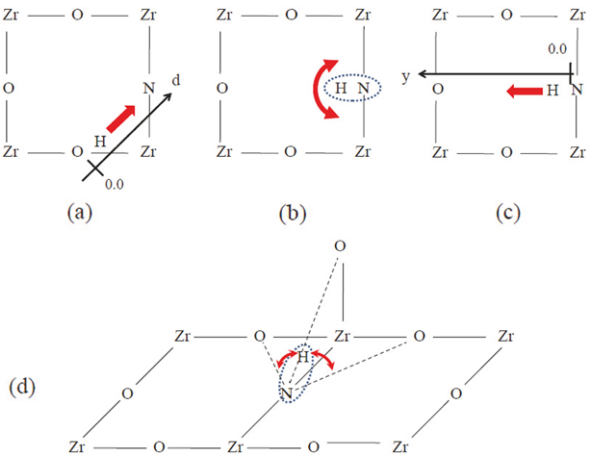

Fig. 14.4 The proton conduction paths in the nitrogen-doped ionics model $Ba_2Zr_4O_3NH$: (**a**) O–N diagonal path (A path), (**b**) N–H rotation path within Zr_4O_4 square (B path), (**c**) N–O path along *y* axis (B′ path), (**d**) three-dimensional out-of-plane proton conduction path around doped nitrogen (C path). The *arrows* denote hydrogen-migration direction

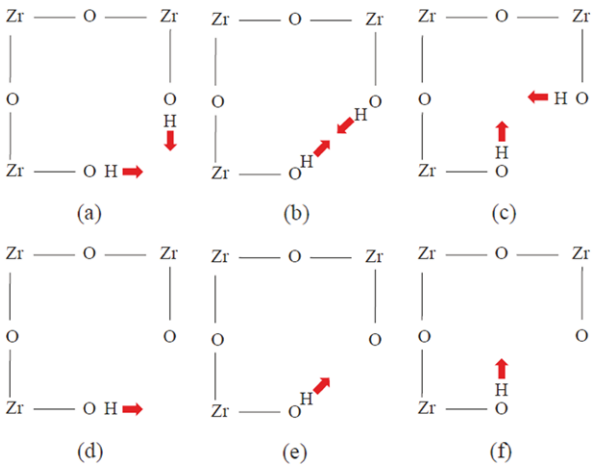

Fig. 14.5 The proton conduction paths in zirconium vacancy doped ionics models: proton conduction paths along (**a**) Zr–O–Zr, (**b**) O–O diagonal line and (**c**) toward centre in $Ba_2Zr_3O_4H_2$ model; proton conduction paths along (**d**) Zr–O–Zr, (**e**) O–O diagonal line and (**f**) toward centre in $Ba_2Zr_3O_4H$ model. The *arrows* denote hydrogen-migration direction

the O2 site. Figure 14.4 illustrates the four proton conduction paths (A, B, B′ and C paths) around doped nitrogen, in the same manner.

To investigate O–H covalent bonding formation around zirconium vacancy, the Zr vacancy-doped ionics models $Ba_2Zr_3O_4H_2$ and $Ba_2Zr_3O_4H$ were constructed. In $Ba_2Zr_3O_4H_2$ model, zirconium vacancy is introduced at the Zr3 site, and the second hydrogen atom is introduced near the O2 site. In $Ba_2Zr_3O_4H$ model, zirconium vacancy is introduced in the same manner (the Zr3 site). Figure 14.5 illustrates three proton conduction paths in $Ba_2Zr_3O_4H_2$ and $Ba_2Zr_3O_4H$ models.

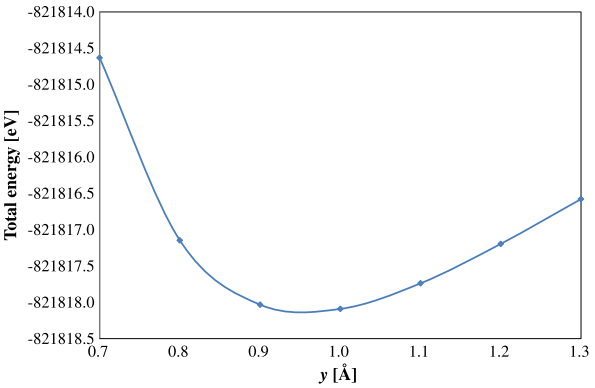

Fig. 14.6 The potential energy curve for proton conduction in B′ path of $Ba_2Zr_4O_4H$ model

14.2.3 Onishi Chemical Bonding Rule

Molecular orbital (MO) analysis is very useful to investigate the mechanism of chemical bonding formation. We constructed Onishi chemical bonding rule to judge chemical bonding character (Covalency or Ionicity) in strongly correlated M–X–M system (M = transition metal, X = O, F etc.) [26]:

1. In MOs including outer shell electrons, check whether the orbital overlap between M and X exists or not.
2. With orbital overlap, bonding character is covalent. Without orbital overlap, bonding character is ionic.

14.3 Results and Discussion

14.3.1 Proton Conduction in $BaZrO_3$ Perovskite

Figures 14.6 and 14.7 show the potential energy curves along y axis and O–O diagonal line, respectively. The minimum total energy was given around 0.9 Å along y axis. The activation energy for O–H rotation within Zr_4O_4 square is 2.26 eV, given by the total energy difference between at local minima along O–O diagonal line and y axis. The activation energy for O–O diagonal path is 1.65 eV. When the hydrogen atom migrates cross Zr_4O_4 square, the three-dimensional, out-of-plane proton conduction path dominates. Hydrogen migrates between two local minima in O–O diagonal path. Figure 14.8 shows the potential energy curve for 3D O–H rotation. The activation energy for 3D O–H rotation is 1.30 eV. It is found that O–H rotation within Zr_4O_4 square needs much energy.

In Fig. 14.9, the all potential energy curves are plotted together. It is found that the much energy is necessary to start proton conduction from the most stable point ($x = 0.0$ Å). The total activation energy was 3.91 eV, which is given by the total energy difference between the most stable point along y axis and local maximum along O–O diagonal path.

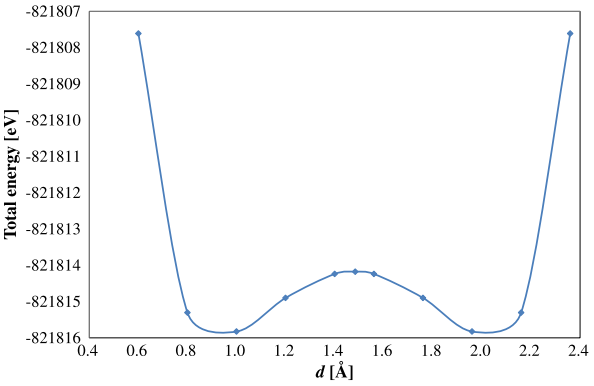

Fig. 14.7 The potential energy curve for proton conduction in A path of $Ba_2Zr_4O_4H$ model

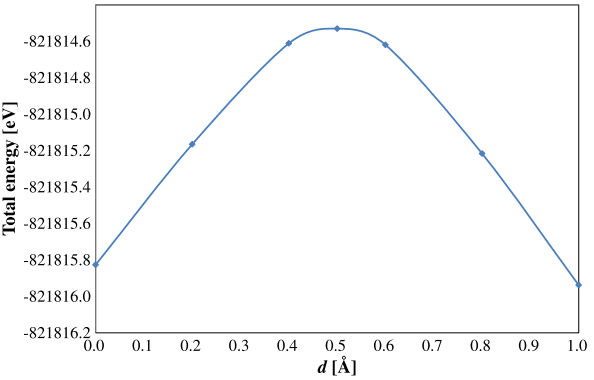

Fig. 14.8 The potential energy curve for proton conduction in C path of $Ba_2Zr_4O_4H$ model

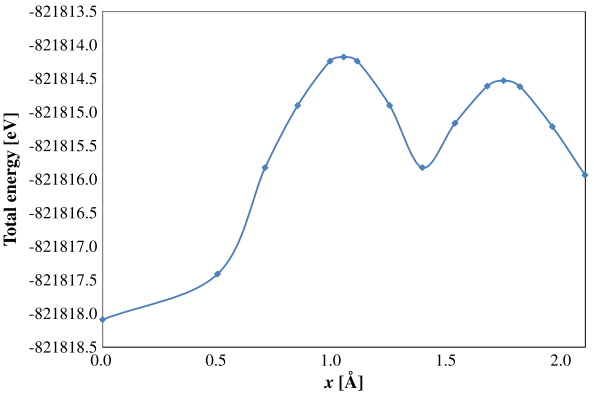

Fig. 14.9 The all potential energy curves for proton conduction in $Ba_2Zr_4O_4H$ model

14.3.2 Hartree-Fock (HF) Exchange in Hybrid Kohn-Sham

Pure Kohn-Sham methods such as LDA, GGA and BLYP underestimate bandgap, since they overestimate orbital overlap. The delocalization effect should be prop-

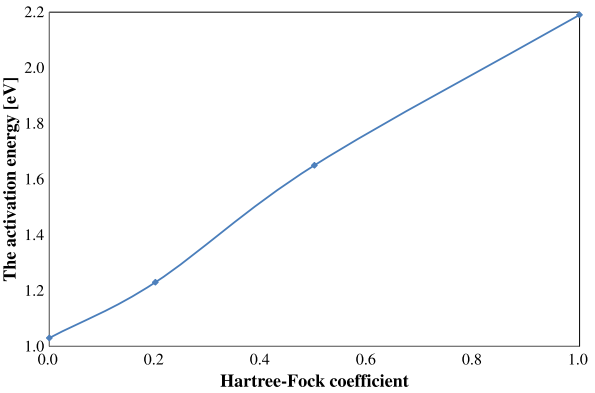

Fig. 14.10 The variation of the activation energy for proton conduction in A path of $Ba_2Zr_4O_4H$ model by changing HF exchange functional coefficient

erly included by using HF exchange. Here, we investigate the dependence of HF exchange on activation energy in O–O diagonal path. Figure 14.10 shows the variation of the activation energy by changing HF exchange functional coefficient. It is found that activation energy is approximately proportional to HF coefficient. The activation energies along O–O diagonal path are 2.19, 1.65, 1.23 and 1.03 eV by HF, BHHLYP, B3LYP and BLYP, respectively. BHHLYP approximately provides the reasonable physical constants for strongly correlated perovskite-type transition metal oxides. It is found that HF and BLYP overestimates and underestimates activation energy along O–O diagonal path.

14.3.3 Chemical Bonding Analysis

Figure 14.11 depicts MOs related to the conductive hydrogen 1s orbital at the minimum and maximum in O–O diagonal path, and the minimum along *y* axis. Figure 14.12 depicts the diagram on MO energies.

It is found that MO129 (MO136) is O–H bonding (antibonding) MO at the local minimum in O–O diagonal path. The energy difference between bonding and antibonding MOs was 4.60 eV. Although bonding and antibonding MOs exist at the maximum in O–O diagonal line, the energy difference became smaller (2.04 eV). It is concluded that O–H covalency is larger than O–H–O covalency, due to the larger orbital overlap. At the minimum along *y* axis, MO123 is O–H bonding, and MO129 and MO135 are O–H antibonding. It is found that antibonding O–H MOs (MO129 and MO135) have the bonding and antibonding interactions, respectively, with barium 5p orbital. The energy difference between O–H bonding MO123 and O–H antibonding MO129 (MO135) was 14.8 eV (17.4 eV). It is concluded that O–H covalency around the minimum is extremely large, and O–H covalency around the local minimum is larger than that around the local maximum in O–O diagonal line.

Let us consider the large mismatch between the calculated (3.91 eV) and experimental (0.44–0.49 eV) activation energies for proton conduction. In AC impedance measurement, the real part, which means electric resistance, is divided into three

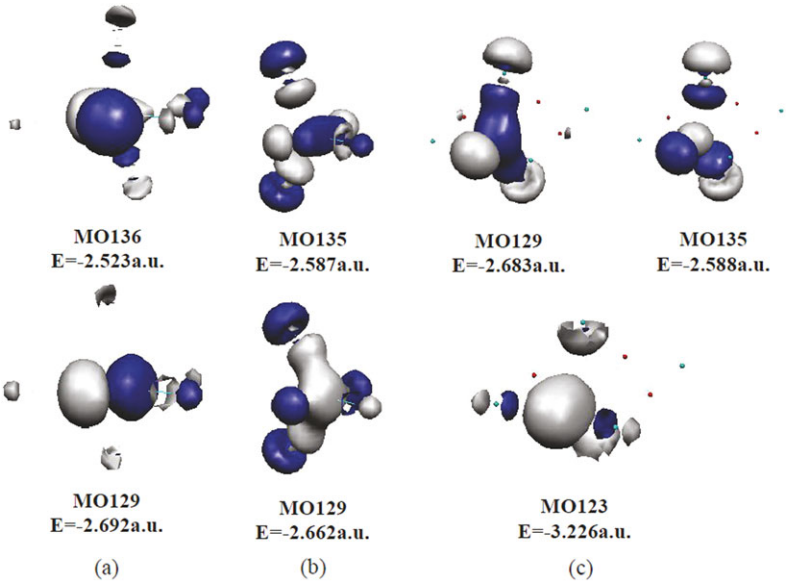

Fig. 14.11 The molecular orbitals (MOs) related the conductive hydrogen 1s orbital: (**a**) the local minimum in O–O diagonal path, (**b**) the local maximum in O–O diagonal path, (**c**) the minimum along *y* axis

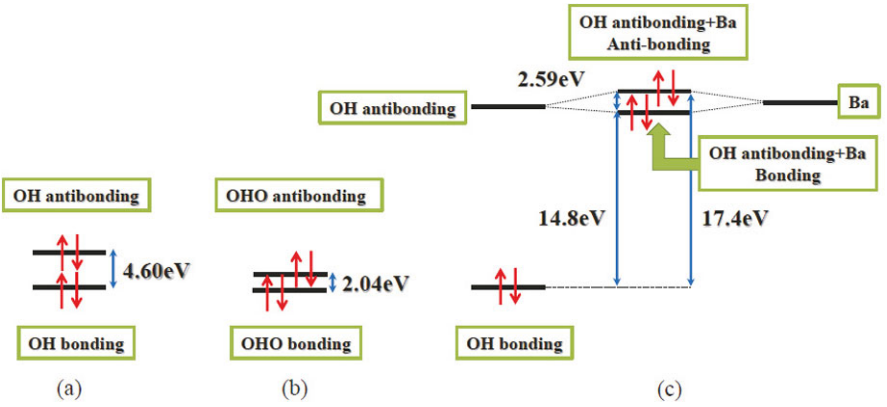

Fig. 14.12 The diagram on molecular orbital energies related the conductive hydrogen 1s orbital: (**a**) the local minimum in O–O diagonal path, (**b**) the local maximum in O–O diagonal path, (**c**) the minimum along *y* axis

contributions in Nyquist plot: bulk, grain boundary and electrode interface. In a conventional ion conductivity measurement, it is assumed that the ion exists as a part of not molecule but sole ion. However, hydrogen exists as a part of O–H bonding or O–H–O bonding rather than ion. In O–H bonding region, O–H rotation oc-

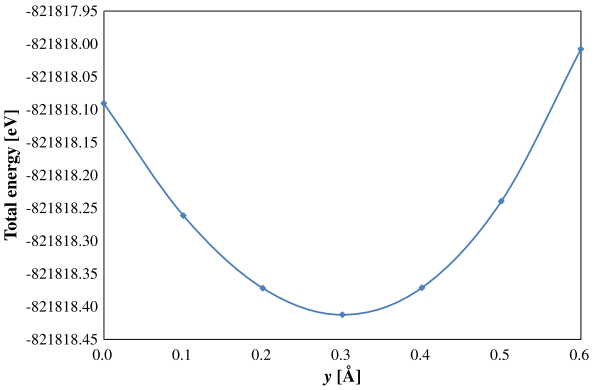

Fig. 14.13 The potential energy curve for OH-conduction along y axis in $Ba_2Zr_4O_4H$ model

curs instead of hydrogen migration. On the other hand, it is considered that hydrogen migration is measured in O–H–O covalent bonding (O–H dissociation region). The low-frequency real part in Nyquist plot corresponded to only O–H–O covalent bonding region. In other words, the experimental activation energy is much underestimated. The calculated large activation energy for proton conduction in $BaZrO_3$ perovskite is consistent with a high temperature (over 500 K) required to start proton conduction. However, in lithium ion conductive perovskite-type titanium oxide, our calculated activation energies approximately corresponded to the experimental ones (under 0.4 eV at room temperature) [17]. The conductive lithium ion forms ionic bonding with other atoms, according to Onishi chemical bonding rule [15]. In AC impedance measurement, as conductivity is simply recognized as lithium ion migration, the low-frequency real part corresponds well to lithium ion conduction.

14.3.4 Proton Pumping Effect: OH-Conduction in Wet Condition

To introduce hydrogen in $BaZrO_3$ perovskite, trivalent cations such as yttrium and scandium are doped at zirconium site. At the same time, oxygen vacancy is created at oxygen site. In wet conditions, OH dissolved from water migrates through oxygen vacancy. We considered O–H-conduction along y axis, where O–H direction is perpendicular to Zr–O–Zr, and O–H distance is kept fixed. When hydrogen in OH exists between oxygen and zirconium in Zr–O–Zr, the total energy is higher, due to the ionic repulsion between hydrogen and zirconium, same as in $SrTiO_3$ perovskite [13].

Figure 14.13 shows the potential energy curve for OH-conduction along y axis. The local minimum was given at 0.3 Å. It means that proton conduction starts from this stable O–H site inside Zr_4O_4 square. We considered the proton conduction path from this site to oxygen. Figure 14.14 shows all potential energy curves in the three proton conduction paths namely O–H rotation within Zr_4O_4 square, short O–O diagonal line and 3D O–H rotation cross Zr_4O_4 square. The activation energies for O–H rotation, short O–O diagonal path and 3D O–H rotation were 1.64, 0.78 and

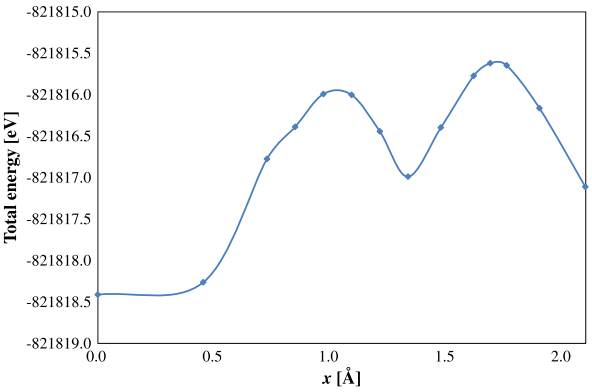

Fig. 14.14 The all calculated potential energy curves in proton conduction paths such as O–H rotation within Zr_4O_4 square, short O–O diagonal line and three-dimensional O–H rotation of $Ba_2Zr_4O_4H$ model

1.36 eV, respectively. They became smaller than in dry conditions except for 3D O–H rotation. The total activation energy became 2.42 eV, given by the total energy difference between the most stable point along y axis and local maximum along O–O diagonal path. It means that wet condition is superior to dry condition, due to this "proton pumping effect". Phonon assisted proton conduction mechanism and tunnelling effect are also considered. However, their effect is smaller, due to the smaller displacement of oxygen atoms in Zr_4O_4 square.

In Y-doped (Sc-doped) ionics model $Ba_2Zr_3YO_4H$ ($Ba_2Zr_3ScO_4H$), where Y (Sc) is doped at Zr3 site in Fig. 14.2, the total activation energy was 4.09 eV (3.01 eV). On the other hand, the activation energies for 3D O–H rotation were 1.79 and 1.76 eV, respectively. It is concluded that Sc-doping is superior to Y-doping for proton conduction.

14.3.5 Nitrogen-Doping at Oxygen Site

To enhance the proton conduction, we considered trivalent anion-doping at oxygen site. In nitrogen doping at oxygen site, hydrogen can exist as a part of NH^{2-}. We calculated the activation energy for nitrogen-doped $BaZrO_3$ perovskite in three proton conduction paths namely N–H rotation around nitrogen, O–N diagonal path and 3D N–H rotation. Figure 14.15 shows the potential energy curve in O–N diagonal path (O is located at $d = 0.0$ Å). The activation energy from N to O is 2.14 eV, and reverse barrier (from O to N) is 0.40 eV. It is found that hydrogen is more stabilized around nitrogen. As the most stable hydrogen position was given in y axis, the activation energies for N–H rotation around nitrogen, and 3D N–H rotation were 2.13 and 1.68 eV, respectively. The total activation energy from nitrogen to nearest-neighbour oxygen is 4.26 eV, which is slightly larger than $Ba_2Zr_4O_4H$ model (3.91 eV). It is concluded that nitrogen-doping enhances proton conductivity, due to introduction of much hydrogen.

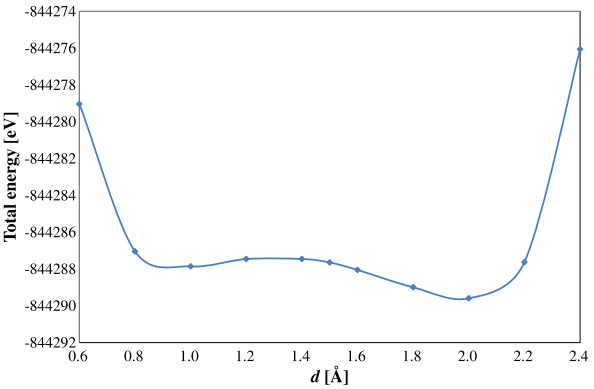

Fig. 14.15 The potential energy curve for proton conduction in O–N diagonal path of $Ba_2Zr_4O_3NH$ model

14.3.6 Hydrogen Defect Around Zirconium Vacancy

We investigated O–H covalent bonding formation around zirconium vacancy. In the $Ba_2Zr_3O_4H_2$ model, the relationship between two hydrogen defects was investigated. The proton conduction mechanism between hydrogen defects around zirconium vacancy was investigated in $Ba_2Zr_3O_4H$ model.

Figure 14.16 depicts the potential energy curves for proton conduction in the $Ba_2Zr_3O_4H_2$ model. The local minima were given in the all curves. The minimum total energy was obtained, when hydrogen atom is located along Zr–O–Zr. It is found that two hydrogen-defects are stabilized when OH covalent bonding is toward zirconium vacancy. It is because the ionic repulsion between conductive hydrogen and barium is smaller. Figure 14.17 depicts the schematic picture on hydrogen defects around zirconium vacancy. Four hydrogen defects are theoretically captured per one zirconium vacancy to compensate charge.

Figure 14.18 depicts the potential energy curve for proton conduction in $Ba_2Zr_3O_4H$ model. Whereas the local minima were given in the all curves, the local maxima were given along Zr–O–Zr and O–O diagonal path. The activation energies for proton conduction along Zr–O–Zr and diagonal line were 1.77 and 1.08 eV, respectively. The minimum energy was given along Zr–O–Zr, the same as $Ba_2Zr_3O_4H_2$ model. The total activation energy for proton conduction along O–O diagonal path was 2.85 eV. Proton conduction along Zr–O–Zr occurs more often than along O–O diagonal path. The activation energy for O–H rotation within Zr_4O_4 square was 3.15 eV. We concluded that conductive hydrogen atoms are trapped around zirconium vacancy, and proton conduction occurs from oxygen to oxygen through zirconium vacancy. The schematic picture is depicted in Fig. 14.19.

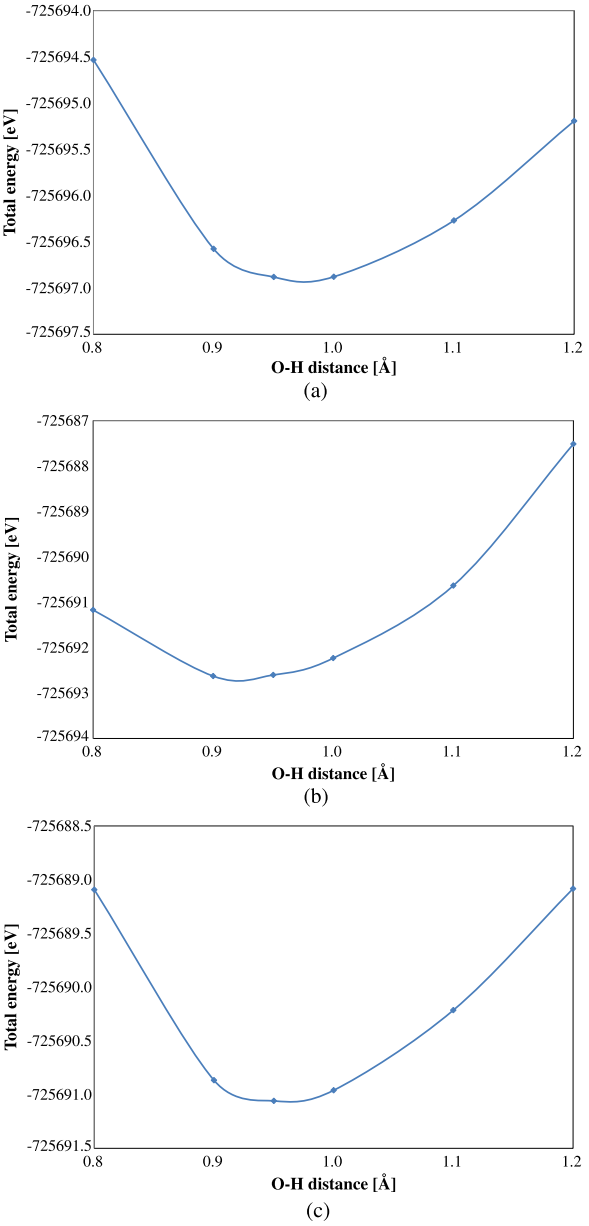

Fig. 14.16 The potential energy curves for proton conduction in $Ba_2Zr_3O_4H_2$ model: proton conduction paths along (**a**) Zr–O–Zr, (**b**) O–O diagonal line and (**c**) toward centre

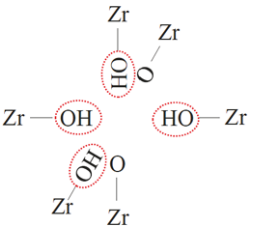

Fig. 14.17 A schematic picture of hydrogen defects around zirconium vacancy in $BaZrO_3$ perovskite

14.4 Concluding Remarks

14.4.1 General Conclusions

In this study, hybrid Kohn-Sham calculations were performed for ionics models to investigate the proton conduction mechanism in $BaZrO_3$ perovskite. We concluded as follows.

1. The activation energies were 2.26, 1.65 and 1.30 eV for O–H rotation within Zr_4O_4 square, O–O diagonal path and 3D O–H rotation across Zr_4O_4 square, respectively. The total activation energy was 3.91 eV, which is calculated from the energy difference between the minimum in O–H rotation and maximum in O–O diagonal path.
2. The activation energy changes, depending on Hartree-Fock coefficient in hybrid Kohn-Sham method. Pure Kohn-Sham underestimates the activation energy.
3. The strong O–H covalent bonding is formed within Zr_4O_4 square. O–H–O covalent bonding is in O–H dissociation region, from the energy difference between bonding and antibonding molecular orbitals. It is considered that hydrogen as a part of O–H covalent bonding is not recognized in the low-frequency real part of AC impedance spectra.
4. Proton pumping effect is responsible for high proton conductivity. It is because the short O–O distance blocks O–H dissociation.
5. Sc-doping is superior to Y-doping at titanium site.
6. N-doping at oxygen site enhances proton conductivity, the same as in $SrTiO_3$ perovskite.
7. Hydrogen defect is located toward zirconium vacancy, to avoid the ionic repulsion with barium. Proton conduction occurs between oxygen atoms around zirconium vacancy. However, hydrogen atom is trapped around zirconium vacancy, due to the higher energy barrier.

14.4.2 Future Prospects

Very recently, we concluded that the defect of hydrogen-molecule (H_2) exists at strontium vacancy at the cubic centre, and H_2 conduction occurs through strontium vacancy and Ti_4O_4 bottleneck in $SrTiO_3$ perovskite [29]. The activation energy (1.4–1.5 eV) was calculated by BHHLYP hybrid Kohn-Sham method. The

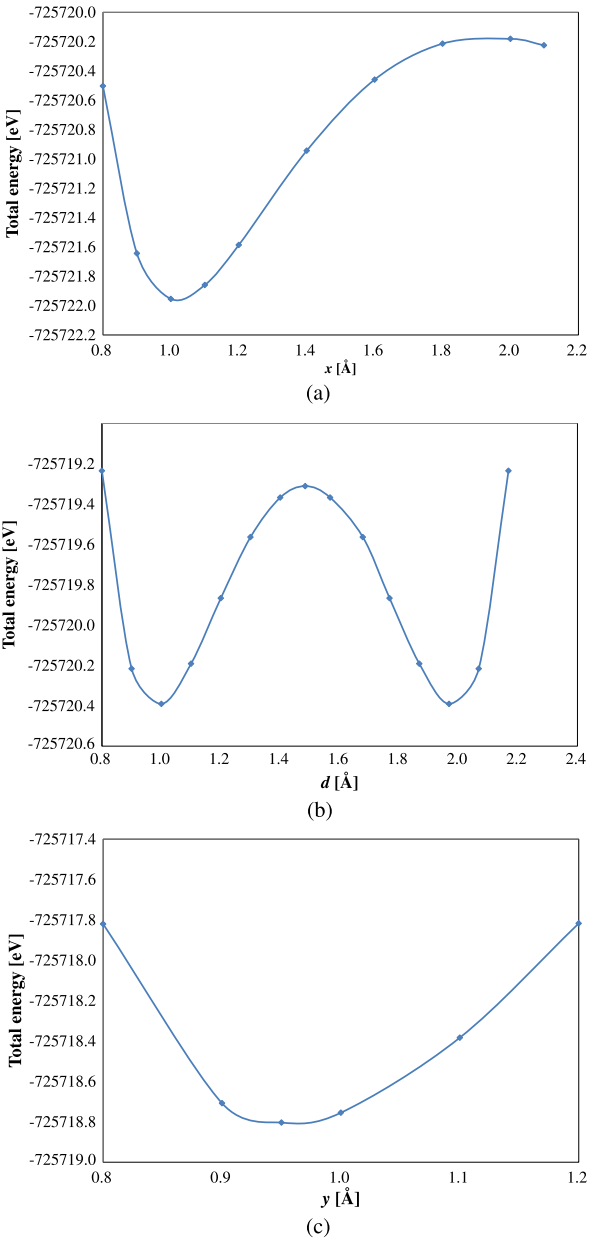

Fig. 14.18 The potential energy curves for proton conduction in $Ba_2Zr_3O_4H$ model: proton conduction paths along (**a**) Zr–O–Zr, (**b**) O–O diagonal line and (**c**) toward centre

proton conductive $SrTiO_3$ and $BaZrO_3$ are used in electrolyte of solid oxide fuel cell (SOFC). In a practical use, safety problem cannot be negligible. The relationship between H_2 defect and safety should be explored.

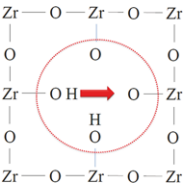

Fig. 14.19 A schematic picture of trapped hydrogen defects and proton conduction around zirconium vacancy

Acknowledgements This work was partially supported by The Norwegian Research Council through the CoE Centre for Theoretical and Computational Chemistry (Grant No. 179568/V30).

References

1. Iwahara H, Yajima T, Hibino T, Ozaki K, Suzuki H (1993) Solid State Ion 61:65–69
2. Kreuer KD (1999) Solid State Ion 125:285–302
3. Bohn HG, Schober T (2000) J Am Ceram Soc 83:768–792
4. Kreuer KD, Adams St, Münch W, Fuchs A, Klock U, Maier J (2001) Solid State Ion 145:295–306
5. Babilo P, Uda T, Haile SM (2007) J Mater Res 22:1322–1330
6. Duval SBC, Holtappels P, Vogt UF, Pomjakushina E, Conder K, Stimming U, Graule T (2007) Solid State Ion 178:1437
7. Kjølseth C, Fjeld H, Pryth Ø, Dahl PI, Estournès C, Haugsrud R, Norby T (2010) Solid State Ion 181:268–275
8. Münch W, Seifert G, Kreuer KD, Maier J (1997) Solid State Ion 97:39–44
9. Münch W, Kreuer KD, Seifert G, Maier J (2000) Solid State Ion 136–137:183–189
10. Shi C, Yoshino M, Morinaga M (2005) Solid State Ion 176:1091–1096
11. Björketun ME, Sundell PG, Wahnström G (2007) Phys Rev B 76:054307
12. Sundell PG, Björketun ME, Wahnström G (2007) Phys Rev B 76:094301
13. Onishi T, Helgaker T (2012) Int J Quant Chem 112:201–207
14. Onishi T, Helgaker T (2013) Int J Quant Chem 113:599–604
15. Onishi T (2009) Solid State Ion 180:592–597
16. Onishi T (2009) Int J Quant Chem 109:3659–3665
17. Inaguma Y, Liquan C, Itoh M, Nakamura T, Uchida T, Ikuta H, Wakihara M (1993) Solid State Commun 86:689–693
18. Bjørheim TS, Stølen S, Norby T (2010) Phys Chem Chem Phys 12:6817–6825
19. Bjørheim TS, Kuwabara A, Mohn CE, Norby T (2012) Int J Hydrog Energy 37:8110–8117
20. Becke AD (1993) J Chem Phys 98:1372–1377
21. Onishi T (2008) Int J Quant Chem 108:2856–2861
22. Onishi T, Takano Y, Kitagawa Y, Kawakami T, Yoshioka Y, Yamaguchi K (2001) Polyhedron 20:1177–1184
23. Tatewaki H, Huzinaga S (1979) J Chem Phys 71:4339–4348
24. Schmidt MW, Baldridge KK, Boatz JA, Elbert ST, Gordon MS, Jensen JH, Koseki S, Matsunaga N, Nguyen KA, Su S, Windus TL, Dupuis M, Montgomery JA (1993) J Comput Chem 14:1347–1363
25. Varetto U ⟨MOLEKEL 4.3.⟩; Swiss National Supercomputing Centre. Manno, Switzerland
26. Bjørheim TS, Kuwabara A, Ahmed I, Haugsrud R, Stølen S, Norby T (2010) Solid State Ion 181:130–137
27. Onishi T (2012) Adv Quantum Chem 64:31–81
28. Onishi T (2010) Int J Quant Chem 110:2912–2917
29. Onishi T, Helgaker T (2012) In "A theoretical study on defect of hydrogen molecule for proton conductive $SrTiO_3$ perovskite". Presented at 14th international congress of quantum chemistry (ICQC)

Chapter 15
Molecular Theory of Graphene

E.F. Sheka

Abstract Odd electrons of benzenoid units and the correlation of these electrons having different spins are the main concepts of the molecular theory of graphene. In contrast to the theory of aromaticity, the molecular theory is based on the fact that odd electrons with different spins occupy different places in the space so that the configuration interaction becomes the central point of the theory. Consequently, a multi-determinant presentation of the wave function of the system of weakly interacting odd electrons is utterly mandatory on the way of the theory realization at the computational level. However, the efficacy of the available CI computational techniques is quite restricted in regard to large polyatomic systems, which does not allow performing extensive computational experiments. Facing the problem, computationists have addressed standard single-determinant ones albeit not often being aware of the correctness of the obtained results. The current chapter presents the molecular theory of graphene in terms of single-determinant computational schemes and discloses how reliable information about the electron-correlated system can be obtained by using either UHF or UDFT computational schemes.

When the paper was written, a splendid conceptually profound 'informal reflection' of Roald Hoffmann appeared in the first issue of the Angewandte Chemie (International edition) that celebrates its 125-year anniversary [1]. Hoffmann's "Small but Strong Lessons from Chemistry for Nanoscience" turned out to be remarkably concordant to the main ideas discussed in the current chapter. This should be expected since the Hoffmann concepts on stabilizing singlet states of biradicals in organic chemistry (see [2] and references therein) and dimeric molecular magnets [3] have laid the foundation of the molecular theory of fullerenes [4, 5], application of which to graphene science is discussed below. These problems are on a knife-edge today that is why, once in full agreement with Hoffmann's answers to the question 'What you can trust about theory?'. I would like to preface the presentation of the text of a quote from the 'informal reflection', placing it as the epigraph

E.F. Sheka (✉)
Peoples' Friendship University of Russia, Miklukho-Maklay, 6, Moscow 117198, Russia
e-mail: sheka@icp.ac.ru

M. Hotokka et al. (eds.), *Advances in Quantum Methods and Applications in Chemistry, Physics, and Biology*, Progress in Theoretical Chemistry and Physics 27,
DOI 10.1007/978-3-319-01529-3_15,

It goes without saying that theory is really of value when it is used to perform numerical experiments that capture a trend. Not numbers, but a trend.

Roald Hoffmann, 2013.

15.1 Introduction

For more than ten years, I have been immersed in an absorbing world of quantum chemistry of sp^2 nanocarbons, a world full of mysteries, hidden obstacles, and wonderful discoveries. My first travelling was stimulated by a wish to find the answer to a very simple question: why is there no fullerene Si_{60} while fullerene C_{60} does exist? A widely spread standard statement "silicon does not like sp^2 configuration" just postulated the fact but did not explain the reason. Moreover, computations, available by that time, showed that Si_{60} molecule could exist. A comparative examination of C_{60} and Si_{60} showed a strange feature in the high-spin states behavior of the molecules. As occurred, a sequence of spin-varying states (singlet (RHF)-triplet-quintet) formed a progressively growing series by energy for the C_{60} molecule while for the Si_{60} one energy of the triplet and quintet states turned out to drop drastically with respect to the RHF singlet. Due to a crucial controversy with the reality, a natural question arose: what is wrong with the molecule singlet state? I will not touch here on the frequent claim that the semiempirical approach is bad. It is not the case, in general, and is absolutely not relevant to carbonaceous and siliceous species due to superior parameterization of both atoms. Actually, all the next stories have shown that the matter was not due to the wrong approximation but was provided by an inherent peculiarity of both molecules. At that time, in 2003, it was shown that the singlet state of the Si_{60} molecule took its correct place below the triplet one if it only is calculated by using the open-shell unrestricted Hartree-Fock (UHF) approximation [4, 6, 7]. Since then, in more than eight dozen papers that followed, I and my colleagues have convinced ourselves and have tried to convince others that UHF approach touches very intimate properties of sp^2 nanocarbons that select them from other carbonaceous species and put them in a particular place. The properties are the result of a significant weakening of the interaction between the odd electrons of the species in comparison with, say, that one in the benzene molecule.

During these investigations we obtained (i) the answer to the initial question concerning the absence of Si_{60} molecule [4], (ii) disclosed regulations that govern chemistry, magnetism, biomedical and photonic behavior of carbonaceous fullerenes [5], (iii) showed a tight similarity in the description of the properties of fullerenes, carbon nanotubes, and graphene molecules [5, 8]. Little by little an applied molecular theory of sp^2 nanocarbons became sharply defined, which revealed itself in the most vivid way in case of graphene. However, graphene, which is a famous nobeliated 2D solid, and molecular theory—if there is no controversy between these subjects?

The answer lies on a surface and follows from a well known definition of graphene: 'Graphene is an allotrope of carbon, whose structure is one-atom-thick

planar sheets of sp^2-bonded carbon atoms that are densely packed in a honeycomb crystal lattice [9]'. This definition clearly exhibits a molecular-crystal duality of this extraordinary substance. From the molecular viewpoint, the extraordinariness is provided with the availability of odd electrons that are responsible for the sp^2 configuration of valence electrons of carbon atoms. The 2D-dimensionality, on the other hand, dictates peculiar properties of a regularly packed honeycomb pattern. Due to this, the graphene properties are similar to those of both polycondensed benzenoid molecules and 2D-dimensional crystals. Obviously, fundamental characteristics of the two forms are tightly interconnected. Thus, as will be discussed below, such seemingly solid state properties as magnetism and mechanics of graphene are of molecular origin.

The above mentioned peculiar duality is embodied in the computational strategy of graphene, as well. On one hand, the solid state microscopic theory of quasiparticles in a 2D space forms the ground for the description of the graphene crystal. On the other hand, quantum molecular theory creates the concept of the graphene molecule. Seemingly, the two theoretical approaches, obviously different from the computational viewpoint, have nevertheless much in common. Thus, the solid state quasiparticles are usually described in the approach based on a unit cell and/or supercell followed by periodic boundary conditions; besides, the unit cell is described at the molecular theory level thus presenting the molecular object in the same way as in the case of the molecular theory. However, the very molecular object provides a crucial difference between the two approaches. In the case of a correct solid state formulation, the cell and/or supercell should be strictly chosen as a known crystalline motive. Accordingly, the two-atomic cell of graphene crystal finds its exhibition in the peculiarities of the crystal electron band structure. However, nowadays, the solid state approach is explored in the graphene science in regard to practically all the phenomena including graphene chemical modification, graphene deformation and magnetization. The two-atomic unit cell of the crystal does not meet conditions needed for examining these complicated events, particularly, related to the chemical modification. The cell is substituted by a supercell, whose structure is taken at one's own choosing, once in the preponderance of cases just 'drawn' in stead off attributed to a reality. Moreover, regular structure of the graphene object is fastened by the periodical boundary conditions. The two features of the solid-state approach, namely, the arbitrarily chosen supercell and the fastened periodicity make clear the Hoffmann answer "Not much" to the question "What you can trust about theory?" [1]. Then Hoffmann continues: "Aside from the natural prejudice for simplicity, people really want translational periodicity in their calculations, for then the quantum mechanical problem reduces to one of the size of the unit cell. But the real world refuses to abide by our prejudices. And it is often an aperiodic, maximally defect-ridden, amorphous world, where emergent function is found in matter that it is as far from periodic as possible". The reality of the graphene science, particularly, related to the chemical modification, strongly witnesses the domination of aperiodic structures. In view of this, the molecular theory of graphene has a convincing preference since its molecular object is created in the course of computations without structural restrictions introduced in advance.

The current chapter is concentrated at the molecular essence of graphene considered from the viewpoint of the molecular theory of sp^2 nanocarbons. The theory is based on two main concepts, which involve the odd-electron origin of the graphene electron system and these electrons correlation. The latter turns out to play the governing role. As will be shown below, such an approach occurs very efficient in describing chemical, magnetic, mechanical, and optical properties of graphene.

15.2 Odd Electrons Correlation

In spite of formally two-atomic unit cell of crystalline graphene, its properties are evidently governed by the behaviour of odd electrons of the hexagonal benzenoid units. The only thing that we know about the behaviour for sure is that the interaction between odd electrons is weak; nevertheless, how weak is it? Is it enough to provide a tight covalent pairing when two electrons with different spins occupy the same place in space or, oppositely, is it too weak for this and the two electrons are located in different spaces thus becoming spin correlated? This supremely influential molecular aspect of graphene can be visualised on the platform of the molecular quantum theory.

To exhibit a trend, a system computational experiment must be carried out meaning that a vast number of computations are to be performed as well as a great number of atoms are to be considered. When speaking about electron correlation, one should address the problem to the configuration interaction (CI). However, neither full CI nor any its truncated version, clear and transparent conceptually, can be applied for the computational experiments, valuable for graphene nanoscience. Owing to this, techniques based on single unrestricted open-shell determinants becomes the only alternative. Unrestricted Hartree-Fock (UHF) and unrestricted DFT (spin polarized, UDFT) approaches form the techniques ground and are both sensitive to the electron correlation, but differently due to different dependence of their algorithms on electron spins [10, 11]. The approach application raises two questions: (1) what are criteria that show the electron correlation in the studied system and (2) how much are the solutions of single-determinant approaches informative for a system of correlated electrons.

Answering the first question, three criteria, which highlight the electron correlation at the single-determinant level of theory, can be suggested. Those concern the following characteristic parameters:

Criterion 1

$$\Delta E^{RU} \geq 0,$$

where,

$$\Delta E^{RU} = E^R - E^U \tag{15.1}$$

presents a misalignment of energy. Here, E^R and E^U are the total energies calculated by using the restricted and unrestricted versions of the software in use.

Criterion 2

$$N_D \neq 0.$$

Here, N_D is the total number of effectively unpaired electrons. The number is determined as

$$N_D = \mathrm{tr}\, D\left(r|r'\right) \neq 0 \quad \text{and} \quad N_D = \sum_A D_A. \tag{15.2}$$

Here, $D(r|r')$ [12] and D_A [13] present the total and atom-fractioned spin density caused by the spin asymmetry due to the location of electrons with different spins in different spaces.

Criterion 3

$$\Delta\hat{S}^2 \geq 0. \tag{15.3}$$

Here,

$$\Delta\hat{S}^2 = \hat{S}_U^2 - S(S+1)$$

presents the misalignment of squared spin. $\hat{S}_U^2$ is the squared spin calculated within the applied unrestricted technique while $S(S+1)$ presents the exact value of $\hat{S}^2$.

Criterion 1 follows from the well known fact that the electron correlation, if available, lowers the total energy [14]. Criterion 2 highlights the fact that the electron correlation is accompanied with the appearance of effectively unpaired electrons that provide the molecule radicalization [12, 13, 15]. Those electrons total number N_D depends on interatomic distance: when the latter is under a critical value R_{cov}^{crit}, two adjacent electrons are covalently bound and $N_D = 0$. However, when the distance exceeds R_{cov}^{crit}, the two electrons become unpaired; $N_D \geq 0$, the more, the larger is the interatomic spacing. In the case of the sp^2 C–C bonds, $R_{\mathrm{cov}}^{crit} = 1.395$ Å [16]. Criterion 3 is the manifestation of the spin contamination of unrestricted single-determinant solutions [13, 15]; the stronger electron correlation, the bigger spin contamination of the studied spin state.

Table 15.1 presents sets of the three parameters evaluated for a number of graphene molecules presented by rectangular (n_a, n_z) fragments of graphene (n_a and n_z count the benzenoid units along armchair and zigzag edges of the fragment, respectively [19]), (n_a, n_z) nanographenes (NGrs) below, by using the AM1 version of the semiempirical UHF approach implemented in the CLUSTER-Z1 codes [18]. To our knowledge, only this software allows for getting all the above three parameters within one computing session. As seen in the table, the parameters are certainly not zero, obviously greatly depending on the fragment size while their relative values are practically non size-dependent. The attention should be called to rather large N_D values, both absolute and relative. The finding evidences that the length of C–C bonds in the considered molecules exceed the critical value $R_{\mathrm{cov}}^{crit} = 1.395$ Å. It should be added as well that the relation $N_D = 2\Delta\hat{S}_U^2$, which is characteristic for

Table 15.1 Identifying parameters of the odd electron correlation in the rectangular graphene fragments [17]

Fragment (n_a, n_z)	Odd electrons N_{odd}	ΔE^{RU} [a] kcal/mol	δE^{RU} %[b]	N_D, e	δN_D, %[b]	$\Delta\hat{S}^2_U$
(5, 5)	88	307	17	31	35	15.5
(7, 7)	150	376	15	52.6	35	26.3
(9, 9)	228	641	19	76.2	35	38.1
(11, 10)	296	760	19	94.5	32	47.24
(11, 12)	346	901	20	107.4	31	53.7
(15, 12)	456	1038	19	139	31	69.5

[a]AM1 version of UHF codes of CLUSTER-Z1 [18]. Presented energy values are rounded off to an integer

[b]The percentage values are related to $\delta E^{RU} = \Delta E^{RU}/E^R(0)$ and $\delta N_D = N_D/N_{odd}$, respectively

spin contaminated solutions in the singlet state [13], is rigidly kept over all the fragments.

Summarizing said above, it is possible to conclude the following.

1. Nowadays, single-determinant computational schemes, based on the open-shell approximation of either Hartree-Fock or DFT approach, are the only alternative for practically valuable computations of polyatomic graphene systems (Nat > 30–40);
2. For electron-correlated systems, the obtained solutions are not exact but spin-mixed;
3. The question arises: which reliable information about electron-correlated system can be obtained by using either UHF or UDFT computational scheme?

Given below has been organized as getting answers to this question.

Answer 1 Broken symmetry approach allows obtaining the exact energy of pure-spin states.

The wave functions of the unrestricted single-determinant solutions satisfy the operator equations for the energy and z-projection of the spin S_z but do not satisfy the operator equation for the squared spin $\hat{S}^2$. This causes a spin contamination of the solution whose extent is determined by $\Delta\hat{S}^2$ (3). Owing to this, one faces the problem of the evaluation of the energies of pure spin states.

The unrestricted broken symmetry (UBS) approach suggested by Noodleman [20] can be considered as the best way to solve the problem. It is the most widely known among the unrestricted single-determinant computational schemes used in practice, both UHF and UDFT. The UBS approach provides the determination of the exact energy of pure-spin states on the basis of the obtained single-determinant results within each of the computational schemes at the level of the theory that is equivalent to the explicit CI. According to the approach, the energy of pure-spin singlet state is expressed as

$$E^{PS}(0) = E^U(0) + S_{\max} J, \tag{15.4}$$

Table 15.2 Energies of singlet ground state and exchange integral of the rectangular graphene fragments,[a] kcal/mole [17]

Fragment (n_a, n_z)	$E^R(0)$	$E^U(0)$	$E^{PS}(0)$	ΔE^{RPS}	δE^{RPS}[b] %	ΔE^{UPS}	δE^{UPS}[b] %	J
(5, 5)	1902	1495	1432	470	24.70	63	4.39	−1.429
(7, 7)	2599	2223	2156	443	17.03	67	3.09	−0.888
(9, 9)	3419	2778	2710	709	20.75	68	2.53	−0.600
(11, 10)	4072	3312	3241	831	20.42	71	2.20	−0.483
(11, 12)	4577	3676	3606	971	21.22	70	1.95	−0.406
(15, 12)	5451	4413	4339	1112	20.40	74	1.70	−0.324

[a]AM1 version of UHF codes of CLUSTER-Z1. Presented energy values are rounded off to an integer

[b]The percentage values are related to $\delta E^{RPS} = \Delta E^{RPS}/E^R(0)$ and $\delta E^{UPS} = \Delta E^{UPS}/E^U(0)$, respectively

where, $E^U(0)$ is the energy of the singlet state of the USB solution while $S_{\max}$ is the highest spin of the studied odd electron system and J presents the exchange integral

$$J = \frac{E^U(0) - E^U(S_{\max})}{S_{\max}^2}. \tag{15.5}$$

Here, $E^U(S_{\max})$ is the energy of the highest-spin-multiplicity state and corresponds to the $S_{\max}$-pure-spin state.

Table 15.2 presents sets of three energies, namely: $E^R(0)$, $E^U(0)$, and $E^{PS}(0)$, alongside with the exchange integrals J related to (n_a, n_z) NGrs considered earlier. As seen in the table, comparing with $E^R(0)$, the odd electron correlation causes lowering of not only $E^U(0)$ energy, but $E^{PS}(0)$ as well, therewith, the pure-spin energy $E^{PS}(0)$ occurs to be the lowest. As seen from the table, the percentage quantities $\delta E^{RPS} = \Delta E^{RPS}/E^R(0)$ and $\delta E^{UPS} = \Delta E^{UPS}/E^U(0)$, where $\Delta E^{RPS} = E^R(0) - E^{PS}(0)$ and $\Delta E^{UPS} = E^U(0) - E^{PS}(0)$ present the corresponding energy misalignment, deviate differently: if δE^{RPS} changes from ∼20 to 25 %, δE^{UPS} varies much less within ∼2–5 %. These values clearly show the measure of incorrectness that is introduced when the graphene molecule energy is described by either restricted or unrestricted computational schemes.

Answer 2 Broken symmetry approach provides exact determination of the magnetic constant.

Obviously, the odd electrons correlation is a necessary reason for the graphene magnetization. However, this, as such, is not enough since there are additional requirements concerning the magnetic constant value equal to the exchange integral J [21] (see Ex. (15.5)). Graphene molecules are among the singlet bodies, whose magnetic phenomenon may occur as a consequence of mixing the ground singlet state with those of high-spin multiplicity [22] following, say, to the van Fleck mixing promoted by the applied magnetic field [23]. Since the effect appears in the

first-order perturbation theory, it depends on the J value that determines the energy differences in denominators. Consequently, J should be small by the absolute value to provide noticeable magnetization. Estimated for molecular magnets [24], the phenomenon can be fixed at $|J|$ of 10^{-2}–10^{-3} kcal/mole or less.

The joint unit cell of graphene crystal involves two atoms that form one C–C bond of the benzenoid unit. Estimation of J value for the ethylene and benzene molecule with stretched C–C bonds up to 1.42 Å in length gives -13 kcal/mole and -16 kcal/mole, respectively. In spite of the molecules do not reproduce the unit cell of graphene crystal exactly, a similar J value of the cell constant is undoubted. Owing to this, the magnetization of the graphene crystal cannot be observed so that the crystal should demonstrate the diamagnetic behaviour only. The latter is supported both theoretically [25] and empirically (see [26] and references therein). To provide a remarkable magnetization means to drastically decrease the magnetic constant $|J|$, which, in its turn, determines a severe strengthening of the odd electron correlation. Since it is impossible to the regular crystal, let us look what can be expected at the molecular level.

Analyzing data published earlier [27, 28] and addressing the discussion presented in the previous section, one may suggest the NGr molecule size as a regulating factor of the electron correlation. As shown in Table 15.2, the magnetic constant $|J|$ decreases when the molecule becomes larger. When speaking about mixing the ground singlet state with those of high-spin ones, obviously, the singlet-triplet mixing is the most influent. As follows from Table 15.2, the energy gap to the nearest triplet state, equal $2|J|$, for the studied molecules constitutes 2.8–0.6 kcal/mole. The value is still large to provide a recordable magnetization of these molecular magnets, but the trend is quite optimistic.

In view of this idea, let us estimate how large should be the graphene molecule to provide a noticeable magnetization. As mentioned earlier, the molecular magnetism can be fixed at $|J| \sim 10^{-2}$–10^{-3} kcal/mole or less. Basing on the data presented in Table 15.2 and supposing the quantity to be inversely proportional to the number of odd electrons, we get $N \sim 10^5$. For rectangular NGrs with N odd electrons, the number of carbon atoms constitutes $\mathrm{N} = N - 2(n_a + n_z + 1)$ that, according to [19], is determined as

$$\mathrm{N} = 2(n_\alpha n_z + n_\alpha + n_z). \tag{15.6}$$

To fit the needed N value, the indices n_α and n_z should be of hundreds, which leads to linear sizes of the NGrs from a few units to tens nm. The estimation is rather approximate, but it, nevertheless, correlates well with the experimental observations of the magnetization of activated carbon fibers consisting of nanographite domains of ~2 nm in size [29, 30]. Recently, has been reported a direct observation of the size-dependent large-magnitude room-temperature ferromagnetism of graphene interpore regions [31, 32]. The maximum effect was observed at the region width of 20 nm after which the signal gradually decreased when the width increased. The behaviour is similar to that obtained for fullerene oligomers [33] that led to the suggestion of a scaly mechanism of the nanostructured solid state magnetism of the polymerized fullerene C_{60} that was confirmed experimentally.

The obtained results highlight another noteworthy aspect of the graphene magnetism attributing the phenomenon to size-dependent ones. The latter means that the graphene magnetization is observed for nanosize samples only, moreover, for the samples whose linear dimensions fit a definite interval, while the phenomenon does not take place at either smaller or bigger samples outside the critical region. An individual benzenoid unit (including benzene molecule) is non-magnetic (only slightly diamagnetic [34]). When the units are joined to form a graphene-like benzenoid cluster, the effectively unpaired electrons appear due to weakening the interaction between the odd electrons followed by their correlation. The correlation accelerates when the cluster size increases, which is followed with the magnetic constant $|J|$ decreasing until the latter achieves a critical level that provides a noticeable mixing of the singlet ground state with high-spin states for the cluster magnetization to be fixed. Until the enlargement of the cluster size does not violate the molecular behavior of the odd electrons, the sample magnetization will grow. However, as soon as the electron behavior becomes spatially quantized, the molecular character of the magnetization will be broken and will be substituted by that one determined by the electron properties of the crystal unit cell [22]. The critical cluster size is determined by the electron mean free path l_{el}. Evidently, when the cluster size exceeds l_{el} the spatial quantization quenches the cluster magnetization. The accurate determination of l_{el} for the odd electrons in graphene is not known, but the analysis of a standard data base for the electron mean free paths in solids [35] shows the quantity should be ~10 nm, which is supported by the experimental data of 3–7 nm electron free path in thin films of Cu-phthalocyanine [36].

Another scenario of getting magnetic graphene is connected with introducing the impurity and structural defects in the graphene body. The best illustration of such scenario reality can be found in a recent publication of the Geim team [26] where a paramagnetic behaviour of graphene laminates consisting of 10–50 nm sheets has been recorded after either their fluorination or bombarding by electrons. The treatment provides the 'spin-half paramagnetism in graphene induced by point defects'. In both cases, the magnetization is weak and is characterized by one moment per approximately 1,000 carbon atoms, which is explained by the authors by clustering of adatoms and, for the case of vacancies, by the loss of graphene's structural stability. Besides, the unit cell contains one additional spin thus lifting the spin multiplicity to doublet. The latter explains the paramagnetic behaviour of the sample while the size of the cell provides small value of the magnetic constant $|J|$ due to large (~40 nm) cell dimension. Therefore, introduced adatoms and point defects cause a magnetic nanostructuring of the pristine crystal that favors the realization of the size-dependent magnetism.

Explaining magnetic behavior of the graphene molecule, we attribute the phenomenon to the correlation of the molecule odd electrons. As was said in Introduction, Criterion 2 highlights the fact that the electron correlation is accompanied with the appearance of the effectively unpaired electrons that provide the molecule radicalization [12, 13, 15]. A natural question arises which characteristic of graphene does control its electrons correlation? Looking for answering the question we have come to Answer 3.

Answer 3 Odd electrons correlation is controlled by lengths of C–C bonds.

Firstly shown by Takatsuka, Fueno, and Yamaguchi [12], the correlation of weakly interacting electrons is manifested through the density matrix, named as the distribution of 'odd' electrons,

$$D(r|r') = 2\rho(r|r') - \int \rho(r|r'')\rho(r''|r')dr''. \tag{15.7}$$

The function $D(r|r')$ was proven to be a suitable tool to describe the spatial separation of electrons with opposite spins, and its trace

$$N_D = \mathrm{tr}\, D(r|r') \tag{15.8}$$

was interpreted as the total number of these electrons [12, 37]. The authors suggested N_D to manifest the radical character of the species under investigation. Over twenty years later, Staroverov and Davidson changed the term by the 'distribution of *effectively unpaired electrons*' [13, 38] emphasizing that not all the odd electrons may be taken off the covalent bonding. Even Takatsuka et al. mentioned [12] that the function $D(r|r')$ can be subjected to the population analysis within the framework of the Mulliken partitioning scheme. In the case of a single Slater determinant, Eq. (15.8) takes the form [13]

$$N_D = \mathrm{tr}\, DS, \tag{15.9}$$

where

$$DS = 2PS - (PS)^2. \tag{15.10}$$

Here, D is the spin density matrix $D = P^\alpha - P^\beta$ while $P = P^\alpha + P^\beta$ is a standard density matrix in the atomic orbital basis, and S is the orbital overlap matrix (α and β mark different spins). The population of effectively unpaired electrons on atom A is obtained by partitioning the diagonal of the matrix DS as

$$D_A = \sum_{\mu \in A} (DS)_{\mu\mu}, \tag{15.11}$$

so that

$$N_D = \sum_A D_A. \tag{15.12}$$

Staroverov and Davidson showed [13] that the atomic population D_A is close to the Mayer free valence index [39] F_A in a general case while in the singlet state D_A and F_A are identical. Thus, plotting D_A over atoms gives a visual picture of the actual radical electrons distribution [13], which, in its turn, exhibits atoms with the enhanced chemical reactivity.

The effectively unpaired electron population is definitely connected with the spin contamination of the UBS solution state. In the case of UBS HF scheme, there is the straight relation between N_D and squared spin $\langle \hat{S}^2 \rangle$ [13]

$$N_D = 2\left(\langle \hat{S}^2 \rangle - \frac{(N^\alpha - N^\beta)^2}{4}\right), \tag{15.13}$$

where

$$\langle \hat{S}^2 \rangle = \left(\frac{(N^\alpha - N^\beta)^2}{4} \right) + \frac{N^\alpha + N^\beta}{2} - \sum_i^{N^\alpha} \sum_j^{N^\beta} |\langle \phi_i | \phi_j \rangle|^2. \tag{15.14}$$

Here, ϕ_i and ϕ_j are the atomic orbitals; N^α and N^β are the numbers of electrons with spin α and β, respectively.

If the UBS HF computations are realized in the *NDDO* approximation (the basis for the AM1/PM3 semiempirical techniques) [40], a zero overlap of orbitals leads to $S = I$ in Eq. (15.10), where I is the identity matrix. The spin density matrix D assumes the form

$$D = \left(P^\alpha - P^\beta \right)^2. \tag{15.15}$$

The elements of the density matrices $P_{ij}^{\alpha(\beta)}$ can be written in terms of the eigenvectors of the UHF solution C_{ik}

$$P_{ij}^{\alpha(\beta)} = \sum_k^{N^{\alpha(\beta)}} C_{ik}^{\alpha(\beta)} C_{jk}^{\alpha(\beta)}. \tag{15.16}$$

Expression for $\langle \hat{S}^2 \rangle$ has the form [41]

$$\langle \hat{S}^2 \rangle = \left(\frac{(N^\alpha - N^\beta)^2}{4} \right) + \frac{N^\alpha + N^\beta}{2} - \sum_{i,j=1}^{NORBS} P_{ij}^\alpha P_{ij}^\beta. \tag{15.17}$$

Within the framework of the *NDDO* approach, the HF-based total N_D and atomic N_{DA} populations of effectively unpaired electrons take the form [42]

$$N_D = \sum_A N_{DA} = \sum_{i,j=1}^{NORBS} D_{ij} \tag{15.18}$$

and

$$N_{DA} = \sum_{i \in A} \sum_{B=1}^{NAT} \sum_{j \in B} D_{ij}. \tag{15.19}$$

Here, D_{ij} are elements of the spin density matrix D that presents a measure of the electron correlation [12, 13, 43], *NORBS* and *NAT* mark the number of orbitals and atoms, respectively.

Explicit expressions (15.18) and (15.19) are the consequence of the wave-function-based character of the UBS HF. Since the corresponding coordinate wave functions are subordinated to the definite permutation symmetry, each value of the spin S corresponds to the definite expectation value of the energy [11]. Oppositely, the electron density ρ is invariant to the permutation symmetry. The latter causes a serious spin problem for the UBS DFT [10, 11]. Additionally, the spin density $D(r|r')$ of the UBS DFT depends on the spin-dependent exchange and correlation functionals and can be expressed analytically in the former case only [11]. Since

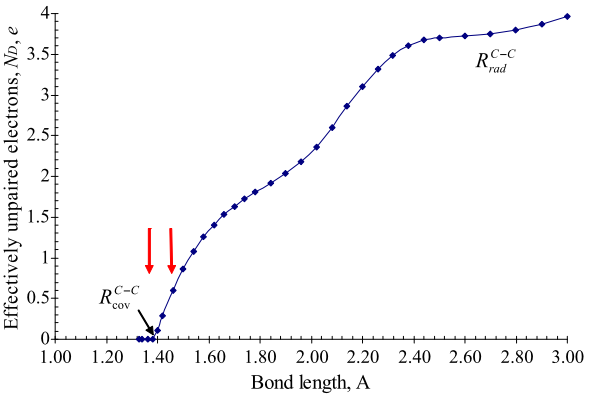

Fig. 15.1 The total number of the effectively unpaired electrons N_D accompanying the stretching of the C–C bond in ethylene. R^{C-C}_{cov} marks the extreme distance that corresponds to the completion of the covalent bonding. R^{C-C}_{rad} matches completion of the homolytic bond cleavage. Two vertical arrows mark the interval of the C–C bond lengths characteristic for sp^2 nanocarbons

the exchange-correlation composition deviates from one method to the other, the spin density is not fixed and deviates alongside with the composition. Serious UBS DFT problems are known as well in relevance to the $\langle \hat{S} \rangle^2$ calculations [44, 45]. These obvious shortcomings make the UDFT approach practically inapplicable in the case when the correlation of weakly interacting electrons is significant. Certain optimism is connected with a particular view on the structure of the density matrix of the effectively unpaired electrons developed by the Spanish-Argentine group [15, 43, 46] from one hand and new facilities offered by Yamagouchi's approximately spin-projected geometry optimization method intensely developed by a Japanese team [47, 48], from the other. By sure, this will give a possibility to describe the electron correlation at the density theory level more thoroughly.

The odd electrons story is counted from the discovery of the benzene molecule made by Michael Faraday in 1825. However, only a hundred years later Hückel suggested the explanation of the deficiency of hydrogen atoms in the molecule to complete the valence ability of its carbon atoms. Extra, or odd, electrons were named as π electrons that, in contrast to σ electrons, interact much weaker while providing the additional covalent coupling between neighbouring atoms. The two electrons are located in the same space, and their spins are subordinated to the Pauli law. Formally, this view on extra π electrons, which lays in the foundation of the aromaticity concept, has been expanded over all sp^2 nanocarbons and has been shared by a number of material scientists in the field until now. However, the concept does not take into account a crucial role of the distance between two neighbouring odd electrons. As seen in Fig. 15.1, which presents a plotting of the total number of effectively unpaired electrons N_D as a function of the C–C distance in the ethylene molecule, the bond stretching from its equilibrium value of 1.326 Å up to $R_{crit} = R^{C-C}_{\text{cov}} = 1.395$ Å does not cause the appearance of the unpaired electrons so that the relevant π electrons are fully covalently bound. However, above R_{crit} the number N_D gradually increases up to a clearly vivid knee that is characterized by $N_D \cong 2$ at $R = 1.76$ Å, which evidences a complete radicalization of the previous π electrons. On the way

Table 15.3 Effectively unpaired electrons in the aromatic molecules, UBS HF singlet state [16]

Molecules	C–C bond length, Å				N_D, e
	Number of bonds				
Benzene	1.395				0.05
	6				
Naththalene	1.385	1.411	1.420	1.430	1.483
	4	2	4	1	
Anthracene	1.387	1.410	1.421	1.435	3.003
	4	6	4	2	
Tetracene	1.388	1.410	1.421	1.436	4.320
	4	8	6	3	
Pentacene	1.388	1.411	1.420	1.436	5.540
	4	10	8	4	

from R_{crit} to $R = 1.76$ Å, the two electrons are not more located in the same space, but electrons with different spins occupy different spaces. Further stretching concerns mainly two σ electrons that, once fully covalently bound until $R = 1.76$ Å, gradually become unpaired just repeating the fortune of π electrons resulting in $N_D \cong 4$ at 2.5 Å.

In spite of clear explanation where unpaired electrons are coming from, the question about their existence still remains due to suspicion of their attribution to an *artifact* caused by the limitations of the single-determinant calculations. Looking for the confirmation of the physical reality of the unpaired electrons leads to Answer 4.

Answer 4 Effectively unpaired electrons are the definite physical reality.

In a series of aromatic hydrocarbon molecules, the unified length of C–C bonds in the benzene molecule exactly fits R_{crit}, which is why $N_D = 0$ as is expected for a truly aromatic molecule. However, even the naphthalene molecule is characterized by a set of C–C bonds, short and long representatives of which have lengths that are below and above R_{crit}, respectively. This slightly dispersive many-length set is further kept in all the aromatic molecules (becoming a two-length one in fullerene C_{60}). As the number of the benzene units grows, the number of long bonds increases, which is followed by increasing N_D (see Table 15.3) [16]. As seen in the table, for the pentacene molecule N_D constitutes 5.4 e so that the molecule is a 5.4-fold radical. The N_D distribution over the molecule atoms in terms of N_{DA} is shown in Fig. 15.2a. As seen in the figure, the main chemical reactivity of the molecule is concentrated in its central part.

This finding could have been one of questionable results of the molecular theory only if it were not for a recent experimental viewing of the molecule by using the

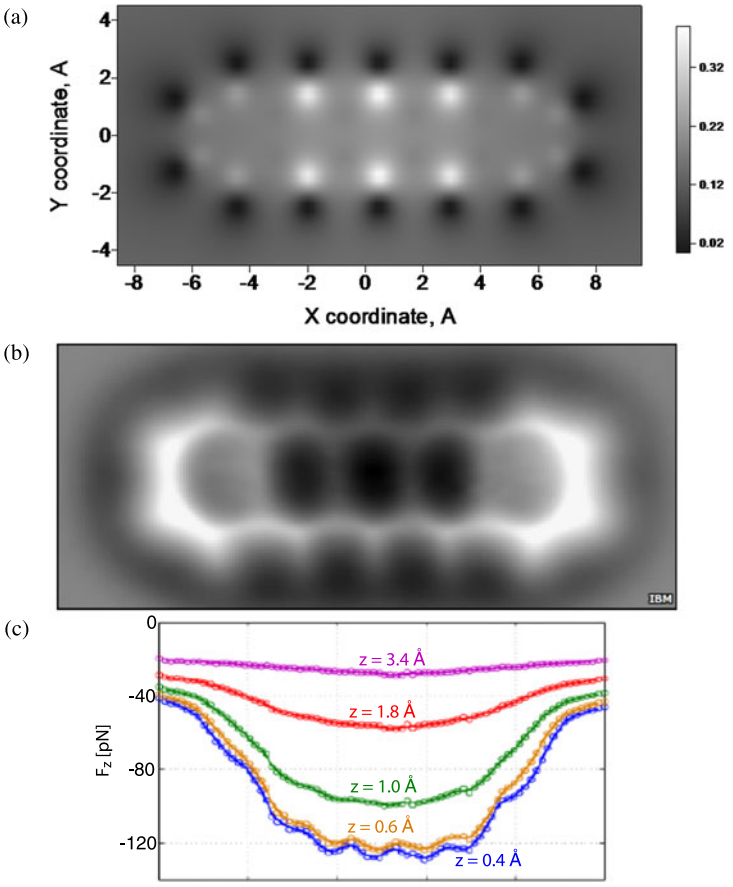

Fig. 15.2 Effectively unpaired electrons of the pentacene molecule. (**a**) Calculated N_{DA} image, UBS HF singlet state. (**b**) AFM imaging of pentacene on Cu(111) using a CO-at-Au tip [49]. (**c**) Extracted vertical force along the molecule long axis [49]

AFM with unprecedented high resolution [49] (see Fig. 15.2b). The molecule image was obtained by using the short-range chemical forces of noncontact AFM. The forces profiles are shown in Fig. 15.2c. As seen in the figure, the least forces and, consequently, the weakest interaction are observed at the molecule ends (the brightest area in Fig. 15.2b) while the strongest interaction (the darkest area in Fig. 15.2b) is characteristic for the molecule central area. Since the interaction of the CO apex of the AFM tip is obviously proportional to the electron density on the atoms above which the tip is located, thus recorded AFM molecule image should be inverted by color with respect to the N_{DA} image map in Fig. 15.2a. This has actually been observed exhibiting the first evidence of the distribution of the effectively unpaired electrons in the sp^2 molecules. The next example concerns a similar imaging of the olympicene molecule that has been synthesized on the eve of the London Olympic

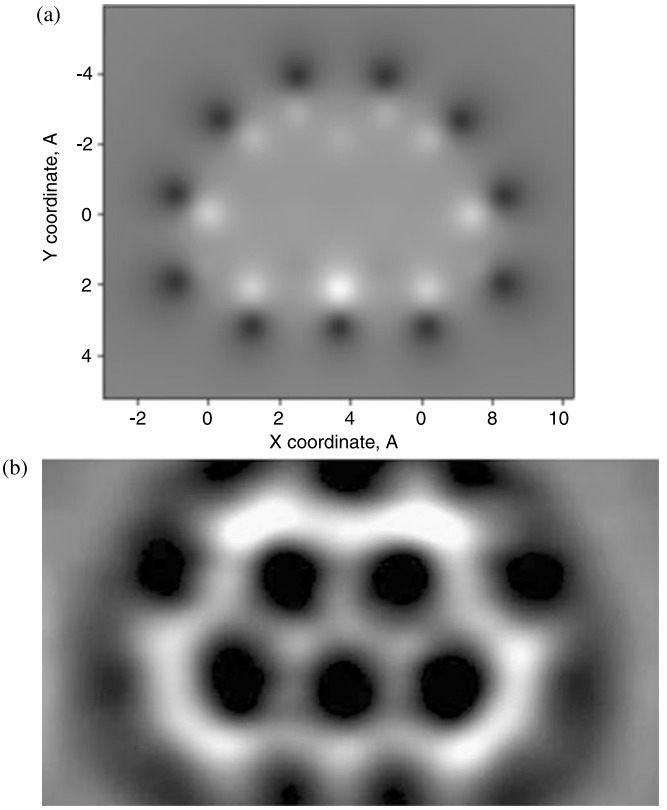

Fig. 15.3 Effectively unpaired electrons of the olympicene molecule. Calculated N_{DA} image, UBS HF singlet state (**a**) and AFM imaging of olympicene on Cu(111) using a CO-at-Au tip [50]

Games 2012 [50]. Figure 15.3 presents the image map of the N_{DA} distribution over the molecule alongside with its AFM image obtained as previously. The color inversion of the two images is clearly seen.

Two vertical arrows in Fig. 15.1 mark the C–C bond length interval that is characteristic for graphene molecules equilibrated in the framework of the UBS HF approach. (It should be mentioned that the application of the restricted version of the same program results in practically non-dispersive value of the C–C bond length of 1.42 Å.) As seen, the C–C bond lengths exceed R_{crit} which leads to a considerable amount of the effectively unpaired electrons, total numbers of which are listed in Table 15.1 for different graphene fragments. Figure 15.4a exhibits a typical image map of the N_{DA} distribution over one of them. The fragment edges are not terminated, and the N_{DA} image map has a characteristic view with a distinct framing of the sample by edge atoms since the main part of the unpaired electrons is concentrated in this area. The N_{DA} image map intensity in the basal plane is of ∼0.3 e in average.

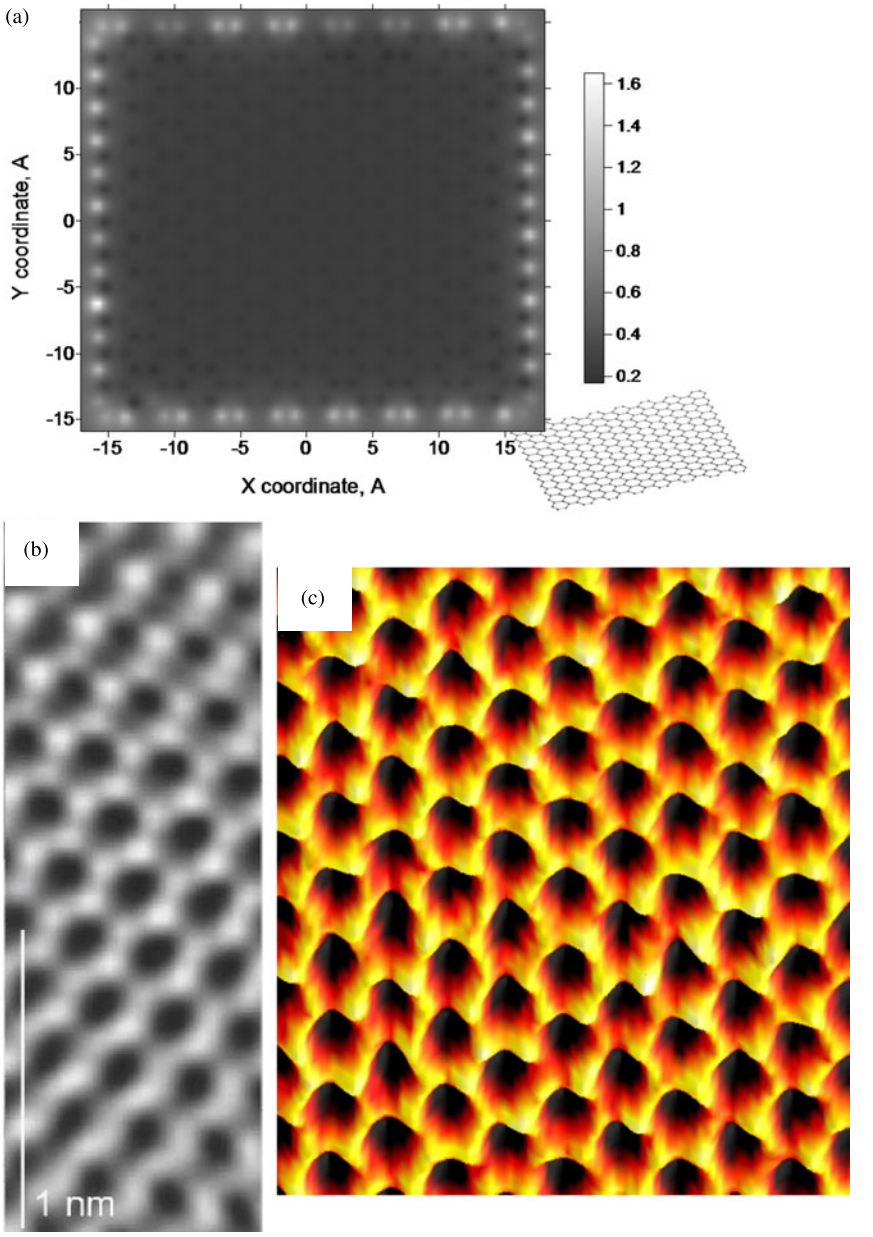

Fig. 15.4 Effectively unpaired electrons of graphene. (**a**) Calculated N_{DA} image of (15, 12) NGr molecule, UBS HF singlet state. (**b**) The atomic-resolved image of a portion of the graphene monolayer [53]. (**c**) The image of a single suspended sheet of graphene taken with the TEAM 0.5, at Berkeley Lab National Center for Electron Microscopy [54]

The peculiarity of the graphene edges had been a topic for intense discussions from the very beginning of the graphene science [51] when they were disclosed by using the tight-binding band calculation within the Hückel approximation [52]. However, they have not been attributed to the effectively unpaired electrons and have been discussed in the context of the graphene spin system peculiarity with respect to the expected magnetic behavior of the sample. In this context, it is worthwhile to refer to one more quote from the Hoffmann 'informal reflection' [1]: "There is a special problem that theory has with unterminated structures—ribbons cut off on the sides, polymers lacking ends. If passivation is not chosen as a strategy, then the radical lobes of the unterminated carbon atoms, or undercoordinated transition metals, will generate states that are roughly in the middle energetically, above filled levels, below empty levels in a typical molecule that has a substantial gap between filled and unfilled levels. If such levels—states, the physicists call them—are not identified as "intruder" states, not really real, but arising from the artifact of termination, they may be mistaken for real states in the band gap, important electronically. And if electrons are placed in them, there is no end to the trouble one can get into. These band gap states are, of course, the origin of the reactivity of the terminated but not passivated point, line, or plane. But they have little to do with the fundamental electronic structure of the material". Supporting the said above, depicted in Fig. 15.4a presents the reactivity image of the graphene molecule. As seen in the figure, not only edge, but basal-plane carbon atoms are chemically active, albeit with different efficacy. Important to note, that the reactivity is distributed over atoms rather inhomogeneously. The recent atom-resolved graphene images convincingly witness this inhomogeneity as can be seen in Figs. 15.4b and c. Therefore, the effectively unpaired electrons of the sp^2 molecules are a physical reality and are assuming their leading place in the molecular theory of graphene.

In the singlet state, the N_{DA} values are identical to the atom free valences [13] and thus exhibit the atomic chemical susceptibility (ACS) [55, 56]. The N_{DA} distribution over atoms plots a 'chemical portrait' of the studied molecule, whose analysis allows for making the definite choice of the target atom with the highest N_{DA} value to be subjected to the chemical attack by an external addend. Therefore, we have come to Answer 5 claiming that peculiarities of the graphene chemistry can be exhibited at the quantitative level, much as this has been done for fullerenes [5].

Answer 5 Computational strategy of the chemical modification of graphene.

The typical chemical portrait of graphene fragment in Fig. 15.4a highlights edge atoms as those with the highest chemical activities, besides rather irregular, while exhibiting additionally the basal atoms ACS comparable with that one of fullerene C_{60} [28, 57]. This circumstance is the main consequence of the odd electron correlation in graphene in regard to its chemical modification. Ignoring the correlation has resulted in a common conclusion about chemical inertness of the graphene atoms with the only exclusion concerning the edge ones. Having this general indication only, a computationist is still in the dark concerning the place of both the first and

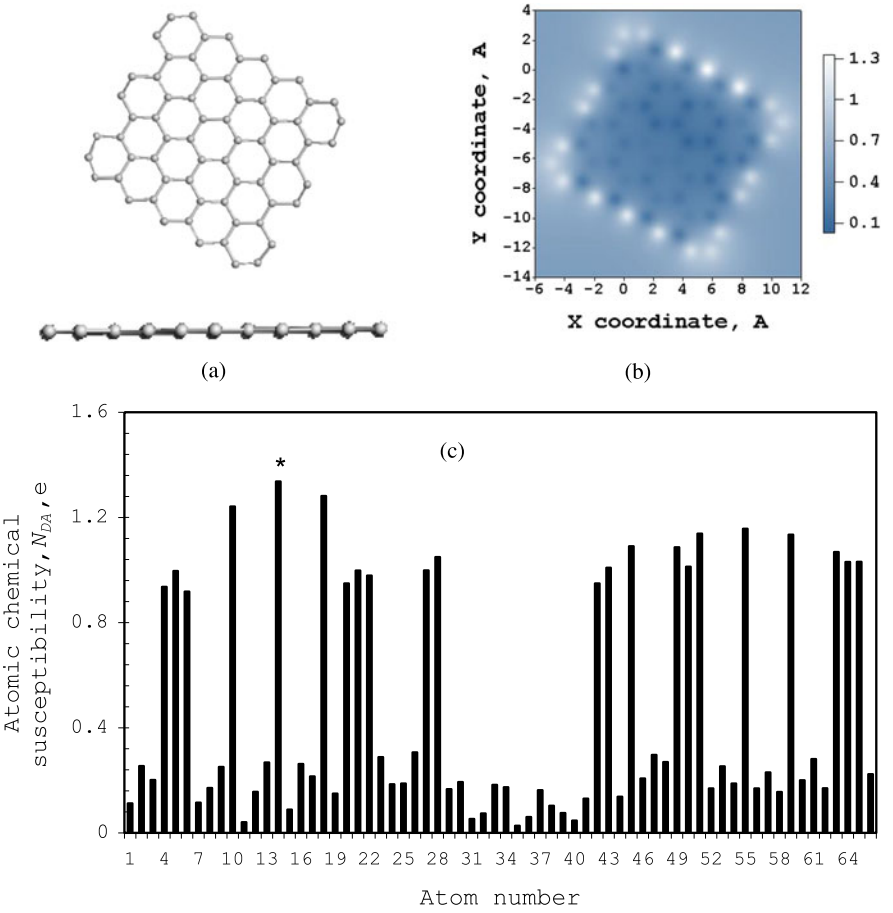

Fig. 15.5 Top and side views of the equilibrium structure of the (5, 5) NGr molecule (**a**); N_{DA} image map (**b**) and N_{DA} distribution over atoms according to the atom numbers in the output file (**c**) [60]

consequent chemical attacks and has to perform a large number of calculations sorting them out over the atoms by using the lowest-total-energy (LTE) criterion (see, for example, [58]). In contrast, basing on the N_{DA} value as a quantitative pointer of the target atom at any step of the chemical attack, one can suggest the algorithmic 'computational syntheses' of the molecule polyderivatives [59]. In what follows the algorithm-in-action will be illustrated by the examples of the hydrogenation and oxidation of the (5, 5) NGr molecule.

(5, 5) NGr Molecule Hydrogenation The equilibrium structure of the (5, 5) NGr molecule alongside with its N_{DA} image map is shown in Fig. 15.5. Panel b exhibits the N_{DA} distribution attributed to the atoms positions thus presenting the 'chemical portrait' of the molecule. Different N_{DA} values are plotted in different colouring

according to the attached scale. The absolute N_{DA} values are shown in panel c according to the atom numbering in the output file. As seen in the figure, 22 edge atoms involving 2×5 *zg* and 2×6 *ach* ones have the highest N_{DA} thus marking the perimeter as the most active chemical space of the molecule. The molecule hydrogenation will start on atom 14 (star-marked in Fig. 15.5c) according to the highest N_{DA} in the output file. The next step of the reaction involves the atom from the edge set as well, and this is continuing until all the edge atoms are saturated by a pair of hydrogen atoms each since all 44 steps are accompanied with the high-rank N_{DA} list where edge atoms take the first place [60]. Thus obtained hydrogen-framed graphene molecule is shown in Fig. 15.6 alongside with the corresponding N_{DA} image map. Two equilibrium structures are presented. The structure in panel *a* corresponds to the optimization of the molecule structure without any restriction. In the second case, positions of the edge carbon atoms and framing hydrogen atoms under optimization were fixed. In what follows, we shall refer to the two structures as a free standing and fixed membrane, respectively. Blue atoms in Fig. 15.6c alongside with the framing hydrogens are excluded from the forthcoming optimization under all steps of the further hydrogenation.

The chemical portraits of the structures shown in Figs. 15.6b and 15.6d are quite similar and reveal the transformation of brightly shining edge atoms in Fig. 15.5b into dark spots. The addition of two hydrogen atoms to each of the edge ones saturates the valence of the latter completely, which results in zeroing N_{DA} values, as is clearly seen in Fig. 15.6e. The chemical activity is shifted to the neighbouring inner atoms and retains higher in the vicinity of *zg* edges, however, differently in the two cases. The difference is caused by the redistribution of the C–C bond lengths of the free standing membrane when it is fixed over perimeter, thus providing different starting conditions for the hydrogenation of the two membranes.

Besides the two types of initial membranes, the hydrogenation will obviously depend on other factors, such as (1) the hydrogen species in use and (2) the accessibility of the membranes sides to the hydrogen. Even these circumstances evidence the hydrogenation of graphene to be a complicated chemical event that strongly depends on the initial conditions, once divided into 8 adsorption modes in regard to atomic or molecular adsorption; one- or two-side accessibility of membranes; and free or fixed state of the membranes perimeter. Only two ones of the latter correspond to the experimental observation of hydrogenated specimens discussed in [61], namely: two-side and one-side atomic hydrogen adsorption on the fixed membrane. Stepwise hydrogenation of the (5, 5) NGr molecule was considered in details in [60]. Here, we restrict ourselves with a brief description of the main results.

Two-Side Atomic Adsorption of Hydrogen on Fixed Membrane The hydrogenation concerns the basal plane of the fixed hydrogen-framed membrane shown in Fig. 15.6c that is accessible to hydrogen atoms from both sides. As seen in Fig. 15.6e, the first hydrogenation step should occur on basal atom 13 marked by a star. Since the membrane is accessible to hydrogen from both sides, one has to check which deposition of the hydrogen atom, namely, above the carbon plane ('up') or below it ('down') satisfies the LTE criterion.

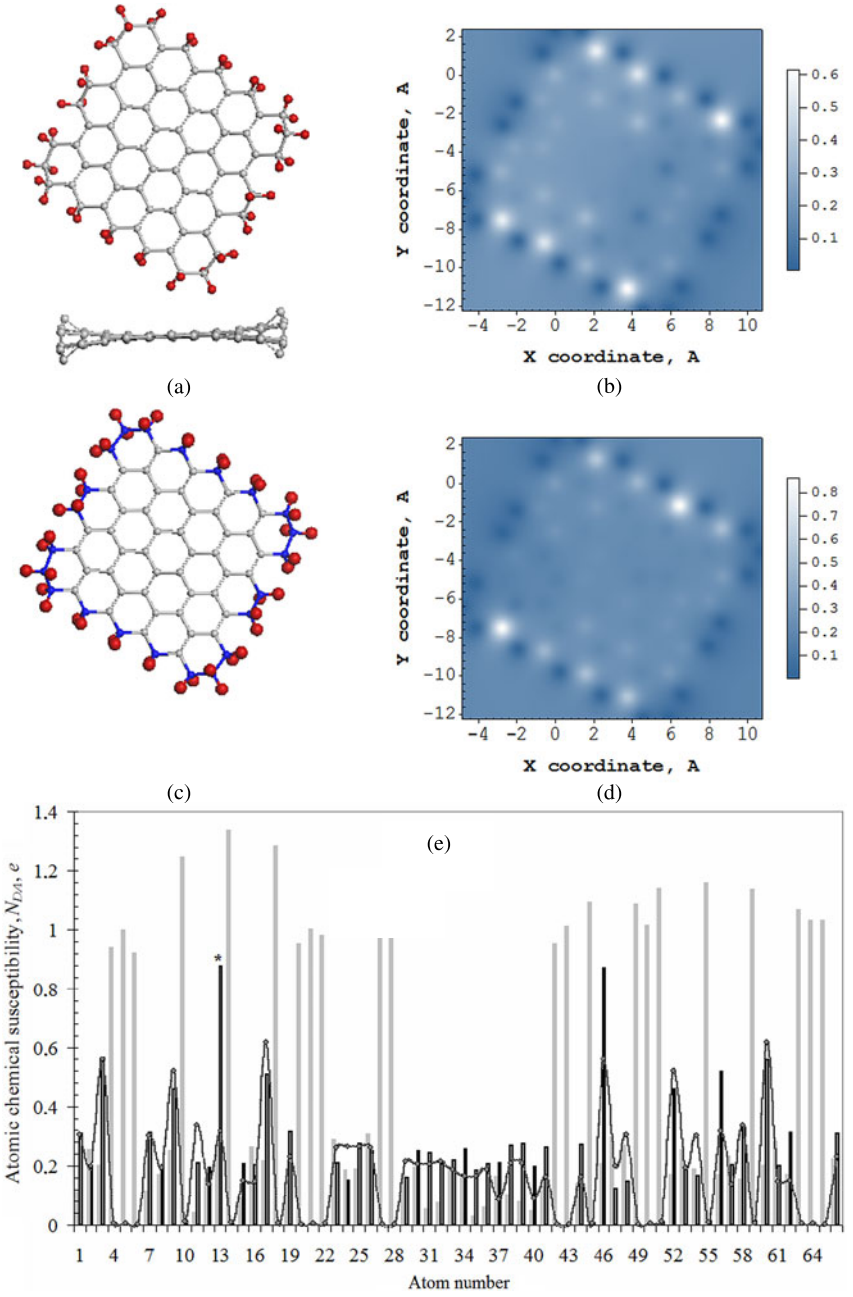

Fig. 15.6 Equilibrium structures of the free standing (top and side views) (**a**) and fixed (**c**) (5, 5) NGr membrane; N_{DA} image maps (**b**, **d**) and N_{DA} distribution over atoms according to the atom numbers in the output file (**e**) [60]. *Light gray* histogram plots the ACS data for the pristine (5, 5) NGr molecule. *Curve* and *black* histogram are related to the membranes in panels (**a**) and (**c**), respectively

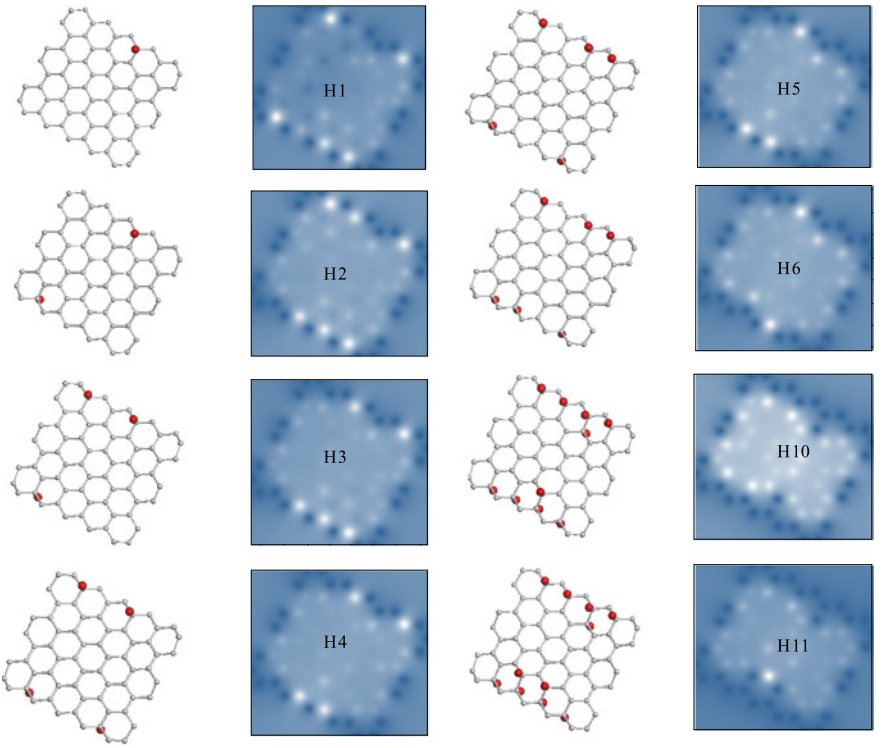

Fig. 15.7 Equilibrium structures (*left*) and N_{DA} image maps (*right*) of the graphene polyhydrides related to the initial stage of the basal-plane hydrogenation. HKs denote hydrides with K hydrogen atoms deposited on the fixed membrane basal plane [60]. Framing hydrogen atoms are not shown to simplify the structure image presentation

After deposition of hydrogen atom on basal atom 13, the N_{DA} map has revealed carbon atom 46 for the next deposition (see H1 N_{DA} map in Fig. 15.7). The LTE criterion favours the down position for the second hydrogen on this atom so that we obtain structure H2 shown in Fig. 15.7. The second atom deposition highlights next targeting carbon atom 3 (see N_{DA} map of H2 hydride), the third adsorbed hydrogen atom activates target atom 60, the fourth does the same for atom 17, and so forth. Checking up and down depositions in view of the LTE criterion, a choice of the best configuration can be performed and the corresponding equilibrium structures for a selected set of the (5, 5) NGr polyhydrides from H1 to H11 are shown in Fig. 15.7. The structure obtained at the end of the 44th step is shown in Fig. 15.8a. It is perfectly regular, including framing hydrogen atoms, thus presenting a computationally synthesized fully saturated chairlike (5, 5) nanographane (NGra) that is in full accordance with the experimental observation of the graphane crystalline structure [61].

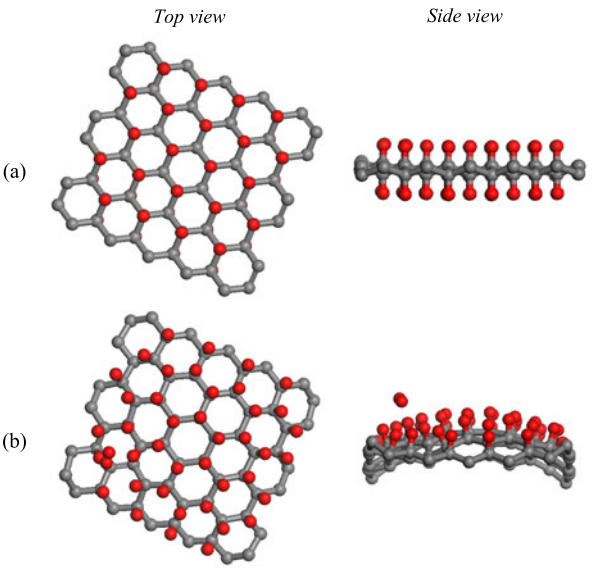

Fig. 15.8 *Top* and *side views* of the equilibrium structures of the saturated graphene polyhydrides formed at the atomic adsorption of hydrogen on the fixed (5, 5) NGr membrane, accessible to the adsorbate from both (1) (**a**) and one (2) (**b**) sides [60]. Framing hydrogen atoms are not shown to simplify the structure image presentation

One-Side Atomic Adsorption of Hydrogen on Fixed Membrane Coming back to the first step of the hydrogenation, let us proceed further with the second and all the next steps of the up deposition only. As previously, the choice of the target atom at each step is governed by the high-rank N_{DA} values. Figure 15.8b presents the saturated graphene polyhydride related to the final 44th step. A peculiar canopy shape of the carbon skeleton of the hydride is solely provided by the formation of the table-like cyclohexanoid units. However, the unit packing is quasi-regular which may explain the amorphous character of the polyhydrides formed at the outer surface of graphene ripples observed experimentally [61]. The reasons of the hydrogen molecule desorption at the 44th step are discussed elsewhere [60].

As for the hydrogen coverage, Fig. 15.9 presents the distribution of C–H bond lengths of the saturated graphene polyhydrides. In both cases, the distribution consists of two parts, the first of which covers 44 C–H bonds formed at the molecule skeleton edges. Obviously, this part is identical for both hydrides since the bonds are related to the framing atoms. The second part covers C–H bonds formed by the hydrogen atoms attached to the basal plane. As seen in the figure, in the case of polyhydride 1, C–H bonds are practically identical with the average length of 1.126 Å and only slightly deviate from those related to framing atoms. This is just a reflection of the regular graphane structure of the polyhydride shown in Fig. 15.8a similarly to highly symmetric fullerene polyhydride $C_{60}H_{60}$ [62]. In contrast, C–H bonds on a canopy-like carbon skeleton of polyhydride 2 are much longer than those in the framing zone, significantly oscillate around the average value of 1.180 Å. In spite of the values markedly exceed a 'standard' C–H bond length of 1.11 Å, typical for benzene, those are still among the chemical C–H bonds, whilst stretched, since the C–H bond rupture occurs at the C–H distance of 1.72 Å [63]. A remarkable

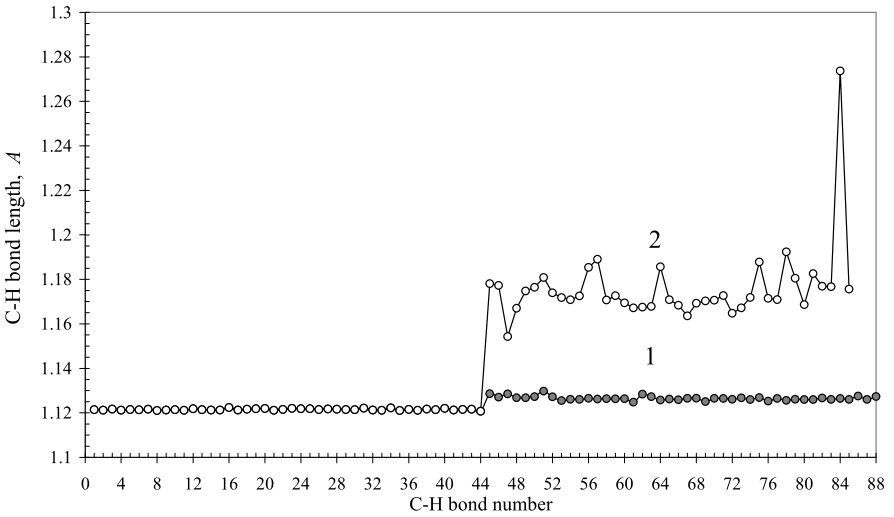

Fig. 15.9 C–H bond length distribution for the saturated graphene polyhydrides 1 (1) and 2 (2) [60]

stretching of the bonds points to a considerable weakening of the C–H interaction for polyhydride 2 in comparison with polyhydride 1, which is supported by the energetic characteristics of the hydrides, as well [60]. The total energies of both hydrides are negative by sign and gradually increase by the absolute value when the number of adsorbed atoms increases. However, the absolute value growth related to polyhydrides 2 is slowing down starting at step 11 in contrast to the continuing growth for polyhydrides 1 [60]. This retardation obviously shows that the one-side addition of hydrogen to the fixed membrane of polyhydrides 2 at the coverage higher than 30 % is more difficult than in the case of the two-side addition of polyhydrides 1, for which the reaction of the chemical attachment of the hydrogen atoms is thermodynamically profitable through over the covering up to the 100 % limit. In contrast, the large coverage for polyhydrides 2 becomes less and less profitable so that at final steps the hydrogen adsorption and desorption become competitive.

(5, 5) NGr Molecule Oxidation Stepwise oxidation of the (5, 5) NGr molecule can be considered similarly to the hydrogenation described above. On the background of a tight similarity in both processes, in general, important difference of the events concerns the fact that instead of atomic hydrogens, which were attacking agents in the first case, a set of oxidants consisting of oxygen atoms O, hydroxyls OH, and carboxyls COOH had to be considered in the latter case. A detailed description of the molecule oxidation is given in [64, 65]. Skipping extended explanations of details given above for hydrogenation, below there is a brief presentation of results of the performed computational experiment, attributed to the main hot points of the graphene oxide (GO) chemistry.

Morphology Empirical experiments reveal a remarkable disordering of the initial graphene structure even by partial oxidation so that the chemically produced graphene polyoxides (GOs) are highly amorphous (see [66–69] and references therein).

The performed computational experiment fully supports this finding since none of the regularly structured GOs has been obtained in the study.

Graphene Oxidation as a Process in General Experimentally was shown that the oxidation of the graphene proceeds in a rather random manner [66]. The saturated at% ratio of oxygen to carbon is ∼20–45 [69–72]. When GOs are heated to 110 °C, there is still about 5–10 at% oxygen left [71–73].

As shown computationally, the oxidation can be considered as a stepwise addition of oxidants to the pristine graphene molecule subordinated to the algorithm governed by the list of high-rank atomic chemical susceptibilities N_{DA}. In numerous cases presented in [64, 65], the algorithm action does cause seemingly random distribution of oxidants over the molecule body in due course of the oxidation process.

The algorithmic approach to the chemical modification of sp^2 nanocarbons does not impose any restriction on the limit at% ratio of any addend attached to the carbon skeleton, in general. This was supported by the results of the 'computational synthesis' of polyderivatives of fullerene C_{60} [5] as well as polyhydrides and polyfluorides of the (5, 5) NGr molecule [60]. However, the initial radicalization of any pristine sp^2 molecule, which is provided by N_D effectively unpaired electrons, is gradually suppressed as the chemical reaction proceeds. The molecule chemical reactivity is little by little worked out approaching zero due to which the reactions stop. This explains why the hydrogenation and fluorination of fullerene C_{60} is terminated at producing $C_{60}F_{48}$ and $C_{60}H_{36}$ polyderivatives, respectively, [59, 62] and why at% ratio of hydrogen to carbon in the experiment of Elias et al. [61] decreases when going from graphene polyhydrides formed from two-side, H-accessible, perimeter-fixed membranes to one-side, H-accessible ripples [60]. The same regularities govern the (5, 5) NGr molecule oxidation, which, as shown, terminates the oxidation at achieving ∼67 at% of oxygen when the oxidation is provided by the addition of either hydroxyls or oxygen atoms. The saturation number involves filling both edge and basal atoms. Since the pristine (5, 5) NGr molecule is rather small, the contribution of edge atoms is significant. If the latter is excluded, the basal plane coverage approaches 48 at% that is quite reasonable and points to a predominant C_2O stoichiometry. The earlier mentioned data of ∼20–45 at% are mainly related to the basal positions of rather big experimental samples for which the contribution of edge atoms is small.

In contrast, the availability of the remaining oxygen in the reduced GOs (rGOs) subjected to heating up to 1100 °C, is connected with the edge atoms of the latter. As shown, these atoms, which include not only perimeter atoms of the rGOs molecules but the atoms framing every defect zone, form a local area with very high chemical reactivity. The oxidants are strongly coupled with the atoms and can leave the molecule jointly with the carbon partners. The number of such atoms depends

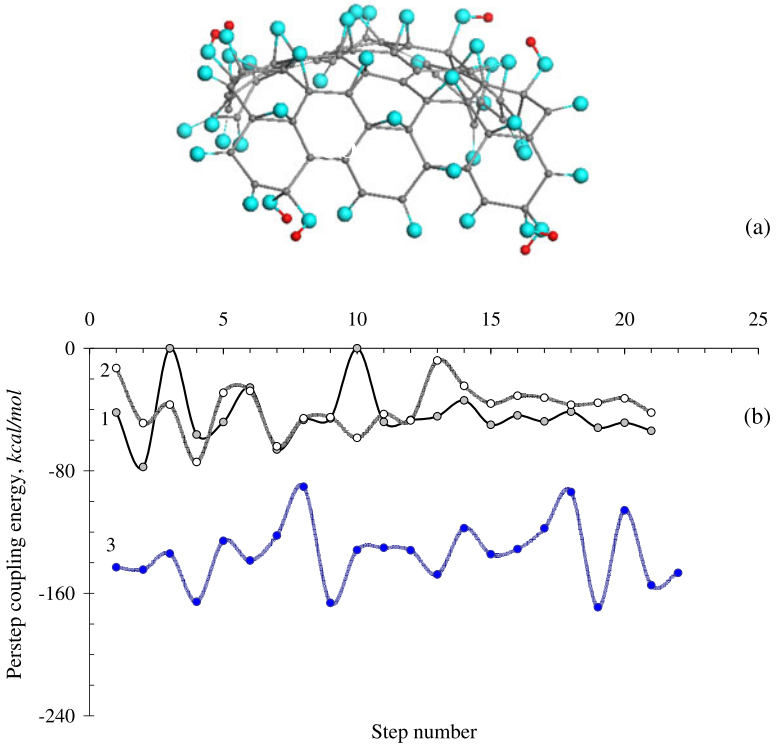

Fig. 15.10 Based on the (5, 5) NGr molecule, the structural model of a top-down exfoliated GO (**a**) and per step coupling energy (**b**) versus step number for the GOs family under subsequent O- and OH-additions to carbon atoms at either the molecule basal plane (*curves 1* and *2*) or edges (*curve 3*) [64, 65]

on linear size of both pristine GO molecules and their inner defects and cannot evidently exceed a few percents, which perfectly correlates with the observed amount of the remaining oxygen.

Chemical Composition of Graphene Oxide Basing on empirical data, the most common opinion attributes COOH, OH, and C = O groups to the edge of the GO sheet, while the basal plane is considered to be mostly covered with epoxy C–O–C and OH groups [66, 69, 74, 75]. At least five structural models were suggested to exhibit the GOs chemical composition [68]. However, none of them could stand comparison with the full set of experimental data.

The performed computations have allowed for forming up a hierarchy of the main three oxidants (O, OH, COOH) with respect to their participation in the graphene oxidation that has shown an extremely low probability of such activity for carboxyls. Basing on the results obtained, it is possible to suggest a reasonable, self-consistent model of a convenient GO presented in Fig. 15.10a. Sure, the model cannot be simply scaled for adapting to larger samples. Obviously, due to extreme sensitivity of

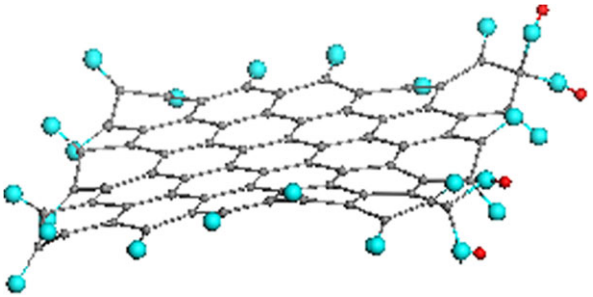

Fig. 15.11 Based on the (5, 5) NGr molecule, the structural model of the reduced top-down exfoliated rGO [64, 65]

the graphene molecule structure and electronic system to even small perturbations caused by external factors, the fractional contribution of O, OH, and C–O–C groups may change in dependence of changing the molecule size, shape as well as of the presence of such impurities as metal atoms [76] and so forth. These facts may explain 'fluidness' of the term "graphene oxide" pointed by Ruoff et al. [66]. However, it is possible to convincingly state that the chemical composition of any GO has been governed by the presence of two zones drastically differing by the coupling of the relevant oxidants with the graphene molecule body so that carbonyl/hydroxyl and epoxy/hydroxyl combinations will be typical for edge and basal areas of all GOs of different size and shape (see Fig. 15.10b).

Besides the chemical composition of chemically produced GOs, the performed calculations are able to suggest the chemical composition of rGOs as well. Discussion based on a two-zone-chemical-reactivity peculiarity of graphene molecules, clearly pointed to a reliable rGO model shown in Fig. 15.11.

Concluding discussion of hydrogenation and oxidation of graphene, some words should be said concerning the computational strategy applicable to the molecule chemical modification, in general. Until now, the computations in this field have been aimed at finding support to one of the available models, the majority of which has been suggested just intuitively. This strategy has been a result of certain limitations provided by a standard computational DFT scheme within the framework of the solid-state periodic boundary conditions, which requires a beforehand given structure of the relevant supercell unit. However, the computational study, based on such concept 'from a given structure to reliable properties' has resulted in wrong conclusions, which, for example, in the case of GO have led to the statement about kinetically constrained metastable nature of GO [77], thus revealing the inability to meet the calls of the GO chemistry at the computational level. In contrast, the molecular theory of graphene does not need any given structure beforehand but creates the structure in the course of the calculations following the algorithms that take into account such fragile features of graphenes as their natural radicalization, correlation of their odd electrons, an extremely strong influence of structure on properties, a sharp response of the graphene molecule behavior on small action of external factors.

The molecular theory not only well works with the graphene chemical modification but opens large possibility in considering the mechanical properties of graphene, in general, and its mechanochemistry, in particular, thus suggesting Answer 6.

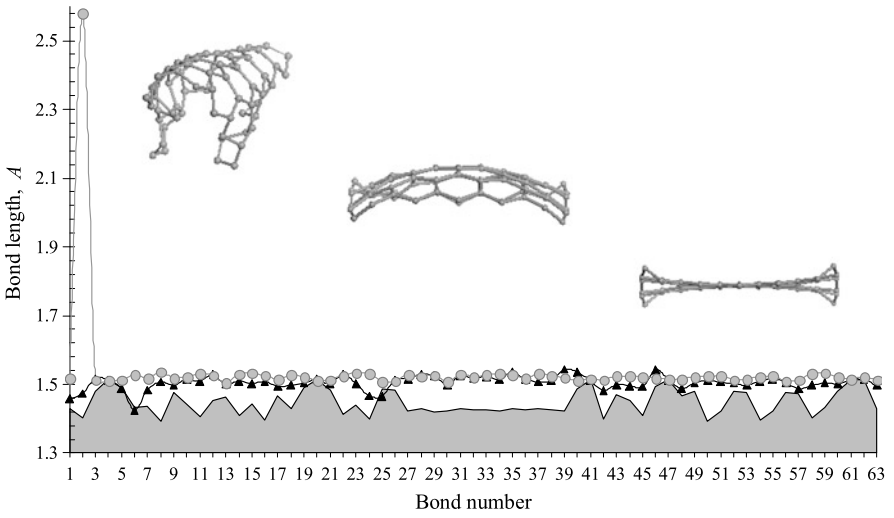

Fig. 15.12 C–C bond length distribution for the carbon skeletons of the pristine (5, 5) NGr molecule (*gray filled region*); canopy-like (*dark triangles*); and basket-like (*gray balls*) fixed membranes [60]

Answer 6 Electron correlation of graphene is strongly influenced by mechanical deformation.

Deformation of graphene is tightly connected with the odd electron correlation since it concerns changing the interatomic distances. As we saw, the latter are very important regulators of the correlation extent thus increasing it when the distances grow. Obviously, strengthening of the electron correlation results in the growths of the number of effectively unpaired electrons N_D as it was shown in Fig. 15.1.

The deformation might be either static or dynamic. The former is caused by the deformation of the carbon skeleton of the graphene molecule due to chemical modification. The C–C bonds stretching occurred in this case can be highlighted when comparing the carbon skeletons of the pristine (5, 5) NGr molecule and those of the canopy-like and basket-like ones subjected to the one-side hydrogen adsorption on either fixed or free standing membrane, respectively [60]. Figure 15.12 presents the views of the skeletons alongside with the distribution of their C–C bond lengths. As seen in the figure, the C–C bonds of both deformed skeletons are elongated, whilst the summary elongation for the basket-like skeleton is evidently bigger than that one for the canopy-like one. The elongation is restricted by the bond length of 1.53 Å, which is dictated by the sp^3 configuration of carbon atoms due to hydrogenation. Naturally, the accumulated deformation may cause some bonds breaking, which occurs for bond 2 of the basket-like skeleton. As a whole, changes in the C–C bond lengths presented in Fig. 15.12 result in decreasing magnetic constant J by the absolute value from -1.43 kcal/mole for the pristine (5, 5) NGr to -0.83 and -0.59 kcal/mole for the canopy-like and basket-like skeletons. Simultaneously,

N_D increases from 31 e to 46 e and 54 e, respectively. Both findings evidence an undoubted strengthening of the odd electron correlation caused by the chemically-stimulated deformation of the carbon skeleton.

Yet another evidence of the deformation effect is presented in Fig. 15.13. The figure shows the redistribution of unpaired electrons density over the skeleton atoms caused by the deformation. As seen in the figure, the skeleton electron-density image greatly changes when the electron correlation becomes stronger (draw attention on a large vertical scale of plottings presented in the top figure). Consequently, if observed by HRTEM, the basket-like skeleton might have look much brighter than the canopy-like one and especially than the least bright pristine molecule. In view of the finding, it is naturally to suggest that raised above the substrate and deformed areas of graphene in the form of bubbles, found in a variety of shapes on different substrates [78, 79], reveal peculiar electron-density properties just due to the stretching deformation that results in strengthening the odd electron correlation. Small (5, 5) NGr molecule presented in Fig. 15.13 cannot pretend to simulate the picture observed for micron bubbles, but it exhibits the general trend that might take place in bubbles, as well. In view of the obvious strengthening of the odd electron correlation caused by the deformation, this explanation looks more natural than that proposed from the position of an artificial 'gigantic pseudo-magnetic field' [78].

A considerable decreasing of the magnetic constants J stimulated by the deformation allows for suggesting a peculiar magnetic behaviour of the deformed graphene regions, such as, say, bubbles, stimulated by both their size and curvature. The two parameters obviously favour decreasing in the constant values thus promoting the appearance of magnetic response localized in the bubble regions.

Besides the formation of bubbles caused by ultrastrong adhesion of graphene membranes to different substrates [80], the dynamic deformation of graphene can be caused by the application of the external stress. The quantum molecular theory suggests considering the graphene molecule deformation and rupture in terms of a mechanochemical reaction [81–83]. The quantum chemical realization of the approach is based on the coordinate-of-reaction concept for the purpose of introducing a mechanochemical internal coordinate (MIC) that specifies the deformational mode. The related force of response is calculated as the energy gradient along the MIC while the atomic configuration is optimized over all other coordinates under the MIC constant-pitch elongation. When applied to the description of the deformation of both (5, 5) NGr [81, 82] and (5, 5) NGra [83] molecules under uniaxial tension, the calculations highlighted a pronounced changing in the number of effectively unpaired electrons N_D of the sample in due course of its deformation. As shown, the changing is different when the deformation occurs either along or normal to the chains of C–C bonds. However, in all cases the changing is quite significant pointing to a considerable strengthening of odd electron correlation due to changes in interatomic spacings. A detailed consideration of a possible regulating mission of the stress with respect to the enhancement of chemical reactivity of carbon atoms and magnetic behaviour of the loaded sample obviously deserves a further thorough study.

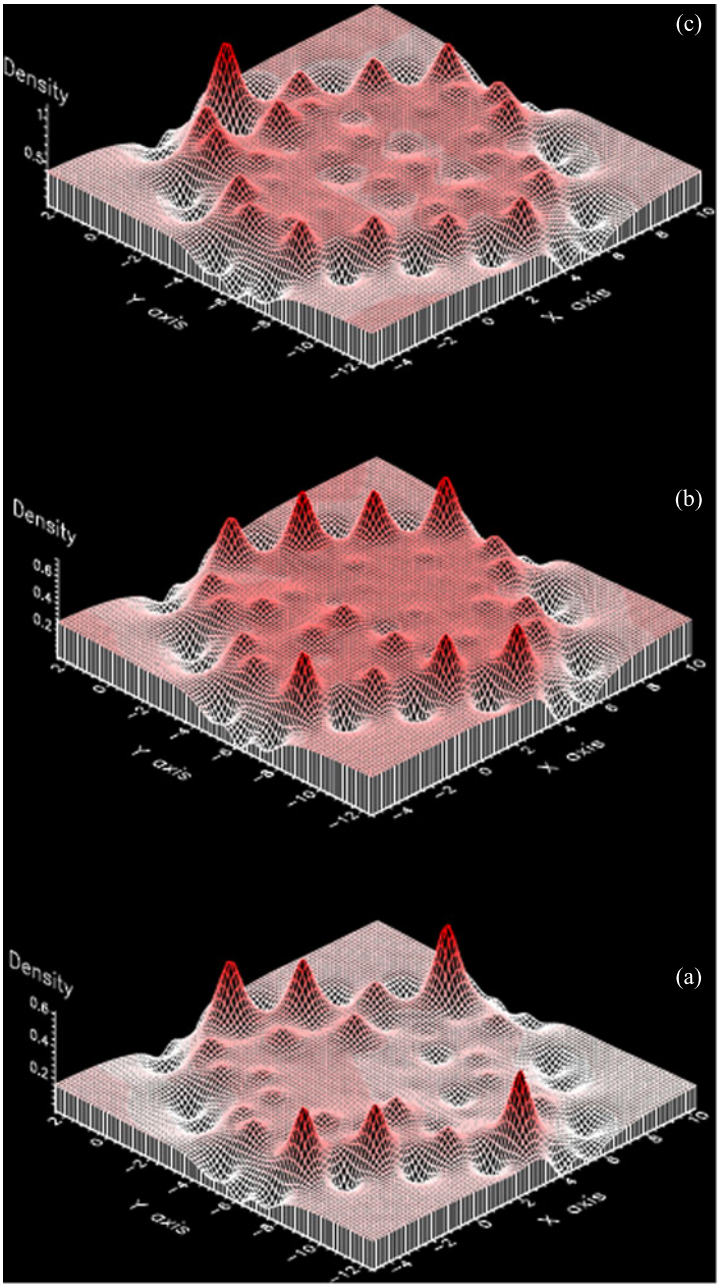

Fig. 15.13 Effectively-unpaired-electron-density images of the carbon skeletons of the pristine (5, 5) NGr molecule (**a**); canopy-like (**b**); and basket-like (**c**) fixed membranes

15.3 Discussion and Conclusive Remarks

The odd electrons of benzenoid units and the correlation of these electrons having different spins are the main building stones of the molecular theory of sp^2 nanocarbons. In contrast to the theory of aromaticity, the molecular theory accepts that the odd electrons with different spins occupy different places in the space so that the configuration interaction (CI) becomes the central point of the theory. Consequently, a multi-determinant presentation of the wave function of the system of the weakly interacting odd electrons is absolutely mandatory on the way of the theory implementation at the computational level. However, the efficacy of the available CI computational techniques is quite restricted in regards large polyatomic systems, which does not allow performing extensive computational experiments. On the other hand, the modern computational science of sp^2 nanocarbons, in general, and graphene, in particular, is, actually, the field of such experiments due to its steadily grown importance caused by prevailing computations over other empirical technique, which is evidently the case of graphene. Facing the problem, computationists have addressed standard single-determinant software albeit not often being aware of how correct are the obtained results. The current paper attempts to present the molecular theory of graphene in terms of the single-determinant computational schemes as well as to analyze the reliability of the obtained results.

The open-shell presentation of the wave functions is the first step towards the multi-determinant computational schemes so that naturally one has to address this form of the function presentation. Unrestricted Hartree-Fock (UHF) and density functional techniques (UDFT) are to be the basic grounds for the techniques used. In spite of a partial suiting of both approaches to the CI ones, both UHF and UDFT schemes provide spin-contaminated solutions with the relevant energies that exceed the pure-spin ones. Much higher energies and, thus, much less reliability correspond to the standard computational HF and DFT schemes in the restricted closed-shell approach. Nevertheless, a predominant majority of the DFT computations related to graphene have been performed in this approximation, which greatly impugns the reliability of the results obtained.

In the case of the unrestricted approach, the situation is better but this does not remove the issue about the result reliability. On the example of the application of the UHF-based theory to graphene, were obtained answers to most of the questions. These answers lead the foundation of the current paper. It should be noted that getting them has required the performance of system computational experiments in the majority of cases.

Before passing to the answers, one should pay attention to the fact that the inner features of the unrestricted computational schemes open the possibility in issuing three criteria that can distinguish electrons systems by the electrons correlation. These criteria are presented by the following quantities: (1) the energy misalignment $\Delta E^{RU} \geq 0$; (2) the total number of effectively unpaired electrons $N_D \neq 0$; and (3) the squared spin misalignment $\Delta \hat{S}^2 \geq 0$. A detailed description of the values is given in the relevant Section. When all the quantities are zero, the electrons are non-correlated (that is the case of the benzene molecule), and the relevant sp^2 systems

subordinate to the theory of aromaticity. In the case of graphene, the values are not zero, which manifests a considerable correlation of its odd electrons. Studying the graphene odd electrons system by using the unrestricted broken symmetry approach, one can obtain the following answers concerning the issue mentioned above.

Answer 1 states that application of both UHF and UDFT techniques in the framework of the broken symmetry approach [20] allows determining the energies of pure spin states quite correctly.

Answer 2 concerns the quantitative description of the graphene magnetism and shows that the broken symmetry approaches provide the exact determination of the magnetic constant. The value is size-dependent and steadily decreases by absolute value when the graphene molecule size increases. The molecules with linear dimension of a few nm can provide the constant small enough for the magnetism of the singlet graphene to be recorded. However, when the size exceeds the electron mean free pass, the magnetism disappears due to quantizing electronic states and coming back to the crystalline graphene unit cell that is diamagnetic.

Answer 3 is related to the graphene characteristic that controls the odd electrons correlation. As shown, this is the C–C bond length that exceeds the critical value $R_{crit} = 1.395$ Å. Above this value two adjacent odd electrons become effectively unpaired, firstly, partially radicalized and then completely radicalized as the C–C distance grows.

Answer 4 addresses the definite physical reality of the effectively unpaired electrons. So far there had been only one case when UBS HF computational results were compared with those obtained by using one of the CI schemes in the form of either CASSCF or MRCI approach [38]. The two techniques were applied to the description of diradical character of the Cope rearrangement transition state. CASSCF, MRCI, and UBS HF calculations have revealed effectively unpaired electrons N_D at the level of 1.05, 1.55, and 1.45 e, respectively, just highlighting that the feature is a characteristic for the electron correlation but not the proximity of the UBS HF approach. Recent successes in the atomic force microscopy with unprecedented high accuracy have allowed seeing the unpaired electrons directly. The recorded molecular images for the pentacene, olympicene, and graphene molecules are in full consent with those calculated in the UBS HF approximation.

Answer 5 concerns the basic grounds of the chemical modification of graphene. As shown, the fractional number of the effectively unpaired electrons related to a given atom N_{DA} is the quantitative indicator of the atom chemical activity (atomic chemical susceptibility) that can be used as a reliable pointer of the target atom entering the reaction. A large scale stepwise reaction can be considered computationally, which leads to the formation of different polyderivatives of graphene. On the example of hydrogenation and oxidation of graphene, was obtained a general view of graphene polyhydrides and polyoxides that well fit the experimental reality.

Answer 6 testifies that molecular theory is quite efficient when considering mechanical behavior of graphene. Leaving outside the theory application to the consideration of the deformational process as such [81–83], the current chapter is concentrated on the consequences, related to the odd electros correlation, that are caused by stretching and rupture of the C–C bonds in the graphene molecules in due course of

deformation. The C–C bonds stretching causes increasing of both the total and fractional numbers of the effectively unpaired electrons. The feature explains changing in the chemical reactivity of graphene during deformation, on one hand, and appearing bright spots on the TEM images in the area of graphene bubbles.

A limited volume of the chapter does not allow touching all the features of the extremely large graphene science. However, the selected topics and answers obtained in the course of their consideration clearly show that the molecular theory of graphene, implemented in the format of the UBS HF computing schemes, is highly efficient and suggests reliable explanations for a number of different graphene peculiarities. These explanations are obtained on the same platform based on quite a few concepts involving the odd electrons of the graphene benzenoid units and their correlation due to weak interaction. Outside the paper, there are still questions concerning the chemical topology of graphene [84, 85], different aspects concerning graphene quantum dots [86, 87], the silicene as siliceous counterpart of graphene [88, 89], the graphene catalytic activity [90, 91], and so forth. The molecular theory of graphene is very successful in dealing with all these issues, not being concentrated on numbers but giving the main attention to clearly seen trends.

The odd electron correlation is not a prerogative of graphene only. Similar phenomenon is characteristic for all sp^2 nanocarbons, including fullerenes and nanotubes as well [5]. The only preference of graphene consists in much larger variety of cases when this inherent characteristic of the class can be visualized.

Acknowledgements The author immensely appreciates fruitful discussions with I.L. Kaplan, E. Brandas, D. Tomanek. O. Ori, F. Cataldo, E. Molinary L.A. Chernozatonski who draw her attention onto different problems of the molecular theory of graphene. The author is deeply grateful to her colleagues N. Popova, V. Popova, L. Shaymardanova, B. Razbirin, D. Nelson, A. Starukhin, N. Rozhkova for support and valuable contribution into the study. A financial support provided by the Ministry of Science and High Education of the Russian Federation grant 2.8223.2013 is highly acknowledged.

References

1. Hoffmann R (2013) Small but strong lessons from chemistry for nanoscience. Angew Chem, Int Ed 52:93–103
2. Hoffmann R (1971) Interaction of orbitals through space and through bonds. Acc Chem Res 4:1–9
3. Hay PJ, Thibeault JC, Hoffmann R (1971) Orbital interactions in metal dimer complexes. J Am Chem Soc 97:4884–4899
4. Sheka E (2003) Violation of covalent bonding in fullerenes. In: Sloot PMA, Abramson D, Bogdanov AV et al (eds) Computational science—ICCS2003. Lecture notes in computer science. Springer, Heidelberg, pp 386–398
5. Sheka EF (2011) Fullerenes: nanochemistry, nanomagnetism, nanomedicine, nanophotonics. CRC Press/Taylor and Francis, Boca Raton
6. Sheka EF (2003) Fullerenes as polyradicals. Internet electronic conference of molecular design, 2003, 23 November–6 December 2003. http://www.biochempress.com. November 28, paper 54
7. Sheka EF (2004) Odd electrons and covalent bonding in fullerenes. Int J Quant Chem 100:375–386

8. Sheka E (2009) Nanocarbons through computations: fullerenes, nanotubes, and graphene. In: The UNESCO-EOLSS encyclopedia nanoscience and nanotechnology. UNESCO, Moscow, pp 415–444
9. Geim AK, Novoselov KS (2007) The rise of graphene. Nat Mater 6:183–191
10. Davidson E (1998) How robust is present-day DFT? Int J Quant Chem 69:214–245
11. Kaplan I (2007) Problems in DFT with the total spin and degenerate states. Int J Quant Chem 107:2595–2603
12. Takatsuka K, Fueno T, Yamaguchi K (1978) Distribution of odd electrons in ground-state molecules. Theor Chim Acta 48:175–183
13. Staroverov VN, Davidson ER (2000) Distribution of effectively unpaired electrons. Chem Phys Lett 330:161–168
14. Benard MJ (1979) A study of Hartree–Fock instabilities in $Cr_2(O_2CH)_4$ and $Mo_2(O_2CH)_4$. J Chem Phys 71:2546–2556
15. Lain L, Torre A, Alcoba DR et al (2011) A study of the relationships between unpaired electron density, spin-density and cumulant matrices. Theor Chem Acc 128:405–410
16. Sheka EF, Chernozatonskii LA (2007) Bond length effect on odd electrons behavior in single-walled carbon nanotubes. J Phys Chem A 111:10771–10780
17. Sheka EF (2012) Computational strategy for graphene: insight from odd electrons correlation. Int J Quant Chem 112:3076–3090
18. Zayets VA (1990) CLUSTER-Z1: quantum-chemical software for calculations in the *s*, *p*-basis. Institute of Surface Chemistry Nat Ac Sci of Ukraine, Kiev
19. Gao X, Zhou Z, Zhao Y et al (2008) Comparative study of carbon and BN nanographenes: ground electronic states and energy gap engineering. J Phys Chem A 112:12677–12682
20. Noodleman L (1981) Valence bond description of antiferromagnetic coupling in transition metal dimers. J Chem Phys 74:5737–5742
21. Illas F, de Moreira IPR, de Graaf C, Barone V (2000) Magnetic coupling in biradicals, binuclear complexes and wide-gap insolators; a survey of ab initio function and density functional theory approaches. Theor Chem Acc 104:265–272
22. Zvezdin AK, Matveev VM, Mukhin AA et al (1985) Redkozemeljnyje iony v magnito-uporjadochennykh kristallakh (Rear Earth ions in magnetically ordered crystals). Nauka, Moskva
23. Van Fleck JH (1932) The theory of electric and magnetic susceptibilities. Oxford at the Clarendon Press, Oxford
24. Kahn O (1993) Molecular magnetism. VCH, New York
25. Koshino M, Ando T (2007) Diamagnetism in disordered graphene. Phys Rev B 75:235333. (8 pp)
26. Nair RR, Sepioni M, Tsai I-L et al (2012) Spin-half paramagnetism in graphene induced by point defects. Nat Phys 8:199–202
27. Sheka EF, Chernozatonskii LA (2010) Chemical reactivity and magnetism of graphene. Int J Quant Chem 110:1938–1946
28. Sheka EF, Chernozatonskii LA (2010) Broken spin symmetry approach to chemical susceptibility and magnetism of graphenium species. J Exp Theor Phys 110:121–132
29. Shibayama Y, Sato H, Enoki T, Endo M (2000) Phys Rev Lett 84:1744
30. Enoki T, Kobayashi Y (2005) J Mater Chem 15:3999
31. Tada K, Haruyama J, Yang HX et al (2011) Graphene magnet realized by hydrogenated graphene nanopore arrays. Appl Phys Lett 99:183111. (3 pp)
32. Tada K, Haruyama J, Yang HX et al (2011) Ferromagnetism in hydrogenated graphene nanopore arrays. Phys Rev Lett 107:217203. (5 pp)
33. Sheka EF, Zayets VA, Ginzburg IYa (2006) Nanostructural magnetism of polymeric fullerene crystals. J Exp Theor Phys 103:728–739
34. Boeker GF (1933) The diamagnetism of carbon tetrachloride, benzene and toluene at different temperatures. Phys Rev 43:756–760
35. Seach MP, Dench WA (1979) Quantitative electron spectroscopy of surfaces: a standard data base for electron inelastic mean free paths in solids. Surf Interface Anal 1:2–11

36. Komolov SA, Lazneva EF, Komolov AS (2003) Low-energy electron mean free path in thin films of copper phthalocyanine. Tech Phys Lett 29:974–976
37. Takatsuka K, Fueno TJ (1978) The spin-optimized SCF general spin orbitals. II. The 2^2S and 2^2P states of the lithium atom. J Chem Phys 69:661–669
38. Staroverov VN, Davidson ER (2000) Diradical character of the Cope rearrangement transition state. J Am Chem Soc 122:186–187
39. Mayer I (1986) On bond orders and valences in the ab initio quantum chemical theory. Int J Quant Chem 29:73–84
40. Dewar MJS, Thiel W (1977) Ground states of molecules. 38. The MNDO method. Approximations and parameters. J Am Chem Soc 99:4899–4907
41. Zhogolev DA, Volkov VB (1976) Metody, algoritmy i programmy dlja kvantovo-khimicheskikh raschetov molekul (Methods, algorithms and programs for quantum-chemical calculations of molecules). Naukova Dumka, Kiev
42. Sheka EF, Zayets VA (2005) The radical nature of fullerene and its chemical activity. Russ J Phys Chem 79:2009–2014
43. Lain L, Torre A, Alcoba DR et al (2009) A decomposition of the number of effectively unpaired electrons and its physical meaning. Chem Phys Lett 476:101–103
44. Wang J, Becke AD, Smith VH Jr (1995) Eveluation of $\langle\hat{S}\rangle^2$ in restricted, unrestricted Hartree-Fock, and density functional based theory. J Chem Phys 102:3477–3480
45. Cohen AJ, Tozer DJ, Handy NC (2007) Evaluation of $\langle\hat{S}\rangle^2$ in density functional theory. J Chem Phys 126:214104. (4 pp)
46. Lobayan RM, Bochicchio RC, Torre A et al (2011) Electronic structure and effectively unpaired electron density topology in closo-boranes: nonclassical three-center two-electron bonding. J Chem Theory Comput 7:979–987
47. Kitagawa Y, Saito T, Ito M et al (2007) Approximately spin-projected geometry optimization method and its application to di-chromium systems. Chem Phys Lett 442:445–450
48. Kitagawa Y, Saito T, Nakanishi Y et al (2009) Spin contamination error in optimized geometry of singlet carbene ($^1A_1$) by broken-symmetry method. J Phys Chem A 113:15041–15046
49. Gross L, Mohn F, Moll N et al (2009) The chemical structure of a molecule resolved by atomic force microscopy. Science 325:1110–1114
50. 'Olympic rings' molecule olympicene in striking image. BBC News Science and Environment (2012-05-28)
51. Fujita M, Wakabayashi K, Nakada K et al (1996) Peculiar localized state at zigzag graphite edge. J Phys Soc Jpn 65:1920–1923
52. Nakada K, Fujita M, Dresselhaus G et al (1996) Edge state in graphene ribbons: nanometer size effect and edge shape dependence. Phys Rev B 54:17954–17961
53. Coleman J (2008) A new solution to graphene production. SPIE Newsroom. doi:10.1117/2.1200810.1336
54. The noise about graphene (2010) Science Centre of Barkley Lab
55. Sheka EF (2006) 'Chemical portrait' of fullerene molecule. J Struct Chem 47:600–607
56. Sheka EF (2007) Chemical susceptibility of fullerenes in view of Hartree-Fock approach. Int J Quant Chem 107:2803–2816
57. Sheka EF, Chernozatonskii LA (2010) Chemical reactivity and magnetism of graphene. Int J Quant Chem 110:1938–1946
58. Allouche A, Jelea A, Marinelli F et al (2006) Hydrogenation and dehydrogenation of graphite (0001) surface: a density functional theory study. Phys Scr T 124:91–94
59. Sheka EF (2010) Stepwise computational synthesis of fullerene C_{60} derivatives. Fluorinated fullerenes $C_{60}F_{2k}$. J Exp Theor Phys 111:395–412
60. Sheka EF, Popova NA (2012) Odd-electron molecular theory of the graphene hydrogenation. J Mol Model 18:3751–3768
61. Elias DC, Nair RR, Mohiuddin TMG et al (2009) Control of graphene's properties by reversible hydrogenation: evidence for graphane. Science 323:610–613
62. Sheka EF (2011) Computational synthesis of hydrogenated fullerenes from C_{60} to $C_{60}H_{60}$. J Mol Model 17:1973–1984

63. Sheka EF, Popova NA (2011) When a covalent bond is broken? arXiv:1111.1530v1 [physics.chem-ph]
64. Sheka EF, Popova NA (2012) Molecular theory of graphene oxide. arXiv:1212.6413 [cond-mat.mtrl-sci]
65. Sheka EF, Popova NA (2012) Molecular theory of graphene oxide. Phys Chem Chem Phys 15:13304–13322
66. Dreyer DS, Park S, Bielawski CW et al (2010) The chemistry of graphene oxide. Chem Soc Rev 39:228–240
67. Zhu Y, Shanthi M, Weiwei C et al (2010) Graphene and graphene oxide: synthesis. Properties, and Applications Adv Mater 22:3906–3924
68. Kuila T, Mishra AK, Khanra P et al (2013) Recent advances in the efficient reduction of graphene oxide and its application as energy storage electrode materials. Nanoscale 5:52–71
69. Wang H, Hu IH (2011) Effect of oxygen content on structures of graphite oxides. Ind Eng Chem Res 50:6132–6137
70. Fujii S, Enoki T (2010) Cutting of oxidized graphene into nanosized pieces. J Am Chem Soc 132:10034–10041
71. Xu Z, Bando Y, Liu L et al (2011) Electrical conductivity, chemistry, and bonding alternations under graphene oxide to graphene transition as revealed by in situ TEM. ACS Nano 5:4401–4406
72. Wang S, Wang R, Liu X et al (2012) Optical spectroscopy investigation of the structural and electrical evolution of controllably oxidized graphene by a solution method. J Phys Chem C 116:10702–10707
73. Mattevi C, Eda G, Agnoli S et al (2009) Evolution of electrical, chemical, and structural properties of transparent and conducting chemically derived graphene thin films. Adv Funct Mater 19:2577–2583
74. Wang L, Zhao J, Sun Y-Y et al (2011) Characteristics of Raman spectra for graphene oxide from ab initio simulations. J Chem Phys 135:184503. (5 pp)
75. Saxena S, Tyson TA, Negusse E (2010) Investigation of the local structure of graphene oxide. J Phys Chem Lett 1:3433–3437
76. Ambrosi A, Chee SY, Khezri B et al (2012) Metallic impurities in graphenes prepared from graphite can dramatically influence their properties. Angew Chem, Int Ed 51:500–503
77. Lu N, Li Zh (2012) Graphene oxide: theoretical perspectives. In: Zeng J et al (eds) Quantum simulations of materials and biological systems. Springer, Dordrecht, pp 69–84
78. Levy N, Burke SA, Meaker KL et al (2010) Strain-induced pseudo-magnetic fields greater than 300 tesla in graphene nanobubbles. Science 329:544–547
79. Georgiou T, Britnell L, Blake P et al (2011) Graphene bubbles with controllable curvature. Appl Phys Lett 99:093103. (3 pp)
80. Koenig SP, Boddeti NG, Dunn ML et al (2011) Ultrastrong adhesion of graphene membranes. Nat Nanotechnol 6:543–546
81. Sheka EF, Popova NA, Popova VA et al (2011) Structure-sensitive mechanism of nanographene failure. J Exp Theor Phys 112:602–611
82. Sheka EF, Popova NA, Popova VA et al (2011) A tricotage-like failure of nanographene. J Mol Model 17:1121–1131
83. Popova NA, Sheka EF (2011) Mechanochemical reaction in graphane under uniaxial tension. J Phys Chem C 115:23745–23754
84. Sheka EF, Shaymardanova LKh (2011) C_{60}-based composites in view of topochemical reactions. J Mater Chem 21:17128–17146
85. Sheka EF (2013) Topochemistry of spatially extended sp^2 nanocarbons: fullerenes, nanotubes, and graphene. In: Ashrafi AR, Cataldo F, Iranmanesh A et al (eds) Topological modelling of nanostructures and extended systems. Carbon materials: chemistry and physics, vol 7. Springer, Dordrecht. doi:10.1007/978-94-007-6413-2_5
86. Razbirin BS, Rozhkova NN, Sheka EF et al (2013) Fractals of graphene quantum dots in photoluminescence of shungite. arXiv:1308.2569v2 [cond-mat. mes-hall]

87. Rozhkova NN, Sheka EF Shungite as loosely packed fractal nets of graphene-based quantum dots. arXiv:1308.0794v1 [cond-mat. mtrl-sci]
88. Sheka EF (2009) May silicene exist? arXiv:0901.3663
89. Sheka EF (2013) Why sp^2-like nanosilicons should not form: insight from quantum chemistry. Int J Quant Chem 113:612–618
90. Tang S, Cao Z (2012) Site-dependent catalytic activity of graphene oxides towards oxidative dehydrogenation of propane. Phys Chem Chem Phys 14:16558–16565
91. Hsu H-C, Shown I, Wei H-Y et al (2013) Graphene oxide as a promising photocatalyst for CO_2 to methanol conversion. Nanoscale 5:262–268

Chapter 16
Topological Mechanochemistry of Graphene

E.F. Sheka, V.A. Popova, and N.A. Popova

Abstract In view of the formal topology, two common terms, namely, the connectivity and adjacency, determine the 'quality' of the C–C bonds of sp^2 nanocarbons. The feature is the most sensitive point of the inherent topology of the species so that such external action as the mechanical deformation should obviously change it and result in particular topological effects. The current chapter describes the effects caused by uniaxial tension of a graphene molecule in due course of the mechanochemical reaction. Basing on the molecular theory of graphene, the effects are attributed to both mechanical loading and chemical modification of the edge atoms of the molecule. The mechanical behavior is shown to be not only highly anisotropic with respect to the direction of the load application, but greatly dependent on the chemical modification of the molecule edge atoms thus revealing the topological character of the graphene deformation.

16.1 Introduction

The modern topology in chemistry covers two large valleys, namely, formal, mathematical and empirical, chemical. The former is concerned with the description of the molecular structures on the basis of the finite topological spaces. The space shows itself as a mathematical image or instrument of the theoretical study. A large collection of comprehensive reviews, related to the topological description of fullerenes from this viewpoint, has recently been published [1]. The second field covers vastly studied topochemical reactions. The space in this case is the physical reality defining the real place where the reactions occur. If the appearance of the mathematical topology in chemistry can be counted off the publication of the Merrifield and Simmons monograph in 1989 [2], the topochemical reactions have been studying from the nineteenth century (see [3] and references therein). The first stage of the study was completed in the late nineteenth-twenties [4] and then obtained a new pulse after appearing the Woodward and Hoffmann monograph, devoted to the conservation of orbital symmetry, in 1970 [5]. Since then, the topochemical reactions

E.F. Sheka (✉)
Peoples' Friendship University of Russia, Miklukho-Maklay, 6, Moscow, 117198, Russia
e-mail: sheka@icp.ac.ru

M. Hotokka et al. (eds.), *Advances in Quantum Methods and Applications in Chemistry, Physics, and Biology*, Progress in Theoretical Chemistry and Physics 27,
DOI 10.1007/978-3-319-01529-3_16,

have become an inherent part of not only organic, but inorganic chemistry, as well. The readers, who are interested in this topic, are referred to a set of comprehensive reviews [3, 6–9], but a few. The current situation in this field can be seen by the example of a direct structural understanding of the topochemical solid state photopolymerization reaction [10].

Nowadays, we are witnessing the next pulse, stimulating investigations in the field, which should be attributed to the appearance of a new class of the spatially extended molecular materials, such as sp^2 nanocarbons. Obviously, the main members of the class such as fullerenes, nanotubes, and numerous graphene-based species are absolutely different from the formal topology viewpoint. Thus, fullerenes exist in the form of a hollow sphere, ellipsoid, or tube consisting of differently packed benzenoid units. Carbon nanotubes present predominantly cylindrical packing of the units. In graphene, the benzenoid units form one-atom-thick planar honeycomb structure. If we address the common terms of the formal topology, namely, connectivity and adjacency, we have to intuitively accept their different amount in the above three species. In its turn, the connectivity and adjacency determine the 'quality' of the C–C bond structure of the species, thus, differentiating them by this mark. Since non-saturated C–C bonds are the main target for chemical reactions of any type, one must assume that identical reactions, involving the bonds, will occur differently for different members of the sp^2 nanocarbon family. Therefore, one may conclude that the spatially extended sp^2 nanocarbons present not only peculiar structural chemicals, but the class of species for which the formal and empirical topology overlap. At the first time, the results, presented in [11, 12] have revealed this tight interconnection in terms of the molecular quantum theory. Not only fullerenes, but carbon nanotubes and graphene (their fragments) have been considered at the molecular level. The obtained results are related to the computational study of the intermolecular interaction between one of the above sp^2 nanocarbon molecules and one of the other addends, among which there are both sp^2 nanocarbons and monoatomic species. The intermolecular interaction lays the foundation of any reaction so that its topological peculiarities may evidence a topochemical character of the reaction under study. However, since the 'quality' of the C–C bonds is the most sensitive point of the inherent topology of the sp^2 nanocarbons, external actions, such as mechanical deformation, on the bonds should obviously result in particular topological effects that accompany the relevant intramolecular reactions. The current chapter is devoted to the discussion of such reactions that are presented by the mechanochemical one related to the uniaxial tension of a graphene molecule.

16.2 Uniaxial Tension of Graphene as a Mechanochemical Reaction

Below we will consider a particular topological effect caused by the influence of both the loading direction and the graphene molecule edge termination on the inherited topology of the molecule. As turned out, the graphene deformation under

external mechanical loading is extremely sensitive to the state of the edge atoms and makes it possible to disclose a topological nature of this sensitivity.

Oppositely to real physical experiments, when changing the object shape under loading is usually monitored, computational experiments deal with the total energy response to the object shape deformation that simulates either tension and contraction or bending, screwing, shift, and so forth. As for graphene, whose mechanical properties are amenable to experimental study with difficulty, the computational experiments take on great significance.

A lot of works are devoted to the calculation of mechanical properties of graphene due to which two approaches, namely, continuum and atomistic ones have been formulated. The continuum approach is based on the well developed theory of elasticity of continuous solid media applied to shells, plates, beams, rods, and trusses. The latter are the structure elements used for the continuum description. When applying to graphene, its lattice structure is presented in terms of the above continuum structure elements and the main task of the calculations is the reformulation of the total energy of the studied atomic-molecular system subjected to changing in shape in terms of the continuum structure elements. This procedure actually involves the adaptation of the theory of elasticity of continuous media to nanosize objects which makes allowance for introducing macroscopic basic mechanical parameters such as Young's modulus (E), the Poisson ratio (ν), the potential energy of the elastic deformation, etc into the description of mechanical properties of graphene. Since the energy of graphene is mainly calculated in the framework of quantum chemistry, which takes the object atom structure into account, the main problem of the continuum approach is a linkage between molecular configuration and continuum structure elements. Nanoscale continuum methods (see Refs. [13–17] and references therein), among which those based on the structural mechanics concept [18] are the most developed, have shown the best ability to simulate nanostructure materials. In view of this concept, graphene is a geometrical frame-like structure where the primary bonds between two nearest-neighboring atoms act like the load-bearing beam members, whereas an individual atom acts as the joint of the related beams [19–22].

The basic concept of the atomistic approach consists in obtaining mechanical parameters of the object from results of the direct solutions of either Newton motion laws [22, 23] or Schrödinger equations [24, 25] under changing the object shape following a particular algorithm of simulation of the wished type of deformation. It should be necessary to issue a general comment concerning calculations based on the application of the DFT computational schemes. All the latter, except the recent one [26], were performed in the framework of restricted versions of the programs that do not take into account spins of the graphene odd electrons and thus ignore the correlation interaction between the latter. Peculiarities of the graphene odd electron behavior is connected with a considerable enlarging of its C–C bonds, which, in its turn, causes a noticeable weakening of the odd electron interaction and thus requires taking into account these electrons correlation [27, 28].

In the case of atomistic approach, not energy itself, but forces applied to atoms become the main goal of calculations. These forces are inputted later into the rela-

tions of macroscopic linear theory of elasticity and lay the foundation for the evaluation of micro-macroscopic mechanical parameters such as Young's modulus (E^*), the Poisson ratio (ν^*), and so on. Nothing to mention that parameters E and E^* as well as ν and ν^* are not the same so that their coincidence is quite accidental. Obviously, the atomistic approach falls in opinion comparing with the continuum one due to time consuming calculations and, as a result, due to applicability to smaller objects. However, it possesses doubtless advantages concerning the description of the mechanical behavior of the object under certain loading (shape changing) as well as exhibiting the deformation and failure process at the atomic level. A serious deficiency of both standard approaches is their close links with the theory of elasticity, which drives the graphene into the Procrustean bed of elastic deformation, depriving it of the right to permanent plastic behavior.

Recently a new atomistic approach has been suggested for the description of the graphene deformation based on considering the failure and rupture process of graphene as the occurrence of a mechanochemical reaction [29–32]. A similarity between the mechanically induced reaction and the first-type chemical ones, first pointed out by Tobolski and Eyring seventy years ago [33], suggested the use of a well developed quantum-chemical approach of the reaction coordinate [34] in the study of the atomic structure transformation under deformation. Firstly applied to the deformation of poly(dimethylsiloxane) oligomers [35], the approach has revealed a high efficacy in exhibiting elastic, plastic, and superplastic regions of the uniaxial tension of the oligomer, disclosing the mechanism of its failure and rupture. It has been successfully applied recently for the description of the uniaxial tension of both graphene [29, 30] and graphane [31] molecules, thus positioning itself as a significant part of the molecular theory of graphene [28].

The main point of the approach concerns the reaction coordinate definition. When dealing with chemical reactions, the coordinate is usually selected among the internal ones (valence bond, bond angle or torsion angle) or is presented as a linear combination of the latter. Similarly, mechanochemical internal coordinates (MICs) are introduced as modified internal coordinates defined in such a way as to be able to specify the considered deformational modes [35, 36]. Thus, uniaxial tension and contraction are described by linear MICs similar to valence bonds. In the case of tensile deformation, the benzenoid pattern of graphene sheets and a regular packing of the units predetermined the choice of either parallel or normal MICs orientation with respect to the chain of C–C bonds. In the rectangular nanographene sheets and nanoribbons the former orientation corresponds to tensile deformation applied to the zigzag edges (*zigzag* mode) while the latter is attributed to the armchair edges (*armchair* mode). The MIC configurations of the two tensile modes of the $(5, 5)$ NGr molecule are presented in Fig. 16.1. The molecule lays the foundation of previously performed computational experiments [29–32] and presents a rectangular fragment of a graphene sheet that is cut along zigzag and armchair edges and contains 5 benzenoid units along each direction. The deformation proceeds as a stepwise elongation of the MICs with the increment $\delta L = 0.1$ Å at each step so that the current MIC length constitutes $L = L_0 + n\delta L$, where L_0 is the initial length of the MIC and n counts the number of the deformation steps. The right ends of

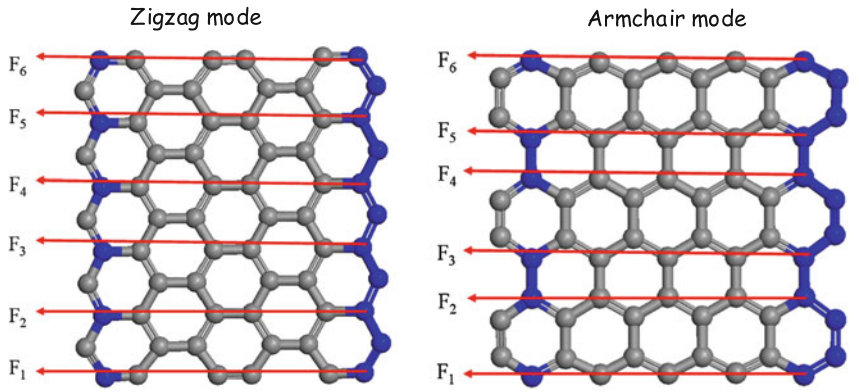

Fig. 16.1 Six mechanochemical internal coordinates of the uniaxial tension of the molecule (5, 5) NGr for two deformation modes. F_1, F_2, F_3, F_4, F_5, F_6 are the forces of response along these coordinates. *Blue atoms* fix the coordinates ends

all the MICs are fixed so that these blue colored atoms are immobilized while the atoms on the left ends of MICs move along the arrows providing the MIC successive elongation, once excluded from the optimization, as well. The relevant force of response is calculated as the energy gradient along the MIC while the atomic configuration is optimized over all of the other coordinates under the MIC constant-pitch elongation. The results presented in the chapter were obtained in the framework of the Hartree-Fock unrestricted (UHF) version of the DYQUAMECH codes [37] exploiting advanced semiempirical QCh methods (PM3 version [38]).

The corresponding forces of response F_i applied along the ith MICs are the first derivatives of the total energy $E(R)$ over the Cartesian coordinates [35]:

$$\frac{dE}{dR} = \left\langle \varphi \left| \frac{\partial H}{\partial R} \right| \varphi \right\rangle + 2\left\langle \frac{\partial \varphi}{\partial R} | H | \varphi \right\rangle + 2\left\langle \frac{\partial \varphi}{\partial P} | H | \varphi \right\rangle \frac{dP}{dR} \tag{16.1}$$

Here, φ is the wave function of an atom in the ground state at fixed nucleus positions, H presents the adiabatic electron Hamiltonian, and P is the nucleus momentum. When the force calculation is completed, the gradients are re-determined in the system of internal coordinates in order to proceed further in seeking the total energy minimum by the atomic structure optimization. Forces F_i are used afterwards for determining all the required micro-macroscopic mechanical characteristics, which are relevant to the uniaxial tension, such as the total force of response $F = \sum_i F_i$, the stress $\sigma = F/S = (\sum_i F_i)/S$, where S is the loading area, the Young's modulus $E = \sigma/\varepsilon$, where both stress σ and the strain ε are determined within the elastic region of deformation.

16.3 Computational Results

Thus arranged computations have revealed that a high stiffness of the graphene body is provided by that one of the benzenoid units. The anisotropy of the unit mechan-

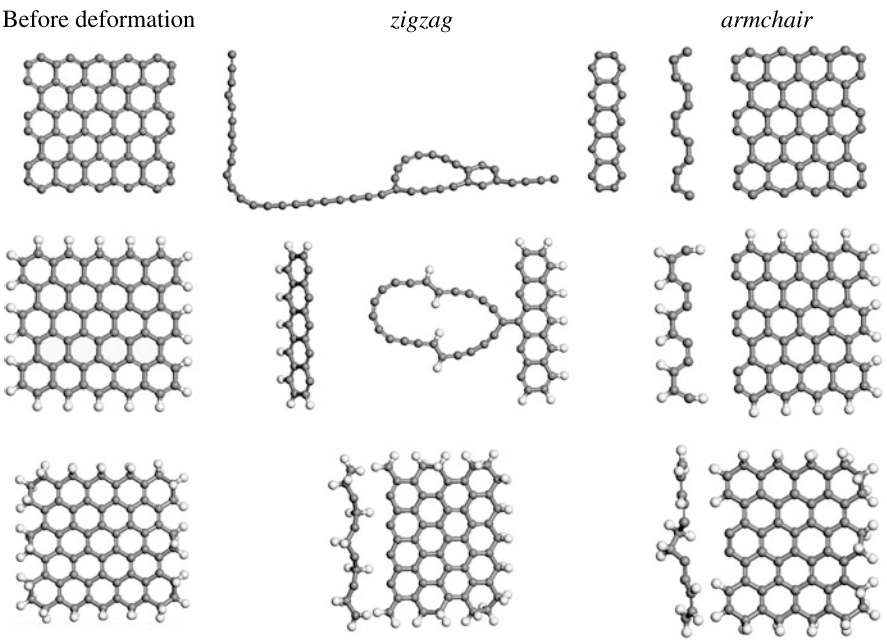

Fig. 16.2 The equilibrium structures of the (5, 5) NGr with different chemical modification of the edge atoms before and after completing the tensile deformation in two modes of deformation. Bare edges (*top*); H_1-terminated edges (*middle*); H_2-terminated edges (*bottom*)

ical behavior in combination with different packing of the units either normally or parallel to the C–C bond chains lays the ground for the structure-sensitive mechanism of the mechanical behavior of the object that drastically depends on the deformation modes [29–31]. The elastic region of tensile deformation of both (5, 5) nanographene (NGr) and nanographane (NGra) molecules is extremely narrow and corresponds to a few first steps of the deformation. The deformation as a whole is predominantly plastic and dependent on many parameters. Among the latter, the most important is the chemical composition of the molecule edge atoms [32].

The equilibrium structures of the (5, 5) NGr molecule before and after uniaxial tension, which was terminated by the rupture of the last C–C bond coupling two fragments of the molecule, are shown in Fig. 16.2. Looking at the picture, two main peculiarities of the molecule deformation should be notified. First concerns the anisotropy of the deformation with respect to two deformational modes. Second exhibits a strong dependence of the deformation on the chemical composition of the molecule edge atoms. As mentioned above, the deformation anisotropy of graphene has been attributed to the mechanical anisotropy of the constituent benzenoid units [29, 30]. The dependence of the deformation on the chemical modification of the framing edge atoms has been revealed for the first time.

As seen in Fig. 16.2, the deformation behavior is the most complex for the naked molecule. The mechanical behavior of the (5, 5) NGr molecule is similar to that of a

tricotage sheet when either the sheet rupture has both commenced and completed by the rupture of a single stitch row (*armchair* mode) or the rupture of one stitch is 'tugging at thread' the other stitches that are replaced by still elongated one-atom chain of the carbon atoms (*zigzag* mode). In the former case, the deformation is one-stage and is terminated on the 17th step of the deformation. In contrast, the deformational mode *zigzag* is multi-stage and consists of 250 consequent steps with elongation of 0.1 Å at each step [29, 30]. The formation of the one-atom chain under zigzag-mode tension of the naked graphene piece has been supported experimentally [39].

Quite unexpectedly, the character of the deformation has occurred to be strongly dependent on the chemical situation at the molecule edges. As seen in Fig. 16.2b, the addition of one hydrogen atom to each of the molecule edge atoms does not change the general character of the deformation: it remains a tricotage-like one so that there is still a large difference between the behavior of *zigzag* and *armchair* modes. At the same time, the number of the deformation steps of the *zigzag* mode reduces to 125.

Even more drastic changes for this mode are caused by the addition of the second hydrogen atoms to the edge ones (Fig. 16.2c). Still, the *armchair* mode is quite conservative while the *zigzag* one becomes practically identical to the former. The tricotage-like character of the deformation is completely lost and the rupture occurs at the 20th step.

Figure 16.3 presents a set of the 'stress-strain' relations that fairly well highlight the difference in the mechanical behavior of all the three molecules. Table 16.1 presents the Young modules that were defined in the region of the elastic deformation. As seen from the table, the Young modules depend on the character of the edge atom chemical modification. As shown in [31], elastic properties of extended molecules such as polymers [35, 40] and nanographenes [31] are determined by dynamic characteristics of the objects, namely, by force constants of the related vibrations. Since benzenoid units provide the determining resistance to any deformation of the graphene molecules, the dynamic parameters of the stretching C–C vibrations of the units are mainly responsible in the case of the uniaxial tension. Changing in Young's modules means changing in the force constants (and, consequently, frequencies) of these vibrations. The latter are attributed to the G-band of graphene that lays the foundation of a mandatory testing of any graphenium system by the Raman spectroscopy. In numerous cases, the relevant band is quite wide which might indicate the chemical modification of the edge zone of the graphene objects under investigation.

Since the deformation-induced molecule distortion mainly concerns the basal atoms, so drastic changes in the deformation behavior points to a significant influence of the chemical state of the edge atoms on the electronic properties in the basal plane. The observed phenomenon can be understood if suggest that (1) the deformation and rupture of the molecule are a collective event that involves the electron system of the molecule as a whole; (2) the electron system of the graphene molecule is highly delocalized due to extreme correlation of the odd electrons; and (3) the electrons correlation is topologically sensitive due to which the chemical termination of the edge atoms so strongly influences the behavior of the entire molecule. The latter has turned out to be the reality, indeed.

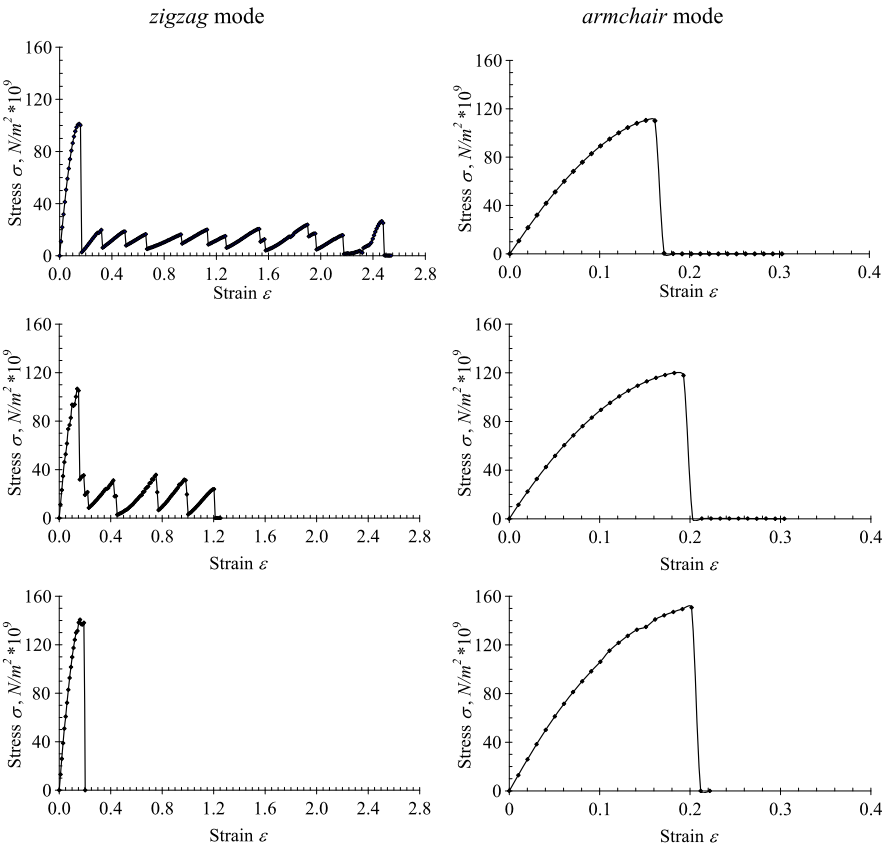

Fig. 16.3 The stress-versus-strain dependences of the tensile deformation of the (5, 5) NGr molecule with the different chemical modification in two deformation modes. Nake molecule (*top*); H_1-terminated edges (*middle*); H_2-terminated edges (*bottom*)

Table 16.1 Young's modules for (5, 5) NGr with different configuration of edge atoms, TPa

Mode	Bare edges	H_1-terminated edges	H_2-terminated edges
Zigzag	1.05	1.09	0.92
Armchair	1.06	1.15	0.95

16.4 Topological Character of the Odd Electron Correlation in Graphene

The performed computations have revealed that the correlation of the odd electrons of the studied molecules changes quite remarkably in the course of the deformation. This result can be illustrated by the evolution of the total number of effectively unpaired electrons N_D during the deformation. The N_D value is a direct characteristic

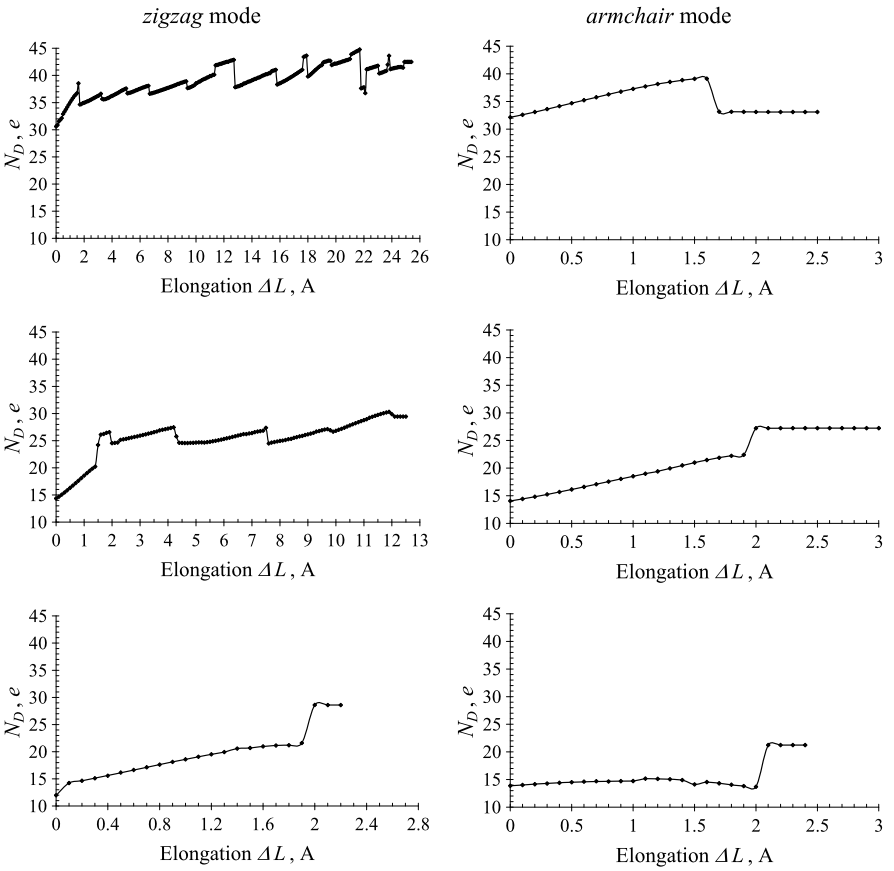

Fig. 16.4 The evolution of the odd electrons correlation in terms of the total numbers of the effectively unpaired electrons under the tensile deformation of the (5, 5) NGr at two deformation modes. Bare edges (*top*); H_1-terminated edges (*middle*); H_2-terminated edges (*bottom*)

of the extent of the electron correlation, on one hand, [28] and molecular chemical susceptibility, on the other, [41]. Changing in N_D reveals changing in the molecule chemical activity induced by deformation.

Figure 16.4 presents the evolution of N_D for the three studied molecules. Since breaking of each C–C bonds causes an abrupt changing in N_D, a toothed character of the relevant dependences related to the *zigzag* mode of the molecule with the naked and H-terminated edges is quite evident. One should draw attention to the N_D absolute values as well as to their dependence on both the chemical modification of the edge atoms and the deformational modes. Evidently, the chemical activity of the molecules drastically changes in the course of the mechanically induced transformation. This changing is provided by the redistribution of the C–C bond lengths caused by the mechanical action. This action combines the positions of both basal plane and edge atoms into the united whole and is topologically sensitive. There-

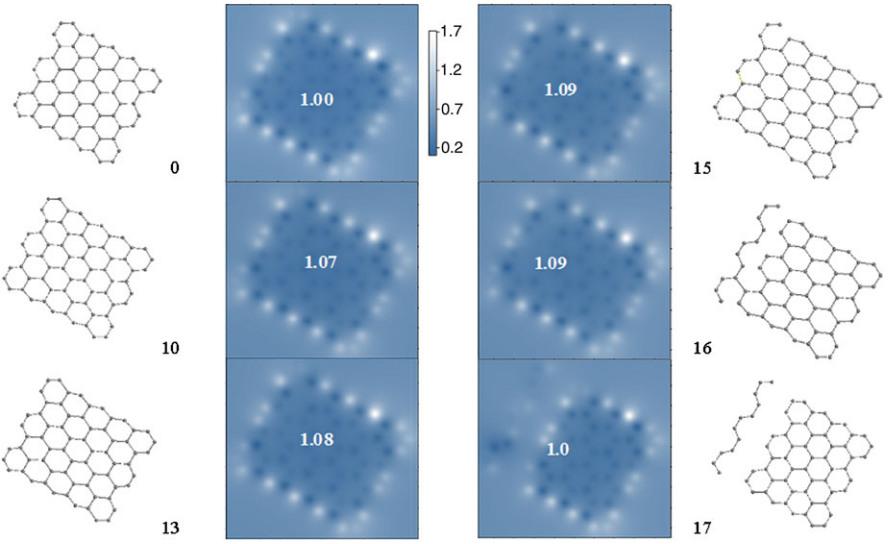

Fig. 16.5 The image N_{DA} maps and the equilibrium structures of the naked (5, 5) NGr molecule in the course of the first stage *armchair*-mode tensile deformation. The *black* and *white* figures number steps and equalizing coefficients, respectively. The same intensity scale is related to all the maps

fore, the redistribution of the C–C bonds over their lengths causes changing in the topological 'quality' of individual bonds. To illustrate the latter, let us look at not the total number of the effectively unpaired electrons N_D, but at the atomic chemical susceptibility distribution over the molecule atoms that is determined by a fractional number of the effectively unpaired electrons N_{DA} at atom A [28].

16.4.1 Naked Graphene Molecule

Figure 16.5 presents a set of the N_{DA} image maps related to the first 17 steps of the *armchair* mode of the molecule uniaxial tension. The set corresponds to gradually increased N_{DA} values up to the 17th step shown at the right-hand top panel of Fig. 16.4. The maps are accompanied by the molecule equilibrium structures. For the maps to be presented in one scale, the N_{DA} data were normalized by equalizing maximum N_{DA} values at each map to that one at the zeroth step that corresponds to the non-deformed molecule. White figures present the equalizing coefficients.

As seen in the figure, the segregation of the atoms into two groups related to the edge and basal plane areas, respectively, which is characteristic for the non-deformed molecules, takes place up to the 16th step inclusively. Obviously, since simultaneously, the total number of the effectively unpaired electrons N_D grows, the redistribution of the N_{DA} values should occur. However, the latter mainly concerns the basal plane atoms leaving the edge atoms only slightly changed due to

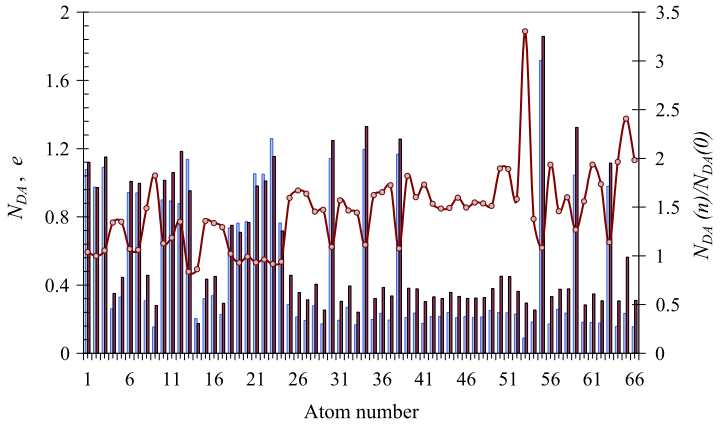

Fig. 16.6 The histograms of the N_{DA} distribution over the atoms of the naked (5, 5) NGr molecule related to the non-deformed (*light*) and the 16th step-deformed (*dark*) *armchair*-mode tensile deformation. The *curve* plots the presented values ratio when $n = 16$

practically constant maximum N_{DA} values of the latter, which follows from the presented equalizing coefficient. Actually, Fig. 16.6 shows the distribution of the absolute N_{DA} values for the zero and 16th steps alongside with their ratio. As seen in the figure, the redistribution concerns basal plane atoms mainly, indeed.

Important to draw attention to both the image N_{DA} maps and the corresponding structures related to the 15th and 16th steps. The structures are drawn by a visualization standard program that is based on tabulated values of the chemical bond lengths. According to the data, there is one broken C–C bond at the 15th step and five of them appear at the 16th step. Since the bonds are ruptured homolytically, one should expect the radicalization of the molecule at these points. Providing the N_{DA} indicative ability of just the very events, the appearance of white spots on the maps should be expected. However, until the 17th step no such spots are observed. This shows that the bonds breaking occurs at much longer interatomic distance in comparison with the standard tabulated data, which supports the conclusion made in [42].

Figure 16.7 presents a similar picture describing changes in the odd electron correlation during the *zigzag*-mode tension of the studied molecule. The first 17 steps cover the first-stage *zigzag*-mode deformation and correspond to the first tooth of the strain-stress and N_D-elongation dependences shown in the left-hand top panels in Figs. 16.3 and 16.4, respectively. In contrast to the previous case, the redistribution of the N_{DA} values occurs quite differently. Although the general image of the maps is kept up to the 16th step, the appearance of strongly stretched C–C bonds can be already noticed at the 15th step while a complete bond breaking becomes absolutely evident at the 17th step only. The effect of the stretched C–C bonds in the basal plane on the N_{DA} value redistribution is well seen in Fig. 16.8. About 5.5-fold changing in the N_{DA} value is characteristic for one of them while edge atoms preserve only slightly changed N_{DA} values.

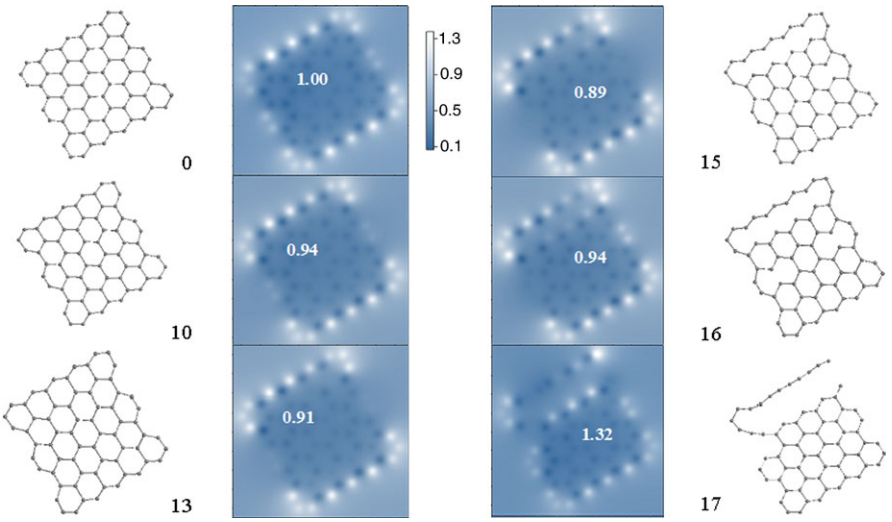

Fig. 16.7 The image N_{DA} maps and the equilibrium structures of the naked (5, 5) NGr molecule in the course of the first stage *zigzag*-mode tensile deformation. The *black* and *white* figures number steps and equalizing coefficients, respectively. The same intensity scale is related to all the maps

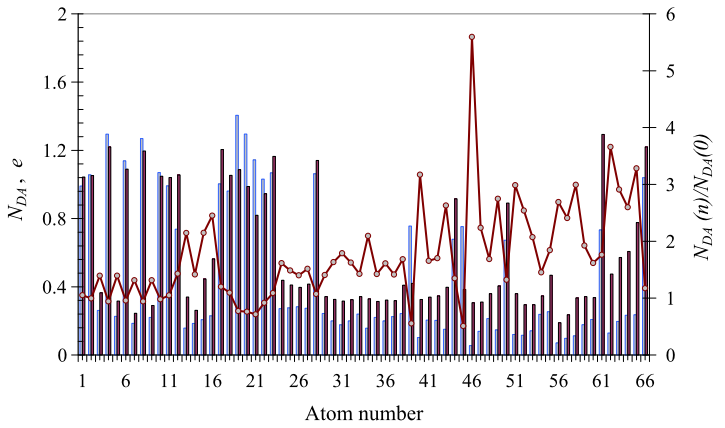

Fig. 16.8 The histograms of the N_{DA} distribution over the atoms of the naked (5, 5) NGr molecule related to the non-deformed (*light*) and the 16th step-deformed (*dark*) *zigzag*-mode tensile deformation. The *curve* plots the presented values ratio when $n = 16$

As was previously mentioned [29, 30], per step elongation (stretching) of the C–C bonds under the *armchair*- and *zigzag*-mode tension is quite different from the geometrical viewpoint. Evidently, this might explain the difference in the N_{DA} values related to the same step of both modes but cannot explain why the character of the redistribution for the two modes is completely different thus attributing the difference to the topological nature of the considered mechanochemical reaction.

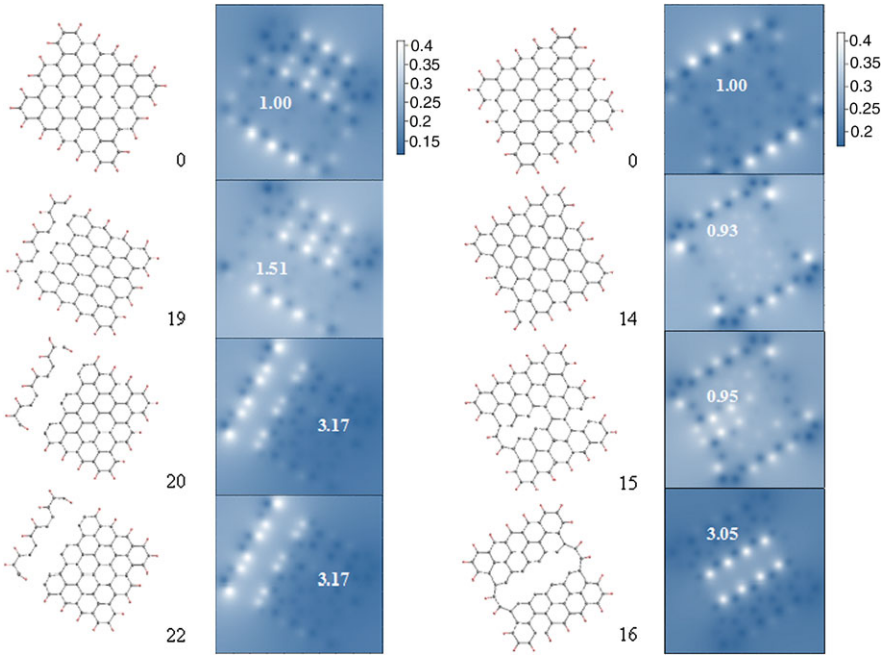

Fig. 16.9 The image N_{DA} maps and the equilibrium structures of the single-hydrogen-terminated (5, 5) NGr molecule in the course of the first stage of the *armchair* (*left*) and *zigzag* (*right*)-mode tensile deformation. The *black* and *white* figures number steps and equalizing coefficients, respectively. Scales are related to all the maps within the deformational mode

16.4.2 Single-Hydrogen Terminated Graphene Molecule

The evolution of the N_{DA} image maps in the course of the *armchair*- and *zigzag*-mode uniaxial tension of the (5, 5) NGr molecule with the single-hydrogen terminated edges is presented in Fig. 16.9. The data are related to the first stage of deformation for both modes. The picture in the figure drastically differs from that one shown in Figs. 16.5 and 16.7. The difference starts from the non-deformed molecule. As seen in the figure, the N_{DA} distributions differ remarkably for the two modes. The two maps are obtained in due course of the following procedure. Firstly, the equilibrium structure of the free standing H_1-terminated (5, 5) NGr molecule was obtained. Afterwards, a set of carbon atoms, which determine six selected MICs (see blue atoms in Fig. 16.1), was fixed, differently for two deformation modes. Then the optimization procedure was repeated for adopting calculation to the new conditions. If in the case of the naked molecule considered in the previous section, this procedure caused only a homogeneous scaling of the N_{DA} values (see scales in Figs. 16.5 and 16.7), a complete reconstruction of the image N_{DA} map occurs in the current case while the maximum N_{DA} values are practically identical. Both findings mean that fixation of the graphene sheet edges provides a considerable change in its

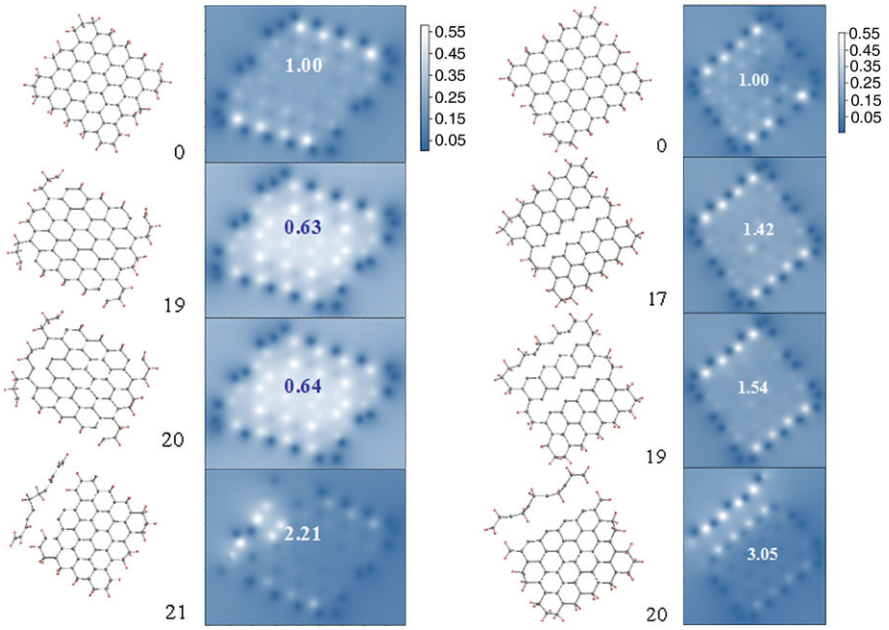

Fig. 16.10 The image N_{DA} maps and the equilibrium structures of the double-hydrogen-terminated- (5, 5) NGr molecule in the course of the first stage of the *armchair* (*left*) and *zigzag* (*right*)-mode tensile deformation. The *black* and *white* figures number steps and equalizing coefficients, respectively. Scales are related to all the maps within the deformational modes

electron distribution. The latter is additionally greatly influenced by the chemical composition of the sheet edge atoms.

Coming back to Fig. 16.9, one can see that, as previously, in the case of *armchair* mode the image maps keep practically unchanged appearance until the 19th step in spite of highly stretched C–C bonds at the latter step. The next 0.1 Å elongation provides simultaneous breaking of six C–C bonds followed with 3-fold increasing of the N_{DA} values. The sample becomes highly radicalized. Concentration of high N_{DA} values in the area of broken bonds drastically changes the image map fully suppressing much less active pristine atoms. Further elongation does not change the situation.

In the case of *zigzag* mode, the map appearance has been kept up to the 14th step after which highly stretched C–C bonds are observed in the middle of the molecule basal plane at the 15th step, whose complete breaking is followed at the 16th step. The sample becomes highly radicalized.

16.4.3 Double-Hydrogen Terminated Graphene Molecule

Addition of the second hydrogen atom to the edge carbons drastically changes the image maps again as seen in Fig. 16.10. In contrast to the previous case, the initial

fixation of edge atoms does not cause changing in both the map appearance and absolute N_{DA} value. However, the molecule becomes non-planar, which greatly influences further deformation. Thus, in due course of the *armchair*-mode tension, the difference in the values of eight framing basal atoms and remainders is gradually smoothed, once equalizing at the 19th step. The situation remains the same for the 20th step in spite of the presence of the stretched C–C bonds. The bond breaking occurs at the 21st step; the sample becomes radicalized with a small area of the radical concentration. Oppositely to the case, the *zigzag*-mode deformation does not cause any smoothing of the N_{DA} values distribution and keeps the non-deformed shape up to the 19th step. The bond stretching is observed at the steps from 17th to 19th, and the bond breaking occurs at the 20th step.

Taking together, Figs. 16.5, 16.7, 16.9, and 16.10 exhibit changing in the odd electron correlation of the graphene molecule under deformation and highlight a strong dependence of the correlation on both the deformational mode configuration and the chemical modification of the molecule edge atoms.

16.5 Conclusion

Presented in the current chapter undoubtedly shows that the chemical modification of the graphene molecule edge atoms has a great impact on its mechanical behavior. The feature results from the significant correlation of the molecule odd electrons followed by their conjugation over the molecule. Thus, the transition from the naked molecule, characterized by the maximal correlation of the odd electrons, to the molecule with the single- and double-hydrogen-terminated edges is followed by a considerable suppression of the correlation related to the edge atoms in the former case and a complete zeroing of the latter in the second case. As turned out, the changes are not local and strongly influence the electronic structure in the region of the basal plane, where the main deformational process occurs, causing the redistribution of the C–C bonds over their lengths, thus, changing 'the quality' of the bonds and providing the topological character of the deformational processes in graphene.

Acknowledgements A financial support provided by the Ministry of Science and High Education of the Russian Federation grant 2.8223.2013 is highly acknowledged.

References

1. Cataldo F, Graovac A, Ori O (eds) (2011) The mathematics and topology of fullerenes. Springer Science+Business Media BV, Berlin
2. Merrifield RE, Simmons HE (1989) Topological methods in chemistry. Wiley, New York
3. Schmidt GMJ (1971) Photodimerization in the solid state. Pure Appl Chem 27:647–678
4. de Jong AWK (1923) Uber die Konstitution der Truxill – und Truxinsauren und uber die Entwiklung des Sonnenlichtes auf die Zimtsauren und Zimisaure – Salze. Chem Ber 56B:818–832

5. Woodward RB, Hoffmann R (1970) The conservation of orbital symmetry. Verlag Chemie, Weinheim. Bergstr
6. Enkelmann V (1984) Polydiacetilenes. Adv Polym Sci 63:91–121
7. Hasegawa M (1986) Topochemical photopolymerization of diolefin crystals. Pure Appl Chem 58:1179–1188
8. Boldyrev VV (1990) Topochemistry and topochemical reactions. React Solids 8:231–246
9. MacGillivray LR, Papaefstathiou GS (2004) Solid state reactivity. Topochemistry. In: Atwood JL, Steed JW (eds) Encyclopedia of supramolecular chemistry. Dekker, New York, pp 1316–1319
10. Guo F, Marti-Rujas J, Pan Z et al (2008) Direct structural understanding of a topochemical solid state photopolymerization reaction. J Phys Chem C 112:19793–19796
11. Sheka EF, Shaymardanova LKh (2011) C_{60}-based composites in view of topochemical reactions. J Mater Chem 21:17128
12. Sheka EF (2013) Topochemistry of spatially extended sp^2 nanocarbons: fullerenes, nanotubes, and graphene. In: Ashrafi AR, Cataldo F, Iranmanesh A et al (eds) Topological modelling of nanostructures and extended systems. Carbon materials: chemistry and physics, vol 7. Springer, Dordrecht. doi:10.1007/978-94-007-6413-2_5
13. Kudin K, Scuseria GE, Yakobson BI (2001) C_2F, BN, and C nanoshell elasticity from ab initio computations. Phys Rev B 64:235406 (10 p)
14. Liu F, Ming P, Li J (2007) Ab initio calculation of ideal strength and phonon instability of graphene under tension. Phys Rev B 76:064120 (7 p)
15. Hemmasizadeh A, Mahzoon M, Hadi E, Khadan R (2008) A method for developing the equivalent continuum model of a single layer graphene sheet. Thin Solid Films 516:7636–7640
16. Wei X, Fragneaud B, Marianetti CA, Kysar JW (2009) Nonlinear elastic behavior of graphene: ab initio calculations to continuum description. Phys Rev B 80:205407 (8 p)
17. Shokrieh MM, Rafiee R (2010) Prediction of Young's modulus of graphene sheets and carbon nanotubes using nanoscale continuum mechanics approach. Mater Des 31:790–795
18. Li C, Chou T-W (2003) A structural mechanics approach for the analysis of carbon nanotubes. Int J Solids Struct 40:2487–2499
19. Sakhaee-Pour A (2009) Elastic properties of single-layered graphene sheet. Solid State Commun 149:91–95
20. Hashemnia K, Farid M, Vatankhah R (2009) Vibrational analysis of carbon nanotubes and graphene sheets using molecular structural mechanics approach. Comput Mater Sci 47:79–85
21. Tsai J-L, Tu J-F (2010) Characterizing mechanical properties of graphite using molecular dynamics simulation. Mater Des 31:194–199
22. Guo Y, Guo W (2003) Mechanical and electrostatic properties of carbon nanotubes under tensile loading and electric field. J Phys D, Appl Phys 36:805–811
23. Bu H, Chen Y, Zou M et al (2009) Atomistic simulations of mechanical properties of graphene nanoribbons. Phys Lett A 373:3359–3362
24. Van Lier G, van Alsenoy C, van Doren V, Geerlings P (2000) Ab initio study of the elastic properties of single-walled carbon nanotubes and graphene. Chem Phys Lett 326:181–185
25. Gao Y, Hao P (2009) Mechanical properties of monolayer graphene under tensile and compressive loading. Physica E 41:1561–1566
26. Topsakal M, Ciraci S (2010) Elastic and plastic deformation of graphene, silicene, and boron nitride honeycomb nanoribbons under uniaxial tension: a first-principles density-functional theory study. Phys Rev B 81:024107 (6 p)
27. Sheka EF, Chernozatonskii LA (2010) Broken spin symmetry approach to chemical susceptibility and magnetism of graphenium species. J Exp Theor Phys 110:121–132
28. Sheka EF (2012) Computational strategy for graphene: insight from odd electrons correlation. Int J Quant Chem 112:3076–3090
29. Sheka EF, Popova NA, Popova VA et al (2011) A tricotage-like failure of nanographene. J Mol Mod 17:1121–1131
30. Sheka EF, Popova NA, Popova VA et al (2011) Structure-sensitive mechanism of nanographene failure. J Exp Theor Phys 112:602–611

31. Popova NA, Sheka EF (2011) Mechanochemical reaction in graphane under uniaxial tension. J Phys Chem C 115:23745–23754
32. Popova VA, Popova NA, Sheka EF (2013) Effect of chemical modification of edge atoms of graphene sheets on their strength. arXiv:1301.0944 [cond-mat.mtrl-sci]
33. Tobolski A, Eyring H (1943) Mechanical properties of polymeric materials. J Chem Phys 11:125–134
34. Dewar MJS (1971) MO theory as a practical tool for studying chemical reactivity. Fortschr Chem Forsch 23:1–63
35. Nikitina EA, Khavryutchenko VD, Sheka EF et al (1999) Deformation of poly (dimethylsiloxane) oligomers under uniaxial tension. Quantum-chemical view. J Phys Chem A 103:11355–11365
36. Khavryutchenko VD, Nikitina EA, Malkin AL et al (1995) Mechanics of nanoobjects. Computational mechanochemistry. Phys Low-Dimens Struct 6:65–84
37. Khavryutchenko VD, Khavryutchenko AV Jr (1993) DYQUAMECH dynamical-quantum modelling in mechanochemistry. Software for personal computers, Institute of Surface Chemistry. Nat Ac Sci of the Ukraine, Kiev
38. Stewart JJP (1989) Optimization of parameters for semiempirical methods I. Method J Comput Chem 10:209–220
39. Jin C, Lan H, Peng L et al (2009) Deriving carbon atomic chains from graphene. Phys Rev Lett 102:205501
40. Tashiro K, Kobayashi M, Tadacoro H (1992) Theoretical evaluation of three-dimensional elastic constants of native and regenerated celluloses: role of hydrogen bonds. Polym J 24:899–916
41. Sheka EF (2011) Fullerenes: nanochemistry, nanomagnetism, nanomedicine, nanophotonics. CRC Press/Taylor and Francis, Boca Raton
42. Sheka EF, Popova NA (2011) When a covalent bond is broken? arXiv:1111.1530v1 [physics.chem-ph]

Chapter 17
Theoretical Analysis of Phase-Transition Temperature of Hydrogen-Bonded Dielectric Materials Induced by H/D Isotope Effect

Takayoshi Ishimoto and Masanori Tachikawa

Abstract We theoretically analyzed the H/D isotope effect for phase transition temperature (T_c) and geometrical changes of hydrogen-bonded dielectric materials by using the multi-component molecular orbital method, which can take account the quantum effect of proton, deuteron, triton, and muon. Taking into account the quantum effect of proton/deuteron using the MC_MO method directly, the difference of T_c, as well as, the geometry and electronic charge difference is universally elucidated. The origin of the isotope effect for hydrogen-bonded dielectric materials is from the difference of the proton/deuteron wave distributions under the anharmonicity of the potential.

17.1 Introduction

The hydrogen-bonded dielectric material is classified into the (anti-) ferroelectric materials having hydrogen bond in the crystal structure. Many hydrogen-bonded dielectric materials have been reported since the discovery of potassium dihydrogen phosphate, KH_2PO_4 (KDP), in 1935 [1]. The hydrogen-bonded dielectric materials have various hydrogen-bonded networks such as three-, two-, one-, and zero-dimensional structures [2–5].

The phase transition of the hydrogen-bonded dielectric materials strongly depends on the nature of hydrogen-bonded networks. The hydrogen bond in the crystal of hydrogen-bonded dielectric materials plays an important role to control various physical properties. In particular, drastic change of the phase transition temperature (T_c) of the hydrogen-bonded dielectric materials upon replacing hydrogen atoms with deuterium is usually called the 'isotope effect'. Sometimes the difference of the T_c between the hydrogen and deuterium compounds is more than 100 K. The problem of its phase transition and the large isotope effect on such physical quantities as the T_c has been one of the most interesting topics in this field. Although there are many models and experimental results with respect to the isotope effect of

M. Tachikawa (✉)
Quantum Chemistry Division, Graduate School of Science, Yokohama-City University, 22-2 Seto, Kanazawa-ku, Yokohama 236-0027, Japan
e-mail: tachi@yokohama-cu.ac.jp

M. Hotokka et al. (eds.), *Advances in Quantum Methods and Applications in Chemistry, Physics, and Biology*, Progress in Theoretical Chemistry and Physics 27,
DOI 10.1007/978-3-319-01529-3_17,

the phase transition, the origin of the isotope effect is not yet completely elucidated. We should address here that the origin of the isotope effect is among the major subjects in condensed matter physics. The history of research of the isotope effect is introduced below.

More than sixty years ago, Slater first investigated the mechanism of the phase transition of KDP using a statistical mechanism [6]. He concluded the order-disorder type phase transition using the classical double-minimum protonic potential functions, while he did not refer to the isotope effect.

Since the chemical nature of the hydrogen and deuterium atoms is believed to be the same, the origin of the isotope effect is related to the difference in *only* their masses. In order to elucidate the isotope effect, various theoretical approaches were proposed after his work. Among the various theoretical models, the proton tunneling model [7–10] has been most widely accepted, since it was supported by the light scattering experiment [11, 12] and high-pressure measurement [13]. In the tunneling model, which occurs in the disordered phase at high temperature, each proton (deuteron) occupies two equilibrium positions with equal probability in a symmetric double well potential, and proton (deuteron) tunneling between these positions opposes localization. Within this model, the phase transition is driven by the direct proton-proton interaction. The isotope effect is explained as the difference of the splitting of energy levels by the proton (deuteron) tunneling amplitudes.

Some serious doubts, however, have been thrown upon the proton tunneling model. Ichikawa has pointed out the importance of the isotope effect on geometry and symmetry of the hydrogen bond for inducing the large isotope effect of the T_c [14]. This is called the "geometrical isotope effect" based on the empirical investigation of KDP families at various temperatures and pressures. This indicates that the large difference of T_c might be interpreted without invoking proton tunneling.

Recent developments in experimental techniques have made it possible to give various novel information. Noda and Kasatani et al. observed the difference in the electronic population around the proton and deuteron by the X-ray diffraction study [15–18]. The total number of electrons around the proton and deuteron in the tripotassium hydrogen disulfate (KHS) and its deuterium compound DKHS are 0.65 and 1.19, respectively. They suggested that the charge difference is important for the occurrence of the large isotope effect. In addition, there is no evidence of the proton (deuteron) tunneling phenomena from the Raman spectroscopic analysis by Tominaga [19]. In this sense, the some experimental results such as the origin of isotope effect on the T_c of hydrogen-bonded dielectric materials cannot be fully understood by only proton tunneling model.

Recently, new models which take into account the quantum effect of nucleus such as proton and deuteron are proposed [20–22]. In particular, Koval et al. [20] studied the nuclear quantum effects of KDP (DKDP) based on the density functional theory (DFT) [23]. The DFT is not fully unveiled the hydrogen-bonded dielectric materials, even though the DFT based on the local density approximation (LDA) [24] and generalized gradient approximation (GGA) [25] with the plane wave basis expansion has been employed with great success to theoretically analyze the various materials. This method is no longer able to predict the difference in the electronic charge distributions around the proton (deuteron) and polarized structures such as hydrogen

bonds. On the other hand, the molecular orbital (MO) and crystal orbital methods based on the one electron approximation are powerful tools for the electronic structure calculation of molecules and clusters. This method is effective for the detailed geometry analysis using the potential energy surfaces. Recently, we have proposed the multi-component MO (MC_MO) method which takes into account the quantum effect of proton and deuteron directly [26]. Here, the quantum effect can include the effect of the anharmonicity due to the zero-point vibration induced by the quantum proton and deuteron. The MC_MO method extends the concept of the conventional MO method not only to the electrons but also to nucleus. It is a great and important challenge to elucidate the origin of the isotope effect.

The computational procedure of the multi-component MO method, which can take into account of the quantum effect of the proton and deuteron directly, is introduced in next section. In Sect. 17.3.1, we show the results of our MC_MO calculation for isotope effect on the phase transition in the $K_3H(SO_4)_2$ and its deuterated $K_3D(SO_4)_2$ in order to theoretically analyze the quantum effect of the proton and deuteron and to show the efficiency of the MC_MO method. In Sect. 17.3.2, the origin of the phase transition and the isotope effect in the squaric acid, which is well known as the organic dielectric material, will be shown through the stabilities, structures, and cluster size dependency of the unit. The phase transition temperature (T_c) difference between H_2SQ and D_2SQ is theoretically evaluated. In Sect. 17.3.3, the T_c and geometrical changes of the mixed $K_3H_{1-x}D_x(SO_4)_2$ and $(H_{1-x}D_x)_2SQ$ crystal is discussed. The T_c of TKHS and T_2SQ substituted from hydrogen to tritium is also predicted. From the above results and discussion, the origin of the isotope effect on the phase transition temperature in hydrogen-bonded dielectric materials is deduced, as shown in Summary.

17.2 Computational Method

The quantum mechanical description of nuclear motion is a problem of central interest in physics, chemistry, and interdisciplinary fields [27–29]. However, quantum chemical molecular orbital (MO) theory has been developed for the description of electronic motion in the molecular system. A multi-component MO (MC_MO) method [26] is proposed to the description of the nuclear motion; that is, both electronic and nuclear wave functions are calculated simultaneously and all the parameters are determined variationally, except for the physical constant [30–32] to express the 'optimized nuclear MO' directly.

The electronic Hamiltonian of an N_e electron and M nuclear system in atomic units is

$$H_e = \sum_{i=1}^{N_e}\left(-\frac{1}{2}\nabla_i^2 - \sum_{\mu=1}^{M}\frac{Z_\mu}{r_{i\mu}}\right) + \sum_{i>j}^{N_e}\frac{1}{r_{ij}} + \sum_{\mu>\nu}^{M}\frac{Z_\mu Z_\nu}{r_{\mu\nu}}, \tag{17.1}$$

where, the i and j indices refer to the electrons, μ and ν to the nuclei and Z_μ represents the nuclear charge. In the conventional MO calculation, the time-independent

Schrödinger equation of the electronic Hamiltonian is solved approximately using the variational method with the nuclei fixed; that is, the motion of the electrons is evaluated in the field of fixed nuclear charges [33, 34]. This electronic Hamiltonian expresses only electronic states and includes no nuclear kinetic energy operator terms. Based on the Born-Oppenheimer (B.O.) approximation [35], two steps are necessary to analyze the nuclear motion. First, the electronic Hamiltonian for all possible nuclear configurations (in principle) is solved to obtain a potential energy hypersurface, which is then used as an adiabatic potential for the analysis of the nuclear motion. However, this treatment is practicable only di- or tri-atomic molecules [36, 37].

In order to obtain both the electronic and nuclear wave functions simultaneously, the total Hamiltonian including the nuclear kinetic-energy operators is used as,

$$H_{tot} = -\sum_{p}^{M} \frac{1}{2M_p} \nabla_p^2 + H_e, \tag{17.2}$$

where the p index refers to the nucleus treated as a quantum wave and M_p is the mass of the pth nuclear particle. For simplicity, one kind of nuclear species is treated as the quantum mechanical wave and the other nuclei as the point charges. It may be a better approximation if the lightest nuclei, such as protons, are dealt with as a quantum wave. Furthermore, in order to obtain better convergence of the total wavefunction at Hartree-Fock level, the independent-particle approximation for the electronic and nuclear wavefunction is adopted as

$$\Psi_{tot} \cong \Phi_0^e \cdot \Phi_0^p. \tag{17.3}$$

The superscript refers to the type of particles; i.e. e for electrons and p for protons. The energy of this system after integration of the spin coordinates is given by

$$\begin{aligned} E = &\sum_{i}^{N_e} n_i^e h_{ii}^e + \sum_{i,j}^{N_e} \left[\alpha_{ij}^e (\phi_i\phi_i|\phi_j\phi_j) + \beta_{ij}^e (\phi_i\phi_j|\phi_i\phi_j)\right] + \sum_{i}^{N_p} n_p^p h_{pp}^p \\ &+ \sum_{p,q}^{N_p} \left[\alpha_{pq}^p (\phi_p\phi_p|\phi_q\phi_q) + \beta_{pq}^p (\phi_p\phi_q|\phi_p\phi_q)\right] - \sum_{i}^{N_e}\sum_{p}^{N_p} n_i^e n_p^p (\phi_i\phi_i|\phi_p\phi_p), \end{aligned} \tag{17.4}$$

where, the p and q indices refer to the nuclei, ϕ_i and ϕ_p are the spatial MOs of an electron and a nucleus, h_{ii}^e and h_{pp}^p are one-electron and one-nuclear integral, $(\phi_i\phi_i|\phi_j\phi_j)$ and $(\phi_i\phi_j|\phi_i\phi_j)$ the Coulomb and exchange integrals of electrons, $(\phi_p\phi_p|\phi_q\phi_q)$ and $(\phi_p\phi_q|\phi_p\phi_q)$ those of nuclei, and $(\phi_i\phi_i|\phi_p\phi_p)$ Coulomb integral between an electron and a nucleus. The coefficients n_i^e and n_p^p are the occupation numbers of ϕ_i and ϕ_p, the α and β are Coulomb and exchange coupling constants and N_e and N_p are the number of electrons and nuclei, respectively.

The effective one-electron (f^e) and a fermion nucleus (f^p) are given by the variational method as

$$f^e\phi_i = \varepsilon_i\phi_i,$$
$$f^e = 2h^e + \sum_i^{Ne/2}(2J_i - K_i) - \sum_p^{Np/2} 2J_p, \tag{17.5}$$

$$f^p\phi_p = \varepsilon_p\phi_p,$$
$$f^p = 2h^p + \sum_p^{Np/2}(2J_p - K_p) - \sum_i^{Ne/2} 2J_i, \tag{17.6}$$

where J and K are the Coulomb and exchange operators, respectively. In Eq. (17.5), the effective field of the electronic MO ϕ_i is due to the motion of the nuclei and the remaining electrons. In Eq. (17.6) that of the nuclear MO ϕ_p is due to the motion of the electrons and remaining nuclei. The ϕ_i and ϕ_p MOs are given by solving Eqs. (17.5) and (17.6) iteratively.

The linear combination of gaussian-type function (LCGTF) for both the electronic and nuclear MOs is used as

$$\phi_i = \sum_r C^e_{ri}\chi^e_r, \tag{17.7}$$

$$\phi_p = \sum_v C^p_{vp}\chi^p_v. \tag{17.8}$$

In Eqs. (17.7) and (17.8), there are three types of parameters such as LCGTF coefficients (C^e, C^p), GTF exponents (α^e, α^p), and centers (R^e, R^p). In the conventional LCGTF-MO calculation, only the LCGTF coefficients (C^e, C^p) are determined by the variational theorem with the other parameters fixed [38].

However, the GTF exponent and center of the nuclear MO have not yet been determined by optimization. The optimization of only GTF exponents [39–42] or only GTF centers [43–45] has been reported. In this study, the fully variational MO (FVMO) method was applied; that is, the parameters such as GTF exponents and centers are also optimized, as well as, the LCGTF coefficients for both the electronic and nuclear GTFs. In the present case, the analytical formulas should be derived for energy derivatives with respect to the GTF parameters in electron and nuclei to optimize the energy in Eq. (17.4). Since, the GTF exponents depend on the GTF centers, a nonlinear optimization must be carried out. The MC_MO method used the updated Hessian matrix, as estimated by the Davidson, Fletcher, and Powell method [46].

17.3 Results and Discussion

17.3.1 Isotope Effect in $K_3H(SO_4)_2$ and $K_3D(SO_4)_2$

Hydrogen bonding materials are one of the most attractive and widely studied systems to investigate the phase transition phenomena in dielectric materials. The drastic change of the phase transition temperature (T_c) of the hydrogen-bonded dielectric

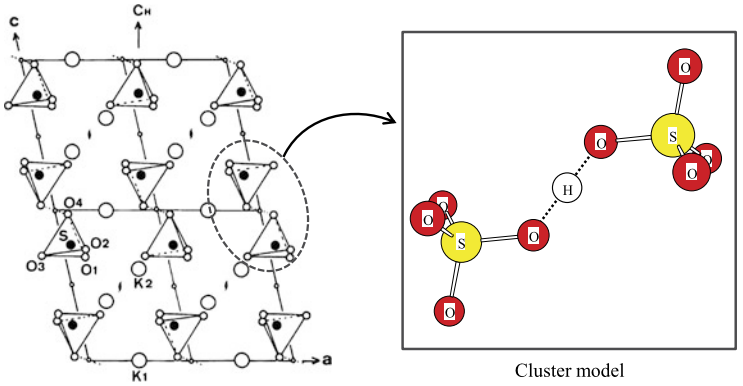

Fig. 17.1 Cluster model for $K_3H(SO_4)_2$ (KHS) crystal

materials upon replacing hydrogen atoms with deuterium is usually called the 'isotope effect'. The isotope effect on the phase transition behavior of the $M_3H(XO_4)_2$ type crystals is remarkably large (M = K, Rb, X = S, Se).

In particular, from the view point of the phase transition tripotassium hydrogen disulfate, $K_3H(SO_4)_2$ (KHS), has unique characteristics among the hydrogen-bonded dielectric materials. The deuterium compound $K_3D(SO_4)_2$ (DKHS) has the phase transition temperature ($T_c = 85$ K), while the hydrogen compound KHS does not show any phase transition [5, 47]. Secondly, the hydrogen-bonded network is restricted to within two SO_4^{2-} ions because KHS is a zero-dimensional hydrogen-bonded dielectric material, i.e. SO_4^{2-} ion is hydrogen-bonded to only one other SO_4^{2-} ion. There is, thus, no effect of the hydrogen-bonded network on the phase transition, as shown in Fig. 17.1. Other $M_3H(XO_4)_2$ type crystals also show similar properties. $Rb_3H(SO_4)_2$ [48] and $Rb_3H(SeO_4)_2$ [49] show no phase changes from room temperature down to the lowest temperature examined (typically 4.2 K), whereas their deuterated analogues undergo phase transitions at 70–100 K. $K_3H(SeO_4)_2$ undergoes a phase transition at 20 K and $K_3D(SeO_4)_2$ at 103 K [50, 51].

Recent precise structure analyses of KHS and DKHS revealed that the structures are isomorphous with each other, and the difference of positional parameters is extremely small [15–18]. Noda and Kasatani [17] obtained an experimental result that the total number of electrons around the proton in KHS and the deuteron in DKHS are 0.65 and 1.19 in the room temperature, respectively. They suggested that the charge difference is important for the occurrence of the large isotope effect.

In here, the isotope effect on the phase transition in the KHS and DKHS is examined. In order to explore the origin of the isotope effect between KHS and DKHS, the multi-component molecular orbital (MC_MO) calculation [52–54] was carried out beyond the adiabatic approximation.

Using the MC_MO calculation, the isotope effect was analyzed with the potential energy surfaces, geometrical changes, and electronic charge densities around the proton and deuteron for the cluster models of KHS and DKHS crystals. The adopted

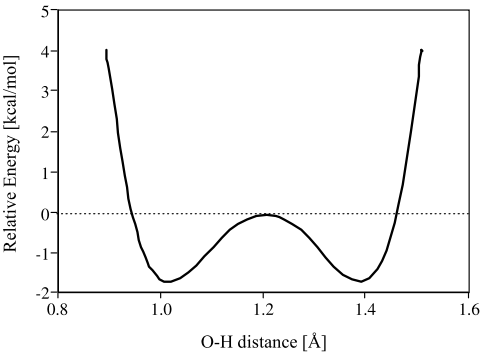

Fig. 17.2 The relation between the O–H distance and the relative energy of cluster model of KHS using the conventional MO method

cluster models of KHS and DKHS are shown in Fig. 17.1. In this MC_MO calculation, the proton and the deuteron are treated as quantum waves, as well as the electrons under the field of S and O nuclear point charges. The positions (geometry) of the S and O point charges were determined by means of ordinary optimization procedures using analytical gradients [55]. The single s-type Gaussian-type function (GTF), $\exp\{-\alpha(r - R)^2\}$, was employed for each protonic or deuteronic basis function, and the GTF variational parameter (α) was optimized. The standard [3s1p]/(4s1p) electronic basis set was used for hydrogen and Pople's 3-21G* basis set [56–58] for S and O. The centers of the electronic GTFs were fixed on each nucleus. All calculations were carried out at the Hartree-Fock level using modified versions of the Gaussian 98 program packages [59].

The potential energy surface is described with the location of the hydrogen atom which is connected the two sulfuric acid ions (SO_4^{2-}) between the oxygen atoms. The geometries in which the hydrogen atom moves from at the center between two oxygen atoms to near one side oxygen atoms were optimized gradually. In this geometry optimization, the hydrogen atom is moved on the straight line between the oxygen atoms because the energy difference is a little in comparison with ordinary O–H···O bending structure. Acquired energies were plotted as a relative energy to the geometrical energy in which the hydrogen atom is centered between the oxygen atoms. The potential energy surface acquired the conventional MO method is shown in Fig. 17.2. The O–H distance in which the hydrogen atom is centered between two oxygen atoms is 1.202 Å. The O–H distance of the most stable geometry is 1.020 Å. The energy difference is 1.70 kcal/mol.

The cluster model of KHS using the conventional MO method describes the potential energy surface of double-well having each stable points of two near oxygens with the hydrogen moving. This potential energy surface is adiabatic potential because the motion of the nucleus does not consider by the conventional MO method. The potential energy surface in Fig. 17.2 is a fundamental model of the conventional tunneling theory. The origin of the isotope effect was believed the difference of the mass of the proton and the deuteron which move above this potential energy surface.

The potential energy surfaces were acquired using the MC_MO method. The potential energy surfaces of KHS and DKHS are shown in Fig. 17.3. The potential energy surface having the double-well is obtained for the DKHS cluster model.

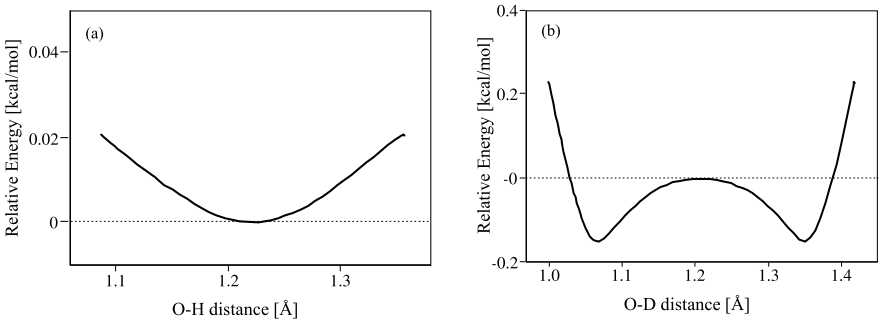

Fig. 17.3 The relation between the O–H (**a**)/O–D (**b**) distance and the relative energy of cluster model of KHS/DKHS using the MC_MO method

The O–D distance of the most stable geometry is 1.100 Å. The energy difference (ΔE^D) is 0.17 kcal/mol. On this potential energy surface (Fig. 17.3(a)), the positive territory of energy corresponds the disordered state in which the deuteron locates at random. The energy territory shifts to the negative together with the falling temperature. The deuteron occupies the orderly two stable points. It is indicated that the drastic changes from the disordered state to ordered state results in the phase transition.

The potential energy surface having the single-well is obtained for the KHS cluster model. The O–H distance of the most stable geometry is 1.224 Å, *that is*, the hydrogen atom locates at the center between two oxygen atoms. On this potential energy surface (Fig. 17.3(b)), the drastic change does not occur in the proton from the disordered state accompanying the falling temperature. It is deduced that the KHS crystal does not have a phase transition because there is no drastic change.

The conventional tunneling model was treated with the motions of the proton and deuteron above the same potential energy surface. However, the potential energy surfaces for the motion of the proton and the deuteron are completely different in shape using the MC_MO method when taking into account of the quantum effect of the proton and deuteron. Thus, the occurrence or absence of the phase transitions of KHS and DKHS can be successfully explained the difference of their shapes.

For the geometrical structures the focus was on the two characteristically stable structures. One structure is geometry (a), in which the hydrogen atom locates at the center between two oxygen atoms. The other is the most stable geometry (b). The two optimized geometries (a) and (b) using the conventional MO method are shown in Fig. 17.4. Geometry (a) has a point symmetry in which the hydrogen atom is centered between two oxygen atoms of two sulfuric acid ions (SO_4^{2-}). On the other hand, the symmetry is broken in geometry (b), and the hydrogen atom is not centered but bonded to one of the oxygen atoms strongly. Geometry (b) is more stable than geometry (a) because of the relaxation of the cluster model including the sulfuric acid ions (SO_4^{2-}). Note that geometries (a) and (b) correspond to the paraelectric and antiferroelectric phases, respectively.

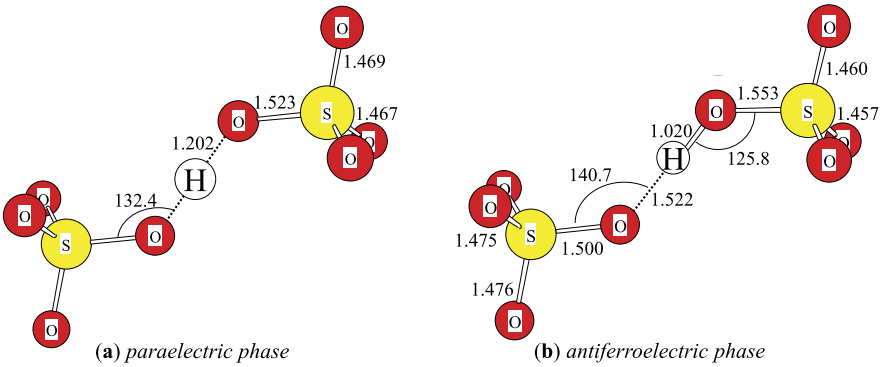

Fig. 17.4 The optimized geometries of KHS cluster model of paraelectric (antiferroelectric) phase using the conventional MO method. The bond lengths and angles are given in angstroms and degrees, respectively

Fig. 17.5 The optimized geometry of KHS cluster model of paraelectric phase using the MC_MO method. The bond lengths and angles are given in angstroms and degrees, respectively

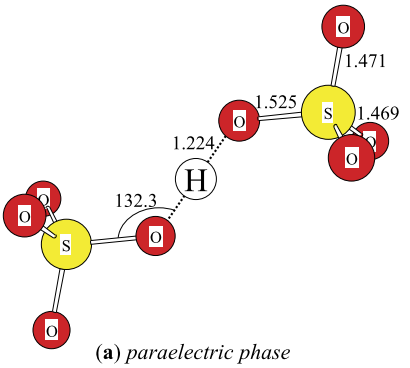

The optimized geometries (a) and (b) using the MC_MO method are also shown. The optimized geometries from KHS and DKHS are shown in Figs. 17.5 and 17.6, respectively. At this level of theory only geometry (a) is obtained for the KHS cluster as the most stable. This result is consistent with the experimental result, where only the paraelectric phase is known for the KHS crystal. Geometry (a) and (b) are obtained for the DKHS cluster as the characteristic stable structures. These results are theoretically reproduced the experimental results in which DKHS crystal is occurred the phase transition from paraelectric phase to antiferroelectric phase.

The most stable geometries of KHS and DKHS are the geometries (a) (Fig. 17.5) and (b) (Fig. 17.6), respectively. The existence of the geometrical isotope effect was theoretically confirmed from the alteration of the whole cluster model. The most stable structures of the KHS and DKHS cluster models obtained using both the conventional MO and the MC_MO methods were analyzed. The most stable structure is geometry (b) (Fig. 17.4) as determined by the conventional MO method. The most stable structures of KHS and DKHS cluster models are geometries (a) (Fig. 17.5) and (b) (Fig. 17.6) by the MC_MO method, respectively.

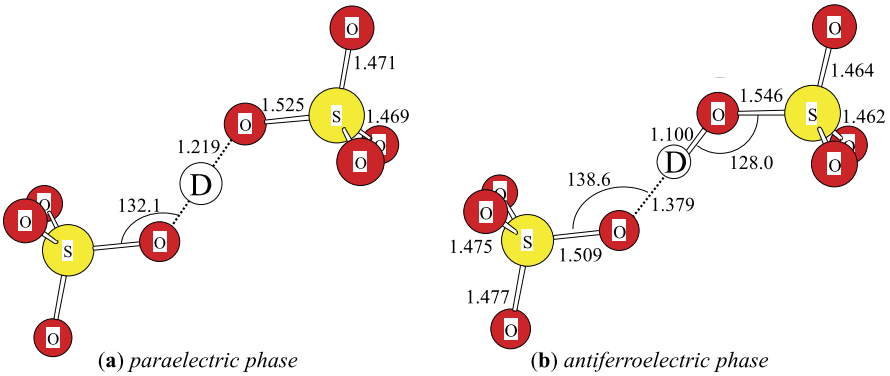

(**a**) *paraelectric phase* (**b**) *antiferroelectric phase*

Fig. 17.6 The optimized geometries of DKHS cluster model of paraelectric (antiferroelectric) phase using the MC_MO method. The bond lengths and angles are given in angstroms and degrees, respectively

Table 17.1 Hydrogen-bonded characters in stable structures of (D)KHS cluster models

	Conventional MO	MC_MO(H)	MC_MO(D)
Exponent	–	16.90	26.12
Electronic Population	−0.307	−0.598	−0.633
O–H Distance [Å]	1.020	1.224	1.100
O···O Distance [Å]	2.542	2.448	2.479

The focus was on the bond lengths and electronic charge density of hydrogen-bonded structures in which are the most stable geometries. The exponents (α) of GTF, which represent the charge distribution, are indicated in Table 17.1. Table 17.1 also shows the electronic charge densities as the gross electronic charge by Mulliken population analysis [60], as well as O–H and O···O distances for the hydrogen bonds. The proton is treated as a point charge by the conventional MO method. The proton and the deuteron are treated as waves using the GTF by the MC_MO method. The exponent of the deuteron (26.12) is larger than that of the proton (16.90), which indicates that the distribution of the deuteron wave shrinks more than that of the proton one. The electronic charge densities around the proton and deuteron are −0.598 and −0.633, respectively. According to these charge distributions of the proton and the deuteron, it was found that the electronic charge density around the deuteron was higher than that of the proton. These results agree with the experimental results of X-ray diffraction studies to KHS by Kasatani et al.

Taking notice of the hydrogen-bonded distances, the O–H distance in KHS cluster and O–D distance in DKHS are calculated to be 1.224 Å and 1.100 Å, respectively. The O···O distance in DKHS cluster (2.479 Å) is longer than KHS cluster (2.448 Å). These geometrical differences are consistent with the well-known the Ubbelohde effect [61] due to the geometrical isotope effect which was proposed by Ichikawa et al. It is found that the difference in the distribution of the proton

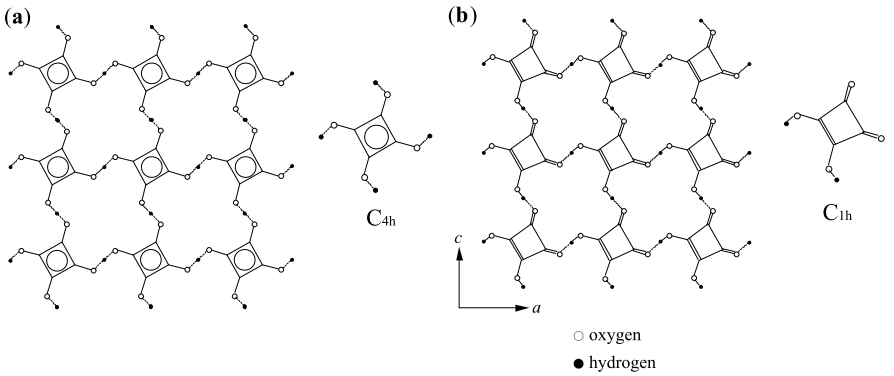

Fig. 17.7 The schematic structure of molecular sheet of the H_2SQ crystal: (**a**) paraelectric and (**b**) antiferroelectric phases

wave and the deuteron wave is reflected in the electronic charge densities around the proton and the deuteron and the hydrogen bonds.

17.3.2 Phase Transition Mechanism and Isotope Effect in Squaric Acid

In the previous Sect. 17.3.1, the isotope effect on the phase transition of KHS and DKHS was examined using the MC_MO method. The importance of the quantum effect of proton/deuteron and the efficiency of the MC_MO method to apply the hydrogen-bonded dielectric material was clearly shown. Hereafter, for the universal understanding of the origin of isotope effect on the phase transition, the focus is on squaric acid.

Squaric acid ($H_2C_4O_4$, abbreviated as H_2SQ) is an organo dielectric material and an effective model system for the design of the organo materials. The H_2SQ crystal has a two-dimensional hydrogen-bonded network between the unit structures of $C_4O_4^{2-}$ [62]. The schematic structure of the molecular sheet and a constituent molecular unit of the H_2SQ crystal are shown in Fig. 17.7. The phase transition of the H_2SQ crystal occurs from (a) the paraelectric phase to (b) the antiferroelectric phase [63, 64]. The temperatures of the phase transition for H_2SQ and D_2SQ (in the deuterated crystal) are 371 K and 516 K, respectively [3]. The temperature is high compared with another inorganic dielectric material such as KDP-type crystals, so that proton tunneling does not occur in the H_2SQ/D_2SQ systems. It has been reported from X-ray diffraction studies that, at the phase transition, the unit structures in the H_2SQ crystal change their symmetry from the high symmetrical C_{4h} (Fig. 17.7(a)) to the low symmetrical C_{1h} (Fig. 17.7(b)) [65–67].

High-pressure effects on the vibrational modes in Raman and infrared spectra, furthermore, have been investigated in H_2SQ/D_2SQ crystals by Moritomo et

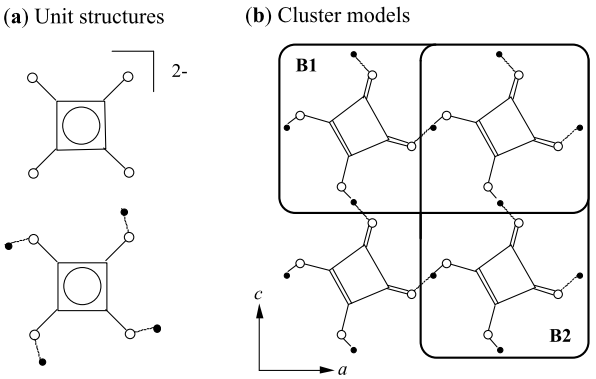

Fig. 17.8 The cluster models in H_2SQ crystal: (**a**) unit structures and (**b**) cluster models of dimer and tetramer. Unit structures are two types of $C_4O_4^{2-}$ and $C_4H_4O_4$. The cluster models of dimer have two kinds of hydrogen-bonded structures *B1* and *B2*

al. [68]. This result suggests that the high pressure causes an anomalous change in the symmetry of constituent molecules, which is possibly induced by deformation of the proton potential from the double-well to single-well type. In addition, recent high-resolution NMR data on the H_2SQ/D_2SQ systems have given detailed hydrogen-bond distance and atomic positions of hydrogen/deuterium [69]. The origin of the isotope effect including the evident structural changes, however, has not as yet been rationalized.

The geometrical and energetic changes for the $(H_2SQ)_n$ ($n = 1$, 2, and 4) clusters were analyzed. Adopted cluster models $(H_2SQ)_n$ ($n = 1$, 2, and 4) are shown in Fig. 17.8. Two structures ($C_4O_4^{2-}$ and $C_4H_4O_4$) of $n = 1$ molecule in Fig. 17.8(a) are the units of the crystal system. The dimer structure of $n = 2$ cluster ($[C_4H_3O_4\text{–}H\text{–}C_4H_3O_4]^{3+}$) and tetramer structure of $n = 4$ cluster ($[(C_4H_3O_4)_4H_4]^{4+}$) are shown in Fig. 17.8(b), respectively. Note that in the dimer structure, there are two kinds of hydrogen bonds from the crystallographic structural point of view. The hydrogen bond in the dimer **B1** spreads to the direction of crystallographic axis a, while that in the dimer **B2** spreads to axis c. All the geometrical parameters of the systems (bond lengths, bond angles, and dihedral angles) were optimized by using the energy gradient method [70].

The isotope effect in the dimer models was analyzed by using the MC_MO method [52–54] which takes explicitly into account the quantum effect of proton (deuteron) and the electronic charge density on the proton (deuteron). In the actual MC_MO calculation for the dimer model, the proton, deuteron, and muon are treated as quantum waves, as well as, the 116 electrons under the field of C and O nuclear point charges. C and O nuclei are treated as +6 and +8 point charges, respectively. The position of point charges for C and O nuclei is determined by ordinary optimization procedures using analytical gradients. The single s-type gaussian type function (GTF), $\exp\{-\alpha(r - R)^2\}$, is employed as each protonic, deuteronic, and muonic basis function, and the GTF variational parameter α is optimized. The standard [3s1p]/(4s1p) for hydrogen electronic basis set, and the Pople's 3-21G basis set [56–58] for C and O were used. Centers of electronic GTFs is fixed on each nucleus. All calculations were carried out based on the Hartree-Fock level by using modified Gaussian 98 program packages [59].

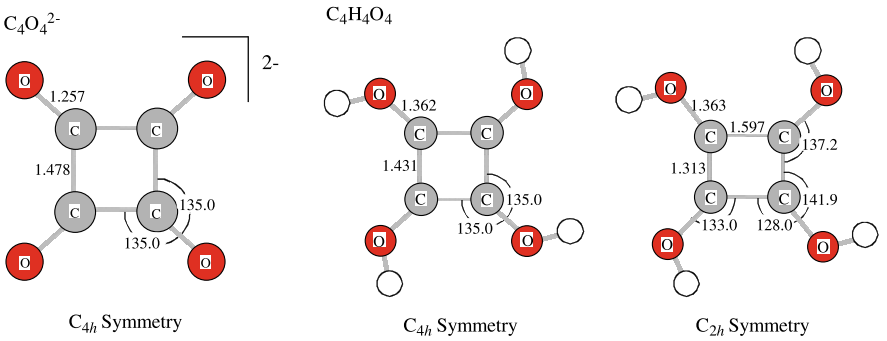

Fig. 17.9 The optimized geometries of unit structures. The bond lengths and angles are shown in angstroms and degrees, respectively

In the H_2SQ crystal, there are π electrons above the molecular sheet formed *via* the two-dimensional hydrogen-bonded networks. The behavior of the π electrons significantly controls the phase transition of the H_2SQ crystal. $C_4O_4^{2-}$ and $C_4H_4O_4$ were treated as the unit structures of the H_2SQ crystal. The optimized geometry for $C_4O_4^{2-}$ having 10π electrons is shown in Fig. 17.9. All C–C and C–O distances are 1.478 Å and 1.257 Å, respectively. The most stable geometry of $C_4O_4^{2-}$ has a high symmetry (C_{4h}) owing to the delocalization of 10π electrons. According to the traditional theory of aromaticity, the high symmetrical geometry is the most stable of the $[4n + 2]\pi$ system. The square geometry of the carbon frames obtained is consistent with aromaticity. The optimized geometries for $C_4H_4O_4$ having 12π electrons are shown in Fig. 17.9. There are two stable geometries for $C_4H_4O_4$. One has the C_{2h} symmetry, while the other has C_{4h}. In contrast to the $C_4O_4^{2-}$ case, the low symmetrical geometry (C_{2h}) is 26.98 kcal/mol more stable than high symmetrical geometry (C_{4h}). According to the Jahn-Teller effect [71], the low symmetrical geometry is energetically more stable than the high symmetrical geometry in which the electronic structure is degenerate for the $[4n]\pi$ system. The geometrical change of the unit according to the Jahn-Teller effect propagates through the entire system of the hydrogen-bonded network. The resulting distortion of the crystal system causes the phase transition. The driving force of the phase transition of H_2SQ crystal was found to be the Jahn-Teller effect of the constituent molecular unit.

The next focus was on the nature of hydrogen-bonded part. The dimer structure of the $n = 2$ cluster includes a hydrogen bond. The optimized geometries of dimer models are shown in Fig. 17.10. The geometry of dimer **A** has C_{4h} symmetry in which the hydrogen atom is at the center between oxygen atoms of each unit. Otherwise, there are two possible structures having lower symmetry with hydrogen atom attached to one of the oxygen atoms. One is the structure denoted by dimer **B1** in which the hydrogen bond and double bonds of C–C form the *axial* conformation. The other structure is dimer **B2** in which they form the *equatorial* conformation (see Fig. 17.8). Dimers **A** and **B1** (**B2**) are regarded as paraelectric and antiferroelectric phases, respectively. The O–H distances of dimer **A**, where hydrogen atom locates at the center between oxygen atoms, are both 1.192 Å. The O–H distances of dimer **B1**

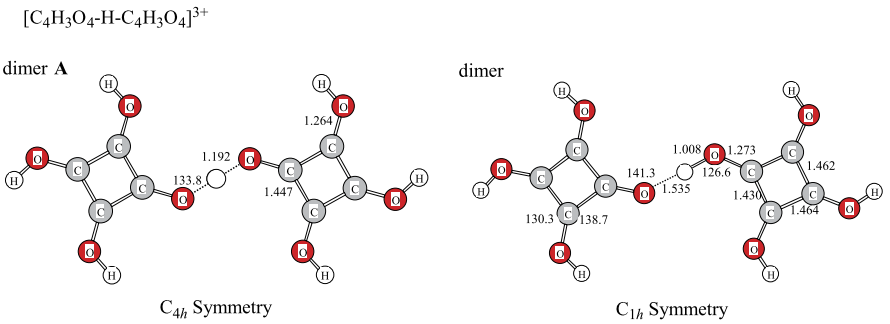

Fig. 17.10 The optimized geometries of dimer. The bond lengths and angles are shown in angstroms and degrees, respectively

are 1.008 and 1.535 Å. Dimer **B1** is 7.33 kcal/mol more stable than dimer **A**. When lowering the symmetry of the unit geometry from C_{4h} to C_{1h}, the hydrogen atom moves from the center between oxygen atoms to near one oxygen atom. The geometry of the dimer then changes from dimer **A** to **B1** (or **B2**). The phase transition from paraelectric to antiferroelectric phase corresponds to the geometrical change from dimer **A** to **B1/B2**. The local geometrical change on the phase transition with the dimer model could be reproduced theoretically. A larger cluster size than the dimer, however, should be required to distinguish the nature of hydrogen bond along a or c axis in H_2SQ crystal.

The optimized geometries of tetramer ($n = 4$) respectively keeping C_{4h} and C_{1h} symmetries are shown in Fig. 17.11. In the structure having C_{4h} symmetry, four hydrogen atoms are at the center between two oxygen atoms. When lowering the symmetry of unit from C_{4h} to C_{1h}, the hydrogen atom moves from the center between oxygen atoms to near one oxygen, as well as, for the dimer model. In the structure having the lower C_{1h} symmetry, intermolecular hydrogen bonds are classified into two types. One is *axial* (c direction) and the other is *equatorial* (a direction) to the C–C double bond (1.424 Å) of the unit moiety. The O–H distances of a and c axis directions are 1.025 Å and 1.030 Å, respectively. The lower symmetry C_{1h} geometry is 9.30 kcal/mol more stable than the higher symmetry C_{4h} geometry. It should be noted that the tetramer model is possible to predict the different nature of the respective hydrogen bonds along a and c axis directions in the crystal.

The calculated results for C_{1h} symmetrical geometries of dimer and tetramer were compared in regard to the antiferroelectric phase with the experimental result by neutron diffraction in antiferroelectric phase [67]. The illustration of the unit structure of H_2SQ crystal in antiferroelectric phase is shown in Fig. 17.12. The optimized geometrical parameters (bond lengths and angles) are summarized in Table 17.2, together with neutron diffraction data.

The unit structure of H_2SQ crystal on antiferroelectric phase is experimentally known to have a trapezoid-like geometry in which C(1)–C(2) bond distance (1.414 Å) is shorter than any other C–C bond distances (1.461∼1.500 Å). That is, in a chemical viewpoint, the bond between C(1) and C(2) atoms is a double bond,

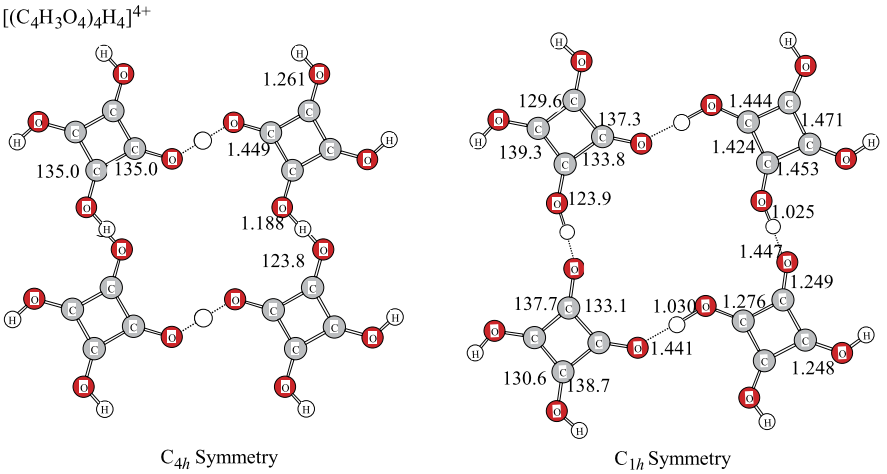

Fig. 17.11 The optimized geometries of tetramer. The bond lengths and angles are shown in angstroms and degrees, respectively

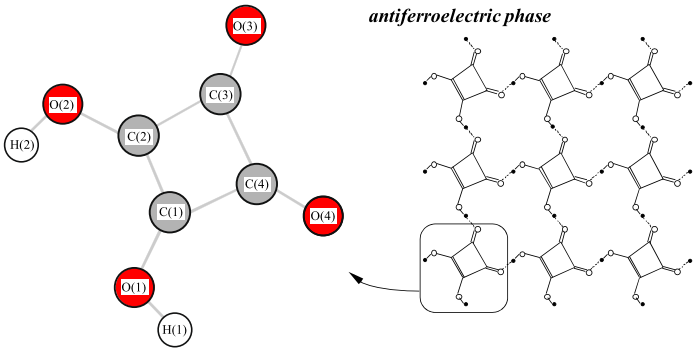

Fig. 17.12 An illustration of unit structure of the H_2SQ crystal in the antiferroelectric phase

while the other C–C bonds are single. The calculated results show that in dimer **B1**, the unit structure $C_4O_4^{2-}$ forms a rhombus-like geometry rather than a trapezoid-like geometry in which C–C bonds are classified into two shorter bonds (1.43 Å) and two longer bonds (1.46 Å). The trapezoid like geometry, where C(1)–C(2) bond distance (1.425 Å) is shorter than any other C–C bond distances (1.444∼1.474 Å) in tetramer model have been reproduced.

From the experimental results using neutron diffraction, the O···O distances along the *a* and *c* axis directions are both about 2.55 Å. Considering the O–H bond, the O–H distances O(2)–H(2) bond (1.037 Å) along the *a* axis direction and O(1)–H(1) bond distance (1.030 Å) along the *c* axis direction are different. The O–H bond distances along the *a* and *c* axis directions of the calculated tetramer model are 1.030 Å and 1.025 Å, respectively, which are in significant agreement with the

Table 17.2 The optimized geometrical parameters of the unit structure of H_2SQ in its antiferroelectric phase. Bond distances and angles are shown in angstroms and degrees, respectively

	Calculation		Experiment
	Dimer	Tetramer	Neutron
C(1)–O(1)	1.276	1.276	1.289(1)
C(2)–O(2)	1.273	1.277	1.287(1)
C(3)–O(3)	1.273	1.244	1.227(1)
C(4)–O(4)	1.239	1.248	1.230(1)
C(1)–C(2)	1.431	1.425	1.414(1)
C(1)–O(4)	1.464	1.454	1.464(1)
C(2)–C(3)	1.432	1.444	1.461(1)
C(3)–C(4)	1.462	1.471	1.500(1)
O(1)–H(1)	–	1.025	1.030(1)
O(2)–H(2)	1.008	1.030	1.037(1)
O(1)···O(3)	–	2.473	2.553(1)
O(2)···O(4)	2.543	2.474	2.554(1)
H(1)···O(3)	–	1.448	1.524(2)
H(2)···O(4)	1.535	1.441	1.517(2)
C(4)–C(1)–C(2)	91.0	90.7	91.66(4)
C(4)–C(1)–O(1)	138.7	138.7	136.14(4)
C(2)–C(1)–O(1)	130.3	130.6	132.21(5)
C(1)–C(2)–C(3)	89.9	91.1	91.72(4)
C(1)–C(2)–O(2)	139.7	139.3	136.85(5)
C(3)–C(2)–O(2)	130.0	129.6	131.43(5)
C(2)–C(3)–C(4)	91.0	89.2	88.40(3)
C(2)–C(3)–O(3)	138.9	137.7	136.59(5)
C(4)–C(3)–O(3)	130.0	133.1	135.01(5)
C(3)–C(4)–C(1)	87.8	88.9	88.23(3)
C(3)–C(4)–O(4)	138.7	137.3	136.48(5)
C(1)–C(4)–O(4)	133.6	133.8	135.30(5)
C(1)–O(1)–H(1)	–	127.4	112.70(7)
C(2)–O(2)–H(2)	126.6	126.7	113.61(7)
C(3)–C(3)···H(1)	–	129.6	118.15(5)
C(4)–O(4)···H(2)	141.3	130.6	116.24(5)

experimental tendency. Not only was the difference of the two hydrogen bond structures along the *a* and *c* axis directions reproduced, but also the unit structure of $C_4O_4^{2-}$. Applying the adequate cluster model as tetramer, it can be found that both local structures represented hydrogen bond structures and generally the systems including unit structures are reproducible.

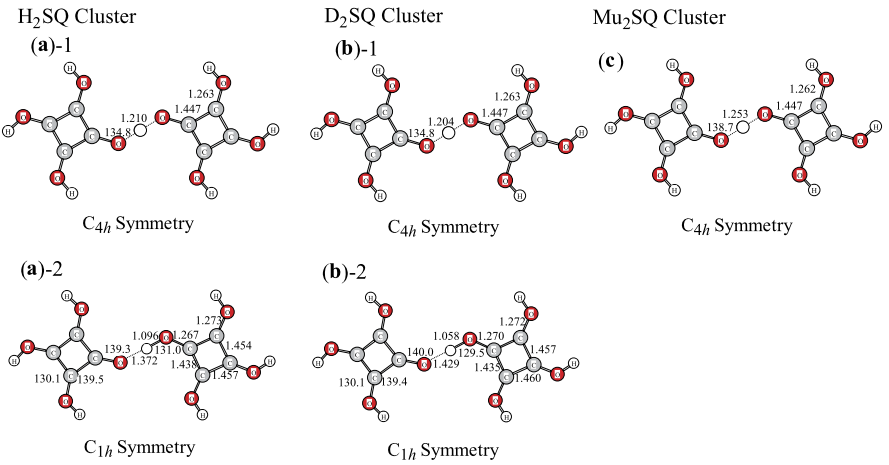

Fig. 17.13 The optimized geometries of H_2SQ, D_2SQ, and Mu_2SQ cluster models of dimer using MC_MO method

Furthermore, the origin of the isotope effect on the phase transition of H_2SQ and D_2SQ crystal was analyzed by applying the MC_MO method taking directly into account the quantum effects of the proton and deuteron. The cluster model used as dimer took note of the hydrogen-bonded part to the a axis. The optimized geometries of the dimer modeled of H_2SQ crystal are shown in Fig. 17.13(a). The high C_{4h} symmetry geometry, where the hydrogen atom is at the center between the oxygen atoms and the low C_{1h} symmetry geometry are shown in Fig. 17.13(a)-1 and Fig. 17.13(a)-2, respectively. The low symmetry geometry ((a)-2) is more stable than high symmetry geometry ((a)-1). The energy difference (ΔE^H) between the (a)-1 and (a)-2 geometries is 6.19 kcal/mol. The corresponding C_{4h} and C_{1h} geometries for deuterated D_2SQ crystal are shown in Fig. 17.13(b)-1 and (b)-2, respectively. The most stable geometry is (b)-2, as for the cluster model of H_2SQ crystal. The calculated energy difference (ΔE^D) between (b)-1 and (b)-2 geometries is 6.57 kcal/mol. Thus, the energy difference between ΔE^H and ΔE^D corresponds to the calculated difference, 192 K, of the phase transition temperature between H_2SQ and D_2SQ crystals by using the dimer model. On the other hand, the experimental difference of the phase transition temperature between H_2SQ and D_2SQ crystal is 145 K [3]. Therefore, the difference of the phase transition temperature of the crystal systems was theoretically reproduced.

The most stable structures of H_2SQ and D_2SQ cluster models ((a)-2, (b)-2) are also presented and the bond lengths and electronic charge densities of H_2SQ with the bond lengths and electronic charge densities of D_2SQ hydrogen-bonded parts were compared. The exponents (α) of the GTF, which represents the charge distribution, are indicated in Table 17.3. Table 17.3 also shows the electronic charge densities as the gross electronic charge by Mulliken population analysis [60], O–H and O···O distances of the hydrogen-bonded parts. The exponent of deuteron is larger than that of proton. This indicates that the charge distribution of the deuteron shrinks more

Table 17.3 The characteristics of the hydrogen bonds in stable structures of $(H/D/Mu)_2SQ$

	Conventional MO	MC_MO(H)	MC_MO(D)	MC_MO(Mu)
Exponent	–	17.65	26.89	4.68
Electronic Population	−0.385	−0.514	−0.545	−0.430
O–H Distance [Å]	1.008	1.096	1.058	1.252
O···O Distance [Å]	2.543	2.468	2.487	2.504

than that of proton. The difference of the distribution reflects the local unit structures. The O–H distance in the H_2SQ cluster and O–D distance in the D_2SQ cluster were calculated to be 1.096 and 1.058 Å, respectively. The O···O distance in D_2SQ cluster (2.487 Å) is longer than H_2SQ cluster (2.468 Å). These geometrical differences are consistent with the well-known Ubbelohde effect due to the geometrical isotope effect [61]. The electronic charge density around the deuteron (−0.545) is larger than one around the proton (−0.514). This result shows the same tendency as obtained from the recent experimental result of X-ray diffraction. It is found that the influence of the isotope effect appears the geometrical structure and electronic charge densities following the change of the wave distribution of the proton and deuteron.

Finally, the T_c of Mu_2SQ was predicted where the hydrogen atom was substituted by a muonium in H_2SQ crystal. The muonium has one electron bound to the muon meson whose mass is 1/9 of hydrogen. The Bohr radius and ionization energy of the Mu (0.5315 Å and 13.54 eV) are significantly close to those of hydrogen (0.5292 Å and 13.60 eV), that is the Mu behaves as an isotope of hydrogen. The average span of life for the Mu is very short (2.20×10^{-6}). There are no experimental results of the phase transition temperature for Mu_2SQ crystal because the experiment for the Mu is very difficult. The MC_MO calculation was applied to the dimer model of the Mu_2SQ crystal. The optimized geometry of the dimer is shown in Fig. 17.13(c). Only the C_{4h} symmetry geometry where the Mu locates at the center between the oxygen atoms was obtained. This geometry corresponds to paraelectric phase. This result clearly predicts that the Mu_2SQ crystal system would not undergo the phase transition. The exponent of the Mu is very small compared the proton, so that the Mu is delocalized itself.

17.3.3 Phase Transition Temperature of Mixed $K_3H_{1-X}D_x(SO_4)_2$, $(H_{1-x}D_x)_2SQ$ and Tritiated TKHS, T_2SQ

In the hydrogen-bonded dielectric materials, partial substitution of protons with deuterons can control the phase transition with varying T_c [72]. Therefore, a proton-deuteron mixed crystal can provide a good opportunity for the study of the dynamics of protons in this class of compounds. Concerning the KHS and H_2SQ

crystals, the phase transition temperature upon changing the deuteron concentration is investigated using the mixed $K_3H_{1-x}D_x(SO_4)_2$ and $(H_{1-x}D_x)_2SQ$ crystals with random substitution of protons with deuterons [73, 74]. In the mixed $K_3H_{1-x}D_x(SO_4)_2$ crystal, the phase transition appearance was reported with increasing deuterium concentration. The deuterium concentration dependent behavior of T_c was described by simple transverse Ising Hamiltonian. However, it is impossible to express the geometrical and electronical changes as well as the T_c between the H- and D-compounds. Therefore, the first-principle calculation is necessary to theoretically analyze the origin of isotope effect for phase transition including geometrical changes. In the mixed $(H_{1-x}D_x)_2SQ$ crystal, the critical temperature T_c for the dielectric phase transition was found to increase linearly with the deuterium concentration. Since, the phase transition of H_2SQ and D_2SQ crystals has large geometrical change, conventional model calculations are not enough to theoretically investigate the relation between phase transition and geometrical changes.

In addition, tritium behaves as an isotope of hydrogen since the mass is three times of hydrogen. Tritium is also well known as a radioactive nuclide that emits β-rays, even a trace amount of tritiated products can be detected with high sensitivity [75]. Tritium is often used to measure the kinetic isotope effect on enzyme catalyzed hydrogen transfer [76, 77]. To date, there is no experimental report about the tritiated hydrogen-bonded dielectric materials. It is a great and important challenge to theoretically elucidate the T_c of tritiated hydrogen-bonded dielectric materials.

In this chapter, the deuterium concentration dependence of phase transition temperature and geometrical changes of mixed $K_3H_{1-x}D_x(SO_4)_2$ and $(H_{1-x}D_x)_2SQ$ crystal in random substitution of protons with deuterons was theoretically investigated. Furthermore, the phase transition temperature of TKHS and T_2SQ crystals that is the tritium substitutions from theoretical prediction was estimated.

In order to describe the proton-deuteron mixed crystal, the mass of proton is adopted as the 1836.59, 2293.59, 2750.59, 3207.58, and 3664.58 a.u. for $x = 0.00$, 0.25, 0.50, 0.75, and 1.00, respectively. These masses are indicated as the average of $H_{1-x}D_x$ in each $K_3H_{1-x}D_x(SO_4)_2$ and $(H_{1-x}D_x)_2SQ$ crystal at the random substitution of protons with deuterons.

In the MC_MO calculation which directly takes into account the quantum effect, the proton, deuteron, and other mixed particles (these particles are called the "light nuclei" in this chapter) are treated as quantum waves, as well as electrons under the field of S, C, and O nuclear point charges. The positions of these point charges are determined by conventional optimization procedures using analytical gradient [70]. The single s-type gaussian type function (GTF), $\exp\{-\alpha(r - R)^2\}$, was employed for each light nuclear basis function in which the GTF variational parameters were optimized, simultaneously. The standard [3s1p]/(4s1p) electronic basis set for hydrogen and Pople's 3-21G* basis set [56, 78] for S, C, and O were used. The centers of electronic GTFs are fixed on each nucleus. All calculations were carried out at the Hartree-Fock level using modified versions of Gaussian/98 program packages [59].

Furthermore, in order to predict the phase transition temperature and geometries of TKHS and T_2SQ in which the triton is substituted from proton, the cluster model was calculated using the MC_MO method by the same procedure of the

Table 17.4 The stable hydrogen-bonded structures of paraelectric and antiferroelectric phases of mixed $K_3H_{1-x}D_x(SO_4)_2$

	D concentration (x)	0.00	0.25	0.50	0.75	1.00
a (*Paraelectric Phase*)	Energy (kcal/mol)	0.00	0.00	0.00	0.00	0.00
	Exponent	16.90	19.17	21.21	23.08	24.81
	Electronic Population	−0.598	−0.600	−0.601	−0.603	−0.604
	O–H Distance (Å)	1.224	1.222	1.221	1.220	1.219
	O···O Distance (Å)	2.448	2.444	2.442	2.440	2.438
b (*Antiferroelectric Phase*)	Energy (kcal/mol)	–	−0.01	−0.07	−0.12	−0.17
	Exponent	–	19.85	22.21	24.32	26.12
	Electronic Population	–	−0.618	−0.624	−0.632	−0.633
	O–H Distance (Å)	–	1.123	1.112	1.105	1.100
	O···O Distance (Å)	–	2.471	2.474	2.477	2.479
	T_c	–	7	25	59	85
	$\Delta\alpha$	–	0.68	1.00	1.24	1.31

mixed $K_3H_{1-x}D_x(SO_4)_2$ and $(H_{1-x}D_x)_2SQ$ above. The mass of triton was treated as 5492.57 a.u.

Before discussing the details of geometrical changes and T_c of mixed $K_3H_{1-x}D_x(SO_4)_2$ crystal, the important two geometries of KHS cluster have already reported in the previous Sect. 17.3.1. In one structure (a) the proton/deuteron locates at the center between two connected oxygen atoms. In the other structure (b) the proton/deuteron is located at one side of two oxygen atoms. These structures, (a) and (b), correspond to the paraelectric and antiferroelectric phases, respectively. First the two characteristics stable structures in mixed $K_3H_{1-x}D_x(SO_4)_2$ crystal were calculated. Table 17.4 lists the relative energies, exponent values, electronic charge densities, and geometrical parameters of two stable structures in the various deuteron concentrations. In the case where $x = 0.00$, (a) is obtained as the most stable structure. When increasing the deuteron concentration (x), (b)s are obtained as the most stable structures. The exponent values that express the charge distributions become larger with increasing x values. In other words, the charge distribution shrinks more when the mass of light nucleus increases. These charge distributions reflect the geometrical parameters and electronic charge densities. The O···O distances in the most stable structure of each x is, 2.448, 2.471, 2.474, 2.477, and 2.479 Å, gradually lengthening with the increase in deuteron concentration. The electronical relaxation also depends on the charge distribution of light nucleus.

Compared with the energy difference between the (a) and (b) at same deuteron concentration, its relative energy corresponds to the T_c. Figure 17.14 shows various deuterium concentration dependencies of T_c in the mixed $K_3H_{1-x}D_x(SO_4)_2$. The experimental results by Moritomo et al. are also plotted in Fig. 17.14. The calculated result is reproduced from the experimental result in the large deuterium concentration field ($x \geq 0.50$). In regard to the appearance area of the phase transition ($x = 0.30 \sim 0.40$), there is a gap between the calculated and experimental results.

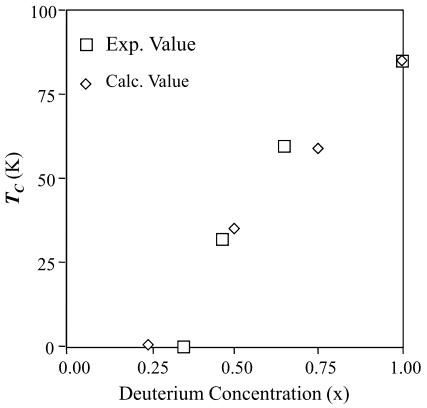

Fig. 17.14 The relationship between the phase transition temperature (T_c) and deuterium concentration of mixed $K_3H_{1-x}D_x(SO_4)_2$ crystal. The experimental and calculated values are plotted as □ and ◇, respectively

As one of the reasons, the cluster size is not enough to describe the surrounding electrostatic effect in this drastically changing area.

Next, the deuterium concentration dependence of the relative energy, exponent value, electronic charge density, and geometrical parameters in the mixed $(H_{1-x}D_x)_2SQ$ crystal were analyzed. It has been demonstrated in the previous Sect. 17.3.2 that the phase transition temperature difference (ΔT_c) between the H_2SQ and D_2SQ crystals theoretically can be obtained as 192 K (experimental ΔT_c is 145 K). In this calculation, two structures corresponding to paraelectric and antiferroelectric phases having C_{4h} and C_{1h} symmetries in each unit were optimized. In addition, the two structures (a) and (b) were treated in this chapter. The calculated results of (a) and (b) are shown in Table 17.5 with the theoretical ΔT_c. The exponent values show the tendency to become large with increasing deuterium concentrations. The geometrical difference and electronic charge densities are also obtained with the same pattern in the mixed $K_3H_{1-x}D_x(SO_4)_2$ crystal. Large difference of exponent values in same deuterium concentration reflects the energy difference, as well as, geometrical and electronical relaxations.

The energy difference becomes large when the deuterium concentration increases. Various deuterium concentration dependence of ΔT_c recalculated from the energy difference are shown in Fig. 17.15 with experimental results. Increasing the deuterium concentration, the ΔT_c increases linearly with x from 0 ($x = 0.00$) to 192 ($x = 1.00$) K. The experimental results suggest that ΔT_c increases linearly with x from 0 K at $x = 0$ to 145 K at $x = 1$. As reproduced, the ΔT_c from H_2SQ to D_2SQ crystals increases linearly with the various deuterium concentration from $x = 0.00$ to $x = 1.00$, although the calculated value has overestimated the experimental one. The energy difference between the (a) and (b) structures is a reasonable approximation for represent the T_c. Hence, not only ΔT_c but electronical and geometrical relaxations of mixed $(H_{1-x}D_x)_2SQ$ crystal have been theoretically obtained.

The energy difference between two cluster model structures for paraelectric and antiferroelectric phase is approximately corresponding to the T_c of mixed $K_3H_{1-x}D_x(SO_4)_2$ and $(H_{1-x}D_x)_2SQ$ crystal in the present chapter. In here, the prediction of the T_cs for TKHS and T_2SQ crystals substituted from hydrogen to

Table 17.5 The stable hydrogen-bonded structures of paraelectric and antiferroelectric phases of mixed $(H_{1-x}D_x)_2SQ$

	D concentration (x)	0.00	0.25	0.50	0.75	1.00
a (*Paraelectric Phase*)	Energy (kcal/mol)	0.00	0.00	0.00	0.00	0.00
	Exponent	16.67	18.94	20.94	22.80	24.58
	Electronic Population	−0.481	−0.485	−0.487	−0.488	−0.490
	O–H Distance (Å)	1.210	1.208	1.207	1.205	1.204
	O···O Distance (Å)	2.420	2.416	2.414	2.410	2.408
b (*Antiferroelectric Phase*)	Energy (kcal/mol)	−6.19	−6.30	−6.40	−6.49	−6.57
	Exponent	17.65	20.20	22.66	24.77	26.89
	Electronic Population	−0.513	−0.523	−0.534	−0.539	−0.546
	O–H Distance (Å)	1.096	1.083	1.070	1.066	1058
	O···O Distance (Å)	2.468	2.474	2.484	2.486	2.496
	ΔT_c	0	57	109	153	192
	$\Delta\alpha$	0.98	1.26	1.72	1.97	2.31

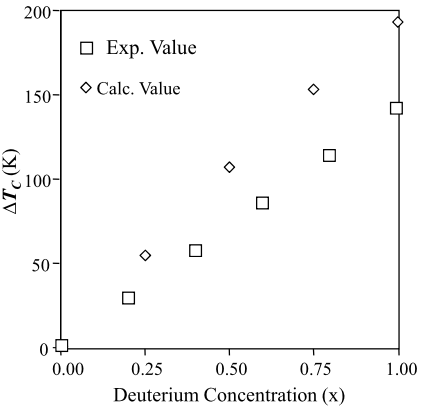

Fig. 17.15 The relationship between the T_c difference (ΔT_c) and deuterium concentration of mixed $(H_{1-x}D_x)_2SQ$ crystal. The experimental calculated values are plotted as □ and ◇, respectively

tritium is attempt. Though there are many experimental studies of T_c for various hydrogen-bonded dielectric materials, no report has been published that T_c includes for a tritium.

At first, the TKHS cluster model was calculated using the MC_MO method. The two stable structures (a) and (b) corresponding to the paraelectric and antiferroelectric phase are shown in Fig. 17.16, respectively. The structure (b) is −0.36 kcal/mol more stable than (a). The T_c of the TKHS crystal is predicted as about 190 K from first-principle calculation. The optimized exponent values of triton, electronic charge densities, and geometrical parameters are listed in Table 17.6 along with the previous calculated results of KHS and DKHS. The exponent value of triton is more localized than those of proton and deuteron. Owning to the localization of triton, the electronic charge density and O···O distance are larger and longer than the other results of the most stable structure.

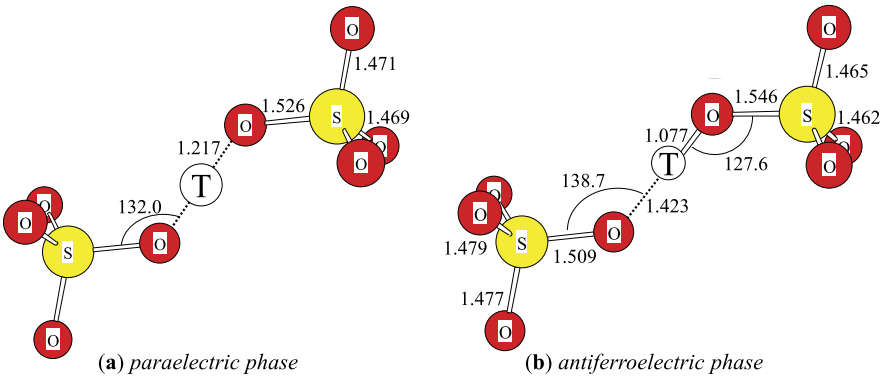

(**a**) *paraelectric phase* (**b**) *antiferroelectric phase*

Fig. 17.16 The stable structures of TKHS cluster models of paraelectric (**a**) and antiferroelectric (**b**) phases. The bond lengths and angles are shown in angstroms and degrees, respectively

Table 17.6 The stable hydrogen-bonded structures of paraelectric and antiferroelectric phases of KHS. The hydrogen in KHS crystal is substituted deuterium, tritium, and muonium

	Substitution	H	D	T	Mu
(*Paraelectric Phase*)	Energy (kcal/mol)	0.00	0.00	0.00	0.00
	Exponent	16.90	24.81	30.93	4.50
	Electronic Population	−0.598	−0.604	−0.606	−0.545
	O–H Distance (Å)	1.224	1.219	1.217	1.257
	O···O Distance (Å)	2.448	2.438	2.434	2.514
(*Antiferroelectric Phase*)	Energy (kcal/mol)	–	−0.17	−0.36	–
	Exponent	–	26.12	33.24	–
	Electronic Population	–	−0.633	−0.651	–
	O–H Distance (Å)	–	1.100	1.077	–
	O···O Distance (Å)	–	2.479	2.500	–
	$\Delta\alpha$	–	1.31	2.31	–

Two stable structures of the T_2SQ cluster model were optimized to analyze the energy difference. Figure 17.17 shows the stable structures obtained. The structure (a) and (b) correspond to the paraelectric and antiferroelectric phases having C_{4h} and C_{1h} symmetries in each unit, respectively. The energy difference between (a) and (b) is −6.99 kcal/mol. In order to estimate the T_c for T_2SQ crystal, the relative energy of D_2SQ result was compared. The energy difference (0.42 kcal/mol) between T_2SQ and D_2SQ corresponds to about 210 K. In the case of D_2SQ, however, since the theoretical ΔT_c has overestimated the experimental results by 25 %, it is necessary to correct ΔT_c between T_2SQ and D_2SQ. As a result of the correction, the ΔT_c between D_2SQ and T_2SQ was deduced to be about 160 K from the temperature difference (210 K) before compensation. The T_c of T_2SQ crystal is about 160 K higher than that of D_2SQ. The T_c of T_2SQ was theoretically predicted to

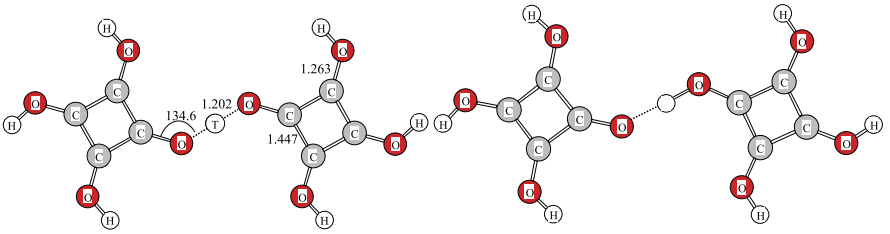

(**a**) *paraelectric phase* (**b**) *antiferroelectric phase*

Fig. 17.17 The stable structures of T_2SQ cluster models of paraelectric (**a**) and antiferroelectric (**b**) phases. The bond lengths and angles are shown in angstroms and degrees, respectively

Table 17.7 The stable hydrogen-bonded structures of paraelectric and antiferroelectric phases of H_2SQ. The hydrogen in H_2SQ crystal is substituted deuterium, tritium, and muonium

	Substitution	H	D	T	Mu
(*Paraelectric Phase*)	Energy (kcal/mol)	0.00	0.00	0.00	0.00
	Exponent	16.67	24.58	30.06	4.28
	Electronic Population	−0.481	−0.490	−0.494	−0.416
	O–H Distance (Å)	1.210	1.204	1.202	1.253
	O···O Distance (Å)	2.420	2.408	2.404	2.506
(*Antiferroelectric Phase*)	Energy (kcal/mol)	−6.19	−6.57	−6.99	–
	Exponent	17.65	26.89	33.82	–
	Electronic Population	−0.514	−0.545	−0.557	–
	O–H Distance (Å)	1.094	1.058	1.048	–
	O···O Distance (Å)	2.468	2.487	2.501	–
	$\Delta\alpha$	0.98	2.31	3.76	–

be about 680 K. Table 17.7 lists the optimized exponent values of triton, electronic charge densities, and geometrical parameters with the calculated results of H_2SQ and D_2SQ. The optimized exponent value of triton also shrinks more than that of deuteron, as well as, the TKHS. Thus, not only the T_c, but also the stable structures of paraelectric and antiferroelectric phase of the unknown T_2SQ crystal were found.

17.4 Summary

The exploration of the isotope effect on the phase transition of hydrogen-bonded dielectric materials is one of the most major subjects in condensed matter physics. Although, many models and theories are proposed concerning the origin of the isotope effect, an universal understanding is far from complete. Even with only the difference between a proton and a deuteron, the phase transition temperature difference must be rationalized as well as the geometrical and electronic relaxation induced by the isotope effect. In order to explain the isotope effect of hydrogen-

bonded dielectric materials, it is essential to elucidate the quantum effect of proton and deuteron from the microscopic view.

In computational details, the importance of the quantum effect of proton and deuteron with not only the T_c, but also the structures and electronic charge difference in the hydrogen-bonded dielectric materials was dealt using the adequate cluster model and multi-component molecular orbital (MC_MO) method which takes into account the quantum effect, such as, an anharmonicity due to the zero-point energy of the proton/deuteron directly.

In Sect. 17.3.1, the isotope effect of $K_3H(SO_4)_2$ (KHS) and $K_3D(SO_4)_2$ (DKHS) was discussed in order to verify the importance of the quantum effect of proton/deuteron and the efficiency of the MC_MO method. The difference between the KHS and DKHS was clearly demonstrated, namely: (1) the shape of potential energy surface, (2) the geometrical parameter including the hydrogen-bond (Ubbelohde effect), and (3) the electronic charge density. These results are universally explained the independent various theories. In conclusion, the origin of the isotope effect of KHS and DKHS is concluded that the difference of the reflection to the geometrical parameters because of the difference in the proton and deuteron wave distributions.

In Sect. 17.3.2, the mechanism of the phase transition of $H_2C_4O_4$ (H_2SQ) was discussed. The main driving force of phase transition in H_2SQ crystal was found to be the Jahn-Teller effect of the constituent molecular unit. The phase transition causes the distortion of the crystal system because the geometrical change of the unit propagates throughout the entire system via the hydrogen-bonded network. In addition, the T_c difference was shown, as well as, the theoretical geometrical difference using the MC_MO method. The H_2SQ and D_2SQ crystals are different in the way which propagates the alternation of the unit induced by the shrinkage distribution of the deuteron as opposed to the proton.

In Sect. 17.3.3, the difference of the T_c, geometry, and electronic charge density of $K_3H_{1-x}D_x(SO_4)_2$ and $(H_{1-x}D_x)_2SQ$ crystals were examined with increasing deuterium concentration. Calculated T_cs of $K_3H_{1-x}D_x(SO_4)_2$ and $(H_{1-x}D_x)_2SQ$ reproduced the experimental results, since the variation of light nuclear quantum effect (i.e. exponent value) has influenced the T_c, geometry, and electronic charge density. Furthermore, the T_c values of tritiated TKHS and T_2SQ are predicted to be equal to 190 and 680 K, respectively. Owing to the localization of charge distribution of triton, hydrogen-bond structure and electronic charge density are longer and larger than in the case of DKHS and D_2SQ.

The major aim of manuscript is to explain the difference of T_c in hydrogen-bonded dielectric materials induced by the H/D isotope effect. The importance of the quantum effect (i.e. anharmonicity) of proton/deuteron for the KHS (DKHS), H_2SQ (D_2SQ), their mixed $K_3H_{1-x}D_x(SO_4)_2$ and $(H_{1-x}D_x)_2SQ$, and tritiated TKHS and T_2SQ which have special features such as hydrogen-bonded networks and T_c were confirmed. Taking into account the quantum effect of proton/deuteron using the MC_MO method directly, the difference of T_c, as well as, the geometry and electronic charge difference is universally elucidate without a tunneling model. In conclusion, the origin of the isotope effect of hydrogen-bonded dielectric materials is the anharmonicity due to the difference of the proton/deuteron wave distribution.

References

1. Busch G, Scherrer P (1935) Naturwissenschaften 23:737
2. Samara GA (1987) Ferroelectrics 71:161
3. Samara GA, Semmingsen D (1979) J Chem Phys 71:1401
4. Negran TJ, Glass AM (1978) Ferroelectrics 21:467
5. Gesi K (1980) J Phys Soc Jpn 48:886
6. Slater JC (1941) J Chem Phys 9:16
7. Blinc R (1960) J Phys Chem Solids 13:204
8. Blinc R, Zeks B (1972) Adv Phys 21:693
9. Tokunaga M, Matsubara T (1966) Prog Theor Phys 35:581
10. Tokunaga M, Matsubara T (1987) Ferroelectrics 72:175
11. Kaminov IP, Damon TC (1968) Phys Rev Lett 20:1195
12. Peercy DS (1975) Rhys Rev B 12:2725
13. Samara GA (1981) Phys Rev Lett 27:103
14. Ichikawa M, Motida K (1987) Phys Rev B 36:874
15. Noda Y, Uchiyama S, Kahuku K, Kasatani H, Terauchi H (1990) J Phys Soc Jpn 59:2804
16. Noda Y, Kasatani H, Terauchi H, Gesi K (1990) J Phys Soc Jpn 59:3249
17. Noda Y, Kasatani H (1991) J Phys Soc Jpn 60:13
18. Noda Y, Kasatani H, Watanabe Y, Terauchi H (1990) J Phys Soc Jpn 59:2804
19. Tominaga Y (1994) J Korean Phys Soc 27:S16
20. Koval S, Kohanoff J, Migoni RL, Tosatti E (2002) Phys Rev Lett 89:187602
21. Suwa Y, Yamauchi J, Kageshima H, Tsuneyuki S (2001) Mater Sci Eng B 79:31
22. Suwa Y, Yamauchi J, Kageshima H, Tsuneyuki S (2001) Mater Sci Eng B 79:98
23. Kohn W, Sham LJ (1965) Phys Rev A 140:1133
24. Hohenberg P, Kohn W (1964) Phys Rev B 136:864
25. Becke AD (1992) J Chem Phys 96:2155
26. Tachikawa M (2002) Chem Phys Lett 360:494
27. Holyland JR (1964) J Chem Phys 40:3540
28. Schwartz ME, Schaad LJ (1967) J Chem Phys 46:4112
29. Helgaker T, Almlof J (1988) J Chem Phys 89:4889
30. Huber H (1979) Chem Phys Lett 62:95
31. Huber H (1980) Chem Phys Lett 70:353
32. Huber H (1980) Theor Chim Acta 55:117
33. Huber H (1981) J Mol Struct, Theochem 76:277
34. Hurley AC (1988) J Comput Chem 9:75
35. Frost AA (1977) In: Scharfer HF III (ed) Methods of electronic structure theory. Morden theoretical chemistry, vol 3. Plenum, New York, p 29
36. Mohallem JR, Dreizler RM, Trsic M (1986) Int J Quant Chem S20:45
37. Faegri K Jr, Almlof J (1986) J Comput Chem 7:396
38. Hashimoto K, Osamura Y (1989) Chem Phys Lett 164:353
39. Hashimoto K, Osamura Y (1991) J Chem Phys 95:1121
40. Hashimoto K, Osamura Y (1992) Can J Chem 70:547
41. Casimir HBG, Polder D (1948) Phys Rev 73:360
42. Milonni PW, Smith A (1996) Phys Rev A 53:3484
43. Milonni PW, Shih M-L (1992) Phys Rev A 45:4241
44. Thirunamachandran T (1983) Mol Phys 40:393
45. Jorgensen P, Simons J (1983) J Chem Phys 79:352
46. Fletcher R (1980) Practical methods of optimization. Wiley, New York
47. Noda Y, Watanabe Y, Kasatani H, Terauchi H, Gesi K (1991) J Phys Soc Jpn 60:1972
48. Gesi K (1981) J Phys Soc Jpn 50:3185
49. Fukai M, Inaba A, Matsuo T, Suga H, Ichikawa M (1993) Solid State Commun 87:939
50. Endo M, Kaneko T, Osaka Y, Ichikawa M (1983) J Phys Soc Jpn 52:3829
51. Matsuo T, Kohno K, Ichikawa M (1994) J Korean Phys Soc 29:S432

52. Tachikawa M, Mori K, Suzuki K, Iguchi K (1998) Int J Quant Chem 70:491
53. Tachikawa M, Mori K, Nakai H, Iguchi K (1998) Chem Phys Lett 290:437
54. Tachikawa M, Mori K, Osamura Y (1999) Mol Phys 96:1207
55. Pulay P (1969) Mol Phys 17:197
56. Binkley JS, Pople JA, Hehre WJ (1980) J Am Chem Soc 102:939
57. Gordon MS, Binkley JS, Pople JA, Pietro WJ, Hehre WJ (1982) J Am Chem Soc 104:2797
58. Pietro WJ, Fracl MM, Hehre WJ, Defrees DJ, Pople JA, Binkley JS (1982) J Am Chem Soc 104:5039
59. Frisch MJ, Trucks GW, Schlegel HB, Scuseria GE, Robb MA, Cheeseman JR, Zakrzewski VG, Montgomery JA Jr, Startmann RE, Burant JC, Dapprich S, Millam JM, Daniels AD, Kudin KN, Strain MC, Farkas O, Tomasi J, Barone V, Cossi M, Cammi R, Mennucci B, Pomelli C, Adamo C, Clifford S, Ochterski J, Patersson GA, Ayala PY, Cui Q, Morokuma K, Malick DK, Rabuck AD, Raghavachari K, Foresman JB, Cioslowski J, Ortiz JV, Stefanov BB, Liu G, Liashenko A, Piskorz P, Imamori I, Gomperts R, Martin RL, Fox DJ, Keith T, Al-Laham MA, Peng CY, Nakayakkara A, Gonzales C, Challacombe M, Gill PMW, Johnson B, Chen W, Wong MW, Andres JL, Head-Gordon M, Replogle ES, Pople JA (1998) Gaussian 98. Gaussian, Inc, Pittsburgh
60. Mulliken RS (1928) Phys Rev 32:186
61. Ubbelohde AR, Gallagher KJ (1955) Acta Crystallogr 8:71
62. Semmingsen D (1973) Acta Chem Scand 27:3961
63. Samuelsen J, Semmingsen D (1977) J Phys Chem Solids 38:1275
64. Ehrhardt K-D, Bauchenau U, Samuelsen EJ, Maier HD (1984) Phys Rev B 29:996
65. Semmingsen F, Feder J (1974) Solid State Commun 15:1369
66. Hollander FJ, Semmingsen D, Koetzle TF (1977) J Chem Phys 67:4825
67. Semmingsen D, Hollander FJ, Koetzle TF (1977) J Chem Phys 66:4405
68. Moritomo Y, Tokura Y, Takahashi H, Mori N (1991) Phys Rev Lett 67:2041
69. Dalal N, Klymachyov A, Bussmann-Holder A (1998) Phys Rev Lett 81:5924
70. Pulay P (1977) In: Schaefer HF (ed) Applications in electronic structure theory. Plenum, New York, p 153
71. Jahn HA, Teller E (1937) Proc R Soc A 161:220
72. Loiacono GM, Balascio JF, Osborne W (1974) Appl Phys Lett 24:455
73. Moritomo Y, Tokura Y, Nagaosa N, Suzuki T, Kumagai K (1993) Phys Rev Lett 71:2833
74. Moritomo Y, Katsufuji T, Tokura Y (1991) J Chem Phys 95:2244
75. Aratono Y, Matsumoto T, Takayanagi T, Kumada T, Komaguchi K, Miyazaki T (1998) J Phys Chem A 102:1501
76. Thomä NH, Meier TW, Evens PR, Leadlay PF (1998) Biochemistry 37:14386
77. Karsten WE, Hwang C-C, Cook PF (1999) Biochemistry 38:4398
78. Gordon MS, Binkley JS, Pople JA (1983) J Am Chem Soc 104:2797

Chapter 18
On Converse Piezoelectricity

Michael Springborg, Bernard Kirtman, and Jorge Vargas

Abstract We review theoretical treatments of large regular non-conducting systems exposed to an electrostatic field. The field will induce a structural change (our primary focus) that depends noticeably upon the surfaces no matter how large the system. Interestingly, the surface effect can be determined by treating the system as infinite and periodic, even though no surfaces are present in that case. Accurate results are presented for a simple model that verify and illustrate our infinite periodic treatment. Approximate calculations are also carried out for a couple of real materials. The breakdown of our treatment for metals is analyzed and, on the basis of that analysis, our approach is extended to account for the strain induced by a metal short-circuiting the opposite surfaces of a semiconductor/insulator.

18.1 Introduction

Piezoelectricity describes the ability of materials (most often, crystals) to produce an electric potential under the influence of an externally applied mechanical stress. For a material that is not short-circuited, the mechanical stress will lead to a separation of opposite electrical charges at opposite crystal surfaces which results in an electric voltage across the material. This effect is reversible in the sense that materials exhibiting the so called direct piezoelectric effect, i.e., the production of electricity when a stress is applied, also exhibit the converse piezoelectric effect, i.e., the production of stress and/or strain when an electric field is applied.

In the present contribution we concentrate on the converse piezoelectric effect. Specifically, we study how the spatial dimensions of a sample exposed to an electrostatic field change as a function of the externally applied voltage, as shown schematically in Fig. 18.1. The materials of interest to us are taken to be macroscopic so that the thermodynamic limit has been reached. This assumption has two interesting consequences that are discussed in this presentation.

Firstly, for a large macroscopic material the surfaces constitute an almost vanishingly small part of the complete system. This would suggest that their contribution

M. Springborg (✉)
Physical and Theoretical Chemistry, University of Saarland, 66123 Saarbrücken, Germany
e-mail: m.springborg@mx.uni-saarland.de

M. Hotokka et al. (eds.), *Advances in Quantum Methods and Applications in Chemistry, Physics, and Biology*, Progress in Theoretical Chemistry and Physics 27,
DOI 10.1007/978-3-319-01529-3_18,

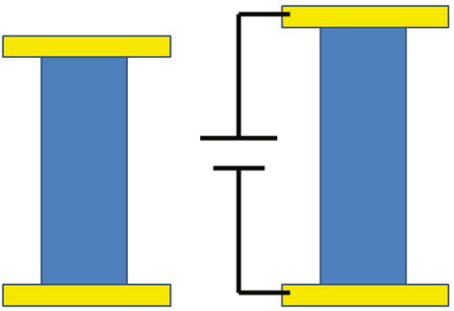

Fig. 18.1 Schematic presentation of the converse piezoelectric effect. The sample to the *left* is placed between two electrodes. When an electrical voltage between the two electrodes is applied, the sample changes its spatial dimensions, as shown in the *right* hand part

to any property, including the converse piezoelectric effect, can be made arbitrarily small simply by considering sufficiently large samples. However, we demonstrate in the present contribution that this is not the case. Certain converse piezoelectric properties have a finite contribution from the surfaces regardless of how large the samples are when the thermodynamic limit has been reached.

Secondly, as a consequence of the above, it might be thought that the converse piezoelectric properties can be calculated only by considering a very large finite system. In general this approach would lead to very large computational demands. The alternative of treating the system as infinite and periodic, but perturbed by the scalar interaction potential due to an external electrostatic field, is also inadequate because this potential is both non-periodic and unbounded. However, in the present work we demonstrate how it is possible to treat the system as infinite and periodic even in the presence of the field and also to include the effects due to the surfaces.

The question of whether surfaces have an effect on piezoelectric properties has been discussed for more than four decades [1–8]. Often, a crystal with polar surfaces was analyzed and arguments for why the crystal terminations should, or should not, play a role in the responses were presented. In the present work, we demonstrate that it is possible to modify the converse piezoelectric responses by modifying the chemical nature of the surfaces, but not completely arbitrarily. Thus, both sets of arguments contain some truth.

Our presentation is structured as follows. In Sect. 18.2 we present our mathematical arguments, which involve comparing a large, finite system to an infinite, periodic one. In that section the focus is on dielectrics,* for which there is an energy gap between occupied and unoccupied electronic orbitals. Then, in Sect. 18.3 results are presented for both a simple model system and a real system. Subsequently, we briefly discuss metallic systems in Sect. 18.4 and in Sect. 18.5 treat the dielectrics when they are short-circuited by a metallic connection. Finally, our results are summarized in Sect. 18.6.

Except where otherwise mentioned, we restrict ourselves, for the sake of simplicity, to systems that are extended in one dimension but finite in the other two, i.e., chain compounds/polymers. Moreover, we use atomic units whereby the elementary charge $|e|$, Planck's constant $\hbar$, and the dielectric constant of vacuum $4\pi\varepsilon_0$ are all set equal to 1.

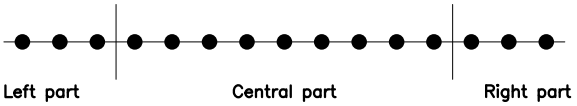

Fig. 18.2 Schematic representation of a long, but finite, regular chain. Each *black circle* represents a building block containing one or more atoms, which is placed regularly along the chain axis (the z axis). The separation into a central and two terminal (*left* and *right*) regions is shown through the vertical lines

18.2 Theoretical Foundations

18.2.1 Large Finite System

When exposed to a uniform electrostatic field the Hamilton operator for a large finite system changes according to

$$\hat{H} \rightarrow \hat{H} - \hat{\boldsymbol{\mu}} \cdot \mathbf{E}, \tag{18.1}$$

where $\hat{H}$ is the Hamilton operator in the absence of the field and we have used the scalar interaction potential with $\mathbf{E}$ as the electrostatic field. Finally, $\hat{\boldsymbol{\mu}}$ is the dipole moment operator for the system of interest.

If the system contains a large number of building blocks that are regularly distributed and identical, except at the surfaces (we will refer to such a system as regular), it may be most convenient to treat it as being infinite and periodic. Moreover, for any extensive property, ξ, that depends on the number of units of the system, N, it is often more useful to consider the corresponding intensive property,

$$\bar{\xi} = \lim_{N\rightarrow\infty} \frac{\xi(N)}{N} = \lim_{N\rightarrow\infty} \frac{1}{\Delta N}\big[\xi(N+\Delta N) - \xi(N)\big], \tag{18.2}$$

where ξ may be, for example, the total energy or any of the components of the dipole moment vector.

For a system like that of Fig. 18.2 the presence of an electrostatic field leads to several complications. First of all, the dipole-moment operator is unbounded so that states with electrons confined to the chain become resonances. Moreover, for sufficiently strong fields, some electrons may tunnel from one end to the other in order to lower the total energy of the system. Finally, for very long chains, such tunneling may occur for any non-vanishing field. These complications make the theoretical treatment of a system like that of Fig. 18.2, when exposed to an electrostatic field, very difficult.

An alternative might be to treat the chain as infinite and periodic. However, since the dipole moment operator is unbounded and does not possess the periodicity of the system, it is not straightforward to formulate the Hamilton operator for that case. One way to formulate the desired operator may be developed by considering the dipole moment for the large, but finite, system and, subsequently, applying Eq. (18.2). The total dipole moment of the system in Fig. 18.2 can be written as

$$\boldsymbol{\mu} = \int \rho(\mathbf{r})\mathbf{r}d\mathbf{r} = \int_C \rho(\mathbf{r})\mathbf{r}d\mathbf{r} + \int_L \rho(\mathbf{r})\mathbf{r}d\mathbf{r} + \int_R \rho(\mathbf{r})\mathbf{r}d\mathbf{r}$$
$$= K_C\boldsymbol{\mu}_C + (\mathbf{R}_R - \mathbf{R}_L)\int_R \rho(\mathbf{r})d\mathbf{r} + \int_L \rho(\mathbf{r})(\mathbf{r} - \mathbf{R}_L)d\mathbf{r} + \int_R \rho(\mathbf{r})(\mathbf{r} - \mathbf{R}_R)d\mathbf{r}, \tag{18.3}$$

where we have made explicit use of the spatial separation into right (R), left (L), and central (C) regions. It is also assumed that the total charge in region L is equal in magnitude to that in region R, but opposite in sign, in order to satisfy overall neutrality (given that the units in C are neutral by construction). In Eq. (18.3) $\rho(\mathbf{r})$ is the total charge density, $\mathbf{R}_R$ and $\mathbf{R}_L$ are typical positions within the right and left regions, respectively, and K_C is the number of units in C. Combining this relation with the second definition of Eq. (18.2) gives immediately

$$\bar{\boldsymbol{\mu}} = \boldsymbol{\mu}_C + Q_R \cdot \mathbf{a}, \tag{18.4}$$

in which Q_R is the total charge of R, $\boldsymbol{\mu}_C$ is the dipole moment of one of the C units, and $\mathbf{a}$ is the lattice constant of C.

It is clear that $\bar{\boldsymbol{\mu}}$ depends on the charge accumulated at the terminations. Thus, it might be thought that upon chemical substitution at the terminations, Q_R can vary essentially arbitrarily (within chemical limits), thereby making all values of $\bar{\boldsymbol{\mu}}$ possible. However, that is not the case as may be seen from the following argument [9, 10]. The set of orthonormal electronic orbitals for the entire system can be transformed into a set of maximally localized orthonormal functions. In terms of these localized functions the density matrix consists of three diagonal blocks, one for each of the regions in Fig. 18.2, whereas the remaining elements are exponentially vanishing. Since the complete density matrix is idempotent, each of the three blocks will be idempotent as well. This implies that the number of electrons associated with each block can change only by an integer and, thus, that Q_R can vary only by an integer.

18.2.2 The Dipole Moment per Unit for the Infinite Periodic System

Per construction, the infinite periodic system is lacking the terminations. Thus, the contribution from the second term in Eq. (18.4) must appear in another form. In order to see how that occurs we need to formulate an expression for the dipole moment per unit of the infinite periodic system. For an infinite, periodic system, the electronic orbitals in an independent particle model can be written as Bloch functions,

$$\psi(\mathbf{r}) = \psi_j(k, \mathbf{r}) = e^{ikz}u_j(k, \mathbf{r}). \tag{18.5}$$

Here $u_j(k, \mathbf{r})$ is a lattice-periodic function, k is a continuous variable in the interval $-\frac{\pi}{a} < k \leq \frac{\pi}{a}$, and a is the lattice constant in the chain direction. In a practical

calculation one considers only a finite set of K equidistant k values, which is equivalent to assuming that the properties are periodic with the periodicity Ka—i.e. they have the symmetry of the Born von Kármán (BvK) zone. This is clearly not the case for the dipole moment operator in the scalar interaction potential. Thus, one must consider an alternative approach.

About 20 years ago alternative formulations allowing for calculation of the dipole moment per unit cell, based on an operator that has (i) the BvK periodicity and (ii) approaches the position operator as the size of the BvK zone approaches infinity, began to appear. Working expressions were initially proposed within the so-called modern theory of polarization [9, 11, 12]; later they were formally developed and generalized from other points of view [13, 14] (see also [15, 16]).

In the description provided here we concentrate on the component of the total dipole moment per unit cell along the chain (z) direction and separate it into an electronic and a nuclear contribution,

$$\bar{\mu}_z = \bar{\mu}_{zn} + \bar{\mu}_{ze}. \tag{18.6}$$

For an independent particle model, the electronic contribution can be written either as [11]

$$\bar{\mu}_{ze} = \bar{\mu}_{\mathrm{R}} \equiv -\frac{a}{2\pi}\,\mathrm{Im}\ln\det \underline{\underline{S}}^{+} = \frac{a}{2\pi}\,\mathrm{Im}\ln\det \underline{\underline{S}}^{-} \tag{18.7}$$

or [9, 12]

$$\begin{aligned}\bar{\mu}_{ze} = \bar{\mu}_{\mathrm{KSV}} &\equiv -\frac{i}{K}\sum_{k=1}^{K}\sum_{j=1}^{B}\left\langle u_j(k,\mathbf{r})\left|\frac{\partial}{\partial k}u_j(k,\mathbf{r})\right.\right\rangle \\ &= -\frac{i}{K}\sum_{k=1}^{K}\sum_{j=1}^{B}\left\langle e^{-ikz}\psi_j(k,\mathbf{r})\left|\frac{\partial}{\partial k}e^{-ikz}\psi_j(k,\mathbf{r})\right.\right\rangle,\end{aligned} \tag{18.8}$$

where B is the number of occupied bands and spin degeneracy is not assumed. These expressions are valid only for systems with an energy gap between occupied and unoccupied orbitals, i.e., semiconductors and insulators; metals will be discussed briefly in Sect. 18.4.

In Eq. (18.7), the dimension of the matrices $\underline{\underline{S}}^{\pm}$ is equal to the number of electrons per BvK zone (i.e., KB) and the elements, in a Bloch wave basis [cf. Eq. (18.5)], are given by

$$\begin{aligned}\left[S_{j_1 j_2}(k_1 k_2)\right]^{\pm} &= \left\langle\psi_{j_1}(k_1,\mathbf{r})\left|e^{\pm i\Delta kz}\right|\psi_{j_2}(k_2,\mathbf{r})\right\rangle \\ &= \delta_{k_1,k_2\pm\Delta k}\left\langle\psi_{j_1}(k_1,\mathbf{r})\left|e^{\pm i\Delta kz}\right|\psi_{j_2}(k_2,\mathbf{r})\right\rangle \\ &= \delta_{k_1,k_2\pm\Delta k}\left\langle u_{j_1}(k_1,\mathbf{r})\left|u_{j_2}(k_2,\mathbf{r})\right.\right\rangle,\end{aligned} \tag{18.9}$$

where $\Delta k = \frac{2\pi}{Ka}$ is the spacing between the k points. Upon organizing the occupied Bloch waves in order of increasing k, the $\underline{\underline{S}}^{\pm}$ matrices have the simple structure shown in Fig. 18.3 with square blocks above and below the $k_1 = k_2$ diagonal (except at the corners). The expressions (18.7) and (18.8) were derived [14] for an independent particle model. In a more recent work [15] we have shown how to generalize this result to the case of a multi-determinant electronic wavefunction.

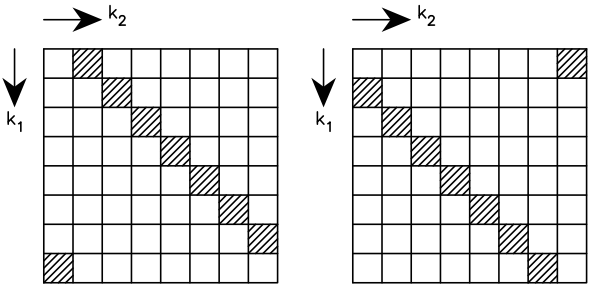

Fig. 18.3 Schematic presentation of the structure of the $\underline{\underline{S}}^{\pm}$ matrices

In order to complete the picture, the nuclear contribution to the dipole moment per unit cell may be obtained simply as

$$\bar{\mu}_{zn} = \sum_m (Z_{mp} - pa) Q_m. \tag{18.10}$$

Here, Z_{mp} is the z component of the position of the mth nucleus in the pth unit cell and Q_m is the nuclear charge.

It is useful to examine Eq. (18.7) from a different perspective. To that end we transform the set of K delocalized Bloch functions in Eq. (18.5) to a set of localized Wannier functions, i.e.

$$\begin{aligned} w_{j,p}(\mathbf{r}) &= \frac{1}{\sqrt{K}} \sum_{k=1}^{K} \psi_j(k, \mathbf{r}) e^{-ikap}, \\ \psi_j(k, \mathbf{r}) &= \frac{1}{\sqrt{K}} \sum_{p=1}^{K} w_{j,p}(\mathbf{r}) e^{ikap}. \end{aligned} \tag{18.11}$$

Here the Wannier function $w_{j,p}$ of the jth band is more or less localized to the pth unit inside the BvK zone. In terms of these functions, one can easily obtain

$$\bar{\mu}_{\mathrm{KSV}} = -\sum_{j=1}^{B} \langle w_{j,0}(\mathbf{r}) | z | w_{j,0}(\mathbf{r}) \rangle. \tag{18.12}$$

(Notice the minus sign that originates from the negative charge of the electrons).

Alternatively, we may consider an LCAO approach in which the single particle orbitals are written as linear combinations of localized basis functions centered on the atoms,

$$\begin{aligned} \psi_j(k, \mathbf{r}) &= \sum_m C_{mj}(k) \chi_m(k, \mathbf{r}), \\ \chi_m(k, \mathbf{r}) &= \frac{1}{\sqrt{K}} \sum_p e^{ikap} \chi_{pm}(\mathbf{r}) \end{aligned} \tag{18.13}$$

with χ_{pm} being the mth atomic basis function of the pth unit. It then follows that

$$\begin{aligned}\bar{\mu}_{ze} &= \bar{\mu}_{\mathrm{KSV}} \\ &= -\frac{i}{K}\sum_j \sum_k \left\langle u_j(k,\mathbf{r}) \middle| \frac{\partial}{\partial k} u_j(k,\mathbf{r}) \right\rangle \\ &= -\frac{1}{K}\sum_{jm}\sum_k e^{ikma}\sum_{pq} C^*_{qj}(k)\Bigg(\underbrace{\langle \chi_{q0}|z-ma|\chi_{pm}\rangle}_{\text{charge}} + \underbrace{i\langle \chi_{q0}|\chi_{pm}\rangle \frac{d}{dk}}_{\text{current}}\Bigg) C_{pj}(k).\end{aligned} \tag{18.14}$$

Hereby, $\bar{\mu}_{ze}$ may be split into so-called charge and current contributions. This separation can also be carried out including the nuclear part, which only affects the charge contribution, to give

$$\bar{\mu} = \bar{\mu}_{\mathrm{charge}} + \bar{\mu}_{\mathrm{current}}. \tag{18.15}$$

It can be shown analytically [15] that the charge contribution corresponds to that part of the dipole moment per unit for a large finite system that has its origin in the dipole moment of a central unit, i.e., $\boldsymbol{\mu}_C$ of Eq. (18.4). Accordingly, the current contribution corresponds to that part of the dipole moment per unit for a large finite system that is due to the charge transfer between the termination regions, i.e., $Q_R \cdot \mathbf{a}$ of Eq. (18.4).

For our arguments it is important to notice that each expression for the dipole moment per unit contains an unknown integer multiple of the lattice constant. In the expression of Eq. (18.7) $\mathrm{Im}\ln\det \underline{\underline{S}}^{\pm}$ is just the phase of the complex number $\det \underline{\underline{S}}^{\pm}$, which contains an unknown integer multiple of 2π. Thus, $\bar{\mu}_{\mathrm{R}}$ is only determined up to an integer times the lattice constant. Equivalently, in evaluating $\bar{\mu}_{\mathrm{KSV}}$ of Eq. (18.8) we may modify each electronic orbital by a phase factor

$$\psi_j(k,\mathbf{r}) \to \psi_j(k,\mathbf{r}) e^{i\phi_j(k)} \tag{18.16}$$

which is arbitrary except for requiring that

$$e^{i\phi_j(\pi/a)} = e^{i\phi_j(-\pi/a)} \tag{18.17}$$

or, equivalently,

$$\phi_j(\pi/a) = \phi_j(-\pi/a) + \tilde{n}_j \cdot 2\pi \tag{18.18}$$

with $\tilde{n}_j$ an integer. As a result the dipole moment per unit is changed by an amount

$$-\tilde{n}\cdot a = -\sum_{j=1}^{B} \tilde{n}_j \cdot a. \tag{18.19}$$

This change modifies the current, but not the charge term. Finally, since the assignment of the Wannier functions in Eq. (18.11) to the individual units is non-unique, the expression of Eq. (18.12) also contains an unknown integer multiple of the lattice constant.

18.2.3 The SCF Equations for the Infinite Periodic System

In the absence of an electrostatic field, and for an independent particle model, the coefficients $\{C_{mj}(k)\}$ of Eq. (18.13) are determined from the well-known SCF equation

$$\underline{\underline{F}}(k) \cdot \underline{C}_j(k) = \varepsilon_j(k) \cdot \underline{\underline{S}}(k) \cdot \underline{C}_j(k). \tag{18.20}$$

Here, $\underline{\underline{F}}(k)$ is the Fock (or Kohn-Sham) matrix, $\underline{\underline{S}}(k)$ is the overlap matrix, $\varepsilon_j(k)$ is the orbital energy, and $\underline{C}_j(k)$ the vector containing the coefficients for the jth orbital. As shown, k is a good quantum number.

When the infinite, periodic system is exposed to an electrostatic field there are different approaches for including the field. One is to use a scalar potential to describe the interaction and, accordingly, to include the dipole term derived from the expression in Eq. (18.14). Alternatively, the effect of the field may be included by using the time-dependent vector potential, $\mathbf{A}(t)$. Then, the (time-dependent) SCF equation is obtained by replacing

$$\hat{\mathbf{p}} \to \hat{\mathbf{p}} + \frac{1}{c}\mathbf{A}(t), \tag{18.21}$$

which leads to

$$\left(\hat{F} - i\frac{\partial}{\partial t}\right)\psi_{j_1}(k, \mathbf{r}, t) = \sum_{j_2} \varepsilon_{j_2 j_1}(k, t)\psi_{j_2}(k, \mathbf{r}, t) \tag{18.22}$$

or, using the LCAO expansion of Eq. (18.13), [13, 17]

$$\begin{aligned} &\underline{\underline{F}}(k,t) \cdot \underline{\underline{C}}(k,t) + E(t) \cdot \left[\underline{\underline{M}}(k) \cdot \underline{C}(k,t) + i\underline{\underline{S}}(k)\frac{\partial}{\partial k}\underline{\underline{C}}(k,t)\right] - i\underline{\underline{S}}(k)\frac{\partial}{\partial t}\underline{\underline{C}}(k,t) \\ &\quad = \underline{\underline{S}}(k) \cdot \underline{\underline{C}}(k,t) \cdot \underline{\underline{\varepsilon}}(k,t). \end{aligned} \tag{18.23}$$

Here, $E(t)$ is the electric field obtained by taking the time derivative of the vector potential.

Independent of whether the scalar potential, or the vector potential for a static field, is used one arrives at the same matrix equation

$$\left(\underline{\underline{F}}(k) + E \cdot \left[\underline{\underline{M}}(k) + i\underline{\underline{S}}(k)\frac{\partial}{\partial k}\right]\right) \cdot \underline{C}_j(k) = \varepsilon_j(k) \cdot \underline{\underline{S}}(k) \cdot \underline{C}_j(k), \tag{18.24}$$

that was originally derived within the so-called vector-potential approach [13, 17]. In this equation

$$\begin{aligned} S_{qp}(k) &= \sum_l e^{ikal}\langle\chi_{q0}|\chi_{pl}\rangle, \\ F_{qp}(k) &= \sum_l e^{ikal}\langle\chi_{q0}|\hat{F}|\chi_{pl}\rangle, \\ M_{qp}(k) &= \sum_l e^{ikal}\langle\chi_{q0}|z - la|\chi_{pl}\rangle = \sum_l e^{-ikal}\langle\chi_{ql}|z|\chi_{p0}\rangle \end{aligned} \tag{18.25}$$

are the overlap, Fock (or Kohn-Sham), and dipole matrices, respectively. It is important to note that k remains a good quantum number, as indicated in Eq. (18.24), and thus translational symmetry is preserved. On the other hand, due to the $\frac{\partial}{\partial k}$ term on the left hand side, Eq. (18.24) is not a simple matrix-eigenvalue relation. Since $\underline{C}_j(k)$ may contain essentially random, j- and k-dependent phase factors, it is a non-trivial problem to solve Eq. (18.24). During the last few years, however, we have presented a numerically stable and accurate procedure for doing so [8, 18–21].

18.2.4 The Total Energy

For the large finite system exposed to an electrostatic field, the total energy can be written as

$$\begin{aligned} E_{\text{tot}} &= E_{\text{kin}}\big[\{\psi_j\}\big] + E_{\text{J}}\big[\rho(\mathbf{r})\big] + E_{\text{xc}}\big[\{\psi_j\}\big] - \mathbf{E}\cdot\boldsymbol{\mu} \\ &\equiv E_{\text{tot},0} - \mathbf{E}\cdot\boldsymbol{\mu}. \end{aligned} \tag{18.26}$$

In principle, the above expression is exact, provided one uses a set of occupied orbitals $\{\psi_j\}$ that yield the exact density. In practice, we will assume that one is using either the Hartree-Fock or the Kohn-Sham independent particle model. The first term in the top line of the right hand side is the kinetic energy contribution; the second term is the classical Coulomb interaction between all charged particles (i.e., electrons and nuclei); and the third term is either the exchange energy for a Hartree-Fock treatment or the exchange-correlation energy for a Kohn-Sham treatment. The last term describes the interaction between the system and the electrostatic field. Since the electronic orbitals, and thereby the electron density, obtained from Eq. (18.24) depend upon the electrostatic field each term in the total energy expression will depend upon E including $E_{\text{tot},0}$ as well as $\boldsymbol{\mu}$.

By considering large finite systems of different (sufficiently large) size it is possible to calculate the total energy per unit, $\bar{E}_{\text{tot}}$. Alternatively, one may consider the infinite periodic system directly. In that case the quantity $\boldsymbol{\mu}$ per unit cell is calculated using the expression of Eq. (18.6) with the nuclear part given by Eq. (18.10) and the electronic part by Eq. (18.14).

18.3 Results for Semiconductors

18.3.1 A Model System

As discussed in the previous section, for the infinite periodic system, $\bar{\mu}$ contains an unknown additive term, i.e.

$$\bar{\mu} = \bar{\mu}_0 - \tilde{n}\cdot a, \tag{18.27}$$

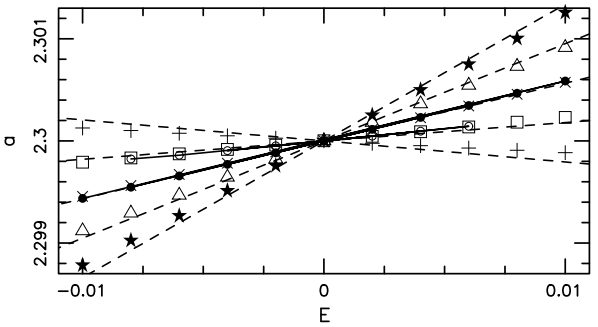

Fig. 18.4 Optimized lattice constant a from a set of representative calculations for the model chain (see text). *Open* and *filled circles* (connected by *solid straight lines*) are for finite chains with 40/41 units, whereas *all other symbols* are for infinite periodic chains with $K = 80$. The finite chain results differ by an end-to-end transfer of two electrons. For the periodic chains, $\times$, *triangles*, *squares*, *stars*, and $+$ mark results for the integer $\tilde{n}$ equal to 0, 2, -2, 4, and -4, respectively. The *dashed straight lines* are linear approximations to the infinite-chain results

where $\bar{\mu}_0$ represents some reference value and the integer $\tilde{n}$ is arbitrary, but related to the orbital phases. On the other hand, for an extended finite system the dipole moment per unit can be written as

$$\bar{\mu} = \mu_C + Q_R \cdot a, \tag{18.28}$$

where the charge Q_R is, in principle, arbitrary although it can change only by an integer. This theoretical limitation on the terminal charge has been termed charge quantization [10] and it has been found in numerical studies [22].

A highly relevant question is whether the properties of the infinite periodic system and those of the large finite system coincide. In order to address that issue we have studied a simple model linear chain [8, 16] with alternating A and B atoms, a lattice constant a, and alternating bond lengths $\frac{a}{2} \pm 2u$. We use a basis set of two AOs per atom and assume that there are 4 electrons per repeat unit. All elements of the Fock and overlap matrices are parametrized as described in detail in [8], where a further description of the model parameters is given. The advantage of studying a model, instead of a real system, is that one can eliminate truncation errors due to summations in real and reciprocal space and to basis set expansions. Furthermore, it becomes possible to study large finite systems without prohibitive computational demands.

We studied both large finite systems and infinite periodic systems as a function of field. In order to study how the properties of the infinite periodic system depend upon the integer $\tilde{n}$ in Eq. (18.27) the orbital phases were modified by hand. For the large finite system the Fock matrix elements of AOs near the terminations were modified in order to vary the terminal charge Q_R in Eq. (18.28).

For the present purpose, the most important results of our model calculations are reproduced in Fig. 18.4 where the optimized lattice constant a is shown as a function of the field E. For other properties, please consult [8]. From the results of Fig. 18.4 we emphasize two findings. First, there are two sets of finite chain results which differ by an end-to end transfer of two electrons. These correspond

to the infinite periodic chain calculations with $\tilde{n}$ equal to 0 and -2. The important point is that the finite chain and infinite periodic chain results lie on top of one another, which means that the properties do coincide. Second, different values of $\tilde{n}$, or Q_R, lead to different results. For the infinite periodic system the integer $\tilde{n}$ exactly mimics the effect of the terminal charge, Q_R, for the large finite system. We hasten to add that the calculations are several orders of magnitude faster for the former system than for the latter. Finally, the variation in a, as a function of E, is what causes all other properties to depend upon the terminal charge. This was also demonstrated in [8, 16], where it was shown that the dependence upon terminal charge is eliminated by keeping a fixed.

The converse piezoelectric effect describes the relative change in the lattice constant as a function of the external electric field. This can be quantified through a converse piezoelectric coefficient,

$$d = \left[\frac{1}{a}\frac{\partial a}{\partial \lambda}\right]\Bigg|_{\lambda=0}, \tag{18.29}$$

where λ can be either the field strength, E, or the potential drop over one unit cell, $V = E \cdot a$. It turns out to make an important difference which of the two is used as will be seen below. In order to determine d for the present model, we expand the total energy per unit cell to second order in the lattice constant, a, the internal coordinate, u, and λ about the field-free optimum geometry (indicated by subscript 0 on a and u),

$$\begin{aligned}
\bar{E}_{\text{tot}} &\equiv \bar{E}_{\text{tot}}(a, u, \lambda) \\
&\simeq \bar{E}_{\text{tot},0} + \lambda\frac{\partial \bar{E}_{\text{tot}}}{\partial \lambda} + \frac{1}{2}(a-a_0)^2\frac{\partial^2 \bar{E}_{\text{tot}}}{\partial a^2} \\
&\quad + \frac{1}{2}(u-u_0)^2\frac{\partial^2 \bar{E}_{\text{tot}}}{\partial u^2} + (u-u_0)(a-a_0)\frac{\partial^2 \bar{E}_{\text{tot}}}{\partial u \partial a} \\
&\quad + \frac{1}{2}\lambda^2\frac{\partial^2 \bar{E}_{\text{tot}}}{\partial \lambda^2} + \lambda(a-a_0)\frac{\partial^2 \bar{E}_{\text{tot}}}{\partial \lambda \partial a} + \lambda(u-u_0)\frac{\partial^2 \bar{E}_{\text{tot}}}{\partial \lambda \partial u}.
\end{aligned} \tag{18.30}$$

All partial derivatives in the above equation are evaluated at a_0, u_0 and $\lambda = 0$. If λ is the field, then $\frac{\partial E_{\text{tot}}}{\partial \lambda} = -\mu$ and, thus, $\frac{\partial^2 \bar{E}_{\text{tot}}}{\partial \lambda \partial a}$ will depend on $\tilde{n}$. In fact, this is the only term on the right hand side in which this integer explicitly appears. On the other hand, if λ is the voltage, V, then $\tilde{n}$ will not appear at all because μ is replaced by μ/a. Setting $\lambda = E$, we may differentiate the right-hand side of Eq. (18.30) with respect to a and u to determine the optimized structure for a given field. This yields

$$\begin{aligned}
a(E) &= a_0 + E\left[\frac{\partial^2 \bar{E}_{\text{tot}}}{\partial E \partial u}\frac{\partial^2 \bar{E}_{\text{tot}}}{\partial u \partial a} - \frac{\partial^2 \bar{E}_{\text{tot}}}{\partial E \partial a}\frac{\partial^2 \bar{E}_{\text{tot}}}{\partial u^2}\right] \\
&\quad \times \left[\frac{\partial^2 \bar{E}_{\text{tot}}}{\partial a^2}\frac{\partial^2 \bar{E}_{\text{tot}}}{\partial u^2} - \left(\frac{\partial^2 \bar{E}_{\text{tot}}}{\partial u \partial a}\right)^2\right]^{-1}, \\
u(E) &= u_0 + E\left[\frac{\partial^2 \bar{E}_{\text{tot}}}{\partial E \partial a}\frac{\partial^2 \bar{E}_{\text{tot}}}{\partial u \partial a} - \frac{\partial^2 \bar{E}_{\text{tot}}}{\partial a^2}\frac{\partial^2 \bar{E}_{\text{tot}}}{\partial E \partial u}\right] \\
&\quad \times \left[\frac{\partial^2 \bar{E}_{\text{tot}}}{\partial a^2}\frac{\partial^2 \bar{E}_{\text{tot}}}{\partial u^2} - \left(\frac{\partial^2 \bar{E}_{\text{tot}}}{\partial u \partial a}\right)^2\right]^{-1}
\end{aligned} \tag{18.31}$$

from which we can determine the converse piezoelectric coefficient, d. The latter can, then, be written in a form similar to Eq. (18.27)

$$d = d_0 - \tilde{n} \cdot d_1, \tag{18.32}$$

where we have used the fact that $\frac{\partial^2 \bar{E}_{\text{tot}}}{\partial E \partial a}$ is directly proportional to $\tilde{n}$. The straight dashed lines in Fig. 18.4 show the curves for

$$a(E) = a_0(1 + d \cdot E) \tag{18.33}$$

with d calculated from Eq. (18.32). Since the several straight lines have different slopes it is clear that the value of the (bulk) lattice constant depends on the surfaces/terminations. Due to coupling between a and u the bond length alternation (not shown) depends upon the surfaces as well. Finally, the close fit of the dashed lines to the 'exact' numerical results in Fig. 18.4 shows that the approximation of Eq. (18.33) is quite reasonable for the fields considered in this model study.

18.3.2 A Real System

The results of the model calculations suggest that the converse piezoelectric effect contains a non-negligible contribution from the surface charges. However, the model was not designed to represent any real system and, accordingly, it is possible that this contribution is overestimated. It is, therefore, relevant to study a real material.

We chose to consider the so-called layered perovskites $R_2Ti_2O_7$ with R being Sm or Gd [23]. Although these systems possess many structural parameters, we reduced these to the two that are closely related to the spontaneous polarization (i.e. the permanent dipole moment per unit volume) that these materials possess. One of the two parameters is the lattice constant, a, in the direction of the spontaneous polarization, and the other, u, describes the distortion from the centrosymmetric structure at which the spontaneous polarization would vanish. All other structural parameters were relaxed to the optimized field-free value for a given a and u. For further details of the calculations, please consult [23].

Assuming that the 2nd order expansion on the right hand side of Eq. (18.30) is sufficiently accurate in this case as well, we can calculate all required quantities approximately from the total energy and dipole moment as a function of a and u using finite-differences (see [23]). The results for the (converse) piezoelectric parameters in Eq. (18.32) are $d_0 = 9.9$ (7.9) 10^{-10} $(\text{V/cm})^{-1}$ and $d_1 = -7.5$ (-7.0) 10^{-11} $(\text{V/cm/(surface cell)})^{-1}$ for R = Sm (R = Gd). Even if these numbers should be taken with some caution due to the finite difference approximations involved in their determination, they do indicate a non-negligible effect of the surfaces. Of course, d_1 must be multiplied by the number of electrons per surface unit cell that are transferred from one surface to the opposite one due, for example, to chemical modifications. For a transfer of ± 2 electrons/(surface cell), our results above correspond to a change in the converse piezoelectric coefficient of about 20 % which is an effect that should be detectable experimentally.

18.3.3 Measuring Surface-Dependent Converse Piezoelectricity

In order to measure the converse piezoelectric coefficient we propose the following approach using, for illustrative purposes, the linear chain shown in Fig. 18.1. Our approach guarantees that surface effects, other than those discussed above, are eliminated as soon as the samples are large enough to reach the thermodynamic limit. We also do not need to assume that the surface regions have an almost vanishing spatial extent. Finally, this approach can be used to separate the coefficients d_0 and d_1 as well as to measure the direct piezoelectric effect.

Let us consider a set of samples that have the same terminations but different lengths. Thus, they differ only in the size of the central region (at least, to a good approximation for a large system). When these samples are exposed to an electrostatic field their length, l, will change. Since the termination regions may respond differently than the central region

$$\begin{aligned} l &= l_R + l_L + K_C \cdot a \\ &= l_{R0}(1 + d_R E) + l_{L0}(1 + d_L E) + K_C a_0 (1 + d_C E), \end{aligned} \tag{18.34}$$

where d_X is the converse piezoelectric coefficient for region X and the subscript 0 again indicates the field-free value. We seek the converse piezoelectric coefficient d_C. To that end it is convenient to re-write Eq. (18.34) as

$$l = l_0(1 + d_C E) + l_{R0}(d_R - d_C)E + l_{L0}(d_L - d_C)E, \tag{18.35}$$

whereas l_{R0} and l_{L0} are independent of the size of the sample, l_0 is not. Thus, a plot of l as a function of l_0 for samples of different lengths, but subject to the same field, will give a straight line with slope $(1 + d_C E)$. Ultimately, by repeating the whole process for another set of samples with different terminal charges, it is possible to separate the bulk converse piezoelectric coefficient into a reference value and a surface-dependent term as done in Eq. (18.32).

18.4 Metals

So far we have assumed that the occupied and unoccupied orbitals are separated by a finite gap, i.e., that the system is insulating or semiconducting. It is natural to ask whether it is possible to treat a metallic system with the approaches presented here. As it turns out, there are aspects in which a metal is fundamentally different from a semiconductor, or an insulator, that make it impossible to do so.

First, we discuss the infinite periodic case. In principle, for a metal the electronic part of the dipole moment per unit could be formulated using an expression like that of Eq. (18.8). The only difference would be that the sum over occupied orbitals would not include the complete band, i.e., the j summation in Eq. (18.8) would have an upper limit that is k-dependent. Although the substitution of Eq. (18.16) is still possible, this means that the conditions of Eqs. (18.17) and (18.18) cannot be used

to fix $\bar{\mu}_{ze}$ (up to an integer multiple of the lattice constant). As a result the electronic dipole moment per unit cell given by Eq. (18.8) may take any value.

A similar result is obtained when attempting to use Wannier functions [see Eq. (18.12)] to calculate $\bar{\mu}_{ze}$. That approach is not applicable because Wannier functions cannot be constructed for fractionally occupied bands.

One could try to calculate $\bar{\mu}_{ze}$ from Eq. (18.7). For a semiconductor/insulator the $\underline{\underline{S}}^{\pm}$ matrices contain K blocks of dimension $B \times B$ (B is the number of occupied bands) with non-vanishing matrix elements between band orbitals of neighboring k values [see Eq. (18.9) and Fig. 18.3] whereas all other matrix elements are zero. Thus, $\det(\underline{\underline{S}}^{\pm})$ will equal the product of the K determinants of each block. For a metallic system, since there are partially occupied bands, some of these square blocks will become rectangular and $\det(\underline{\underline{S}}^{\pm})$ will vanish. Thus, as above, $\bar{\mu}_{ze}$ can take any value.

Next we turn to the case of a very large finite system, for which the energy gap between occupied and unoccupied orbitals approaches zero as the system size grows. As pointed out by Resta [24], one can construct localized orbitals for such small band gap semiconductors even though it is not possible to do so for a metal. Indeed, in our model zero field calculations these long finite chains behaved similarly to ordinary semiconductors. However, as soon as a field was turned on, it became no longer possible to identify a central region even for the longest chains, which were more than one order of magnitude longer than those discussed earlier in Sect. 18.3.1). Moreover, the dipole moment per unit increased supralinearly with chain length. Upon fitting the latter property to a power series in the applied field,

$$\bar{\mu} = \bar{\mu}^{(0)} + \bar{\alpha}E + \frac{1}{2}\bar{\beta}E^2 + \frac{1}{6}\bar{\gamma}E^3 + \cdots, \tag{18.36}$$

we found that the polarizability per unit, $\bar{\alpha}$, as well as the hyperpolarizabilities per unit, $\bar{\beta}$ and $\bar{\gamma}$, also grow rapidly with system size in accord with the behavior for a perfect metal. Thus, the field causes a charge redistribution throughout the complete system and, as a result, the charge associated with the chosen surface region can take any value.

18.5 Short-Circuited Semiconductor

The results of the last two sections will now be used to study a system ('device') like that of Fig. 18.5. This system contains a semiconductor placed between two metal capacitor plates connected through a metal so that the semiconductor is short-circuited. We assume that there is a non-vanishing polarization **P** inside the semiconductor in the direction perpendicular to the capacitor plates. **P** is related to the dipole moment per unit cell through

$$\mathbf{P} = \frac{1}{\Omega}\bar{\boldsymbol{\mu}} \tag{18.37}$$

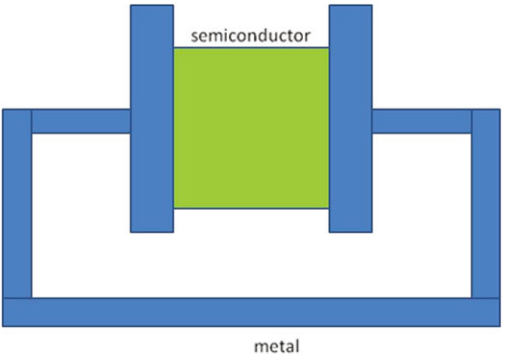

Fig. 18.5 Schematic representation of a semiconductor short-circuited by two metal plates connected to one another via a metal

with Ω being the unit cell volume. Inside the semiconductor, assuming that the polarization is uniform, there will be an electrostatic field

$$E_0 = -4\pi P. \tag{18.38}$$

When the semiconductor is free-standing, this field will give rise to a potential drop from one side to the other. However, when the semiconductor is short-circuited, as in Fig. 18.5, there will be no potential drop and, instead, the electrostatic field of Eq. (18.38) will induce a compensating external uniform electrostatic field $E = -E_0$ originating from charge redistribution within the metal.

For the semiconductor in the(induced) electrostatic field of the metal we may rewrite the total energy of Eq. (18.26) as

$$\bar{E}_{\text{tot}} = \bar{E}_{\text{tot},0} - E\,\Omega\,P. \tag{18.39}$$

Here P is the self-consistent polarization of the semiconductor and E is the self-consistent external electrostatic field of the metal. In this expression we insert the value of $E = -E_0$ determined by Eq. (18.38), with P now being the self-consistent polarization, to obtain

$$\bar{E}_{\text{tot}} = \bar{E}_{\text{tot},0} - 4\pi\,\Omega\,P^2. \tag{18.40}$$

In this derivation, as noted above, we have used the fact that the charge distribution within the metal is completely delocalized and will reorganize to exactly compensate the potential drop over the semiconductor due to the (self-consistent) polarization of the latter. This situation would, clearly, be different if the two metal plates were connected via another semiconductor.

The structural parameters of the short-circuited semiconductor may be determined by minimizing the total energy of Eq. (18.40). However, we shall here determine a simple estimate of the changes in the structure due to the short-circuiting. Thereby, $\bar{E}_{\text{tot},0}$ and P of Eq. (18.40) are both expanded to second order in the two parameters a and u, and the derivatives in the resulting expression are evaluated numerically by finite differences [23]. $\bar{E}_{\text{tot},0}$ depends on both the structure and the electronic wavefunctions, and the latter depend on whether the system is short-circuited or not. As one approximation, we shall ignore this difference, whereby all quantities entering the second order expansion can be extracted from calculations without

Table 18.1 The relative change in the optimized lattice constant, i.e., the strain δ, for the device of Fig. 18.5 and the two systems of Sect. 18.3.2

$\tilde{n}$	Sm	Gd
−2	0.075	−0.257
−1	−0.032	−0.030
0	−0.057	−0.056
1	−0.069	−0.069
2	−0.076	−0.077

inclusion of an electrostatic field. As a further approximation, we shall assume that this second order expansion is sufficiently accurate to describe the structural changes due to short-circuiting even if these are far from being infinitesimally small.

The relative change in the optimized lattice constant with respect to the isolated chain value a_0, i.e., the strain

$$\delta = \frac{a - a_0}{a_0}, \tag{18.41}$$

is given in Table 18.1 for different values of $\tilde{n}$. These results demonstrate a couple of points. First, there is a highly non-trivial dependence on $\tilde{n}$. Second, the structural changes are significant, though not large; they vary up to about 8 percent. A single exception is found in the case of the Gd-based compound for $\tilde{n} = -2$. The reason for this exception is to be found in the highly non-linear dependence of δ on $\tilde{n}$ which, in turn, is associated with a near-cancellation of terms in the denominator [cf. Eq. (18.31)] of the expression for a.

As emphasized above, our approach is based on several approximations. Thus, the results of Table 18.1 may be considered only as a rough estimate for the effects of short-circuiting.

18.6 Summary

In this work we have studied properties of large regular systems. Such systems contain a large number of regularly arranged, identical units and only in the surface regions may there be deviations from this regularity. We have focused on a single property, namely the converse piezoelectric effect, which describes how the spatial extensions of the system change upon application of an external electrostatic field.

A central result of our work is that the quantitative converse piezoelectric coefficient depends on the surfaces of the system, in particular on the surface charge. This dependence does not vanish in the limit of an almost infinitely large system, but the coefficient also cannot take on an arbitrary numerical value. It turns out that the surface effect can be accounted for in theoretical studies which assume that the system is infinite and periodic, even though there are no surfaces in that case. The surfaces have a finite effect on bulk properties, independent of system size, and despite the fact that they have essentially vanishing volume compared to the total volume in a large sample.

We also sketched our theoretical approach for including an external electrostatic field in calculations on infinite periodic systems, as is necessary to determine the converse piezoelectric coefficient. This approach involves development of an appropriate dipole moment operator containing both 'charge' and 'current' terms. It also leads to the introduction of an (unknown) integer multiple of the lattice constant into the phases of the crystal orbitals. Many details are non-trivial and could not be discussed here, but for a complete and more thorough description the interested reader is referred to [16].

Results are shown from earlier model calculations on semiconductor chains that verify and illustrate our theoretical treatment. More recent calculations for real materials are included as well. They involve some approximations but, nonetheless, confirm that the surface effect is significant, though not very large for the particular materials studied.

The infinite periodic treatment we have presented is applicable only for semiconductors and insulators. It is shown to be inapplicable to metals because the electronic charge cannot be localized to a central region and, by the same token, the electronic dipole moment may take any arbitrary value. For a large finite system the electronic dipole moment grows supralinearly with chain length.

Based on our analysis of a metallic system we studied an idealized device where a semiconductor (or insulator) is sandwiched between two metallic capacitor plates and short-circuited by connecting the plates through the metal. If the free-standing semiconductor is spontaneously polarized (i.e. has a permanent dipole moment) it will have an associated internal electric field. When attached to the metal the latter will respond by creating an (external) field that exactly compensates the internal one. The external field, in turn, will induce a change in the polarization of the semiconductor, and so forth. This leads ultimately to a total energy for the semiconductor that depends upon the square of its self-consistent polarization. Using the results for the real material, we were able to estimate the relative change in the lattice constant, i.e. the strain, due to short-circuiting the semiconductor.

Acknowledgements One of the authors (MS) is very grateful to the International Center for Materials Research, University of California, Santa Barbara, for generous hospitality. Another author (JV) is very grateful to CONACYT, Mexico, and DAAD, Germany, for financial support. Moreover, this work was supported financially by the German Research Council (DFG) through project Sp439/37. We thank Adlane Sayede, Université Lille Nord de France, France, for the ab initio results behind our discussion in Sect. 18.3.2 and Stanislaw Krukowski, Polish Academy of Sciences, Warsaw, Poland, for discussions about the system of Sect. 18.5.

References

1. Woo JWF (1971) Phys Rev B 4:1218
2. Martin RM (1972) Phys Rev B 5:1607
3. Martin RM (1972) Phys Rev B 6:4874
4. Woo JWF, Landauer R (1972) Phys Rev B 6:4876
5. Nelson DF, Lax M (1976) Phys Rev B 13:1785

6. Kallin C, Halperin BI (1984) Phys Rev B 29:2175
7. Tagantsev AK (1986) Phys Rev B 34:5883
8. Springborg M, Tevekeliyska V, Kirtman B (2010) Phys Rev B 82:165442
9. Vanderbilt D, King-Smith RD (1993) Phys Rev B 48:4442
10. Kudin KN, Car R, Resta R (2007) J Chem Phys 127:194902
11. Resta R (1994) Rev Mod Phys 66:899
12. King-Smith RD, Vanderbilt D (1993) Phys Rev B 47:1651
13. Kirtman B, Gu FL, Bishop DM (2000) J Chem Phys 113:1294
14. Springborg M, Kirtman B, Dong Y (2004) Chem Phys Lett 396:404
15. Springborg M, Kirtman B (2011) Theor Chem Acc 130:687
16. Springborg M, Kirtman B, Dong Y, Tevekeliyska V (2012) AIP Conf Proc 1461:116
17. Bishop DM, Gu FL, Kirtman B (2001) J Chem Phys 114:7633
18. Springborg M, Kirtman B (2007) J Chem Phys 126:104107
19. Springborg M, Kirtman B (2008) Phys Rev B 77:045102. Erratum, M. Springborg and B. Kirtman, Phys. Rev. B, 77, 209901 (2008)
20. Springborg M, Kirtman B (2009) Can J Chem 87:984
21. Springborg M, Tevekeliyska V, Kirtman B, Champagne B, Dong Y (2010) Z Phys Chem 224:617
22. Springborg M, Kirtman B (2008) Chem Phys Lett 454:105
23. Sayede A, Bruyer E, Springborg M (2012) Phys Rev B 86:125136
24. Resta R (2002) J Phys Condens Matter 14:R625

Part IV
Structure and Processes in Biosystems

Chapter 19
Analysis of Water Molecules in the Hras-GTP and GDP Complexes with Molecular Dynamics Simulations

Takeshi Miyakawa, Ryota Morikawa, Masako Takasu, Akira Dobashi, Kimikazu Sugimori, Kazutomo Kawaguchi, Hiroaki Saito, and Hidemi Nagao

Abstract In the Hras-GTP and GDP complexes, the coordination bonds between Mg^{2+} and oxygen atoms are very important. In this study, we use AMBER03 and our calculated force field parameters, and perform MD simulations of Hras-GTP and GDP complexes with water solvents. It is shown that the number of water molecules in the first hydration sphere is larger in GDP than in GTP. The duration time and the direction of water molecules in the first hydration sphere in GTP is not so different from those in GDP. It is shown that water molecules are distributed evenly around PG, although they are not distributed evenly around PB. This difference can be the reason why the hydrolysis of GTP in Hras-GTP is easier than the hydrolysis of GDP in Hras-GDP.

19.1 Introduction

Hras is a product of proto-oncogene *Hras*, and is included in the signaling process to induce the cell division and cell differentiation. Hras is one of G-proteins, which act as molecular switch.

In inactive state, Hras forms a complex with GDP (guanosine diphosphate). Hras is in inactive state if Hras is in non-cancerous cell and if cell division is not needed. When EGF (epidermal growth factor) binds EGFR (epidermal growth factor receptor), the signal of cell division and differentiation propagates to Hras. When the signal reaches Hras, GEF (guanine nucleotide exchange factor) binds Hras. This promotes the dissociation of GDP from Hras. Because the concentration of GTP (guanosine triphosphate) is much higher than the concentration of GDP in cytoplasm, active Hras-GTP complex is made. Because Hras-GTP has higher affinity to Hras binding protein than Hras-GDP, the signal of cell division and cell differentiation propagates to nuclei through the path including the Hras binding protein. When the signal of cell division and cell differentiation reaches nuclei, the expression of genes which are coding the protein needed for cell division and cell differentiation

T. Miyakawa (✉)
School of Life Sciences, Tokyo University of Pharmacy and Life Sciences, 1432-1 Horinouchi, Hachioji, Tokyo 192-0392, Japan
e-mail: takeshi@toyaku.ac.jp

M. Hotokka et al. (eds.), *Advances in Quantum Methods and Applications in Chemistry, Physics, and Biology*, Progress in Theoretical Chemistry and Physics 27,
DOI 10.1007/978-3-319-01529-3_19,

are enhanced. In non-cancerous cell, GTP in Hras-GTP complex is hydrolyzed to GDP in appropriate time. When inactive Hras-GDP complex is made, the propagating of the signals of cell division and cell differentiation is stopped [1].

To study the hydrolysis of GTP in Hras-GTP complex, we investigate the structure of Hras-GTP. In about 30 % of human cancer cells, at least one of Ras family, which consists of Hras, Kras and Nras, is mutated [2]. The mutated Hras protein has different structure from wild type Hras. This change of structure suppresses the hydrolysis of GTP in Hras-GTP complex. As a result, the mutated Hras-GTP sends continuously signals of cell division and cell differentiation [3]. The structure of Hras-GTP complex is important for the hydrolysis of Hras-GTP. The suppression of the hydrolysis of GTP is important to generate the tumor in the cell with the mutated Hras-GTP complex. Investigating the structure of Hras-GTP complex is important in order to prevent mutated Hras-GTP complex generating the tumor.

In 1990, the structures of Hras-GTP complex [4] and Hras-GDP complex [5] were investigated by X-ray crystallography analyses. These analyses showed that the structures of Hras-GTP complex and Hras-GDP complex are different in switch I, which consists of 30–38 residues, and in switch II, which consists of 60–72 residues.

In order to understand the mechanism of the hydrolysis of GTP in Hras-GTP complex, we consider the role of water molecules in GTP hydrolysis by the analysis of the position and direction of water molecules. The reaction mechanism of GTP hydrolysis is classified mainly in two types. One is that the P–O bond is cleaved after the attack of OH^-. The other is that the P–O bond is cleaved and the water molecule attacks the intermediate of hydrolysis. In order to know which mechanism is preferred in Hras complex, we compare the positions of water molecules around GTP and GDP. If some differences are found, the former mechanism is preferred.

While some researches suggest associative transition states [4, 6–12], other researches suggest mostly dissociative transition states [13–24]. We focused on the orientation of water instead of OH^- because most of these researches suggest that GTPase catalyzes GTP hydrolysis reactions by neutralizing the negative charge development at β- or γ-phosphate of GTP and by correct positioning of the nucleophilic water molecule *via* a conserved Gln residue in the switch II region. Because oxygen atoms in γ-phosphate of GTP are not protonated in Hras-GTP complex, a water molecule attacks γ-phosphate in either case of dissociative mechanism or associative mechanism.

In fact, the MD simulations of these complexes in water solvent have been performed in the former studies by several scientists [25–29]. In those studies, some calculated the potential parameters with a small basis set [25, 26]. Others did not write the used parameters in detail in their paper [27, 28]. Still others used the potential parameters of guanosine nucleotide calculated in water, not in Hras protein complex [29].

Using the parameters in AMBER03 [30] and the parameters calculated by us [31], we performed MD simulations of Hras-GTP and Hras-GDP complexes in water solvent. From the trajectories of MD simulations, we analyzed the position and direction of water molecules.

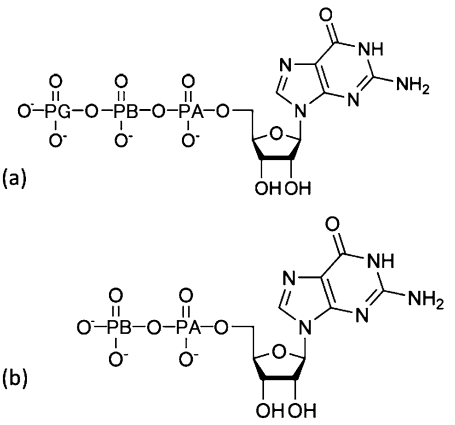

Fig. 19.1 The chemical structure of guanosine triphosphate, GTP (**a**), and of guanosine diphosphate GDP (**b**). The identification of the phosphorus atom is explicitly indicated in each chemical structure

19.2 Method

19.2.1 MD Simulation

In Fig. 19.1, we show the chemical structures of GTP (a) and GDP (b). PA is the phosphorus atom nearest to the guanosine in GTP. PB is the second nearest phosphorus atom and PG is the third nearest phosphorus atom. In GDP the same identification is used.

We use the structures of PDBID:121P determined by X-ray crystallography for GTP and PDBID:1Q21 determined by X-ray crystallography for GDP as initial states. Because 121P contains the GCP, which is the slowly hydrolyzable GTP analogue, we start with GCP and substitute C atom in GCP to O atom in order to change GCP to GTP. We use TIP3P model for water molecules [32]. We add counterions to the system in order to neutralize the total charge of the system. For bonds containing hydrogen atom, SHAKE algorithm [33] is used. The energy of the system is minimized. We heat the temperature of the solvent water to 300 K under *NPT* condition, while we constrain the Hras, GTP/GDP and crystallization water by harmonic force with 50 kcal/mol. The harmonic constraints are taken off gradually at 300 K. Without harmonic constraints, the system is equilibrated at 300 K for 500 ps under *NPT* condition. We used Langevin thermostat [34, 35] for temperature coupling and Berendsen's method [36] for pressure coupling. MD simulations are performed with the time step 1.0 fs.

19.2.2 Analysis

We calculate the radial distribution function (RDF) of water molecules with respect to the phosphorus atoms in guanine nucleotides (GTP, GDP) of the Hras-GTP and Hras-GDP complexes. We define the first hydration radius as the distance which

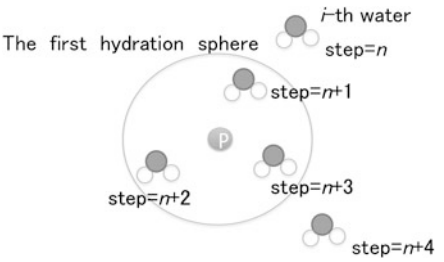

Fig. 19.2 The schematic picture of snap shots of from step $= n$ to step $= n + 4$ of i-th water molecule and the first hydration sphere

gives the local minimum of RDF between the first peak and the second peak. We also define the first hydration sphere as the sphere whose radius is the first hydration radius and whose center is the position of the phosphorus atom.

Here, we explain how to estimate the duration time of the i-th water molecule in the first hydration sphere as shown in Fig. 19.2. The snap shot of trajectories is recorded for every time interval $\Delta_{\text{snap\_shot}}$. At step $= n$ and $n + 4$, the i-th water is outside the first hydration sphere. From step $= n + 1$ to $n + 3$, the i-th water is inside the first hydration sphere. When the i-th water is inside the first hydration sphere in two successive snap shots, we assume that the i-th water stayed inside the first hydration sphere during the intervals. In this case, the i-th water is inside the first hydration sphere from step $= n + 1$ to step $n + 3$. We assume the entrance time as step $= n + 0.5$ and the leaving time as step $= n + 3.5$. We estimate the duration time as $3\Delta_{\text{snap\_shot}}$.

We define the occurrence ratio of duration time of water molecules in the first hydration sphere. The occurrence ratio is proportional to the number of events with corresponding duration time, when an event starts with the entrance of water molecule in the first hydration sphere and stops with the leaving the sphere. Here, the number of events are divided by the summation of events throughout the simulation. This divided number is the occurrence ratio of events with corresponding duration time.

19.3 Results and Discussion

We check the averaged structures and fluctuations throughout the MD simulations of Hras-GTP and Hras-GDP complexes, although these data are not shown in this paper.

Averaged structures throughout the MD simulations of Hras-GTP and Hras-GDP complexes are different at the switch I and the switch II regions. In particular, as shown in crystal structures [4, 5] and shown in the paper of MD simulations by Kobayashi et al. [29], α helix in switch II of Hras-GDP complex is shorter than α helix of Hras-GTP complex.

We compare the fluctuations of structures of Hras-GTP and Hras-GDP complexes by performing PCA (principal component analysis) in switch I and II regions. The fluctuations of structures of Hras-GDP are larger than Hras-GTP around

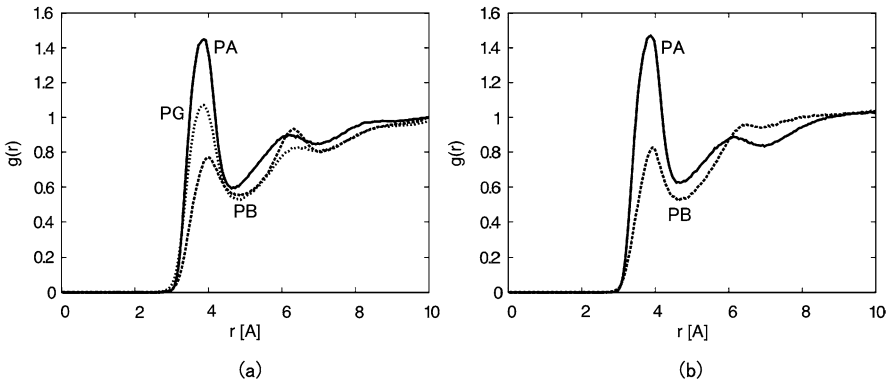

Fig. 19.3 The radial distribution functions of water molecules with respect to the phosphorus atoms in GTP (**a**), and in GDP (**b**)

Table 19.1 The first hydration radius with respect to phosphorus atom in guanosine nucleotide and the averaged number of water molecules in the first hydration sphere

Guanosine nucleotide	Phosphorus atom	Radius (Å)	Averaged number of water
GTP	PA	4.63	0.91
GTP	PB	4.88	0.65
GTP	PG	4.88	0.90
GDP	PA	4.68	3.23
GDP	PB	4.63	1.73

THR35 in switch I, as shown in the paper of MD simulations by Kobayashi et al. [29], because THR35 binds Mg coordinately in the Hras-GTP complex although THR35 does not bind Mg coordinately in the Hras-GDP complex.

We calculate the radial distribution function (RDF) of water molecules with respect to the phosphorus atoms in guanine nucleotides (GTP, GDP) of the Hras-GTP and Hras-GDP complexes as shown in Fig. 19.3.

In Table 19.1, we show the values of hydration radius, which are defined in Sect. 19.2.2. The values are from 4.63 Å to 4.88 Å. The averaged number of water molecules in the first hydration sphere are calculated and summarized in Table 19.1. It is shown that the averaged number around phosphorus atoms in GDP has larger value than those in GTP. The hydration of the phosphorus atoms weaken the Coulomb interaction between phosphorus atoms and atoms in the residues around the phosphorus atoms. Thus, the fact that the averaged number around phosphorus atoms in GDP has larger value than those in GTP suggests that GDP dissociates from Hras more easily than GTP. In vital cells, neither GDP nor GTP dissociates from Hras, unless other proteins are connected.

We compare the atomic charges calculated by quantum chemistry in our previous work [31] in the Hras-GTP complex and in the Hras-GDP complex, in order to

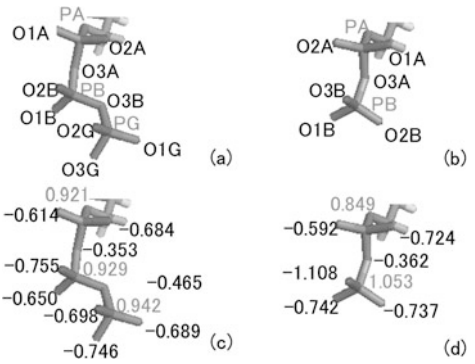

Fig. 19.4 Identification of atoms in molecular structure of GTP (**a**), and of GDP (**b**). The atomic charges in GTP (**c**), and in GDP (**d**) calculated by quantum chemistry in our previous work [31]

confirm that the difference in atomic charges does not cause the larger value of averaged number of water molecules in GDP than in GTP. As is shown in Fig. 19.4, the values of atomic charges in GDP are almost the same in GTP except O3B. One reason why the averaged number of water molecules is larger in GDP than in GTP is that water molecules are less restricted in GDP than in GTP.

In Fig. 19.5, we show the occurrence ratio of duration time of water molecules in the first hydration spheres, which is defined in Sect. 19.2.2. The horizontal axis is the evaluated duration time. The vertical axis is the occurrence ratio of duration time of water molecules, which is defined in Sect. 19.2.2. When duration time is shorter than about 5 ps, the occurrence ratio is proportional to $t^{-1.4}$ in PA, PB and PG. When duration time is longer than about 5 ps, the occurrence ratio does not follow power law, and curves of PA are different from the curves of PB and PG. This suggests that the network of water molecules is conserved in 5 ps.

Next, we consider the reason why the hydrolysis of GTP in Hras-GTP is easier than the hydrolysis of GDP in Hras-GDP, although the duration time is not so different, and the averaged number of water molecules in the first hydration spheres in GDP is larger than in GTP. By analogy of the typical hydrolysis of a ester, the mechanism of hydrolysis can be dissociative when the water molecule attacks from the extension of a O3B-PG line to γ-phosphate. In order to ascertain whether the water molecule attacks from the extension of a O3B-PG line to γ-phosphate, we calculate the angular distribution of water molecules around PG in Hras-GTP and around PB in Hras-GDP. When we calculate the angular distribution of water molecules around PG in Hras-GTP, we define PG as the origin as shown in Fig. 19.6. The O3B-PG line is z axis. The plane which includes PG and which is perpendicular to z axis is the x–y plane. The projection of the PG-O1G line onto the x–y plane is x axis. The angle from the z axis to the j-th water is θ, and the angle from the x axis to the j-th water on the x–y plane is ϕ. In the same manner, when we calculate the angular distribution of water molecules around PB in Hras-GDP, we define PB as the origin. The O3A-PB line is z axis. The plane which includes PB and which is perpendicular to z axis is the x–y plane. The projection of the PB-O1B line onto the x–y plane is x axis.

Figure 19.7 shows the angular distribution of water molecules in the shell with radius from 3.5 Å to 4.0 Å around PG in Hras-GTP (a) and around PB in Hras-

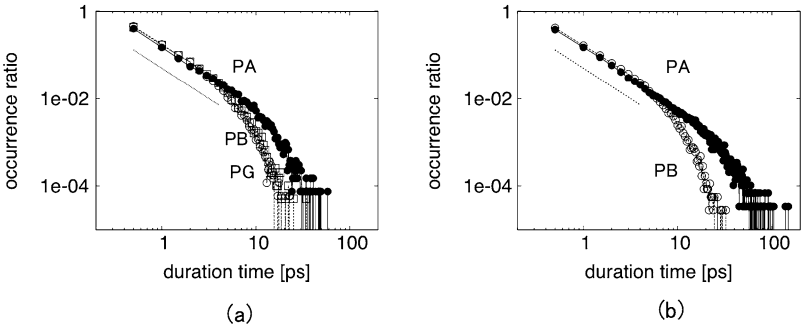

Fig. 19.5 The occurrence ratio of entrance event with corresponding duration time of the water molecules in the first hydration sphere with respect to the phosphorus atoms in GTP (**a**) and in GDP (**b**). *Filled circles* are PA, *open circles* are PB, and *open rectangles* are PG. The *lines* are the guide to the eyes, which are proportional to $t^{-1.4}$

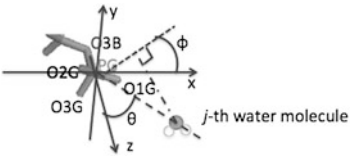

Fig. 19.6 The coordinates used for angular distribution of water molecules around PG in Hras-GTP

GDP (b). The angular distribution of water molecules in Hras-GTP is different from those in Hras-GDP. Water molecules are distributed in $\theta < 30°$ around PG in Hras-GTP although water molecules are not distributed in $\theta < 30°$ around PB in Hras-GDP. Only in the area $\theta \sim 30°, \phi \sim 0°$, the density of water molecules in Hras-GTP is higher than those in Hras-GDP. The hydrolysis of GTP in Hras-GTP is easier than the hydrolysis of GDP in Hras-GDP, although the duration time is not so different, and the averaged number of water molecules in the first hydration spheres in GDP is larger than in GTP. Thus, the fact that the density of water molecules in Hras-GTP is higher than those in Hras-GDP in the area $\theta \sim 30°, \phi \sim 0°$ suggests that the hydrolysis of GTP in Hras-GTP complex can be triggered by the attack of water molecules to γ-phosphate from the direction $\theta \sim 30°, \phi \sim 0°$. This difference of the positions of water molecules between GTP and GDP suggests that the associative transition state is preferred for the hydrolysis.

We also calculate the distribution of the direction of waters. We define the direction of waters by the angle between PG-O(H_2O) line and O(H_2O)-G(H_2O) line, where O(H_2O) is the oxygen atom of the water molecule and G(H_2O) is the center of mass of the water molecule. Figure 19.8 shows the direction angle of water molecules averaged over the volume element such that $r_0 < r < r_1, \theta_0 < \theta < \theta_0 + \Delta\theta, \phi_0 < \phi < \phi_0 + \Delta\phi$, where $r_0 = 3.5$ Å, $r_1 = 4.0$ Å, and $\Delta\theta = \Delta\phi = 9°$. The values of averaged direction of water molecules are distributed from 40° to 50°. In detail, at the area $\theta \sim 30°, \phi \sim 0°$, the averaged directions in Hras-GTP are distributed also in direction angle $< 50°$ as shown by the complicated contour of 50° in Fig. 19.8(a), although the averaged directions in Hras-GDP are distributed in di-

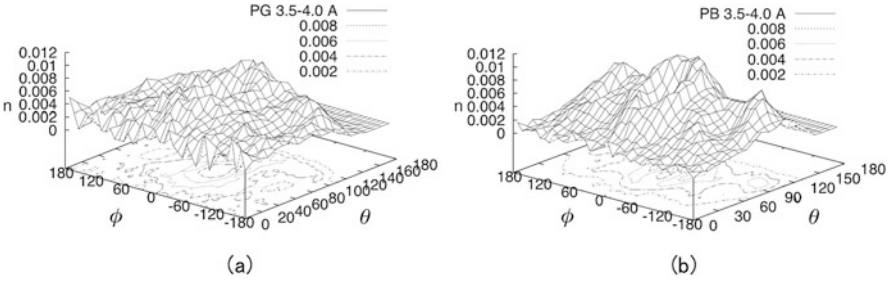

Fig. 19.7 The angular distribution of used for angular distribution of water molecules in the shell with radius from 3.5 Å to 4.0 Å around PG in Hras-GTP (**a**) and around PB in Hras-GDP (**b**)

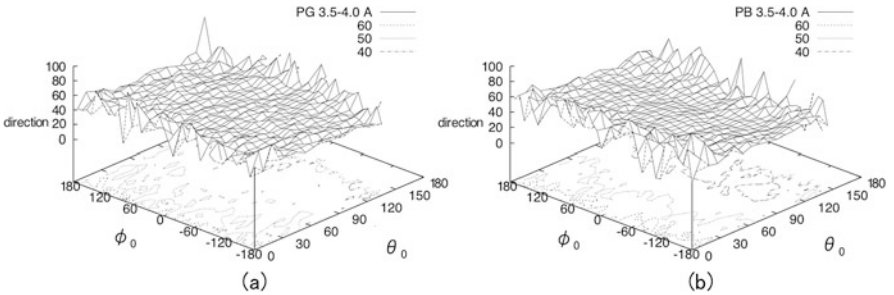

Fig. 19.8 The direction angle of water molecules averaged over the volume element such that $r_0 < r < r_1, \theta_0 < \theta < \theta_0 + \Delta\theta, \phi_0 < \phi < \phi_0 + \Delta\phi$, where $r_0 = 3.5$ Å, $r_1 = 4.0$ Å, and $\Delta\theta = \Delta\phi = 9°$

rection angle $> 50°$ as shown by the simple contour of 50° in Fig. 19.8(b). The direction of water molecules is related to the capability of water molecules sitting on the space restricted by the atoms in the phosphate of guanine nucleotide. This difference of direction angle between in Hras-GTP and in Hras-GDP possibly causes the difference of density at the area $\theta \sim 30°, \phi \sim 0°$. In future work, in order to confirm the relation between the direction of water molecules and the density of water molecules, we need to investigate the restrictions on water molecules around PG in GTP and PB in GDP by the amino acid residues, Mg^{2+}, and crystallization water. And we need to investigate the possible directions of water molecules around PG in GTP and around PB in GDP.

19.4 Summary

Differences of structures between Hras-GTP and Hras-GDP are presented in switch I and II regions. The value of the first hydration radii defined from the RDF of water molecules with respect to phosphorus atoms in GTP and GDP is from 4.63 to 4.88 Å. Averaged number of water molecules in the first hydration sphere with

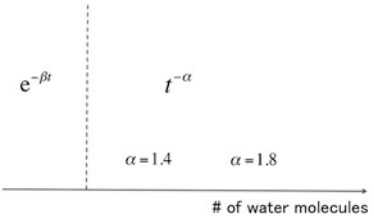

Fig. 19.9 The categories of the occurrence ratio of duration time by the number of water molecules

respect to the phosphorus atoms is larger in GDP than in GTP. Occurrence ratio of duration time is proportional to $t^{-1.4}$ when duration time is less than about 5 ps. PA has a long tail in occurrence ratio of duration time. This suggests that the network of water molecules is conserved in 5 ps. Here, for short-time behaviour, we will explain three cases. (1) When we analyzed the occurrence ratio of duration time of water molecules in the first hydration sphere around atoms in areas in which water molecules rarely come in, we found that the occurrence ratio decay exponentially, (data are not shown). (2) When we analyzed the occurrence ratio of duration time around C_α atoms near the protein surface, we found that the power is about -1.8, and conserved time is about 10 ps or more, (data are not shown). (3) In our case of Fig. 19.5, the occurrence ratio of duration time is proportional to $t^{-1.4}$ when duration time is less than about 5 ps, because the water molecules around GTP or GDP are partially restricted, and the entering and the leaving the area around GTP or GDP are not so rare.

We can categorize them into two: In one category ((1) above), the occurrence ratio of duration time of water molecules in the first hydration sphere is proportional to exponential function, when the number of water molecules is very small. In the other category ((2) and (3) above), the occurrence ratio of duration time is proportional to the power of t, when the number of water molecules is not very small. In detail, the power index is small and conserved time is long when the number of water molecules is large, while the power index is large and conserved time is short when the number of water molecules is small, as is drawn schematically in Fig. 19.9. The water molecules are distributed evenly around PG in GTP although not evenly around PB in GDP. This suggests that the hydrolysis of GTP can be triggered by the attack of water molecule to the γ-phosphate by an appropriate direction. The direction distribution of water molecules around PG in GTP is slightly different from the distribution around PB in GDP. This slight difference in distribution of direction possibly causes the difference in the density distribution of water molecules.

Acknowledgements This work was supported by JSPS KAKENHI Grant Number 24540442. The computations were in part carried out at the Research Center for Computational Science, Okazaki, Japan.

References

1. Alberts B, Johnson A, Lewis J, Raff M, Robertss K, Walter P (2002) Molecular biology of the cell, 5th edn. Garland, New York

2. Downward J (2003) Nat Rev Cancer 3:11–22
3. Goodsell DS (1999) Oncologist 4:263–264
4. Pai EF, Krengel U, Petsko GA, Goody RS, Kabsch W, Wittinghofer A (1990) EMBO J 9:2351–2359
5. Milburn MV, Tong L, deVos AM, Brünger A, Yamaizumi Z, Nishimura S, Kim SH (1990) Science 247:939–945
6. Coleman DE, Berghuis AM, Lee E, Linder ME, Gilman AG, Sprang SR (1994) Science 265:1405–1412
7. Frech M, Darden TA, Pedersen LG, Foley CK, Charifson PS, Anderson MW, Wittinghofer A (1994) Biochemistry 33:3237–3244
8. Glennon TM, Villa J, Warshel A (2000) Biochemistry 39:9641–9651
9. Langen R, Shweins T, Warshel A (1992) Biochemistry 31:8691–8696
10. Privé GG, Milburn MV, Tong L, de Vos AM, Yamaizumi Z, Nishimura S, Kim SH (1992) Proc Natl Acad Sci USA 89:3649–3653
11. Schweins T, Geyer M, Scheffzek K, Warshel A, Kalbitzer HR, Wittinghofer A (1995) Nat Struct Biol 2:36–44
12. Schweins T, Warshel A (1996) Biochemistry 35:14232–14243
13. Maegley KA, Admiraal SJ, Herschlag D (1996) Proc Natl Acad Sci USA 93:8160–8166
14. Admiraal SJ, Herschlag D (1995) Chem Biol 2:729–739
15. Herschlag D, Jencks WP (1989) J Am Chem Soc 111:7587–7596
16. Skoog MT, Jencks WP (1984) J Am Chem Soc 106:7597–7606
17. Allin C, Armadian MR, Wittinghofer A, Gerwert K (2001) Proc Natl Acad Sci USA 98:7754–7759
18. Allin C, Gerwert K (2001) Biochemistry 40:3037–3046
19. Cepus V, Scheidig AJ, Goody RS, Gerwert K (2001) Biochemistry 37:10263–10271
20. Du X, Frei H, Kim SH (2000) J Biol Chem 275:8492–8500
21. Wang JH, Xiao DG, Deng H, Webb MR, Callender R (1998) Biochemistry 37:11106–11116
22. Zhu G, Liu J, Terzyan S, Zai P, Li G, Zhang XC (2003) J Biol Chem 278:2452–2460
23. Cheng H, Sukal S, Deng H, Leyh TS, Callender R (2001) Biochemistry 40:4035–4043
24. Herschlag D, Jencks WP (1986) J Am Chem Soc 108:7938–7946
25. Foley CL, Pedersen LG, Charifson PS, Darden TA, Wittinghofer A, Pai EF, Andersen MW (1992) Biochemistry 31:4951–4959
26. Worth GA, Edge C, Richards WG (1995) J Mol Model 1:123–142
27. Mello LV, van Aalten DMF, Findlay JBC (1997) Protein Eng 10:381–387
28. Futatsugi N, Tsuda M (2001) Biophys J 81:3483–3488
29. Kobayashi C, Saito S (2010) Biophys J 99:3726–3734
30. Duan Y, Wu C, Chowdhury S, Lee MC, Xiong W, Zhang G, Yang R, Cieplak P, Luo R, Lee T, Caldwell J, Wang J, Kollman P (2003) J Comput Chem 24:1999–2012
31. Miyakawa T, Morikawa R, Takasu M, Sugimori K, Kawaguchi K, Saito H, Nagao H (2012) Prog Theory Chem Phys 26:525–543
32. Jorgensen WL, Chandrasekhar J, Madura JD, Impey RW, Klein ML (1983) J Chem Phys 79:926–935
33. Ryckaert J-P, Ciccotti G, Berendsen HJC (1977) J Comput Phys 23:327–341
34. Adelman SA, Doll JD (1976) J Chem Phys 64:2375–2388
35. Grest GS, Kremer K (1986) Phys Rev A 33:3628–3631
36. Berendsen HJC, Postma JPM, van Gunsteren WF, DiNola A, Haak JR (1984) J Chem Phys 81:3684–3690

Chapter 20
Bath Correlation Effects on Inelastic Charge Transport Through DNA Junctions

Tal Simon, Daria Brisker-Klaiman, and Uri Peskin

Abstract The effect of correlations in bath-assisted inelastic transport through DNA molecular junctions is studied. Assigning physical meaning to the correlated bath modes, we examine the relative contributions of different types of nuclear modes to the inelastic transport. In particular, we demonstrate that intra-strand (backbone modes) and inter-strand (Hydrogen bonds) modes have different contributions to the current, and thus can be associated with a measurable phenomenon. This work emphasizes the important effect of bath correlations on quantum transport, as pointed out recently also in the context of electron energy transport in biomolecular environment. The approach presented in this work is complementary to detailed atomistic simulations which account for specific intra-molecular and intermolecular vibrational modes.

20.1 Introduction

The mechanism of charge transport (CT) through DNA has been under intensive study. Much of the work was devoted to photochemical experiments in which charge (hole, typically) is transiently injected into one end of the molecule, and the rate of transport through the molecule is monitored. Most experiments which aim to identify the CT mechanism in DNA focus on the effects of the number of base pairs [1–5], or the temperature [6, 7]. Different mechanisms were attributed to the transport process under different conditions, including tunneling (superexchange), or hopping (kinetic transport) [8–13] in the off-resonant regime, and ballistic or inelastic transport in resonant tunneling [14, 15]. Only few experiments measured directly the single molecule conductance of DNA [4, 6, 16–18] in a molecular junction setup [19, 20], where a molecule is placed between two macroscopic leads and the steady state current is measured. Particularly interesting are experiments in which the connection strategy between the double helix structure and the two electrodes in a junction configuration can be controlled [18].

U. Peskin (✉)
Schulich Faculty of Chemistry, Technion—Israel Institute of Technology, Haifa 32000, Israel
e-mail: uri@tx.technion.ac.il

M. Hotokka et al. (eds.), *Advances in Quantum Methods and Applications in Chemistry, Physics, and Biology*, Progress in Theoretical Chemistry and Physics 27,
DOI 10.1007/978-3-319-01529-3_20,

Our recent theoretical study focused on specific highly ordered DNA sequences and proposed that for some connection strategies the transport may be dominated by coherent ballistic charge transport, whereas for other connection strategies the transport is dominated by inelastic hopping between de-localized orbitals of the double helix structure [14, 15]. The inelastic processes induced by the intra-molecular nuclear modes and/or the solvent environment were modeled by coupling the electronic transport Hamiltonian to a harmonic bath. In Ref. [15] each nucleobase was coupled to a local environment (bath) of nuclear modes, and these local environments were uncorrelated.

In this work we examine the effect of correlations between nuclear baths on the measured current through the molecule. Assigning physical meaning to the correlated bath modes, our theoretical study highlights the relative importance of different nuclear motions to the inelastic transport. In particular, we demonstrate that intra-strand (e.g., backbone) modes and inter-strand (e.g., hydrogen bonds) modes have different effects on the inelastic current.

The paper is organized as follows: In Sect. 20.2 we review the model for hole transport through DNA, based on a tight-binding parameterization of a double helix structure. In Sect. 20.3 our model of correlated baths is introduced and in Sect. 20.4 the current is formulated in terms of a reduced density matrix. Numerical results that illustrate the effect of bath correlations on the inelastic current are given in Sect. 20.5 and analyzed in Sect. 20.6. Conclusions and future perspectives are drawn in Sect. 20.7.

20.2 The Rigid Double Helix Model

Our model for hole transport through DNA is based on a tight-binding ladder molecular Hamiltonian, used in our earlier work [14, 15] on coherent elastic transport in ordered DNA sequences. The model takes explicit account of the double strand nature of the structure, beyond the 1D sequence of base pairs. This level of detail is often unnecessary for simulating transport through DNA [21, 22], but it is essential for modeling different connection strategies between the four terminals of the double strand structure and the electrodes [15, 18]. The model parameterization is based on the work by Voityuk et al. [23–25] for the on-site hole energies and hopping integrals:

$$\hat{H}_M = \sum_{n=1}^{2N} \varepsilon_n d_n^\dagger d_n + \left\{ \sum_{n=1}^{N-1} \alpha_{n,n+1} d_n^\dagger d_{n+1} + h.c. \right\} + \sum_{n=N+1}^{2N-1} \left\{ \alpha_{n,n+1} d_n^\dagger d_{n+1} + h.c. \right\} + \sum_{n=1}^{N} \left\{ \beta_n d_n^\dagger d_{n+N} + h.c. \right\}. \tag{20.1}$$

The operators $d_n^\dagger (d_n)$ represent a creation (annihilation) of a hole at the nth nucleobase site. It is convenient to rewrite the molecular Hamiltonian in terms of the

creation ($a_m^\dagger$) and annihilation (a_m) operators of a single hole in Molecular Orbitals (MOs), $\hat{H}_M = \sum_{m=1}^{2N} \varepsilon_m a_m^\dagger a_m$, where each MO is a superposition of the local nucleobases orbitals, $a_m^\dagger \equiv \sum_{n=1}^{2N} u_{n,m} d_n^\dagger$. Each (many body) molecular eigenvector is then associated with a unique set of hole occupation numbers $\{n_m\}$ ($n_m \in 0, 1$) in the MOs.

In the molecular junction scenario the molecule is coupled to two charge (electronic) reservoirs, which enables flow of holes into and out of the molecule. The coupling between the system and the reservoirs is introduced here by the leads Hamiltonian [26],

$$\hat{H}_{leads} = \hat{H}_R + \hat{H}_L; \qquad \hat{H}_J = \sum_{j_J} \varepsilon_{j_J} b_{j_J}^\dagger b_{j_J} + \left\{ \sum_{j_J} \xi_{j_J} b_{j_J}^\dagger \sum_n \lambda_{n,J} d_n + h.c. \right\}, \tag{20.2}$$

where $b_{j_J}^\dagger$ (b_{j_J}) is the creation (annihilation) operator of a hole at the jth orbital of the Jth electrode. The connection strategy between the double strand structure and the two leads is captured in a matrix $\{\lambda_{n,J}\}$ which obtains the value 1 when the nth site is coupled to the Jth electrode and zero otherwise. The state to state coupling parameters, $\{\xi_{j_J}\}$, are defined by the electrodes spectral densities.

20.3 Correlated Nuclear Baths

Nuclear vibrations of the molecule and its environment are modeled in terms of collections of harmonic baths modes. In our earlier work, the charge at each nucleobase site was coupled to a specific bath representing local vibrations. Here we introduce correlation between the baths by allowing non-local coupling, i.e. groups of modes that are coupled simultaneously to several nucleobase sites. Denoting the number of baths as N_b, and the number of sites, $2N$, the corresponding nuclear Hamiltonian reads,

$$\begin{aligned} \hat{H}_{nuc} &= \sum_{n_b=1}^{N_b} \hat{H}_{n_b}; \\ \hat{H}_{n_b} &= \sum_{j_{n_b}}^{N_{n_b}} \hbar\omega_{j_{n_b}} \left(c_{j_{n_b}}^\dagger c_{j_{n_b}} + \frac{1}{2} \right) + \sum_{j_{n_b}}^{N_{n_b}} \frac{\eta_{j_{n_b}}}{\sqrt{2}} \left(c_{j_{n_b}}^\dagger + c_{j_{n_b}} \right) \sum_{n=1}^{2N} W_{n,n_b} d_n^\dagger d_n \end{aligned} \tag{20.3}$$

and the full Hamiltonian takes the form,

$$\hat{H} = \hat{H}_M + \hat{H}_{leads} + \hat{H}_{nuc}. \tag{20.4}$$

$c_{j_{n_b}}^\dagger$ ($c_{j_{n_b}}$) are the creation (annihilation) operators of a vibration quantum at the jth nuclear mode associated with the n_bth nuclear bath. The microscopic coupling parameters are related to the spectral density of each bath, defined as, $J_{n_b}(\hbar\omega) = 2\pi \sum_{j_{n_b}} \eta_{j_{n_b}}^2 \delta(\hbar\omega - \hbar\omega_{j_{n_b}})$. W_{n,n_b} defines the strength of coupling between the nth nucleobase and the n_bth bath, where the choice $W_{n,n_b} = \delta_{n,n_b}$ defines an uncorrelated bath model, and $W_{n,n_b} = \text{const}$ corresponds to a fully correlated bath. For the

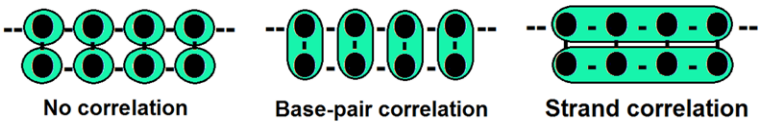

Fig. 20.1 Three types of bath correlations. In each case different sites are grouped into subspaces, where each subspace is coupled to common nuclear bath modes

comparative study below the number of baths was kept equal to the number of nucleobases, $N_b = 2N$, and the coupling strength for each bath was normalized, such that $\sum_{n=1}^{2N} W_{n,n_b} = \sum_{n_b=1}^{2N} W_{n,n_b} = 1$.

The correlation introduced by coupling a group of nuclear modes to a group (electronic subspace) of nucleobase sites is natural to specific types of vibronic coupling in the double stranded DNA. For example, vibrations associated with a particular base-pair (e.g., hydrogen bonds) would be mainly affected by hole hopping from one base-pair to another, and less affected by hole hopping within the base-pair. In contrast, vibrations within a given strand (e.g., backbone vibrations) would be mainly affected by hole hopping from one strand to another, and less affected by hole hopping within the same strand. Below, we focus on these two types of bath correlations (see Fig. 20.1). The first would be termed "base pair" correlation, where each base pair constitutes a molecular subspace which is coupled to a specific bath. The second would be termed "strand" correlation where each strand constitutes a molecular subspace, coupled to a specific bath. These two types of bath correlations are introduced by the matrices $\mathbf{W} = \frac{1}{2}\mathbf{C}^{(2)} \otimes \mathbf{I}^{(N)}$ and $\mathbf{W} = \frac{1}{N}\mathbf{I}^{(2)} \otimes \mathbf{C}^{(N)}$, respectively, where $\mathbf{C}^{(M)}$ is a matrix of size $M \times M$ with $C_{m,n} = 1$, and $\mathbf{I}^{(M)}$ as the $M \times M$ identity matrix.

20.4 Steady State Currents

The current calculations are based on a second order approximation in the coupling to the electronic and nuclear reservoirs [26]. The weak molecule-electrodes coupling regime is fundamentally interesting since the electronic properties of the molecular bridge (e.g. the MOs) are expected to dominate the current. In a conductance experiment, the molecule-electrodes coupling strength can be controlled by the linking group between the electrodes and the DNA strand. The presence of long linkers and the relatively small currents measured (in the 10–100 nA regime [18]), justify our weak coupling assumption. The vibronic coupling was also restricted to the weak coupling limit, thus effects of strong vibronic coupling, such as transport through vibronic pathways [27] or vibrationally induced coherences [28] are excluded, and the focus is on the sole effect of weakly coupled bath modes. We note that the treatment can be extended to include strong coupling to particular nuclear modes by including the relevant nuclear degrees of freedom within the molecular (system) Hamiltonian such that the system eigenstates are vibronic states, but this is beyond our scope in the present work. Within these assumptions each one of the electrodes

(hole reservoirs) and the local nuclear environments (phonon reservoirs) maintains a quasi equilibrium density. Invoking a Markovian second order approximation in the system-reservoirs coupling, and accounting for rapid de-phasing (decay of coherences) between molecular eigenstates [26, 29], the time evolution of the molecular (reduced) density matrix in the presence of interaction with the reservoirs is cast into population transfer rates between the electronic eigenstates of the molecular system. Denoting the hole population at the mth eigenstate as, $P_m(t)$, the following set of equations is obtained [15, 30],

$$\frac{\partial}{\partial t}P_m(t) = \left(\sum_{J\in R,L}\left[k_J^{(ele)}\right]_{m,m'} + \sum_{n_b=1}^{N_b}\left[k_{n_b}^{(nuc)}\right]_{m,m'}\right)P_{m'}(t). \tag{20.5}$$

The rate constants for electrode-induced molecular transitions are given by [15, 26],

$$\left[k_J^{(elec)}\right]_{m,m'} = (1-\delta_{m,m'})\left(\Gamma^{J;e}_{m,m'} + \Gamma^{J;h}_{m',m}\right) - \delta_{m,m'}\sum_{m''\neq m}\left(\Gamma^{J;e}_{m'',m} + \Gamma^{J;h}_{m,m''}\right), \tag{20.6}$$

where $\Gamma^{J;h/e}_{m,m'} = |\sum_n \lambda_{n,J}\langle m|d_n|m'\rangle|^2 J_J(E_{m'}-E_m) f_J^{(h/e)}(E_{m'}-E_m)/\hbar$ are single hole hopping rates out of or into the molecule. These rates depend on the voltage via the Fermi occupation numbers for holes at the two electrodes,

$$f_J^{(h)}(E) \equiv \frac{1}{1+e^{(E-\mu_J)/K_BT}}; \qquad f_J^{(e)}(E) \equiv 1 - f_J^{(h)}(E)$$

and on the microscopic coupling parameters, $\{\xi^2_{j_J}\}$, via the electrode conductance band spectral density [26].

The rate constants for nuclear-induced molecular transitions are given by [15, 30],

$$\left[k_{n_b}^{(nuc)}\right]_{m,m'} = (1-\delta_{m,m'})\left(\Gamma^{n_b;em}_{m,m'} + \Gamma^{n_b;ab}_{m',m}\right) - \delta_{m,m'}\sum_{m''\neq m}\left(\Gamma^{n_b;em}_{m'',m} + \Gamma^{n_b;ab}_{m,m''}\right), \tag{20.7}$$

where $\Gamma^{n_b;em/ab}_{m,m'} = |\langle m|\sum_n W_{n,n_b} d_n^\dagger d_n|m'\rangle|^2 J_{n_b}(E_{m'}-E_m) g^{(em/ab)}(E_{m'}-E_m)/\hbar$ are rates of phonon emission and absorption during the respective molecular transitions. These rates are related to the phonon thermal occupation factors at the respective nuclear reservoir, $g^{(ab)}(\hbar\omega) = \frac{1}{e^{\hbar\omega/K_BT}-1}$; $g^{(em)}(\hbar\omega) = \frac{e^{\hbar\omega/K_BT}}{e^{\hbar\omega/K_BT}-1}$, and they depend on the microscopic vibronic coupling parameters $\{\eta^2_{j_{n_b}}\}$ via the nuclear bath spectral density.

Transient left-to-right currents [31] are associated with the net rate of hole transitions from the left electrode into the molecule. The steady state current is associated with the infinite time limit, and depends explicitly on the steady state populations of the molecular eigenstates (coherences, if present, do not appear in the current formula), i.e. [26]

$$I_{L\to R} = \lim_{t\to\infty}\sum_{m,m'} 2e\left[\kappa_L^{(ele)}\right]_{m,m'} P_{m'}(t) N_m, \tag{20.8}$$

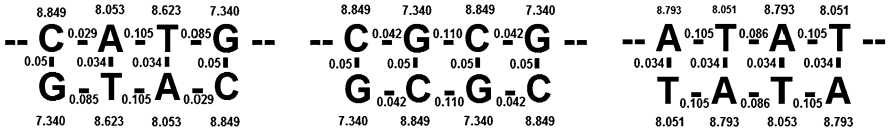

Fig. 20.2 Three types of DNA sequences. Each sequence is represented by a tight binding model Hamiltonian, with on-site hole energies and hopping matrix elements (in eV), taken from Refs. [23–25]. In each sequence only one of the strands (upper) is coupled to the two electrodes

Table 20.1 Calculated currents (nA)

	No correlation	Base-pair correlation	Strand correlation
- -CGCG- - GCGC	19.5	7.8	9.0
- -ATAT- - TATA	47.7	43.7	23.9
- -CATG- - GTAC	50.8	40.7	10.4

where $N_m = \sum_{n=1}^{2N} \delta_{n_m,1}$ is the hole occupation number at the mth eigenstate. Notice that the infinite time limit assures that the entire frequency band of the dynamical fluctuations is accounted for in the current calculation [21].

20.5 Results

Steady state currents were calculated for hole chemical potentials, $\mu_L = \mu_0 + e\Phi/2$, $\mu_R = \mu_0 - e\Phi/2$. The values $\mu_0 = 7$ eV and $e\Phi = 4.5$ eV were chosen to assure that the entire "band" of molecular orbitals is within the Fermi conductance window [15]. The metallic nature of the electrodes was captured using a semi-elliptic band model [33], $J_J(E) = 2\pi \sum_{j_J} \xi_{j_J}^2 \delta(E - \varepsilon_{j_J}) \cong \frac{\xi_J^2}{\gamma_J^2}\sqrt{4\gamma_{j_J}^2 - (E-\mu_J)^2}$, with a band width parameter, $\gamma_J = 5$ eV, and a molecule-electrode coupling parameter, $\xi_J = 0.02$ eV. For the nuclear baths an Ohmic model was invoked, where, $J_{n_b}(\hbar\omega) = \frac{2\pi\eta_{n_b}^2}{\hbar\omega_{C,n_b}^2}\omega e^{-\omega/\omega_{C,n_b}}$ for $\omega > 0$, and zero otherwise. To account for the net effect of bath correlations, the different baths were all associated with the same spectral density, $\eta_{n_b} \equiv \eta = 0.1$ and $\hbar\omega_{C,n_b} \equiv \hbar\omega_C = 0.25$ eV for $n_b = 1, 2, \ldots, M$. The temperature of the system was set to zero (using a numerical value 10^{-6} K). This choice fixes the direction of energy flow from the system into the bath. Energy flow into the molecular system, following thermal activation of low frequency modes ($\hbar\omega \ll K_B T$), is therefore explicitly blocked.

The calculated currents for three different sequences (Fig. 20.2) are presented in Table 20.1 for three different types of bath correlations (see Fig. 20.1). Notice

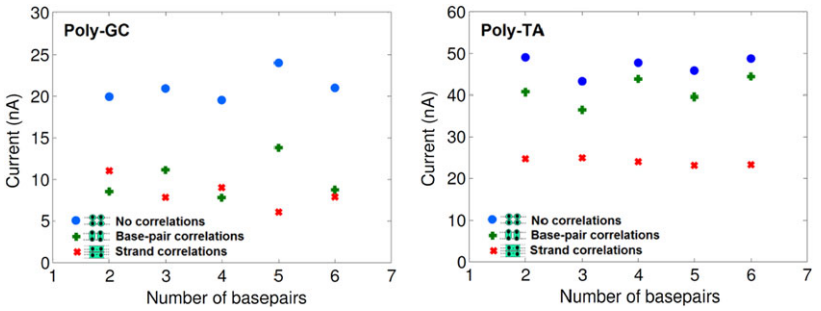

Fig. 20.3 Inelastic currents through poly-GC and poly-TA sequences at varying lengths. The *circles*, *pluses* and *crosses* correspond to no bath correlations, base pair correlations and strand correlations respectively

that each orbital in these structures can be classified as a G-type, T-type, C-type or A-type, according to the bases which dominate the probability amplitude distribution over the molecular sites [14, 15]. The connection strategy between the double stranded structure and the two electrodes (see Fig. 20.1) was chosen to assure that the transport is predominantly inelastic [15], by coupling the source and drain electrodes to orbitals of different types. This way a charge entering a specific MO from the source, can exit to the drain only through a different MO at a different orbital energy. The different bath correlations correspond to 'no correlation', 'base pair correlation' and 'strand correlation' according to the discussion in Sect. 20.3.

The effect of bath correlations is found to be specific to each particular strand. In poly-GC, both strand correlations and base pair correlations reduce significantly ($\sim$50 %) the inelastic current, suggesting that inelastic transitions from C-type to G-type orbitals are not dominated by base pair or intra-strand vibrations. In contrast, in poly-TA and CATG, the currents induced by base pair correlations seem to be still smaller than, but similar to the currents induced in the absence of any bath correlations. This suggests that vibrations within each base-pair are less effective in promoting inelastic transitions from A-type to T-type orbitals in these sequences. The same trends are observed for poly-GC and poly-TA sequences of varying length (Fig. 20.3). In all cases the inelastic current is largest in the absence of any bath correlations. However, in poly-GC, both strand and base-pair correlations reduce the current significantly, whereas in poly-AT base-pair correlations tend to reduce the current only slightly.

20.6 Discussion

The specific efficiency of bath induced charge transport in each sequence, as well as the general observations, can be rationalized by inspecting the rate constants for

the dominant inelastic processes. First we notice that the general expression for a bath-induced molecular transition rate,

$$\Gamma_{m,m'}^{n_b;em/ab} = \left| \langle m | \sum_{n=1}^{2N} W_{n,n_b} d_n^\dagger d_n \left| m' \right\rangle \right|^2 J_{n_b}(E_{m'} - E_m) g^{(em/ab)}(E_{m'} - E_m)/\hbar,$$

is simplified in the low temperature limit ($\hbar\omega \gg K_B T$), since phonon emission processes are favored over phonon absorption. This amounts to setting the respective phonon occupation factors, $g^{(em)}(\hbar\omega) \approx 1$ and $g^{(ab)}(\hbar\omega) \approx 0$ in the rate expression. The overall rate of an inelastic transition from a (many body) system eigenstate, $|m'\rangle$, to another eigenstate, $|m\rangle$ reads in this case,

$$\begin{aligned} K_{m,m'} &\equiv \sum_{n_b=1}^{N_b} \left[k_{n_b}^{(nuc)} \right]_{m,m'} = \sum_{n_b=1}^{N_b} \Gamma_{m,m'}^{n_b;em} \\ &= \sum_{n_b=1}^{N_b} \frac{1}{\hbar} \left| \langle m | \sum_{n=1}^{2N} W_{n,n_b} d_n^\dagger d_n \left| m' \right\rangle \right|^2 J_{n_b}(E_{m'} - E_m), \end{aligned} \tag{20.9}$$

where $E_{m'} > E_m$. Using the expansion of single hole molecular orbitals (MOs) in the local sites basis, $a_l^\dagger \equiv \sum_{n=1}^{2N} u_{n,l} d_n^\dagger$, the electronic coupling term at the nth site can be expressed in terms of the MOs creation and annihilation operators, i.e., $\langle m | d_n^\dagger d_n | m' \rangle = \sum_{k,l=1}^{2N} u_{n,l}^* u_{n,k} \langle m | a_l^\dagger a_k | m' \rangle$. This term vanishes, unless the two many body eigenstates, $|m'\rangle$ and $|m\rangle$, are identical except for the (hole) occupation in precisely two of the orbitals, one of which is occupied only at the mth state while the other is only occupied at the m'th state. Denoting these orbital indexes as l_m and $k_{m'}$ respectively, it follows that $\langle m | d_n^\dagger d_n | m' \rangle = u_{n,l_m}^* u_{n,k_{m'}}$. A non-vanishing transition between the many-body states $|m'\rangle$ and $|m\rangle$ would therefore involve a single "MO Hopping" event at the corresponding rate,

$$K_{m,m'} = \sum_{n_b=1}^{N_b} \frac{1}{\hbar} \left| \sum_{n=1}^{2N} W_{n,n_b} u_{n,l_m}^* u_{n,k_{m'}} \right|^2 J_{n_b}(E_{m'} - E_m). \tag{20.10}$$

Let us define a partial overlap between the $k_{m'}$ and the l_m orbitals, with respect to the n_b bath, $S_{l_m,k_{m'}}^{n_b} \equiv \sum_{n=1}^{2N} W_{n,n_b} u_{n,l_m}^* u_{n,k_{m'}}$. It follows that,

$$K_{m,m'} = \sum_{n_b=1}^{N_b} \frac{1}{\hbar} \left| S_{l_m,k_{m'}}^{n_b} \right|^2 J_{n_b}(E_{m'} - E_m) \tag{20.11}$$

i.e., each bath contributes to the rate of hopping between two orbitals according to the partial overlap between these orbitals. The partial overlap for each bath is defined as the overlap, projected onto the partial (sub) space of sites which are simultaneously coupled to that bath.

One can readily see that for a fully correlated bath (uniformly coupled to all sites, $W_{n,n_b} = \text{const}$), the respective rate vanishes due to the orthogonality of the different orbitals. In contrast, as observed in the numerical calculations presented above, a

maximal rate is obtained in the absence of any bath correlations, where each nucleobase site is associated with its own local bath, i.e., $W_{n,n_b} = \delta_{n,n_b}$, and $K_{m,m'} = \frac{J(E_{m'}-E_m)}{\hbar} \sum_{n=1}^{2N} |u_{n,l_m}|^2 |u_{n,k_{m'}}|^2$. This can be proved within our normalization convention for the overall vibronic coupling strength, $\sum_{n=1}^{2N} W_{n,n_b} = \sum_{n_b=1}^{2N} W_{n,n_b} = 1$, and when the same spectral density is assumed for all baths,

$$\begin{aligned} K_{m,m'} &= \frac{J(E_{m'} - E_m)}{\hbar} \sum_{n_b=1}^{2N} \left| S^{n_b}_{l_m,k_{m'}} \right|^2 \\ &\leq \frac{J(E_{m'} - E_m)}{\hbar} \sum_{n_b=1}^{2N} \sum_{n=1}^{2N} |W_{n,n_b}|^2 |u_{n,l_m}|^2 |u_{n,k_{m'}}|^2 \\ &\leq \frac{J(E_{m'} - E_m)}{\hbar} \sum_{n_b=1}^{2N} \sum_{n=1}^{2N} W_{n,n_b} |u_{n,l_m}|^2 |u_{n,k_{m'}}|^2 \\ &= \frac{J(E_{m'} - E_m)}{\hbar} \sum_{n=1}^{2N} |u_{n,l_m}|^2 |u_{n,k_{m'}}|^2. \end{aligned} \tag{20.12}$$

An upper bound for the inelastic transport rates is therefore obtained in the absence of any correlation between bath modes associated with different nucleobases. Indeed, according to our model a correlated motion of nuclei from two different sites is not coupled to charge transport between these sites. Only charge transport into or out off either one of the two sites is coupled the correlated motion. Therefore, the introduction of bath correlations reduces the number of vibronic coupling channels and diminishes the overall inelastic current.

For partially correlated baths the inelastic transition rates are very sensitive to the partial overlaps, which vary from one type of bath correlations to another. In Table 20.2 partial overlaps are presented for two sequences. In each case the overlap was calculated between orbitals that are coupled to the source electrode and orbitals that are coupled to the drain electrode. As one can see, strand correlations are associated with relatively small partial overlaps in the two sequences, in agreement with the relatively low currents obtained for this type of correlations in all studied cases (see Table 20.1, Fig. 20.3). Base pair correlations on the other hand have more significant partial overlaps, and particularly for the poly-TA sequence, in consistency with the calculated currents involving A-type to T-type inelastic transitions.

The overlap between any two orbitals is most sensitive to the relative phases of the probability amplitudes at different sites, and therefore reflects the orbitals nodal structure. Large partial overlap within a given subspace indicates a similar nodal structure of the two orbitals within that subspace. Consider for example the inelastic transition from the A-type 2 and the T-type 2 orbitals in the poly-TA sequence. Figure 20.4 demonstrates the respective orbital structures. As one can see both orbitals have a node between the two strands, but a different nodal structure between the base-pairs. As a consequence, these two orbitals have different nodal structure along a single strand but the same nodal structure for each base pair. This is consistent with the much smaller partial overlap obtained for the strand correlations vs.

Table 20.2 Partial overlap integrals between molecular orbitals

Poly-GC: Base pair correlations				
IN\OUT	G-type 1	G-type 2	G-type 3	G-type 4
C-type 1	0.0011	0.0008	0.0002	0
C-type 2	0.0007	0.0012	0	0.0002
C-type 3	0.0163	0	0.0012	0.0008
C-type 4	0	0.0163	0.0007	0.0011

Poly-GC: Strand correlations				
IN\OUT	G-type 1	G-type 2	G-type 3	G-type 4
C-type 1	0	0	0.0034	0
C-type 2	0	0	0	0.0034
C-type 3	0.0031	0	0	0
C-type 4	0	0.0031	0	0

Poly-TA: Base pair correlations				
IN\OUT	G-type 1	G-type 2	G-type 3	G-type 4
A-type 1	0.0171	0.0026	0.0098	0
A-type 2	0.0021	0.0183	0	0.0098
A-type 3	0.0427	0	0.0183	0.0026
A-type 4	0	0.0427	0.0021	0.0171

Poly-TA: Strand correlations				
IN\OUT	G-type 1	G-type 2	G-type 3	G-type 4
A-type 1	0	0	0.0039	0
A-type 2	0	0	0	0.0039
A-type 3	0.003	0	0	0
A-type 4	0	0.003	0	0

base pair correlations in this case. While the details should depend strongly on the sequence and on the type of correlations, we point out that similar nodal structures, and thus larger partial overlaps, are more likely to occur for more compact subspaces as in the case of base pair correlations. We therefore speculate that baths with short range correlations are more significant than baths with long range correlations in promoting inelastic charge transport through the types of sequences studied above.

20.7 Conclusions

The effect of nuclear baths correlations on charge transport through models of DNA junctions was studied using a reduced density matrix formulation. Different types

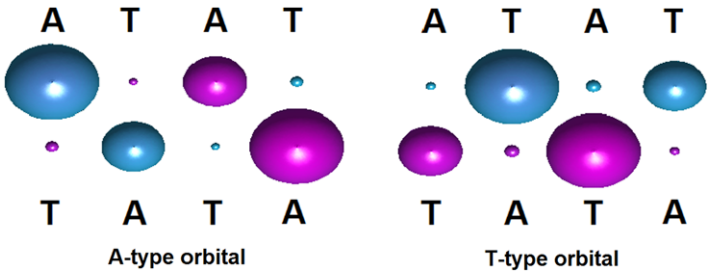

Fig. 20.4 Two representative orbital plots for a poly-AT sequence. The color changes correspond to changes in the sign of the probability amplitude between different sites

of correlations were introduced accounting for different types of vibrations inherent to the double-strand structure. In particular, base-pair correlations correspond to nuclear vibrations within each base pair, as, e.g., the hydrogen bonds between bases, whereas strand correlations correspond to vibrations within each strand, as, e.g., DNA backbone vibrations. The inelastic currents for given sequences and given connections to the electrodes were found to be highly sensitive to the specific type of bath correlations, suggesting that the relative role of different type of vibronic couplings can be associated with a measurable phenomenon.

Analysis of the inelastic transition rates relates the effect of bath correlations to partial overlap integrals between specific molecular orbitals of the DNA sequence. These integrals are defined within subspaces of sites that are coupled to common bath modes. Our model analysis of the studied DNA sequences suggests that long-range correlations (such as strand correlations) in the vibronic coupling are likely to be less efficient than short range correlations (such as base pair correlations) in promoting inelastic currents through DNA.

On a more basic level this work emphasizes the important effect of bath correlations on quantum transport, as highlighted recently also in electron energy transport in bio-molecular environment [28, 32]. Inelastic charge transport through biomolecules was studied extensively using both atomistic simulations and minimal models. We believe that the analysis in terms of bath correlations, as introduced above, provides an important bridge between these two types of approaches. While atomistic simulations are often too detailed to enable understanding of the principles in action, generic models are often too simplified to provide reasoning for the complexity of the biological structures. In this work, a systematic study of the effect of bath correlations on the inelastic transport enabled us to point to the relative role of specific nuclear motions (e.g., hydrogen bonds or backbone modes) although they were not explicitly included in the generic model. These results naturally call for more detailed atomistic simulations which can demonstrate the role of specific nuclear vibrations in the DNA and its surroundings on the inelastic transport efficiency [13, 21, 33, 34], according to their type of correlation.

Acknowledgements This research was supported by the US-Israel Binational Science foundation and by the German-Israeli Foundation for Scientific Research and Development.

References

1. Lewis FD, Wu T, Zhang Y, Letsinger RL, Greenfield SR, Wasielewski MR (1997) Science 277:673
2. Giese BB (2000) Acc Chem Res 33:631
3. Schuster GB (2000) Acc Chem Res 33:253
4. Xu B, Zhang P, Li X, Tao N (2004) Nano Lett 4:1105
5. Nogues C, Cohen SR, Daube S, Apter N, Naaman R (2006) J Phys Chem B 110:8910
6. Porath D, Bezryadin A, de Vries S, Dekker C (2000) Nature 403:635
7. O'Neil MA, Barton JK (2004) J Am Chem Soc 126:11471
8. Grozema FC, Berlin YA, Siebbeles LDA (2000) J Am Chem Soc 122:10903
9. Gutiérrez R, Porath D, Cuniberti G (2000) DNA conduction: the issue of static disorder, dynamic fluctuations and environmental effects. In: Baranovski S (ed) Charge transport in disordered solids with applications in electronics. Wiley, New York
10. Shih C-T, Roche S, Römer RA (2008) Phys Rev Lett 100:018105
11. Gutiérrez R, Caetano RA, Woiczikowski BP, Kubar T, Elstner M, Cuniberti G (2009) Phys Rev Lett 102:208102
12. Zilly M, Ujsághy O, Wolf DE (2010) Phys Rev B 82:125125
13. Skourtis SS, Waldeck DH, Beratan DN (2010) Ann Rev Phys Chem 61:461–485
14. Brisker-Klaiman D, Peskin U (2010) J Phys Chem C 114:19077
15. Brisker-Klaiman D, Peskin U (2012) Phys Chem Chem Phys 14:13835
16. Braun E, Eichen Y, Sivan U, BenYoseph G (1998) Nature 391:775–778
17. Cohen H, Nogues C, Naaman R, Porath D (2005) Proc Natl Acad Sci USA 102:11589
18. Guo X, Gorodetsky AA, Hone J, Barton JK, Nuckolls C (2008) Nat Nanotechnol 3:163
19. Joachim C, Gimzewski JK, Aviram A (2000) Nature (London) 408:541
20. Nitzan A, Ratner MA (2003) Science 300:1384
21. Gutiérrez R, Caetano RA, Woiczikowski BP, Kubar T, Elstner M, Cuniberti G (2009) Phys Rev Lett 102:208102
22. Conwell EM, Rakhmanova SV (2000) PNAS 97:4556
23. Voityuk AA, Jortner J, Bixon M, Rösch N (2000) Chem Phys Lett 324:430
24. Voityuk AA, Rösch N, Bixon M, Jortner J (2000) J Phys Chem B 104:9740
25. Voityuk AA, Bixon M, Jortner J, Rösch N (2001) J Chem Phys 114:5614
26. Peskin U (2010) J Phys B, At Mol Opt Phys 43:153001
27. Abu-Hilu M, Peskin U (2005) J Chem Phys 122:021103
28. Volkovich R, Caspary Toroker M, Peskin U (2008) J Chem Phys 129:034501
29. May V, Kuhn O (2011) Charge and energy transfer dynamics in molecular systems. Wiley-VCH, Weinheim
30. Volkovich R, Härtle R, Thoss M, Peskin U (2011) Phys Chem Chem Phys 13:14333
31. Volkovich R, Peskin U (2011) Phys Rev B 83:033403
32. Rebentrost P, Mohseni M, Kassal I, Lloyd S, Aspuru-Guzik A (2009) New J Phys 11:033003
33. Peskin U (2012) Mol Phys 110:729
34. Berlin YA, Voityuk AA, Ratner MA (2012) ACS Nano 6:8216

Index

M. Hotokka et al. (eds.), *Advances in Quantum Methods and Applications in Chemistry, Physics, and Biology*, Progress in Theoretical Chemistry and Physics 27,
DOI 10.1007/978-3-319-01529-3,